MILD COAL PRETREATMENT TO ENHANCE LIQUEFACTION REACTIVITY

R.L. Miller, K. Shams, and R.M. Baldwin

Chemical Engineering and Petroleum Refining Department
Colorado School of Mines
Golden, Colorado 80401

ABSTRACT

This paper reports results from an on-going process development study in which coal is converted to liquid products at relative mild reaction conditions. The process consists of three main steps: 1) mild pretreatment of the feed coal at ambient conditions using methanol (or other common organic solvent) and a trace amount of hydrochloric acid to enhance dissolution reactivity and dry the coal, 2) low severity thermal dissolution to obtain a very reactive coal-derived residual intermediate product amenable to upgrading, and 3) catalytic upgrading of the residual products to distillate liquids. We have found that mild pretreatment of Wyodak subbituminous coal using methanol/HCl can provide an improvement in THF conversion of greater than 30 wt% at 350° C reaction temperature. Possible explanations for the observed reactivity enhancement include mild alkylation at oxygen sites in the coal's organic phase, leaching of selected elements from the coal's mineral matter phase, or formation of chlorinated species such as $FeCl_3$ which are known to be active coal dissolution catalysts.

INTRODUCTION

Much of the recent research in direct coal liquefaction seeks to develop methods for dissolving coal at low reaction severity (defined as temperatures below 350° C and pressures of 1000-1500 psi). The incentives for developing a viable low severity liquefaction process are numerous; they include: 1) reduced hydrocarbon gas production resulting in reduced feed gas consumption and enhanced hydrogen utilization efficiency, 2) suppressed retrogression of primary coal dissolution products resulting in enhanced distillate and residuum product quality, 3) production of high boiling residuum which is less refractory and thus more amenable to catalytic upgrading in a conventional second-stage hydrocracker, 4) substitution of less expensive off-the-shelf vessels, piping, valves, pumps, etc. in place of expensive, custom-designed units, and 5) less severe slurry handling and materials of construction problems as a result of lower operating temperatures and pressures.

Researchers at several locations including the Pittsburgh Energy Technology Center (1), the University of North Dakota Energy and Environmental Research Center (2), Carbon Resources, Inc. (3), and the Colorado School of Mines (4) have investigated various methods for improving coal reactivity and liquid yields at mild reaction conditions. These studies showed that coal can be readily converted to tetrahydrofuran (THF) soluble products via selective chemical attack rather than thermal bond scission, but that the rate and extent of coal dissolution at mild conditions is strongly dependent upon intrinsic coal reactivity. Thus the problem of optimizing low severity liquefaction conversion becomes one of maximizing coal reactivity at these conditions.

The objective of this paper is to present recent experimental data in which mild chemical pretreatment using methanol or other common organic solvent and hydrochloric acid is used as a method to improve intrinsic coal reactivity at low reaction severity. The original basis for this work derives from studies by Sternberg (5), Liotta (6), Sharma (7) and others where alkylation was used as a method for rendering coal soluble in THF or toluene to aid in structural analysis. Sharma's work demonstrated the ability to mildly alkylate coal using alkyl alcohols. Limited work has been reported in which the liquefaction reactivity of alkylated coals has been studied. Schlosberg et al. (8) measured the reactivity of alkylated Wyodak subbituminous and Illinois #6 bituminous coals in tetralin at 427° C, 1500 psi hydrogen pressure and 130 min. reaction time. A 10-21 wt% (maf and alkyl group-free basis) increase in cyclohexane conversion was noted for the alkylated coals.

EXPERIMENTAL PROCEDURE

The entire suite of eight coals from the Argonne Premium Coal Sample Bank was used as the source of feed coals for this study. Ultimate analyses for these coals are listed in Table I. Coal samples were stored under argon in sealed ampules prior to pretreatment and liquefaction experiments.

Pretreatment experiments were performed using a liquid phase technique we developed based on the gas phase alkylation chemistry reported by Sharma (7). Coal was pretreated by suspending 5 g of undried coal in 40 cm^3 of methanol and 0.1 cm^3 of concentrated hydrochloric acid in a 100 cm^3 round bottom flask and continuously stirring the coal/methanol slurry on a magnetic stirring plate for 3 hrs. The flask was connected to a cooling water condenser to reduce solvent losses by evaporation. Several experiments were completed in which dry nitrogen was used to blanket the coal/methanol slurry; elemental analyses of the treated coals showed no difference in the extent of oxidation when the system was purged with nitrogen and when it was vented to the atmosphere. Several blank experiments using hexane or acetone in place of methanol were also completed.

After pretreatment, most of the organic solvent was decanted off and the moist coal sample washed with three 50 cm^3 aliquots of fresh solvent to remove residual acid. Any remaining solvent was recovered by roto-evaporation and vacuum drying (50° C, 10-20 millitorr pressure, 24 hrs.). Untreated coal samples were vacuum dried at the same conditions before liquefaction. After drying, all treated and untreated coal samples were stored at room temperature in a vacuum dessicator (0.1 torr) before analysis or liquefaction. Reactor runs were scheduled so that each coal sample was stored for less than 12 hours before use.

Liquefaction experiments were conducted in a 20 cm^3 tubing bomb reactor attached to an agitator and immersed in a fluidized sandbath. Low severity reaction conditions were set at 350° C reaction temperature, 1000 psig initial cold hydrogen pressure, and 30 min. reaction time. Dihydrophenanthrene (DHP) was used as hydrogen donor solvent (2/1 solvent/coal wt. ratio) in these runs. Coal conversion was measured using THF extraction data corrected for the intrinsic THF solubilities of treated and untreated coals. Solubility measurements were conducted at ambient conditions and consisted of three steps: 1) sonicating the liquid products from the tubing bomb reactor (or feed coal sample) in excess THF for 10 min., 2) centrifuging the mixture at 2000 rpm for 15 min., and 3) decanting THF-soluble products and excess THF from the THF-insoluble residuum. This procedure was repeated at least two times until no additional THF-soluble products were recovered. Remaining THF-insolubles were dried at 100° C for 24 hours to remove residual THF, weighed, and finally ashed. Coal conversion to THF-soluble products was computed as follows:

$$\underset{\text{(wt\% maf basis)}}{\text{Coal conversion}} = \frac{M_f - M_p}{M_f} \times 100$$

where: M_f = mass of maf THF-insoluble coal charged

M_p = mass of maf THF-insoluble products recovered (corrected to satisfy the ash balance)

RESULTS AND DISCUSSION

Baseline reactivity data for the untreated and treated Argonne coals are shown in Figures 1 and 2. Each of these data points represents the average of 2-3 reactor experiments. The average standard deviation for the dataset shown is ± 1.8 wt%.

At the low severity reaction conditions studied, three of the high volatile bituminous coals [Illinois #6 (72.1 wt%), Blind Canyon (69.6 wt%), and Pittsburgh #8 (57.0 wt%)] gave the highest THF conversions. Wyodak subbituminous coal was the next most reactive coal (44.4 wt%), while Pocahontas low volatile bituminous coal was the least reactive sample studied (15.6 wt%). These

reactivity data follow the same trends reported for the Argonne coals by several other investigators.

Pretreatment with methanol and HCl using the procedure described earlier enhanced low severity liquefaction reactivity for all eight Argonne coals. The absolute increase ranged from only 5.5 wt% for Blind Canyon coal to 31.5 wt% for Wyodak coal, and averaged 18.0 wt% for the eight coals. No simple trends in reactivity improvement with chemical or physical properties of the coals are obvious, although the reactivity of pretreated low rank coals (Wyodak and Beulah-Zap) increased much more than reactivity of the six bituminous coals.

Interestingly, replacement of methanol with hexane during coal pretreatment also enhanced low severity liquefaction reactivity. Since hexane cannot participate in the alkylation chemistry proposed by Sharma (7), other effects must also be contributing to the observed reactivity enhancement. Some possibilities include: 1) leaching of calcium, magnesium, iron, and perhaps other species from the coal mineral matter, and 2) formation of chlorinated mineral species such as $FeCl_3$, which are known to be active coal dissolution catalysts (9,10). Other as yet unknown effects are certainly possible as well. Several additional sets of experiments and analyses are currently being conducted to begin elucidating the existence and importance of these effects.

Figure 3 compares the effect of our mild pretreatment method using methanol/HCl with low severity reactivity enhancement data for Wyodak coal samples alkylated using the Liotta (6) and Sternberg (5) alkylation techniques. As shown, our method provided a significant reactivity improvement even though the extent of alkylation was very low. These data also indicate that effects in addition to alkylation at oxygen and carbon sites in the organic coal structure are contributing to the observed improvements in coal liquefaction reactivity.

ACKNOWLEDGMENT

We wish to acknowledge financial support from the U.S. Department of Energy under Contract Nos. DE-AC22-88PC88812 and DE-FG22-90PC90289.

LITERATURE CITED

1. Bockrath, B.C.; Illig, E.C.; Finseth, D.H.; Sprecher, R.F. Prepr. Pap. - Am. Chem. Soc., Div. Fuel Chem., 29, 5, 76, 1984.

2. Farnam, S.A.; Wolfson, A.C.; Miller, D.J.; Gaides, G.E.; Messick, D.D. Prepr. Pap. - Am. Chem. Soc., Div. Fuel Chem., 30, 2, 354, 1985.

3. Porter, C.R.; Knudson, C.L.; Rindt, J.R. Prepr. Pap. - Am. Chem. Soc., Div. Fuel Chem., 31, 4, 70, 1986.

4. Miller, R.L.; Baldwin, R.M. Prepr. Pap. - Am. Chem. Soc., Div. Fuel Chem., 31, 4, 152, 1986.

5. Sternberg, H.; Delle Donne, C.L. Fuel, 53, 172, 1974.

6. Liotta, R. Fuel, 58, 724, 1979.

7. Sharma, D.K.; Sarkar, M.K.; Mirza, Z.B. Fuel, 64, 449, 1985.

8. Schlosberg, R.H.; Neavel, R.C.; Maa, P.S.; Gorbaty, M.L. Fuel, 59, 45, 1980.

9. Derbyshire, F.J. Catalysis in Coal Liquefaction: New Directions for Research; IEA Coal Research: London, June 1988.

10. Anderson, L.L.; Miin, T.C. Fuel Proc. Tech., 12, 165, 1986.

Table I

Ultimate Analysis of Feed Coals

Wt% Dry Basis	Wyodak	Beulah-Zap	Illinois #6	Pittsburgh #8
Carbon	68.4	65.9	65.7	75.5
Hydrogen	4.9	4.4	4.2	4.8
Nitrogen	1.0	1.0	1.2	1.5
Sulfur	0.6	0.8	4.8	2.2
Oxygen	16.3	18.2	8.6	6.7
Ash	8.8	9.7	15.5	9.3
Coal Rank	Subbit.	Lignite	HVB	HVB
Symbol	Wy	BZ	Ill	Pit

Table I (cont.)

Ultimate Analysis of Feed Coals

Wt% Dry Basis	Blind Canyon	Lewiston-Stockton	Upper Freeport	Pocahontas
Carbon	76.9	66.2	74.2	86.7
Hydrogen	5.5	4.2	4.1	4.2
Nitrogen	1.5	1.3	1.4	1.3
Sulfur	0.6	0.7	2.3	0.7
Oxygen	10.8	7.8	4.8	2.3
Ash	4.7	19.8	13.2	4.8
Coal Rank	HVB	HVB	MVB	LVB
Symbol	BC	LS	UF	POC

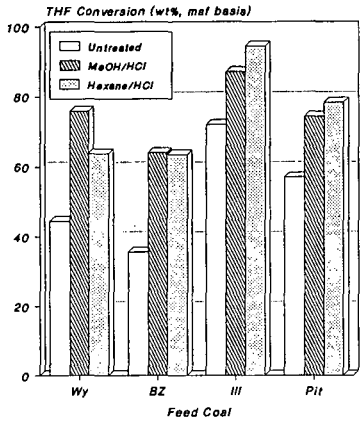

Figure 1. Effect of Pretreatment with MeOH/HCl and Hexane/HCl on Low Severity Liquefaction Reactivity of Argonne Coals

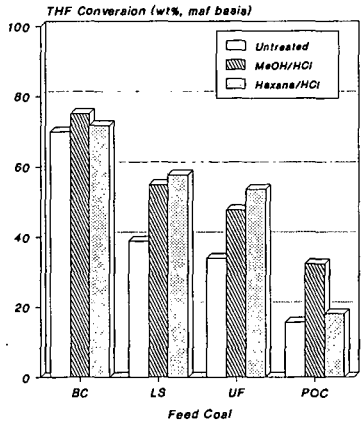

Figure 2. Effect of Pretreatment with MeOH/HCl and Hexane/HCl on Low Severity Liquefaction Reactivity of Argonne Coals

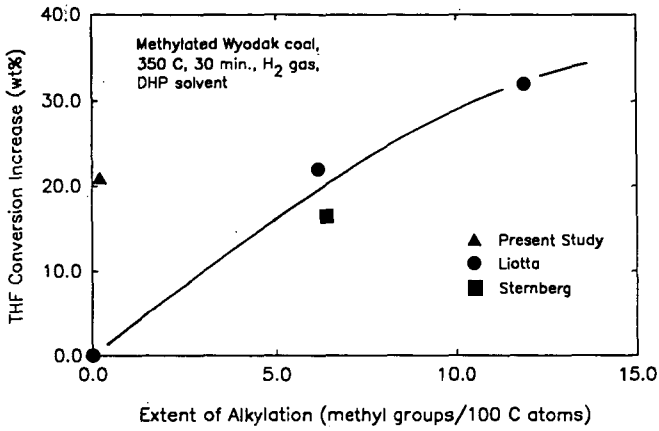

Figure 3. Liquefaction Reactivity Enhancement as a Function of Alkylation Extent for Three Pretreatment Methods

WATER PRETREATMENT OF COAL

Michael A. Serio, Peter R. Solomon, Erik Kroo, and Sylvie Charpenay

Advanced Fuel Research, Inc.
87 Church Street
East Hartford, CT 06108

Keywords: Pretreatment, Coal, Liquefaction, Pyrolysis

INTRODUCTION

Water pretreatment of coal has been studied previously as a means to increase the yields of liquid products from pyrolysis or liquefaction of coal. However, the mechanisms of this process and the applications to coals of a wide range of ranks are still a subject of considerable debate. Bienkowski et al. (1,2) have studied the effect of steam pretreatment on coal liquefaction. They used a Wyodak coal which had been carefully stored (under water) to avoid weathering. The experimental conditions were adjusted to provide 750 psig steam for 30 minutes in either a pretreatment (~200°C) stage and/or liquefaction stage. Pretreatment of the suction dried coal at 200°C increased the conversion to extractable products at 400°C from 30.5 to 38.5%. If the pretreatment was carried out at 240°C, the conversion was increased to 40.3%. However, increasing the pretreatment temperature even further to 320°C led to a smaller conversion (33.8%). In a later paper, Bienkowski et al. (2) tried ammonia addition to both reaction stages and obtained even better results than with steam alone.

The explanation offered by Bienkowski et al. (1,2) for the effect of steam pretreatment was that it allows breaking of hydrogen bonds, loosening of the coal matrix and stabilization of some of the reactive components of the coal. This effect appears to be enhanced by the presence of ammonia which can also provide hydrogen bonding and which may undergo chemical reactions with oxygen functional groups.

Graff and Brandes (3-5) have observed higher yields of liquid products from pyrolysis or solvent extractions of steam pretreated Illinois No. 6 coal. The steam pretreatment was done in a stainless steel microreactor at 50 atm (~ 750 psig) and 320-360°C. A similar pretreatment of coal in a helium atmosphere had no effect. If the steam-pretreated coal was exposed to air, both the improvements obtained in the pyrolysis and extraction yields were lost. The mechanism for the pretreatment was explained as partial depolymerization of the coal due to disruptions of hydrogen bonds. Recent evidence has suggested that the treatment increases the number of hydroxyl groups in the coal (5). It was postulated that the steam reacts with the ether linkages in coal, forming hydroxyl groups and reducing the number of covalent crosslinks in the coal (5).

Recent work by Khan et al. (6) involved the steam pretreatment of a set of five coals which covered a wide range of coal rank. The pretreatments were done at 300-320°C and 1100-1300 psig steam. The steam pretreatment was found to reduce the concentration of oxygen functional groups for the low rank coals, but did not have much effect on higher rank coals (or increased the amount of oxygen). Under pyrolysis conditions, the low rank coals showed increases in tar yields, when pyrolyzed at a rapid rate. When the steam-treated coals were pyrolyzed at a slow heating rate, the tar yields did not increase significantly for any of the coals tested.

Ross et al. (7,8) have studied the liquefaction of Illinois No.6 coal in CO/H_2O systems at high pressure (4000-5000 psig) and high temperatures (400°C), where the water is supercritical. The conversion was measured in terms of toluene solubility (TS) and the results were found to be superior to those obtained in tetralin under the same conditions. The CO/H_2O system was most effective (indicating a kinetic isotope effect) followed by CO/H_2O and H_2/H_2O. The latter treatment was not very effective for demineralized coal. The results have been explained in terms of an ionic mechanism involving the initial formation of formate ion, as explained in Ref. 7, whereby hydrogen is donated to the coal.

Recent work by Ross and coworkers has addressed the use of liquid water as a pretreatment step to liquefaction in a conventional donor solvent (9,10). Work was done on Illinois No. 6 coal and

Wyodak subbituminous coal. The results did not show a significant effect of water pretreatment on increasing the conversion to toluene solubles in a donor liquefaction solvent. However, significant changes were observed in the composition and molecular weight distributions of the liquid products.

EXPERIMENTAL

Sample Selection

The selection of coal samples was made from the Argonne Premium Sample Bank. Since pretreatment is potentially most useful for lower rank coals which are subject to retrograde reactions, the coals selected were the Zap Lignite, the Wyodak subbituminous and the Illinois No. 6 bituminous, which are also being used in a complementary study (11). It is also planned to study coals which have been dried and/or aged, as there is evidence from the work of Graff and Brandes (3-5) and Bienkowski et al. (1,2) that the pretreatment is less effective on such coals, and that aging can reverse the beneficial effects of the pretreatment. The work to date has been done on the raw Zap and Wyodak coals.

Reactor for Steam/Water Pretreatment

A new reactor system was developed for this program, which is shown as a schematic in Fig. 1. This system was designed to carry out high pressure (up to 6000 psig), high temperature (up to ~ 400°C) steam or water pretreatment of coal in a closed bomb reactor, which is also interchangeable with our current liquefaction reactor and product collection system. A schematic of the reactor is shown in Fig. 2. The inner volume of the bomb (20 ml) is divided into upper and lower parts by a stainless steel screen and glass wool. The screen is secured on the capillary tube and the glass wool is replaced after every experiment to keep the coal from being blown out on evacuation during the gas collection phase. After 1-3 g coal is fed into the bomb and the reactor head is screwed on to get a gas tight seal, the system is purged with N_2 or evacuated, the high temperature, high pressure valve on the reactor base is closed, and the water is injected directly into the coal through the capillary tube with a ~ 0.1-1.0 ml/min rate. Deaerated and deionized water is used throughout the reaction.

Simultaneously with the water injection, the reactor is immersed into the fluidized sand bath held at the required temperature. The pressure is measured in the water feed capillary tubing directly after the pump. The amount of water pumped in and the temperature determines whether steam and/or water pretreatment is done.

After the reaction, the bomb is quickly quenched with water, flooded with up to 300-600 psig N_2 and depressurized with a 0.8 liter previously evacuated sampling tank. The yields of product gases, e.g., H_2, CO_2, CO, CH_4, C_2H_6, CH_2H_4, CH_2H_2, and H_2S are determined by GC. After opening the reactor, the pretreated coal is taken out of the reactor by washing it with deionized water and filtering under an N_2 atmosphere. N_2 was passed through the coal sample for about an hour to obtain a sample with approximately the same moisture content as the starting coal sample. In addition to the reactor, an N_2 purged glove box was also constructed to facilitate all the product work up in an oxygen-free environment. It is equipped with a lock which can be evacuated or filled with N_2 to transfer the reactor to the box.

RESULTS

An extensive series of steam pretreatment experiments was done on the Zap lignite using subcritical water at a pressure of 4000 psig and temperatures of 250, 300, and 350°C. Selected experiments were done for the Wyodak coal at 350°C, 4000 psig. The pretreatment times varied from 5 minutes to 5 hours. The pretreatment experiments with the Zap lignite over a wide range of temperatures and times give a fairly consistent picture based on analysis of the evolved gases during the pretreatment step and analysis of the solid residues by a variety of techniques (TG-FTIR, solvent extraction, FT-IR, x-ray, liquefaction). The TG-FTIR technique is a programmed pyrolysis instrument which includes on-line analysis of gases by FT-IR spectroscopy and on-line measurement of weight loss with a TGA (12,13).

The TG-FTIR analysis of residues produced at all three temperatures shows a sharp increase in tar at relatively short pretreatment times. The results for the tar yield for pretreatment at 350°C are shown in Fig. 3 for the Zap and in Fig. 4 for the Wyodak. The significant increase in tar does not persist at long pretreatment times. These changes are delayed and attenuated as the pretreatment temperature is reduced, as shown in Fig. 5 for the Zap lignite. However, there is a monotonic increase in the pyridine extractables (not shown) with increasing pretreatment time and a monotonic decrease in CO_2, as shown in Fig. 6 for the Zap lignite. The changes in the CO_2 evolution result primarily from changes in the organic CO_2, as shown by comparing Figs. 6a and 6b. The amount of CH_4 produced upon pyrolysis of the coal increased with increasing pretreatment time, as shown in Fig. 7. The results for the trends in the yields of tar, CH_4, CO_2 and pyridine extractables suggest that steam pretreatment is similar to a geological aging of the coal since these trends are nearly identical to the rank variations in these quantities. By this it is meant that the low rank Zap lignite exhibits behavior which is more characteristic of a higher rank coal after water pretreatment. This explanation is also consistent with the fact that the benefits of steam or water pretreatment are not observed for high rank coals (6). The similarity betwen the effects of steam pretreatment and geological aging has also been noted by Ross and coworkers (9,10). Landais and Monthioux have discussed the analogy between pyrolysis in confined systems and geological aging (14).

When liquefaction experiments are done on the steam pretreatment residues produced at 350°C, without shaking of the liquefaction reactor, no benefit to liquefaction yields is observed and, in fact, the yields are reduced. These results are shown in Fig. 8a. The liquefaction experiments were done in dihydrophenanthrene for 30 minutes at 400°C. A limited number of liquefaction experiments, which include shaking, have been done on the steam pretreated Zap residues produced at 350°C over a range of pretreatment times. These results are shown in Fig. 8b. These indicate a modest (10-20%) benefit to liquefaction yields at long pretreatment times (~ 5 hours).

An explanation for the effect of reactor shaking may be that the steam pretreatment process makes the coal agglomerate and thus more difficult to liquify. The agglomeration of coal by steam pretreatment was reported by Graff and Brandes (3-5) and Khan et al. (6) and has been observed in our own work.

Samples of residues from pretreatment experiments done at 350°C with Zap lignite were subjected to x-ray analysis. The results are summarized in Table 1, below.

TABLE 1

Effect of Water Pretreatment Time at 350°C, 4000 psig on Mineral Compositions for Zap Lignite

Time (min)	Na	Ca	Al	S(o)	Ash
0	0.31	1.09	0.33	0.30	6.86
10	0.00	1.30	0.45	0.20	6.70
60	0.02	0.99	0.40	0.22	5.83
180	0.02	1.38	0.55	0.22	7.60
240	0.00	1.18	1.09	0.24	9.66

The total ash content was found to go through a minimum after about one hour pretreatment time and then increase with further increases in pretreatment time. This is in agreement with results obtained independently from a TGA combustion experiment, although the reasons for this are not yet clear. One possibility is segregation of the ash. For the individual ash components, the most significant trends were elimination of Na, and increases in Al, Si, and Fe with increased pretreatment time. The increases in Al and Fe may be due to partial dissolution of the reactor system. Little change was found for Mg, Ca, Ti, and organic sulfur.

Some of the residues from the 350°C experiments have also been analyzed by FT-IR. The preliminary results suggest that there is a reduction in oxygen functional groups during water pretreatment as was found by Khan et al. (6). Hopefully, the FT-IR results will allow us to verify some aspects of the chemistry of steam pretreatment which we suspect involves the interaction of H_2O, carboxyl groups and/or cations to produce methyl and hydroxyl groups. This is based on the fact that the beneficial effects of steam pretreatment are likely a result of a reduction in retrogressive reactions. Our previous work has suggested that carboxyl groups and cations are significantly involved in retrogressive reactions (15).

CONCLUSIONS

The preliminary conclusions are as follows:

1. The analysis of pyrolysis data from water pretreated Zap lignite (reduction in CO_2 yield, maximum in tar yield, increase in CH_4 yield, reduction in CO yield, maximum in extractables yields) shows a strong similarity to a geological aging process.

2. These changes are delayed and attenuated as the pretreatment temperature is reduced. The preliminary results for a Wyodak subbituminous coal are qualitatively similar.

3. The changes in the mineral composition due to water pretreatment are highly mineral specific.

4. Preliminary IR data is consistent with a general reduction of oxygen groups during water pretreatment.

5. The results from liquefaction experiments on samples produced to date indicate only modest benefits in donor solvent liquefaction.

ACKNOWLEDGEMENTS

The support of this work by the U.S. D.O.E. Pittsburgh Energy Technology Center under Contract No. DE-AC22-89PC89878 is gratefully acknowledged.

REFERENCES

1. Bienkowski, P.R., Narayan, R., Greenkorn, R.A., Choa, K.W., IEC Res., **26**, 202, (1987).
2. Bienkowski, P.R., Narayan, R., Greenkorn, R.A., and Choa, K.C., Ind. Eng. Chem. Res. **26**, 206, (1987).
3. Graff, R.A. and Brandes, S.D., Proceed. of the New Fuel Forms Workshop, U.S. DOE Fossil Energy, p. 35, (1986).
4. Graff, R.A. and Brandes, S.D., Energy & Fuels, **1**, 84, (1987).
5. Brandes, S.D., Graff, R.A., Gorbaty, M.L., and Siskin, M., Energy & Fuels, **3**, 494, (1989).
6. Khan, M.R., Chen, W.-Y., and Suuberg, E.M., Energy & Fuels, **3**, 223, (1989).
7. Ross, D.S., Green, T.K., Mansani, R., and Hum, G.P., Energy & Fuels, **1**, 287, (1987).
8. Ross, D.S., Green, T.K., Mansani, R., and Hum, G.P., Energy & Fuels, **1**, 292, (1987).
9. Ross, D.S. and Hirschon, A., ACS Div. of Fuel Chem. Prepr., **35**(1), **37**, (1990).
10. Ross, D.S., Hirschon, A., Tse, D.S., and Loo, B.H., ACS Div. of Fuel Chem. Prepr., **35**(2), 352, (1990).
11. Serio, M.A., Solomon, P.R., Bassilakis, R., Kroo, E., Malhotra, R., and McMillen, D., "Fundamental Studies of Retrograde Reactions in Direct Liquefaction", Quarterly Reports under DOE/PETC Contract No. DE-AC22-88PC88814, (1989).
12. Carangelo, R.M., Solomon, P.R., and Gerson, D.J., Fuel, **66**, 960, (1987).
13. Whelan, J.K., Solomon, P.R., Deshpande, G.V., and Carangelo, R.M., Energy & Fuels, **2**, 65, (1988).
14. Monthioux, M., Fuel, **67**, 843, (1988).
15. Solomon, P.R., Serio, M.A., Deshpande, G.V., and Kroo, E., Energy & Fuels, (1990).

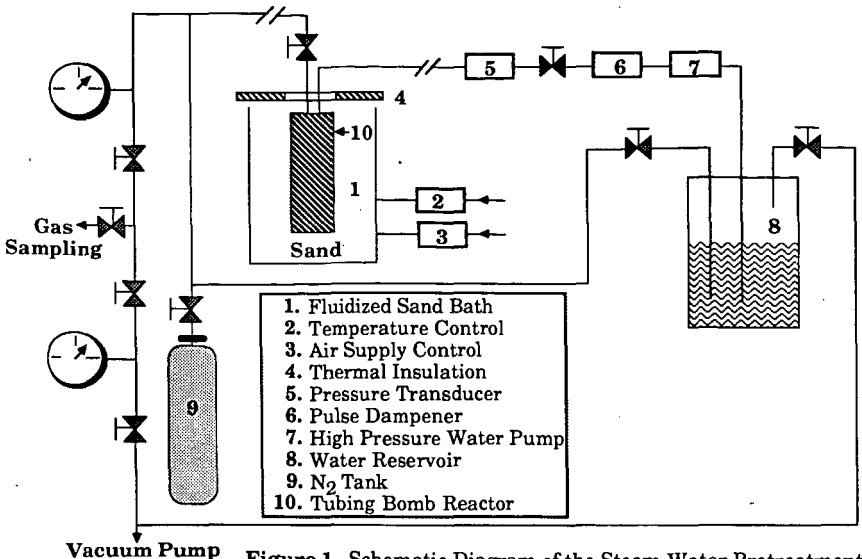

Figure 1. Schematic Diagram of the Steam-Water Pretreatment Reactor System.

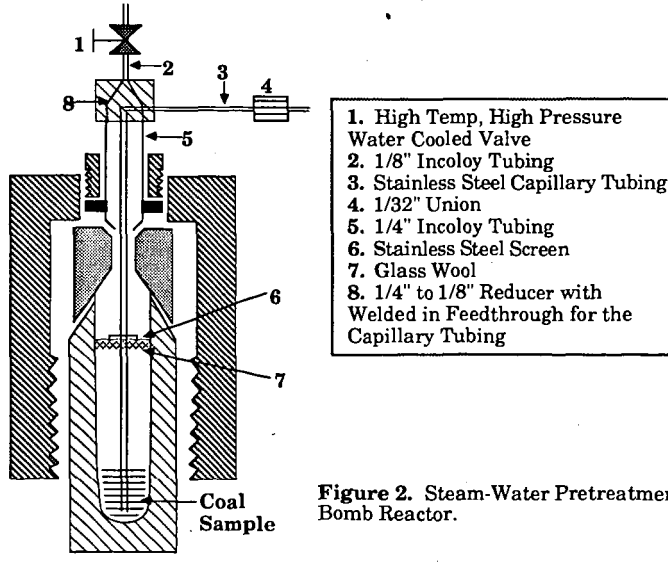

Figure 2. Steam-Water Pretreatment Bomb Reactor.

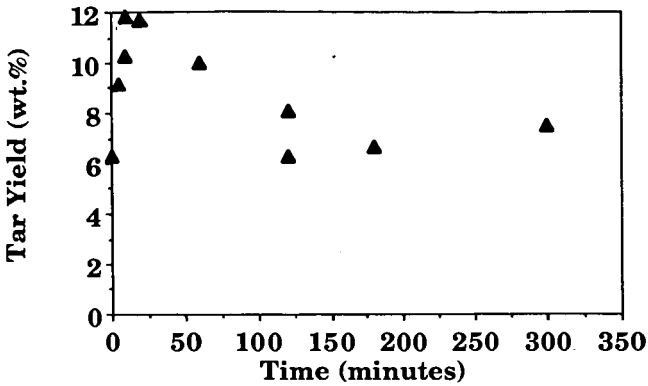

Figure 3. Tar Yield Data from Pyrolysis of Water Pretreated Zap Lignite (350°C, 4000 psig).

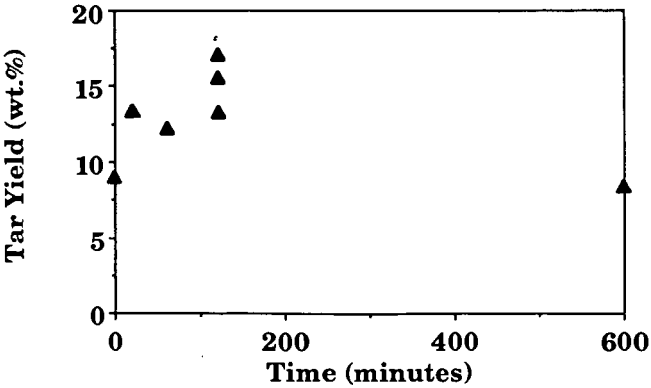

Figure 4. Tar Yield Data from Pyrolysis of Water Pretreated Wyodak Coal (350°C, 4000 psig).

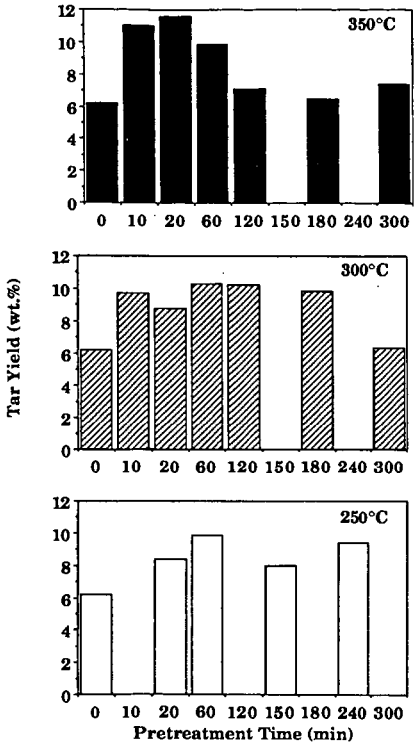

Figure 5. Tar Yield Data from Pyrolysis of Water Pretreated Zap Lignite Produced at Three Temperatures (4000 psig).

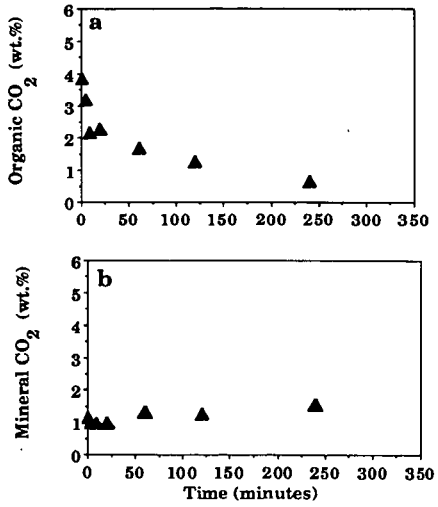

Figure 6. CO_2 Yield Data from Pyrolysis of Water Pretreated Zap Lignite (350°C, 4000 psig).

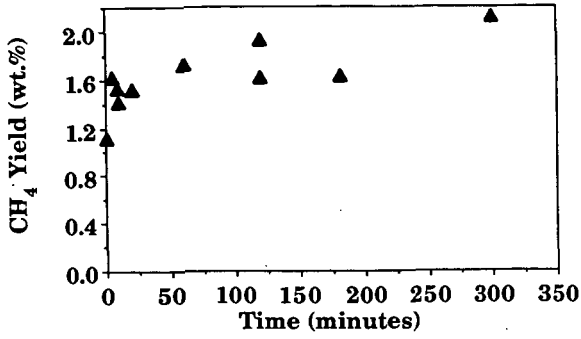

Figure 7. CH_4 Yield Data from Pyrolysis of Water Pretreated Zap Lignite (350°C, 4000 psig).

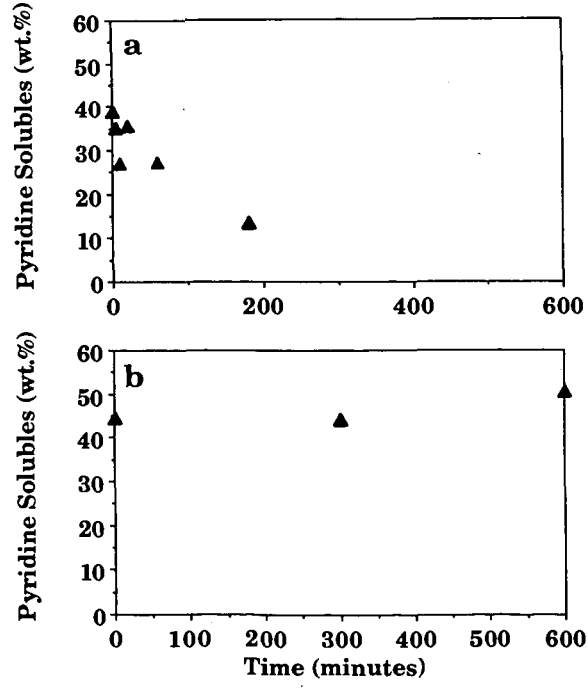

Figure 8. Pyridine Solubles Yields from Liquefaction Experiments with Water Pretreated Zap Lignite (350°C, 4000 psig).

Pretreatment for Coal Liquefaction

N. R. Pollack[1], G. D. Holder[2], and R. P. Warzinski

U.S. Department of Energy, Pittsburgh Energy Technology Center
Pittsburgh, PA 15236

Keywords: coal liquefaction, pretreatment, mass transfer limitations

Abstract

Pretreatment of Illinois No. 6 coal using two different procedures at moderate temperatures, 100°C to 300°C, resulted in small (up to 8%) but consistent increases in subsequent liquefaction yields. In a hydrothermal pretreatment, coal and water were heated together and then separated. The increase in yields due to this pretreatment are probably due to a chemical change in the coal. A method of modelling chemically effective pretreatments is proposed. The other pretreatment that increased liquefaction yields involved soaking the coal at 300°C in a coal-derived solvent prior to liquefaction. Particle size experiments were also performed to determine if mass-transfer resistance was a factor. At short contact times, liquefaction yields were greater with smaller particles, whereas, at longer contact times, the yields approached the same limiting value regardless of the initial coal particle size.

Introduction

The use of pretreatments, including catalyst dispersion, to enhance the liquefaction of coal has recently drawn considerable interest. Such pretreatments are proposed to open up the pores of the coal, provide a more intimate contact of catalyst and coal, and possibly affect the ultimate reaction chemistry by chemically altering the nature of coal prior to the liquefaction step. In this paper, such pretreatments will be classified into two types: **Type I**, which are those primarily aimed at reducing mass-transfer limitations between the coal and liquefaction media; and **Type II**, which are those designed to affect the liquefaction chemistry.

Examples of Type I pretreatments include those which open the pores of the coal allowing the solvent and hydrogen to more easily penetrate the coal particle or those in which a catalyst or other chemical, such as a hydrogen donor, is placed within the pores of the coal so that it is at the reaction site when liquefaction begins. Note that the process of catalyst deposition may affect the morphology of the catalyst and would need to be distinguished from mass-transfer-related effects. With the exception of catalyst morphology effects, all of these pretreatments are designed to overcome mass-transfer limitations. Type I pretreatments would therefore be ineffective if such limitations do not exist in the particular liquefaction scheme under investigation.

Only those pretreatments that produce a change in the chemical structure, surface properties, or molecular arrangement of the coal prior to liquefaction can be classified as Type II pretreatments. If the same effect can be produced by just adding the reagent(s) to the liquefaction step, then a separate pretreatment would not be necessary.

---

[1] Calgon Carbon Corporation, Robinson Township PA 15205

[2] University of Pittsburgh, Pittsburgh, PA 15216

For example, in order for a hydrothermal pretreatment to be judged a Type II pretreatment, the water must produce an effect that is different than would be obtained by just adding water to the liquefaction solvent. This concept is fundamental in evaluating any Type II pretreatment.

Background

During the past several years, coal pretreatments have received increased attention as a means of improving the liquefaction process by either lowering the reaction severity or improving yields under conventional liquefaction conditions. Examples of Type I pretreatments include solvent swelling or presoaking in the liquefaction solvent, both of which have been previously reported to enhance liquefaction yields (1,2,3,4). The most straightforward Type I pretreatment would be a reduction in particle size. This subject has been reviewed by Whitehurst et al. (5). They concluded that, while some variations in conversion were observed for different particle sizes, there were no significant mass-transfer limitations in coal liquefaction, especially when good hydrogen-donor solvents were used in well-agitated systems. In other processes, however, such as high-temperature solvent extraction (5,6) and for chemical reactions at temperatures below those used for conventional liquefaction (7), the presence of significant intraparticle mass-transfer limitations was sometimes observed. Since the presence of mass-transfer limitations is dependent on the type of process and on the mechanics of the system being used, it is therefore judicious to investigate this matter in the development of a Type I pretreatment.

Common Type II pretreatments used for coal liquefaction are alkylation and hydrothermal processing. A recent example of an alkylation pretreatment is the work by Baldwin et al. (8). In this work, mild O-alkylation was shown to be a beneficial pretreatment for a subbituminous coal. The benefit was associated with the suppression of cross-linking reactions that take place during the initial stages of coal thermolysis. The effects were most pronounced at lower reaction severity. Concerning hydrothermal pretreatments, improvements in pyrolysis conversions resulting from steam and hot water pretreatments were originally reported by Brandes et al. (9), and Bienkowski et al. (10). Mochida also reported an improvement in liquefaction yields in a pyrene solvent system associated with a boiling-water pretreatment (11). Ross and coworkers report some improvement in product quality from donor-solvent liquefaction of a hydrothermally pretreated coal (12). Although these various systems have been studied, the mechanism and the actual benefit of hydrothermal pretreatments in liquefaction systems are still not fully understood.

Experimental

Two samples of Illinois No. 6 coal were used in the work reported here. Elemental analyses are contained in Table 1. One sample was ground to minus 48-mesh and minus 325-mesh top sizes. From a second sample of lump-size coal, a 10x48 mesh fraction was screened out after passing the coal through a delumper and a jaw mill. Part of the 10x48 fraction was further ground in a ball mill for 15 minutes under argon to produce a minus 230-mesh sample. The coal-derived liquefaction solvent was a hydrogenated heavy distillate obtained from the V1074 separator at the Advanced Coal Liquefaction Test Facility in Wilsonville, Alabama.

A 38 cm^3 (2.54-cm o.d., 12.7-cm long) stainless-steel microautoclave was used to perform the high-temperature pretreatments and the liquefaction tests. During operation, the microautoclave is

horizontally positioned and agitated by a Burrell wrist-action shaker. The microautoclave is rapidly heated to reaction temperature by immersion in a hot sand bath and quenched after reaction in water. Zero-contact-time experiments involved quenching the microautoclave as soon as reaction temperature was attained. The internal temperature and pressure are continuously monitored.

The liquefaction tests were performed on 3 g of coal or treated coal that was mixed with 9 g of solvent in the microautoclave. A 1000 psig hydrogen or nitrogen cold charge was used in these tests. Liquefaction conversions are measured by methylene chloride and n-heptane solubility and are based on the dry, ash-free, insoluble residues. The standard error in the conversion determinations is less than 4% in both cases. Additional details are available elsewhere (13, 14).

The hydrothermal pretreatments were performed using 5 g of coal and 10 g of water under an initial nitrogen pressure of 500 psig. After 30 minutes at 300°C, the microautoclave was quenched and transferred to a nitrogen-filled glove box where it was vented and opened. The contents were removed with deionized water and filtered to remove the excess water. A portion of the sample was then placed back in the microautoclave for the liquefaction test. Another portion was analyzed to determine the moisture and ash content of the pretreated sample.

In the presoak pretreatments, the microautoclave was heated to 300°C for 10 minutes before being transferred to another sandbath that was preheated to liquefaction temperatures. In one case, the presoak pretreatment was performed by placing the microautoclave and its contents in a cold sandbath and gradually bringing it up to liquefaction temperature over a period of about 2 hours.

Results and Discussion

Results of a Type I pretreatment on the minus 48-mesh sample of Illinois No. 6 coal are shown in Figure 1. The pretreatment involved presoaking the coal in the Wilsonville V1074 recycle solvent prior to liquefaction. In one case, indicated by PS in Figure 1, the presoak was carried out at 300°C for 10 minutes prior to immersing the reactor in another sand bath at liquefaction temperature. In another case, indicated by SH in Figure 1, the microautoclave was slowly heated to reaction temperature over a period of about 2 hours. At 400°C, both presoaking and slow heating led to small increases in conversion to both methylene-chloride and n-heptane solubles. The increases were less for the longer experiment in which slower heating was used. The magnitudes of the observed increases were of the same order of magnitude as that observed by Narain (4) but less than those observed by others (1,3).

Figure 1 also shows that increasing the liquefaction temperature to 425°C results in the pretreatment effect being absent in the case of the n-heptane conversions and negative for the conversions measured with methylene chloride. These results represent part of a larger body of experimental data yet to be reported (13), but they serve to illustrate the sensitivity we observed for this type of pretreatment with respect to the actual liquefaction conditions used.

To further assess the role of mass transfer limitations in donor-solvent liquefaction, experiments with Illinois No. 6 coal of various mesh sizes were conducted. Results of using these fractions in the Wilsonville V1074 solvent system are shown in Figure 2. Any benefits of using the smaller particle sizes in this system are only observed at very short contact times and diminish as contact time increases. As

with the presoak results described above, liquefaction at 425°C diminishes any benefit observed at the lower temperature.

Another set of experiments on this subject was performed to isolate the effect of solvent/coal contact using the more carefully sized coal particles (see the Experimental section for details). The liquefaction tests in this case were conducted at 400°C in tetralin under an inert atmosphere. As before, the results, contained in Figure 3, show that a small but consistent increase in methylene-chloride and n-heptane conversions accompany the use of the smaller-sized particles. The magnitude of the increase diminishes with increasing contact time but is still evident at 20 minutes. Analysis of the methylene-chloride-insoluble product produced from the 10X48 mesh sample showed the presence of particles larger than 48 mesh for the 0 and 5 minute tests but no evidence of the original particles at 20 minutes.

In summary of the above, the small influence that initial particle size has on ultimate (longer contact time) yields indicates that the same asymptotic yields are reached although the initial conversion is moderately inhibited by the larger particles. The asymptotic behavior also implies that the reactions are delayed slightly but not significantly changed in nature. The results from these tests and the presoak experiments indicate that mass-transfer limitations may exist under certain conditions and that, in these cases, Type I pretreatments may be effective in reducing these limitations. However, under conventional liquefaction conditions, large benefits should not be expected from Type I pretreatments. Such pretreatments may have greater utility under lower-severity conditions where coal particles do not disintegrate rapidly and the rates of the liquefaction reactions are slower. The work described here indicates that the largest effect related to any mass-transfer limitations probably occurs during the initial heating to liquefaction temperatures, since only small improvements are observed even in zero-contact-time experiments.

The effect of using a hydrothermal (Type II) pretreatment on Illinois No. 6 coal is shown in Figure 4. The pretreatments resulted in a small but consistent improvement in the methylene-chloride solubles (2%) and the heptane solubles (6%) compared to the yields obtained for untreated coals. In other work, similar but less consistent results were obtained for a Wyodak coal (13). These results are consistent with those of Ross and coworkers (12), which show similar small improvements in the yields of toluene soluble material after a hydrothermal pretreatment at 250°C. They also noted an improvement in the product quality due to the pretreatment as determined from FIMS data. They postulate that the pretreatment disrupts chemical associations between the organic and mineral phases of the coal causing the release of organic matter. In other work, Mochida et al. (11) speculate that hydrothermal pretreatments remove divalent cations such as Ca^{2+} and Mg^{2+}, which link oxygen functionalities and thereby impede liquefaction. In the pyrolysis work of Brandes et al. (9), the proposed reason for increased yields is the chemical interaction of the steam used in the pretreatment with oxygen functional groups in the coal. Although the hypothesized mechanisms for hydrothermal pretreatment are varied, the consensus is that it is a chemical effect and therefore classified as a Type II pretreatment. Also, in previous work, the addition of water directly to the liquefaction reactor was not found to cause any benefit in the conversion results or product quality (12,14).

The primary way by which Type II pretreatments can affect the degree of conversion as measured by solvent solubility is to change the rate at which soluble and/or insoluble products are produced. To be effective, the pretreatment must accelerate the rate at which soluble products are

produced, in the same manner that a catalyst would, or decelerate the rate at which insoluble products are produced. A simple first-order model can be used to describe the production of soluble and insoluble products from coal:

$$\text{Coal} \xrightarrow{k_S} \text{Soluble Products}$$

$$\text{Coal} \xrightarrow{k_I} \text{Insoluble Products}$$

where k_S and k_I represent the rate constants for the reactions indicated. Using the first-order models, it is possible to determine the relative rate constants, k_S/k_I, before and after pretreatment by solving the following equation.

$$k_S + k_I = -\ln[1-x_S(1 + k_I/k_S)]/t$$

where x_S is the fractional conversion to solubles at time t. Since two unknowns are present, conversions must be available at more than one reaction time. It should be noted that the k_S/k_I ratio would remain the same if both rates changed by the same amount (if the pretreatment caused the same final state to be reached only at a different time). Also note that the model does not explicitly account for the production of gases.

For the hydrothermal pretreatments shown in Figure 4, the k_S/k_I ratio for the methylene-chloride-soluble products improves from 1.47 prior to pretreatment to 1.61 after pretreatment. This small increase could be due either to an increase in the rate of formation of soluble products or to a decrease in the rate of formation of insoluble products.

The ratio, k_S/k_I, has been calculated for other chemical pretreatments reported in the literature. For hydrothermal pretreatment of oxidized coal prior to liquefaction in an aqueous-KOH/CO system (14), k_S/k_I for methylene-chloride-soluble products increased from 0.37 to 1.82. Alkylation of Wyodak Coal prior to donor-solvent liquefaction (8) caused the ratio for tetrahydrofuran-soluble products to increase from 0.54 to 2.22. Comparing these values with the ratio calculated for the experiments in Figure 4 shows that hydrothermal pretreatment prior to donor-solvent liquefaction has a smaller effect than the other pretreatments and liquefaction systems mentioned. Note that the largest effect of pretreatment comes when the initial ratio of k_S/k_I is quite small (0.4 to 0.5) owing either to a low rate of formation of soluble products or a high rate of formation of insoluble products.

Conclusions

The results of the experiments reported in this paper show that presoaking (a Type I pretreatment) in the liquefaction solvent resulted in small but consistent increases in conversions in a donor-solvent liquefaction system at temperatures below 425°C. Additional tests with different particle sizes confirmed the existence of mass-transfer limitations in the early stages of liquefaction under similar conditions. Overall, the benefit of using a Type I pretreatment will depend on the mass-transfer limitations relative to liquefaction rates in the system of interest. The greatest utility of Type I pretreatments will likely be in the development of lower-severity processes in which mass-transfer limitations would be greater and liquefaction rates lower. The effect of Type I pretreatments in catalytic systems also needs further investigation.

A Type II, hydrothermal pretreatment, also resulted in small but consistent increases in conversion in a donor-solvent liquefaction system. Other Type II pretreatments reported in the literature, such as alkylation, provide a greater benefit. A simple first-order model was used to compare the relative effectiveness of these Type II pretreatments. It is also important to note that benefits from Type II pretreatments can be due to an increase in formation of soluble products and/or to a reduction in the formation of insoluble products. These considerations should be taken into account when investigating Type II pretreatments.

Disclaimer

Reference in this report to any specific product, process, or service is to facilitate understanding and does not imply its endorsement or favoring by the United States Department of Energy.

References

1. Rincon, J.M., Cruz, S., and Jairo, R. Proceedings, Int. Conf. on Coal Science, Volume II October 23-27, 1989, 851.
2. Snape, C.E., Derbyshire, F.J., Stephens, H.P., Kottenstette, R.J., and Smith, N.W. Fuel Proc. Technol. 1990, 24, 119.
3. Wham, R. M. Fuel, 1987, 66, 283.
4. Narain, N.K., Appell, H.R., and Utz, B.R. Prepr. Pap., Amer. Chem. Soc., Div. Fuel Chem. 1983, 28(1), 161.
5. Whitehurst D.D., Mitchell T.O., and Farcasiu M. in "Coal Liquefaction: The Chemistry and Technology of Thermal Processes," Academic Press, New York, 1980 pp 91-112.
6. Woodfine, B., Steedman, W., and Kemp, W. Fuel, 1989, 68, 293.
7. Larsen, J.W. and Lee, D. Fuel, 1983, 62, 1351.
8. Baldwin, R.M., Nguanpraesert, O., Kennar, D.R., and Miller, R.L. Prepr. Pap., Amer. Chem. Soc., Div. Fuel Chem. 1990, 35(1), 70.
9. Brandes, S.D., Graff, R.A., Gorbaty, M.L., and Siskin, K. Energy & Fuels, 3, 494.
10. Bienkowski, P.R., Narayan, R., Greenkorn, R.A., and Chao, K. Ind. Eng. Chem. Research 1987, 26(2), 202 and 206.
11. Mochida, I., Moriguchi, Y., Iwamoto, K., Fujitsu, H., Korai, Y., and Takeshita, K. Proceedings, Japan/U.S. NSF Chemistry of Coal Liquefaction Meeting 1985, 25.
12. Ross, D.S. and Hirschon, A.S. Prepr. Pap., Amer. Chem. Soc., Div. of Fuel Chem. 1990, 35(1), 37.
13. Pollack, N.R. Ph.D. Thesis, Chemical Engineering Department, University of Pittsburgh, in preparation.
14. Pollack, N.R., Holder, G.D., and Warzinski, R.P. Proceedings, Seventh Annual Pittsburgh Coal Conference 1990, Pittsburgh, Pa., 689.

Table 1. Elemental Analyses of Illinois No. 6 Coals Used.

Sample Designation	Moisture	Ash	----moisture and ash free---- C	H	O	N	S
-48 mesh	7.2	23.1	78.0	5.3	9.0	1.5	6.2
-325 mesh	5.2	22.9	77.3	5.3	9.7	1.5	6.1
10X48 mesh	9.5	16.2	83.2	4.8	5.2	1.5	5.4
-230 mesh	5.8	16.6	81.0	4.5	7.6	1.5	5.4

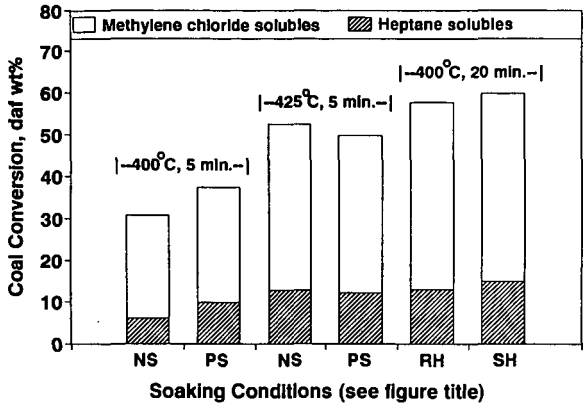

Figure 1. Effect of thermal soaking on the conversion of Illinois No. 6 coal in Wilsonville V1074 solvent. Liquefaction times and temperatures shown in the graph. All tests were under 1000 psig H_2 cold pressure. (NS - No Soaking, PS - Presoaked at 300°C for 10 min., RH - Rapid Heating, SH - Slow Heating)

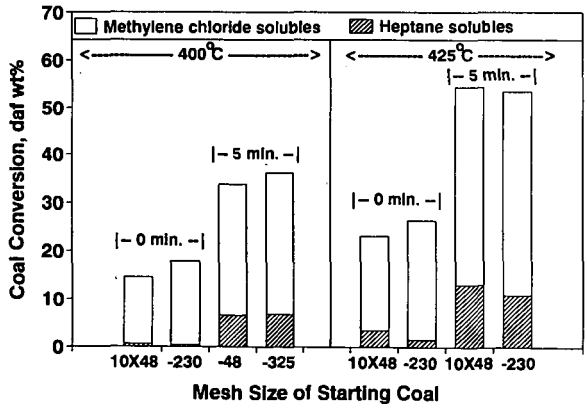

Figure 2. Effect of particle size on the conversion of Illinois No. 6 coal in Wilsonville V1074 solvent. Reaction times and temperatures shown in graph. All tests were under 1000 psig H_2 cold pressure.

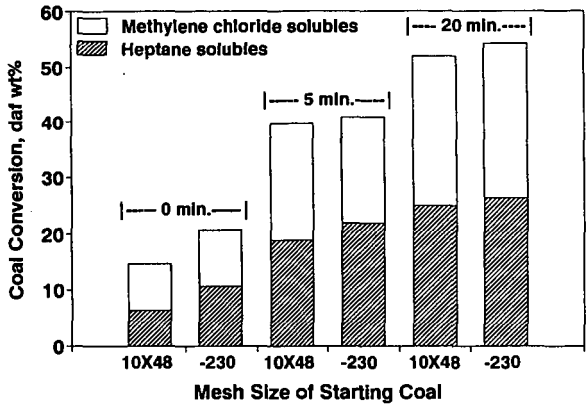

Figure 3. Effect of particle size on the conversion of Illinois No. 6 coal at 400°C for various times at reaction temperature. All tests were performed in tetralin under 1000 psig nitrogen cold pressure.

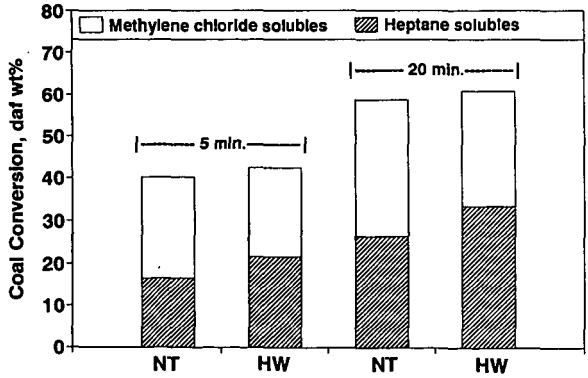

Figure 4. Effect of hydrothermal pretreatments on the conversion of Illinois No. 6 coal in tetralin at 400°C under 1000 psig (cold) H_2. NT - No treatment, HW - 15 minute pretreatment at 300°C under 500 psig (cold) N_2.

EFFECT OF HYDROTHERMAL PRETREATMENT FOR COPROCESSING

Doris S. Tse, Albert S. Hirschon, Ripudaman Malhotra, Donald F. McMillen, and David S. Ross

Chemistry Laboratory
SRI International Menlo Park, California 94025-3493

KEYWORDS: Water, Pretreatment, Coprocessing

ABSTRACT

We report here effects of hydrothermal pretreatment on coprocessing of three different coals from the Argonne Premium Coal Sample Program. Aqueous pretreatment has resulted in a marked beneficial effect in terms of conversion to hexane solubles for Wyodak subbituminous coal and Zap lignite. The effect on the Illinois No. 6 coal was negligible to slightly detrimental. Hydrothermal pretreatment of Wyodak subbituminous coal (1 part) at 250°, 300°, and 350°C for 30 min followed by coprocessing with Maya ATB (2 parts) at 425°C for 1 h, resulted in 26.0%, 23.5%, and 23.5% hexane insolubles based on total feed. Without hydrothermal pretreatment, 31.5% of the feed ended up as hexane insolubles. Use of a donor solvent, tetralin, in place of water during pretreatment produced 27.5% hexane insolubles, and thus was not as effective as hydrothermal pretreatment for the Wyodak coal. Coupling of phenolic constituents and the effect of water in minimizing such retrogressive reactions provide a possible explanation of these results Support for this hypothesis was found in model compound studies with catechol. We observed that while coupling of catechol on kaolin proceeds very rapidly such that after 3 h at 350°C only 38% of the catechol was recovered, addition of water dramatically mitigated the coupling, with 96% recovery.

INTRODUCTION

The impact of water on coal conversion under different process conditions has been a subject of interest and controversy for some time. Recent studies have shown that mild hydrothermal treatment of an Illinois No. 6 coal substantially enhances conversion into soluble products. For instance the convertibility of an Illinois No. 6 coal into toluene-soluble products increased from ~ 35% to almost 70% when the coal was treated for 30 minutes with water at 250°C under nitrogen, and then subjected to conversion in CO/water systems.(1) Similar favorable effects of mild hydrothermal pretreatment have also been reported for conversions in pyrene (2) and for rapid hydropyrolysis.(3,4) However, the benefits of water pretreatment are clearly not general in that they are not observed for all coals under all combinations of pretreatment and subsequent processing conditions.

We present here results from a study we undertook to determine whether the beneficial effects of mild hydrothermal pretreatment can be exploited in the context of coprocessing. The objectives of this study were to explore the range of benefits, with respect to coal type, temperature of pretreatment, and the manner of water removal. In a parallel study, we have examined the impact of water on clay-catalyzed coupling of phenolics. Together, the two studies strongly indicate that the beneficial impact of water is due to the suppression of retrogressive coupling reactions.

EXPERIMENTAL

The coals used in this study were Wyodak-Anderson seam subbituminous coal, Illinois No. 6 seam high volatile bituminous coal, and Beulah-Zap seam North Dakota lignite; all coals were obtained from the Argonne premium coal bank and used as received. To minimize exposure to air and the time between pretreatment and coprocessing, both the steps were conducted in the same microautoclave. The reactor (43 mL) was charged with approximately 2.25 g of the coal and subjected to pretreatment conditions. Aqueous pretreatment was conducted at 250°, 300°, or 350°C for 0.5 h. After cooling, the excess water was pipetted out. Approximately 4.5 g of Maya ATB was added to the reactor, which was then filled with 1200 psig of hydrogen (cold). The reactor was shaken at 425°C for 1 h in a fluidized sandbath. Before opening the reactor, it was cooled in dry ice to prevent volatiles from escaping. Conversion to hexane solubles was the principal diagnostic used in this study, although other parameters such as THF-solubles, elemental composition, and FIMS-volatility were also determined for selected cases.

RESULTS AND DISCUSSION

Table 1 presents data from the coprocessing studies with Argonne premium samples of Wyodak coal and Maya ATB for a variety of pretreatment conditions. Experiment 1 in Table 1 gives conversion of Maya alone with no coal added and Experiment 2 gives the result for coprocessing without any pretreatment. These entries represent base-line values to be used for determining the effect of various pretreatments shown in subsequent lines. Using the baseline conversion of Maya alone, we can determine the theoretical conversions of coal assuming that there is no interaction between the coal and and resid. For instance, 18% by weight of hexane insoluble (HI) material was obtained after treating Maya under these thermal coprocessing conditions. If coal were added (in a ratio of 1 part coal to 2 parts Maya), then we would have obtained a yield of 12% if all of the coal had been converted to hexane soluble material. In contrast, if none of the coal had been converted, a value of 45% insoluble material would have been obtained. As shown in the table the results ranged from 22 to 34% hexane insoluble material, indicating that a significant portion of the coal had been converted.

Effect of Pretreatment Conditions on Coprocessing of Wyodak and Maya ATB

From the data in Table 1 we can immediately see that there is a marked beneficial impact of hydrothermal pretreatment with the yield of hexane-insolubles being reduced from 32% without pretreatment to 26% with pretreatment at 250°C (Experiments 3 and 4). Hydothermal pretreatment at 300°C further reduces hexane-insolubles yield to 24%. Increasing the pretreatment temperature to 350°C results in no further benefit in terms of conversion to hexane-solubles. The additional conversion is not merely due to the extra heating that pretreatment provides. Dry heating of coal for 30 min at 350°C prior to coprocessing is in fact deleterious and results in 34% hexane-insolubles. Even thermal pretreatment in tetralin, a donor solvent, is not as beneficial as hydrothermal pretreatment.

Baldwin et al. have shown that mild pretreatment treatment of several coals with with acidic alcohol solutions results in enhanced conversion during subsequent coprocessing.(5) The premise of their work was that the pretreatment alkylates the coals thus preventing the phenolic and carboxylic groups from undergoing retrogressive reactions and lowering the yields. However, another possibility is that the pretreatment actually dewatered the coal, and the removal of water under mild conditions aided in the enhanced conversions. To test this hypothesis we used acetone which is also completely miscible with water, but which cannot alkylate hydroxyls. However, this treatment was somewhat deleterious and resulted in a slight increase in hexane-insolubles: 34% compared to the base line case of 33%.

To determine if the pretreatment effect was limited to the coal, we treated the Maya ATB at 350°C in water. The water was removed, and Maya ATB was then subjected to treatment at 425°C in nitrogen (Experiment 15) and in hydrogen (Experiment 16). In both cases the conversion was no different from that of no pretreatment. The fact that the HI yields under nitrogen and hydrogen for pure Maya are the same is interesting, and suggests that perhaps the upgrading of the Maya is

primarily a disproportionation reaction, where the hydrogen utilized for the upgrading comes directly from the Maya ATB itself. This conclusion is in concert with the findings of Savage et al., (6) and Khorasheh et al.(7) who have reported that presence of hydrogen does not increase the yield of the distillates (which is often equated to hexane-solubles) under thermal and catalytic processing of resids and gas oils, although it reduces coke formation.

Effect of Coal Rank on Hydrothermal Pretreatment

Table 2 presents data from the coprocessing studies with Argonne premium samples of Wyodak, Illinois No. 6, and North Dakota coals and lignite. Although bituminous coals are generally more easily converted than subbituminous coals, coprocessing of Wyodak and Illinois No. 6 coals without pretreatment led to about the same extent of conversion, yielding 32-34% hexane-insoluble material. However, although the pretreatment of Wyodak gave a significant enhancement of conversion, no benefit for the Illinois No. 6 coal was observed. Hydrothermal pretreatment of the lignite at 350°C was moderately beneficial. It should be remembered that we had optimized the pretreatment conditions using the Wyodak coal; and *a priori* have no reason to assume that these conditions are optimal for other coals as well. The lignite may show a more pronounced effect with a lower temperature hydrothermal pretreatment. Nevertheless, these results show that the beneficial effects of hydrothermal pretreatment are not specific to the Wyodak coal and that other low rank coals also show qualitatively similar enhancement in conversion.

Possible Chemical Basis for Hydrothermal Pretreatment

Various factors could explain the phenomenon of hydrothermal pretreatment and how it relates to the ultimate convertibility of coal. One possibility is that morphologogical changes affect mass transfer rates because the water contact increases pore volume and therefore opens the coal structure for subsequent conversions. However, other, more chemical explanations must also be considered. Because the impact of hydrothermal pretreatment was generally more pronounced for low rank coals, which have relatively large amount of dihydric phenols, and because dihydric phenols are particularly prone to coupling reactions, we investigated the effects of mineral/organic interactions by use of model phenol systems such as phenol and catechol, and mineral systems such as montmorillonite and kaolinite. In previous work we have shown that unless H-donor solvents are present, phenolics such as catechol and resorcinol undergo rapid coupling reactions (8). Trewhella et al., have also reported that the presence of hydrogen donors such as tetralin significantly reduces the polymerization of phenolic compounds to larger ring furans (9).

We conducted a series of experiments in which catechol was heated in a sealed quartz ampoule in the presence of kaolin, a common clay mineral found in coals, and in the presence or absence of water or tetralin. Under the experimental conditions a substantial amount of catechol was converted to polymeric materials and not recovered. The product mixture was analyzed by GCMS to determine the amount of unconverted catechol and the small yields of phenol. Table 3 presents data on the self-coupling reactions of catechol in the temperature range from 300° to 400°C, and how it is modified by kaolin, tetralin, and water. As shown in this table, only a small amount of the catechol underwent any condensation reactions when heated by itself to 400°C for 1 h (Experiment 1). It remained essentially as catechol (75%) or phenol (18%) with only 7% of material unaccounted for. Reaction at 350°C (Experiment 4) results in even less of coupling products. However addition of kaolin markedly accelerated coupling reactions. For instance, after 3 h at 350°C a mixture of catechol and kaolin (Experiment 5) contains only 46% of the original catechol (and 4% phenol), compared to 92% and 1% with no clay added (Experiment 4). Addition of water, on the other hand, results in inhibition of these coupling reactions. In Experiment 6 water was added to the mixture, and 89% of the catechol was recovered, and 1% phenol was formed. Analogous effects of clay and water were observed at 400°C. Addition of clay promotes coupling of catechol with only 2% of the catechol being recovered (Experiment 2), while in the presence of water, 84% was recovered (Experiment 3). These results are very interesting, and suggest that pretreatments and/or conversions in the presence of water should minimize crosslink formation by phenols of this type and lead to larger yield and/or a better quality product.

CONCLUSIONS

We have shown here that hydrothermal pretreatment of low rank coals enhances conversion to hexane-solubles during subsequent coprocessing. We further showed that for the Wyodak coal, the benefit increased from an increase in the pretreatment temperature from 250° to 300°C, but no additional benefits were derived by further increase of temperature to 300°C. Dry thermal pretreatment is deterimental and even thermal pretreatment in donor solvents is not as effective as aqueous pretreatment. We suspect that some of the benefits seen here evolve from changes brought about in clay-promoted retrogressive condensation chemistry. In a small study conducted to understand this phenomena we have shown that water markedly attenuates the clay-catalyzed coupling of phenolics.

Acknowledgment: Support for this work by the US Department of Energy under Contract No. DE-AC22-88PC88802 is gratefully acknowledged.

REFERENCES

1. A. S. Hirschon, D. S. Ross, L. L. Ackerman, "Low Severity Conversion of Activated Coal," SRI Quarterly Report, DOE/PC/79936-4 (October 1988).

2. I. Mochida, K. Iwamoto, T. Tahara, Y. Korai, H. Fujitsu, K. Takeshita, *Fuel*, **1982**, *61*, 603.

3. R. A. Graff, S. D. Brandes, *Energy and Fuels*, **1987**, *1*, 84-88.

4. P. Bienkowski, R. Narayan, R. Greenkorn, K-C Chao, *Ind. Eng. Chem. Res.*, **1987**, *26*, 202.

5. R. L. Miller, M. E. Armstrong, R. M. Baldwin, *ACS Div. Fuel Chem. Prep.* **1989** *34* (3), 873-880.

6. P. E. Savage, M. T. Klein, S. G. Kukes, *Energy and Fuels*, **1988**, *2*, 619.

7. F. Khorasheh, H. A. Rangwala, M. R. Gray, I. G. Dalla Lana, *Energy and Fuels*, **1989**, *3*, 716.

8. D. F. McMillen, S.-J. Chang, S. E. Nigenda, and R. Malhotra, *ACS Div. Fuel Chem. Prep.* **1985**, *30*(4), 414.

9. M. J. Trewhella, A. Grint, *Fuel* **1988**, *67*, 1135.

Table 1

COAL CONVERSION FROM COPROCESSING MAYA ATB AND WYODAK COAL IN MICROAUTOCLAVE[a]

Experiment	Pretreatment[b]	HI (wt%)	Coal Conversion[b]
1	Maya (no coal)	18	--
2	None	32	40
3	250 °C	26	53
4	250 °C	27	53
5	300°C	23	66
6	300°C	24	63
7	350°C	22	69
8	350°C	25	60
9	Thermal 350°C	34	33
10	Thermal 350°C	34	33
11	Vac Dried 56°C	34	33
12	Acetone Dried	33	36
13	Tetralin 350°C	28	52
14	Tetralin 350°C	27	55
15	Maya (no coal, 350 pret)	20	--
16	Maya (no coal, 350 pret)	23	--

a. Reactions of coal and Maya ATB at 425°C for 1 h at and 1200 psi H_2. HI refers to Hexane insoluble fractions.

b. Coal conversion calculated assuming that the insoluble material from the Maya remains the same during the coprocessing experiment.

Table 2

COPROCESSING OF COALS OF DIFFERENT RANK WITH MAYA ATB IN MICROAUTOCLAVE[a]

Experiment	Coal	Pretreatment	Hexane Insoluble	Coal Conversion[b]
1	None	None	18	--
2	Wyodak	None	32	40
3	Wyodak	350°C	22	69
4	Wyodak	350°C	25	61
5	Illinois No. 6	None	34	33
6	Illinois No. 6	350°C	35	30
7	Lignite	None	28	52
8	Lignite	350°C	24	64

a. Reactions of coal and Maya ATB at 425°C for 1 h at and 1200 psi H_2.
b. Coal conversion calculated assuming that the insoluble material from the Maya remains the same during the coprocessing experiment.

Table 3.

EFFECT OF WATER ON CLAY-CATALYZED COUPLING REACTIONS OF CATECHOL

				Mass Balance (Mol%)		
Run	Description	Temp (°C)	Time (h)	Catechol	Phenol	Remainder
1	Catechol	400	1	75	18	7
2	Catechol/ Kaolin	400	1	2	0.2	98
3	Catechol/ Kaolin/water	400	1	84	3	13
4	Catechol	350	3	92	1	7
5	Catechol/ Kaolin	350	3	38	4	52
6	Catechol/ Kaolin/water	350	3	89	1	10
7	Catechol/ Kaolin	300	5	83	8	9
8	Catechol/ Kaolin/water	300	5	99	0	0

LOW TEMPERATURE SWELLING OF ARGONNE PREMIUM COAL SAMPLES: EFFECT ON PORE STRUCTURE

Dennis R. Spears, Lowell D. Kispert and Lidia Piekara-Sady

Box 870336, Chemistry Department,
The University of Alabama, Tuscaloosa, AL 35487-0336

ABSTRACT

Changes in the pore structure of Argonne Premium Coal Samples (APCS) upon slurrying at different temperatures with the solvents toluene, nitrobenzene and pyridine were followed using an EPR spin probe method. At room temperature, spherical shaped pores in coal slurried with nitrobenzene become elongated and cylindrical at 60°C. Coal slurried with pyridine exhibits few detectable spherical shaped pores at room temperature but exhibits significant concentrations of elongated pores at 60°C. This change in pore structure was attributed to the break-up of the hydrogen bonding network by the pyridine solvent.

INTRODUCTION

The organic portion of coal consists of an entangled, extensively cross-linked network of high-molecular weight subunits. The subunits vary in composition and are cross-linked by both covalent and hydrogen-bonding linkages (1). The network, although polymeric in nature, is still not well understood. Adding to the difficulties in understanding coal structure is the porous nature of coal (2). Guest molecules of varying molecular weight are trapped within the network and within the pore system (3). Because coal is polymeric in nature, classical solvent swelling techniques have been used to better understand the structure of coal.

Solvent swelling of coal is important for several reasons. Solvent swelling studies have been used to estimate the average molecular weight between crosslinks (4), and to understand the bonding between subunits (5,6). Understanding solvent swelling is important because organic solvents affect the pore structure of coal, as well as density, mechanical strength, and spectral properties. Further, many coal beneficiation processes, especially liquefaction, take place in organic solvents.

The pore structure of coal has been extensively characterized (7,8). Swelling solvents act upon coal via diffusion into the pore structure. Catalysts can penetrate into accessible areas during conversion processes. Among the many techniques used to characterize the pore structure of coal has been the use of spin probes and electron paramagnetic resonance spectroscopy (EPR) (9-16).

Until the early part of this decade, EPR was used primarily to study the concentration of free radicals in coal and determine g-values. However, in 1981 Silbernagel et al. (9) showed the possibility of diffusing spin probes into coal as observed by EPR spectroscopy. TEMPOL (4-hydroxy-2,2,6,6-tetramethylpiperidine-1-oxyl) was placed in a hexane solution and diffused into either Wyodak or Illinois No. 6 coal. The broadening and reduction of the nitroxide spin probe EPR signal was associated with the diffusion of the TEMPOL molecules into the coal matrix. This experiment suggested that surface adsorption and diffusion of spin probes into coal was possible (9).

This method has been expanded in our laboratory (10). EPR studies of doped Alabama and Penn State Coal Sample Bank (PSOC) coals were carried out, showing it possible to estimate the relative accessibility of different sized spin probes to the pore structure of coals in the presence of a swelling solvent (10-16). Spin probes of different sizes and shapes are diffused into different coal samples swelled with toluene. A nonswelling solvent such as cyclohexane is used to wash away the spin probes not trapped in the porous structure. Relative pore shapes and size distributions can then be

determined by EPR measurement of the spin concentration of the probes trapped within the matrix. In this paper, changes in both pore size and shape with coal rank and swelling solvent were determined as a function of swelling temperature for the Argonne Premium Coal Samples (APCS).

EXPERIMENTAL

All eight Argonne premium coal samples were used in this study. The compositions of these coals on a dry, mineral matter-free basis are shown in Table 1. The coals were doped with spin probes using a procedure described previously (13-16). The coals were swelled with either toluene, nitrobenzene or pyridine solutions of the desired spin probes. This paper details the results of the spin probe commonly known as TEMPOL, I, spin probe V (4-octadecanoylamino-2,2,6,6-tetramethylpiperidine-1-oxyl) and spin probe XIII (4-nonylamino-2,2,6,6-tetramethylpiperidine-1-oxyl). The structures of these probes are given in Figure 1. I was obtained from Aldrich and V and XIII were obtained from Molecular Probes. Spin probe I is roughly spherical in shape while probes XIII and V are elongated. The coals were swelled either at room temperature or at 333 K.

RESULTS AND DISCUSSION

The ability of a solvent to swell a given coal depends upon many factors, including the polarity of the solvent, temperature of solvolysis and rank of the coal. The swelling conditions used in this study were fairly mild. At room temperature with n-alkyl amine solvents, equilibrium swelling ratios require weeks to reach (17). The intention in this study was not to reach swelling equilibrium but rather an equilibrium uptake of the spin probe. This was found to occur after 12 hours.

Nonpolar solvents interact with coal in accordance with regular solution theory; polar solvents swell coal by disrupting hydrogen bonds. Coal is cross-linked with both covalent and hydrogen-bond cross-links. Hydrogen bonding is especially important for lower rank coals, but diminishes in importance with rank (5). Hydrogen bonding is believed to be associated with oxygen functionalities (18), and the oxygen content of coal decreases with rank. Thus, polar solvents show a lessened ability to swell higher ranked coals. Further, the degree of solvent polarity affects the ability of a solvent to disrupt hydrogen bonds and swell coal (19). Swellability also decreases with rank for nonpolar solvents, probably due to high covalent cross-link density in higher ranked coals.

The concentration of spin probe I as a function of swelling solvent and carbon content of the APCS coals, at 298 K, is shown in Figure 2. Carbon content was used as an indicator of rank throughout this study. Of the three solvents used in this study, pyridine was the most polar, toluene the least. At room temperature, the spin concentration of spherical TEMPOL in the swelled coals decreased with rank for coals swelled with either toluene or nitrobenzene. For coals below about 85 % carbon content (dmmf) swelled in nitrobenzene contained a higher spin probe concentration than coals swelled in toluene. For coals with greater than 85 % carbon content (dmmf), there was no significant difference in spin probe concentration regardless of rank or swelling solvent. Coals swelled with pyridine did not retain TEMPOL to any significant degree.

Coal has been shown by SANS (20, 21) experiments to contain spherically shaped pores. Coal swelled in a mild swelling solvent like toluene at room temperature still retains a significant quantity of spherical pores. At room temperature, nitrobenzene, a moderately polar swelling solvent, caused an increase in the number of the spherically shaped pores and a subsequent increase in the number of trapped smaller spherical shaped probe I. However, when coal underwent more severe swelling, such as in pyridine, pores lost their sphericity and became enlarged and elongated or cylindrical (20, 21) in shape. As a result, the spherical TEMPOL molecules are not retained when the coals were washed with cyclohexane.

The severity of swelling is not only affected by solvent polarity, but also by temperature. An increase in swelling temperature from 288 K to 333 K, while small, had a significant effect on the pore

structure of coal. In Figure 3, the concentration of spin probe I as a function of swelling solvent and carbon content of the APCS coals at 333 K is shown. Again, for higher ranked coals (above 85 % carbon content), spin probe concentration did not vary significantly regardless of rank or swelling solvent. For lower ranked coals, toluene-swelled coals retained a significant number of spherically shaped pores, while coals swelled in pyridine did not. Interestingly, at 333 K, coals swelled in nitrobenzene no longer contain significant quantities of spherically shaped pores.

The swelling process using nitrobenzene and pyridine result in a break-up of the hydrogen bonding system, causing an elongation of the pore structure. For nitrobenzene this was most noticeable using spin probe XIII at 298 K and at 333 K. Spin probe XIII is long and cylindrical in shape. When the APCS coals were swelled in nitrobenzene at room temperature (Figure 4), a significant number of cylindrical pores were present, as were numerous spherical pores. When the swelling temperature was increased to 333 K, the spherical pores all but disappeared, and the number of cylindrical pores increased significantly (Figure 5).

Lack of space prevents a discussion of the effect of temperature on the optimal elongation length deduced using several different spin probes for each solvent as a function of coal rank. However using spin probe V shows that almost no detectable spin probes of the size for which probe V would be trapped occurred at room temperature for toluene, or nitrobenzene or pyridine. However at 333 K, pyridine exhibited significant and measurable concentration of elongated pores similar to that of probe V while none were observed for toluene or nitrobenzene solvents. The variation in concentration with coal rank was similar to that exhibited by spin probe XIII in nitrobenzene.

The effect of temperature on the spin probe concentration of spin probe I depicted in Figures 2-5 appears to suggest the following. For coals swelled in toluene, the number of spherically shaped pores increased with temperature. Higher temperatures increased the ability of toluene to swell coal, but not enough to cause pore elongation. For nitrobenzene, spin probe concentration of I decreases with temperature. Like toluene, higher temperatures increase the ability of nitrobenzene to swell coal. At room temperature, nitrobenzene swelled the APCS coals enough to open up spherical pores. At 333 K, conditions were severe enough for nitrobenzene to cause pore elongation. Pyridine was such a severe swelling solvent for coal that even at room temperature pore elongation occurred.

Extensive Electron Nuclear Double Resonance (ENDOR) studies have shown that little chemical interaction occurs between the coal structure and the spin probes. Lack of space prevents a full discussion of the probe location in the pores of the coal.

CONCLUSION

The use of nitroxide spin probes with swelling solvents is a simple way in which to gain an understanding of the pore structure of coals and how it changes in the presence of swelling solvents. Coal contains significant quantities of spherically shaped pores increasing with decreasing rank. If coal is mildly swelled with nitrobenzene, the number of spherically shaped pores increases. As solvent polarity increases, or as swelling temperature increases such as with pyridine, swelling conditions become more severe. As swelling severity increases, pores become elongated as evidenced by a decrease in the number of spherically shaped pores and a similar increase in the number of elongated pores. Finally, regardless of the severity of swelling conditions within the range studied, the pore structure of high rank coals changes very little.

ACKNOWLEDGEMENT

This work was supported by the U. S. Department of Energy, Pittsburgh Energy Center, University Coal Research Program grant No. DE-FG22-90PC90284.

REFERENCES

1. Peppas, N. A.; Larsen, J. W.; Lucht, L. M.; Sinclair, G. W. *Proc. Int. Conf. on Coal Science*, Pittsburgh, **1983**, 280.

2. Bartholemew, C. H.; White, W. E.; Thornock, D.; Wells, W. F.; Hecker, W. C.; Smoot, L. D. *Prepr. Pap.-Am. Chem. Soc., Div. Fuel Chem.* **1988**, *33*, 24.

3. Given, P. H. In *Coal Structure*; Gorbaty, M. L.; Larsen, J. W.; Wender, I.; Eds.; Academic: New York, 1984, Vol. 3.

4. Lucht, L. M.; Peppas, N. A. *Fuel* **1987**, *66*, 803.

5. Larsen, J. W.; Green, T. K.; Kovac, J. *J. Org. Chem.* **1985**, *50*, 4729.

6. Quinga, E. M. Y.; Larsen, J. W. *Energy and Fuels* **1987**, *1*, 300.

7. Mahajan, O. P. In *Coal Structure* ; Meyer, R. A.; Eds.; Academic: New York, 1982.

8. Tricker, M. J.; Grint, A.; Audley, G. J.; Rainey, V. S.; Wright, C. J. *Fuel* **1983**, *62*, 1092.

9. Silbernagel, B. G.; Ebert, L. B.; Schlosberg, R. H.; Long, R. B. *Adv. Chem. Ser.* **1981**, *No. 192*, 23.

10. Wuu, S. K.; Kispert, L. D. *Fuel* **1981**, *64*, 1681.

11. Kispert, L. D.; Corray, L. S.; Wuu, S. K. *Prepr, Pap.-Am. Chem. Soc., Div. Fuel Chem.* **1987**, *32*, 286.

12. Cooray, L. S.; Kispert, L. D.; Wuu, S. K. *Prepr. Pap.-Am. Chem. Soc., Div. Fuel Chem.* **1988**, *33*, 32.

13. Goslar, J.; Cooray, L. S.; Kispert, L. D. *Fuel*, **1989**, *68*, 1402.

14. Goslar, J.; Kispert, L. D. *Fuel*, **1990**, *69*, 564.

15. Goslar, J.; Kispert, L. D. *Energy and Fuels* **1989**, *3*, 589.

16. Spears, R.; Goslar, J.; Kispert, L. D. In *Techniques in Magnetic Resonance for Carbonaceous Solids*; Botto, R.; Sanada, Y., Eds.; ACS Symposium Series No. 229; American Chemical Society: Washington, DC, 1991, in press.

17. Green, T. K.; West, T. A. *Fuel* **1986**, *65*, 298.

18. Larsen, J. W.; Baskar, A. J. *Energy and Fuels* **1987**, *1*, 230.

19. Hall, P. J.; Marsh, H.; Thomas, K. M. *Fuel* **1988**, *67*, 863.

20. Gethner, J. S. *J. Appl. Phys.* **1986**, *59*, 1068.

21. Winans, R. E.; Thiyagarajan P. *Prepr. Pap.-Am. Chem. Soc., Div. Fuel Chem.* **1987**, *32*, 227.

Table 1. Major element composition of Argonne Premium Coal Samples, dmmf basis.

Coal	% C	% H	% N	%S	%O
Upper Freeport	88.08	4.84	1.60	0.76	4.72
Wyodak-Anderson	76.04	5.42	1.13	0.48	16.90
Illinois No.6	80.73	5.20	1.43	2.47	10.11
Pitsburgh No. 8	84.95	5.43	1.68	0.91	6.90
Pocahontas	91.81	4.48	1.34	0.51	1.66
Blind Canyon	81.32	6.81	1.59	0.37	10.88
Lewis-Stockton	85.47	5.44	1.61	0.67	6.68
Beulah-Zap	74.05	4.90	1.17	0.71	19.13

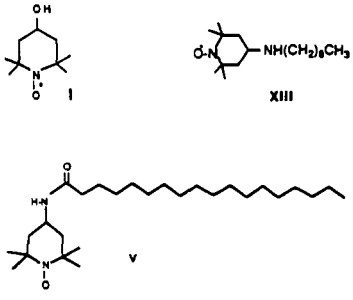

Figure 1. Molecular structure of spin probes I, V and XIII.

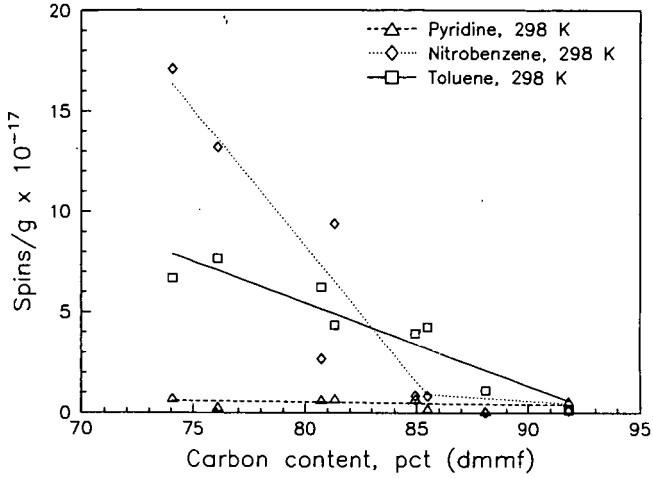

Figure 2. Spin probe concentration of spin probe I (spins/g x 10^{17}) vs. carbon content (pct (%), dmmf basis) for APCS coals swelled 298 K in toluene (□), nitrobenzene (◊), and pyridine (Δ).

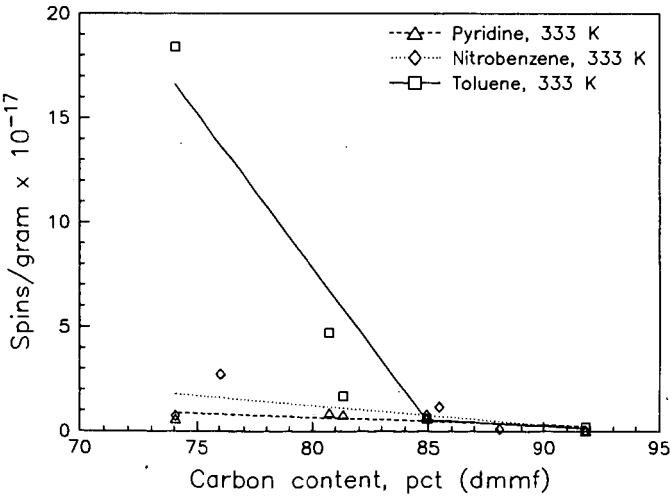

Figure 3. Spin probe concentration of spin probe I (spins/g x 10^{17}) vs. carbon content (pct (%), dmmf basis) for APCS coals swelled 333 K in toluene (□), nitrobenzne (◊), and pyridine (Δ).

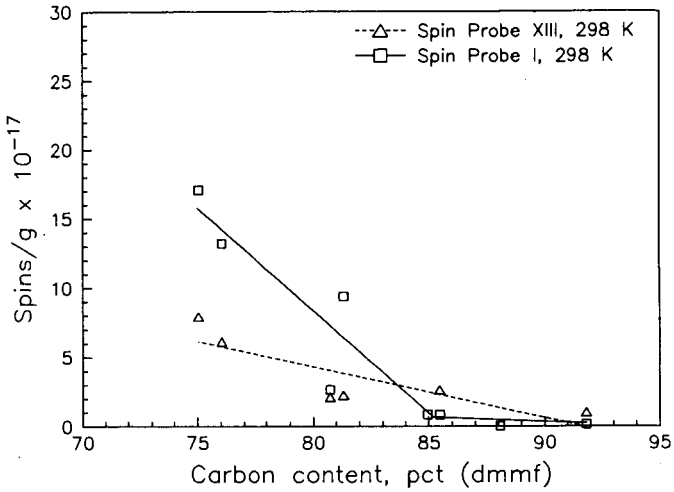

Figure 4. Spin probe concentration of spin probe I (□) and XIII (Δ) in nitrobenzene at 298 K vs. carbon content (pct (%), dmmf basis) for APCS coals.

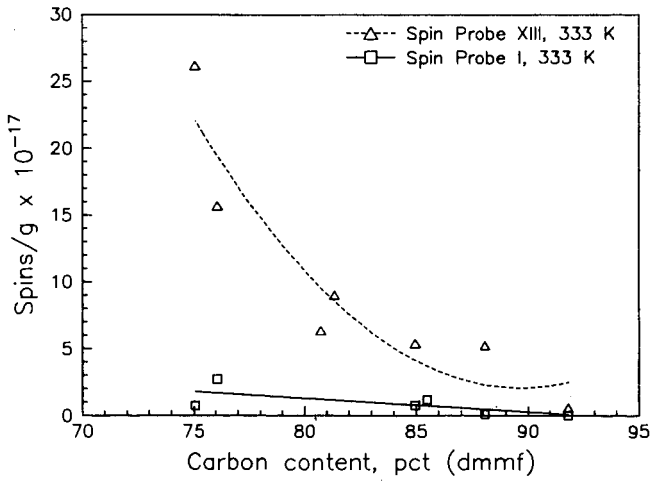

Figure 5. Spin probe concentration of spin probe I (□) and XIII (Δ) in nitrobenzene at 333 K vs. carbon content (pct (%), dmmf basis) for APCS coals.

SWELLING PRETREATMENT OF COALS FOR IMPROVED LIQUEFACTION

Levent Artok, Harold H. Schobert, Gareth D. Mitchell* and Alan Davis*
Fuel Science Program and Energy and Fuels Research Center*
The Pennsylvania State University
University Park, Pa 16802

Keywords: Molybdenum sulfide catalyst, catalyst dispersion, coal swelling, low severity liquefaction.

INTRODUCTION

The organic fraction of coal can be considered to be a large three-dimensional crosslinked macromolecular network of aromatic clusters connected by etheric and aliphatic bridges with the lower molecular weight species trapped in both open and closed pores or weakly bound to the network[1-2]. The coal network can be swollen using appropriate solvents, leading to the expansion of the pores in it. The extent of swelling is rank-dependent. The swelling of coal facilitates impregnation of catalysts and diffusion of reagents towards the reactive sites of coal. Therefore, it can be presumed that the swelling as a pretreatment operation may increase conversion and quality of yield obtained from liquefaction.

Rincon and Cruz[3] found that the conversion of a Colombian coal increased when it is swollen with tetrahydrofuran (THF). Joseph[4] determined a direct correlation between the extent of preswelling and the conversion of coal under liquefaction conditions.

In our work, the effect of swelling on liquefaction has been investigated with and without catalyst at a pretreatment temperature of 275°C using $(NH_4)_2MoS_4$ [ATTM] as a catalyst precursor. In addition, the activities of ATTM and MoS_3 catalyst precursors were compared for unswollen coals at 275°C.

EXPERIMENTAL

Coal preparation

Samples of Blind Canyon high volatile bituminous coal (PSOC-1503 and DECS-6) and Big Brown Texas lignite (PSOC-1444 and DECS-1) collected at different dates were used for this work. The origin and analyses of the coals are given in Table 1. The coals were ground without drying to minus 60 mesh and stored under a nitrogen atmosphere.

Catalyst preparation

ATTM was synthesized in our laboratory following the procedure of Naumann[5]. Molybdenum trisulfide was prepared by acidifying an aqueous solution of ATTM with formic acid, followed by washing the precipitate and drying at 110°C in a vacuum oven.

Sulfur analysis of the molybdenum compounds was performed by the Penn State Materials Characterization Laboratory using a Leco iodimetric titration sulfur analyzer and in the Penn State Combustion Laboratory using a Leco Model SC-132 sulfur analyzer. Carbon, hydrogen, nitrogen analyses were performed using a Leco Model CHN-600 elemental analyzer. Molybdenum analysis and water analysis by the Karl Fisher method were performed by Galbraith Laboratories, Inc. Elemental values and water content of samples are given in Table 2.

Measurement of swelling ratio

One gram of air-dried coal (PSOC-1444 and PSOC-1503) was placed in a 15 ml conical graduated screw-top centrifuge tube and centrifuged at 2900 rpm for 10 minutes and the height of the coal in the tube was recorded in ml/g. Twelve ml of solvent was added to the coal in two increments. The first 6 ml was combined with the coal and the mixture was stirred carefully until all the coal particles were wetted, then

the remaining solvent was added and the tube was sealed with a cap. After a period of time (6-30h) the tube was centrifuged again at 2900 rpm for 10 min and the height was recorded. The volumetric swelling ratio is defined as Q=h2/h1, where h1=height of unswollen coal and h2=height of swollen coal.

The swelling procedure of coals

The coal samples (DECS-1 and DECS-6) were swollen using methanol, pyridine, THF and 10% tetrabutylammonium hydroxide (TBAH) solution of 1:1 (v/v) ratio water:methanol mixture. The coal samples, which were predried at 110°C in vacuum, were mixed with the swelling reagent to give approximately a solvent-to-coal ratio of 3:1 (v/w) and were stirred for 6 hours under nitrogen. The solvent was removed and dried at 50°C in vacuum. In the case of pyridine, the sample was dried at 100°C in vacuum in an attempt to remove pyridine completely. In the case of TBAH, a TBAH solution was added to undried coal and only methanol and water of the mixture were removed, so that TBAH was retained in the swollen coal matrix.

Impregnation of swollen and unswollen coals with catalyst precursors

The catalyst precursor was loaded onto the coal in an amount based on 1% molybdenum (as the metal, not the molybdenum compound) on a dry ash free (daf) basis regardless of whether the coal had been swollen or not. Unswollen coals were impregnated with a water solution of ATTM or suspension of molybdenum trisulfide. The procedure consisted of dissolving or suspending the molybdenum salts in enough distilled water to give an approximate water-to-coal ratio of 1:1 (v/w). Then this solution or suspension was added to the coal sample and stirred 30 min before solvent removal. Excess water was removed from the mixture at room temperature in vacuum. The mixture was continuously being stirred during this procedure. Subsequently, the mixture was quenched in a dry ice-acetone bath until it became frozen and was then freeze dried, followed by vacuum drying at room temperature.

In the case of swollen coal, the swelling reagent (except TBAH) was removed in vacuum at room temperature. While the coal was still wet with swelling reagent, enough ATTM solution (which had been prepared by dissolving ATTM in 1:1 (v/v) ratio methanol:water mixture) to give solution-to-coal ratio of 1:1 (v/w) was added to coal and stirred for 30 min. In the case of TBAH, ATTM was dissolved in a 10% TBAH solution of 1:1 ratio(v/v) water:methanol mixture, then this solution was added to undried coal and stirred for 6 hours in order to give enough time for swelling of coal under nitrogen. After stirring, excess solvent was removed at room temperature in vacuum while it was continuously being stirred, and finally vacuum drying was applied at 50°C for the coals swollen with methanol, THF or TBAH, or at 100°C for pyridine-swollen coal. TBAH was allowed to remain in the coal.

The TBAH content of samples, whether catalyst-impregnated or not, was calculated from the increase of the nitrogen content of the coals, measured with a Leco Model CHN-600 analyzer.

Liquefaction reaction and yield fractionation

The liquefaction reactions were performed in horizontal microautoclave reactors (tubing bomb) of nominal 25 ml capacity. The procedure was the same for both preswollen and unswollen coals and also the same whether they had been impregnated with a catalyst or not.

Five grams of each prepared coal sample and five grams of phenanthrene were placed in the tubing bomb. After mixing the contents with a spatula, the reactor was sealed, pressurized to 1000 psi with nitrogen and checked for leaks. The depressurized tubing bomb was purged with hydrogen twice, pressurizing and depressurizing to 1000 psi. Subsequently, the tubing bombs, pressurized to 1000 psi with hydrogen, were attached to a vertically oscillating system fluidized sand bath which was heated to 283 °C. Immediately after the tubing bombs were placed in the sand bath, the thermostat was reset to 275°C, which was the desired pretreatment temperature. The tubing bombs attained a temperature of 275 °C in about 30 seconds. All the pretreatment experiments were done in duplicate 30 min. reaction times. During this period, the tubing bombs were oscillated through an amplitude of 2 cm at 350 cycles/min.

At the end of the reaction, the reactors were rapidly quenched to room temperature by immersion in cold water. After venting the gas, the contents of each bomb were quantitatively washed into a tared ceramic thimble using toluene and Soxhlet extracted with toluene under nitrogen until the solvent appeared colorless. The toluene extract was concentrated to 10-20 ml by rotary evaporation. The extract was diluted with 400 ml of hexane. The mixture was stirred for 1 h and asphaltenes were allowed to settle overnight and separated with 0.45 micron filter. The filtrate containing hexane-solubles was evaporated by rotary evaporation to remove the hexane. Toluene insolubles were Soxhlet-extracted with THF to separate preasphaltenes and the solid residue under nitrogen atmosphere. THF was removed from the extract by rotary evaporation. Preasphaltenes, asphaltenes and residue were dried overnight in vacuum at 110°C. The conversion was calculated by subtracting residue weight (catalyst corrected) from the weight of coal and dividing by the daf weight of the coal. It was assumed that the catalyst precursor transformed to the same product as ATTM processed without coal in hydrogen at 275°C (Table 2).

RESULTS AND DISCUSSION

Swelling of coals

Solvent swelling ratios with contact time for four different solvents are given in Tables 3 and 4 for Texas lignite (PSOC-1444) and the Blind Canyon hvCb (PSOC-1503), respectively. The maximum level of swelling was attained within 6 h; additional solvent-coal contact in excess of 26 h did not produce a significant increase in swelling ratio. The level of swelling experienced for each coal was slightly different with respect to the individual solvents. For the Texas lignite, swelling increased in order of methanol < THF < pyridine < 10% TBAH; for the Blind Canyon hvCb coal the order was 10% TBAH < methanol < THF < pyridine. Note that the level of the swelling for the different solvents appears to be rank-dependent. Lignites are more crosslinked than bituminous coals. Therefore, lignites give less swelling and extractability for methanol, THF and pyridine than bituminous coals. Lignites have more acidic functional groups (phenolic hydroxyl and carboxylic groups) than bituminous coals; therefore, swelling of lignite increases with increasing basicity of solvents. TBAH is quite basic and has been shown to react strongly with the types of oxygen functionalities in most lower rank coals[6]. Joseph[4] determined for the Illinois #6 bituminous coal that the highest swelling was obtained with 15% TBAH compared with those of THF and methanol. This can be explained, in part by the much higher oxygen functionality of the Illinois #6 coal than that of the Blind Canyon coal and the tendency for TBAH to react with these functional groups[6].

Comparison of MoS_3 and ATTM catalysts for pretreatment

Table 5 shows the conversion data of thermal (non catalytic) and catalyst-impregnated coals. The conversions of coals with both catalysts are greater than those obtained without catalyst. ATTM effectively enhances preasphaltenes and asphaltenes formation for both coals and also improves oil yield for Blind Canyon coal (DECS-6), but not for of the Texas lignite (DECS-1). MoS_3 improved only preasphaltene yield for the Texas lignite; it has not affected formation of asphaltenes and of oil. For the Blind Canyon coal with MoS_3, preasphaltenes were 8% greater than those obtained without catalyst. This yield was even higher than obtained with ATTM, and greater conversion was obtained than with ATTM. However, oil yield was not improved with MoS_3. The conversion of Illinois #6 coal with MoS_3 was found to be comparable to that obtained with ATTM[7]. ATTM was reacted at 275°C under hydrogen atmosphere (1000 psi cold) without coal in order to determine the fate of ATTM at the preliquefaction conditions used in this work. Elemental analysis of the product shows 3.26% of nitrogen (Table 2). The different activities of these catalysts with both coals, may be due to dependence of dispersion on the type of coal and on the destructive effect of ammonia, released from decomposition of ATTM, on catalytic activity of molybdenum sulfide catalyst.

The effect of preswelling on liquefaction

The conversion results of solvent swollen coals without catalyst impregnation are given in Tables 6 and 7. The treatment with methanol enhanced oil formation, decreased preasphaltenes and asphaltenes for the Texas lignite (DECS-1); enhanced oil and preasphaltenes, decreased asphaltenes for the Blind Canyon coal (DECS-6). THF is the least effective swelling reagent in terms of liquefaction of the Texas lignite. It

provided great conversion with its high swelling ability for the Blind Canyon coal (Q=1.9). THF pretreatment increased total conversion of the Blind Canyon coal from 17.7% to 22.1% and oil formation from 4.9% to 9.2%, but its effect on formation of preasphaltenes is not significant and did not influence formation of asphaltenes. The pyridine pretreatment provided greater total conversion and oil formation for the Texas lignite than those obtained from methanol- and THF- treated coals. However, this treatment diminished formation of preasphaltenes for this coal. The pyridine treatment for Blind Canyon coal, surprisingly, decreased total conversion from 17.7% to 16.0%, formation of preasphaltenes from 10.7% to 6.4%, asphaltenes from 2.1% to 1.3%, but increased formation of oil from 4.9% to 9.2%. TBAH treatment provided the highest conversion for the both coals relative to the other solvents, even though 10% TBAH solution in 1:1 water:methanol mixture swelled the Blind Canyon coal least. There might be two reasons for the high conversion with TBAH addition onto coals. The first is the swelling effect. The evaporation of methanol and water from mixture increases the concentration of TBAH. The TBAH thus, concentrated by evaporation can increase the level of swelling of the coal, even for Blind Canyon. Second, in a reaction of 40% TBAH in a tubing bomb at the same reaction conditions as pretreatment experiments (but without coal), butane and butene were observed in the gaseous products. It can be expected that TBAH likely transformed to amine compounds. Therefore, TBAH is going to act as a solvent precursor. It has been found that amines are very good promoters for coal liquefaction[8-9-10]. The nitrogen contents of residue, preasphaltenes and asphaltenes were found to be higher for TBAH-swollen coal than those of unswollen coal. This increase can be attributed to incorporation of amines. Therefore, assuming that TBAH transformed to tributylamine, the amount of tributylamine incorporated in residue, asphaltenes and preasphaltenes can be determined from their difference of nitrogen content and those of the respective products from unswollen coal (Table 10). Incorporation of tributylamine in the residue of the Texas lignite is greater than in Blind Canyon, and addition of catalyst increased this incorporation. Addition of TBAH provided the highest increase in yields of preasphaltenes, asphaltenes and oil for the Texas lignite compared to those of coals swollen with other solvents. For the Blind Canyon coal, TBAH addition provided the greatest conversion, yields of preasphaltenes and asphaltenes, but a lower yield of oil relative to those for coals swollen with the other solvents. For the Texas lignite, conversion without catalyst increased in the order of none < THF < methanol < pyridine < TBAH. For the Blind Canyon coal conversion without catalyst increased in the order of pyridine < none < methanol < THF < TBAH. The extractive ability of a particular solvent is related to the swelling effect of that solvent for a particular coal. A good extractive solvent can disrupt weak bonds in the coal network or in material trapped in the coal structure. Therefore, the molecules released by this disruption and the weakened structure can be liquefied at less severe conditions.

Comparative conversion data of ATTM-impregnated swollen Texas lignite and Blind Canyon are given in Tables 8 and 9. For the Texas lignite with ATTM catalyst the effect of swelling on formation of preasphaltenes and asphaltenes decreases, except for TBAH. The greatest conversions and formation of all types of products were obtained with TBAH addition. If these data were compared with those obtained without catalyst, it can be seen that addition of ATTM increased total conversion and formation of preasphaltenes and asphaltenes, but did not change the amount of oil. The order of conversion can be given as none < THF, methanol < pyridine < TBAH for the Texas lignite. For the Blind Canyon coal methanol treatment decreased yield of asphaltenes, but did not affect conversion and yields of other products. THF treatment decreased formation of preasphaltenes and asphaltenes, while it provided the greatest yield of oil relative to other solvents. However, THF treatment did not affect total conversion. Pyridine treatment decreased formation of preasphaltenes and asphaltenes while increasing total conversion and formation of oils. TBAH addition seemed to decrease the activity of the molybdenum sulfide catalyst, because the conversion of TBAH-treated coal was less than unswollen coal. The addition of ATTM to swollen coals increased significantly total conversion and formation of yields for the Blind Canyon coal except TBAH added coal.The order of conversion is noticed as TBAH < none, methanol, THF < pyridine

CONCLUSIONS

Without swelling pretreatment, impregnation of both coals increased conversion at 275°C. The increased conversion was mainly a result of an increased yield of preasphaltenes. In the absence of catalyst, swelling the Texas lignite before liquefaction improves conversion, with the increase mainly a result of additional (oil+gas) yield. The relative effectiveness of various solvents for improving conversion is in the same general order as their effectiveness at swelling the coal. Preswelling with methanol or

pyridine has little effect on liquefaction of the Blind Canyon coal, but both THF and TBAH provide increased conversion, as a result of improved preasphaltene yields. With this coal, the effectiveness of solvents at improving liquefaction is not in the same order as their ability to swell the coal. The combined effect of catalyst addition and swelling is to enhance conversion of the lignite, with a doubling of conversion obtained by impregnation with ATTM and swelling by TBAH. The yields of all products are enhanced by this pretreatment. In contrast, little improvement in total conversion of the Blind Canyon coal is obtained by combining ATTM impregnation and solvent swelling, but changes in the relative proportions of the products can be obtained.

ACKNOWLEDGEMENTS

The authors are grateful for the financial support provided for this work by the U. S. Department of Energy. The authors are also pleased to acknowledge useful discussions with Dr. J. T. Joseph of the Amoco Corporation.

REFERENCES

1. Hombach, H. P., Fuel, 1981, 60, 663.
2. Given, P. H. Marzec, A., Barton, W. A., Lynch, L. J., Gerstein, B.S., Fuel, 1986, 65, 155.
3. Rincon, J. M.,and Cruz, S., Fuel, 67, 1162.
4. Joseph, J. T., Beneficial effects of preswelling on coal liquefaction, Fuel, in press.
5. Naumann, A. W., United States Patent, 1981, 4243554.
6. Liotta, R., Rose, K., and Hippo, E., J. Organic Chemistry, 1981, 46, 277.
7. Utz, B. R., Cugini, A. V. and Frommell, E. A., Preprints Div. Fuel Chem., Am. Chem. Soc., 1988, 34(4), 1423.
8. Kazimi, F., Chen, W. Y., Chen, J. K., Whitney, R. R., Zimny, B., Preprints Div. Chem, Am. Chem Soc., 1985, 30(4), 402.
9. Tagaya, H., Sugai, J., Onuki, M. and Chiba, K.,Energy & Fuel, 1987, 1, 397.
10. Miller, R. L., Baldwin, R. M. and Kennar, D. R., Preprints Div. Chem. Am. Chem. Soc., 1990, 35(1), 9.

Table 1. Characteristics of coals.

Sample No.	PSOC-1444	PSOC-1503	DECS-1	DECS-6
Seam	Unnamed	Blind Canyon	Bottom	Blind Canyon
County	Freestone	Emery	Freestone	Emery
State	Texas	Utah	Texas	Utah
Province	Gulf	Rocky Mt.	Gulf	Rocky Mt.
Sampling Date	3/30/85	10/01/85	12/11/89	6/07/90
ASTM rank class	Lignite	hvC b	Sub	hvB b
Moisture Content % wt	31.91	10.35	30.00	4.73
Min. Matter % wt (dry)	19.02	4.36	17.97	6.67
Elem. Comp. (% dmmf)				
C	76.21	80.80	76.13	81.72
H	4.71	6.12	5.54	6.22
N	1.42	1.55	1.5	1.56
S (org)	1.36	0.54	1.05	0.40
O (diff)	16.29	10.58	15.78	10.10

Table 2. Elemental analysis of ATTM, MoS_3 and the product obtained from microautoclave reaction of ATTM at 1000 psi (cold) hydrogen gas at a temperature of 275 °C.

Catalyst	%N	%H	%Mo	%S	%H_2O	nS:nMo
ATTM	10.81	3.10	37.01	49.15	ND	3.98
MoS_3	ND	ND	44.45	50.50	1.39	3.41
HATTM*	3.26	1.40	49.74	39.40	6.36	2.38

ND = Not determined.
* = Hydrogenated ATTM

Table 3. Change in solvent swelling ratio (Q) with time for the Texas Lignite (PSOC-1444).

Methanol		THF		Pyridine		TBAH	
Time (h)	Q	Time (h)	Q	Time (h)	Q	Time (h)	Q
5.0	1.1	6.0	1.2	6.5	1.6	6.0	2.6
11.5	1.1	16.5	1.2	21.5	1.6	14.5	2.6
23.0	1.1	22.0	1.3	42.0	1.6	24.5	2.7
27.5	1.1	28.0	1.3				

Table 4. Change in solvent swelling ratio (Q) with time for the Blind Canyon hvCb coal (PSOC-1503).

Time (h)	Methanol Q	THF Q	Pyridine Q	TBAH (10%) Q
6.0	1.2	1.9	2.4	1.2
10.0	1.3	1.8	2.3	1.2
20.0	1.3	1.8	2.2	1.2
26.0	1.3	1.8	2.3	1.2

Table 5. The activity of ATTM and MoS_3 on liquefaction of (Texas lignite) DECS-1 and (Blind Canyon hvB) DECS-6 coals at 275°C.

Coal	Catalyst	Conversion %(daf)			
		Total	Preasph.	Asphal.	Oil +Gas
DECS-1	None	6.6	2.8	2.2	1.6
"	ATTM	9.0	3.9	3.6	1.5
"	MoS_3	7.2	3.9	1.7	1.6
DECS-6	None	17.7	10.7	2.1	4.9
"	ATTM	25.0	15.1	3.0	6.9
"	MoS_3	26.9	19.0	3.3	4.6

Table 6. Effect of preswelling treatment on liquefaction of Texas lignite (DECS-1) at 275°C.

Sol. Treat.	Conversion %(daf)			
	Total	Preasphalt.	Asphal.	Oil +Gas
None	6.6	2.8	2.2	1.6
Methanol	8.4	2.2	1.8	4.4
THF	7.4	2.9	0.9	3.6
Pyridine	10.0	1.7	2.0	6.4
TBAH	17.5	5.2	3.9	8.4

Table 7. Effect of preswelling treatment on liquefaction of Blind Canyon hvB (DECS-1) at 275°C.

Sol. Treat.	Conversion %(daf)			
	Total	Preasphalt.	Asphal.	Oil +Gas
None	17.7	10.7	2.1	4.9
Methanol	19.8	12.2	1.6	6.0
THF	22.1	11.1	2.2	9.2
Pyridine	16.0	6.4	1.3	8.2
TBAH	24.0	15.1	3.6	5.3

Table 8. Effect of preswelling on liquefaction of Texas Lignite with ATTM catalyst at 275°C.

Sol. Treat.	Conversion %(daf)			
	Total	Preasphalt.	Asphal.	Oil+Gas
None	9.0	3.9	3.6	1.5
Methanol	9.5	2.8	2.2	4.5
THF	9.3	3.1	2.8	3.4
Pyridine	11.8	2.9	2.4	6.5
TBAH	18.7	6.2	4.6	7.9

Table 9. Effect of preswelling on liquefaction of Blind Canyon hvB with ATTM at 275°C.

Sol. Treat.	Conversion %(daf)			
	Total	Preasphalt.	Asphal.	Oil + Gas
None	25.0	15.1	3.0	6.9
Methanol	24.7	15.4	2.4	6.9
THF	25.1	12.4	2.4	10.3
Pyridine	26.7	14.6	2.6	9.5
TBAH	23.7	13.5	3.9	6.3

Table 10. The percentage of tributyl amine incorporated to residue, preasphaltenes and asphaltenes of TBAH treated Texas lignite (DECS-1) and Blind Canyon hvB (DECS-6) after hydrogenation with or without ATTM.

Coal	ATTM	Incorporation of TBAH %(dry)		
		Residue	Preashalt.	Asphal.
DECS-1	No	3.2	4.7	5.0
DECS-1	Yes	4.3	3.8	5.5
DECS-6	No	1.7	2.1	8.6
DECS-6	Yes	4.3	3.8	5.5

Morphology and Liquefaction Characteristics of Pyridine-Extracted Illinois No. 6 Coal

R. P. Warzinski and G.D. Holder[1]

U.S. Department of Energy
Pittsburgh Energy Technology Center
Pittsburgh, PA 15236

Keywords: coal liquefaction, pyridine extraction, morphology

Introduction

The primary goal of preconversion processing of coal prior to direct liquefaction is to alter the coal in some fashion so that hydrogenation reactions are favored and detrimental, regressive reactions are limited during the subsequent liquefaction. For example, catalytic hydrogenation at 300-350°C has been shown to favorably influence the yield and composition of products produced during catalytic liquefaction at 400°C (1). Other work has indicated that the glassy nature of coal itself may promote retrogressive pathways that would not exist if the coal structure had more mobility and flexibility (2). Altering the structure of coal by solvent swelling has also been shown to result in improved conversion in noncatalytic, donor-solvent liquefaction (3). As others have postulated, this may be due to the improved penetration and diffusion of reagents in the distorted structure of the swollen coal (4,5) and/or to the possible reduction in the glass transition temperature (used loosely for coal) of the swollen product (6,7).

When coal is swollen and extracted with pyridine, extensive morphological changes are known to occur (4,8,9). The magnitude of the changes in the surface area and porosity of the pyridine-insoluble product may be influenced by the manner in which the residual pyridine is removed. Work with highly porous, silica aerogels indicates that processes involving evaporative removal of a swelling solvent may result in partial collapse of the expanded structure owing to surface-tension effects on the walls of the pores generated by the leaving solvent (10). Maximum porosity is achieved in these systems if non-evaporative methods of solvent removal are used. One such method that avoids the formation of a liquid-vapor interface in the solvent removal process is the dissolution and removal of the swelling solvent by a supercritical fluid (SCF).

In the work reported here, three Illinois No. 6 coal samples were swollen and extracted with pyridine and then subjected to both vacuum drying and SCF extraction with CO_2 to remove the residual pyridine. Differences in morphological features and liquefaction behavior were observed depending on which technique was used. Tests were also performed to compare the liquefaction behavior of the pyridine-soluble fraction with the pyridine-insoluble portion of the coal.

Experimental

The work reported here was performed on three samples of minus 100-mesh Illinois No. 6 coal. Two were from the Burning Star mine and were prepared at the Pittsburgh Energy Technology Center. The third was from

[1] University of Pittsburgh, Pittsburgh, PA 15216

the Argonne Premium Coal Sample program. Elemental analyses of these coals are contained in Table 1.

Pyridine swelling and initial extraction were performed in an Erlenmeyer flask. The coal was added to an excess (approximately 6.5:1 on a weight basis) of reagent-grade pyridine and stirred for approximately two days with a magnetic stirrer. The slurry was then transferred to a cellulose Soxhlet thimble and exhaustively extracted with fresh pyridine until the extract was nearly colorless (pale yellow). The thimble was then removed and the excess pyridine allowed to drain away. The pyridine-insoluble product (PIP) recovered from the Soxhlet thimble contained about 2.5 times its original weight in pyridine. The pyridine-soluble product (PSP) was recovered by rotary evaporation.

Vacuum-dried samples of the PIP were prepared by placing a portion of the material recovered from the Soxhlet thimble in an oven at 110°C to 115°C under full vacuum supplied by a mechanical vacuum pump. The sample was dried in this fashion until the weight loss after a 1-hour interval was less than 0.5%.

Another portion of the PIP from the Soxhlet thimble was extracted with supercritical CO_2 (T_c - 31°C, P_c - 1056 psig) to remove the excess pyridine. The SCF extractions were performed in either a small (1.0 cm i.d. by 25.0 cm long) or large (2.2 cm i.d. by 50.0 cm long) empty HPLC column. The column was wrapped with heating tape, insulated, and connected to a high-pressure ISCO syringe pump filled with liquid CO_2 (375 cm^3 capacity). A back-pressure regulator was used after the column to control the pressure during the extraction. Thermocouples inserted into tee fittings at each end of the column were used to monitor the extraction temperature. With the larger column, another thermocouple was clamped to the surface at its midpoint. Auto-transformers were used to control the heating tapes on the column and on the inlet and exit lines. During the extraction, the column temperature was maintained at 40°C to 45°C and the back-pressure regulator was set at 2000 psig.

When using the small column approximately 12 g of the PIP was extracted. After heating the column, the extraction involved first pumping about 135 ml of CO_2 (as measured on the syringe pump scale) at 10 ml/hour and then 270 ml at 40 ml/hour. The unit was then slowly depressurized through a needle valve while maintaining the temperature at 40°C. The column was then removed and transferred to a nitrogen-filled glove box for sample recovery.

When using the large column, approximately 100 g of the PIP was extracted. The procedure was similar to that for the small column except that more CO_2 was used and at faster flow rates (525 ml at 40 ml/hour then 560 ml at 200 ml/hour). However, on a g-CO_2/g-coal basis, the amount of CO_2 used was less for the larger column, 11 g-CO_2/g-coal as compared to 34 g-CO_2/g-coal for the smaller column.

Surface area measurements, helium densities, and mercury densities were performed at the Center for Micro-Engineered Ceramics at the University of New Mexico by Dr. Douglas Smith. The surface area measurements included a five-point nitrogen analysis at 77 K and a four-point CO_2 analysis at 298 K. The nitrogen measurement provides an estimation of the surface area present in pores with diameters greater than 0.4 nm; whereas, the carbon dioxide measurement is believed to represent the total surface area of coal, including occluded pores (8,9).

Liquefaction tests were performed in a 38 cm^3 (2.54-cm o.d., 12.7-cm long) stainless-steel microautoclave, which was horizontally positioned in a fluidized sandbath and agitated at 360 cycles-per-minute by a Burrell wrist-action shaker. The microautoclave was rapidly heated to reaction temperature by immersion in the hot sand bath and quenched after reaction in water. The internal temperature and pressure were continuously monitored. The microautoclave was charged with approximately 3 g of coal or extraction product, 6 g of tetralin (if used), 1600 to 5000 ppm (based on metal) of a molybdenum-containing catalyst precursor (if used), 0.3 g of carbon disulfide, and 1000 psig hydrogen. When using a catalyst precursor, it was dissolved in only enough solvent to form a wet paste with the sample. The solvent was then removed, usually under vacuum at 60°C, before the liquefaction test. Liquefaction tests were carried out at 425°C for either 20 or 60 minutes. Liquefaction conversions were measured by sequential extraction with either of two sets of solvents -- methylene chloride/n-heptane or tetrahydrofuran/ cyclohexane -- using pressure filtration to separate the soluble products from the residues. Conversions were determined from the insoluble residues and are expressed on a dry, ash-free basis.

Results and Discussion

Sample 1 from the Burning Star mine was the first sample swollen and extracted in pyridine. Based on the as-received coal and the actual amount of solvent-free PIP recovered, 15% of this coal sample was extracted by pyridine. One portion of the PIP from the Soxhlet thimble was vacuum dried and another portion was extracted with supercritical CO_2 using the small column.

As previously mentioned, the objective of performing the SCF extraction was to remove the pyridine by a non-evaporative process that would avoid the formation of a vapor/liquid interface. A model based on the Peng-Robinson equation-of-state was used to estimate the vapor/liquid phase behavior for the CO_2/pyridine system (11). A binary interaction parameter of 0.080 was used in this calculation. Using this model, the mixture critical point at 40°C was estimated to be near 1160 psig. The operational conditions used, 2000 psig at 40°C, are well above this point. At these conditions, the CO_2 should initially dissolve in and expand the pyridine present in the sample, moving the interface out of the coal pores and quickly causing it to disappear without evaporation. The pyridine concentration in the pores would then be reduced by the continued addition of supercritical CO_2 until all of the physically entrapped pyridine was removed. As opposed to vacuum-drying, no surface-tension effects would be exerted on the walls of the pores by the leaving solvent. In fact, the SCF expansion of the pyridine phase may have the opposite effect in exerting a positive force, which would tend to maintain the porosity of the sample.

Both vacuum drying and SCF extraction should remove all of the physically entrapped, but not chemically associated, pyridine from the PIP. The elemental analyses in Table 1 show that the nitrogen contents of the vacuum-dried and SCF-extracted PIP are similar. Based upon elemental analyses and material balances, 6% to 10% pyridine is estimated to remain in the PIP after either procedure.

Table 2 contains the surface area and density results for both the vacuum-dried and SCF-extracted samples. Also shown in this table are the results from a CO_2-extraction experiment in which all of the conditions were the same as for the SCF extraction, except that the

temperature was maintained at 25°C. Under these subcritical conditions, the extraction would be performed with liquid CO_2. The results in Table 2 show that the vacuum-dried PIP has less nitrogen surface area and porosity than the starting coal, while the CO_2 surface area remains about the same. On the other hand, the end result after removal of the pyridine by SCF extraction is an increase in both the nitrogen and CO_2 surface areas and in the resulting porosity. Compared to vacuum drying, SCF extraction produces a PIP that has 6.5 times the nitrogen surface area, 1.9 times the CO_2 surface area, and 4.2 times the porosity.

The data in Table 2 also show that liquid-CO_2 extraction results in a product with nitrogen and CO_2 surface areas that are respectively equal to and greater than the untreated coal but less in both cases than the supercritical-CO_2 extracted sample. The porosity, however, appears to be more like the vacuum-dried sample than the one from supercritical-CO_2 extraction. This initial data supports the hypothesis that the SCF extraction not only eliminates surface-tension forces that would tend to collapse the expanded structure of the PIP but generates forces that help to maintain the expanded structure.

To further investigate this phenomenon, the Argonne Premium Coal sample was subjected to the same treatment described above, except the liquid-CO_2 extraction was not performed. The handling of the untreated coal and the Soxhlet extraction were performed under nitrogen to limit the exposure of this coal to air. This coal sample was found to be 33% soluble in pyridine (based on as-received coal and actual weights recovered). This is twice that of the Burning Star sample discussed above. Similar differences in pyridine extractability between premium and non-premium Illinois No. 6 coal samples have been reported (12,13). Surface area and density results for the vacuum-dried and SCF-extracted samples are also contained in Table 2. All of the trends noted previously for the Burning Star sample are observed in the results for the Argonne coal. The changes in the nitrogen surface areas are particularly noteworthy. The porosity achieved with the SCF extraction was nearly the same as for the Burning Star sample.

Analysis of the SCF-extracted PIP from the Burning Star sample over a period of time showed the increases in surface areas and porosity to be a transitory phenomenon. Surface area and porosity determinations made on fresh aliquots taken from the sample over a four-month period are shown in Figure 1. These results show that the nitrogen surface area, the carbon dioxide surface area, and the porosity decrease with time. The last reported nitrogen and porosity values are even less than for the starting coal and approach the values for the vacuum-dried sample, which are represented in Figure 1 by the open symbols.

Microautoclave liquefaction tests were performed on a second sample of the Burning Star coal which was swollen and extracted with pyridine as before. To prepare enough material, the large column was used for the SCF extraction. The pyridine solubility of this second sample was 23%, which is higher than the first sample of this coal but still less than the Argonne sample.

The vacuum-dried and SCF-extracted samples of the PIP from the second sample of Burning Star coal were used in both thermal and catalytic microautoclave liquefaction experiments to determine the effects of the different morphology on conversion. Ammonium heptamolybdate (AHM) was used as the catalyst precursor at about 5000 ppm (based on metal) in the catalytic tests. A summary of these results is contained in Figure 2. The first two pair of tests in this figure were made using tetralin,

both with and without AHM. The conversions to methylene chloride and heptane solubles were slightly higher in both cases for the SCF-extracted PIP than for the vacuum-dried sample, and the greatest difference occurred in the heptane conversion in the catalytic case. The last pair of tests was performed without added solvent, again with 5000 ppm AHM. In this case, the conversions were measured in tetrahydrofuran and cyclohexane. This particular liquefaction and solvent-analysis system accentuates the effects of the pretreatment procedures on the liquefaction conversions.

From these results, the morphological changes associated with the SCF-extracted samples appear to facilitate liquefaction of these samples, especially in the presence of a catalyst. A possible explanation is that the expanded structure caused by this treatment permits the catalyst precursor to better penetrate these samples during the impregnation procedure, resulting in the improved liquefaction conversions. Investigation in this area is continuing to further substantiate and understand these results.

Additional microautoclave tests on both the PSP and the PIP were performed to investigate the fate of these materials during liquefaction. Figure 3 shows the results of subjecting the PSP to liquefaction with and without solvent and catalyst. In these tests, the contact time at 425°C was 60 minutes and the catalyst precursor was ammonium tetrathiomolybdate (ATM) added from water. The first set of bars shows the pre-liquefaction solubilities of the PSP in tetrahydrofuran and cyclohexane. The next test shows that, in the absence of both catalyst and hydrogen-donor solvent, the solubility in tetrahydrofuran drops sharply while the cyclohexane solubility increases. The remaining data in Figure 3 show that the presence of either a hydrogen-donor solvent or catalyst prevents the retrogressive behavior observed in the absence of these compounds. In the data set shown, the presence of a catalyst provides higher conversions than when a hydrogen-donor solvent is used.

The liquefaction results for the SCF-extracted PIP are contained in Figure 4. No hydrogen-donor solvent was used in any of these tests. Adding ATM as previously described improved both the tetrahydrofuran and cyclohexane conversions. A further improvement in the conversions was also noted when the ATM was added from pyridine and then subjected to extraction with supercritical CO_2 to remove the pyridine. In this case, greater penetration of the ATM into the PIP is likely since the pyridine would re-swell the PIP and facilitate transport of the ATM into the particles. Removing the pyridine with supercritical CO_2 would prevent the ATM from being pulled back out of the particles with the leaving solvent, as might be the case if vacuum drying were used. This aspect of the work is under further investigation.

Summary

Our work has shown that a coal sample can be prepared with an expanded structure, that is, one in which the porosity is two to four times as great as the starting coal. This effect is due both to the removal of pyridine-soluble material and to the means of removing the residual pyridine from the insoluble portion. A non-evaporative procedure, such as SCF extraction, leaves the coal structure, at least temporarily, in an expanded state, whereas vacuum drying causes an immediate collapse of the extracted coal. Upon liquefaction, conversions were consistently

higher for samples subjected to SCF extraction compared to vacuum drying. The greatest benefit was observed in the catalytic tests.

Additional liquefaction tests were performed on both the PSP and PIP. The PSP formed a more refractory product when subjected to liquefaction in the absence of both a catalyst and a hydrogen-donor solvent. The presence of either the catalyst or the solvent reduced this retrogressive behavior. The benefit of a catalyst in this situation was marginally greater than the presence of a hydrogen-donor solvent. The importance of a catalyst was also noted in the liquefaction of the PIP. Dispersal of a catalyst precursor in a manner that may be superior to aqueous impregnation resulted in marginal improvements in liquefaction conversions of the PIP.

Acknowledgements

The authors would like to thank Jerry Foster and Richard Hlasnik for performing the experiments reported.

Disclaimer

Reference in this report to any specific product, process, or service is to facilitate understanding and does not imply its endorsement or favoring by the United States Department of Energy.

References

1. Derbyshire, F., Davis, A., and Lin, R. Energy & Fuels 1989, 3(4), 431-434.
2. Buchanan, A.C., Britt, P.F., and Poutsma, M.L. Prepr. Pap., Amer. Chem. Soc., Div. Fuel Chem. 1990, 35(1), 217-224.
3. Rincon, R.M. and Cruz, S. Fuel 1988, 67(8), 1162-1163.
4. Brenner, D. Fuel 1983, 62(11), 1347-1350.
5. Larsen, J.W., Green, T.K., Choudhury, P., and Kuemmerle, E.W. "Coal Structure," M.L. Gorbaty and K. Ouchi, eds., Adv. Chem. Ser. 1981, 192, 277-291.
6. Lucht, L.M., Larson, J.M., and Peppas, N.A. Energy & Fuels 1987, 1(1), 56-58.
7. Larsen, J.W., and Mohammadi, M. Energy & Fuels 1990, 4(1), 107-110.
8. Harris Jr., E.C., and Petersen, E.E. Fuel 1979, 58(8), 599-602.
9. Klotzkin, M.P. Fuel 1985, 64(8), 1092-1096.
10. Schmitt, W.J., Grieger-Block, R.A., and Chapman, T.W. "Chemical Engineering at Supercritical Fluid Conditions," M.E. Paulitis, et al., eds., 1983, Ann Arbor Science, Ann Arbor, 445-460.
11. Peng, D.-Y. and Robinson, D. B. Ind. Eng. Chem. Fundam. 1976, 15(1), 59-64.
12. Buchanan, D.H. and Mai, W. Prepr. Pap., Amer. Chem. Soc., Div. Fuel Chem. 1987, 32(4)m 293-300.
13. Buchanan, D.H., Osborne, K.R., Warfel, L.C., Mai, W., and Lucas, D. Energy & Fuels 1988, 2(2), 163-170.

Table 1. Elemental analyses.

Sample Designation	Moisture	Ash	C	H	O	N	S
		---------moisture free--------					
Burning Star Sample 1							
Untreated Coal	3.5	10.4	69.1	4.7	11.6	1.4	2.9
Pyridine-Insoluble Product							
Vacuum Dried	3.0	12.1	65.7	4.3	12.3	2.1	3.0
SC-CO_2 Extracted	3.4	11.1	67.0	4.3	11.9	2.3	2.9
Liquid CO_2 Extracted	4.5	11.4	66.8	4.2	12.9	2.5	3.0
Burning Star Sample 2							
Untreated Coal	2.1	8.6	70.6	5.0	12.0	1.5	2.4
Pyridine-Insoluble Product							
Vacuum Dried	1.0	9.8	69.6	4.7	13.4	2.5	2.5
SC-CO_2 Extracted	3.2	10.1	70.1	4.9	11.4	2.9	2.4
Pyridine-Soluble Product	10.5	0.6	80.7	6.0	8.8	2.4	1.2
Argonne Premium Sample							
Untreated Coal	4.5	14.8	65.6	4.5	9.4	1.2	4.9
Pyridine-Insoluble Product							
Vacuum Dried	2.4	17.4	63.0	4.1	10.5	2.2	4.8
SC-CO_2 Extracted	1.6	17.5	63.0	4.2	9.6	1.9	5.0

Table 2. Surface area and density results.

Sample Designation	Surface area, m^2/g		Density, g/cm^3		Porosity*
	N_2	CO_2	He	Hg	
Burning Star Sample 1					
Untreated Coal	12.3	93.4	1.47	1.33	0.10
Vacuum Dried	2.6	91.6	1.47	1.40	0.05
SC-CO_2 Extracted	17.0	170.7	1.46	1.16	0.21
Liquid CO_2 Extracted	12.6	143.9	1.47	1.38	0.06
Argonne Premium Sample					
Untreated Coal	25.8	76.8	1.46	1.38	0.05
Vacuum Dried	1.7	90.3	1.46	1.42	0.03
SC-CO_2 Extracted	36.0	111.2	1.47	1.19	0.19

*Porosity = Hg density(1/Hg density - 1/He density)

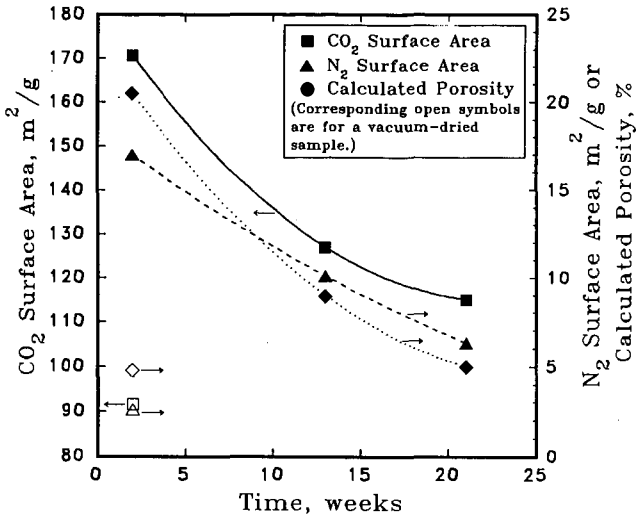

Figure 1. Morphological changes in the SCF-extracted pyridine-insoluble product with time.

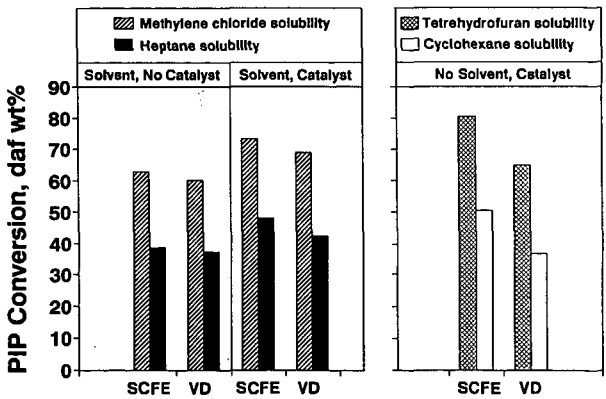

Figure 2. Thermal and catalytic liquefaction of SCF-extracted and vacuum-dried pyridine-insoluble product with and without tetralin and 5000 ppm AHM. SCFE - Supercritical Fluid Extracted. VD - Vacuum Dried. Micro-autoclave tests performed at 425°C, 20 min., 1000 psig hydrogen (cold).

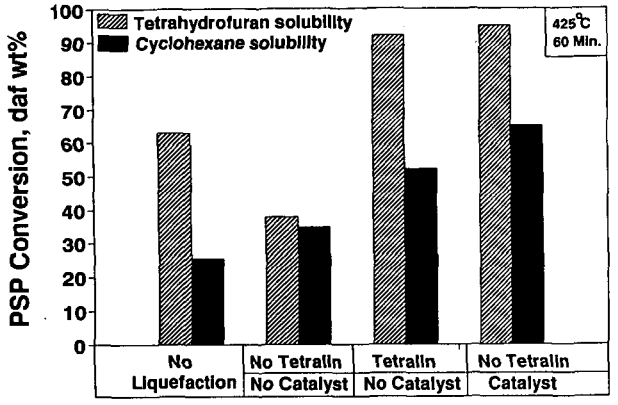

Figure 3. Conversion of pyridine-soluble product in thermal and catalytic liquefaction tests. 1600 ppm Mo added as ATM in the catalytic test. All tests were under 1000 psig hydrogen (cold).

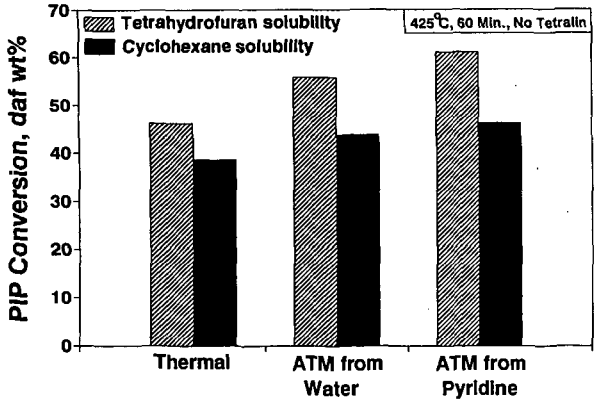

Figure 4. Thermal and catalytic liquefaction of SCF-extracted pyridine-insoluble product. 1600 ppm Mo as ATM applied by incipient wetness from water and by using a pyridine solution followed by SCF extraction. All tests were under 1000 psig hydrogen (cold).

MICROBIAL HYDROGENATION OF COAL AND DIPHENYL METHANE

M.I.H. Aleem[1], D. Bhattacharyya [2] G.P. Huffman[3], R.I. Kermode[2] M.V.S. Murty[1,2]
H. Venkatachalam[2], and M. Ashraf[1]
School of Biological Sciences[1], Department of Chemical Engineering[2], and
The Consortium for Fossil Fuel Liquefaction Science[3]
University of Kentucky, Lexington, Kentucky 40506

Keywords: Coal biohydrogenation, Microbial hydrogenation of diphenyl methane, H_2-transferring hydrogenase in *Sulfolobus* and *Desulfovibrio*.

ABSTRACT

The ability of *Desulfovibrio desulfuricans* and *Sulfolobus brieleyi* to catalyze the hydrogenation of coal and model compounds was investigated using Warburg-manometry in an atmosphere of H_2 without O_2. *D.desulfuricans* catalyzed H_2 uptake at a rate of 48 µmol/h and 0.0701 µmol/h with methylene blue (MB) and diphenyl methane (DPM) respectively, while the uptake rate by KCERL #91182 coal was 4.63 µmol/g coal/h. *S.brieleyi* was 8-12 times more effective catalyst yielding hydrogenation values of 619 µmol H_2 taken up/µmol MB/h and 0.5357 µmol H_2 taken up/ µmol DPM/h, while catalyzing the hydrogenation of coal at a rate of 44.1 µmol/g coal/h. The precipitated iron in the biodesulfurized coal by *S.brierleyi* was mainly in the form of super paramagnetic FeOOH as determined by the ^{57}Fe low temperature Mössbauer spectroscopy. These very fine paramagnetic particles (50-200 Å) exhibited good catalytic behaviour with higher liquefaction yield. Coals biotreated with *D.desulfuricans* also enhanced the chemical coal liquefaction yield by 5.67%.

INTRODUCTION

Bioprocessing of coal is emerging as a new technology for coal cleaning and coal conversion processes[1-7]. Coal conversion under milder conditions continues to offer the potential for improved liquefaction of coal. The overall success of liquefaction may entail improved coal pretreatment, disposable catalysts, upgrading of coal liquids in terms of removal of nitrogen and organic sulfur, and novel hydrogen generation and utilization techniques. The development of these techniques as applied to the above objectives offers an alternative approach if appropriate microbial cultures and environmental conditions can be established. Our earlier work[8-14] has demonstrated that under appropriate culture conditions, over 90% of the pyritic sulfur from coals can be removed by the mesophilic sulfur oxidizing autotrophic bacteria *Thiobacillus ferroxidans* and *Thiobacillus thioxidans*, but these bacteria were incapable of removing organic sulfur. However, the thermophilic archaebacterium *Sulfolobus brierleyi* was able to remove over 95% of the pyritic sulfur and over 30 % of the organic sulfur from the untreated coal when the cells of *S.brierleyi* were acclimatized.

The general reported area of biological conversion of substrate materials to higher quality fuels and chemicals are bioconversion of coal, lignite, and peat; hydrogen production by anaerobic microorganisms; and desulfurization. The aerobic biosolubilization of low-rank coal to polar water soluble products has been demonstrated[15-18]. The microbial desulfurization of oil-water emulsions and metabolism of dibenzothiophene has been demonstrated in our recent work[12]. In addition, the in-situ formation of catalyst, FeOOH crystals on coal particles in the presence of *Sulfolobus brierleyi* for enhanced liquefaction has been observed in our laboratories[10,14]. To our knowledge the direct microbial hydrogenation of untreated coal or the model compounds has not so far been demonstrated. We report here the results of our preliminary experiments.

MATERIALS AND METHODS

Organisms: Methods for growth and cell preparations for *sulfolobus brierleyi* have been described previously[9]. *Desulfovibrio desulfuricans* (ATCC strain No. 7757) was grown anaerobically in DSM medium #63 as described in the DSM catalogue (Deutche Sammlung Von Mikroorganismen: German Collection of Organisms), Grisebachstrasse 8, D-3400 Gottingen, Germany. The cells were obtained by centrifugation (under anaerobic conditions) at 10,000 x g for 30 minutes and washed thrice with 0.05M phosphate buffer(pH 7.4). The cells were suspended in the same buffer and kept anaerobic at 4°C until use.

Hydrogenase Assay: The enzyme activity in *D.desulfuricans* was determined by Warburg manometry at 30°C and pH 7.4 and at 60°C and pH 2 in *S.brierleyi* with H_2 as the electron donor and methylene blue as the electron acceptor in an atmosphere of H_2 under anaerobic conditions. The reaction mixture had a total volume of 3 ml and contained 0.2 ml of 40% KOH in the center well of the reaction

flask to absorb any CO_2 released. Where applicable, the concentration of methylene blue or diphenyl methane was 4.2 and 6.5 mM respectively. Where indicated the concentration of untreated KCERL #91182 coal was 4.5%. The side arm of the Warburg flasks contained 0.3ml of the bacterial suspensions (approximately 3mg protein). The reaction flasks were shaken for 10 minutes under H_2 atmosphere for temperature equilibriation before tipping-in the cells from the side arm. The H_2 uptake was recorded at 10-20 minute time intervals.

Mössbauer Spectroscopy: This technique provided a quantitative measurement of the reactions of pyrite and its transformations in Western Kentucky # 11 coal treated for biodesulfurization by *Sulfolobus brierleyi*. The techniques were essentially the same as described previously[14]. The coal liquefaction product yields (wt. %) determinations were performed by the University of Kentucky Center for Applied Energy Research using tetralin as a solvent, 800 psig H_2, and 427°C.

Samples for Mössbauer Spectroscopy: The samples of a Western Kentucky #11 coal were desulfurized using *Sulfolobus brierleyi* in a coal-water slurry aerated with air containing 10% CO_2.

RESULTS AND DISCUSSION

Comparative Rates of H_2-Uptake Catalyzed by *Sulfolobus brierleyi* and *Desulfovibrio desulfuricans*

Several aerobic and anaerobic bacteria possess hydrogenases but the ability of these microorganisms to catalyze the hydrogenation of coal and/or model compounds has not so far been reported. We have used an aerobic sulfur-oxidising thermoacidophilic archaebacterium *Sulfolobus brierleyi* and an anaerobic sulfate-reducing mesophilic bacterium *Desulfovibrio desulfuricans*. Since both organisms possess hydrogenase enzymes, the data in Table 1 show that both organisms transferred reducing equivalents, e.g., electrons from H_2 to methylene blue, a conventional method used for measuring the hydrogenase activity in microorganisms. The comparative H_2 uptake rates catalyzed by the cells of *D.desulfuricans* and *S.brierleyi* were 48 and 619 µmoles of methylene blue reduced per hour respectively. The respective specific activities of the cellular enzyme were about 16 and 206 µmoles/h/mg protein indicating that the hydrogenase from *S.brierleyi* was about 13 times more potent than the hydrogenase from *D.desulfuricans*. While the hydrogenase of *S.brierleyi* was oxygen insensitive, the enzyme from *D.desulfuricans* might have been inactivated during the preparation of cells since oxygen is extremely toxic to the growth of *D.desulfuricans*. Thus the much lower activity of hydrogenase might not reflect its real potential. It is indeed significant, however, that the cells from both organisms were able to transfer H_2 to both diphenyl methane and untreated coal. Here again the specific activity of H_2-transferring enzyme e.g. hydrogenase was much lower in *D.desulfuricans* than that in *S.brierleyi*. The significant H_2 transfer rate catalyzed by *S.brierleyi* to the model compound diphenyl methane as well as to the untreated coal at 60°C is an important finding since the archaebacterium is capable of not only removing sulfur from coal[8-13] but is also able to catalyze coal hydrogenation which should lead to higher liquefaction yields.

Mössbauer Spectroscopy of the Biodesulfurized Coal: The behaviour and transformation of pyrite in the bioprocessed coal can be demonstrated by ^{57}Fe Mössbauer spectroscopy. The data is shown in Figure 1 for two biodesulfurized Western Kentucky #11 coals from two different desulfurization tests (tests K87 and 22) in which the pyrite content was significantly reduced by pretreatment with *S.brierleyi*. In the upper spectrum (K87) the pyritic sulfur was decreased from 3.3% to 0.1%, while in the lower spectrum (K22) the pyritic sulfur content fell from 1.2 to 0.1%. In both cases significant amounts of iron-bearing oxidation products were precipitated from the solution. Ferric sulfate (Jarosite) was the main oxidation product of pyrite (upper spectrum). In the lower spectrum, iron precipitation occurred when the CO_2 was shut off, and was primarily in the form of superparamagnetic FeOOH which is easily distinguished from pyrite and Jarosite in low-temperature Mössbauer spectra. Such paramagnetic phases have very fine particle sizes (50-200 Å) and therefore, they exhibit good catalytic behaviour during during liquefaction as indicated by data in Table 2 where the liquefaction conversion of the parent coal for run 22 was compared to that of biodesulfurized samples taken before and after the disruption of the CO_2 flow which caused the precipitation of superparamagnetic FeOOH. The higher conversion percentage of liquefaction for sample 22B compared to sample 22A indicates the catalytic nature of FeOOH which raised the conversion percentages of the desulfurized coal back to about that of the untreated pyrite-rich coal. Hence the knowledge of the forms of iron in bioprocessed coal provided by Mössbauer spectroscopy can provide strategies for optimization of sulfur reduction and other conversion technologies.

Acknowledgements: This research was supported by a US Department of Energy contract # DE-FC22-90PC90029.

1. Couch, G.R., Biotechnology and Coal, IEA Coal Research Report., 1987, KTIS/TR 38, London.
2. EPRI Report, First Annual Workshop on Biological processing of Coal, 1988, EPRI ER-5709-SR, Palo Alto, California.
3. Ehrlich, H.L., and Holmes, D.S. (Editors), Workshop on Biotechnology for the Mining, Metal Refining, and Fossil Fuel Processing Industries, Wiley, New York, 1986.
4. Attia, Y.A.(Editor), Processing and Utilization of High-Sulfur Coals, Elsevier, Amsterdam, 1985.
5. Markuszewski, R., and Wheelock, T.D. (Editors), Processing and Utilization of High-Sulfur Coals III, Elsevier, Amsterdam, 1990.
6. Olson, G.I., Brinckman, F.E., and Iverson, W.P., Processing of Coal with Microorganisms. EPRI Final Report, EPRI AP-4472, 1986, Palo Alto, California.
7. Dugan, P.R., Microbiological Desulfurization of Coal and its Increased Monetary Value, Biotechnology, Bioengineering Symposium, 1986, 16, 185-204
8. Khalid, A.M. and Aleem, M.I.H., Biological Desulfurization of Coal by *Sulfolobus* and *Thiobacillus* species. Amer. Soc. Microbio. Annual Meeting., Miami Beach, Florida, Abstract 051, 1988.
9. Khalid, A.M., Bhattacharyya, D. and Aleem, M.I.H., Sulfur Metabolism and Coal Desulfurization Potential of *Sulfolobus brierleyi* and *Thiobacilli*, S.Yunker (Editor), Proc. Symposium on Biological Processing of Coal and Coal-Derived Substances, EPRI ER-6572, 1989, pp. 2-19 to 2-36, Palo Alto, California.
10. Bhattacharyya, D., Hsieh, M., Francis, H., Kermode, R.I., and Aleem, M.I.H., Biological Desulfurization of Coal by Mesophilic and Thermophilic Microorganisms, Resour., Conserv. Recycl., 1990,3,81-96.
11. Khalid, A.M., Bhattacharyya, D., and Aleem, M.I.H., Coal Desulfurization and Electron Transport-Linked Oxidation of Sulfur Compounds by *Thiobacillus* and *Sulfolobus* species. Pierce, G.E. (Editor), Development in Industrial Microbiology (Soc. Ind. Microbiology), 1990, 31,115-126
12. Khalid, A.M., Aleem, M.I.H., Kermode, R.I., and Bhattacharyya, D., Bioprocessing of Coal and Oil-Water Emultions and Microbial Metabolism of Dibenzothiophene. Resour., Conserv., Recycl., 1991,5 (in press)
13. Khalid, A.M., Bhattacharyya, D., Hseih, M., Kermode, R.I., and Aleem, M.I.H., Biological Desulfurization of Coal, Markuszewski, R., and Wheelock, T.D. (Editors), Third International Conference on Processing and Utilization of High-Sulfur Coals III, Elsevier, Amsterdam, 1990, pp. 469,480.
14. Huffman, G.P., Huggins, F.P., Francis, H.E., Mitra, S., and Shah, N., Structural Characterization of Sulfur in Bioprocessed Coal, Markuszewski, R., and Wheelock, T.D., (Editors), Third International Conference on Processing and Utilization of High-Sulfur Coals III, Elsevier, Amsterdam, 1990, pp. 23-32.
15. Cohen, M.S., Bowers, W.C., Aronson, H., Gray, E.T., Cell-free Solubilization of Coal by *Polyporus versicolor*, Appl. Environ. Microbio.., 1987, 53, 2840-43.
16. Pyne, J.W., Stewart, D.L., Fredricson, J., and Wilson, B.W., Solubilization of Leonardite by an Extracellular Fraction from *Coriolus versicolor*, Appl. Environ. Microbio.., 1987, 53, 2844-48.
17. Scot, C.D., Strandberg, G.W., and Lewis, N.S., Micribial Solubilization of Coal, Biotechnol. Prog., 1986, 2, 131-139.
18. Wilson, B.W., Bean, R.M., Franz, J.A., Thomas, B.L., Cohen, M.S., Aronson, H., and Grey, E.T., Microbial Conversion of Low Rank Coal: Characterization of Biodegraded Product, Energy Fuels, 1987, 1, 80-84.

Table 1

Comparative Rates of Hydrogen Uptake Catalyzed by *Sulfolobus brierleyi* and *Desulfovibrio desulfuricans*

Organism	Substrate	Hydrogen uptake
		μmol/g coal/h
S.brierleyi	Coal	44.10
D.desulfuricans	Coal	4.63
		μmol/μmol DPM*/h
S.brierleyi	DPM	0.5357
D.desulfuricans	DPM	0.0701
		μmol/μmol MB**/h
S.brierleyi	MB	619
D.desulfuricans	MB	48

See 'Materials and Methods' for experimental conditions.

* - DPM - Diphenyl methane ** - MB - Methylene blue

Table 2

Liquefaction product yields (wt.%) of biodesulfurized coal

Tetralin, 800 psig H_2 (ambient)

	385°C			427°C		
	Parent Coal	22A[a]	22B[b]	Parent Coal	22A[a]	22B[b]
Gas	2	12[c]	3	4	5	6
Oil	10		8	39	41	39
Asphaltene	22	24	20	32	29	33
Preasphaltene	39	21	36	13	10	12
IOM[d]	28					
Conversion	72	57	67	87	84	90

[a]Biotreated, before FeOOH precipitation. [b]Biotreated after FeOOH precipitation
[c]Gas and oil not determined separately for this sample. [d]Insoluble organic matter or residue.

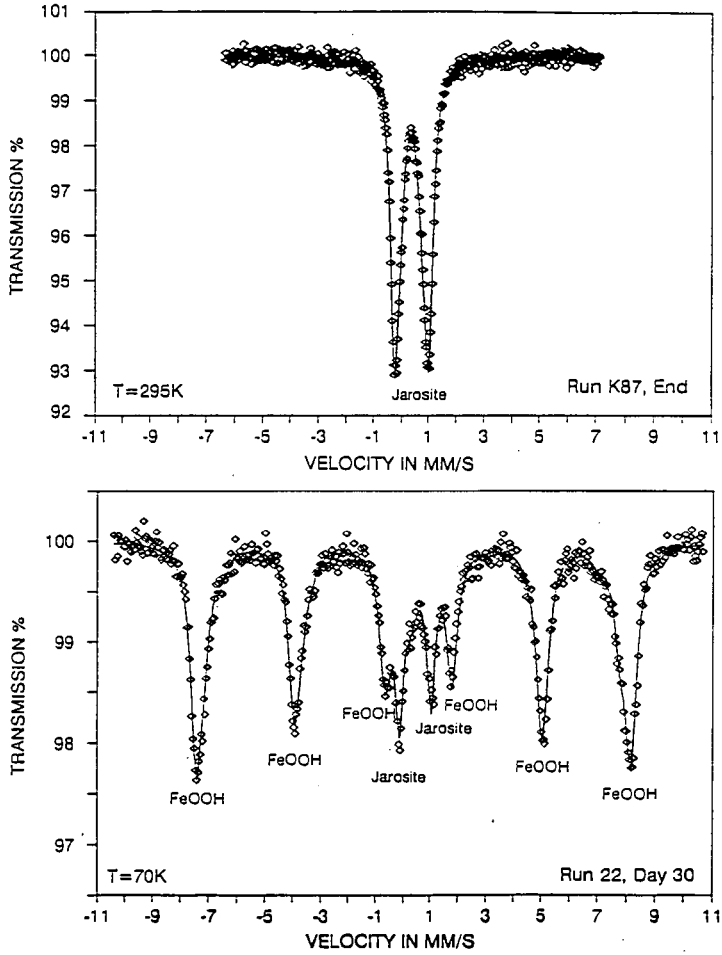

Fig. 1. Mössbauer spectra of biodesulfurized samples of Western Kentucky coals.

AGGLOMERATION OF LOW-RANK COAL AS A PRETREATMENT FOR DIRECT COAL LIQUEFACTION

G. A. Robbins, R. A. Winschel, C. L. Amos
CONSOLIDATION COAL COMPANY
Research & Development
4000 Brownsville Road
Library, PA 15129

Keywords: Oil Agglomeration, Direct Liquefaction, Coal Cleaning

INTRODUCTION

Oil agglomeration is an effective technique for recovering and deashing coal fines. In addition to conventional uses of oil agglomeration, certain features make it attractive as a pretreatment for coal liquefaction. The small coal grind size required for liquefaction may improve the release of mineral contaminants from the coal. These sizes may be more easily handled by oil agglomeration than by conventional cleaning methods. The use of process-derived oil eliminates the additional cost of the agglomerating oil. It also has been shown that pyrite is not effectively removed from coal fines by oil agglomeration (1), since its surface is readily coated by oil. Pyrite is recognized as a liquefaction catalyst (2) and retention of this mineral can be beneficial in liquefaction processes. The economic incentive for lowering the ash content of liquefaction feedstocks result from: 1) the potential of down-sizing or eliminating deashing equipment, 2) improved yields from more efficient ash rejection, 3) reduced erosion/abrasion of equipment, and 4) slightly improved organic throughputs resulting from reduced ash inventory in the system.

The goal of this work was to determine if coal liquefaction process oils are effective in cleaning low-rank coals (subbituminous and lignite) by agglomeration. Previous work of this nature in this laboratory has been limited to characterization of oils for the agglomeration of bituminous coal (3). The work reported here has been described in complete detail in DOE reports (4,5). The coals tested consisted of three subbituminous coals, a Texas lignite, and a bituminous coal (for comparison and establishing operating conditions). The agglomerating oils included petroleum-derived No. 2 diesel fuel and No. 6 fuel oil, two Lummus Integrated Two-Stage Liquefaction (ITSL) distillates from bituminous coal runs, and a Wilsonville ITSL distillate from a run with Texas lignite. Past bench-scale work at Consol using similar equipment has provided results which were scalable to commercial operation at 40 tph (6).

EXPERIMENTAL

The coals used in the tests are described in Table 1. All coals were run-of-mine; several were supplied previously ground. The agglomerating oils and surfactant are described below, and selected properties are shown in Table 2.

- Diesel Fuel No. 2 - Purchased locally.
- Fuel Oil No. 6 - API gravity 13, low sulfur grade.
- Lummus Run 3LCF9 - A sample of the 500 x 850°F distillate second-stage product produced in October 1982 at the Lummus ITSL PDU during a period of run 3LCF9 using Old Ben No. 1 Mine (Indiana V) coal.
- Lummus Run 3LCF7 - A composite sample of the 850°F⁻ distillate portion of the second-stage heavy-oil product made during Run 3LCF7 of the Lummus ITSL PDU with Old Ben No. 1 Mine (Indiana V) coal.

- Wilsonville Run 255 - A sample of the recycle distillate inventory (V-1074) from 5/2, 4, 6, 7/88 during Run 255, made while the plant processed Martin Lake (Texas) lignite, nominal b.p. about 650 x 1000°F.
- Cresylic Acid No. 83 Black (Merichem Company, Houston, Texas).

Agglomeration experiments were performed in a cylindrical stainless steel vessel (Figure 1). The drive motor is rated at 1700 rev/min. The test procedure is shown in Figure 2. A cylindrical heating mantle was used when tests were made above ambient temperature.

Inversion, or phase separation, was manifested by a distinct change in the sound produced by the mixing action and by changes in color and texture at the surface of the slurry. In some tests, additional oil was added to increase agglomerate size. The reject material was dried at 105°C to constant weight (at least two hours), and then weighed and ashed at 800C to constant weight (three hours or more).

The agglomerates were allowed to air-dry until they were visibly dry (16-48 hours). Moisture and ash were determined on the agglomerated products.

Organic recoveries, ash rejections, and ash balances were determined as shown below:

Organic Recovery =

$$\left[1 - \frac{\text{mass of dry reject - mass of ash in reject}}{\text{mass of MAF coal + mass of oil}}\right] \times 100\% \qquad (1)$$

Ash Rejection =

$$\left[\frac{\text{mass of coal ash charged - mass of ash in product}}{\text{mass of coal ash charged}}\right] \times 100\% \qquad (2)$$

Ash Balance =

$$\left[\frac{\text{mass (ash) in agglomerates + mass (ash) in dry reject}}{\text{mass of coal ash charged}}\right] \times 100\% \qquad (3)$$

Though not determined, oils were assumed to be ash-free for the calculations. The ash balance calculations (Table 3) do not account for any water-soluble ash. However, elemental analyses of products, rejects and water-soluble ash from two runs were used to obtain complete ash elemental balances and rejection selectivities.

RESULTS AND DISCUSSION

General

Results are reported for nineteen successful agglomeration tests performed with six coal samples (lignite through hvAb) and five different agglomerating oils. Unsuccessful trials are described in another report (4), but not presented here. Table 3 gives the conditions and results of all the successful agglomeration trials (i.e., those runs which produced agglomerates). Organic recoveries ranged from 85% to 100% and were greater than 98% for all the low-rank coal tests. Ash rejections ranged from -1% to 72%. The low-rank coal tests gave ash rejections of up to 56%. Ash balances were 73% to 108% (not accounting for water-soluble rejected ash).

After initial work with a variety of coals, efforts were concentrated on Texas lignite and Wyodak subbituminous coal. Of ten tests conducted with Texas lignite, four produced agglomerates with a petroleum oil and one produced agglomerates with a coal liquefaction oil (fortuitously, the lignite-derived oil). Ash rejection with

No. 6 fuel oil ranged from 39 to 56%, while the lignite-derived oil gave 39% ash rejection. Organic recoveries were always greater than 98% and ash balances ranged from 73% to 100%.

Wyodak subbituminous coal was successfully agglomerated with three different coal liquefaction oils and one petroleum-derived oil. Ash rejections with the coal liquefaction oils ranged from 6 to 19%. With No. 6 fuel oil, ash rejections were 1 to 15%. Organic recoveries were about 98% and ash balances ranged from 88 to 102%.

A chart of the coal/oil combinations used appears below.

CHART OF COAL/OIL COMBINATIONS TESTED FOR AGGLOMERATION

Oils	COALS					
	Texas Lignite	Wyodak (Coarse) Subbit.	Wyodak (Fine) Subbit.	Rosebud Subbit.	Kemmerer Subbit.	Pittsburgh Seam Bitum.
Diesel Oil	-	--	----	---	+	++
No. 6 Fuel Oil	++++	+	+	0	0	0
Lummus 3LCF9 Oil	-	+	++	++	+	+
Lummus 3LCF7 Oil	--	+	0	0	0	0
W'ville Run 255	+-	0	+	0	0	0

- = No agglomeration
+ = Agglomeration
0 = No test performed with this combination

The low-rank coals are ranked Kemmerer > Wyodak fine ≈ Wyodak coarse ≈ Rosebud > Texas lignite in terms of ease of agglomeration. Kemmerer coal appears to be equivalent to Pittsburgh seam coal in ease of agglomeration, but the Kemmerer coal had a very low initial ash content and thus gave low ash rejections. There was no difference evident in the response to agglomeration of -200 mesh (finely ground) compared with -28 mesh (coarsely ground) Wyodak coal. Some mineral liberation effect may have been evident, since the coarser grind size gave a maximum ash rejection of 10%, compared to 19% for the finer grind size.

The oils appear to be ranked No. 6 fuel oil > the three coal liquefaction oils > diesel oil in agglomerating ability. Every coal liquefaction oil successfully agglomerated one of the Wyodak coals, but no data are available to directly compare them in agglomeration of other coals. It appears that appropriate agglomeration temperatures for the oils are: room temperature for diesel oil and the two Lummus oils; 38°C for Wilsonville oil; and 54°C for No. 6 fuel oil. Note that no systematic attempt was made to optimize the agglomeration temperature for each oil. Precedent for effective temperatures for No. 6 fuel oil and the two Lummus oils was established in earlier work using bituminous coals (3).

Effects of Promoter and pH

It was reported elsewhere that cresylic acid promoted the agglomeration of lignite (7). Cresylic acid was used as a surfactant or additive in five runs, with the following effects: 1) it was necessary for the agglomeration of the lignite with the lignite-derived oil at the conditions tested (Run 35), 2) it appeared to improve ash rejection (Wyodak subbituminous coal (Runs 23 and 36), but not lignite), 3) it improved the slow kinetics of agglomeration of the lignite, and 4) it lowered the ash balance. In Run 30 (no cresylic acid), the induction period for phase inversion

was about 40 minutes. In Run 33, with cresylic acid, the induction period was about 6 minutes. Obviously, this has significant consequences for any commercial application of this technology. The lignite is the only coal that was successfully agglomerated which showed any significant kinetic limitation in agglomeration; the other coals had induction periods of two minutes or less. In Run 35, the induction time was about 12 minutes. A similar run made without cresylic acid was terminated after one hour without agglomeration. These results indicate that cresylic acid speeds up the agglomeration of the lignite.

In several agglomeration trials, the pH was adjusted by the addition of various reagents prior to oil addition, without effect in most cases. The one exception was Run 31, in which the slurry pH was adjusted from 6.8 to 2.0 by the addition of HCl. The run was otherwise identical to Run 30. The lower pH resulted in faster agglomeration (phase inversion after 9 minutes instead of 40 minutes), higher ash rejection (56% vs 46%) and a lower ash balance (73% vs 96%). This is very similar to some of the effects caused by the addition of cresylic acid. Note that cresylic acid had no effect on slurry pH.

Elemental Balances

It is necessary to analyze the rejected water (filtrate) to close ash and ash elemental balances. Complete ash and elemental balances were obtained from one agglomeration run with Martin Lake (Texas) lignite (Run 35) and one run with Clovis Point (Wyodak seam) subbituminous coal (Run 35).

Liquid and solid samples were analyzed in duplicate by ICP-atomic emission spectroscopy. Average elemental results were used to calculate a mass balance for ash and for each element. The balances for ash and ash elements relative to the feed coal (i.e., feed coal has 100% of each component) are shown in Figure 3. Ash elemental analyses for the feed coals are given in Table 1. Ash balances shown are on an SO_3-containing and an SO_3-free basis. SO_3 retention is an artifact of the ashing process. The SO_3-free ash balances are a better representation of the coal mineral balances. In coal liquefaction, the fate of the mineral matter is more important than the fate of the ash. For the Wyodak coal test (Run 36), ash rejection was 19.2% (whole-ash and SO_3-free ash bases). For the lignite test (Run 35), the ash rejection was 38.7% (SO_3-containing basis) and 44.3% (SO_3-free basis). This suggests that SO_3-free ash rejections may be uniformly greater than the whole-ash rejections reported for the lignite tests. This results from the selective retention of Ca (and hence SO_3) in the product from the lignite run. Except for ash and ash SO_3, all other components yield the same rejection results when treated on either basis. Overall ash balances were 93 to 96%. Ash balances for individual elements ranged from 89 to 113% for Run 35 and from 84 to 125% for Run 36. The balance for Na_2O was the highest (113% and 125%) observed. Other elements gave balances lower than 106%, with most in the 89 to 96% range. Sodium was greatly reduced in the product agglomerates, and most of it ended up in the water.

Shown in Figure 4 is the selectivity for rejection of each of the ash elements, computed on an SO_3-free basis, for each of the runs. Selectivity was obtained by:

$$\text{Selectivity for Rejection} = \frac{\text{wt oxide in product}}{\text{wt oxide in feed}} \times \frac{\text{wt ash in feed}}{\text{wt ash in product}} \times 100\% \qquad (4)$$

The values thus obtained are less than 100% for components selectively rejected from the product (i.e., rejected to a greater degree than the overall ash) and greater than 100% for components selectively retained in the product. It is evident that Al_2O_3, TiO_2, Fe_2O_3, CaO and MgO were selectively retained in the products and SiO_2 and Na_2O were selectively rejected from the projects in both runs, although retention of Fe_2O_3, CaO and MgO was small in Run 36 (Wyodak). K_2O was rejected and P_2O_5 retained in Run 35 (lignite), but no selectivity for either was observed in Run 36

(Wyodak). Also, ash SO_3 was retained in Run 35 (lignite), but showed no selectivity in Run 36 (Wyodak). The fates of the ash elements are clearly illustrated in Figures 3 and 4.

CONCLUSIONS

This work demonstrated that low-rank coals can be cleaned by agglomeration with coal liquefaction oils. To the authors' knowledge, this is the first time cleaning of low-rank coal by agglomeration with coal liquefaction oils has been demonstrated. It is expected that agglomeration performance, e.g., ash rejection and induction time could be further improved by additional testing.

The Texas lignite is readily cleaned by oil agglomeration, with ash rejections of 50% and higher possible. The Wyodak and Kemmerer coals used here appear less amenable to cleaning by agglomeration, the best ash rejections being about 15 to 20%. The Kemmerer coal may have been particularly difficulty to deash because of its low original ash content (3.6%). Rosebud coal showed little or no cleanability under the conditions used; however, the conditions may have been less than ideal.

Each of the coal liquefaction oils tested agglomerated at least one of the Wyodak coals. The apparent ranking of the coals in ease of agglomeration (not necessarily deashing) is Pittsburgh Seam ≈ Kemmerer > Wyodak fine ≈ Wyodak coarse ≈ Rosebud > lignite. The apparent ranking of the oils in agglomerating ability (but not deashing) is fuel oil No. 6 > the three coal liquefaction oils > diesel oil.

Ash elemental results show some form of iron, a potential liquefaction catalyst, is selectively retained in the agglomeration products. also selectively retained are the elements Ti, Ca and Mg. Sodium, a potential poison to supported catalysts is selectively rejected. The concentrations of all ash elements, even those that were selectively retained, are lower in the agglomerated product than in the feed coal.

ACKNOWLEDGMENTS

The Wilsonville oil sample and the low-rank coals were provided by Dr. Charles Cantrell from the Wilsonville pilot plant laboratory. Lummus-Crest, Inc. supplied the Lummus oils. Fuel oil was provided by Boswell Oil Co. of Dravosburg, Pennsylvania. Cresylic acid was provided by the Merichem Company, Houston, Texas. This work was funded by the U.S. Department of Energy under contract Nos. DE-AC22-84PC70018 and DE-AC22-89PC89883.

REFERENCES

1. Perrot, G. St. J.; Kinney, S. P. *Chem. Met. Engr.* 1921, 25 (5), 182.

2. Mazzoco, N. J.; Klunder, E. B.; Drastman, D. *Study of Catalytic Effects of Mineral Matter Level on Coal Reactivity*; U.S. Department of Energy, 1981; DOE/PETC/TR-81/1.

3. Winschel, R. A.; Burke, F. P. *Fuel* 1987, 66 851.

4. Winschel, R. A.; Robbins, G. A., Burke, F. P. "Coal Liquefaction Process Solvent Characterization and Evaluation, Technical Progress Report, April 1 through June 30, 1988"; DOE Contract No. DE-AC22-84PC70018, May 1989.

5. Burke, F. P.; Winschel, R. A.; Robbins, G. A. "Coal Liquefaction Process Solvent Characterization and Evaluation, Final Report"; DOE Contract No. DE-AC22-84PC70018, September 1989.

6. Theodore, F. W. in 4th Int. Symp. on Agglomeration; Capes, C.E., Ed.; AIME: Warrendale, PA, 1985; p. 883.

7. Ikura, M.; Kelly, J. F.; Capes, C. E. "Beneficiation of Lignite by Oil Agglomeration as an Integral Part of Coprocessing"; presentation at the 195th National Meeting of the American Chemical Society, Toronto, Ontario, Canada, June 1988, response to question about identity of surfactant used.

TABLE 1

FEED COAL IDENTIFICATION AND ANALYSES COAL/OIL AGGLOMERATION

Designation	Code	Mine	Seam	State	Apparent Rank	Moisture wt %, as det.	Ash, wt % MF
Pittsburgh Seam	MC	--	Pittsburgh	WV	hvAb	1.39	26.15
Wyodak (Coarse)	WC	Clovis Point	Upper & Lower Wyodak	WY	sub.	24.6	8.35
Wyodak (Fine)	WF	Clovis Point	Upper & Lower Wyodak	WY	sub.	20.8	8.41
Kemmerer	KC	Kemmerer	Adaville	WY	sub.	17.9	3.55
Texas Lignite	TC	Martin Lake	Wilcox	TX	lig.	25.9	15.4
Rosebud	RC	Rosebud	Rosebud	MT	sub.	22.98	7.41

Major Elements, Oxide wt % of Ash (As Determined)										
SiO_2	Al_2O_3	TiO_2	Fe_2O_3	CaO	MgO	Na_2O	K_2O	P_2O_5	SO_3	Unaccounted
Texas Lignite										
50.09	13.51	1.10	4.45	13.12	3.14	1.00	0.62	0.15	13.36	-0.54
Wyodak (Fine)										
28.88	13.32	0.70	6.46	22.60	3.80	1.67	0.25	0.70	22.06	-0.44

Notes and Code: Samples WC, WF, KC, TC and RC supplied by the Wilsonville pilot plant laboratory.
Sample MC supplied by Consol.
Sample WF supplied as -200 mesh.
Samples MC, WC, KC, TC and RC supplied as chunks, ground at Consol to -28 mesh.
Ash elemental analyses were not obtained from coals MC, WC, KC and RC.

TABLE 2

SPECIFIC GRAVITIES AND ^{1}H-NMR PROTON DISTRIBUTIONS OF AGGLOMERATION OILS AND ADDITIVE

Oil Designation	Specific Gravity	Cond Arom	Uncond Arom	Cyclic Alpha	Alkyl Alpha	Cyclic Beta	Alkyl Beta	Gamma
No. 2 diesel oil	0.842	2.9	6.0	4.8	7.7	13.5	39.0	26.1
No. 6 fuel oil	0.899	5.3	2.3	7.1	6.4	13.3	44.8	20.8
Lummus 3LCF9	1.041	20.3	6.6	16.4	9.0	20.0	16.6	11.1
Lummus 3LCF7	1.022	13.2	6.6	15.8	0.6	23.2	19.5	13.2
Wilsonville Run 255	0.931	7.5	5.2	13.6	8.8	19.2	29.5	16.2
Cresylic acid	-	1.9	24.5	7.4	35.5	4.5	12.5	5.3

TABLE 3

CONDITIONS AND RESULTS OF SUCCESSFUL AGGLOMERATION TRIALS

Run No.	Feed Coal	Agglom. Oil	Slurry pH, Initial/ Final (Agent)	Notes	Added Oil at Phase Inver-sion/ Total, mL	Product			MF Reject		Organic Recov., %	Ash Rejec-tion, %	Ash Bal., %
						Moisture, wt %	MF Ash, wt %	Air Dry Mass, g	Mass, g	Ash, wt %			
5	Pittsburgh	Diesel	6.1/10.0 (NaOH)	-	3/14	6.58	9.12	105.32	30.76	55.7	86.7	72.2	81.0
6	Pittsburgh	Diesel	6.1/8.5 (NaOH)	1	3/30	8.75	8.97	135.18	38.92	60.9	88.7	65.7	107.9
8	Pittsburgh	3LCF9	8.4/8.4	-	10/35	3.24	8.37	119.99	38.90	50.2	84.8	69.9	90.7
9	Kemmerer	3LCF9	7.3/7.3	-	8/14	14.2	2.83	134.38	0.71	64.2	99.8	10.4	102.1
11	Kemmerer	Diesel	7.3/7.3	-	8/22	10.3	2.62	126.65	1.18	81.1	99.8	18.3	107.9
20	Rosebud	3LCF9	6.3/6.3	-	7/25	8.56	6.05	130.16	0.11	52.9	100.0	-0.9	101.7
21	Rosebud	3LCF9	6.3/6.3	-	7/15	9.69	6.20	122.33	0.18	71.5	100.0	4.0	97.8
22	Wyodak coarse	3LCF9	5.2/5.2	-	13/25	9.83	6.02	131.60	0.18	62.0	99.9	9.2	92.2
26	Wyodak coarse	3LCF7	5.2/5.2	-	10/13	18.2	6.62	131.23	0.61	67.3	99.8	9.7	95.5
27	Wyodak coarse	#6 fuel	5.3/5.3	-	9/10	10.7	7.50	115.97	0.29	90.0	100.0	1.3	102.0
23	Wyodak fine	3LCF9	5.1/5.1	-	15/45	8.56	5.48	156.40	0.52	74.0	99.9	5.9	98.8
29	Wyodak fine	#6 fuel	5.2/5.2	-	10/25	21.7	5.66	159.03	1.14	77.4	99.8	15.4	95.3
36	Wyodak fine	3LCF9	5.1/5.1	2	21/21	12.8	5.76	133.89	2.43	25.4	98.4	19.2	88.2
37	Wyodak fine	Run 255	5.1/5.1	2	20/20	12.0	6.06	129.65	2.09	30.8	98.7	17.0	90.8
28	Texas lignite	#6 fuel	7.1/7.1	-	20/23	19.7	8.19	132.20	6.09	91.4	99.5	39.0	100.0
30	Texas lignite	#6 fuel	6.8/6.8	-	15/15	11.4	7.77	111.56	6.59	91.8	99.4	46.2	96.3
31	Texas lignite	#6 fuel	6.8/2.0 (HCl)	-	15/15	28.6	6.67	131.32	4.44	93.2	99.7	56.2	72.9
33	Texas lignite	#6 fuel	6.7/6.7	2	15/15	22.9	8.73	121.87	5.73	81.6	98.9	42.5	90.3
35	Texas lignite	Run 255	6.7/6.7	2	16/16	11.2	8.78	112.13	5.54	78.6	98.7	38.7	91.8

*Runs conducted at ambient temperature with diesel, 3LCF7 and 3LCF9 oils. Runs conducted at 38°C with Run 255 oil and 54°C with fuel oil #6.
Note 1: 25 g coal added after final oil addition.
Note 2: Promoted by 1.87 g cresylic acid.

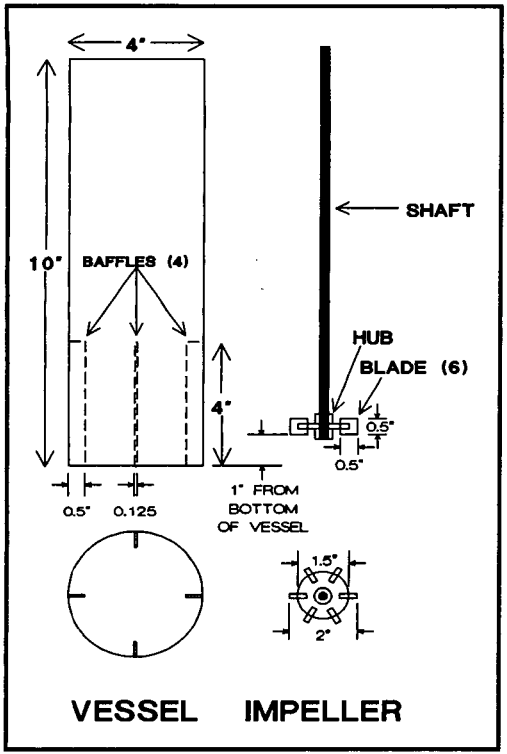

Figure 1. Apparatus for Bench-Scale Agglomeration Tests.

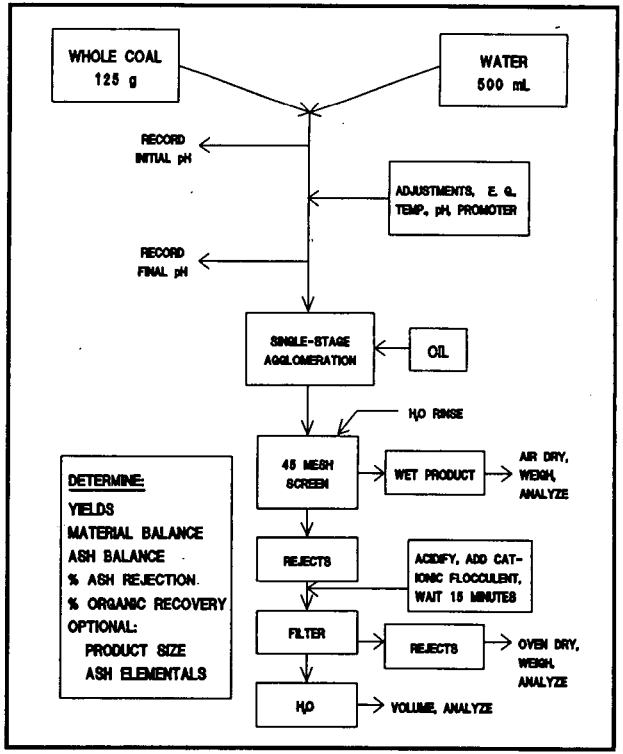

Figure 2. Agglomeration Test Procedure.

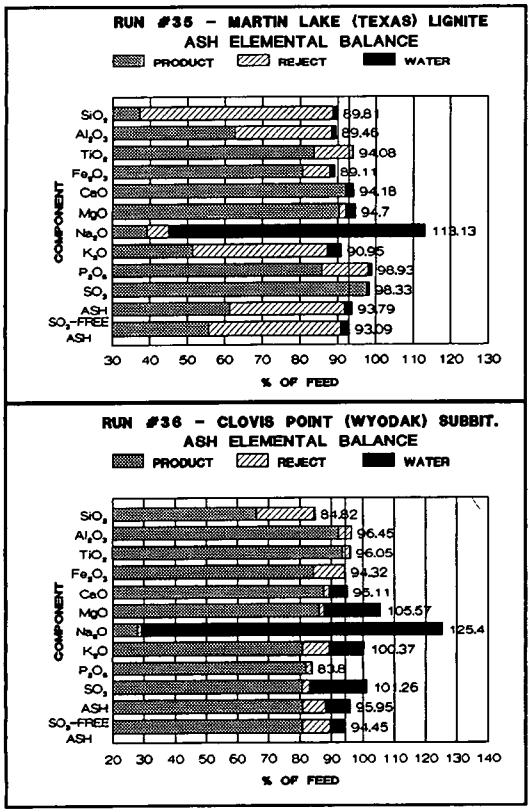

Figure 3. Ash Elemental Balance for Selected Runs.

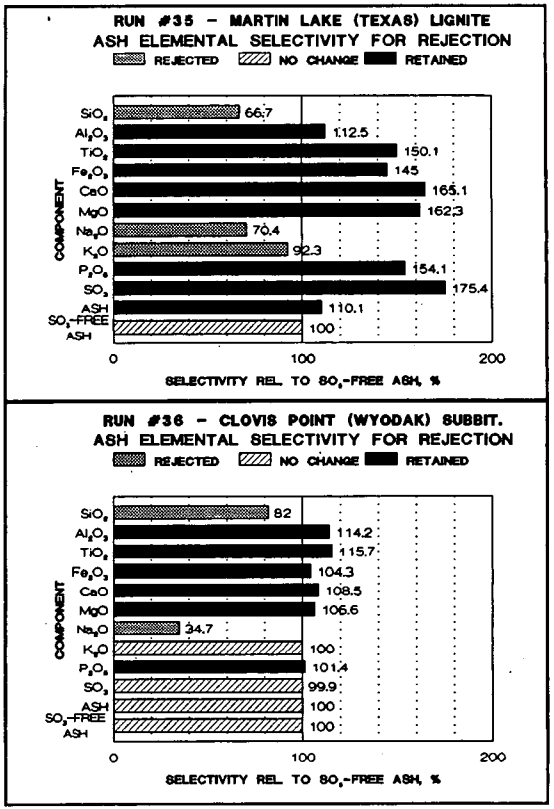

Figure 4. Ash Elemental Selectivity for Rejection for Selected Runs.

COAL BENEFICIATION: PROCESS DEVELOPMENT FOR LIQUEFACTION

Cronauer, Donald C. and Swanson, April J.
Amoco Oil Company, Naperville, IL 60566

ABSTRACT

Research was undertaken to evaluate techniques for removing mineral matter and unreactive components from coal for subsequent liquefaction. A sample of Burning Star Mine, Illinois No. 6 seam, bituminous coal was crushed, sieved, and gravity separated. The yields of fines (-60 mesh), float (1.40 gravity) and sink fractions were 30%, 46% and 24%, respectively. The ash levels were 14.9%, 6.5% and 18.3%, respectively. In the treatment of Martin Lake Texas lignite, the yield of fines was only 14%, but it contained 24% ash. To remove metal salts of organic acids in the lignite, the coarse fraction (+60 mesh) was treated with sulfurous acid and then gravity separated. The ash levels of the treated float and sink fractions were 5.6% and 39.3%, respectively. The overall recovery of the float fraction was 62%. Fractions of these coals were liquefied in a two-stage, bench-scale unit. The preferred feeds for high coal conversion were the float fractions. Both the sink and -60 mesh fine fractions should be rejected and used as fuel. However, in the case of Illinois No. 6 coal, the sink fraction gave a low-boiling product, presumably due to catalytic activity of the remaining mineral matter which had a high iron content.

INTRODUCTION

Several papers[1-5] have reported that coal liquefaction conversion is related to the concentration of macerals in the feed coal. Specifically, vitrinites convert well; liptinites liquefy well, but somewhat slowly; and inertinites liquefy only to a limited extent.

Coal beneficiation provides a means to separate the more reactive macerals from the mineral matter and less reactive macerals. Minerals can often be liberated by sufficient size reduction, and the unreactive maceral fusinite, which is charcoal-like, breaks into small particles during crushing and is concentrated in the fine fractions. Maceral density increases in the order liptinite < vitrinite < inertinite. Therefore, a portion of the inertinites along with minerals can be concentrated in the high-density fractions isolated by "sink/float" gravity separation.

In addition to mineral matter, low rank coals contain high levels of organic acids that bond cations. These consist of alkali and alkaline earth cations attached to carboxylates. Mochida et al.[6] have shown that pretreatment of lignites with 0.4M HCl significantly increased conversion during liquefaction. We use sulfurous acid because of its low cost, easy recoverability, and less corrosive nature. Sulfurous acid hydrolyzes organic acid salts present as exchangeable ions in low rank coals. The resulting metal bisulfites are washed from the coal and subsequently precipitated.

The second aspect of this paper deals with the liquefaction of treated coal samples. These are liquefied at conditions that are representative of those in use at the Advanced Coal Liquefaction Facility located in Wilsonville, AL. Descriptions of this process have been published.[7-9]

In this facility, unconverted solids are separated from liquefaction product using the ROSE-SR process of Kerr-McGee Corp. The mineral-rich "ash concentrate" stream carries along a sizable amount of heavy liquefaction product[10-11] which is either lost, used as fuel, or gasified. If the level of mineral matter and unreactive coal in the liquefaction feed stream is low, organic losses also are low.

The objectives of our work were to prepare samples of beneficiated Illinois No. 6 bituminous coal and Martin Lake, Texas, lignite and to evaluate the liquefaction behavoir of the various coal fractions using a two-stage, continuous flow unit.

EXPERIMENTAL

Fresh samples of Illinois No. 6 seam coal (Consolidation Coal Co. Burning Star Mine) and Martin Lake lignite (courtesy of Texas Utilities Electric, Dallas, TX) were obtained. Portions were pulverized under nitrogen and subsequently stored at 40°F.

Coal liquefaction solvents were obtained from the Wilsonville facility. They were derived from the liquefaction of similar coals (the same coal in the case of Illinois coal and Black Thunder subbituminous coal-derived product for the lignite runs.). Analyses are given in Table I.

Bulk samples of beneficiated coal were prepared at Hazen Research, Inc., Golden, CO. The Hazen facility includes coal crushing and wet screening units and a closed circuit sump-pump-cyclone unit. Water and magnetite media were added to the feed sump, the resulting slurry was pumped to the cyclone, and cyclone products were recycled to the sump. The specific gravity of each charge was determined and the amount of magnetite adjusted accordingly. The 8x60 mesh coal was added to the media at a ratio of about 1:5. When stable flow conditions were established, timed samples of the cyclone overflow and underflow were collected. The product samples were wet-screened at 60 mesh to remove the magnetite. Recovered coal was filter-pressed and dried under nitrogen at room temperature at Amoco.

A portion of the 8X60 mesh lignite was agitated with sulfur dioxide saturated water. The liquid was decanted, and the resulting lignite was flushed with water. The lignite was then wet screened with additional water flush prior to sampling and gravity separation.

Pilot plant-scale liquefaction runs were made in a two-stage unit that operates in a once-through, continuous mode with regard to H_2, solvent, and coal, and in a batch mode with regard to catalyst. Each stage functions as a continuous, stirred-tank reactor (CSTR), as previously described.[14]

Presulfided Amocat-1C catalyst was used in both reactors. Operating temperatures in the two stages were 790°F and 740°F, and nominal residence times were 1.5 and 1 hour, respectively. Feed slurries with Illinois No. 6 coal were 33/67 coal/solvent, and those with Martin Lake lignite were 25/75.

Catalyst was lined out for about one week. Subsequent samples were run for about three days. A solvent only period was also included.

Coal conversion is defined in terms of tetrahydrofuran (THF), toluene, and hexane soluble material as determined by Millipore filtration. Modified ASTM distillations were carried out with subsequent to atmospheric pressure. Products were analyzed for C, H (Leco), N (AutoKjeldahl), S (X-ray fluorescence), metals (Inductively Coupled Plasma spectroscopy/ICP).

Because resid is present in the feed solvent and is generated from the liquefaction of the lignite, the yield of resid from the lignite is calculated as a difference between the measured level in the product and that observed in the reference solvent only period. A "negative" yield may result if less resid is recovered than determined in the solvent only run.

RESULTS

Coal Beneficiation:

Illinois No. 6 Coal: The results of the beneficiation of fresh Illinois No. 6 coal are summarized in Figure 1. Coal crushing and screening resulted in a 70% recovery of 8X60 mesh coal, designated "coarse". The "fines" (-60 mesh) could not be handled by heavy media beneficiation. A sample of the coarse coal was sink/float beneficiated at a specific gravity of 1.35. This resulted in a 66/34 (dry coal basis) split between the overflow and underflow of the cyclone. On the basis of coal feed, the product yields were: 30% fines, 46% overflow (float), and 24% underflow (sink).

Results of elemental analyses of the recovered fractions are shown in Table II. The feed coal contained about 12% ash. The levels of ash in the fines and sink fractions were high at about 15% and 18%, respectively. The float fraction contained 6.5% ash. This latter value is typical of that observed for such treatment of Illinois coal.[12] High levels of sulfur in the fines and sink fractions were likely due to high levels of pyrite in these fractions. The fines had a marginally low H/C ratio when compared to the other samples (0.79 vs. 0.82); this may have been due to a high level of inertinites.

Martin Lake Lignite: As shown in Figure 2, the yield of fines from crushing was only 14%. An additional 2% was generated during the sulfurous acid treatment step. Sink/float separation of the treated lignite was done at a gravity of 1.40. The resulting split between overflow and underflow was 76/24 on a dry coal basis. The overall product distribution was: 16% fines, 62% overflow (float), and 22% underflow (sink).

Analyses of lignite samples are given in Table III. The fines fraction had a very high ash level (24% vs. 15% in the feed); therefore, this fraction might better be used as fuel and not as a liquefaction feedstock. Sulfurous acid treatment of the coarse fraction resulted in about a 30% reduction of ash. From previous studies[13] with this lignite, the 30% ash reduction was due primarily to the partial removal of alkali and alkaline earth metals. Gravity separation of the treated coarse fraction resulted in a sizable improvement in ash levels (5.6% vs. 39.3% for the float and sink fractions, respectively). However, further inspection of the sink fraction indicated that magnetite had not been effectively removed. The correct ash level in the sink fraction should be about 31%.

As also shown in Table III, there was an increase in sulfur and oxygen contents in the treated samples in comparison with the feed lignite. About 1 to 2% SO_2 was retained in the lignite as a result of treatment.

Liquefaction of Illinois No. 6 Coal Samples:

Differences were observed in conversion, resid yield, and hydrogen consumption from the liquefaction of the coal fractions, as shown in Table IV. The sink fraction produced low conversion to THF solubles, indicative of a high inertinite content. However, liquid product from the sink fraction was of very high quality, containing virtually no resid. Conversely, product from the float fraction was heavy, containing twice as much resid as product from the reference coarse coal. Therefore, sink/float beneficiation of Illinois No. 6 coal apparently does more than just change the level of unconverted coal and ash. The removal of some of the mineral components, which probably had catalytic properties, affected the upgrading aspects of liquefaction.

The effect of beneficiation is also indicated by the level of hydrogen consumption. An internal catalyst was present in the sink fraction, as indicated by hydrogen consumptions of 6.0% for the sink fraction and 4.7% for the float fraction. Iron was the likely internal catalyst as shown from the metals analyses in the unconverted coal solids (Table V). The sink sample was enriched in Fe, and to a lesser extent Ca.

Liquefaction of Martin Lake Lignite Samples:

Conversion of sulfurous acid-treated lignite to THF solubles was higher than that of the untreated lignite (Table VI), but the product contained much more resid. The second lignite liquefaction run was made only with samples of sulfurous acid treated lignite. Surprisingly, conversions of both the sink and float samples were lower than that of the coarse treated material that was used as their feedstock; see Table VII. The treated sink fraction gave only 69% conversion, which is consistent with a high inertinite level, as found in analogous laboratory-scale samples.[12]

The yield of resid from sulfurous acid-treated lignite was significantly higher than from untreated lignite, 12% vs. -6%, respectively. The difference between resid yields is not as great as shown, because contributions from solvent conversion changed throughout the run. However, there was at least 10% more resid produced from the treated lignite.

High yields of distillable product, defined as 975°F- liquids, were obtained from the treated float and sink fractions. In fact, no resid was recovered from processing the treated float fraction. There was a negative yield in the case of the sink fraction, indicating that some of the resid present in the feed solvent was being converted in addition to that generated from the lignite. The sink fraction was heavily contaminated with magnetite, which apparently acted as an upgrading catalyst.

CONCLUSIONS

Beneficiation of Illinois No. 6 coal using sequential size selection and gravity separation was effective in obtaining an improved coal liquefaction feedstock. However, there were both positive and negative effects. Ash and inertinite removal by rejection of the sink fraction would decrease liquid losses in the solids separation step. Offsetting this, internal mineral matter catalyst is also rejected thereby resulting in heavier liquefaction products. Sulfurous acid treatment and sink/float beneficiation of Martin Lake lignite is clearly beneficial. Ash levels in the lignite were reduced, conversion was slightly increased, and an all-distillate product was generated.

ACKNOWLEDGMENTS

The authors are indebted to Drs. J. T. Joseph and A. Basu for their effort in getting the sulfurous acid research underway, Drs. O. P. Mahajan and R. E. Lumpkin for advice, and DOE for partial funding under Contract DE-AC22-88PC88819.

REFERENCES

1. Given, P.H., Cronauer, D.C., Spackman, W., Lovell, H.L., Davis, A., Biswas, Fuel, 1975, 54, 40.
2. Dyrkacz, G.R., Horwitz, E.P., Fuel, 1982, 61, 3.
3. King, H.H., Dyrkacz, G.R., Winans, R.E., Fuel, 1984, 63, 341.
4. Parkash, S., Lali, K., Holuszko, M., du Plessis, M.P., Liq. Fuels Tech., 1985, 3(3), 345.
5. Semones, G.B., Carlin, D.H., Shi, X., Albright, L.F., Ind. Eng. Chem. Process Des. Dev., 1985, 24, 1091.
6. Mochida, I., et al., Fuel, 1983, 62, 471.
7. Lamb, C.W., Nalithan, R.V., Johnson, T.W., PREPRINTS: Am. Chem. Soc., Div. Fuel Sci., 1986, 31(4), 240.
8. Nalithan, R.V., Lee, J.M., Johnson,, TW., "Status of Coal Liquefacton at Wilsonville", DOE Contractor's Conference on Direct Coal Liquefaction, Monroeville, PA, October 20-22, 1986.
9. Gollakota, S.V., "Recent Progress at Wilsonville in the Direct Liquefaction of Two Low-ash Powder River Basin Coals and a Deep-cleaned Pittsburgh Seam Coal", DOE Contractor's Review Meeting on Direct Liquefaction, September 24—26, 1990.
10. Leet, W.A., Lee, F.S.-C., Gandy, R., Cronauer, D.C., PREPRINTS: Am. Chem. Soc., Div. Fuel Sci., 1987, 32(3), 352.
11. Leet, W.A., Cronauer, D.C., PREPRINTS: Am. Chem. Soc., Div. Fuel Sci., 1987, 32(3), 234.
12. Burke, F.P., personal communication.
13. Cronauer, D.C., Joseph, J.T., Davis, A., Quick, J.C., Luckie, P.T., "The Beneficiation of Martin Lake Texas Lignite", Submitted for Publication.
14. Tait, A.M., Swanson, A.J., Pacheco, M.A., "Multistage Coal Liquefaction Catalyst Development", Final Report EPRI Contract RP 2561-02, Submitted for Publication.

FIGURE 1

IL NO. 6 BENEFICIATION PROCEDURE

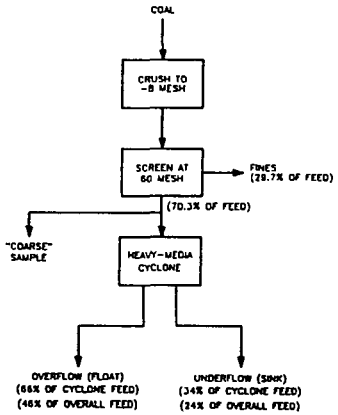

FIGURE 2

LIGNITE BENEFICIATION PROCEDURE

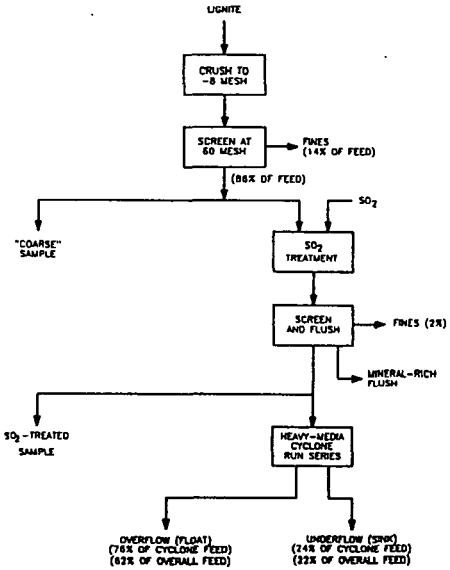

TABLE I

SOLVENT ANALYSES

Wilsonville Run	257	258
Wilsonville Coal	Il. No. 6	Black Thunder
Elemental Analyses, Wt%		
C	89.26	89.54
H	8.83	8.28
N	0.57	0.80
S	.08	.05
O	1.26	1.33
Distillation, Wt%		
IBP-650°F	0.36	8.83
650-975°F	55.78	53.70
975+°F	43.86	37.46
Solubility, Wt%		
THF insolubles	0.12	0.09
Toluene involubles	1.07	1.31
Hexane insolubles	7.96	15.33

TABLE II

ANALYSES OF BENEFICIATED IL NO. 6 COAL SAMPLES

ULTIMATE ANALYSES
(Dry Basis)

	Feed	Fines	Coarse	Overflow (Float)	Underflow (Sink)
Carbon	69.0	66.8	70.0	73.9	63.3
Hydrogen	4.7	4.4	4.8	5.1	4.3
Nitrogen	1.5	1.5	1.4	1.6	1.2
Sulfur	3.5	3.8	3.4	2.9	4.7
Ash	11.9	14.9	10.7	6.5	18.3
Oxygen (Diff)	9.4	8.6	9.7	10.0	8.2

TABLE III

ANALYSES OF BENEFICIATED HARTIN LAKE LIGNITE SAMPLES

ULTIMATE ANALYSES
(Dry Basis)

	Feed	Fines	Coarse	SO_2 Treated Coarse	Float	Sink
Carbon	63.3	56.8	64.4	63.4	68.3	43.3
Hydrogen	4.5	4.0	4.6	4.3	4.9	3.2
Nitrogen	1.2	1.2	1.2	1.3	1.4	0.9
Sulfur	1.5	1.6	1.5	2.4	1.5	2.8
Ash	14.6	23.6	13.1	10.0	5.6	39.3
Oxygen (Diff)	14.9	12.8	15.2	18.6	18.3	10.5

TABLE IV

LIQUEFACTION OF DENSITY BENEFICIATED IL. NO. 6 COAL

Coal Sample	Coarse	Float	Sink
Conversion	94.6	94.7	92.7
C_1-C_3 Hydrocarbon	3.2	6.5	6.0
C_4-360°F	9.5	5.4	12.5
360-650°F	38.4	29.5	35.8
650-975°F	23.6	26.5	27.7
975+°F Resid	9.3	18.6	0.5
Hydrogen Consumption	5.6	4.7	6.0

TABLE V

METALS IN UNCONVERTED COAL
(WEIGHTS ARE REPORTED RELATIVE TO ALUMINUM)

COAL	COARSE	FLOAT	SINK
CA	0.33	0.14	0.39
FE	2.07	1.57	2.72
MG	0.08	0.07	0.08
NA	0.05	0.05	0.04
K	0.22	0.23	0.23
TI	0.05	0.05	0.04
V	0.00	0.01	0.00
ZN	0.01	0.01	0.02
MN	0.00	0.01	0.00
CR	0.01	0.01	0.01
NI	0.00	0.01	0.00

TABLE VI

WATER/SO_2-BENEFICIATED MARTIN LAKE LIGNITE

LIGNITE SAMPLE	UNTREATED	WATER/SO_2 BENEFICIATED
CONVERSION	84.7	91.3
C_1-C_3 HYDROCARBON	7.3	6.2
C_4-360°F	13.2	14.1
360-650°F	33.5	33.1
650-975°F	24.7	9.6
975+°F	-6.3	12.0
HYDROGEN CONSUMPTION	7.4	7.4

RESULTS FROM UNTREATED FINES WERE INCONCLUSIVE BECAUSE THE PILOT PLANT OPERATED AT 0.5 RELATIVE SPACE VELOCITY DUE TO PUMPING DIFFICULTIES.

TABLE VII

COMBINED WATER/SO_2-BENEFICIATION AND DENSITY BENEFICIATION

LIGNITE SAMPLE	WATER/SO_2-BENEFICIATED		
	TREATED FEED	FLOAT	SINK
CONVERSION	91.0	86.4	68.9
C_1-C_3 HYDROCARBON	8.6	10.2	7.3
C_4-360°F	9.6	7.9	9.6
360-650°F	29.5	37.9	40.0
650-975°F	9.7	14.7	13.3
975+°F RESID	16.5	0	-23.0
HYDROGEN CONSUMPTION	6.4	6.4	8.4

CTSL™ CATALYTIC TWO-STAGE LIQUEFACTION COUPLED WITH COAL CLEANING

Alfred G. Comolli
Edward S. Johanson
Sudhir V. Panvelker
Gabriel A. Popper

Hydrocarbon Research, Inc.
100 Overlook Center, Suite 400
Princeton, New Jersey 08540

Key words: CTSL, Liquefaction, Beneficiation

Introduction

The overall objective of the CTSL process, which has been under DOE sponsored Bench-Scale development since 1983, is to achieve higher distillate yields, better quality products and to lower production and capital costs in relation to existing direct coal liquefaction technologies.

CTSL is a two-stage direct liquefaction process using close-coupled ebullated-bed reactors with the first stage operating at milder temperatures than the second stage (see Figure 1). Cobalt or nickel molybdenum on alumina catalysts are used to produce an all distillate slate of products with low sulfur and nitrogen contents. The lower temperature first stage promotes hydrogenation of the coal derived oils and of the recycled solvent prior to hydrocracking and additional heteroatom removal in the second stage.

Efforts have been underway to improve economics of the process by improving yields while reducing erosion and solids separation requirements through cleaning and beneficiation of the coal prior to liquefaction. Various techniques have been examined and tested in HRI's Bench-Scale unit. The Bench-Scale unit consists of a two-stage continuous ebullated-bed reactor system with on-line fractionation and optional on-line fixed-bed hydrotreating. At a nominal capacity of 50 pounds of coal per day, this size unit clearly defines process chemistry of a CSTR system with operations in a batch mode with respect to catalysts. Scale-up is on a 1/1 basis to the next larger PDU operations size on a selected equilibrium catalyst activity basis.

HRI has examined various modes of beneficiation//cleaning and evaluated them in both single and two-stage processing. Some of the techniques evaluated were: Heavy Media Cleaning, Electrostatic Precipitation, Oil Agglomeration of Pulverized Coal, Oil Agglomeration of Micronized Coal and Chemical Leaching.

Program

Present direct coal liquefaction studies at HRI are sponsored by DOE under a three year contract from 1988 to fiscal 1992. The baseline coal for cleaned and beneficiated coal studies has been Illinois #6 Burning Star coal with a typical analysis as shown in Table 1. The evaluations of heavy media and electrostatically cleaned coals occurred in a preceding contract in 1986, the oil agglomeration tests were recently completed in 1990.

Objective

The specific objectives of these studies were to quantify the reactivity differences resulting from beneficiation and to determine the processing advantages resulting in solid separation and product handling.

Studies

Five samples of Illinois #6 Burning Star Mine coal cleaned by different techniques were evaluated in continuous two-stage ebullated-bed bench-scale operations to examine their liquefaction behavior. The five cleaning techniques were: heavy media density separation, electrostatic precipitation, chemical leaching and oil agglomeration of pulverized and micronized coal. Operations and results of the cleaned coals were compared directly with a sample of conventionally cleaned (washed) coal from the mine and run at near identical conditions.

The coal samples were prepared at other laboratories briefly as follows: Heavy Media cleaned coal was cleaned at the Bituminous Coal Research facility in Monroeville, PA using magnetite as the dense phase with a total recovery of about 67 W% of the feed coal. Coal cleaned and beneficiated by electrostatic precipitation was prepared in a proprietary process by AED, Advanced Energy Dynamics of Natick, Mass. using a vertical belt separator feeding -70 mesh dried coal supplied by HRI. Recovery was 47% with a possible of 85% using a finer grind and rotary apparatus. The coal prepared by the "Ash Lite", Resource Engineering, Inc. leaching method also used -70 mesh coal from HRI and was prepared in Waltham, Mass. with a reported carbon yield of over 90% and an ash reduction to 3.6%. A major change was noted with an increase in the chlorine content of the coal from 0.06 W% to 1.8 W% after cleaning.

A coal sample was prepared at Homer City, PA by Bechtel under contract to DOE using spherical agglomeration with heptane and asphalt while feeding coal pulverized to less than 50 mesh. The coal was supplied with a hard asphalt content of 1.9 W% and 6.8 W% moisture and fed to the bench unit as received.

A fifth cleaned and beneficiated coal was prepared in Syracuse, NY by the proprietary "OTISCA" coal process and supplied as a 35% slurry in water. This coal is also cleaned using light solvents and a fine micronized coal of 5 micron median diameter. This was the only coal sample that required special handling to remove the water to low levels prior to liquefaction.

Maceral analysis were obtained on each of the coals in addition to ash and sulfur and other heteroatoms to determine the degree of beneficiation and effects on liquefaction and reactivity of the coals in a catalytic ebullated-bed system. A 1/32" extrudate catalyst of alumina promoted with nickel molybdate was used in all the sample evaluations and start-up oil was a Wilsonville derived heavy distillate from Illinois Coal. The operating conditions were 2500-2800 psig system pressure, reaction temperatures of 750/800°F, space velocity of 45 lbs/hr/ft^3 of settled catalyst and oil/coal ratio of 1.1/1 except for the OTISCA coal at about 2 to 1.

Results and Discussion

The coal prepared by REI using the "Ash Lite" process showed lower reactivity than other samples when screened on a microautoclave scale and failed due to a high pressure drop after operating 13 hours in the continuous bench-scale apparatus. As a result, only minimal data was obtained on this sample.

Each of the other coals operated smoothly showing enhanced reactivity when compared with untreated, mine washed coal. In the OTISCA coal/water slurry tests coals were compared on the same micronized size and water concentration basis.

The proximate and petrographic analysis of the coal samples are presented in Table 2. In each cleaning technique, the coals are beneficiated by a reduction in the inerts and fusinite. A summary of normalized yields and performance data are presented in Table 3. Comparisons are made with mine washed coal and with unagglomerated micronized coal.

Coal Conversion - The coal conversion follows the decrease in inertinite and ash contents showing higher conversion ranging from 89 to 96 W%. The lower coal conversions for the micronized coal studies may be attributed to the use of 10% lower slurry coal concentration and subsequent lower residence time.

Resid Conversion - Residual oil or 975°F+ conversion (basis = 100-unconverted coal and residual oil) is considerably improved as the ash content is reduced, ranging from 82 to 92% for the lowest ash coal.

Distillate Yields - Distillate yields follow a similar pattern, ranging from 66 to 69% for the uncleaned coals to 71 to 76 W% MAF for the cleaned and beneficiated coals. A bar chart comparison is shown in Figure 2 with the spherical oil agglomerated cleaned coal showing the highest yield at 76.2 W% of MAF coal. The electrostatically cleaned coal falls outside the pattern; this may be the result of some oxidation as shown by high sulfate sulfurs.

Product Quality - The quality of the oils produced was generally enhanced by cleaning, showing higher hydrogen contents and lower heteroatom levels. Table 4 illustrates the improved quality of the 500-650°F product as obtained with coal cleaned by spherical agglomeration.

Conclusions

- Coal cleaning and beneficiation (reduction of inert organic matter) by methods studied herein produces higher coal conversion and distillate yields in ebullated bed reaction systems.
- The improved productivity is accompanied by lower solid removal requirements and a probable lower erosion rate in let-down valves and lines.
- The highest yields were obtained with the heavy media cleaned and spherical oil agglomeration products.
- Residual oil conversion appears to correspond directly with ash content (see Figure 3) which may be the result of reducing catalyst poisons.

Economic studies are currently underway to determine the product cost benefit of using cleaned coal techniques. The two methods currently under consideration based on the results of this study are heavy media and spherical oil agglomeration cleaning.

Acknowledgments

The authors thank the U.S. Department of Energy and Pittsburgh Energy Technology Center and Drs. Edgar B. Klunder, Project Manager, Richard F. Hickey, Supervisory Chemical Engineer at PETC, Dr. Eneo Moroni of DOE Germantown, and the HRI staff for their technical support and guidance in this work.

References

1. A.G. Comolli, et al "Low Severity Catalytic Two-Stage Liquefaction Process - Illinois Coal Studies", DOE/PC/80002-T2, September, 1988.

2. A.G. Comolli, et al "Two Stage Close-Coupled Catalytic Liquefaction of Coal", Seventh Quarterly Report, DOE-88818-7, 1 April 1990-30 June 1990.

3. A. Davis, et al "Catalyst Dispersion and Activity under Conditions of Temperature-Staged Liquefaction", Technical Progress Report, DOE PC-898774, July to September 1990.

4. Mike Schaal, Horst Huettenhain and Shelby Rogers, "Spherical Agglomeration of an Advanced Physical Fine Coal Cleaning Technology", Bechtel Research and Development under DOE, EPRI Contract 1988-1990.

TABLE 1

FEED COAL ANALYSES

ILLINOIS NO. 6 BURNING STAR MINE

Feed Designation	(Run-of-Mine)	(Agglomerated)
Ultimate Analysis (W%, Dry Basis)		
Carbon	65.12	74.75
Hydrogen	4.57	5.23
Sulfur	3.80	2.90
Nitrogen	1.33	1.53
Ash	15.21	4.62
Oxygen (by difference)	9.97	10.97
Sulfur Forms (W%, Dry Basis)		
Sulfate	0.12	0.05
Pyrite	1.84	0.59
Organic	1.74	2.23
Mineral Analysis of Ash (W%, Ignited		
Silica, SiO_2	49.50	38.40
Alumina, Al_2O_3	19.62	18.00
Titania, TiO_2	0.90	0.99
Ferric Oxide, Fe_2O_3	20.52	28.02
Lime, CaO	4.08	4.96
Magnesia, MgO	1.04	1.10
Potassium Oxide, K_2O	1.76	1.70
Sodium Oxide, Na_2O	0.85	1.30
Sulfur Trioxide, SO_3	1.09	4.11
Phosphorous Pentoxide, P_2O_5	0.31	0.31
Undetermined	0.33	1.11

TABLE 2

CLEANED, BENEFICIATED COAL ANALYSIS

Ultimate, W% Dry	Mine Washed	Heavy Media Cleaned	Electrostatic Cleaned	Chemical Cleaning	Oil Agglom. Pulverized	Oil Agglom. Micronized	Micronized Unagglom.
Carbon	70.4	73.9	74.3	74.0	74.8	75.9	69.3
Hydrogen	4.5	4.9	4.7	4.8	5.2	5.2	4.5
Nitrogen	1.4	1.5	1.5	1.9	1.5	1.5	1.3
Sulfur	3.6	2.8	3.1	3.2	2.9	2.7	3.5
Ash	10.6	5.8	4.9	3.6	4.6	3.5	10.6
Oxygen (Diff.)	9.5	12.1	11.4	10.8	11.0	11.3	10.7
Sulfur Forms, W% Dry							
Sulfate	0.12	0.25	0.30	0.01	0.05	0.07	0.11
Pyrite	1.8	0.5	0.7	1.1	0.6	0.6	1.3
Organic	1.7	2.1	2.0	2.3	2.2	2.1	2.0
Petrographic, V%							
Total Reactives	88.2	91.5	92.6	90.1	91.9	84.5(1)	81.1(1)
Total Inerts	11.8	8.5	7.4	9.9	8.1	15.5	19.9
Fusinite	1.9	0.3	0.5	0.8	3.3	NA	NA

(1) Performed at a different laboratory

TABLE 3

YIELDS AND PERFORMANCE OF CLEANED COALS

	Mine Washed	Heavy Media Cleaned	Electrostatic Cleaned	Oil Agglom. Pulverized	Oil Agglom. Micronized	Micronized Unagglom.
Yields, W% MAF						
C_1-C_3	5.9	6.2	6.7	7.3	8.3	5.6
C_4-390°F	17.1	19.0	18.9	22.3	21.6	18.1
390-650°F	32.9	35.7	32.4	33.1	39.6	29.0
650-975°F	19.2	18.6	20.1	17.3	11.9	19.2
975°F+	8.3	8.3	9.5	4.9	1.4	7.5
Performance, W% MAF						
Coal Conversion	93.0	96	96.2	95.4	93.3	89.3
975°F+ Conv.	84.7	87.8	86.6	90.2	91.9	82
C_4-975°F+ Yield	69.2	73.3	71.4	76.2	73.1	66.3
Hydrogen Consumption	7.1	7.5	7.3	7.0	7.9	6.7

TABLE 4

DETAILED COMPARISON OF SPHERICAL AGGLOMERATED COAL

Coal Feed	Agglomerated		R-O-M
Ash in Coal Feed, W%	4.62	4.62	15.21
NiMo Catalyst Age. Lb Coal/Lb Cat.	106	233	319
Yields, W% MAF Coal			
C_1-C_3 Hydrocarbon Gases	7.9	7.6	8.9
C_4-975°F Liquids	75.0	76.2	68.8
975°F+ Residual Oil	2.0	5.1	7.1
H_2O, NH_3, H_2S, CO_x	17.1	13.8	16.4
Hydrogen Consumption	7.7	7.4	7.4
Coal Conversion	94.5	95.4	93.7
Product (Recycle) Resid. Conc., W%	16.6	26.7	31.0
Properties, 500-650°F Product			
Hydrogen, W%	11.57	11.39	11.08
Nitrogen, W%	0.11	0.10	0.13
Sulfur, W%	<0.01	<0.01	<0.02

HRI EBULLATING-BED CATALYTIC TWO-STAGE COAL LIQUEFACTION (CTSL) PROCESS

SIMPLIFIED FLOW PLAN

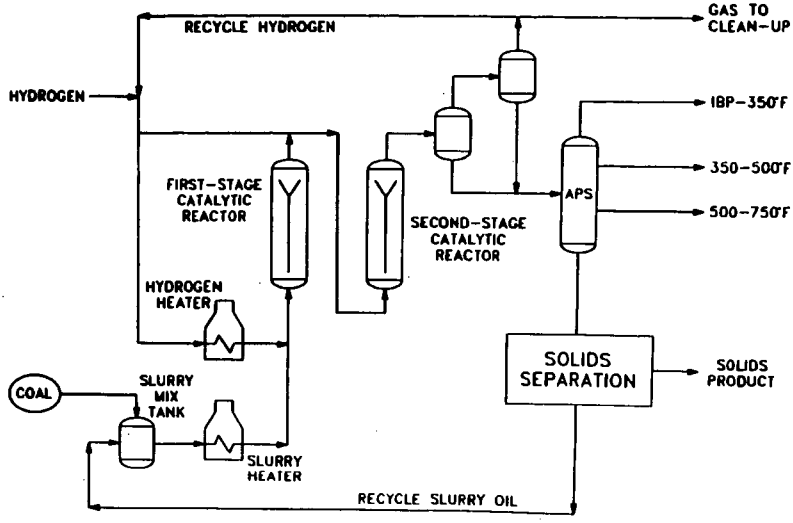

FIGURE 1

FIGURE 2

CLEANING METHOD EFFECT ON DISTILLATE YIELDS

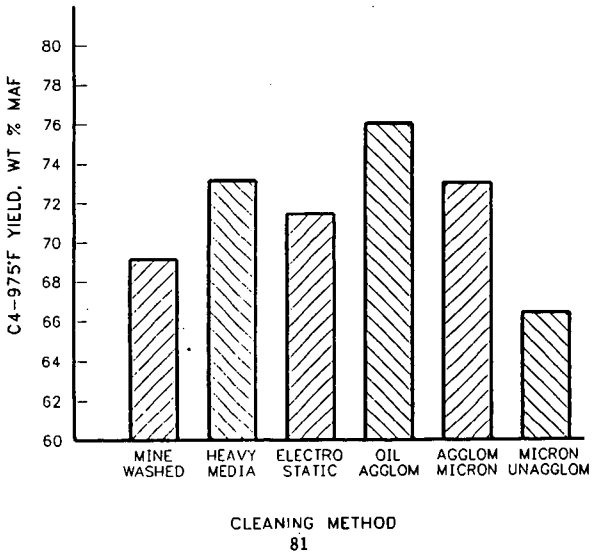

FIGURE 3

ASH EFFECT ON RESIDUAL
OIL CONVERSIONS IN EBULLATED BEDS

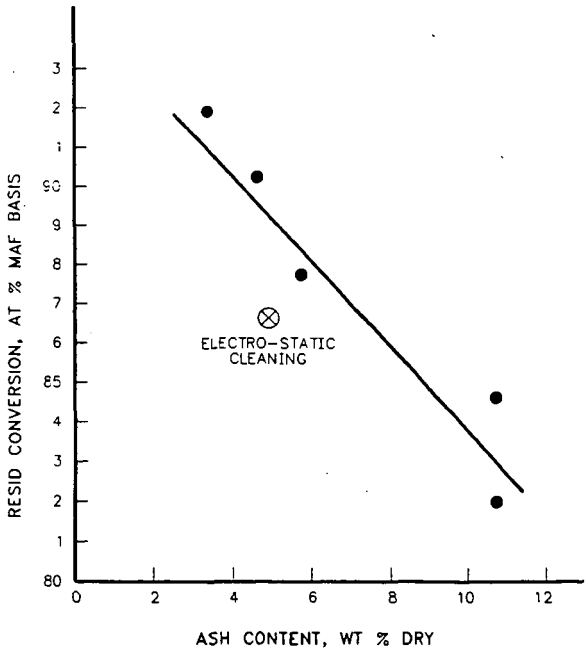

PRECONVERSION TREATMENTS OF LOW-RANK COAL

John R. Rindt, Melanie D. Hetland, Randal S. Sauer,
William M. Sukalski, and Leslie W. Haug
University of North Dakota Energy and Environmental Research Center
Box 8213, University Station
Grand Forks, ND 58202

Keywords: direct liquefaction, low-severity preconversion treatments

INTRODUCTION

Coal can be converted to very high yields of oil using a two-stage processing approach. To obtain even higher yields, however, it may be necessary to control the processing conditions to which coal is subjected in a manner that significantly reduces the role that repolymerization, recombination, and/or coking reactions play in the conversion process. Improvements in conversion and distillate yields may be possible if the conversion stage is subdivided into a low-severity preconversion treatment and a noncatalytic conversion step. This multistep first stage could produce a completely soluble product, theoretically increasing the effectiveness of the second-stage catalytic upgrading.

EXPERIMENTAL METHODS

A three-year program, funded by the U.S. Department of Energy under Contract Number DE-FC21-86MC10637, is underway to investigate various preconversion treatments and methods of increasing the conversion of LRCs to soluble material during the first stage. As a first step, low-severity preconversion treatments were screened to evaluate their impact on the direct liquefaction of Indian Head lignite. Several schemes were devised, and an experimental matrix was developed to screen them. Screening was carried out using the 20-cm^3 microreactor system and the 1-gallon hot-charge autoclave system. Six pretreatment schemes were tested in each system. For comparative purposes, two single-step tests were performed in the microreactor system using H_2 as the reductant: one at 372°C and the other at 423°C.

Testing proceeded in two steps. The first step consisted of the preconversion treatment at the matrix-specified temperature for 60 minutes. In the case of the microreactor system, half of the microreactors were removed after preconversion treatment and the products analyzed. The remaining six duplicate microreactors were charged with hydrogen and treated at approximately 410°C for 20 minutes. When the autoclave system was used, a sample was removed for analysis following the preconversion treatment. The remaining material was then reacted with H_2 at nominally 410°C for 20 minutes. The higher than usual, first-stage temperatures were used during these studies in order to highlight the differences between the products.

RESULTS AND DISCUSSION

It should be kept in mind that, for this discussion, liquefaction is considered to be comprised of two steps: the first stage and the catalytic upgrading (second) stage. Only preconversion treatment and the first stage were studied during this work; catalytic upgrading of the products was not studied.

Microreactor Tests

Preconversion Treatment Screening Tests The conversions to THF solubles that were achieved by the six preconversion treatment schemes screened in the microreactor system are presented in Table 1. The table presents the conversions to THF-soluble material after the preconversion treatment and after the first-stage processing. Initial discussion will focus on the conversion following the first-stage processing.

The first reactant combination consisted of Indian Head lignite, A04 (coal-derived anthracene oil) solvent, and H_2. Conversions achieved with this combination after preconversion treatment and subsequent first-stage processing ranged from 37.1% at a preconversion treatment temperature of 175°C to 67.4% at a temperature of 110°C. This combination was compared with the second scheme, which consisted of lignite, A04 solvent, and CO. It was hypothesized that the nascent hydrogen produced during the water/gas shift reaction ($CO + H_2O \rightarrow CO_2 + 2H\cdot \rightarrow CO_2 + H_2$) would be used more readily by the coal than hydrogen added as the reducing gas. Differences were noted in the conversion to THF solubles of the two schemes. These differences increased as the preconversion treatment temperature increased, so that a marked difference was noted at 250°C. At this temperature, the conversion for the A04/H_2 combination was 63.4% and the conversion for the A04/CO combination was 79.1%. The water/gas shift reaction is more active at 250°C than it is at the lower treatment temperatures. Therefore, it appears that the nascent hydrogen was more readily used by the coal than the hydrogen that was added as the reducing gas.

The third combination tested consisted of lignite, cresylic acid (CA1), and CO. This combination was chosen to determine if some of the material that physically prohibits the reaction of the coal with the hydrogen could be extracted with CA1. The results did not indicate that this was the case, as the CA1/CO scheme resulted in lower conversions at each temperature than did the A04/CO combination. For example, at 175°C the CA1/CO combination resulted in a 26.4% conversion, while the A04/CO scheme's conversion was 40.7%. At 250°C, the CA1/CO conversion was 72.1%, compared with 79.1% conversion for the A04/CO scheme.

The fourth combination made use of lignite, CA1, CO, and sodium. The use of sodium as a promoter for the addition of hydrogen to the coal structure was evaluated in this combination. A substantial increase in conversion (from 72.1% to 92.9%) was noted when sodium was present in the system at 250°C. Based upon the limited data available, it appears that sodium did promote the addition of hydrogen to the coal structure.

The fifth combination made use of lignite and tetralin in the absence of a reducing gas to determine if hydrogen transferred directly from the solvent to the coal. This approach was quite successful at the lowest preconversion treatment temperature (110°C), achieving an 87.5% conversion. A relatively low conversion of 56.4% was noted at 250°C, presumably due to the absence of CO as a reducing gas and its part in the water/gas shift reaction.

The sixth combination was performed using lignite, tetralin, and CO to determine if the hydrogen-donating solvent requires a reducing gas in order for the hydrogen transfer to take place. At 110°C, the tetralin-only system achieved an 87.5% conversion, while the tetralin/CO combination achieved a 48.8% conversion. The results were reversed at 250°C, where the tetralin/CO combination achieved a conversion of 86.3% and the conversion of the tetralin-only scheme was 56.4%. Presumably the water/gas shift reaction was a factor in the higher conversion of the tetralin/CO combination at 250°C.

Single-Step Processing Table 2 presents the conversions achieved during single-step processing using the microreactor system. The tests were performed for comparison to the first six preconversion treatment screening tests. The average conversion to THF solubles using tetralin as the solvent was approximately 90% during single-step processing at 430°C. This is slightly better than the conversion attained at a preconversion treatment temperature of 250°C for the tetralin/CO combination or that achieved by the tetralin alone at a treatment temperature of 110°C. It does not appear that the preconversion treatment had a significant impact on the conversion of lignite to THF-soluble material when tetralin was used as the solvent.

The conversion to THF solubles achieved using A04 as the solvent at a processing temperature of 430°C probably averaged near 60%, as the 76.4% conversion seems to be

out of line with the other two values. A conversion of 60% during single-step processing was somewhat less than that attained after preconversion treatment at either 110° or 250°C, but is greater than that achieved after treatment at 175°C. As was the case with tetralin, it does not appear the preconversion treatment had a significant impact on the conversion of lignite to THF-soluble material when AO4 was the solvent.

When CA1 was used as the solvent during single-step processing at 430°C, the resulting conversion was approximately 45%. This value is considerably worse than that achieved by preconversion treatment at either 110° or 250°C. This seems to indicate that preconversion treatment can improve the conversion of lignite to THF-soluble material when a cresylic acid solvent is used.

Autoclave Tests

The remaining six preconversion screening tests (the seventh through twelfth combinations) were performed in the 1-gallon, hot-charge autoclave system at a nominal temperature of 175°C. The data obtained during these tests are presented in Table 3. Most of the tests were performed to investigate the addition of H_2S to the combinations of solvents and reducing gases tested in the first six (microreactor) tests. Previous studies indicated that the use of H_2S catalyzes the reactor walls. Relative to the reactor volume, the wall effects due to this catalysis are sufficient to skew the results when the testing is performed in the microreactor system. Although the use of H_2S also catalyzes the walls of the autoclave system, the effects on the products are less pronounced due to the larger volume-to-surface area ratio, resulting in a truer indication of the effects of H_2S on a given reaction.

The seventh combination tested consisted of lignite, tetralin, and argon. The resulting conversion of 78.9% was compared with that of the eighth combination, which consisted of lignite, tetralin, argon, and H_2S as a reaction promoter. The presence of H_2S resulted in a conversion of 85.3%. The use of H_2S in this instance appears to improve the conversion of lignite to soluble material.

The ninth combination tested consisted of lignite, AO4, argon, and H_2S and resulted in a conversion of 80.0%. The conversion was not as high as that achieved using tetralin and H_2S. The fact that AO4 is not as good a hydrogen-donating solvent as tetralin may account for the difference in conversion.

The tenth combination made use of lignite, AO4, CO, and H_2S to evaluate both the reaction-promoting capabilities of H_2S in the presence of a reducing gas and the effect of H_2S on the water/gas shift reaction. The resulting conversion of 83.0% was higher than the 80.0% achieved by the AO4/argon/H_2S combination. This may indicate that the presence of a reducing gas slightly improves the conversion and/or that the H_2S enhances the water/gas shift reaction.

The eleventh combination consisted of lignite, CA1, CO, and H_2S. This scheme was not especially successful when compared with the other combinations. A conversion of 70.9% was achieved, less than the 83.0% achieved using AO4 solvent. This same trend was noted in the data from the microreactor tests.

The final test was the primary combination test using AO4 and H_2, and it achieved the lowest conversion of all combinations tested in the autoclave system, a 60.7% conversion of coal to THF-soluble material.

Trends Noted After Preconversion Treatment Only

Conversions to THF solubles were determined for most of the tests following the preconversion treatment. These values are presented in Tables 1 and 3. When comparing the conversions after preconversion treatment only, it is possible to

discern some major differences between the reactions taking place with the different combinations.

At treatment temperatures of 175°C or less, tests performed using A04 as the solvent always had a negative conversion to soluble material of nominally -10% following preconversion treatment. In other words, at that point in the processing, the reaction had actually polymerized some of the feed slurry. In the presence of A04, upgrading of the insoluble organic matter (IOM) to soluble resid and distillable oils must take place primarily during the first stage.

Conversion to THF solubles after preconversion treatment using CA1 was positive with only one exception. This indicates that the CA1 solvent begins its conversion at very low-severity conditions, possibly through solubilization of portions of the coal.

At 250°C, the conversion to THF-soluble material was nearly as high after preconversion treatment as it was after liquefaction processing. This is most likely due to the effect of the water/gas shift reaction at this temperature. As would be expected, tests involving CO at this temperature exhibited the highest levels of conversion to THF solubles.

Comparison of Product Slates of Autoclave Tests

Evaluation of the data should not be restricted to conversion to THF-soluble materials, but should also include the product slates when possible. Due to sample size, product slates could be determined for the products of the autoclave tests only. Tables 4 and 5 present the product slates after preconversion treatment and first-stage processing, respectively. The values are presented in terms of moisture- and ash-free (maf) coal fed to the system. The product slates of the preconversion treatments will be examined first.

The tests using the light-oil solvents (tetralin and CA1) resulted in the conversion of more coal to soluble resid than the tests performed with A04 as the solvent, as shown in Table 4. The coal was probably solubilized by these solvents during the pretreatment. For the tests performed using A04, a significant portion of the coal remained as insoluble organic matter (IOM) after the preconversion treatment was completed. Table 6 presents the solvent recoveries realized during these tests. As the table shows, the solvent recoveries for the tetralin and CA1 tests were lower after the preconversion treatment than the A04 recoveries, indicating that these solvents reacted with the coal during the preconversion treatment while the A04 did not. As would be expected, the lack of gas production indicates that very little gasification took place during this pretreatment step.

Other observations can be made when the various preconversion treatment schemes are compared based upon the product slates of the first-stage processing, as given in Table 5.

An increase in CO_2 production indicated that more decarboxylation took place during the tetralin/argon test than during the tetralin/argon/H_2S test. The presence of H_2S resulted in the production of less soluble resid and IOM and more light oils and water from the coal. The H_2S seemed to aid in the conversion of the soluble resid present in the coal. During the test performed without H_2S, soluble resid equal to approximately 60 wt% of the maf coal fed to the reactor was produced at the expense of the production of light oils.

The liquid product of the A04/Ar/H_2S combination contained more IOM and soluble resid than the product of the tetralin/Ar/H_2S test. This is probably due to the heavier nature of the solvent and the reactions which took place during the preconversion treatment step.

When CO was used with the AO4/H_2S combination instead of argon, more CO, CO_2, and soluble resid were produced from the coal, while less of the coal remained as IOM. The AO4/CO/H_2S combination required less of the coal-derived light oils for upgrading to soluble resid than the AO4/argon/H_2S scheme. However, more of the coal went to middle oil production in the presence of argon than CO. In other words, the test performed with argon resulted in the upgrading of more of the coal to lighter products than the test with CO.

When CA1 was used as the solvent instead of AO4 in the CO/H_2S scheme, CO was consumed rather than produced by the coal. All of the soluble resid present in the coal as well as some of that present in the CA1 solvent after preconversion treatment were upgraded to water and light oils. This was significant when compared to the nonproduction of light oils during the test with AO4. However, nearly twice as much of the coal remained as IOM at the end of the test with CA1 as at the end of the test using AO4. It appears that CA1 upgrades the solubilized material better than AO4, but the lighter nature of the solvent does not permit the upgrading of the heavier insoluble material.

Comparison of the AO4/H_2 combination to the AO4/CO/H_2S combination reveals that less gas was produced during the H_2 test. The H_2 test failed to upgrade approximately 40% of the coal, which appears in the product as IOM. Of the coal which was upgraded during the AO4/H_2 test, approximately half went to soluble resid and half went to middle oils. By comparison, the majority of the upgrade during the AO4/CO/H_2S test was to soluble resid with very little coal upgrading to distillable oils.

When comparing the AO4/H_2 and the AO4/argon/H_2S combinations, the argon/H_2S was more successful in upgrading the coal to soluble resid. Similar quantities of coal went to middle oils for both tests, but considerably more of the coal remained as IOM when treated with H_2.

CONCLUSIONS

- In the presence of AO4, upgrading of IOM took place primarily during the first stage, whereas when CA1 was used as the solvent, conversion began at very low-severity conditions.
- Nascent hydrogen from the water/gas shift reaction was more readily used than hydrogen from the reducing gas.
- If any material physically prohibits conversion, it was not extractable with cresylic acid solvent.
- Sodium appeared to promote hydrogen addition to coal.
- Hydrogen-donating solvents were the most successful at converting coal to soluble material.
- The use of H_2S as a reaction promoter appeared to enhance conversion and result in generally lighter liquids than those produced when H_2S was not present.

It appears that conversion of lignite to THF-soluble material can be improved through the use of specific, solvent-dependent preconversion treatment. Small increases in conversion are possible with AO4 solvent, while larger differences are possible when CA1 is the solvent of choice. This indicates that preconversion treatment can prevent some of the retrograde reactions that take place when CA1 is used as the solvent.

TABLE 1

RESULTS OF PRETREATMENT SCHEMES TESTED IN THE MICROREACTOR SYSTEM

Run Numbers	Pretreatment Temperature	Solvent	Reducing Gas[a]	Additive	% Conversion to THF Solubles: After Pretreatment	% Conversion to THF Solubles: After 1st Stage[b]
T380, T381	110°C	AO4[c]	H_2	--[d]	-5.9	67.4
		AO4	CO	--	-8.4	66.3
		CA1[e]	CO	--	9.5	*[f]
		CA1	CO	Na[g]	*	63.9
		Tetralin	--	--	-9.0	87.5
		Tetralin	CO	--	*	48.8
T378, T379	175°C	AO4	H_2	--	-7.4	37.1
		AO4	CO	--	-11.0	40.7
		CA1	CO	--	7.2	26.4
		CA1	CO	Na	-0.5	*
		Tetralin	--	--	-9.3	*
		Tetralin	CO	--	-9.8	*
T376, T377	250°C	AO4	H_2	--	51.5	63.4
		AO4	CO	--	77.6	79.1
		CA1	CO	--	66.3	72.1
		CA1	CO	Na	74.0	92.9
		Tetralin	--	--	45.1	56.4
		Tetralin	CO	--	74.0	86.3

[a] 1000 psi charged.
[b] Nominal conditions of 420°C and 1000 psi H_2.
[c] Coal-derived anthracene oil.
[d] None used.
[e] Cresylic acid solvent.
[f] Samples not available for analysis.
[g] 0.05 g NaOH dissolved in 0.05 g H_2O

TABLE 2

SINGLE-STEP LIQUEFACTION TESTS PERFORMED IN THE MICROREACTOR SYSTEM[a]

Run Number	Maximum Temperature	Solvent	% Conversion to THF Solubles
T372	398°C	Tetralin	78.7
		AO4	69.8
		AO4	73.5
T373	433°C	Tetralin	89.1
		Tetralin	91.4
		AO4	57.3
		AO4	61.9
		AO4	76.4
		CA1	43.8
		CA1	47.4
		CA1	43.0

[a] Using H_2 as the reductant.

TABLE 3

RESULTS OF PRETREATMENT SCHEMES TESTED IN THE AUTOCLAVE SYSTEM

Solvent	Reducing Gas	Additive	Run Number: Pretreatment	Run Number: First Stage	% Conversion to THF Solubles: After Pretreatment[a]	% Conversion to THF Solubles: After 1st Stage[b]
Tetralin	Ar	--[c]	N459	N460	*[d]	78.9
Tetralin	Ar	H_2S	N457	N458	23.0	85.3
AO4	Ar	H_2S	N455	N456	-10.6	80.0
AO4	CO	H_2S	N463	N464	-9.2	83.0
CA1	CO	H_2S	N461	N462	1.8	70.9
AO4	H_2	--	N453	N454	-12.4	60.7

[a] At nominal conditions of 175°C and 1000 psi reducing gas.
[b] At nominal conditions of 410°C and 1000 psi H_2.
[c] None used.
[d] Sample not available for analysis.

TABLE 4

PRODUCT SLATES OF AUTOCLAVE PRETREATMENT TEST
FOLLOWING PRETREATMENT ONLYa

	Pretreatment Scheme				
	N457 Tet/Ar/H_2S	N455 AO4/Ar/H_2S	N463 AO4/CO/H_2S	N461 CA1/CO/H_2S	N453 AO4/H_2
Gas					
CO	0.00	0.00	-3.22	-0.12	0.00
H_2	0.36	0.39	0.40	0.53	0.17
CO_2	1.44	1.47	11.46	7.28	1.38
C1-C3	0.05	0.10	0.00	0.00	0.00
H_2S	-7.60	-0.93	-2.51	-4.07	0.00
Liquid					
H_2O	-0.68	1.55	-3.48	-1.73	-1.00
Distillable Oils	-69.16	-27.15	-20.77	-85.18	-37.21
Soluble Residue	96.85	12.97	8.29	84.05	24.34
Ash	1.77	1.01	0.66	1.05	-0.03
IOM	76.98	110.60	109.17	98.18	112.35

[a] Values are wt% based upon 100 g MAF coal in; positive values indicate production of a component; negative values indicate consumption.

TABLE 5

PRODUCT SLATES OF AUTOCLAVE PRETREATMENT TESTS FOLLOWING FIRST-STAGE PROCESSING[a]

	Pretreatment Scheme				
	N457 Tet/Ar/H_2S	N455 AO4/Ar/H_2S	N463 AO4/CO/H_2S	N461 CA1/CO/H_2S	N453 AO4/H_2
Gas					
CO	0.71	0.50	0.37	-3.06	0.43
H_2	-0.83	-1.99	-6.21	-1.36	-0.71
CO_2	15.37	11.93	9.40	10.73	10.18
C1-C3	2.32	2.17	1.49	1.71	1.45
H_2S	0.70	6.31	5.27	2.82	0.11
Liquid					
H_2O	4.37	8.30	0.79	8.58	-1.11
Distillable Oils	-4.34	102.50	12.23	76.51	23.15
Soluble Residue	59.70	-40.42	56.63	-29.98	27.26
Ash	-2.55	-4.05	0.06	-1.14	-0.07
IOM	24.55	14.75	19.97	29.06	39.31

[a] Values are wt% based upon 100 g MAF coal in; positive values indicate production of a component; negative values indicate consumption.

TABLE 6
SOLVENT RECOVERIES OF AUTOCLAVE TESTS

Pretreatment Scheme	Run Number	Solvent Recovery, wt% After Preconversion Treatment	After First Stage
Tet/Ar[a]	N459	*[b]	98.74
Tet/Ar/H_2S	N457	77.09	138.31
AO4/Ar/H_2S	N455	90.84	103.07
AO4/CO/H_2S	N463	90.43	97.24
CA1/CO/H_2S	N461	71.88	133.41
AO4/H_2	N453	82.54	110.99

[a] Tet = tetralin; Ar = argon; CA1 = cresylic acid solvent.
[b] Not available for analysis.

EFFECT OF ACTIVATION CONDITIONS ON DISPERSED IRON CATALYSTS IN COAL LIQUEFACTION

Cugini, A.V., Utz, B.R., Krastman, D., and Hickey, R.F.
U. S. Department of Energy, Pittsburgh Energy Technology Center
P.O. Box 10940, Pittsburgh, PA 15236
and
Balsone, V.
Gilbert Commonwealth, Inc., Library, PA 15129

INTRODUCTION

Ongoing research at PETC has focused on improved means of developing high surface area, well dispersed slurry catalyst options for direct coal liquefaction applications.[1] Compared to supported hydroliquefaction catalysts now being employed, such catalysts can exhibit superior characteristics for use in a coal dissolution reactor, particularly with respect to loss of activity and contact with reactants during the early stages of coal liquefaction. If properly dispersed and activated, molybdenum is sufficiently active to be employed for coal liquefaction at low concentrations (<0.1 wt% based on coal). However, owing to the difficulty of recovering expensive transition elements such as molybdenum after use, iron has continued to be of interest as the basis of an economical and disposable catalyst for coal liquefaction.

The catalytic activity obtained by direct introduction of iron into the feed slurry in the form of readily available minerals such as oxides or sulfide (pyrite) concentrates is generally low. Such approaches are typically ineffective unless relatively high concentrations (several wt% based on coal) of iron are added.[2-4] Among the factors usually contributing to the low activity are poor initial dispersion and low surface area of the added iron phase, and a tendency for aggregation and loss of surface area (sintering) of the catalytically active iron sulfide (pyrrhotite) phase under coal liquefaction conditions.[5]

A variety of methods have been employed to increase the initial dispersion of iron in coal liquefaction systems. Catalyst precursors have been introduced by physically mixing very small particles into the feed slurry, deposition from aqueous solutions, addition in oil soluble forms, and impregnation of the feed coal by water soluble compounds.[6-12] Exploratory studies using such approaches have provided evidence for increased activity with reduction of iron particle size, the need for available sulfur donating species if non-sulfide precursors are used, and the inhibiting effect of coal on the agglomeration and growth of small particles of some iron catalyst precursors under liquefaction conditions. The studies also suggest that iron may be an effective liquefaction catalyst at concentrations well below 1 wt% of the feed coal by utilizing the proper precursors, introduction techniques, and activation conditions.

Based upon a review of past research and initial screening tests, an approach combining both coal impregnation and precipitation techniques to generate a highly active dispersed iron catalyst has shown considerable promise in liquefaction tests at PETC.[13] In effect, the carbonaceous matrix of the coal is being used as a support not only to disperse added iron but also to help sustain the initial high dispersion achieved subsequent to activation. Effort to date has been primarily directed toward a hydrated iron oxide (FeOOH) precursor, since sub-micron oxide particles are readily formed under the proper conditions.[14] The approach being pursued appears to be of rather general applicability in coal liquefaction, utilizes no expensive reagents, minimizes the iron requirement, and is capable of being adapted for use on a larger processing scale.

EXPERIMENTAL

Feedstocks

Experiments were conducted with -200 mesh Illinois No. 6 (Burning Star No. 2) coal obtained from the Consolidation Coal Company. Analyses of the ground coal are given in Table 1.

Second stage heavy distillate from recent operations in a close-coupled integrated two-stage liquefaction mode at the Wilsonville Advanced Coal Liquefaction Test Facility was used as the liquefaction vehicle.[15] The bituminous coal was slurried with second stage vacuum tower overheads (V-1074) from Run 257 (Illinois No. 6 coal). Properties of the vehicle are summarized in Table 2.

Catalyst Precursors

For use in experiments testing the effect of physically mixing catalyst precursors into the feed slurry, FeOOH was prepared by precipitation from a ferric nitrate solution (200 g/L) with sufficient ammonium hydroxide to provide a three-fold excess of NH_4+ to Fe. A sample of Fe_2O_3, with a nominal particle size of one micron, was used as obtained from Spang and Company, Butler, PA. A pyrite concentrate was used that originated from the Robena coal preparation facility of the U.S. Steel (now USX) Corporation. All other chemicals and reagents were ACS grade.

Two molybdenum catalyst precursors were tested to establish a basis for comparison with the iron catalysts. These precursors were ammonium heptamolybdate (AHM) and ammonium tetrathiomolybdate (ATTM). The use of these precursors to form a dispersed MoS_2 catalyst at liquefaction conditions has been documented. [1,16 and 17]

FeOOH was also dispersed onto the feed coals by an incipient wetness impregnation/precipitation approach. A solution of 1 g of ferric nitrate, $Fe(NO_3)_3 \cdot 9H_2O$ dissolved in 40 g of distilled water was used to wet 50 g of the ground bituminous coal to incipient wetness. The wet paste was added rapidly to a solution containing 20 g of ammonium hydroxide (29% NH_3) and 200 g of distilled water. Pressure-filtration of the aqueous coal suspension through a 0.45 micron filter resulted in a clear filtrate. The iron loaded coal was vacuum dried at 40°C.

X-Ray diffraction studies were conducted with a Rigaku computer-controlled diffractometer equipped with a long fine-focus Cu X-ray tube, a receiving graphite monochromator to provide monochromatic Cu-K_a radiation, and a scintillation detector.

Liquefaction Tests

Catalyst screening tests were conducted in 40-mL microreactors for 1 hour at 425°C using a 10g total charge of 2:1 vehicle (tetralin) to coal ratio. In tests comparing the effect of an added source of sulfur to ensure sulfiding of the iron, 0.1 g of CS_2 was added to the charge. Heat-up rates of 2-3 minutes were obtained by immersing the microreactor in a fluidized sand bath preheated to 425°C. Coal conversion was calculated from the solubility of the coal-derived products in methylene chloride and in heptane determined by a pressure filtration technique, based on weight of insoluble residue.[18]

Semi-batch (batch slurry, flow through gas) tests were performed in a 1-L stirred-tank reactor system to obtain more definitive product yield and conversion information and sufficient product for additional characterization. The feed charge consisted of 500 g of 30 wt% coal slurry. Reactions were run at 425°C for 1 hour under 2500 psig of H_2/3%H_2S. The gas feed rate was 4 SCFH. A 100 g aliquot of the reactor product was subjected to a single-stage vacuum distillation to approximate the 650°F-, 650°F-950°F, and 950°F+ content. The 650°F- fraction was separated by

distillation at a pressure of 50 torr to a vapor temperature of 462°F. The product distillation was taken to a pressure of 5 torr and vapor temperature of 610°F to approximate the 950°F+ yield. A second 100 g aliquot of the reactor product was used to determine solubility yields following the general product workup scheme outlined in Figure 1. The product gas composition was determined by on-line gas chromatography monitoring and by the analysis of gas burette samples.

Further tests were performed in a computer-controlled 1-L bench-scale continuous liquefaction unit. A schematic of the unit is shown in Figure 2. For experiments with iron, an intermediate stage was added to assist in activating the catalyst precursor. The residence time in this intermediate stage was approximately 20 minutes. Continuous operations were carried out with a 30 wt% coal slurry, reactor temperature of 435°C, 2500 psig H_2/3%H_2S, and 1-h residence time. The gas flow rate was 4 SCFH; the slurry feed rate was 240 g/h. The product workup scheme in Figure 1 was followed.

Activation Studies:

The 40 mL microautoclave reactor was used to investigate the effect of activation temperature on the transition of FeOOH to pyrrhotite. In these experiments, FeOOH was impregnated onto carbon black rather than coal to eliminate the interferences caused by the indigenous pyrite in the coal. The carbon black was Raven 22 Powder obtained from Columbian Chemicals Co. The iron loaded carbon black and tetralin were rapidly heated (under H_2 in the presence of CS_2) to temperatures of 100°C, 150°C, 200°C, 250°C, 300°C, 350°C, and 400°C and held at temperature for 5 minutes. The products were mixed with THF and filtered through a 0.45-micron filter paper. The filter cake, containing the iron loaded carbon, was recovered and analyzed by X-Ray diffraction.

RESULTS AND DISCUSSION

Catalyst Screening Experiments

A series of microautoclave screening experiments was initially conducted with Illinois No. 6 coal and a variety of iron additives. Results with no added iron, several iron oxide preparations, and AHM are compared in Figure 3. Coal conversions to heptane and methylene chloride solubles were similar in the presence of 5000 ppm iron as 1-micron particles of iron oxide or in the presence of H_2S (from addition of 0.1 wt% CS_2) with no added iron. Although not shown, introduction of 5000 ppm iron in the form of powdered coal-derived pyrite or dilute solutions of ferrous sulfate or ferrous ammonium sulfate gave results comparable to physically mixing the powdered iron oxide into the tetralin/coal charge. Tests with powdered FeOOH gave some improvement in coal conversions. These conversions were further enhanced by addition of a sulfiding agent. The highest catalytic activity was developed after dispersion of the FeOOH precursor on the coal surface by an incipient wetness impregnation/precipitation procedure. Coal conversions with 2500 ppm iron added by this procedure were comparable to those obtained by addition of 1500 ppm molybdenum as a dilute solution of AHM. The screening studies indicate that the presence of hydrogen sulfide (or another sulfur source) is required to transform the FeOOH precursor into its most active form.

The general trends in liquefaction activity of the iron oxides in Figure 3 are consistent with expectations based on particle size considerations. The initially high metal dispersion that may be attained by solution impregnation can be largely lost in the subsequent drying procedure. The PETC procedure minimizes this problem by rapidly precipitating and fixing the precursor onto the coal surface in an insoluble form before drying. It is important that the coal surfaces only be wetted to incipient wetness during the impregnation step prior to precipitation. A procedure in which the coal is suspended in the impregnating solution and then treated with base to

deposit FeOOH on the coal has been described by Mukherjee and coworkers.[8] As shown in Figure 4, results obtained by this approach are only marginally better than those obtained by physically mixing the FeOOH precursor into the coal/solvent feed.

Liquefaction Tests

Semi-batch stirred autoclave tests were conducted with Illinois No. 6 coal. Conversions at 425°C to soluble and distillate products obtained with the impregnated FeOOH, AHM, and no added catalyst are compared in Figure 5. Yield structures for 2500 ppm added iron (as impregnated FeOOH) and 1500 ppm molybdenum (as aqueous AHM) are presented in Table 3. The yield structure for the two cases appears to be similar. However, for the particular liquefaction conditions and active metal concentrations chosen, a higher total distillate yield was obtained from the iron catalyst. Elemental analysis of the distillation product fractions indicated little difference between the products from using FeOOH or AHM as the catalyst precursors.

The transitions involved in the generation of pyrrhotite from impregnated FeOOH were studied in a series of microautoclave experiments. The results are given in Table 4. These results indicate that a transition from amorphous to crystalline form occurs between 300°C and 350°C, after which crystalline pyrrhotite is observed. It is likely that pyrrhotite is present at temperatures below 350°C. The pyrrhotite present below 350°C must be smaller than 100 Å, since it was not detectable by X-Ray diffraction. Consequently, it may be expected that pyrrhotite formed prior to 350°C would exhibit a higher liquefaction activity than the pyrrhotite formed at 350°C.

A continuous unit evaluation of the impregnated iron catalyst was made with Illinois No. 6 coal. Table 5 compares product yields in this test using FeOOH and an activation temperature of 275°C with those obtained in a continuous unit test using dispersed molybdenum, added as aqueous ammonium tetrathiomolybdate (ATTM), as the catalyst. Under these liquefaction conditions, the observed conversions with iron are comparable to the observed conversions with molybdenum.

The effect of varying the intermediate temperature was investigated in a series of continuous liquefaction tests. Table 6 summarizes the results. The highest levels of conversion and smoothest operation were observed at 275°C. At 350°C, coal conversions were lower than at 275°C and operation of the unit was more difficult; minor plugging problems were observed. Below an activation temperature of 275°C the FeOOH may not have been fully sulfided (converted to pyrrhotite) and, therefore, did not exhibit the same catalytic activity as the pyrrhotite formed at 275°C. The decrease in coal conversion and more difficult unit operation at the higher activation temperature suggest that the pyrrhotite formed at 350°C was catalytically less active than at 275°C. This may be due to formation of the pyrrhotite having a larger crystallite size at 350°C than at 275°C. However, the results could also be attributed to thermal soaking differences between 275°C and 350°C. However, in earlier studies with the molybdenum system[17], it was reported that the effect of thermal soaking was not observed. It has not been established that 275°C represents the optimal intermediate temperature; 275°C is an activation temperature that results in higher coal conversions using the dispersed iron catalyst than activation temperatures that are significantly different. Further studies of the effect of the activation temperature and residence time are being made.

Owing to differences in surface properties, functionality, and liquefaction characteristics between bituminous and subbituminous coals, it cannot be assumed that the exact iron catalyst precursor dispersion and activation conditions that are optimal for a bituminous coal are directly transferable to the case of a subbituminous coal. Preliminary semi-batch studies suggest that higher concentrations of an added sulfiding agent are required to fully activate the iron catalyst on low-sulfur bituminous coals. The optimal catalyst activation temperature in continuous operations may also be different for subbituminous coals. Extension of the current iron dispersion and activation approach to a subbituminous coal is currently under investigation.

SUMMARY

A procedure for dispersing a finely divided form of iron on coal has been developed that yields a highly active catalyst for direct coal liquefaction applications. Feed coal is impregnated with Fe^{3+} by an incipient wetness procedure. Subsequently, the high dispersion and interaction with the coal surfaces is maintained by conversion of the added iron to an insoluble hydrated iron oxide (FeOOH). Proper activation of this dispersed hydrated iron oxide under typical liquefaction conditions is shown to result in an effective disposable catalyst for the conversion of coal. In batch or semi-batch operations proper activation can be achieved during heat-up of the reactants. In continuous operations, an activation reactor stage is required.

Using iron concentrations as low as 2500 ppm (based on coal), batch liquefaction tests were conducted with Illinois No. 6 coal slurried with solvents from the Wilsonville Advanced Coal Liquefaction Test Facility. Conversions of the coal to distillate and soluble products at 425°C under 2500 psig of H_2/3% H_2S for 1-h compared favorably with conversions under the same conditions using 1500 ppm of molybdenum added as ammonium heptamolybdate (AHM).

Bench-scale continuous-unit tests to better define the activation sequence of the iron catalyst in continuous operations were conducted with Illinois No. 6 coal. At an activation temperature of 275°C (and activation residence time of 0.33 hour) and a final reactor temperature of 435°C and residence time of 1 hour, the conversions observed with the impregnated FeOOH catalyst precursor were again similar to the conversions observed using added Mo. Significantly varying the activation temperature from 275°C results in poorer liquid yields and unit performance. Below 275°C sulfiding of the FeOOH precursor may be a problem; above 275°C the growth of pyrrhotite crystals may be detrimental to the liquefaction activity of the iron.

ACKNOWLEDGEMENTS

The authors would like to thank Sidney S. Pollack and Elizabeth A. Frommell for their assistance in the X-ray diffraction study.

DISCLAIMER

Reference in this report to any specific commercial product, process, or service is to facilitate understanding and does not necessarily imply its endorsement or favoring by the United States Department of Energy.

REFERENCES

1. Lett, R.G., Cugini, A.V., Utz, B.R., Krastman, D., Cillo, D.L., and Jin, G.T. Dispersed Catalyst Approaches in Coal Liquefaction and Coprocessing. Proceedings 6th Korea - U.S.A. Joint Workshop on Coal Utilization Technology, 91-106. Seoul, Korea, October 17-18, 1989.

2. Mazzocco, N.J., Klunder, E.B., and Krastman, D. Study of Catalytic Effects of Mineral Matter Level on Coal. DOE/PETC/TR-81/1.

3. Garg, D., and Givens, E.N. Pyrite Catalysis in Coal Liquefaction. Ind. Eng. Chem. Process Des. Dev., 1982, 21, 113-117.

4. Paranjape, A.S., and Rhodes, D.E. Use of Iron Oxide and Hydrogen Sulfide to Improve Integrated Two-Stage Coal Liquefaction. Proceedings DOE Direct Coal Liquefaction Contractors' Review Meeting, 34-59. Albuquerque, NM, October 17-18, 1984.

5. Stohl, F.V. The Effects of Iron Sulfide Surface Area Variations on Coal Liquefaction. Fuel, 1983, 62, 122-126.

6. Andres, M., Charcosset, H., Chicke, P., Davignon, L., Djega-Mariadassou, G., Joly, J.-P., and Pregermain, S. Catalysis of Coal Hydroliquefaction by Synthetic Iron Catalysts. Fuel, 1982, 62, 69-72.

7. Djega-Mariadassou, G., Besson, M., Brodzki, D., Charcosset, H., Huu, T.V., and Varland, J. Evaluation of Highly Dispersed Catalysts During Hydroliquefaction of Coal. Fuel Processing Technology, 1986, 12, 143-153.

8. Mitra, J.R., Chowdhury, P.B., and Mukherjee, D.K. A Comparative Study on Deposited and Mixed Iron Oxide Catalysts for Hydrogenation of Coal. Fuel Processing Technology, 1984, 8, 283-291.

9. Anderson, R.R., and Bockrath, B.C. Effect of Sulfur on Coal Liquefaction in the Presence of Dispersed Iron or Molybdenum Catalysts. Fuel, 1984, 63, 329-333.

10. Watanabe, Y., Yamada, O., Fujita, K., Yoshinobu, T., and Suzuki, T. Coal Liquefaction Using Iron Complexes as Catalysts. Fuel, 1984, 63, 752-755.

11. Weller, S., and Pelipetz, M.G., Coal Hydrogenation Catalysts Studies of Catalyst Distribution. Ind. Eng. Chem., 1951, 43, 1243-1246.

12. Garg, D. and Givens, E.N. Effect of Catalyst Distribution in Coal Liquefaction. Fuel Processing Technology, 1983, 7, 59-70.

13. Utz, B.R., and Cugini, A.V. Method for Dispersing Catalyst Onto Particulate Material. Patent Application Filed.

14. Naono, H., and Nakai, K. Thermal Decomposition of q-FeOOH Fine Particles. J. Colloid and Interface Sci., 1989, 128, 146-156.

15. Wesnor, J.D., Pinkston, T.E., Moore, D.L. Recent Progress at the Advanced Coal Liquefaction Facility in the Direct Liquefaction of Coal. Proceedings DOE Direct Liquefaction Contractors' Review Meeting, 23-42. Pittsburgh, PA, October 2-4, 1989.

16. Utz, B.R., Cugini, A.V., and Frommell, E.A., Dispersed- Phase Catalysis in Coal Liquefaction. Novel Materials in Heterogeneous Catalysis, ACS Symposium Series No. 437, 289-299 (1989).

17. Derbyshire, F.J., Catalysis in Coal Liquefaction: New Directions for Research, IEACR/08, IEA Coal Research, London (1988).

18. Utz, B.R., Appell, H.R., and Blaustein, B.D. Solubility Characterization of Coal-Derived Products Using Pressure Filtration. Fuel, 1984, 63, 1671-1676.

Table 1. Analyses of Illinois No. 6 (Burning Star).

Proximate Analysis, (As Received)	**wt%**
Moisture	4.2
Volatile Matter	36.9
Fixed Carbon	48.2
Ash	10.7
Ultimate Analyses, (Moisture Free)	**wt%**
Carbon	70.2
Hydrogen	4.8
Nitrogen	0.9
Sulfur	3.1
Oxygen (Difference)	9.9
Ash	11.1
Sulfur Forms	**wt%**
Sulfatic	0.03
Pyritic	1.2
Organic	1.9

Table 2. Properties of V-1074 oil.

Ultimate Analysis	wt%
Carbon	89.1
Hydrogen	9.8
Oxygen (Direct)	0.9
Nitrogen	0.4
Sulfur	0.04
Ash	<0.1
850°F⁻ (Vol%)	65
Heptane Insols, wt%	0.2
M_n (daltons)	360[a]
H^*_{ar}	0.15
f_a	0.43

[a]VPO, tetrahydrofuran, 40°C

Table 3. **Product yields from liquefaction of 30 wt% Illinois No. 6 coal and 70 wt% V-1074 in a semi-batch mode non-catalytically, with added iron (FeOOH) and added molybdenum (AHM). (Semi-batch 1-L autoclave; Reactor Temp. = 425°C, Time at Temperature = 1 hour, Pressure = 2500 psig, 97%H_2/3%H_2S; Fe conc. = 2500 ppm, Mo. conc. = 1500 ppm, Gas Feed Rate = 4 SCFH.)**

Yield Structure (Ash Free Basis), Wt%

Component	Non-Catalytic	FeOOH	AHM
C_1-C_4	3.2	3.0	2.3
C_5-950°F	71.8	82.9	81.5
950°F$^+$ Solubles	10.0	6.2	8.6
Heptane Insolubles	15.3	8.3	8.6
Non-Hydrocarbon Gases	1.0	1.0	1.0
Hydrogen	(1.3)	(1.6)	(2.0)

Table 4. **Microautoclave Iron Activation Studies Using Carbon Black and Tetralin 1000 psig H_2 Cold Pressure with Added CS_2 Using 2500 ppm Iron as Hydrated Iron Oxide on Carbon**

Final Reactor Temperature °C	Dominant Iron Phase by X-Ray Diffraction	Pyrrhotite Area Under Curve	Estimated Crystallite Size
100	Amorphous		
150	Amorphous		
200	Amorphous		
250	Amorphous		
300	Amorphous		
350	Pyrrhotite	87	400Å
400	Pyrrhotite	158	400Å

Table 5. **Product yields from liquefaction of 30 wt% Illinois No. 6 coal and 70 wt% V-1074 in a continuous mode with added iron (FeOOH) and added molybdenum (ATTM). (Continuous 1-L autoclave; Reactor Temp. = 435°C, Pressure = 2500 psig, 97%H_2/3%H_2S; Fe conc. = 2500 ppm, Mo conc. = 1000 ppm, Gas Feed Rate = 4 SCFH; Slurry Feed Rate = 240 g/h.**

Yield Structure (Ash Free Basis), Wt%

Component	FeOOH	ATTM
C_1-C_4	3.4	3.2
C_5-950°F	82.7	83.5
950°F$^+$	15.0	14.5
Non-Hydrocarbon Gases	1.4	1.4
Hydrogen	(2.5)	(2.6)

Table 6. **Continuous Unit Iron Activation Studies Using Illinois No. 6 Coal and Wilsonville Recycle Solvent (30 wt% Coal in Solvent), 2500 psig (3% H_2S in H_2) Using 2500 ppm Iron as Hydrated Iron Oxide on Coal**

Reactor #1 Temp. °C	Reactor #2 Temp. °C	Total Product: % 950°F+ in Total Product	Total Product: % Methylene Chloride Insolubles	Total Product: % Heptane Insolubles	Comments
150	435	***	***	***	Plugged - after 12 hours
275	435	15	7.6	14.2	Smooth Operation - 32 hours
350	435	22	12.4	20.6	Rough Operation - 32 hours
50	435	***	***	***	Plugged - after 2 hours
275	435	16	6.4	13.0	Smooth Operation - 72 hours Normal Shutdown

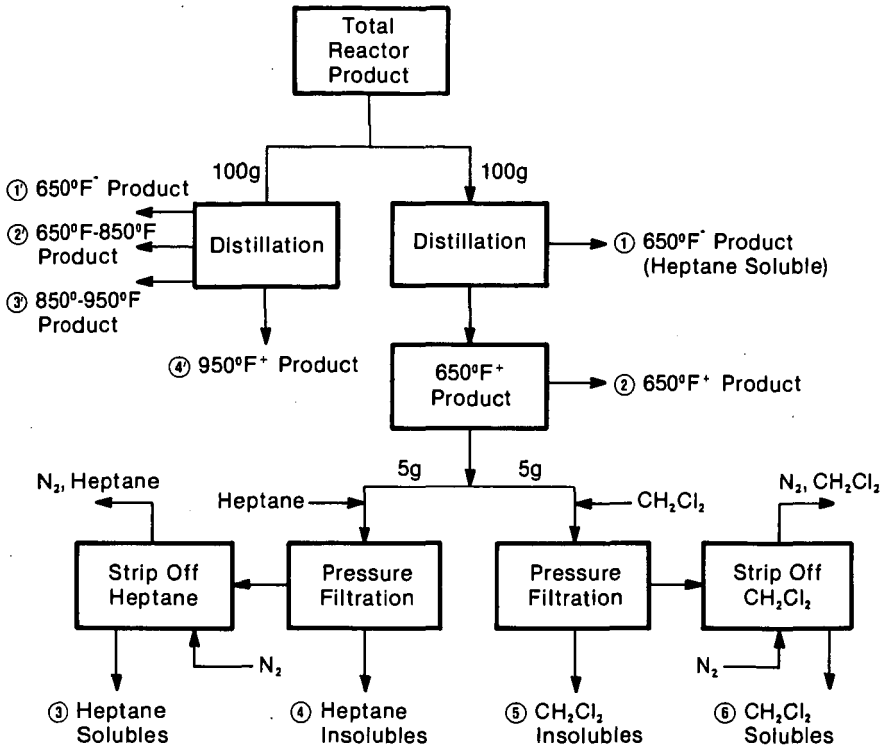

FIGURE 1. PRODUCT WORKUP SCHEME FOR 1-LITER SEMI-BATCH AND CONTINUOUS UNIT OPERATIONS.

No./19.008

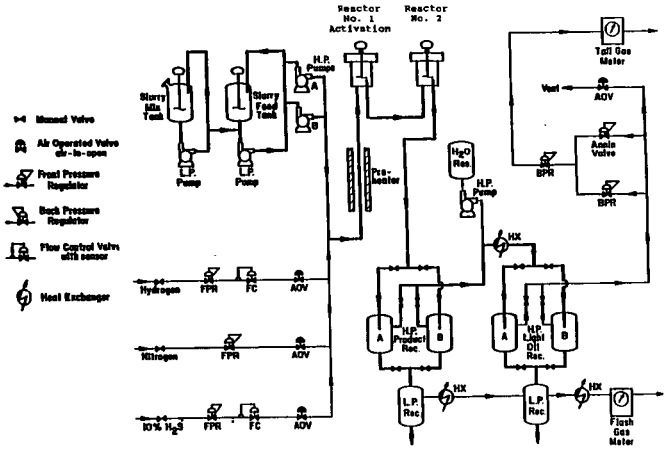

Figure 2. Bench-scale continuous unit configuration.

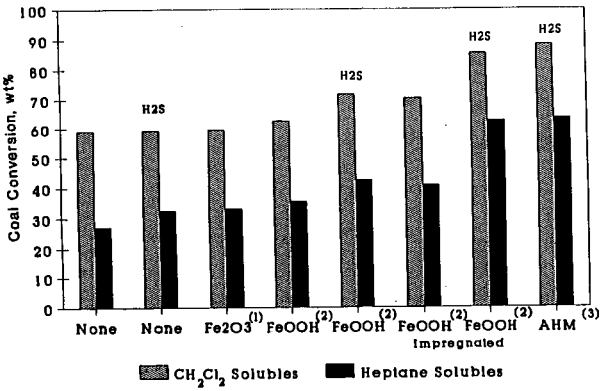

(1) 5000 ppm; (2) 2500 ppm; (3) 1500 ppm

Figure 3. Effect of catalysts on coal conversion. (Microautoclave runs; 425°C, 1h, 2500 psig H_2, 2:1 tetralin:Illinois No. 6 coal)

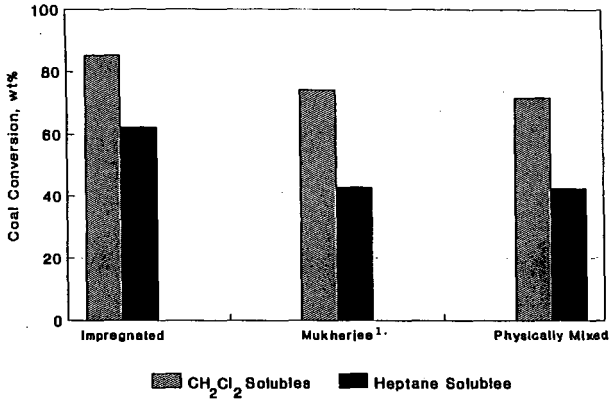

1. Coal/Catalyst mixture prepared according to procedure outlined in reference 8.

Figure 4. **Effect of impregnation on coal conversion. (Microautoclave runs; 425°C, 1h, 2500 psig H_2, 0.1 g CS_2, 2:1 tetralin:Illinois No. 6 coal)**

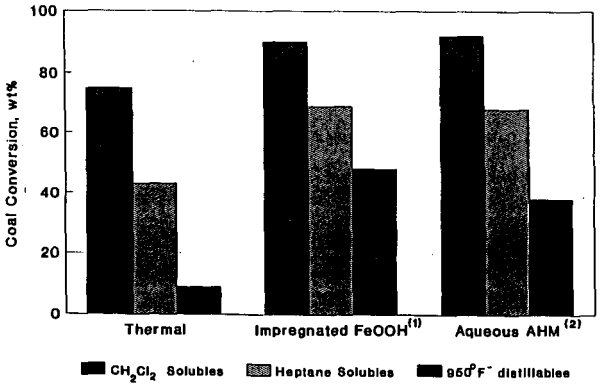

(1) 2500 ppm; (2) 1500 ppm

Figure 5. **Effect of catalysts on coal conversion. (1-L semi-batch experiments; 425°C, 1h, 2500 psig, 97% H_2/3%H_2S at 4 SCFH)**

DESIGNED COAL LIQUEFACTION CATALYSTS

A. S. Hirschon and R. B. Wilson Jr.

SRI International
Inorganic and Organometallic Chemistry Program
Menlo Park, California 94025

Keywords: coal liquefaction; catalysts; preconversion

ABSTRACT

The effects and ramifications of using highly dispersed catalysts for coal liquefaction are discussed. We have briefly explored several types of iron and molybdenum based complexes as precursors to high dispersion catalysts. The precursors were either organometallic complexes or water soluble salts and were impregnated into coals of various ranks. The molybdenum catalysts were found to be very effective for an Illinois #6 bituminous coal whereas the iron catalysts were not. In contrast, the iron catalysts were found to be very effective for lignite conversions. Both a H-donor conversion system and a non-donor system were compared, using tetralin and n-hexadecane, respectively. In each case the organometallic precursor gave greater yields of toluene soluble material, with differences being most dramatic in the hexadecane system. The yields using the organometallic molybdenum precursors in hexadecane were found to be almost as great as those in the tetralin system, indicating that with a good enough catalyst precursor, donor solvents are not needed.

INTRODUCTION

One of the keys to a successful coal liquefaction process is the control of preconversion reactions. Coal is composed of numerous functional groups and classes of molecules. Depending on reaction conditions, these groups may either undergo polymerization and char formation, or bond breaking reactions to form gases and coal liquids. These reactions may occur at quite low temperatures, and thus finding appropriate process conditions and reactive catalysts to control these reactions is critical. For instance, several workers have shown that phenolics tend to polymerize into difficult to upgrade materials unless treated by some means such as a donor solvent such as tetralin (1,2). Current liquefaction processes have shown the benefits of staging the severity of the liquefaction process in order to control preconversion reactions, but are limited in choices of catalyst. Supported catalysts are often used for these processes but suffer in that they only interact with the liquefaction solvent, and have very poor intimate content with the individual coal molecules. The function of these supported catalysts is primarily to transfer hydrogen to the liquefaction solvent. A more efficient process would involve highly dispersed catalysts that have intimate contact with the coal molecules, have high surface areas or are soluble so that only small amounts of catalysts are needed, and most importantly, would be active at preconversion conditions to limit the amount of retrogressive reactions that occur in the initial stages of coal liquefaction.

Generally, efforts to use dispersed catalysts during coal liquefaction utilize precursors that are not activated until high temperatures (3-6). For instance, molybdenum is often added as either the oxide, the thiolate water soluble salt, or as molybdenum naphthenate, so the molybdenum must first be transformed from the oxide to the trisulfide, and finally transformed to the disulfide, the most active form of the catalyst. However, the conversion of the trisulfide to disulfide occurs only under high temperatures, in excess of 350°C (7). Likewise, a commonly used iron precursor, iron oxide, is difficult to convert to the active pyrrhotite and requires high temperature activation. A soluble organometallic precursor, iron carbonyl has also been investigated; however, it likewise is difficult to activate and tends to form iron carbides and oxides during the activation process (6).

In recent work we have investigated precursors designed to have the correct stoichiometry of the active catalyst (8-10). These precursors can form high surface area catalysts that are active at low temperatures, and thus may limit the polymerization or retrogressive reactions that occur during coal preconversion. The following work describes our efforts to study the reactivities and effects of these types of catalysts for coal liquefaction. Our goals are to synthesize and test soluble complexes that are as close to the correct stoichiometry and structure of the active catalyst during the coal liquefaction. Thus we hope that our catalysts, since they do not require high temperature activation, will cause bond breaking reactions at lower temperatures than are currently possible with dispersed catalysts, and may therefore aid in reducing retrogressive reactions.

EXPERIMENTAL

The coals used were PSOC 1098 Illinois #6 and Beulah-Zap North Dakota lignite from the Argonne coal bank. The ratio of catalyst to coal was approximately 0.6 mmoles of metal per gram of coal. The organometallic molybdenum catalyst was $Cp_2Mo_2(\mu\text{-}SH)_2(\mu\text{-}S)_2$, referred to as MoS_2(OM), and was prepared by modification of method of Dubois et al. (11). Pentacarbonyl iron was obtained from Aldrich, and the sulfur-containing iron cluster, $(\mu\text{-}S_2)Fe_2(CO)_6$ was prepared by the method of Bogan et al. (12). Ammonium tetrathiomolybdate, MoS_4(Aq), was obtained from Alfa Chemicals. The organometallic catalysts were impregnated into the coal in tetrahydrofuran (THF) with the exception of the iron complexes, where the reaction solvent was used. The THF was removed by evaporation under vacuum at room temperature. The molybdenum salt was added as an aqueous solution. The coal liquefaction experiments were conducted in a 300 mL Autoclave Engineers stirred reactor using 5.0 g of coal, 30 g of liquefaction solvent, and 500 psig hydrogen. Temperatures of either 400°C or 425°C for 20 minutes using either tetralin or n-hexadecane were used for these conversions. After the reaction had cooled, the coal liquid and residue were taken up in THF. The THF was removed under reduced pressure and the residue taken up in toluene. The product was filtered through a medium porosity filter and separated into toluene soluble (TS) and insoluble (TI) fractions. The toluene and residual tetralin, if used, were then removed from the TS under reduced pressure. The TS and TI fractions were then dried at 76°C for 12 h under vacuum (< 0.1 mm). The conversions were calculated from the amount of toluene-insoluble material and are based on daf basis, or the carbon balance, as in the case of the lignite.

RESULTS AND DISCUSSION

Data from coal conversions in tetralin and hexadecane solvent systems are presented in Tables 1 and 2, respectively. The Illinois #6 coal gave quite high conversions to toluene soluble material even under the mild conditions of 500 psig hydrogen pressures and 400°C when tetralin was used for the coal liquefaction, as expected for a high volatile bituminous coal. Also as expected, it gave poor conversions in the absence of catalyst in the non-donor hexadecane solvent. The tetralin appeared to moderate the effects of the catalysts, so that the range of conversions was only about 13%. For example, the conversion to toluene soluble material in the absence of catalyst in tetralin was 48%,

compared to 53% when impregnated with aqueous molybdenum, and 61% the coal was impregnated with organometallic molybdenum. A similar range was observed with the conversion temperature increased to 425°C. The iron catalyzed reactions, utilizing $Fe(CO)_5$ and the iron sulfido dimer, $(\mu\text{-}S_2)Fe_2(CO)_6$, designated as Fe_2S_2 showed no apparent effect from the non-catalyzed conversions. However, the TS product of the Fe_2S_2 catalyst was a tar while the product from the $Fe(CO)_5$ catalyzed reaction was a brittle solid. Experiments with model compounds have shown that the $Fe(CO)_5$ tends to form tars as well as metal carbides and oxides, whereas the $[SFe(CO)_3]_2$ shows no evidence of polymerization reactions or other products besides iron sulfides, and we suggest that further investigation of these products will show that the latter gives a better quality product.

The oxygen content of the TS product of the catalyzed conversions were found to be lower than those of the non-catalyzed runs. For instance, the molybdenum catalyzed reactions had the lowest oxygen content of 4.6 to 4.8% oxygen, the iron catalyzed reactions gave a 5% oxygen content, and the base line runs an oxygen content of 6-6.5%. The lower oxygen content is one of the goals of our work, since many of the retrogressive reactions are thought to center through this group. In future work we hope to determine whether the reduction of oxygen occurs during the preconversion reactions as we speculate, or during the more severe reactions during coal conversion.

Table 2 lists conversions in hexadecane. The use of hexadecane rather that a typical conversion medium was induced by the desire to use a non-reacting, non-donor conversion medium that would not interfere with the study of the catalysts. As shown in the table, most of the conversions are quite low, as expected. For instance in the absence of catalyst the Illinois #6 coal was converted to 25% toluene soluble material, compared to 48% in tetralin. However, in the presence of the molybdenum catalysts, the conversions were greatly enhanced. For instance, the aqueous molybdenum impregnation gave a conversion of 41% and the organometallic molybdenum impregnation resulted in a conversion of 54%, which is nearly as great as when tetralin was used as the conversion medium. The iron catalyzed conversions showed little effect from the non-catalyzed runs for the Illinois #6 coal; however, showed a significant improvement for the conversion of lignite, with conversions of approximately 40% toluene soluble compared to 24% with no catalyst. Thus the iron complexes appear to be best suited towards low rank coals, presumably due to their increased oxygen functionalities. The Fe_2S_2 catalyst appears to have slightly more asphaltenes in the product distribution, but future work will be needed to further study any differences in reactivities between these catalysts.

CONCLUSIONS

Dispersed catalytic liquefaction has several distinct advantages over conventional thermal or catalytic liquefaction. In the presence of hydrogen, a suitably dispersed catalyst can provide a highly reducing environment within the coal matrix, thus eliminating the need for a good hydrogen donating solvent. An added advantage to these catalysts is that they can promote certain bond cleavage reactions during the liquefaction step. If they can aid in removing the heteroatoms, namely oxygen and nitrogen, during the early stages in coal liquefaction, then the detrimental retrogressive reactions would be minimized. Thus a better quality coal liquid product would be produced that would be easier and less expensive to hydrotreat. The high activity of the molybdenum sulfido complex, we believe, is because the catalyst was impregnated in a highly active form, and thus does not require subsequent activation during the liquefaction step, and thus is active during the preconversion reactions preventing retrogressive reactions. The organometallic iron complexes were found to be effective for low rank coals, and in future work we hope to understand their role in liquefaction in order to better design a more effective liquefaction catalyst.

ACKNOWLEDGEMENTS

The authors gratefully acknowledge the partial support of this work by the Department of Energy under Contract DE-FG22-87PC79936.

REFERENCES

1. M. J. Trewhella and A. Grint, Fuel (1988) 67, 1135-1138.

2. D. F. McMillen, S.-J. Chang, S. E. Nigenda, and R. Malhotra, ACS Fuel Preprints (1985) 30(4), 414.

3. F. J. Derbyshire, A. Davis, M. Epstein, and P. Stansberry Fuel (1986) 65, 1233-1240.

4. F. J. Derbyshire, A. Davis, R. Lin, P. Stansberry, and M.-T. Terrer, ACS Fuel Preprints (1985) 30(4), 326-332.

5. A. Mastral, F. Derbyshire, Fuel (1988) 67, 1477-81.

6. D. Herrick, J. Tierney, and I. Wender, Energy and Fuels (1990) 4, 231-236.

7. D. Huntley, T. Parham, R. Merrill, and M. Sienko, Inorg. Chem., (1983) 22, 4144-4146.

8. A. S. Hirschon, R. B. Wilson Jr., and R. M. Laine, ACS Fuel Preprints (1986) 31(1) 310-317.

9. A. S. Hirschon, R. B. Wilson Jr., and R. M. Laine, ACS Pepr. Preprints (1987) 32(2) 268-270.

10. A. S. Hirschon and R. B. Wilson Jr., ACS Pepr. Preprints (1989) 34(3) 881-886.

11. B. A. Cowens, R. C. Haltiwanger, and M. R. DuBois, Organometallics (1987) 6, 995-1004.

12. L. E. Bogan, Jr., D. A. Lesch, and T. B. Rauchfuss, J. Organometallic Chem. (1983), 250, 429-438.

Table 1

Conversion to Toluene Soluble Products in Tetralin[a]

Catalyst	T (°C)	% TS	% O
None	400	48	6.0
MoS_4(Aq)	400	53	4.8
MoS_2 (OM)[b]	400	61	4.6
$Fe(CO)_5$	400	47	5.0
Fe_2S_2	400	49	5.1
None	425	69	4.0
MoS_2(OM)[b]	425	84	2.3
MoS_4(Aq)	425	76	4.0

[a]Reaction conducted in 300-mL autoclave with 5 g Illinois #6 coal in 30 g solvent and 500 psi H_2 at for 20 min.
[b]OM refers to organometallic precursor.

Table 2

Conversion to Toluene Soluble Products in Hexadecane[a]

Catalyst	Coal	T (°C)	% TS
None	Ill. # 6	400	25
$Fe(CO)_5$	Ill. # 6	400	24
Fe_2S_2	Ill. # 6	400	29
MoS_4(Aq)	Ill. # 6	400	41
MoS_2(OM)	Ill. # 6	400	54
None	Lignite	425	24
$Fe(CO)_5$	Lignite	425	41
Fe_2S_2	Lignite	425	39

[a]Reaction conducted in 300-mL autoclave with 5 g coal in 30 g solvent and 500 psi H_2 at for 20 min.
[b]OM refers to organometallic precursor.

DRYING OF BEULAH ZAP LIGNITE

Karl S. Vorres*, Donald Molenda* and
Yuhong Dang**, Vivak M. Malhotra**
*Chemistry Division, Building 211
Argonne National Laboratory
Argonne, IL 60439
**Physics Department
Southern Illinois University at Carbondale
Carbondale, IL 62901-4401

Keywords: drying, liquefaction, differential scanning calorimetry (DSC), FTIR, TGA

INTRODUCTION

The drying of low rank coal is important in effective liquefaction of this abundant resource. It has been said by several researchers that a small reduction of moisture in these coals does not adversely affect the liquefaction behavior, however a very large amount of drying does have an adverse effect on the rates of this reaction. It has been felt that this behavior may be due to the possible irreversible change in physical pore structure that was believed to accompany drying.

It is generally recognized that the physical structure of coal is composed of three components: an organic matrix, inorganic matter, and an extensive network of pores. It is also believed that the pore network usually contains water in 'as-mined' coals. Mraw and Silbernagel (1) suggested that the amount of water present in as-mined coals provides a measure of pore volume. However, Kaji et al. (2) examined the water-holding capacity, specific surface area, and pore volume of 13 coals from various locations, ranging from lignite to anthracite, and found no correlation between the water-holding capacity and the pore volume. Based on the assumption that the total coal oxygen is distributed uniformly through the coal and the functional-group oxygen increases with oxygen content, Kaji et al. found a linear relationship between the hydrophilic sites and the water-holding capacity of coal. It seems to us that the relationship between the total oxygen content of coal and the water-holding capacity is more fortuitous than real since oxygen-functional groups are not the only hydrophilic sites in coal (3). Moreover, the presence of minerals, especially smectite lattices, and various cations will also strongly influence the coal-water interactions.

Vorres et al. (4) and Vorres and Kolman (5) adopted the approach of ascertaining the kinetics of vacuum drying of coal as a means to understand the complex coal-water interactions. From isothermal thermogravimetry analysis, i.e., the weight loss vs. time at fixed temperature, Vorres and his co-workers indicated that the dehydration of Illinois No. 6 in the form of a block, -20 mesh, and -100 mesh, follows a desorption kinetics mechanism. Thus, they concluded that the rate controlling mechanism of dehydration is governed by the surface of coal. In addition, Vorres and his co-workers indicated that the particle size and the history of coal also affect the dehydration kinetics of coal. More recently, Abhari and Isaacs (6) used the thermogravimetric

analysis (TGA) technique to explore the drying kinetics of six coals from the Argonne coal-sample bank. They evoked a bulk moisture/pore moisture model to explain the observed drying kinetics for the six coals, in which the order of kinetics, i.e., the order of dehydration showed a strong dependence on the rank of coal. In calculating the kinetics parameters from the weight loss data, these researchers assumed that water in coal is held by the physisorption process. This assumption is at variance with the temperature dependent NMR results (7) and the contention of Kaji et al. (2).

In this paper, we report our recent results on the kinetics of water's desorption from Beulah-Zap lignite coal, as determined by thermogravimetric analysis (TGA) and the differential scanning calorimetry (DSC) technique. The kinetic analysis of DSC was further complimented by determining the mechanism of air drying of lignite coal with the help of an in-situ Desorption Kinetics via Fourier transform infrared (ISDK-FTIR) technique.

EXPERIMENTAL

Isothermal Thermogravimetry

Coal drying was done with a Cahn model 121 thermobalance attached to an IBM PC/XT microcomputer. Vendor-supplied software was used to monitor the progress of individual runs, and convert data files to a form that could be further studied with Lotus 123.

The data were obtained as files of weight at 10 second intervals. For runs longer than 10 hours, the runs were modified to work with data points at 20 second intervals.

The typical sample size was about 140 mg. The sample was placed in a platinum hemispherically-shaped pan. Sample sizes included the two mesh sizes of the usual Argonne Premium Coal Samples (-100 and -20 < 841u) and also one or two small pieces which came from lumps which have been stored under nitrogen since the time of the acquisition of the original samples. A sample of -400 mesh (< 37u) material was prepared at Southern Illinois University at Carbondale with a Brinkmann Micro-Rapid mill.

Data were analyzed by testing the weight loss as a function of time with 13 different kinetic expressions including geometrical, unimolecular, first and second order diffusion to establish a best fit. Lotus 123 was used for analysis of individual run data.

Samples were quickly transferred from freshly opened ampoules or bottles which had been kept in constant humidity chambers with water at room temperature (293°K). In the thermobalance system a period of 5 minutes was used to stabilize the system and initiate data acquisition. Room temperature runs were made with and without the furnace in place. The furnace was used for runs at 313 and 353°K. A typical run is shown in Figure 6.

For comparison, a run was made at room temperature under vacuum with the -20 mesh material.

The gas atmosphere was cylinder nitrogen (99.99%) used without further purification and passed over the sample at a rate of about 100 cc/min.

Differential Scanning Calorimetry (DSC) Measurements

The kinetics of water's desorption from lignite coal was evaluated using a non-isothermal approach in which the coal sample temperature was progressively raised at a constant heating rate (8-10). Janikowski and Stenberg (11) and Elder and Harris (12) from their DSC measurements have shown that when coal samples are subjected to thermal treatment a broad endothermic peak is observed at around 323 K - 423 K. This broad peak has been associated with the water loss from the coal. Therefore, a careful DSC experiment at 300 K < T < 473 K under inert environment can provide information on the kinetics of water's desorption from coal. We chose -20 mesh and -400 mesh particle size coal to explore the kinetics of water's desorption from coal. The as-received sample of Beulah-Zap lignite coal was of -20 mesh size, and the sample was received in a sealed ampule. A part of the -20 mesh coal sample was ground in a Brinkmann Micro-Rapid mill to reduce its particle size to -400 mesh. The ground sample was sieved through a -400 mesh sieve, and the -400 mesh particles were collected for DSC measurements.

The desorption of water from -20 mesh and -400 mesh particle size lignite coal was determined with the help of a well calibrated (13,14) Perkin-Elmer DSC7 system. Prior to recording the DSC curves, the lignite coal samples were kept at a 93% relative humidity (RH) for 48 hours in a humidity controlled chamber. Afterwards, about 20 mg of the samples were accurately weighed on a microbalance. The samples were then loaded in Al pans and sealed with the help of Al lids. A number of holes were drilled in the Al lids to ensure the easy escape of water vapors from the Al pans. In loading the coal samples in the Al pans, extreme care was exercised so that mechanical compacting of the particles did not control the overall desorption kinetics of water. The DSC curves were recorded at a heating rate of 10 K/min. under the controlled He purge. After the DSC runs, the sample pans were again weighed to ascertain weight loss due to the thermal treatment.

In-situ Desorption Kinetics via Transmission-FTIR (ISDK-FTIR) Measurements

The air drying kinetics of Beulah-Zap lignite coal was determined using the ISDK-FTIR technique (15). In this approach, a thin film of coal (particle size -400 mesh) was painted onto a laser grade ZnSe optical flat. The thin film was equilibrated at 93% RH in a humidity controlled chamber for 48 hours at room temperature. The desorption kinetics of water from coal was determined by mounting the coal sample in the FTIR spectrometer's sample chamber. The sample chamber was purged with a controlled flow of dry air in order to maintain a constant humidity of 9% RH. The FTIR spectra of coal were recorded as a function of time in the transmission mode. The spectra were collected by employing a fast scanning (25 scans/sec) Nicolet 740 FTIR spectrometer with a fast response liquid nitrogen cooled MCT detector. One hundred interferograms were collected at 4 cm^{-1} resolution to produce the

coal sample's FTIR spectrum. To monitor the desorption kinetics of water, a Nicolet 620 computer, interfaced with the spectrometer, was programmed to collect 100 interferograms after an interval of every 48 seconds. After the collection of 20 spectra, the time interval was increased to 80 seconds for the next 20 spectra and then subsequently to a time interval of 180 seconds. The collected interferograms were stored on a hard disk and after the completion of the experiment, the interferograms were Fourier transformed and co-added to produce the desired FTIR spectrum.

RESULTS AND DISCUSSION

Isothermal Thermogravimetry

The data were normalized to one gram of starting sample weight. The best fit of the data were obtained with a unimolecular decay kinetic expression. Plots of ln (water left) versus time gave a characteristic shape. The plot indicates a consistent slope for about 85% of the moisture loss of the coal. A transition then occurs. The rate is then reduced to about half of the earlier rate. The kinetic parameters are given in Table 1. Values of R squared in the regression coefficient from Lotus 123 were greater than .99 for all but two of the runs. Rate coefficients, k, were obtained from the rate of change of the ln (water left) in mg water/gram of original sample as a function of time in seconds. For a number of runs, the data did not initially fit the straight line. For these, the data included in the determination of the rate constant did not start at zero. The range of time included for the determination is indicated in the table. In the cases of initial lack of fit the rates were always above the line, indicating a more rapid moisture loss.

In general the highest R squared values are associated with the data obtained from the blocks, indicating a greater consistency with data from a singular piece of material.

The use of vacuum to remove moisture is seen to be capable of much more rapid removal of water than a stream of dry nitrogen. The ratio of the rate coefficients is an order of magnitude greater, and would imply an rate advantage to this technique for engineering for rapid processing of pulverized fuel.

The initial removal of about 85% of the moisture and then a transition to a slower rate of water loss implies a structural rearrangement. It is believed that the pores of the particles are changed after this amount of water is lost in a manner that makes the further loss of water more difficult.

DSC Results

Figure 1 reproduces the DSC curves obtained at a heating rate of 10 $Kmin^{-1}$ for -20 mesh and -400 mesh particle size Beulah-Zap lignite coal. As pointed out earlier, Janikowski and Stenberg (11) observed similar endothermic broad peaks in their DSC curves at $323\ K < T < 423\ K$ from various lignite and subbituminous coal samples. At $323\ K < T < 473\ K$, water is expected to be desorbed

from the coal sample. It is worthwhile to point out here that vacuum dried samples of Beulah-Zap lignite coal showed no exothermic peaks at 323 K < T < 473 K. Therefore, consistent with the observations of Janikowski and Stenberg, we also believe that the broad peak at around 373 K, as seen in Fig. 1, is produced due to the water loss from coal.

The general kinetic expression for the decomposition of a solid is

$$\frac{d\alpha}{dt} = A\exp(-E/RT)f(\alpha). \qquad (1)$$

In Eq. 1, is the fractional conversion at a time t, k is the rate of reaction, E is the activation energy in J/mol, R is the gas constant in J/mol.K, A is the frequency factor, and T is the temperature in K. Since our DSC measurements were conducted in a non-isothermal mode, Eq. 1 was modified to take into account the constant heating rates used, i.e.,

$$\frac{d\alpha}{dT}\frac{dT}{dt} = A\exp(-E/RT)f(\alpha). \qquad (2)$$

Substituting B for the constant heating rate dT/dt used, Eq. 2 can be rewritten as

$$\frac{d\alpha}{dT} = \frac{A}{B}\exp(-E/RT)f(\alpha). \qquad (3)$$

Rearranging and integrating Eq. 3, we obtain

$$F(\alpha) = \frac{ART^2}{BE}\left(1-\frac{2RT}{E}\right)\exp(-E/RT). \qquad (4)$$

and

$$F(\alpha) = \int_0^{\alpha}\frac{d\alpha}{f(\alpha)} \qquad (5)$$

Eq. 4 can be further simplified by taking logs, i.e.,

$$\ln\left(\frac{F(\alpha)}{T^2}\right) = \ln\frac{AR}{BE}\left(1-\frac{2RT}{E}\right)-\frac{E}{RT} \qquad (6)$$

The fraction of the sample reacted, i.e., was determined by measuring the ratio of the partial area at temperature T to the total peak area of the appropriate DSC curves shown in Fig. 1. The isothermal kinetic expressions, given in Refs. 16 and 17, representing various decomposition models were converted into non-isothermal kinetic expressions to determine the desired F() functions. The experimental data was then fitted to 12 non-isothermal kinetic models depicting geometrical models, the Unimolecular model, sigmoid rate models, diffusion models, and the 2nd order-diffusion model. A least squares procedure, in conjunction with Eqs. 4, 5, and 6, was adopted to ascertain the kinetics mechanism of water's desorption from lignite coal. Our calculations suggest that the Unimolecular kinetic model and 2nd-order diffusion kinetic model are simultaneously operative for the desorption of water from -20 mesh Beulah-Zap lignite coal; while for -400 mesh particle size coal, only the 2nd-order diffusion mechanism is effective. The activation energy barriers for Unimolecular decay and 2nd-order diffusion models were determined from Eq. 6. For -20 mesh particle size lignite coal the activation energies associated with Unimolecular decay model and 2nd-order diffusion model were 54 KJ/mol (12.94 Kcal/mol) and 78.5

KJ/mol (13.8 Kcal/mol), respectively. The activation energy of the 2nd-order diffusion model for - 400 mesh particle size Beulah-Zap lignite coal was 88.2 KJ/mol (21.1 Kcal/mol). The individual contributions of these kinetic models to the overall desorption of water from lignite coal were determined by fitting the experimental data to the temperature dependence of α (T), i.e.,

$$\alpha(T) = C_1(1-\exp(-Y(T))) + C_2\left(1-\frac{1}{Y(T)+1}\right), \qquad (7)$$

where, $C_1 + C_2 = 1$, and

$$Y(T) = \frac{ART^2}{BE}\left(1-\frac{2RT}{E}\right)\exp(-E/RT).$$

In Eq. 7, the first term on the right hand side represents the Unimolecular decay kinetics, while the second term depicts the 2nd-order diffusion kinetics. C_1 and C_2 for -20 mesh particle size coal were 0.23 and 0.77, respectively, while for -400 mesh particle size $C_1 = 0$ and $C_2 = 1$. Figure 2 compares the experimentally observed (T) with the calculated values for -20 mesh and -400 mesh particle size Beulah-Zap lignite coal. As can be seen from Fig. 2, the agreement between the calculated values and the experimentally observed values is excellent.

The Unimolecular decay kinetics of decomposition of a solid represents a system in which each molecule has an equal probability of undergoing decomposition. In a complex system like lignite coal, the bulk type water, present as a film around the particle or present as pore water in large pores, is expected to display evaporation like characteristics. This should be especially true for water which is away from the surface of coal or is around or near the mouth of large pores. Consequently, it is argued that the observed Unimolecular decay kinetics for -20 mesh particle size coal represents the loss of bulk type water from the Beulah-Zap lignite coal. The 2nd-order diffusion kinetics represents a recombination process in which product molecules are produced with excess energy. The excess energy is then utilized in re-energizing the reactant molecules. It seems to us the water molecules hydrogen bonded to the oxygen functional groups in narrow pores and surface water in large pores will desorb via the 2nd-order diffusion mechanism. As the particle size of coal is reduced to - 400 mesh from -20 mesh , the large pores concentration in coal sample is expected to decrease. Therefore, the observation of desorption of water from - 400 mesh particle size coal via 2nd-order diffusion mechanism is not unreasonable.

ISDK-FTIR Results

Figures 3 and 4 show the observed desorption kinetics of water at T = 294 K from the - 400 mesh particle size Beulah-Zap lignite coal in the water's stretching and bending regions, respectively. The desorption results can be summarized as follows: (1) Three broad vibrations were observed in the O-H stretching region at 3614, 3373, and 3222 cm^{-1} as reflected by the FTIR difference spectrum at t min., i.e., FTIR spectrum at 0 min. - FTIR spectrum at t min. In the water's bending region, positive bands at 1628, 1552, 1458, and 1384 cm^{-1} and a negative band at 1740 cm^{-1} were

found in the difference spectrum. The observed desorption kinetics for the water's stretching and bending modes are shown in Fig. 5. Attempts were made to determine the desorption kinetic mechanism(s) for 3614, 3373, 3222, and 1628 cm^{-1} bands by subjecting the intensity loss data to 12 desorption kinetics models as described in Refs. 15, 16, and 17. All the water bands, be they stretch modes or bend modes, displayed a 2nd-order diffusion mechanism. Therefore, our ISDK-FTIR results support and are consistent with our conclusion from DSC measurements that water from small particles of lignite coal desorbs via a 2nd-order diffusion mechanism.

ACKNOWLEDGMENTS

One of the authors (KSV) gratefully acknowledges the support of the U. S. Department of Energy, Pittsburgh Energy Technology Center for the part of the work dealing with the kinetics of drying.

REFERENCES

1. Mraw, S. C. and B. G. Silbernagel, Am. Inst. Physics Proceedings 70, 332 (1981).

2. Kaji, R., Y. Maranaka, K. Otsuka, and Y. Hishinuma, Fuel 65, 288 (1986).

3. Laskowski, J. S., Am. Chem. Soc. Preprints Fuel Chem. Div. 32 (1), 367 (1987).

4. Vorres, K. S., R. Kolman, and T. Griswold, Am. Chem. Soc. Preprints Fuel Chem. Div. 33 (2), 333 (1988).

5. Vorres, K. S. and R. Kolman, Am. Chem. Soc. Preprints Fuel Div. 33 (3), 7 (1988).

6. Abhari, R. and L. L. Isaacs, Energy & Fuels 4, 448 (1990).

7. Unsworth, J. F., C. S. Fowler, N. A. Heard, V. L. Weldon, and V. J. McBrierty, Fuel 67 1111 (1988).

8. Wendlandt, W. W., " Thermal Analysis", 3rd Ed., John Wiley, New York, 1986.

9. Cassel, R. B. and W. P. Brennan, Proc. 15th North American Thermal Analysis Society Conf., Paper #87, 402-406 (1986).

10. Maycock, J. N., Thermochimica Acta 1 389 (1970).

11. Janikowski, S. K. and V. I. Stenberg, Fuel 68, 95 (1989).

12. Elder, J. P. and M. B. Harris, Fuel 63, 262 (1984).

13. Jasty, S., P. Robinson, and V. M. Malhotra, Submitted to Phys. Rev. B (1990).

14. Jasty, S. and V. M. Malhotra, Submitted to Phys. Rev. B (1990).

15. Mu, R. and V. M. Malhotra, Submitted to Fuel (1990).

16. Malhotra, V. M. and A. A. Ogloza, Phys. & Chem. of Minerals 16, 386 (1989).
17. Malhotra, V. M., S. Jasty, and R. Mu, Appl. Spectrosc. 43, 638 (1989).

Table 1.

Kinetic Coefficients for Beulah-Zap Lignite
(k values are in units of 10^{-5} mg water/gm original sample sec^{-1})

Data at 293°K

Run#	Mesh	k	duration (sec)	R squared	
2	-100	9.0	9,000-20,000	.99993	
4	-100	10.	0-19,000	.9996	
14	-20	10.	0-20,000	.9998	
18	Block	11.	0-	.998	
22	-20	7.0	2,000-8,000	.97	+
23	-100	7.0	5,000-23,000	.9998	
24	Block	10.	0-6,000	.99997	
25	-400	11.	5,000-8,000	.9992	
26	-400	11.	0-8,000	.9993	
27	Block	8.0	0-12,000	.999991	

Data at 313°K

Run#	Mesh	k	duration (sec)	R squared	
3	-100	24.	1,000-7,000	.998	
6	-100	14.	2,000-8,000	.97	+
11	-20	24.	3,000-9,000	.998	
16	Block	23.	2,500-5,500	.9990	
19	Block	19.	1,000-9,000	.9995	

Data at 353°K

Run#	Mesh	k	duration (sec)	R squared
5	-100	99.	700-2,700	.997
7	-100	127	700-2,100	.9990
10	-20	131	900-2,100	.997
15	Block	85	1,100-2,900	.9994

Run in vacuum at 293°K

Run#	Mesh	k	duration (sec)	R squared
V6	-20	108.	1,000-3,000	.997

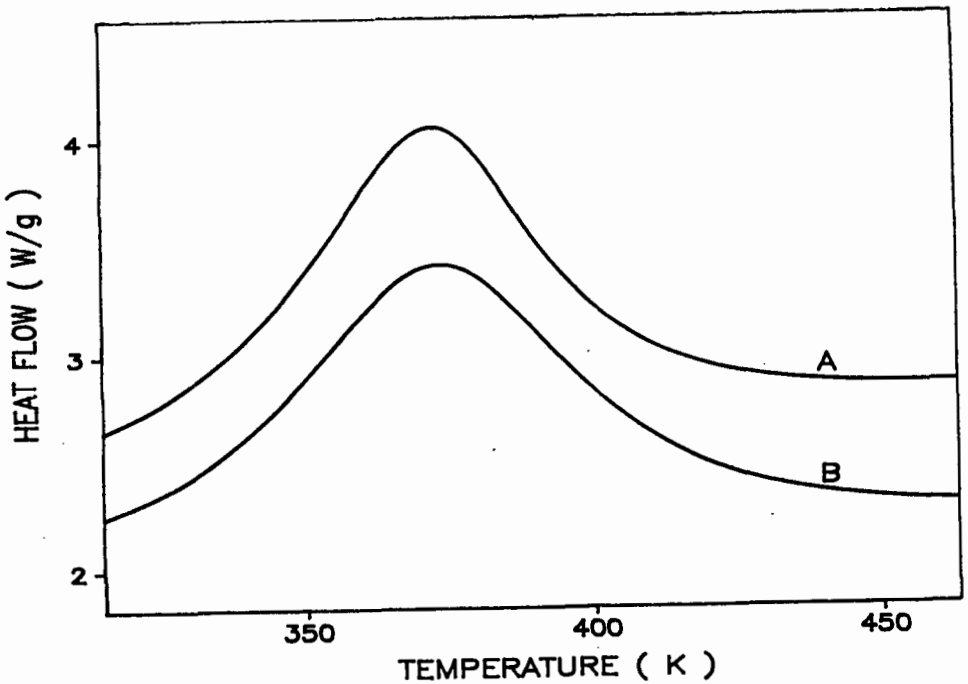

Fig. 1 The DSC curve shows the endothermic peak due to the desorption of water from Beulah-Zap lignite coal. (A) < 841 particle size, (B) < 37 particle size.

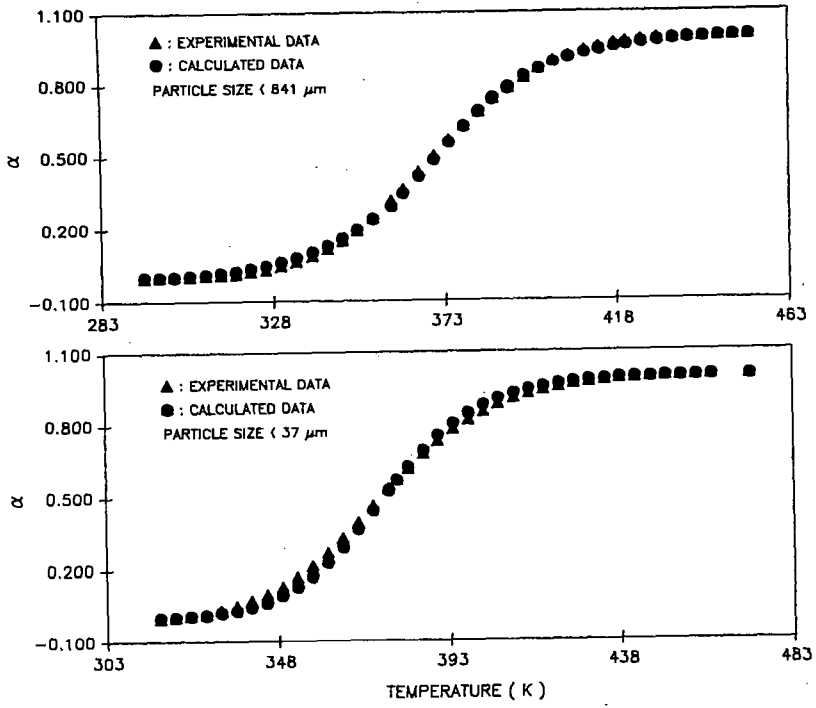

Fig. 2 This graph compares the experimentally observed desorption of water data with calculated values of Eq. 7.

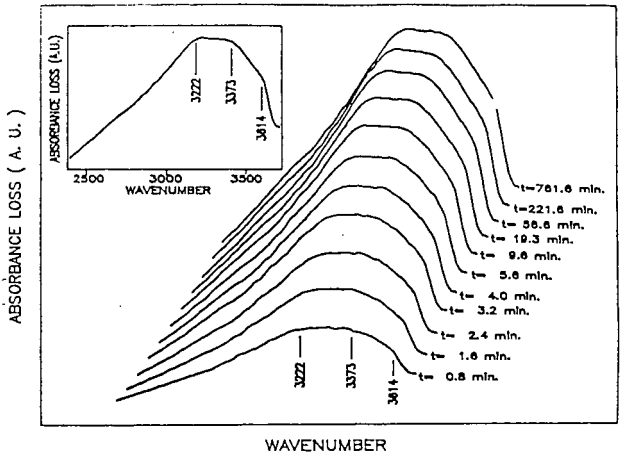

Fig. 3 FTIR difference spectra at t min. show the desorption kinetics of various types of water from < 37 particle size Beulah-Zap lignite coal in the water's stretching region.

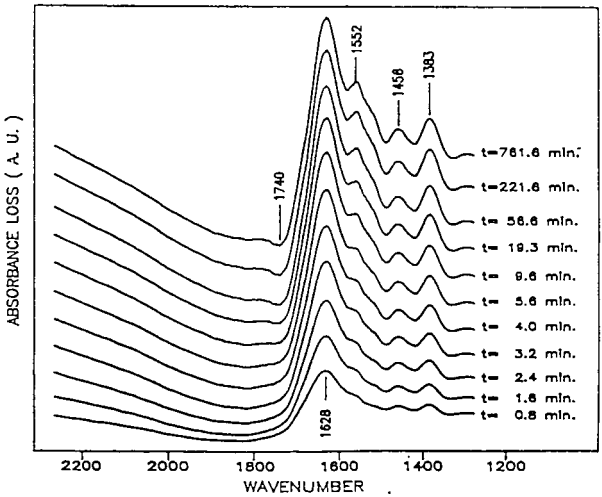

Fig. 4 FTIR difference spectra at t min. show the desorption kinetics of water from the lignite coal in the water's bending region.

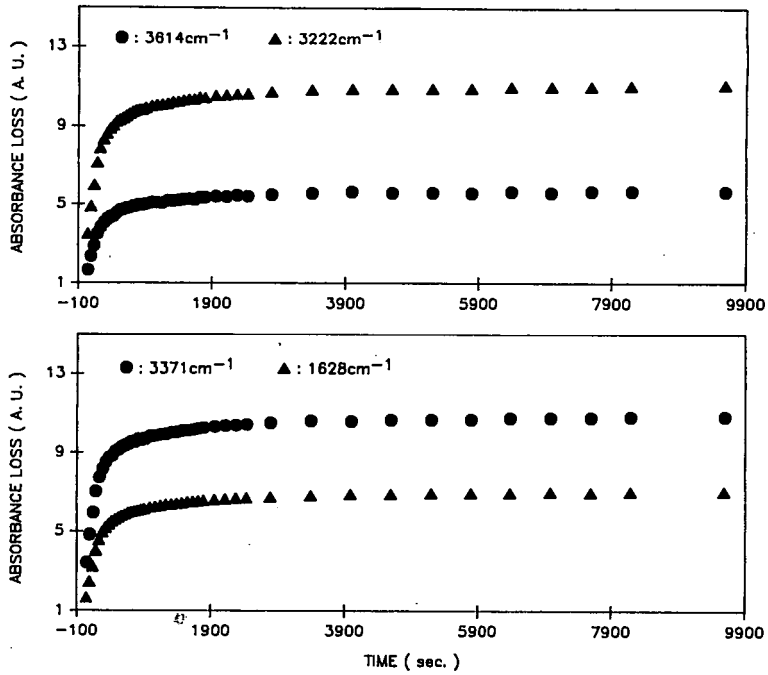

Fig. 5 Isothermal desorption kinetics of 3614, 3371, 3222, and 1628 cm^{-1} bands measured by monitoring the absorbance loss generated from difference spectrum at (t-0) min.

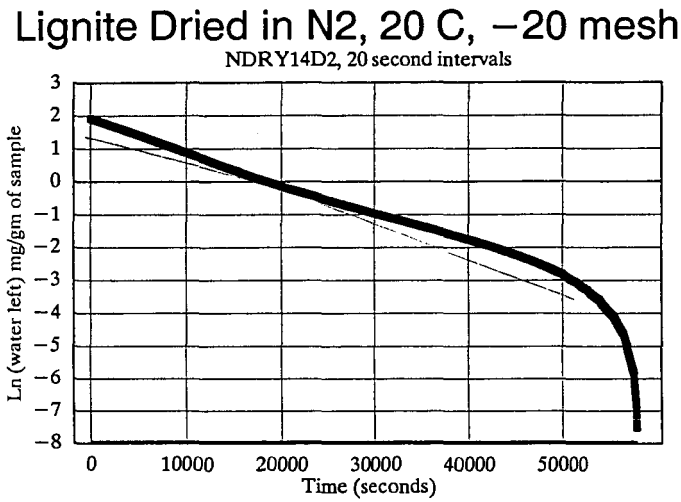

Figure 6. Typical Isothermal Thermogravimetry Run. Note two segments at different slopes after about 85% moisture loss.

HOT-WATER UPGRADING OF LOW-GRADE COAL: FUNDAMENTALS AND SLURRY RHEOLOGY

M. Rashid Khan and Todd Potas*
Texaco Research & Development,
P.O. Box 509, Beacon, NY 12508

*The University of North Dakota, Energy & Environmental Research Center, Grand Forks, ND 58202

ABSTRACT

Extensive bench-scale and pilot-plant studies have been conducted to better understand the fundamentals of hot-water drying of coal and the rheology of treated coal-water slurry. There was an increase in the heating value of the hot-water dried coal via decarboxylation. The formation of tar and extractables reduces the surface area and accessibility of water into the coal structure. As a result of decarboxylation and tar formation, the treated coal becomes relatively more hydrophobic. The slurry prepared from the hot-water dried coal was highly stable towards settling. The moisture reabsorption for the hot-water dried coal was minimal. Finally, the energy density of the slurry prepared from the hot-water dried coal approached those prepared from bituminous coals.

INTRODUCTION & BACKGROUND

The use of coal via gasification offers an excellent avenue to generate electric power with an increased efficiency for both energy recovery from coal as well as removal of pollutants (i.e., sulfur and nitrogen containing species). High-temperature pressurized, entrained-flow gasifiers (such as those used in The Texaco Coal Gasification Process) offer attractive options for integrated gasification combined cycle applications due to their high-throughput and low-level of contaminant production.

In many coal utilization processes, coal-water slurry fuel is used (1-5). Transport of coal into the gasifier by slurrying it with water offers several advantages: (a) the pumping technologies are proven and reliable, valves and flow measurement devices can be used; (b) the slurry feed is homogeneous, predictable and safe; (c) the presence of water in the slurry acts as a temperature moderator; resulting in reduced thermal wear. The high inherent moisture of low-rank coal (LRC), however, prevents the formation of coal slurry with high solids content needed for efficient operation. This necessatitates a method for preparing a slurry that is pumpable and still contains high energy density (i.e., solids content) to permit gasification at a reasonable rate of oxygen consumption. This implies the need to irreversibly reduce the moisture content of the coal.

Hot-water drying (also known as "hydrothermal treatment" or "wet carbonization") of coal, initiated several decades ago (6-9),

offers an excellent avenue to efficiently achieve the objectives of a suitable slurry for gasification. The aim of this study is to review the fundamental aspects of hot-water drying of low-rank coals.

EXPERIMENTAL

Hot-water drying of coal was conducted in various reactors: batch autoclave reactors, and a continuous thermal treatment reactor. One of the batch reactors consists of a 3.8 liter electrically heated autoclave and numerous thermocouples and pressure transducers. The unit was designed so that the reactant materials could be charged rapidly into a preheated autoclave from a piston-type accumulator. This allowed the charge materials to reach operating temperature in the relatively short time of 5 to 10 minutes. It also allowed for close control of residence times as the entire contents of the autoclave reactor charged into a 7.6 liter quench vessel at room temperature to end the drying and pyrolysis reactions rapidly. After quenching, the evolved gases were vented through cold traps (and were metered and analyzed). Description of the continuous thermal treatment reactor is presented elsewhere (4,5).

RESULTS & DISCUSSION

Influence of Pretreatment Temperature/Residence Time: For a given viscosity, the dry-solids content increased with the increasing processing temperature. The viscosity versus solids contents for slurries made from treated (at various temperatures) Indian Head Lignite is shown in Figure 1. At a viscosity of 800 cP, the

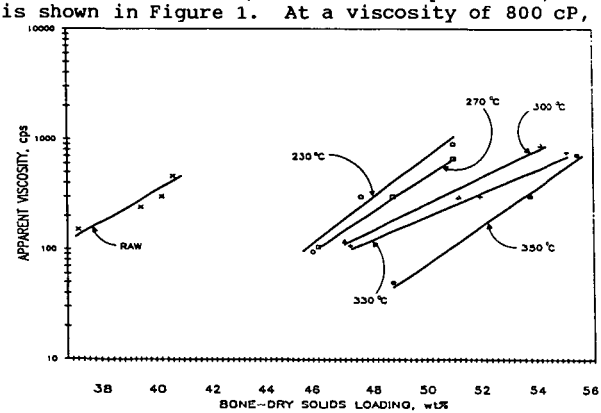

Figure 1. Apparent viscosity at 410 s^{-1} and 28°C versus solids content for coal/water slurry prepared from Indian Head Lignite before and after hydrothermal treatment

solids content increased from 42.5% to 55.5% (at a shear rate of 410 sec^{-1} at 28 °C) after processing at 350°C. In addition, the higher the pretreatment temperature, the higher the solids contents, for a given viscosity of 800 cP. The slurry energy content also increased by pretreatment at 330°C (1,4).

As a result of pretreatment at 330°C, the slurry prepared from Indian Head lignite contained 150 percent of the heat content of the raw slurry. An increase in pretreatment temperature resulted in an increase in heating values for all coals (Figure 2), although to a lesser extent for higher rank coals. The influence of residence time of pretreatment on the slurry solids content is shown in Figure 3. The longer the residence, the greater the slurryability of the products. An increase in pretreatment temperature also reduced the equilibrium moisture content for all coals (Figure 4), measured soon after pretreatment.

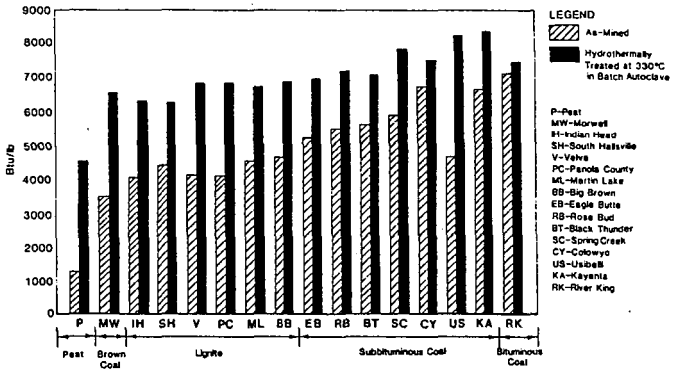

Figure 2. Slurry heating value (dry-basis) of raw and 330°C treated coal at maximum solids concentration.

Influence of Coal Type: The lower the rank of the coal, the greater the reductions in equilibrium moisture content (Figure 4) upon pretreatment. This effect is attributable to the higher concentrations of oxygen functional groups and the associated water molecules present in the lower rank coals.

The changes to the coal structure as a result of hydrothermal treatment were irreversible, and the coal maintained a low equilibrium moisture content in either air or water, unlike the untreated coal.

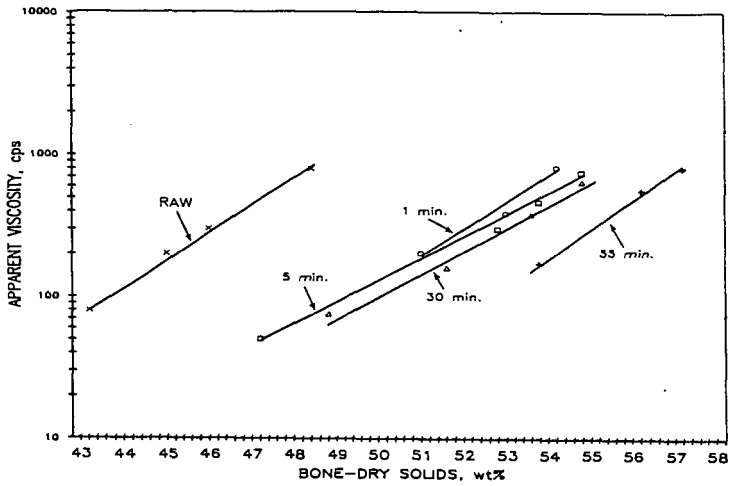

Figure 3. Apparent viscosity versus solids content for a subbituminous coal (Spring Creek, Montana) processed at 330°C at various residence times in a continuous reactor.

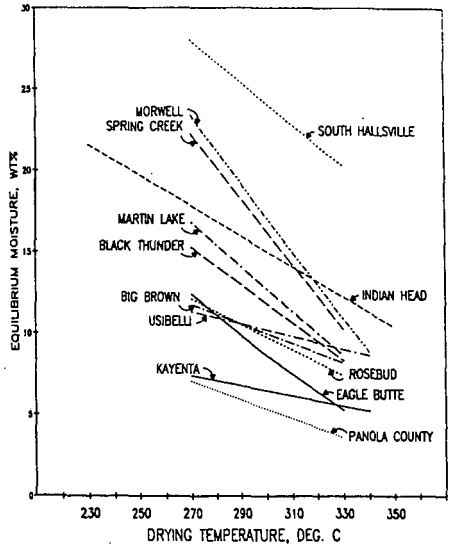

Figure 4. Equilibrium moisture versus pretreatment (hot-water-drying) temperature of various coals.

CP/MAS: Cross Polarization/Magic Angle Spinning (CP/MAS) Solid State C^{13}-NMR spectroscopy provided interesting results on the effects of hot-water drying on the structure of the processed coal. Spectra for as-received and the hydrothermally treated coals (at 330°C, Indian Head lignite) are shown in Figure 5. The raw lignite contained large quantities of aliphatic material, long chain waxes and alkanes. However, when the coal was hydrothermally treated at 330°C there was a dramatic reduction in these groups, perhaps as a result of cracking and extraction. Many coals examined exhibited a significant weight-loss due to expulsion of carboxylic groups during thermal treatment. The carboxylic groups, unlike aliphatic compounds, do not contribute significantly to the heating value of coal. Thus, the loss of these oxygenated functional groups actually enhances the energy density of the product.

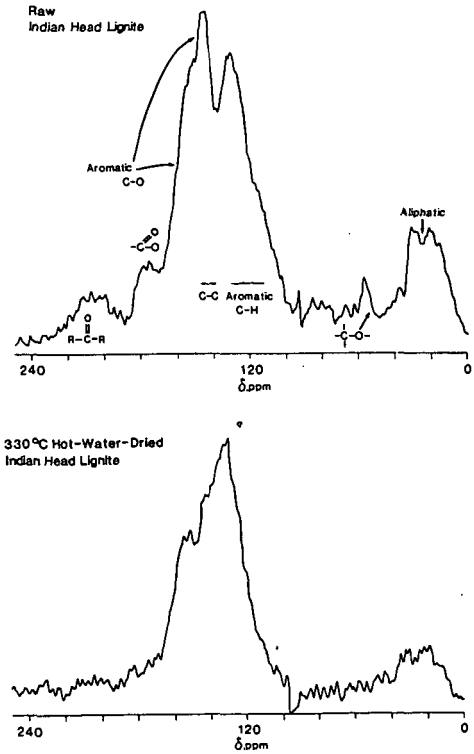

Figure 5. Solid-state ^{13}C NMR spectra for as-mined and 330°C hot-water dried Indian Head (North Dakota) lignite.

Evolved Products: Table 1 provides additional data on the influence of pretreatment temperature on coal structure, and on the nature of the evolved products as a result of heat-treatment. After hydrothermal treatment of Indian Head Lignite at 340°C, the yield of phenolics, alcohols and hydrocarbon gases represented less than 1 wt% of the raw maf coal, while the yield of decarboxylation products (CO_2, CO and H_2O) represented nearly 18% of the products. Decarboxylation of coal had a major effect on reducing the hydrophilic nature of coal, as reflected by the decreases in the equilibrium moisture content.

Formation of Extractables: A significant impact of hydrothermal-treatment was also reflected in the exuded tar yield from the treated coal. The yield of extractables (tar) was significantly increased as a result of hydrothermal treatment (Figure 6). The

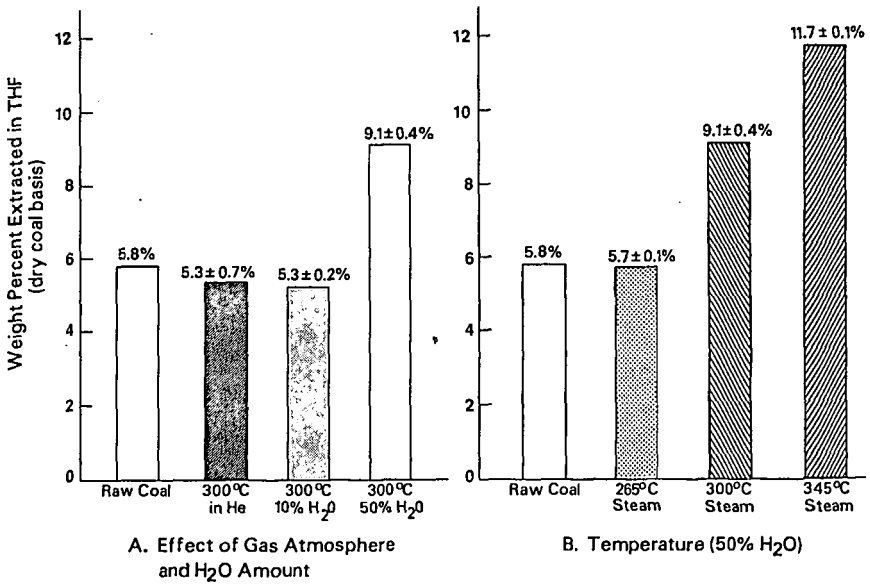

Figure 6. Effect of hot-water-drying of coal on extractable yield

Table 1

COMPARISON OF MATERIAL BALANCE RESULTS FOR HYDROTHERMALLY TREATING INDIAN HEAD LIGNITE IN A COLD-CHARGE AUTOCLAVE

Coal	Indian Head				
Process Temp., °C	231	272	302	333	348
Process Pressure, Psig	400	900	1,400	2,300	2,500
Net Yields - wt% maf coal[a]					
Decarboxylation and Dehydration Products ($CO+CO_2+H_2O$)	1.6	9.8	13.8	14.8	17.5
Pyrolysis Product Gases ($H_2+C_1-C_4+H_2S+NH_3$)	0.0	0.0	0.2	0.2	0.1
Pyrolysis Product Liquids (Phenols, Methanol, Acetone, MEK)	0.0	0.2	0.4	0.4	0.8
Residual maf coal	98.1	92.2	87.7	85.9	83.1
Energy Recovery, %	100.0	98.2	97.8	98.4	96.6
Product Coal Characteristics					
Heating value, mf basis, Btu/lb	10,400	10,800	11,200	11,400	11,600
Equilibrium Moisture, wt %	20.9	18.0	14.5	13.5	7.4
lbs ash/MM Btu	14.83	13.28	13.44	13.93	14.02
lbs sodium/MM Btu	0.53	0.47	0.42	0.42	0.27
lbs sulfur/MM Btu	1.03	0.98	1.00	1.02	0.94
Coal-Water Slurry Properties[b]					
Maximum measured solids concentration, wt%	51.0	50.9	54.2	55.3	55.6
Apparent viscosity, cps					
at 100 sec^{-1} and 28°C	1,770	1,530	1,280	1,420	1,190
at 410 sec^{-1} and 28°C	890	650	860	740	710
Heating value, Btu/lb	5,300	5,500	6,070	6,300	6,450

[a]Net yields do not total 100% because of errors introduced by the changing inorganic content of the coal and the changing ways it behaves when samples are ashed.

[b]The data shown is for samples which were first filtered without washing and then reslurried in deionized water. For some coals significant improvements were seen when the filter cake was washed.

yield of tar was quantified by extracting the treated coal with tetrahydrofuran (THF), as described elsewhere (3). For the Illinois No. 6, the yield of extractables increased significantly with the increase in pretreatment temperature. The influences of gas atmosphere (amount of water) and temperature of pretreatment are shown in Figure 6.

Surface Area of Treated Products Compared to Feed: An important change involved the sealing of the coal pores which exuded the tar. The influence of tar condensation on coal pores (and openings) and surfaces resulted in a decrease in the surface area (i.e., accessibility) as well as the hydrophilic nature of coal. As a result, the surface area of the hot-water dried coal decreased by 30 to 40%, as determined by BET (Brunauer, Emmett, and Teller) approach.

REFERENCES:

1. Potas, T. et.al "Preparation of Hydrothermally Treated LRC-Water Slurries", Chem. Engr. Comm., Vol. 44, pp 133-151, 1986.

2. Khan, M. R., W. Chem. and E. Suuberg, "Influence of Steam Pretreatment on Coal Composition and Devolatilization," Energy & Fuels 3, March/April, 1989.

3. Khan, M. R., "An Overview of Mild Gasification Research," Proceedings, Gasification Contractors' Meeting, US Dept. of Energy, June 27-29, 1989.

4. Willson, W. G. et. al, "Low-Rank Coal Water Slurries for Gasification," Final Report by UNDEERC, EPRI Report No. AP-4262, Nov., 1985.

5. Potas, T. A. et. al, "Pilot Scale Preparation of Lignite and Sub-bituminous Coal Water Fuels," Coal/Water Slurry Preparation and Utilization Conference, Orlando, FL, May 1985

6. H. Klein, "The Fleissner Method of Drying Lignites; Its Underlying Chemical and Physical Principles", BRAUN Kohle 29, 1-30, 1930.

7. G. A. Wiltsee, "Low-Rank Coal Research" Quarterly Report July-September, 1984. University of North Dakota Energy Research Center. Technical Report DOE/FE/60181-1682. Technical Information Center. U.S. Department of Energy.

8. H. Fleissner, U.S. Patent 1,632,829, 1927; H. Fleissner, U.S. Patent 1,679,078, 1928.

9. B. Stanmore, D. N. Baria and L. E. Paulson, "Steam Drying of Lignite: A Review of Processes and Performance", DOE/GFETC/RI-82/1, (DOE 82007849), 1982.

TEMPERATURE AND HIGH SHEAR VISCOSITY ON THE HANDLING OF COAL-WATER SLURRIES

Frank Ohene, Keith Bowman, Antonio Williams and Bryan Obonna
Chemistry Department, Grambling State University
Grambling, La 71270
and
John P. Dooher
Physics Department, Adelphi University
Garden City, NY 11530

ABSTRACT

An experimental study of the effect of high shear rheology and temperature on coal-water slurry, (CWS), was studied. Slurries for this study were formulated in our laboratory from four different coals, ranging from subbituminous western coal to eastern bituminous coals in order to gain a broader understanding of the CWS behavior. All the slurries exhibited a non-Newtonian flow and the packing efficiency of the particles was found to govern the slurry behavior.

(Key Words: rheological, viscosity, particle size distribution)

INTRODUCTION

Coal-Water Slurries have the potential of a near-term replacement for fuel oil [1]. The fundamental understanding of the preparation and handling of highly loaded CWS with low viscosity and desirable atomization and combustion properties is necessary in the commercialization of the CWS [2].

The design of flow systems of suspensions with high solids content such as Coal-Water Slurries, require a detailed rheological knowledge of the suspension [3]. Mathematical models such as Bingham plastic model, Power law model, or H.-Bulkley model have been used to define the flow properties of such suspensions [4,5]. For most suspensions however, the governing parameters have to be determined experimentally. This is due to the variability in characteristics such as the particle size distribution, shape of the particles, concentration of solids, surface chemistry of the particles, and dispersants used to stabilize the suspensions [6,7].

Solids concentration and particle size have been recognized as important hydraulic variables and particle size distribution (PSD) is of considerable importance in CWS formulation [8]. However, no universally acceptable method for its incorporation into models and correlations has been established. Thus, the specific influence of the various particle size fractions on the rheology of CWS continue to receive attention.

This paper reports the results of an experimental technique of examining the various particle size fractions on CWS rheology, using a combination of a Haake RV-20 concentric cylinder viscometer and an Extrusion Rheometer.

EXPERIMENTAL

The coals used in all the experiments were from the Pennsylvania State University Coal Data Bank. The Proximate and Ultimate analyses of the coals are as shown in Table 1.

The coal samples were ground to a distribution as shown in Figure 1 and carefully screened to obtain size fractions of: -400 mesh, +400/-325 mesh, +325/-270 mesh, +270/-200 mesh and +200/-100 mesh using standard U.S sieve screens. Slurries were prepared from blended distributions as shown in Table 2 and using either an ammonium naphthalene sulfonate (A-23) or Igepal 990 as an additive. Each slurry was made using a dosage of 0.3% dispersant based on dry coal and at a pH of 10. The packing concentrations were calculated from particle size distribution measurements obtained by using a Microtrac Particle Size Analyzer Model 2600, and a program based on truncated log-normal distribution which has been developed at the Adelphi Center for Energy Studies. The packing concentrations calculated increased with increase in the number of fines (-325 mesh) to a value of 40 % fines by weight. Above a value of 40% fines, the packing concentration decreased.

Rheological Testing

A Haake RV-20 concentric cylinder viscometer and an Extrusion Rheometer were used to determine the rheological properties of the CWS at low and high shear rates. In The RV-20, the slurry is sheared in the annular gap between a rotating bob and a stationary cup. The torque necessary to rotate the bob at a given speed is measured by a torsion spring. The drive unit consists of a driving motor, a tachometer- generator, and a reduction gear. The stator is surrounded by a temperature tempering vessel (enclosed in a steel container to prevent moisture loss) connected with a constant temperature bath. The temperature can be controlled to $\pm$ 0.01°C.

The viscometer is integrated with an IBM ps/2 data acquisition and analysis system. The signals from the viscometer is monitored twice per second and converted to torque and rotational speed values. Viscosity as a function of shear rate was computed using one of the following flow models:

$\tau=\tau_o + \mu_p\gamma^{\cdot}$ (Bingham law) (1)

$\tau=K\gamma^{\cdot n}$ (Power law) (2)

$\tau= \tau_o + K\gamma^{\cdot n}$ (H.-Bulkley law) (3)

Where:

τ_o is the yield value

K is the flow consistency number

n is the flow behavior index.

n= 1 for a Newtonian flow

< for a pseudoplastic material

and > for a dilatant material.

Figure 2 shows a typical flow curve for a CWS formulated at 65% solids content generated in this viscometer. The shear rate, to which the sample was subjected, was continuously increased from zero to a maximum determined by the viscosity of the CWS (curve 1). Curve 2 decreased to zero, curve 3 increased to a maximum, and curve 4 decreased to zero. The viscosity measurements were taken from curve 3, which represents the fluid

after it has been sheared and its structure broken down.

RESULTS AND DISCUSSION:

Effect of Particle Size Distribution on Rheology of CWS.

Figure 3 shows the effect of particle size distribution on the flow behavior of the slurries. Table 3 lists the rheological data evaluated from these flow curves. The particle size distribution was formulated according to the information contained in Table 2, and all the slurries contained 65% solids content and 0.3% A-23 dispersant.

Rheological analyses of the flow curves show that the flow behavior changed from dilatant to pseudoplastic as the packing concentration increased. Also, the viscosity was found to decrease with increase in the packing concentrations of the slurries. This is an indication that a wider distribution is indeed necessary for more efficient packing.

Effect of Shear Rate on Flow Behavior

Figure 4 is the flow behavior of 63% solids loading of the four coals listed in Table 1. Their rheological properties are listed in Table 4. All the samples exhibit a pseudoplastic behavior with yield at this slurry concentration. PSOC-1493 and 1494 however, have higher yield values and viscosities relative to PSOC-1487 and 1475.

Previous studies on the effect of coal properties on slurry quality show that the acidic functional groups on the coal surface as well as the equilibrium moisture content of the coal samples have an adverse effect on the slurry quality [9,10,11]. ESCA analysis of these samples show a higher degree of carboxylic functional groups on PSOC-1494 and 1493 relative to PSOC-1475 and 1487. The differences in the flow patterns observed may be due to their characteristic properties.

High shear Rheology of 65% solids content of PSOC-1475 was determined using an Extrusion Rheometer. This device determines the apparent viscosity of the slurry under flowing conditions. The CWS volume flow rate, Q, and pressure drop , ΔP, were measured for laminar flow through a tube of Length, L, and radius, R. The shear stress, τ_p, and the shear rate, $\gamma^{\cdot}$, were obtained from the pipeline flow data as follows:

The shear stress at the pipe wall, τ_p, can be defined as:

$$\tau_p = \frac{R}{2}\left(\frac{\Delta P}{L}\right) \qquad (4)$$

against a pipe flow characteristic, Γ, given by:

$$\Gamma = \frac{4\,(Q)}{\pi R^3} \qquad (5)$$

where $\Delta P/L$ is the pressure gradient along the tube of length , L

Q is the volumetric flow

and R is the tube inside radius.

Γ relates to $\gamma^{\cdot}$ through the Rabinowitsch-Mooney relation [12]:

$$\gamma^{\cdot}_p = (1/4)\Gamma[(3+(d \ln\Gamma/d \ln\tau_p)] \quad (6)$$

The apparent viscosity of the suspension then is given by

$$\eta = \tau_p/\gamma^{\cdot}_p \quad (7)$$

The data obtained from the Extrusion Rheometer are shown in Table 5. Figure 5 is the rheogram generated from this data. Rheological analysis shows that the rheogram can be described by the relation:

$$\tau = 1.4 + 0.84\ (\gamma^{\cdot})^{0.96} \quad (8)$$

The apparent viscosities of the slurry as a function of shear rate are listed in Table 6. There is a decrease in viscosity with increase in shear rate to a value of 4000 s^{-1} due to the existence of yield stresses, but the viscosity remains fairly constant after a shear rate of 4000 s^{-1}.

Effect of Temperature

The variation of viscosity of 67% solids of PSOC-1475 as a function of temperature is shown in Figure 6. The viscosity of CWS was found to decrease with increase in temperature between 19 °C and 50 °C. However, with Igepal 990 as an additive, there was an increase in viscosity between 45 °C and 60 °C. It is apparent that the flow behavior of the slurry in the low temperature range is governed by the behavior of water. Above 45°C, the flow behavior is dependent on the additive. The change in flow behavior can be caused by changes in the solubility behavior or changes in the interaction of the additive with the coal particles at higher temperatures [13]. This may explain the increase in viscosity with increase in temperature when Igepal 990 was used as a dispersant.

The high temperature behavior of CWS is of interest with regard to their atomization behavior. Thus, CWS prepared using Igepal 990 as an additive will require special handling techniques at higher temperatures.

CONCLUSION

An experimental technique of examining the influence of particle size distribution and high shear rheology of CWS has been made. The results of the study indicate a range of rheological behavior depending on solids content, particle size distribution, and coal type. Solids with low packing efficiency have relatively high time-independent yield points and also have high viscosities at a shear rate of 100 s^{-1}.

Slurries prepared from coals with low moisture content however, have low time-independent yield values compared to slurries prepared with high moisture content.

The behavior of a slurry at high temperatures is dependent on the additive type. With Igepal 990 as an additive, the slurry viscosity increases with increase in temperature indicating that preheating of such a slurry may present handling problems.

REFERENCES:

1. Manfred, R. F., and Ehrlich, S., "Combustion of Clean Coal-Water Slurry", Proc. Am. Power Conf. 1982, **44**, 1042.

2. Kikkawa, H., Okiura, K., Arikawa, Y., Hitachi, K., and Kure, K., "Development of Highly Loaded CWM Preparation System". Proc. Sixth Int'l. Symp. on Coal Slurry Fuels Preparation and Utilization, 1984, 949.

3. Faddick, R.R., Proc. 3rd Int'l Conf. on Hydr. Transp. of solids in Pipes. Banff, Canada, 1976, May 18-21.

4. Hoffman, R. L., Trans. Soc. Rheol., 1972, **16**, 155.

5. Dinger, D. R., Funk, J. E., Jr., and Funk, J. E., Sr., " Rheology of High Solids Coal-Water Mixture." Proc. 4th Intl. Symp. on Coal Slurry Combustion, Orlando, Fl., (1982)

6. Cluine, J. S., and Ingram, B.T., in "Adsorption from solutions at the Solid/Liquid Interface." (G.D. Praffit and C. H Rochester, Eds.), Academic Press, New York, 1983, p. 105.

7. Fuerstenau, D. W., Resenbaum, J. M. and J. Laskowski, Colloids and Interface Science, 1983, **8**, 153.

8. Mooney, M., "Viscosity of a Concentrated Suspension of Spherical Particles", J. Coll. Sci., 1951, **6**, 162.

9. Botsaris, G. D. and K. N. Astill, "Effect of Interaction Between Particles On The Viscosity Of Coal Water Slurries". Proc. 6th Intl. Symp. on Coal Slurry Combustion and Technology, Orlando, Fl., 1984, 304.

10. Casassa, E. Z., G. D. Parfitt, A. S. Rao and E. W. Toor, "The Effects of Surface Active Agents On Coal-Water Slurry Stability". Proc. 6th Intl. Symp. on Coal Slurry Combustion and Technology, Orlando, Fl., 1984, 251.

11. Ohene, F., Third Quarterly Report. DOE/DE-FG22-88PC925 (1988).

12. Antonini, G., Francois, O., Gislais, P., and A. Touret, "A Direct Rheological Characterization Of Highly Loaded Coal-Water Slurries Flowing Through Pipes". Proc. 6th Intl. Symp. on Coal Slurry Combustion and Technology, 1984, 899.

13. Rosen,M. J. "Surfactants and Interfacial Phenomena". Wiley Interscience, New York, 1978.

ACKNOWLEDGEMENT

The authors will like to thank the U. S. Department of Energy for Financial Support.

Table 1

Proximate and Ultimate Analyses Of Coal Samples.

	PSOC-1494 Kentucky #9	PSOC-1487 Adaville#1	PSOC-1493 Illinois#6	PSOC-1475 Elkhorn#3
Proximate Analysis				
% Moisture	7.12	18.99	9.43	3.37
% Ash	10.97	4.55	13.74	3.22
% Volatile	35.77	34.67	34.34	36.03
% Fixed Carbon	46.14	41.78	42.50	57.38
ULTIMATE ANALYSIS				
% Ash	10.97	4.55	13.74	3.22
% Carbon	65.32	57.96	59.98	78.38
% Hydrogen	3.98	4.09	3.74	5.20
% Nitrogen	1.14	0.84	1.15	1.44
% Total Sulfur	4.50	1.06	4.51	0.95
% Oxygen	6.97	12.50	7.41	7.45
C/O	9.37	4.64	8.09	10.45
FC/VM	1.29	1.21	1.24	1.59
HG Index	72.00	61.10	62.20	58.70

Table 2

Weight Fractions And Packing Concentrations

WT %>200 MESH	WT% -200/325 MESH	WT %<325 MESH	PACKING CONCENTRATION
53.7%	8.5%	37.8%	83.4%
47.7%	9.4%	42.9%	83.1%
41.7%	9.0%	49.3%	83.6%
43.6%	9.4%	47.0%	76.4%
53%	8.3%	39.7%	85.3%
36.2%	15.4%	48.4%	72.1%
26.5%	18.1%	55.4%	73.4%
9.6%	15.6%	74.8%	69.6%
58.1%	2.2%	39.7%	85.2%

Table 3

Rheological Properties Of 65% (PSOC-1475) CWS
With Varying Packing Concentrations.

PACKING	n	τ_o	K	R^2	η_{100}(mPas)
69.6	1.036	3.25	0.276	0.99	335
72.1	0.970	2.01	0.340	0.97	320
73.4	0.907	1.76	0.322	0.98	301
76.4	0.884	4.10	0.827	0.97	248

Table 4

Rheological Properties of 63% CWS.

Sample	n	τ_o	K	R^2	η_{100}(mPas)
1494	0.680	24.0	0.676	0.86	445
1493	0.729	11.3	1.42	0.98	527
1487	0.913	0.250	0.879	0.93	293
1475	0.916	0.082	0.238	0.99	180

Table 5

Extrusion Rheometer Flow Data.

Weight of Slurry/s	Pressure (psig)	Shear Rate(s^{-1})	Shear Stress(mPa)	Viscosity mPa.s
1.6195	10	1181	7860	665
2.55	20	1866	15721	642
5.4995	30	4008	23581	588
7.3921	40	5391	31441	583
9.999	50	7292	39302	539
11.615	60	8471	47162	557
14.237	70	10383	55022	530
15.4417	80	11262	62882	558
17.4041	90	12692	70743	557
20.2955	100	14801	78603	531

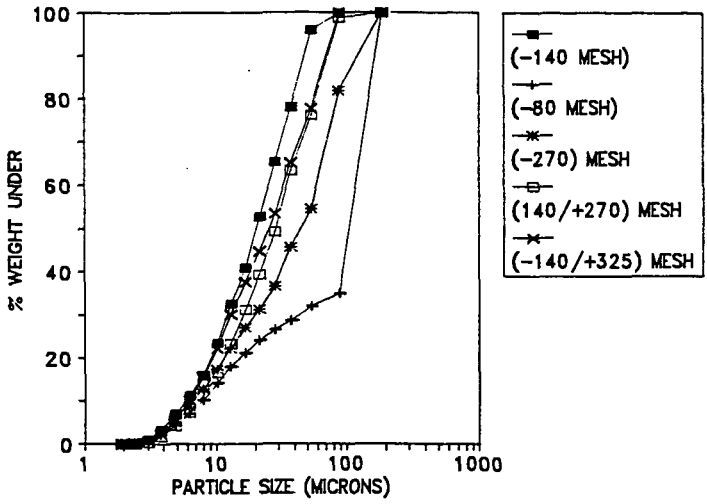

FIGURE 1. PARTICLE SIZE DISTRIBUTION

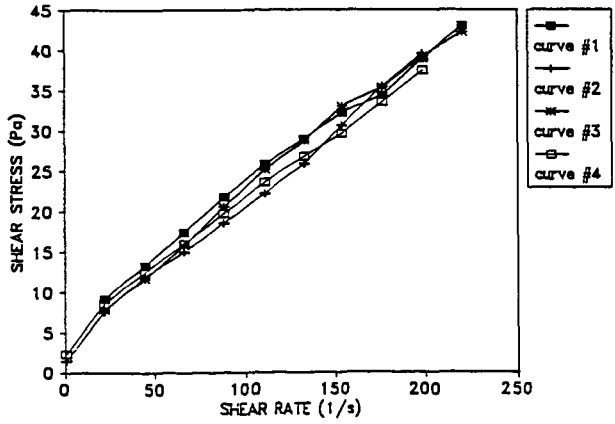

FIGURE 2. FLOW CURVE OF 65% CWS.

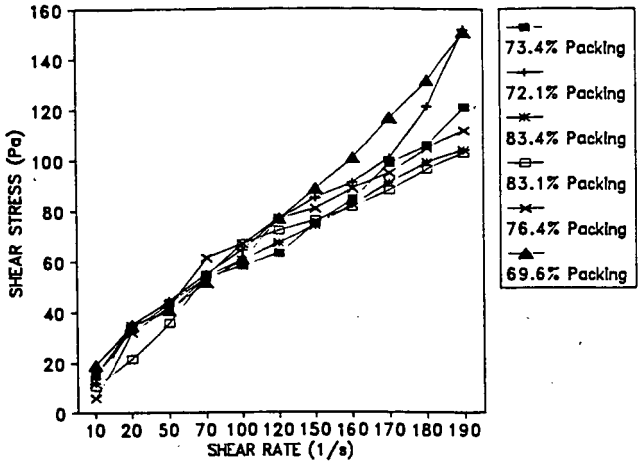

FIGURE 3. THE EFFECT OF PARTICLE SIZE DISTRIBUTION ON THE FLOW BEHAVIOR OF 65% CWS

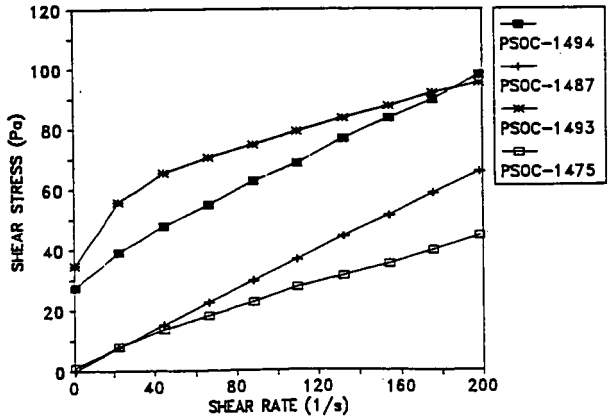

FIGURE 4. VARIATION OF VISCOSITY AS A FUNCTION OF TEMPERATURE

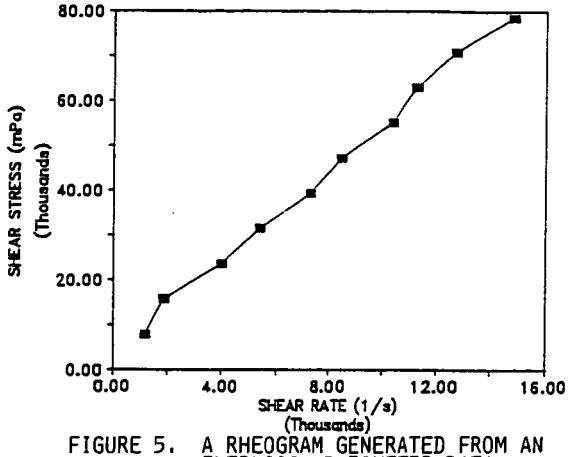

FIGURE 5. A RHEOGRAM GENERATED FROM AN EXTRUSION RHEOMETER DATA

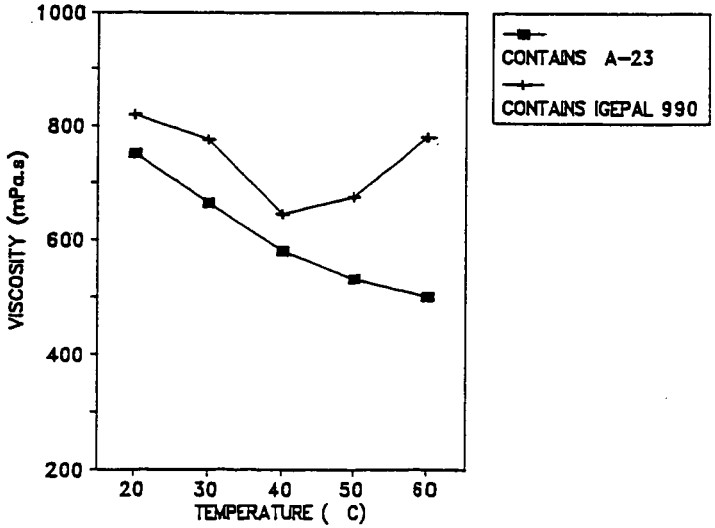

FIGURE 6. VARIATION OF VISCOSITY AS A FUNCTION OF TEMPERATURE

ENHANCED COAL HYDROGASIFICATION VIA OXIDATIVE PRETREATMENT

Martin E. Toomajian, Michael G. Lussier, and Dennis J. Miller
Department of Chemical Engineering
Michigan State University
East Lansing, MI 48824.

Key Words: Hydrogasification, Pretreatment, Oxidation

INTRODUCTION

Coal hydrogasification is not commonly viewed as a competitive route to gaseous fuels and thus has not been studied as extensively as steam gasification. Relative to steam gasification, hydrogasification requires higher pressures to make the reaction thermodynamically favorable; more importantly, hydrogen is presently too expensive to be considered a viable reactant for large-scale coal conversion. Hydrogasification is, however, a useful research tool for improving the understanding of other coal gasification processes. Further, hydrogasification is the primary reaction in at least one coal conversion process, the HYDROCARB process [1], and could be an important means of enhancing methane yields in gasification processes such as that developed by Exxon [2].

The reaction of carbon with pure hydrogen offers a unique opportunity to study the role of oxygen in gasification, since any oxygen present during gasification must be initially associated with the solid. Generally, oxygen is present in bulk carbon and as chemically-bound functional groups on the carbon surface. The desorption of these functional groups as CO or CO_2 may be the rate-limiting step in oxidative gasification; desorption also leaves "nascent", or reactive, sites at which further reaction occurs [3]. Thus, oxidizing the carbon surface prior to conversion should increase the concentration of active sites for gasification.

Exposure to molecular oxygen and immersion in concentrated nitric acid are two common methods of oxidative pretreatment of carbonaceous solids. Partial combustion in oxygen may convert some carbon and open new pore structure, while HNO_3 pretreatment does not significantly alter total surface area or carbon structure [4].

For steam and CO_2 gasification, it has been shown that oxidative pretreatment enhances both catalyzed and uncatalyzed gasification rates. In uncatalyzed gasification, Keleman and Freund [5] determined that prior oxidation of a glassy carbon enhances the dissociative adsorption of O_2 and CO_2 on the surface, thus enhancing gasification rate. In catalyzed gasification, Mims and Krajewski [6] determined that catalyst activity is related to the presence of surface oxygen groups. Keleman et al. [7] and Saber et al. [8] showed that surface oxygen groups have a stabilizing effect on alkali salt catalysts and aid in activating the catalysts. Finally, Ohtsuka et al. [9] found that HNO_3 pretreatment increases the gasification rate by six-fold.

The presence of oxygen also strongly affects hydrogen gasification rates. Cao and Back [10] determined that adding 0.1% oxygen to hydrogen increases the rate of methane formation by an order of magnitude, and Blackwood [11] reported that hydrogasification rate depends on oxygen content of the reacting wood char. Otake and Jenkins

[12] showed that methane formation is directly related to desorption of oxygen complexes as carbon monoxide.

Previous work in our laboratory with model carbons [13,14] illustrated that pretreatment via partial combustion produces up to a two-fold increase in uncatalyzed hydrogasification rate. Also, HNO_3 oxidation results in as much as a three-fold enhancement of the K_2CO_3-catalyzed rate and a lesser (50%) increase in the uncatalyzed rate. Based on the work of Walker [3], Zoheidi [15] postulated that desorption of oxygen groups occurs during heatup. This desorption creates reactive sites at which hydrogen attacks to form methane. Treptau and Miller [14] used x-ray photoelectron spectroscopy to verify that surface oxygen groups desorb before gasification temperatures are reached.

In this paper, we present initial results of oxidative treatment of coal char for the purpose of enhancing hydrogasification rates and overall conversion of coal to methane. Oxidation both before and during the course of carbon conversion is investigated.

EXPERIMENTAL

A coal char, a demineralized coal char, and a Saran char were used as solid reactants in this study. The coal chars were prepared from an Illinois #6 coal (PSOC 1493), and the Saran char was prepared from Saran (Dow MA 127) resin powder. Ultimate analysis of the three chars are given in Table 1.

The chars were prepared by heating coal or Saran resin in a 4.8 cm ID quartz tube furnace under nitrogen at 10°C/min to 900°C and holding for 30 minutes. A portion of the coal char prepared was then demineralized by contacting repeatedly with concentrated HF and concentrated HCl at 55-60°C, vacuum drying in nitrogen at 110°C, and then reheating under nitrogen to 900°C to remove residual volatiles. A sample of each of the three chars was loaded with 10 wt% K_2CO_3 by drying a slurry of char and K_2CO_3 solution at 90°C for several hours.

Oxidative treatments were performed prior to gasification and following partial gasification in hydrogen by exposing chars to air at 375°C in the quartz tube furnace. For oxidation prior to gasification (preoxidation), approximately five grams of char were oxidized in an air flow of 50cc/min. For oxidation following partial gasification, char samples were removed from the gasification reactor, placed in the quartz tube furnace, and oxidized in stagnant air.

Hydrogasification was conducted in a high temperature, high pressure, differential flow reactor. The pressure vessel, furnace, gas collection system, and gas analysis system are all described in detail by Zoheidi [15] with the exception that a Varian Model 3300 Gas Chromatograph is now used for gas analysis. Samples were gasified at 700-800°C in 500 psi pure hydrogen. Rates were measured by timed collection of product gases.

Char samples were analyzed via several procedures both before and after gasification and oxidative treatment. X-ray photoelectron spectroscopy (XPS) was used to determine the surface concentration of oxygen on samples treated at different temperatures and reactor conditions. A vacuum pretreatment reactor [14] enabled us to heat samples to 1000°C under high vacuum or in the presence of reactant

gases. Samples were transferred to the XPS instrument (PHI Model 5400) using a vacuum transfer vessel to avoid sample contamination.

A high pressure Sartorious microbalance was used to determine the total surface area by carbon dioxide adsorption. Prior to CO_2 introduction, the system was evacuated to a pressure of less than one Torr and samples were heated to 150 °C until no further weight loss was observed. The sample was then cooled to room temperature and carbon dioxide pressure was increased incrementally while the sample weight gain was recorded. The Dubinin-Radushkevitch method [16] was used to calculate the total surface area.

Sample pH was determined as a measure of the type of surface oxygen groups present in a manner similar to the ASTM standard method [17]. The char samples were wetted in a 0.1 molar potassium chloride solution and boiled under reflux for 2 hours. A standard 0.1 molar KCl solution was boiled concurrently with the char suspension. The solutions were then cooled to room temperature and the pH of each measured using a Fisher Scientific Accumet 950 pH/ion Meter. The difference in pH between the sample and the standard determines the nature of the surface oxygen groups: a positive change indicates basic groups and a negative change results from acidic surface groups.

RESULTS

The absolute rates reported in the figures for hydrogasification are based on initial mass of carbon in the sample as determined by ultimate analysis (Table 1). Except for gasification of as-received coal char (Figure 2), all gasification runs were carried out for two hours at steady state conditions. Only steady state data are shown; the absence of data at low conversion is the result of carbon conversion at unsteady state.

The rate of hydrogasification of coal char sharply decreases with conversion, undergoing an eight-fold decrease over the first 20% carbon conversion. Preoxidation of demineralized char at 375°C results in up to a 6.3% wt. loss (Table 2), but it does not result in any significant enhancement in gasification rate (Figure 1) or in the total surface oxygen content as measured by XPS (Table 2). The pH measurements indicate, however, that a greater fraction of the surface oxygen groups, following oxidation, are acidic in nature (Table 2).

Results of oxidative treatment (375°C) following partial gasification are shown for coal char in Figure 2. The intermediate oxidations result in a two- to three-fold enhancement in rate upon further hydrogasification. The observed rate enhancement decays as gasification proceeds and after about 5% conversion, the rate returns to approximately that of the nonoxidized sample. Two oxidation times are presented; however, there does not appear to be any added benefit in long oxidation. A slight weight gain of the chars was recorded from the oxidation.

In Figure 3, the effect of adding K_2CO_3 (10% by weight) to coal char is presented. The presence of the catalyst significantly increases the hydrogasification rate, and intermediate oxidation of the catalyzed char results in about a 50% enhancement in rate. There was significant carbon weight loss upon oxidation (20%) so Figure 3 reports rate versus carbon conversion in gasification.

The results of intermediate oxidation of Saran char are given in Figure 4. Again, approximately a two-fold rate enhancement is observed.

DISCUSSION

In earlier work on model carbons [13,14], we postulated the active sites for methane formation are formed by desorption of oxygen functional groups. This desorption occurs during heatup to gasification temperature; Figure 5 illustrates that upon heating coal char to gasification temperature, all excess surface oxygen has desorbed. Since no oxygen is present in the reactant gas in hydrogasification, active sites can only arise from oxygen groups initially on the surface or in the bulk solid. The active sites from surface groups are consumed as carbon is converted, and gasification rate declines accordingly. This drop in gasification rate is evidenced in all results presented.

Oxidative pretreatment (Figure 1) did not result in a large increase in the gasification rate of coal char. The pretreatment had little effect because the sample was already well oxidized as evidenced by the XPS results in Table 2. Thus, few additional sites were formed via oxidation. Following partial gasification of the char, however, active sites have been consumed and the char is in a reduced state. Oxidation at 375°C then placed new oxygen groups on the carbon surface; these new groups desorb upon reheating to gasification temperature to produce active sites for methane formation. These sites are consumed as reaction proceeds and the rate decays back to that of the nonoxidized sample.

Catalyzed gasification rate enhancement from oxidation is in agreement with the results obtained by Saber et al. [8] and Keleman et al. [5] discussed in the introduction. The added stability of potassium species on the carbon surface during gasification is especially important in the reducing hydrogen environment, and thus the rate enhancement from oxidation may be greater in hydrogen than in oxidizing environments.

Changes in carbon structure and morphology occur during gasification, and thus may account for some of the observed gasification behavior. Since the coal char is heterogeneous, the most reactive carbon gasifies first; thus, the decreases in rate may arise from changes in carbon reactivity as well as loss of active sites. The gasification rate, however, is not related to the total surface area of the chars. While the rate decreases markedly, the total surface area remains essentially constant at 290 ± 15 m^2/g sample for the coal char and 750 ± 35 m^2/g sample for the Saran char over the carbon conversion range of 0% to 34%. Also, the Saran char total surface area was initially twice that of the coal char while its gasification rate was similar to that of the char. Further, total surface did not vary significantly over the course of oxidation, indicating that the rate enhancement resulted from fixation of oxygen groups and not from the opening of new pore structure.

Finally, although preoxidation of the coal char did not significantly increase the amount of surface oxygen, it did change the nature of the oxygen groups. The sample surface pH decreased by a factor of two indicating a one hundred-fold increase in surface

acidity. This fixation of acidic surface groups is characteristic of oxidation at 375°C in air. The importance of the type of oxygen group on the rate enhancement is not clear, but it is currently under investigation.

CONCLUSIONS

Oxidation via exposure to molecular oxygen enhances hydrogasification rate of coal chars and model carbons provided the char surface is not previously oxidized. Oxidation following partial gasification results in a two- to three-fold increase in gasification rate for all chars studied, while oxidation of a char previously saturated with oxygen had little effect. Work continues toward increasing rate enhancement via oxidative treatment and in understanding the importance that different types of oxygen groups have on the extent of enhancement.

ACKNOWLEDGMENTS

The support of the United States Department of Energy through grant #DE-FG22-89PC8977 is gratefully acknowledged. and the sample of Saran resin supplied by the Dow Chemical Company is appreciated.

REFERENCES

1. M. Steinberg, 1987 International Conference on Coal Science, 11, 953, Elsevier, Amsterdam-Oxford-New York-Tokyo, (1987).
2. R.L. Hirsch, J.E. Gallagher Jr., R.R. Lessard, R.D. Wesselhoft, Science, 215, 121 (1892).
3. P.L. Walker Jr., Carbon, 28, 261 (1990).
4. J.S. Noh and J.A. Schwarz, Carbon, 25, 675 (1990).
5. S.R. Kelman and H. Freund, ACS Division Fuel Chemistry Prepr., 32, 318 (1987).
6. C. A. Mims and J. J. Krajewski, Journal of Catalysis, 102,140 (1986).
7. S.R. Keleman, H, Freund, and C.A. Mims, Journal of Catalysis, 97, 228 (1986).
8. J.M. Saber, J.L. Falconer, and L.F. Brown, Journal of Catalysis, 90, 65 (1984).
9. Y. Ohtsuka, K. Itagaki, K. Higashiyama, A. Tomita, and Y. Tamai, Neaoyo Kyokaishi, 60, 437 (1981).
10. J.R. Cao and M. H. Back, Carbon, 23, 141 (1985).
11. J.D.Blackwood, Aust. J.Chem., 12, 14 (1959).
12. Y. Otake and R. G. Jenkins, ACS Division Fuel Chemistry Prepr., 32, 310 (1987).
13. H. Zoheidi and D.J. Miller, Carbon, 25, 265 (1987).
14. M.H. Treptau, D.J. Miller, Carbon, In press (1991).
15. H. Zoheidi, Ph.D. Dissertation, Michigan State University, East Lansing, Michigan (1987).
16. S.J. Gregg, K.S.W. Sing, Adsorption, Surface Area and Porosity, 2nd Ed, Academic Press Inc, New York, (1982).
17. ASTM Standard Designation: D 3838-80.

Table 1. ULTIMATE ANALYSIS OF SAMPLES
(Weight % - Dry Basis)

Element	Coal Char	Demineralized Coal Char	Saran Char
C	75.30	93.01	96.36
H	.53	.27	.53
N	1.34	1.62	1.04
S	3.55	1.82	.43
Ash	17.33	2.28	.08
O (by diff)	1.95	.73	1.56
Cl	-.--	.25	-.--
F	-.--	.02	-.--
	100	100	100

Table 2. XPS AND pH RESULTS FOR DEMINERALIZED COAL CHAR
(XPS Pretreatment Temperature -->200 °C)

Oxidative Pretreatment Char Burnoff (%)	Treatment Time at 375°C (hr)	XPS Surface O/C Ratio	ΔpH
0.0	0	.0921	0.77
2.3	120	.0971	-1.3
6.3	160	.1036	-2.8

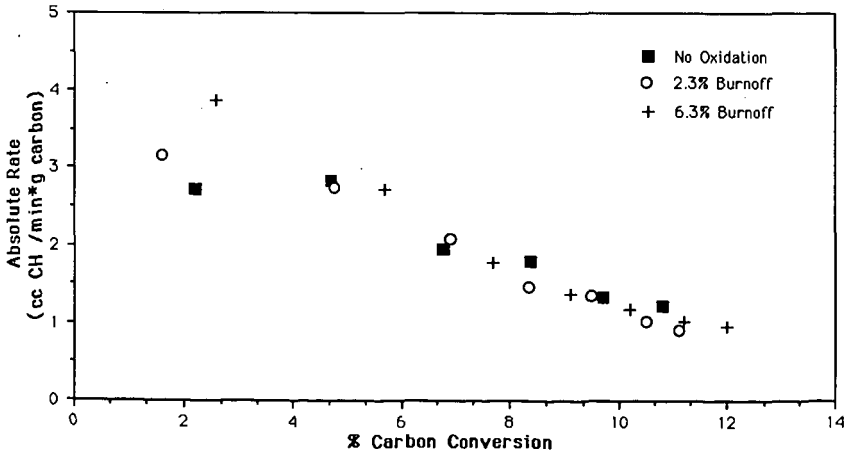

Figure 1. Effect of Preoxidation on Gasification Rate of Demineralized Coal Char

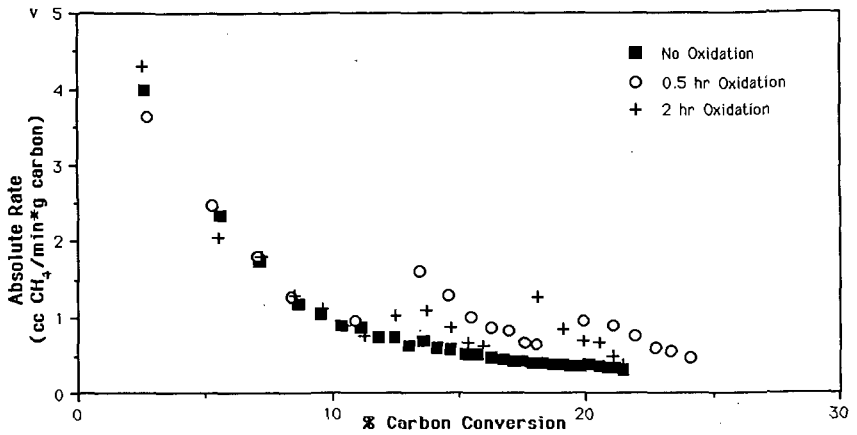

Figure 2. Effect of Two Intermediate Oxidations on the Gasification Rate of Coal Chars

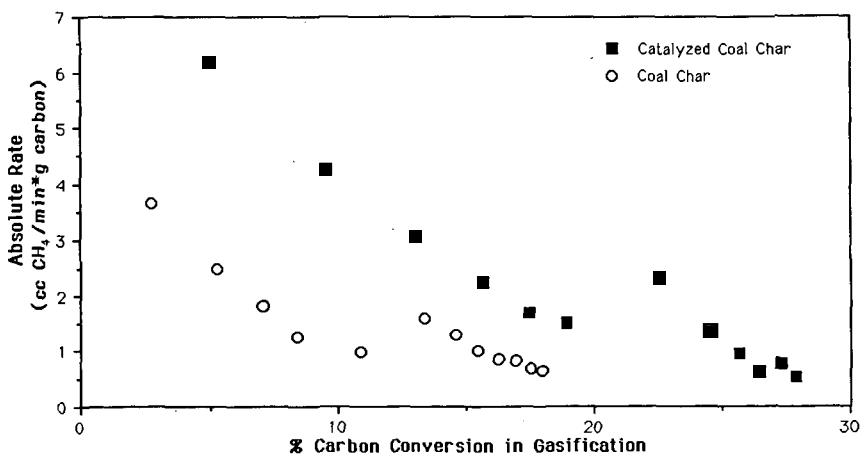

Figure 3. Effect of Intermediate Oxidation on Gasification of K CO -Catalyzed and Uncatalyzed Coal Char

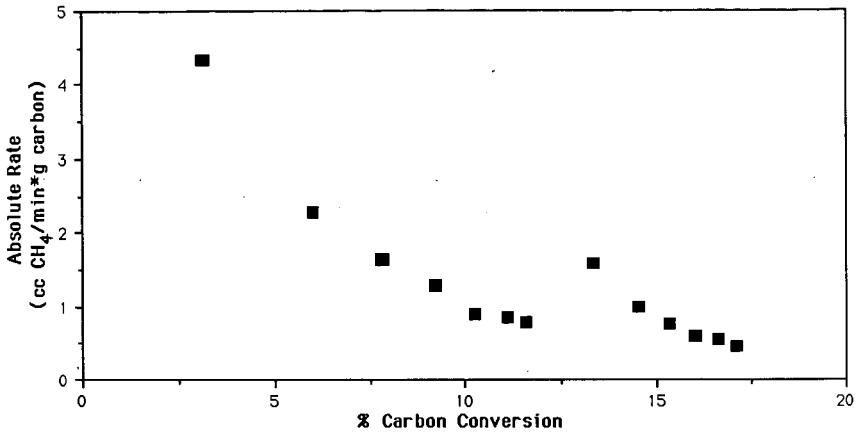

Figure 4. Effect of Intermediate Oxidation on Saran Char

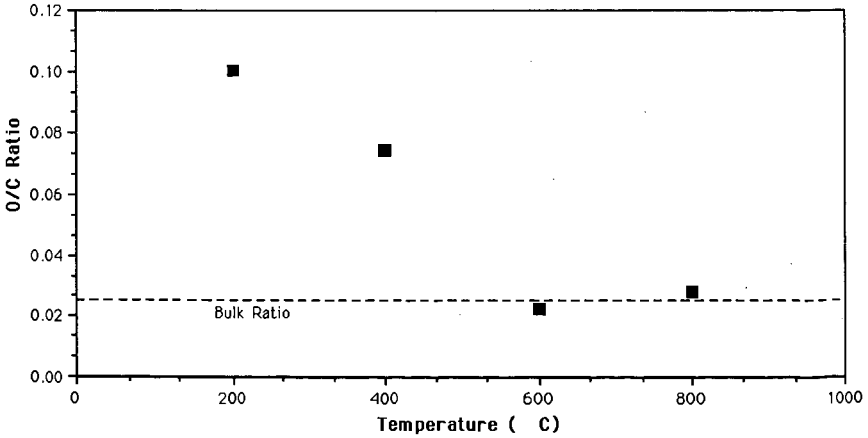

Figure 5. XPS Results for Coal Char
Heated to Gasification Temperature

A MULTIPRODUCT SLATE FROM MILD GASIFICATION OF WYOMING COAL

Robert Ness, Jr., Ted Aulich, Laura Sharp, and Brian Runge
University of North Dakota Energy and Environmental Research Center
Box 8213, University Station
Grand Forks, ND 58202

Keywords: mild gasification, metallurgical coke substitute, mild gasification condensables

INTRODUCTION

Coal is the largest indigenous energy resource in the United States. As consumption of petroleum products and electricity increases in the United States, it becomes increasingly important to develop processes that enable the wider use of coal, including its use as a feedstock for petroleum product substitutes in energy and chemical markets. One such process, called "mild gasification," is under development at the University of North Dakota Energy and Environmental Research Center (EERC) and is similar to the petroleum-refining process in that several coal products are produced that meet the needs of different end users. Thus, within the process economic boundaries, production of a high-value product can be maximized at the expense of a lower value product. The capability to alter product distributions, either by changing feedstocks or processing conditions, permits timely response to the ever-changing market. AMAX Coal Company described the "coal refinery" concept at the Twelfth International Conference on Slurry Technology (1).

In the mild gasification process, for which research is sponsored by the Morgantown Energy Technology Center (METC) of the U.S. Department of Energy (DOE), a rapid devolatilization of coal under mild conditions of temperature and pressure produces three products: a reactive char, a valuable hydrocarbon condensate, and a low-Btu gas. The process under development at EERC would produce activated carbon, metallurgical coke substitutes, diesel fuel additives, and chemical feedstocks.

The objective of the EERC program is to develop a continuous mild gasification process that has the flexibility to enable balancing process economics with the demands of the marketplace. Earlier stages of the program focused on the use of Indiana No. 3 bituminous and Wyodak subbituminous coal in a 1- to 4-lb/hr reactor, to optimize product yields over a variety of reaction conditions. Data generated were used to design and construct a 100-lb/hr mild gasification process development unit (PDU) under Task 4 of the program. This report describes the results of tests performed in the PDU using Wyodak coal.

ECONOMIC CONSIDERATIONS

The economic feasibility of mild gasification is contingent upon obtaining a premium value for the char, probably as a metallurgical coke substitute in the U.S. steel production industry, which is showing signs of economic recovery and is in a position to take advantage of new technology. The value of the condensable hydrocarbon product as a fuel (or fuel additive) is unpredictable and unstable because of dependency on the coal/oil price differential, which was favorable during the oil supply crises in the late 70s and early 80s, but less conducive to coal research during the last eight to ten years.

A new iron-making process developed by Pellet Technology Corporation (PTC) can use mild gasification char in highly reactive iron ore/char pellets that greatly increase throughput in a conventional blast furnace. The pellets can also be used in smaller, more efficient ore reduction equipment such as hot-blast cupolas and direct reduction systems. The competitive char value in the PTC process would be equivalent to that of calcining grade petroleum coke, which is estimated at 30 to 45 dollars per ton, with a market potential of 15 to 20 millon tons per year (2).

The best use of the mild gasification condensables may be their conversion to benzene and phenol, which are subject to essentially no market volume limitations and may command prices of $1.00 and $2.00 per gallon, respectively (2). The best opportunity for condensables in the transportation fuels' market is as a fuel additive for medium-speed railroad diesel engines. Other possibilities for condensables include their use as feedstocks for production of carbon black (used in rubber goods, pigments, printer's ink, and in the production of carbon electrodes for aluminum ore reduction), creosote, cresylic acid, pitch, and rubber-processing oil, and as a briquetting binder and a coal dust suppressant. The best use of mild gasification process gas (from a 1,000-ton per day facility) will be as on-site plant fuel, with excesses used for cogeneration of electricity. Table 1 shows product specifications for PTC pellets and metallurgical coke and the boiling point fractions obtainable from mild gasification condensables along with their potential uses.

EQUIPMENT DESCRIPTION

The PDU was constructed to provide proof of concept for an integrated mild gasification system operating on specific design coals and to produce char and liquid products for upgrade testing and market evaluation. The system was designed to process 100 lb/hr (dry basis) of feed coal and incorporate capabilities for drying, carbonizing, and calcining caking and noncaking coals in fluid-bed reactors and for separating char, liquid, and gaseous products. The system was designed to enable both integrated operation of the carbonizer and calciner and independent operation of either the carbonizer or calciner. This report deals with tests performed using the carbonizer.

Heat for carbonization is principally supplied by hot flue gas from stoichiometric combustion of natural gas. (In a commercial-scale process, heat would be provided by combustion of process-derived gas and waste coal from a coal-cleaning operation in a fluid-bed combustor.) Provisions for carbonizer steam injection were made to take advantage of the sulfur-removal and condensables quality improvement effects of steam, as seen in previous work (3).

Figure 1 is a diagram of the PDU carbonization area and shows the major components of the system. For operation with Wyoming feed coal, the coal is screened to a size of 1/4 inch by 0. The carbonizer was designed as a spouted bed gasifier, based on favorable results with caking coals in the COALCON and KRW gasifier systems. The operative principle allowing use of caking coal in this design is the dilution of the entering coal by internal recycle of char to the bottom of the tapered bed, where high velocity and low-bed density also reduce agglomeration. Char residence time can be varied by bed height, with the design residence time being 30 minutes. The carbonizer operates at temperatures from 900 to 1500°F (480 to 820°C) with steam partial pressures from 10 to 60% of the total reactor pressure. Feed coal is entrained and fed into the bottom of the reactor using preheated nitrogen (575°F/300°C). Char can be drawn from a variety of locations and injected into a nitrogen-purged tote bin.

The condensables quench and separation system was designed to produce separate tar and oil fractions that meet primary product requirements. In addition, the quench system should provide trouble-free operation without a tendency to plug and, ideally, should produce no wastewater condensables. One objective of this work is to enable recovery from the gas stream of both a tar and an oil product using direct contact tar and oil venturi scrubbers (called the tar scrubber and the sieve tower, respectively) and direct contact water scrubbers. In the venturi scrubbers, the scrubbing liquid is injected into the gas stream above the throat of the venturi.

During operation with Wyoming coal, the tar venturi scrubber was used to remove particulates remaining in the gas stream (that were not removed by the cyclones) and condense boiling point fractions of liquid products ranging in temperature from 350

to 700°F (175 to 380°C). Further cooling occurred in the sieve tower, again using recycled product liquor. This unit operates at an exit temperature just above the dew point of the product gas, approximately 160 to 180°F (70 to 80°C). The product gas then passed through a water scrubber, which cooled the gas stream to 80 to 100°F (27 to 38°C), and a demister to ensure that organic material did not escape and pass through the flare system. (An optional quench system uses two water scrubbers to condense all of the tar, oil, and water from the system before the product gas is flared.)

PRODUCT YIELDS

Table 2 shows product yield and material balance data obtained from Carbonizer Test P010, performed using Wyodak coal. As shown in the table, the char yield was 49 percent of the weight of the moisture- and ash-free (maf) coal fed to the reactor, the condensable yield was 9%, and the gas yield was 42%. The yield calculations involved accounting for the CO_2, N_2, and H_2O contents of the product gas and condensable streams that resulted from the combustion of natural gas to provide system heat.

CHAR ANALYSIS AND METALLURGICAL COKE SUBSTITUTE PRODUCTION

Table 3 shows the results of proximate and ultimate analyses performed on the char products obtained from Test P010. The steel industry has specified that for a coal char product to be suitable for use as a coke substitute, its sulfur and ash contents should be less than 1 and 10 wt%, respectively. Table 3 shows that the Wyodak char meets the sulfur specification and only slightly exceeds the ash limit. Pellet Technology Corporation (PTC) utilized Wyodak char from an EERC test performed under conditions similar to those employed for Test P010 as a metallurgical coke substitute in iron ore-reducing tests. The PTC tests were performed using pellets made from Wyodak char, iron ore, lime, and silica. After pressing, the pellets were dried and hardened. Pellets made with a 10 wt% (of total pellet weight) binder comprised of calcium oxide and silica exhibited satisfactory strength, density, and abrasion resistance.

The results of the ore reduction tests, in which the pellets were subjected to temperatures of 2500 and 2700°F (1370 and 1480°C), showed that iron ore reduction times for char-iron ore pellets could be reduced by as much as 80%, compared to reduction times required for coke-iron ore pellets. The fact that the Wyodak char-iron ore pellets were reduced in about 5 minutes (as opposed to the 25 minutes required for coke-iron ore pellets) is thought to be due to the high reactivity of the Wyodak char.

LIQUIDS ANALYSIS

Simulated Distillation To enable comparison of condensable product streams with petroleum fuels, simulated distillation of each P010 liquid product sample was performed using capillary gas chromatography. The technique works as follows: A condensables sample (liquid or tar) is dissolved in methylene chloride at a concentration of approximately 20 milligrams per milliliter (mg/mL), internal standards are added, and the mixture is injected into a gas chromatograph (GC). The temperature in the GC oven is maintained at 122°F (50°C) for two minutes, after which it is raised to 626°F (330°C) at a rate of 14.4°F (8°C) per minute. The chromatogram obtained is compared with a chromatogram of a carefully prepared mixture of normal alkanes (C7, C8, C9..., C25) obtained under identical chromatographic conditions. Since the boiling point of each alkane is known, the relationship of boiling point to GC retention time can be calculated. Once this relationship is determined, the boiling point of any compound in the sample can be approximated based on a comparison of the unknown compound's GC retention time to the retention times of the alkane standard compounds that "bracket" the unknown compound; i.e., if an unknown compound has a retention time midway between the

retention times of C7 and C8, the compound is assigned a boiling point midway between the boiling points of C7 and C8. After assigning boiling points to all compounds detected in a sample (this operation is computerized because in most samples, about 200 to 400 compounds are detected), a plot is generated of cumulative "area percent" of a sample distilled versus temperature. Area percent refers to how the GC detector quantitates, on a relative basis, each compound in a sample. (In the ASTM D-86 distillation method, the distillate is quantitated on the basis of volume percent distilled.) Comparison of ASTM D-86 and simulated distillation data obtained for Diesel #2 and a sieve tower liquids sample showed that the simulated distillation technique yields boiling-point data that is nearly identical to data yielded by the ASTM method.

Separation of Coal-Derived Material Some of the condensables samples obtained from Test P010 contained not only coal-derived material, but also petroleum products, which were used as start-up fluids in the tar scrubber and sieve tower. Mandan Decant Oil, a heavy fuel oil resid from the Amoco Oil Refinery in Mandan, North Dakota, was circulated through the tar scrubber during reactor heat-up, and Diesel #2 was circulated through the sieve tower. A method is being developed at EERC to deter-mine the amounts of diesel fuel and decant oil in a condensables sample using a computerized chromatogram subtraction technique.

The technique involves determining the contributions of diesel fuel and decant oil to the total chromatogram for a condensables sample. This is done by comparing a condensables sample chromatogram with chromatograms of diesel fuel and decant oil. The diesel fuel chromatogram is multiplied by a factor (between 0 and 1) and the resulting chromatogram is subtracted from the condensables chromatogram. This operation is performed as many times as necessary until a factor is found that yields a "difference chromatogram," with many components having area-percent magnitudes near zero. The factor that yields such a difference chromatogram is then multiplied by 100% to yield the percentage diesel fuel in the condensables sample. The same process is repeated using the original condensables chromatogram and the decant oil chromatogram. Subtracting the factored diesel fuel and decant oil chromatograms from the original condensables chromatogram yields a chromatogram that represents the coal-derived material. A simulated distillation curve can then be constructed from this chromatogram. Figure 2 shows the simulated distillation of coal-derived material (Test P010) from the tar scrubber, sieve tower, and the water scrubber. Based on the chromatogram subtraction technique described above, the tar scrubber condensables were estimated to be 100% coal-derived, the sieve tower condensables 93% coal-derived, and the water scrubber condensables (excluding water) 91% coal-derived. The figure shows that the coal liquids condensed in the sieve tower are lighter than the petroleum liquids, and the coal liquids condensed in the water scrubber are heavier than the petroleum liquids. It must be emphasized that the chromatogram subtraction technique is still under development and more work is needed to ensure its validity.

As-Recovered Condensables Analysis Tables 4 and 5 show results of analyses of the condensables obtained from the test. These tables, along with Table 3, show that the sulfur content of the char products is roughly equal to that of the feed coal, and that the sulfur contents of the tar scrubber and sieve tower liquids were significantly higher than that of the feed coal. The reason for the high-sulfur concentrations of these liquids is that they contain not only coal-derived condensables, but also the decant oil and/or diesel fuel start-up fluids. As shown in Table 5, the sulfur content of the decant oil is about 1.9%. On the basis of the sulfur contents of the tar scrubber and sieve tower liquids, it can be inferred that these liquids, with the possible exception of TS-3 (the latest tar scrubber sample obtained), contain some petroleum products.

Proximate analysis was performed on the tar scrubber samples since these samples likely contained significant amounts of coal fines that were not removed by the cyclones. Figure 3 compares the fixed carbon and ash contents of the tar

scrubber liquids with the ash content of tetrahydrofuran (THF) insolubles from the tar scrubber liquids. The linear increases in the THF-insoluble and ash contents indicate that the THF-insolubles are coal fines and not polymerized tar compounds. This buildup of coal fines occurred because insufficient amounts of coal liquids were being condensed into the tar scrubber recycle cooling fluid to fill the unit to the level at which recycle coolant is pumped out of the system.

REFERENCES

1. Woessner, P.W. "The Coal Refinery, A Concept," Presented at the Twelfth International Conference on Slurry Technology, New Orleans, LA, April 1987.

2. Willson, W.G.; Ness, R.O.; Jha, M.; Sinor, J.E. "Development of an Advanced, Continuous Mild Gasification Process for the Production of Co-Products," Literature Survey Results, report to DOE on Contract DE-AC21-87MC24267; University of North Dakota Energy and Environmental Research Center, Grand Forks, ND, January 1988.

3. Ness, R.O. "Development of an Advanced Continuous Mild Gasification Process for the Development of Co-Products," Final Technical Progress Report for the Period February 1988-March 1989, DOE Contract DE-AC21-87MC24267; University of North Dakota Energy and Environmental Research Center, Grand Forks, ND, December 1989

TABLE 1
CHAR PRODUCT SPECIFICATIONS AND CONDENSABLES USES

	PTC Process[a]	Formcoke
% Volatile Content	12	3-6
% Ash	10	10
% Sulfur	<1	<1

Condensable Boiling Point Fractions	
ibp - 330°F	Gasoline Octane Enhancer, Benzene
330° - 430°F	Cresylic Acids, Phenols
430° - 700°F	Diesel Fuel Blends
700° - 1020°F	Briquetting Binders, Anode Carbon

a Pellet Technology Corp. Process

TABLE 2
CARBONIZER MATERIAL BALANCE & YIELD SHEET

	1 KG In	2 KG CH_4 Comb. Prod.	3 KG Out	4 Yields	5 N Yields	6 Vol. %
MAF (Coal/Char)	509		506	99	49	
H_2O in (Coal/Char)	181		4	-35	-35	
H_2O in (Steam/Cond.)	0		317	62	49	
H_2O in Gas		165	100	-13	-13	
H_2O Total					0	
Ash	35		67	6	0	
Cond. Total			63	12	9	
ibp-165			0	0	0	
165-220			9	2	1	
220-375			28	5	4	
375-550			28	5	5	
550-1000			-2	0	0	
BP>1000			0	0	0	
Char Fines			0	0	0	
Residue			0	0	0	
Gas Total	2,698	2,533	2,846	62	42	
H_2			9	2	2	4.6
CO_2		202	546	67	64	12.5
C_3H_6			3	1	1	0.1
H_2S			1	0	0	0.0
C_2H_4			4	1	1	0.2
C_2H_6			5	1	1	0.2
O_2	529	-294	0	-46	-46	0.0
N_2	2,096		2,201	21	5	78.9
CH_4	74	-74	30	6	6	1.9
CO	0		47	9	9	1.7
Btu/scf						45.2
KJ/L						1.7
scf/100 lb						6,974.0
SL/100 Kg						370,548.8
Total	3,424	3,424	3,903	194	100	
Mat. Balance			114.0			

Run No.	P010	1 Mass into the system
Feed Coal	Wyodak	2 Mass change due to the combustion of natural gas
Temperature	1100°F	3 Mass out of the system
Pressure	14.7 psia	4 Yields based on MAF coal feed
Res. Time	0.50hrs	5 Normalized yields based on 100% material closure
		6 Product gas composition out of condensation train

Fluidization Gas: Natural Gas with 80% Excess air, 6% Steam, 78% N_2, 7% CO_2, 0% CO, 0% H_2, 9% O_2, 100 Total

% loss to gas	22.00	% loss to char off-take leg	61.00
% loss to tank 504	17.00	% loss to primary/secondary cyclone	0.00

TABLE 3

ANALYSIS OF P010 WYODAK COAL CHAR

	Feed Coal 1/4 x 0	Product Char 1	Product Char 2	Primary Cyclone Char
Proximate Analysis (wt%)				
Moisture	25.0	0.3	0.8	3.7
Volatiles	33.8	18.5	17.6	18.5
Fixed Carbon	36.3	69.5	69.9	66.8
Ash	4.8	11.7	11.7	11.0
Ultimate Analysis (wt%)				
Hydrogen	6.2	2.6	2.3	2.7
Carbon	51.0	78.6	78.3	76.1
Nitrogen	0.7	1.3	1.3	1.3
Sulfur, mf[1]	0.4	0.7	0.5	0.5
Oxygen	36.8	5.2	5.9	8.4
Ash	4.8	11.7	11.7	11.0
Heating Value (Btu/lb)	9,065	12,582	12,355	12,134

[1] Moisture-free basis.

TABLE 4

ANALYSIS OF P010 TAR SCRUBBER LIQUIDS[1]

Proximate Analysis (%)	TS1[2]	TS2	TS3
Moisture	0.6	0.1	0.4
Volatiles	79.0	74.0	62.9
Fixed Carbon	17.9	22.8	31.8
Ash	2.5	3.2	4.9
Sulfur (wt%)	1.5	1.4	1.3
THF-insolubles (wt%)	17.1	18.6	29.6
Melting Point (°C)	53.0	65.0	85.0

[1] The tar scrubber "liquids" were solid at room temperature.
[2] Tar scrubber samples 1-3 were collected at 8-hour intervals during the test.

TABLE 5
ANALYSIS OF P010 SIEVE TOWER AND WATER SCRUBBER LIQUIDS

	ST1	ST2	ST3	Diesel #2	Decant Oil
Sulfur, wt%	1.2	1.2	0.9	0.0	1.9
		WS1 Organic[2]	WS2 Organic		WS3 Organic
Water Content, wt%[3]		22.3	13.9		0.2
		WS1 Aqueous	WS2 Aqueous		WS3 Aqueous
Phenolics, mg/L[4]					
Phenol		4,800	4,300		2,500
Cresols		3,100	2,130		1,300
C2-Phenols		500	340		220
Total Phenols		8,400	6,770		4,020
TOC[5], mg/L		6,800	6,300		5,170

[1] Sieve tower samples 1-3 were obtained at 8-hour intervals from bottom tray of sieve tower.

[2] Water scrubber samples 1-3 were obtained at 8-hour intervals. Each sample contained an organic and an aqueous phase. The organic phase comprised 14, 14, and 18 wt% of the WS1, WS2, and WS3 samples, respectively.

[3] Values determined using Karl Fisher analysis.

[4] Values estimated using gas chromatography/flame ionization detection.

[5] Total organic carbon.

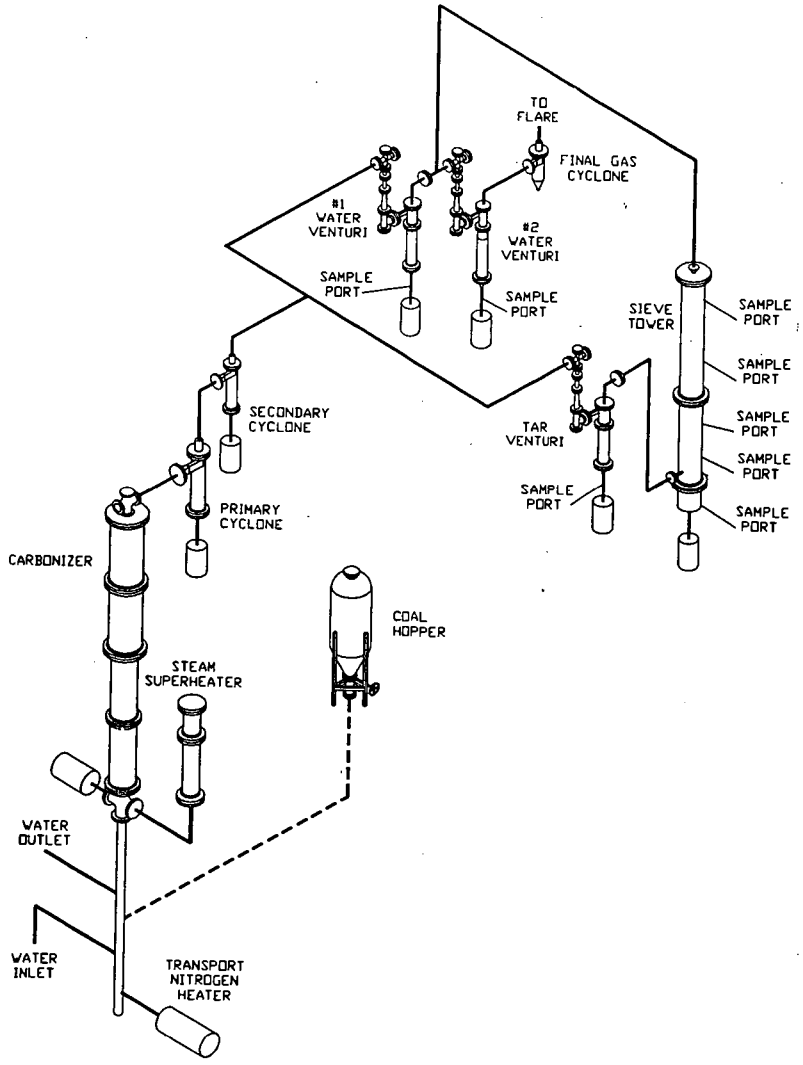

Figure 1. Diagram of the PDU carbonization area.

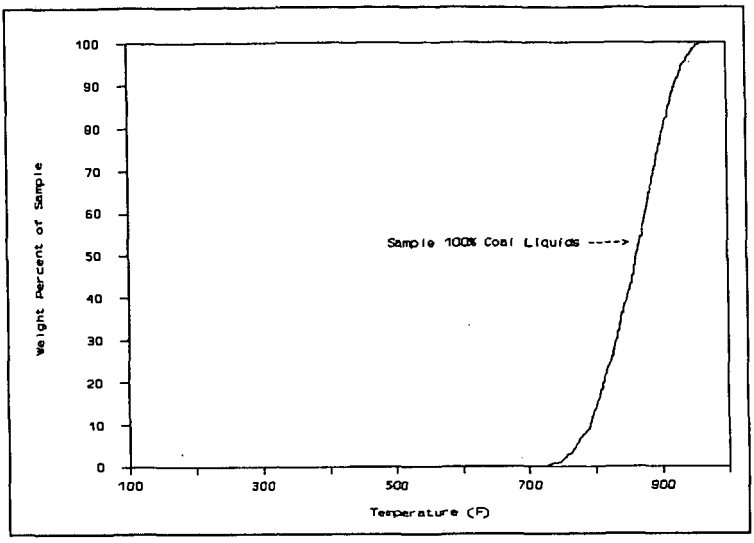

Figure 2a. Simulated distillation of coal liquids condensed in tar scrubber.

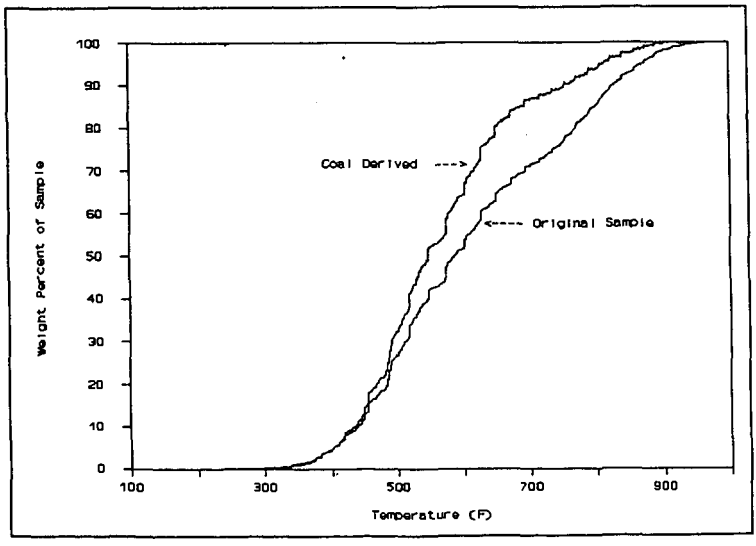

Figure 2b. Simulated distillation of coal liquids condensed in sieve tower.

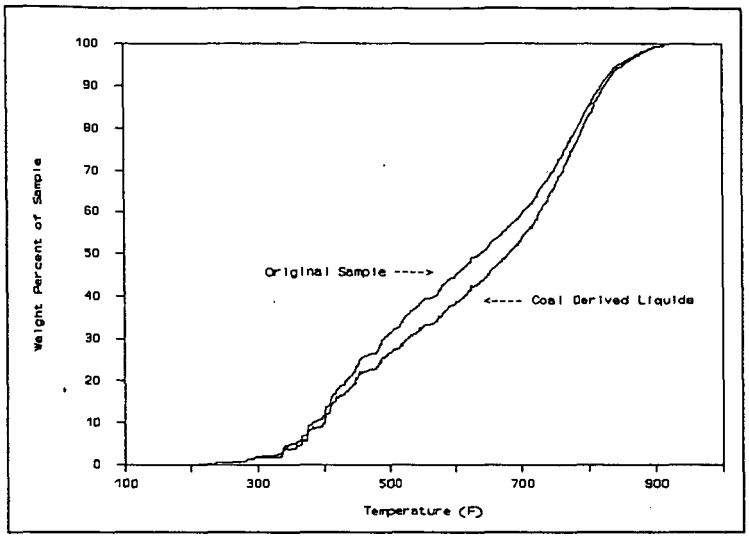

Figure 2c. Simulated distillation of coal liquids condensed in water scrubber.

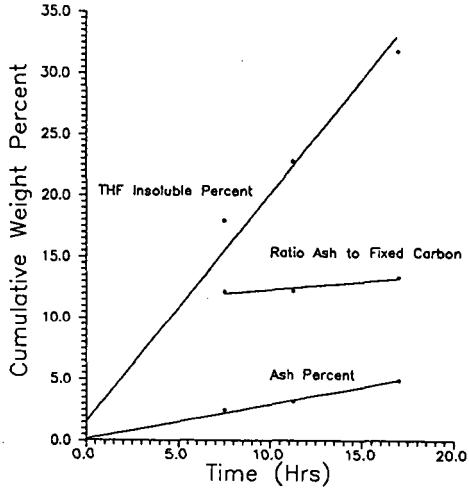

Figure 3. Weight percent of coal fines in tar scrubber liquids.

COMPOSITION AND PARTICLE-SIZE EVOLUTION OF KENTUCKY #9

Thomas Erickson, Christopher Zygarlicke, Murali Ramanathan, and Bruce Folkedahl
University of North Dakota Energy and Environmental Research Center
Box 8213, University Station
Grand Forks, ND 58202

Keywords: coal, inorganic transformations, predictive method

INTRODUCTION

The size and composition of ash resulting during coal combustion involves both chemical and physical processes. Ash particles formed during coal combustion depend largely upon the association of the inorganic species in the coal. In order to accurately model the ash formation processes, detailed information on the distribution of minerals with respect to coal particles is essential.

The combustion of Kentucky #9 coal was analyzed through a three-step approach to track particle-size and compositional evolution. First, the coal was characterized with advanced analytical techniques to determine the original size and type of the minerals present. Second, the coal was combusted under carefully controlled conditions to produce fly ash. The fly ash was characterized with analytical techniques similar to those used with the coal. Third, two separate predictive methods were produced from comparison of the two data sets as well as previous investigations (1,2).

EXPERIMENTAL APPROACH

A utility-sized (70% -200 mesh) sample of Kentucky #9 coal was received from the coal sample bank at Foster Wheeler. The coal was characterized by computer-controlled scanning electron microscopy (CCSEM), x-ray fluorescence (XRF), proximate-ultimate analysis, and automated- and manual-imaging techniques in conjunction with the CCSEM technique. The above analysis combined to provide a wide base of knowledge on the coal in terms of the minerals present, their size distributions, and the bulk chemistry of the coal.

The coal was combusted in a vertically oriented laminar flow furnace (drop-tube furnace) at 1500°C, for approximately 2.5 seconds in an environment to simulate the fouling conditions present during combustion in a pulverized coal-fired furnace. The ash was immediately cooled and quenched with nitrogen upon leaving the furnace. The resultant ash was analyzed with CCSEM. The information obtained from the ash is particle size and particle composition.

COAL AND ASH CHARACTERIZATION

The CCSEM data for both the coal and the formed fly ash were analyzed with the use of a classification method, designed by UNDEERC, specifically for CCSEM data. The fly ash data was first corrected for the spherical orientation of the particles. Figure 1 is a SEM photograph of the fly ash produced and shows that a spherical (circular) orientation of the particles is predominant. When analyzing the size of spheres with a random, cross-sectional, two-dimensional technique, the average measured diameter is lower than the actual average diameter (3). The following equation was applied to correct for this underestimation:

$$D_A = D_M * 4/Pi \qquad \text{[Eq. 1]}$$

where D_A is the actual diameter and D_M is the measured diameter. Table 1 shows the compositional classifications as determined from the CCSEM analysis for both the coal and fly ash. It is noted that the classification of CCSEM data is not specific to crystalline types; it classifies by composition only. Figure 2 shows the

particle-size distribution for the coal and fly ash (corrected for spherical orientation) as determined by CCSEM. The reason for the fly ash distribution being smaller than the mineral size distribution can only be from the fragmentation of mineral particles during combustion. Since pyrite is the only major mineral classified to undergo fragmentation under combustion conditions, and it comprises a substantial amount of the minerals, an "iron-free basis" may give a better understanding of the transformations that occur. Figure 3 shows both the mineral and fly ash distributions on an "iron-free basis." The mineral distribution is now smaller than the fly ash which shows evidence of coalescence of minerals during combustion. Table 2 shows the new classification of the two samples on an "iron-free basis."

The coal was also investigated for the inclusion of minerals inside coal particles (inherent) and the presence of minerals not associated inside a carbon structure (extraneous) (4). Figure 4 shows an SEM photograph of a cross section of the coal mounted in epoxy. The minerals (brighter areas) can be seen to exist in both the coal (grey areas) and epoxy (dark areas). Every particle classified with the CCSEM routine (>2000 particles) was also classified as inherent or extraneous.

PREDICTIVE METHOD 1

Method 1 uses the coal CCSEM results on an "iron-free basis" to predict fly ash formation on an "iron-free basis." The iron-containing species are omitted with the assumption that they lead primarily to the formation of iron oxide and small amounts of iron rich aluminosilicates and silicates. The two categories used in Method 1 are inherent and extraneous particles. The extraneous particles are assumed to not interact with other extraneous or inherent particles during the combustion process. The inherent particles are assumed to randomly coalesce during the process. A random number (with upper and lower limits) of the inherent particles is chosen at random and coalesced to form a single fly ash particle. The sizes and compositions of the coalescing particles are used to generate the size and composition of the resulting fly ash particles. 3000 particles are created from the inherent data and processed through the CCSEM classification program. The inherent and extraneous compositions are combined to form the resultant data. Table 3 shows the composition of the particles produced by Method 1, along with the experimental fly ash composition. Both compositions are similar with differences noted with aluminosilicate particles. A likely explanation for the difference is that the CCSEM classification program incorporates a large number of aluminosilicate classifications and thus must draw fine lines from classification to classification. The total aluminosilicates found for Method 1 and experimental ash are 54.8 and 55.3, respectively, which supports the above statement. The particle-size distributions for both the experimental data and predictive Method 1 are shown in Figure 5. The distributions are very close, and a slight modification in coalescence extremes would be expected to fit better with little change in composition.

PREDICTIVE METHOD 2

Method 2 does not involve the "iron-free basis" of the previous method. The entire data set is used, and predictions are on a total basis. The role in inherent and extraneous particles are similar to Method 1. The inherent pyrite is allowed to coalesce with a small loss in volume due to the release of sulfur during combustion. The extraneous pyrite is assumed to produce iron oxide in a reduced amount also due to the release of sodium. Table 4 shows the compositions predicted, along with those of the fly ash. The iron oxide composition appears to be very high and is believed to be a result of sampling error prior to CCSEM analysis. The pyrite analyzed here is almost double that of a previous reporting. By reducing the pyrite (→ iron oxide) and renormalizing the data, a much closer composition is achieved and is also shown in Table 4.

CONCLUSIONS

Method 1 shows very good agreement with the experimental fly ash data. The use of an iron-free basis allows the study of direct coalescence of minerals in the absence of mineral fragmentation. A proper algorithm for iron removal is essential, and previous results used assumptions that may induce limited amounts of error.

Method 2, with the correction in pyrite to fit previously reported values, also looks very good. At the current time, the investigation of pyrite fragmentation is crucial in determining the total size distribution of the ash; thus it has not been addressed here.

CCSEM analysis coupled together with inherent and extraneous classifications are showing great promise for predicting fly ash formation from coal data. The next step is a coal particle-by-coal particle analysis technique.

REFERENCES

1. Zygarlicke, C.J.; Toman, D.L.; Benson, S.A. "Trends in the Evolution of Fly Ash Size During Combustion," Prepr. Pap.--Am. Chem. Soc., Div. Fuel Chem. 1990, 35(3), 621-636.

2. Zygarlicke, C.J.; Steadman, E.N.; Benson, S.A. "Studies of Transformation of Inorganic Constituents in a Texas Lignite during Combustion," Progress in Energy and Combustion. Science Review, 1990, 16, 195-204.

3. Zygarlicke, C.J.; Toman, D.L.; Steadman, E.N.; Brekke, D.W.; Erickson, T.A. "Combustion Inorganic Transformation," Quarterly Technical Progress Report to United States Department of Energy on Contract No. DE-FC21-86MC10637; University of North Dakota Energy and Environmental Research Center, Grand Forks, ND, 1990.

4. Zygarlicke, C.J.; Steadmen, E.N. "Advanced SEM Techniques to Characterize Coal Minerals," Scanning Microscopy 1990, 4(3), 579-590.

TABLE 1

CCSEM RESULTS FOR THE MAJOR COMPONENTS OF KENTUCKY #9 COAL AND FLY ASH

Classifications	Coal	Fouling Ash
Quartz	9.5	8.4
Iron Oxide	0.2	11.2
Calcite	1.0	2.2
Kaolinite	4.3	2.5
Montmorillonite	3.8	6.3
K-Aluminosilicate	13.6	15.2
Fe-Aluminosilicate	0.1	9.9
Aluminosilicate	0.5	6.7
Mixed Aluminosilicate	0.2	5.0
Pyrite	44.7	1.5
Si-Rich	2.4	8.7
Unknowns	16.2	17.5

TABLE 2

IRON-FREE MAJOR COMPONENTS OF KENTUCKY #9 COAL AND FLY ASH

Classifications	Coal	Fouling Ash
Quartz	17.70	10.9
Calcite	3.00	2.9
Kaolinite	8.00	6.0
Montmorillonite	10.50	14.4
K-Aluminosilicate	36.00	22.5
Aluminosilicate	2.45	10.7
Mixed Aluminosilicate	0.70	1.7
Si-Rich	6.20	11.9
Unknowns	8.30	9.7

TABLE 3

COMPARISON OF PREDICTIVE METHOD 1 AND EXPERIMENTAL FLY ASH DATA ON AN IRON-FREE BASIS

Classifications	Method 1	Fouling Ash
Quartz	12.9	10.9
Calcite	2.7	2.9
Kaolinite	5.6	6.0
Montmorillonite	10.8	14.4
K-Aluminosilicate	33.9	22.5
Aluminosilicate	4.0	10.7
Mixed Aluminosilicate	0.5	1.7
Gypsum	2.3	1.9
Apatite	2.6	0.5
Si-Rich	8.2	11.9
Unknown	12.8	9.7

TABLE 4

COMPARISON OF PREDICTIVE METHOD 2 AND EXPERIMENTAL FLY ASH COMPOSITION
(A modification of Method 2 is also shown due to the inconsistency of pyrite.)

Classifications	Method 2	Fouling Ash	Modified
Quartz	8.0	8.4	9.3
Iron Oxide	30.0	11.2	15.6
Calcite	1.6	2.2	1.9
Kaolinite	2.6	2.5	3.0
Montmorillonite	4.4	6.3	5.1
K-Aluminosilicate	19.3	15.2	22.5
Fe-Aluminosilicate	4.7	9.9	5.4
Aluminosilicate	2.1	6.7	2.4
Mixed Aluminosilicate	0.4	5.0	0.4
Gypsum	1.4	1.5	1.6
Apatite	1.6	0.4	1.9
Si-Rich	4.7	8.7	5.5
Unknowns	17.7	17.5	19.9

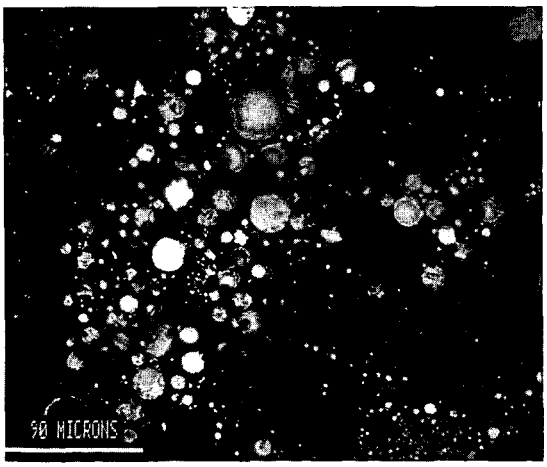

Figure 1. SEM photograph of Kentucky #9 fly ash formed under fouling conditions at 1500°C for 2.5 seconds.

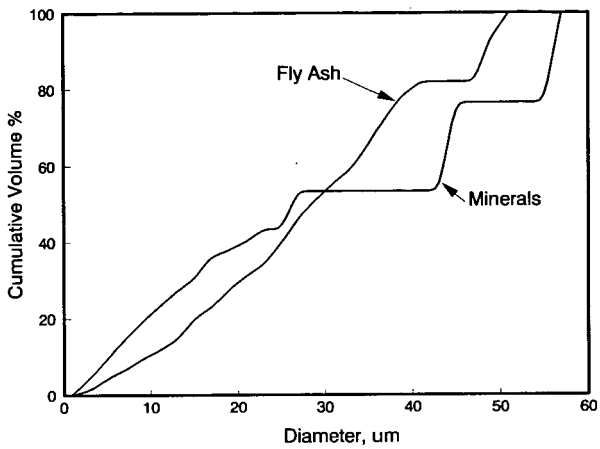

Figure 2. CCSEM particle-size distributions for Kentucky #9 coal and fly ash.

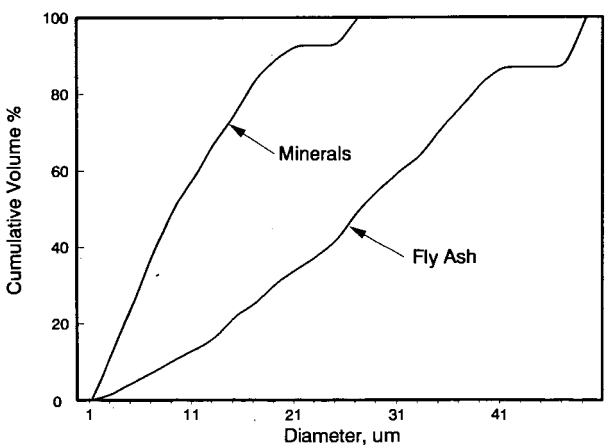

Figure 3. Iron-free particle-size distribution for Kentucky #9 coal and fly ash.

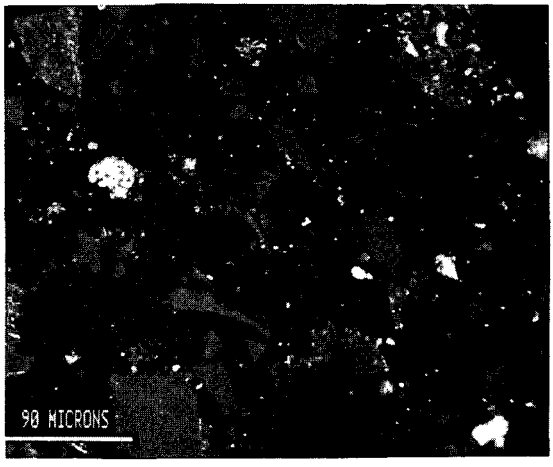

Figure 4. SEM (BEI) photograph of Kentucky #9 coal mounted in epoxy. Bright area-minerals, grey area - coal, dark area - epoxy.

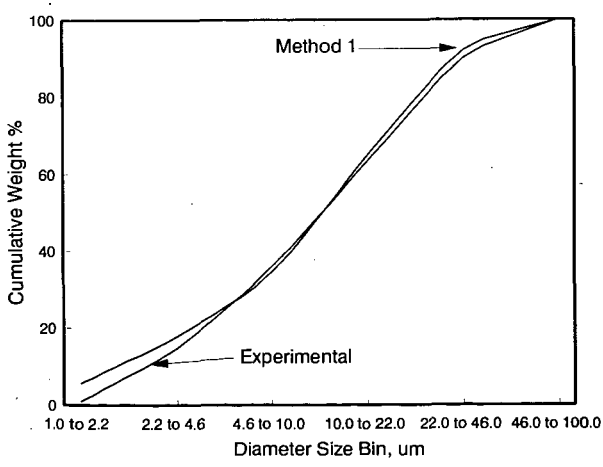

Figure 5. Particle-size distributions of experimental fly ash and predictive Method I particles on an iron-free basis.

GRAPHICAL REPRESENTATION OF CCSEM DATA FOR COAL MINERALS AND ASH PARTICLES.

Naresh Shah, G.P. Huffman, F.E. Huggins, Anup Shah
233 Mining and Mineral Resources Building
University of Kentucky, Lexington, KY 40506-0107.
W.J. Mershon , G. Casuccio
R.J. Lee Group, Inc.,
350 Hochberg Road, Monroeville, PA 15146.

Introduction:

Since its inception, Computer Controlled Scanning Electron Microscopy (CCSEM) has proved to be a powerful tool for materials science (1-4). In coal research, CCSEM has been used to obtain important physical mineralogical information about coal (5,6). Several factors make CCSEM the method of choice in this area. Bulk mineralogical and chemical methods are time consuming and limited. Furthermore, such methods are incapable of providing physical characteristics like size and shape of coal mineral particles which clearly play important roles in ash formation during combustion (7) and catalysis during liquefaction (8). Besides coal mineral analysis, CCSEM has been used to identify and characterize ash particles to gain insight into deposition and fouling characteristics of coals during the coal combustion phenomena. Recent research emphasis in the CCSEM field has been on investigating mineral-maceral associations (9).

CCSEM is basically a statistical analysis method. Thousands of individual particles are analyzed in the course of a single sample analysis and for every one of them chemical composition from X-ray EDS spectra and dimensional (size) parameters from back scattered electron imaging are obtained. These data are then statistically analyzed to infer mineralogical characteristics of the sample. Traditionally, all the statistical data thus obtained is listed in a tabular format. Although such information is very useful and can not be easily obtained by other means, some rather important information and relationships may be obscured in such typical statistical analysis. Graphical representation of CCSEM data provides the means for revealing this hidden complementary information. Though such information may not be easily quantifiable, it can provide the user with a completely different perspective about the sample. Graphical representation of CCSEM data often unveils trends and correlations in a very user friendly way and the information, which usually is difficult to extract from tables, can be easily displayed and understood. In this paper, we show some of the graphical representations our group has developed and used to analyze various problems in coal research.

Size distribution:

Determination of particle size distributions is one of the oldest applications of CCSEM. Bar and line charts make data presentation very user friendly. Stacked charts help in understanding size distribution trends of different minerals in the same sample or the same mineral in different samples. Commercial CCSEM instruments invariably provide software to display such trends. Figure 1 shows pyrite size distributions for some of the Argonne premium sample bank coals (6).

Binary diagrams:

To study the interaction between any two components, we have developed a binary diagram representation. Two component CCSEM data are plotted as a number or volume percentage frequency as a function of concentration of one of the components. Since the data is normalized to 100 percent to represent only two components, it also displays the same information with decreasing concentration of the second component. Figure 2 shows Fe-S binary diagrams for the Argonne Beulah coal. Figure 2a is a plot of number percentage distribution as a function of Fe and S concentrations for all the particles with more than 80% combined counts for Fe and S from EDS spectrum. Since the particles can have different sizes, number percentage representation alone is not quite adequate. We have also incorporated the size information in binary diagram (Figure 2b). If we know density as a function of the concentration, such plots can be easily converted to actual weight distribution.

In some cases, representing just two components is not sufficient and interactions of a single component with a combination of phases or a mineral with several elements (e.g. illite, kaolinite) is important. To display such interactions graphically, we have modified binary diagrams so that one of the ends can be a combination of components. Figure 3 shows several such diagrams for a series of Beulah ash samples collected by University of Arizona's combustor on a size segregating impactors. Graphical representation of such data clearly shows the trends in reaction mechanism. With increasing impactor number (smaller size ash particles), there is more interaction between the aluminosilicate phase with CaO forming a glassy phase.

Ternary diagram:

Pseudobinary diagrams like the one mentioned above (where two components are lumped together), do not provide the interactions between all the components in the ash chemistry. A true ternary diagram, as shown in Figure 4, displays individual particles with sum of x-ray counts for the three components > 80%. Figure 4 shows the same sample as in Figure 3a. Using such a ternary diagram representation, we were able to confirm the presence of a nepheline ($NaAlSiO4$) phase in ashes of low rank coals with large alkali content. Such a phase can play an important role in the fouling and deposition characteristics of the coal during combustion (10).

As a logical extension to ternary diagrams, we can also draw pseudoternary and higher order diagrams in one of two ways. Just like pseudobinary diagrams, we can represent several phases lumped together on one of the vertices of the ternary diagram. Such alumina-silica-base ternary diagrams, where base is a combination of several basic elements (viz. Na, Mg, K, Fe etc.) have been traditionally used by refractory engineers (11). We are currently working on extending such diagrams to include melting point and viscosity information for the ash particles. Such information should provide further insight into stickiness of the ash particles and thereby the fouling and deposition characteristics of such ashes. Alternatively, we can use a color display to represent a fourth dimension in the ternary diagrams. By assigning different colors or different symbols to different concentrations we can display the concentration of the fourth phase on the ternary diagram by different colors (or symbols).

To make this tool more user friendly, we have developed an interactive computer program. In this program, the user can display data in any combinations of components at the three vertices. The user can also select to display a fourth component by different

color or a combination of up to five components on one of the vertices. Using a mouse, the user can further select a subset of the data displayed by positioning a smaller variable size triangle on this ternary diagram. The size distribution information of the interactively selected data subset can then be displayed.

One of the major drawbacks of such a ternary diagram is its inability to show number distribution within the ternary diagram. If two particles have the same composition, they overlap giving only one point on the ternary diagram which can be quite misleading. To overcome this problem, we have added the fourth dimension in the ternary diagram by displaying it in a perspective view. Figure 5 is a number density distribution of Ca-Si-Al ternary diagram for Beulah ash collected on an impactor filter (#1) of University of Arizona combustor (Note the correspondence to Figures 3a and 4). As is clearly evident, the points at both the Ca and Si vertices on the ternary diagram actually represent a large number of particles. Such concentration information is not readily available on the simple ternary diagrams.

Often the physical size information provided by CCSEM is not enough as such information does not reveal anything about the morphology or the association of the particles. To resolve this problem, we have improved CCSEM data acquisition program by including real-time microimaging (12). Once the particle is identified and its x-ray spectrum is obtained, the SEM beam is controlled by the computer to raster the area bounded by a minimum rectangle totally surrounding the particle. The video image of the particle is then captured and stored on the computer with the EDS spectrum as well as the standard physical dimensions and X-ray counts. Since the raster is narrowed down from the entire frame to just the particle dimensions, we can also get a virtual magnification of the particle. These video images can be called up by a mouse driven selection of the particles on a ternary diagram. Figure 6 shows such a digitally stored backscattered electron image of a single coal particle sitting on a beryllium substrate. An experienced user can then deduce something about the morphology and juxtaposition of these particles. We are using such digital images to investigate mineral-maceral association.

Conclusions:

The amount of information generated by CCSEM is difficult to assimilate just by tabular presentations and some important trends have been obscured in conventional analysis. We are developing graphical tools to represent the standard information in a more friendly representation as well as to depict information previously hidden. Further progress in such CCSEM analysis will be carried out by including n-dimensional analyses and video image processing.

REFERENCES

1. R.J. Lee, F.E. Huggins, G.P. Huffman, Scanning Electron Microscopy, 1, (1978), 561-568.
2. F.E. Huggins, D.A. Kosmack, G.P. Huffman, R.J. Lee, Scanning Electron Microscopy, 1, (1980), 531-540.
3. R.J. Lee, J.F. Kelly, Scanning Electron Microscopy, 1, (1980), 303-310.
4. G.P. Huffman, F.E. Huggins, R.W. Shoenberger, J.S. Walker, F.W. Lytle, R.B. Greegor, Fuel, 65, (1986), 621-632.

5. W.E. Straszheim, J.G. Yousling, R. Markuszewski, in Mineral Matter and Ash in Coal (Ed.: K. Vorres), American Chemical Society, (1986), 449-461.
6. N. Shah, R.A. Keogh, F.E. Huggins, G.P. Huffman, A. Shah, B. Ganguly, S. Mitra, ACS Div. of Fuel Chem. Preprints, 35(3), (1990), 784-792.
7. G.P. Huffman, F.E. Huggins, N. Shah, A. Shah, Prog. Energy Combust. Sci., 16, (1990), 243-251.
8. F.V. Stohl, ACS Div. of Fuel Preprints, 34(3), 1989, 814-818.
9. W.E. Straszheim, R. Markuszewski, Energy & Fuels, 4, (1990), 748-754.
10. J. J. Helble, S. Srinivasachar, A. A. Boni, S. G. Kang, A. F. Sarofim, J. M. Beer, N. Gallagher, L. Bool, T. W. Peterson, J. O. L. Wendt, N. Shah, F. E. Huggins, and G. P. Huffman, Proc. Sixth Ann. Pitt. Coal Conf., 1, (1989), 81-89.
11. "Phase Diagrams for Ceramist", Volumes 1-5, American Ceramic Society, (1964).
12. B.C. Henderson, I.M. Stewart, G.S. Casuccio, American Lab., (Nov. 1989).

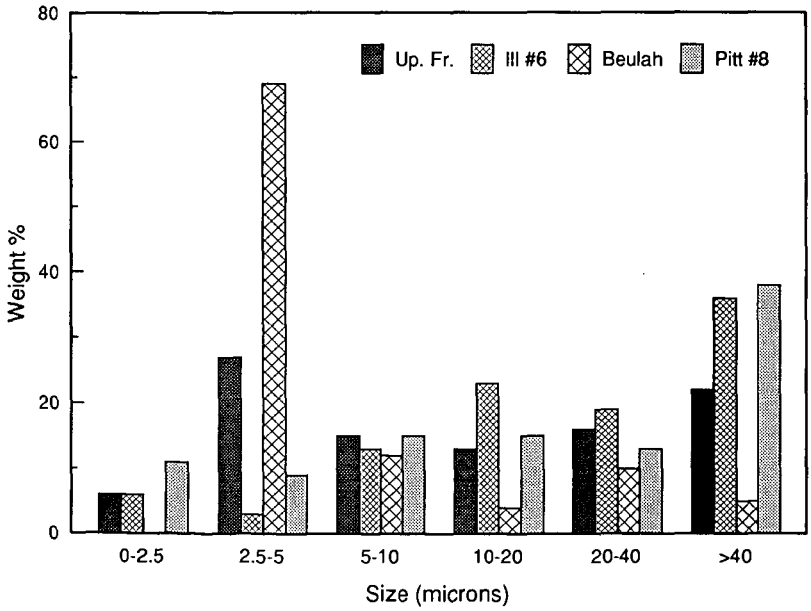

Fig. 1. Example of size distribution obtained by CCSEM for pyrite in several Argonne coals.

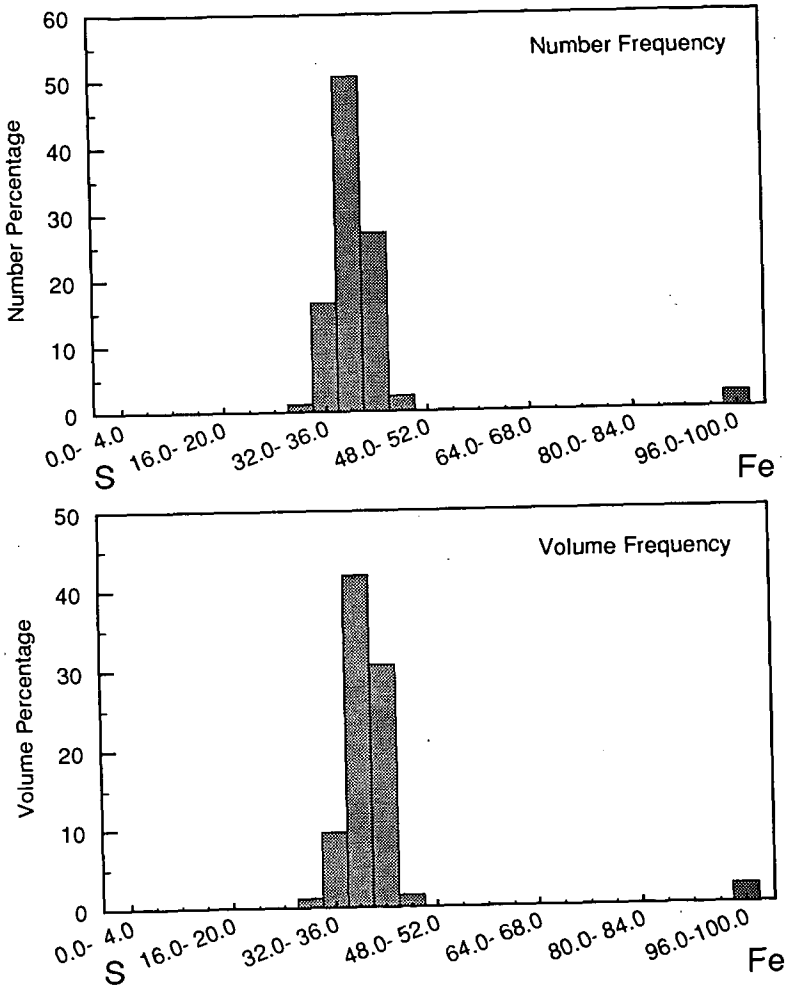

Fig. 2. Examples of Fe-S binary composition diagrams for Beulah coal.

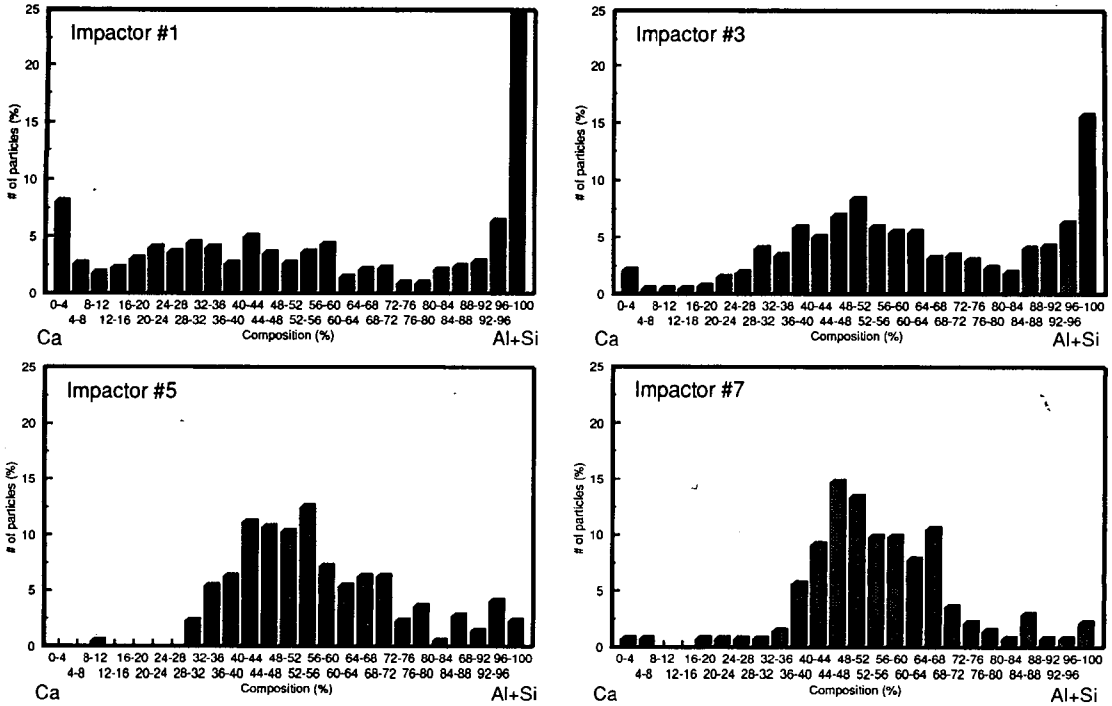

Fig. 3. Ca-Al+Si pseudo binary diagram for Beulah ash collected on size segregating impactor filters. Note the decrease in number of pure Ca and Al+Si particles and increase in glassy Ca+Al+Si mixture particles with increasing impactor number (decreasing size).

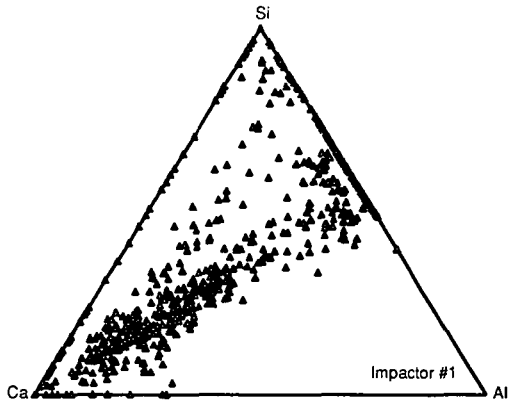

Fig. 4. Ca-Al-Si ternary diagram for Beulah ash

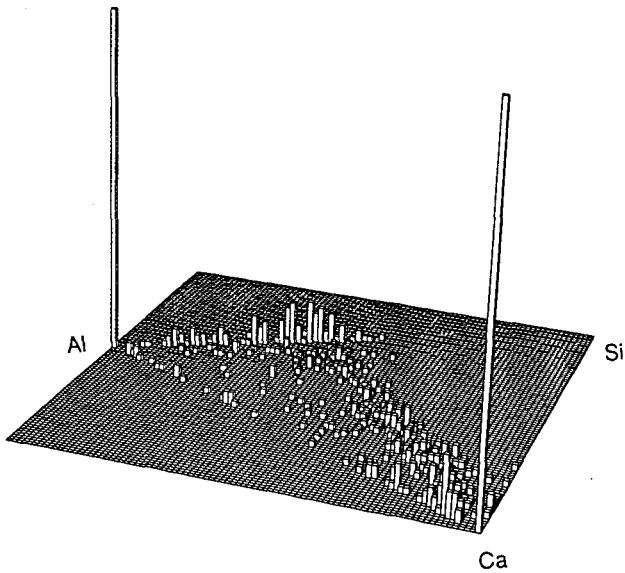

Fig. 5. Ca-Al-Si ternary diagram for Beulah ash showing number frequency.

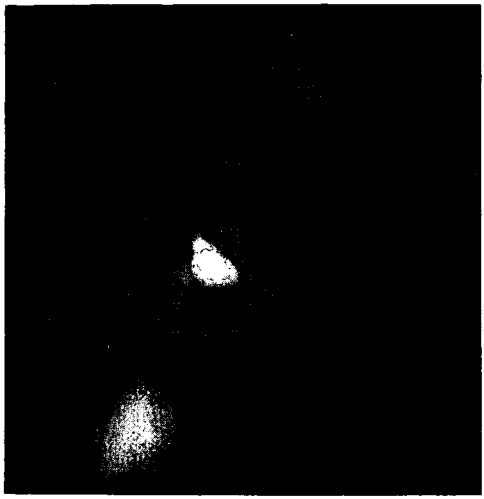

Fig. 6. Digitally stored backscattered electron image of a coal particle on a beryllium substrate. Note a bright mineral particle included within the dark coal matrix.

THE BEHAVIOR OF CLAY MINERALS UNDER COMBUSTION CONDITIONS

J.J. Helble, S. Srinivasachar, and A.A. Boni
PSI Technology Company
20 New England Business Center
Andover MA 01810

Keywords: Coal Combustion, Ash, Deposition

ABSTRACT
The mineral matter in pulverized coal contains a significant amount of clays such as kaolinite, illite, montmorillonite, and other aluminosilicates. During combustion, these minerals often melt and coalesce to form larger ash particles which, if their composition and viscosity are in the appropriate range, may stick to wall surfaces upon impact, leading to deposition. To assess the importance of these transformations in determining ash particle stickiness, combustion and deposit initiation experiments were conducted with montmorillonite, two forms of kaolinite, and several U.S. coals. For the montmorillonite, which contained calcium, magnesium, and iron as modifier ions, vitrification was evident upon exposure to 1500°C oxidizing atmospheres. For the kaolinites - essentially pure aluminosilicates - however, little morphological change was noted. As a result of the difference in modifier ions concentrations, the montmorillonite produced lower viscosity "stickier" particles more prone to adhere to tube surfaces. A comparison of these results with those obtained in a pulverized coal combustion study displayed similar trends. During combustion, if coalescence between clay minerals and dispersed modifier ions such as calcium occurred, the resulting ash particles readily adhered to high temperature tube surfaces. In the absence of modifier species coalescence, reduced values of ash stickiness were observed.

BACKGROUND
To properly select coals for a particular boiler, a reliable prediction of the extent of deposition is clearly desirable. Historically, many empirical indices have been employed for this purpose, but these are only reliable for a limited range of fuels under certain well-defined conditions (1,2). Much of the uncertainty associated with these indices stems from their use of *bulk* ash chemistry to describe processes which are initiated by *individual* ash particles. Fundamental laboratory studies have presented convincing evidence for the need to identify individual ash particle properties and determine how these are derived from the parent coal's mineralogy in addressing deposit initiation and growth (3,4). Although much can learned from studies conducted with pulverized coals, the importance of individual mineral and ash species may be lost in such a complex system. For this reason, studies with individual minerals have been conducted to isolate their transformations in a combustion environment, and to determine whether the resulting ash particles may contribute to inertial deposition. In previous efforts, the role of pyrite and illite have been explored (5,6) and compared to results obtained with synthetic glass particles where viscosity was identified as a key parameter in

deposit initiation. Here we extend our study to two commonly encountered clays - kaolinite and montmorillonite - and explore their role in deposit initiation.

EXPERIMENTAL APPROACH

Equipment

All experiments were conducted in an externally heated laminar flow drop tube furnace, described in detail elsewhere (5). In brief, particles were injected at the top of the reactor into premixed, preheated gases containing 0 - 3 percent O_2 in N_2. Temperatures in the reaction zone were held constant during an individual experiment in the range 1000 to 1500°C. At the exit of the reactor, particles were either (a) sampled isokinetically via a water-cooled nitrogen-quenched collection probe and deposited in a filter for subsequent analysis, or (b) inertially impacted on a deposit collection probe. In the deposit collection probe, particles accelerated through a ceramic converging section to impact uncooled 1.25-3.2 mm diameter mullite tubes oriented perpendicular to the flow. Particles which were sufficiently deformable - "sticky" - adhered to the substrate. Morphological examination of the particles was subsequently conducted by scanning electron microscopy (SEM) on an Amray Model 1820 SEM. Chemical analysis of individual particle and deposit samples was by energy-dispersive x-ray analysis (EDAX).

Sample Selection

Kaolinite and montmorillonite clay samples were obtained from the Source Clays Depository at the University of Missouri - Columbia. Samples were mined from several well-characterized locations, steam dried, pulverized in a hammer mill, remixed, and then riffled prior to shipping. No additives were used in the preparation of these clays. The well-crystallized kaolinite was taken from Washington County Georgia; the poorly crystallized kaolinite from Warren County, Georgia; and the montmorillonite, from Apache County, Arizona. Detailed analyses of these samples have been collected and published in reference (7); chemical composition analysis of each sample taken from (7) is presented in Table I (weight loss on heating is the additional term which will sum the compositions to 100%).

The San Miguel lignite presented for comparison has been discussed in detail elsewhere (3). High clay contents in the parent coal made it an ideal choice for comparison with the clays of this study. Mineralogy of the high-ash San Miguel (51% ash on a dry basis), obtained by computer-controlled SEM at the University of Kentucky, was dominated by zeolite silicates (64 weight percent of the minerals), with significant quantities of montmorillonite (16%) and quartz (12%) also present. Kaolinite levels were only 2% in this lignite, which is lower than the 6-20% levels often encountered in U.S. coals. Note that the coal sample was utilized in an as-received form, with 70% < 75 μm in size. Clay samples were dry-sieved to 38/53 μm prior to testing.

RESULTS AND DISCUSSION

Experiments were first conducted with the well-crystallized kaolinite (K-WC) to determine whether melting or vitrification occurred during combustion processing.

In Figure 1, an SEM micrograph shows typical large kaolinite crystals surrounded by a fairly high concentration of submicron-sized fine particulate. The chemical composition of the larger particles was typically 42-44% Al_2O_3, with the balance silica. Little was noted in the way of modifier ions in the untreated K-WC particles examined. Poorly crystallized kaolinite samples (K-PC) also contained a large number of fine particles in the feed material. Silica-to-alumina ratios for the individual K-PC particles examined were comparable to those observed for the K-WC sample. In contrast to the well-crystallized sample, however, low levels of titania (1-2%) were frequently observed. Silica-rich particles containing nominal 5% potassium (as oxide) were also observed as impurities in the K-PC sample.

Subsequent to reaction in 3% oxygen at 1500°C for 2.9 seconds, little change was noted in either the K-WC or the K-PC samples as shown in Figure 2. In the well-crystallized sample, titania levels of 1-2% were occasionally noted, with no apparent change in the silica-to-alumina ratio observed. For the K-PC sample, some coalescence of the submicron fines is evident upon close examination of the micrograph (Fig. 2b). The chemical composition of these particles, as determined by SEM-EDAX, was comparable to that of the parent K-PC particles. Titania was again consistently observed as an impurity at the 2-6 percent level (oxide, by weight). Iron oxide levels of $\leq$ 2 weight percent were noted in several particles.

Examination of the third clay in this study - montmorillonite - yielded strikingly different results. Initially the particles were similar to the raw kaolinite in that they were of angular shape as seen in Figure 3. Silica-to-alumina ratios in these particles were approximately 3.5/1, with 10% of the particle composed of the modifier ions magnesium, calcium, and iron; most particles sampled were similar in composition to the bulk composition reported in Table I. Subsequent to processing at 1500°C for one second, however, vitrification is apparent in several of the particles seen in Figure 4a. After complete processing at 1500°C for 2.9 seconds (similar to what minerals might encounter in a boiler environment), nearly complete melting was apparent (Fig. 4b).

Because of the high modifier ion content of the montmorillonite, it was expected to produce sticky ash particles prone to deposit over a fairly wide range of conditions. In contrast to this, little deposition was expected from either the K-PC or the K-WC samples. To test this, deposition experiments were conducted with all three samples at deposit impaction surface temperatures of 1275 to 1675 K. Under all conditions examined to-date, little or no deposition was noted with either kaolinite sample as shown in Figure 5. For the montmorillonite, however, capture efficiencies comparable to those of the San Miguel lignite ash previously examined were obtained. Detailed examination of the San Miguel lignite ash had indicated that calcium plus magnesium plus potassium levels of most particles were greater than 10% as oxides, by weight, yielding viscosities below the 10^8 poise believed necessary for adhesion (3). This produced particles with viscosities low enough to permit the particle to remain on the impaction surface subsequent to contact -i.e., viscosities were low enough to absorb the energy of collision. For the calcium

montmorillonite ash particles examined herein, the sum of the modifier ions calcium plus magnesium plus iron was in the range 6-12% for the individual particles studied. Note that this range is comparable to the San Miguel ash particles so similar viscosities are expected. Exact computation requires analysis for the final form of iron (ferrous v. ferric) and is currently underway.

A marked difference in deposit morphology was also noted between the kaolinite and montmorillonite samples, as expected. As Figure 6a shows, only a few glassy particles were retained on the tube surface for the K-WC sample. EDAX analysis of these particles showed them to be illitic in nature and therefore expected to adhere under the conditions of this study (cf. Figure 5). In Figure 6b, the molten adhesive nature of the montmorillonite particles at 1425°C deposition conditions is clearly evident. For this deposit, chemical composition was comparable to that noted both for the raw sample and for individual transformed particles: 20 wt% silica, 67% alumina, 5% each of magnesia and calcia, and 2.4% iron (ferric) oxide.

These results suggest that any mineral interactions which produce aluminosilicate ash particles with approximately 10% modifier ion concentration will give rise to extremely sticky ash particles, prone to deposit upon inertial impaction with wall surfaces. Kaolinite alone is of little concern because of a relative absence of modifier ions, but interactions with dispersed species such as calcium and magnesium could produce ash particles prone to adhere to tube surfaces. Ash particles derived from minerals such as illite and montmorillonite which are rich in modifier ions can deposit without the need for interaction with other species.

ACKNOWLEDGEMENTS
The authors wish to thank Mr. Jeffrey Moore of PSIT for performing many of the experiments described herein. Financial support of the US DOE Pittsburgh Energy Technology Center, grant DE-AC22-86PC90751, is also gratefully acknowledged.

REFERENCES
1. Bryers, R.C., *Proc. EPRI Conf. on the Effects of Coal Quality in Power Plants*, October (1987).
2. Winegartner, E.C., *ASME Research Committee Report on Corrosion and Deposits from Combustion Gases* (1974).
3. Srinivasachar, S., Helble, J.J., and Boni, A.A., *Proc. 23rd Symposium (Int'l) on Combustion*, The Combustion Institute (in press) (1990).
4. Baxter, L.L., Hencken, K.R., and Harding, N.S., *Proc. 23rd Symposium (Int'l) on Combustion*, The Combustion Institute (in press) (1990).
5. Srinivasachar, S., Helble, J.J., and Boni, A.A., *Progr. Energy and Combust. Sci.* ***16***, 281 (1990).
6. Srinivasachar, S., Helble, J.J., Boni, A.A., Shah, N., Huffman, G.P., and Huggins, F.E., *Progr. Energy and Combust. Sci.* ***16***, 293 (1990).
7. Van Olphen and Fripiat, eds., Data Handbook for Clay Materials and Other Non-Metallic Minerals,, Pergamon Press, New York (1979).

Table 1. Clay Chemical Composition

	Weight Percent								
	SiO_2	$A\ell_2O_3$	TiO_2	Fe_2O_3	FeO	MgO	CaO	Na_2O	K_2O
Kaolin-well crystallized	44.2	39.7	1.39	0.13	0.08	0.03	-	0.013	0.05
Kaolin-poorly crystallized	43.9	38.5	2.08	0.98	0.15	0.03	-	-	0.065
Ca-montmorillonite	60.4	17.6	0.24	1.42	0.08	6.46	2.82	0.063	0.19

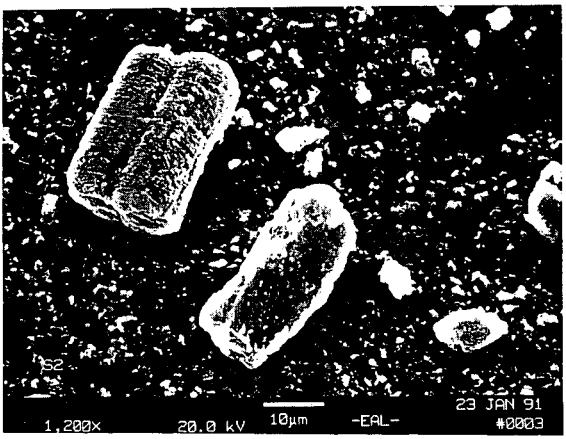

Figure 1. Raw Sample of Well-Crystallized Kaolinite

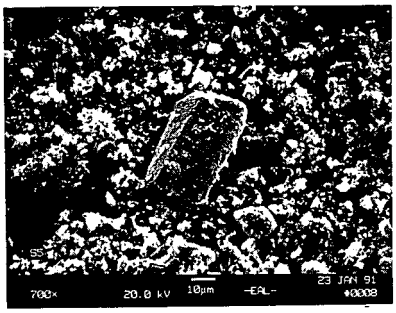

(a) Well Crystallized Kaolinite

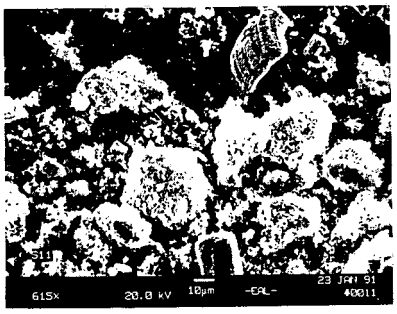

(b) Poorly Crystallized Kaolinite

Figure 2. Kaolinite Samples After Processing at 1500°C in 3 Percent O_2 for 2.9s

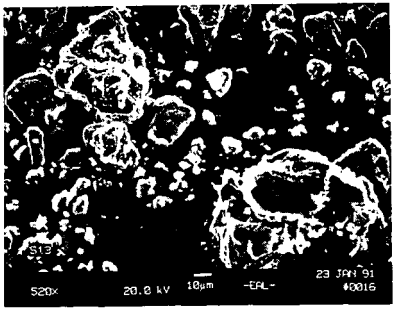

Figure 3. Raw Sample of Calcium-Montmorillonite

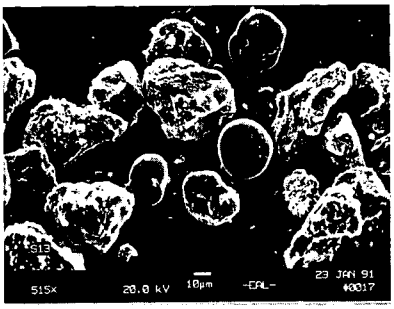

(a) 1s

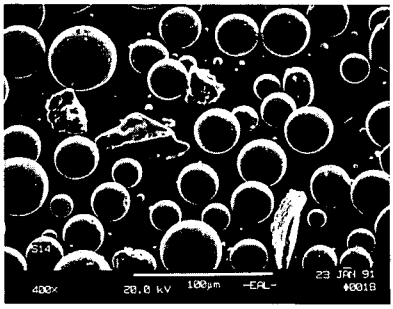

(b) 2.9s

Figure 4. Montmorillonite Samples After Processing at 1500°C in 3 Percent O_2

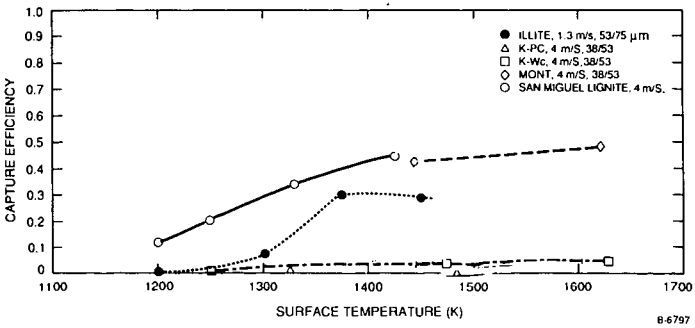

Figure 5. Comparison of Clay Sample Collection Efficiencies with Coal Ash Collection Efficiencies. Combustion conditions as noted

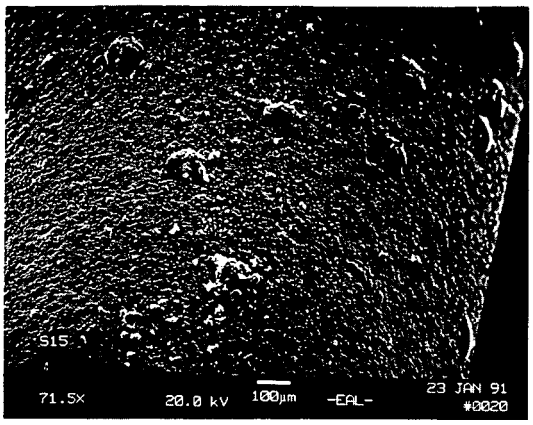

(a) Well Crystallized Kaolinite

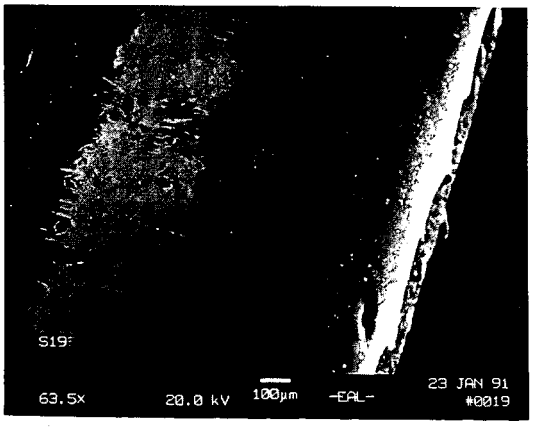

(b) Ca-Montmorillonite

Figure 6. Morphology of Initial Deposits Collected at 1425°C After Processing at 1500°C, 3 Percent O_2

Alkali/Silicate Interactions During Pulverized Coal Combustion

Neal Gallagher, Thomas W. Peterson and Jost Wendt, Chemical Engineering Department, University of Arizona, Tucson, AZ 85721.

Keywords: coal combustion, alkali, aluminosilicates, aerosols

Introduction

During the combustion of pulverized coal, inorganic ash constituents result in the formation of submicron aerosol and large ash particles. It is evident that chemical transformations involving this mineral matter plays an important role in the ultimate size distribution and chemical composition of these particles. One such mineral matter transformation mechanism suggested by data collected in this laboratory is reaction of sodium (or sodium containing species) with aluminosilicates. This observation led to the postulated mechanism of sodium mobilization within a burning char particle reacting with inherent aluminosilicate particles. Mobile sodium which reached the surface of the char particle was assumed to escape to the bulk flue gas environment. Previous work by Lindner and Wall (1988) however suggested that sodium reaction with aluminosilicates takes place primarily after the sodium escapes the char particle. This work attempts to determine the relative importance of sodium reaction with aluminosilicates inside and external to the char particle.

Experimental Work

Experimental facilities included a 17kW down-fired pulverized coal combustor which supported premixed self-sustained flames of pulverized coal. Fly-ash samples were extracted from the combustor and diluted with quench air using an isokinetic probe. Size segregation of the fly-ash samples was accomplished using a Mark II Andersen 1 ACFM cascade impactor. Impaction substrates were 0.2 μm Flouropore filters coated with polyethylene glycol 600 and the after-filter was an uncoated Flouropore filter. The size segregated samples were subjected to atomic absorbance for bulk elemental analysis at the University of Arizona and CCSEM analysis at the University of Kentucky.

Experiments were performed using numerous pulverized coal samples. The data reported herein represent results obtained from an Australian Coal (Loy Yang) and a North Dakota Lignite (Beulah). Loy Yang was chosen since it had a relatively high sodium to aluminosilicate ratio in the original coal, but overall low aluminosilicates (see Table I). In addition to conventional combustion experiments with this coal, experiments were conducted in which an aluminosilicate additive (94 g kaolinite per kg additive-free coal) was included in the coal feed. The kaolinite had a mass mean diameter of 0.5 μm, density 2.63 g/cm^3, and aerodynamic size of 0.81 μm. The purpose of these "doped" runs was to ascertain the effect on Na behavior of the aluminosilicate materials. Table I also shows the original ash analysis in addition to the calculated ash analysis for the doped coal experiments.

The results from the Loy Yang experiments in the absence of additive can be summarized by Figure 1. Here, the fraction oxide of the major elemental species is plotted as a function of the impactor collection plate. TF represents the Total Filter analysis, AF the after-filter analysis and Plates 1 to 8 the larger to smaller particle sizes for the aerodynamic cut-off diameter.

Enrichment of sodium in the smaller sizes is apparent. The sustantial fraction of the sodium found in the smaller sizes could be due to either surface condensation or homogeneous nucleation, but it is clear in either case that the fraction of species in the smallest size range might be indicative of the amount of Na that reached the vapor phase.

When the kaolinite additive is included, a substantial shift in the Na distribution with respect to particle size is witnessed (Figure 2). Not all Na has been taken up by the kaolinite, however, as attested by the large Na fraction still found in the after-filter. This result is not surprising, since it is likely that any remaining submicron aerosols will still be dominated by those species which most easily vaporize. In examining the cumulative mass fraction of the Na that appears on each stage, about 75% of the Na was found in a size range less than 0.65μm in the absence of additive. When kaolinite was included, that fraction fell to about 12%. The additive has significantly changed the overall sodium distribution, but it is still unclear as to whether the mechanism was due to increased condensation, or chemical reaction of the Na with the aluminosilicates.

The experiments with the Loy Yang were conducted because this coal has the rather unusual property of high Na fraction and low aluminosilicate fraction in the parent ash. The Beulah Lignite coal also has relatively high Na content, but contains silicate material in the form of quartz, kaolinite, illite, montmorillonite, mixed silicates and miscellaneous silicates. The Beulah lignite contains approximately 0.065 g Na/g silicates, whereas the doped Loy Yang contained 0.052 g Na/g silicates. Previous work done here showed that the lower the sodium to silicate ratio the higher the fraction of sodium captured. The fraction of sodium not captured was taken as the fraction found on impactor plate 8 and the after-filter (less than 0.65 μm). From this argument alone it would be expected that the doped Loy Yang would exhibit a lower fraction of sodium in a size range less than 0.65 μm than the Beulah Lignite. Figure 3 compares the cumulative fraction sodium oxide as a function of impactor plate for the Beulah Lignite and the doped Loy Yang experiments. These results suggest that because a fraction of the silicate-containing materials in the Beulah Lignite is included within the char matrix (as opposed to being entirely extraneous, as is the case with the kaolinite-doped Loy Yang), there is more efficient Na capture by the silicate materials.

Further examination of the Beulah lignite data also suggests that perhaps a pure condensation mechanism may not be sufficient to explain the behavior of the Na in the presence of the silicate-containing materials. Figure 4 plots the fraction of the impactor sample that is Na oxide vs. the inverse-square of the cut-off diameter. Under pure condensation, such a plot would yield a straight line. This is true for particles in the very small size ranges, but this behavior deviates for larger particles, in spite of the fact that there is a non-negligible amount of Na in these larger particles. Examination via CCSEM (these analyses were performed at the University of Kentucky) of the composition of the individual particles on the largest impactor plate (Plate 1, Figure 5) also shows that, while many of the aluminosilicate-bearing particles had essentially no Na in them, those that did contain Na did so in a fairly narrow range of Na-Al+Si compositions.

Finally, impactor samples collected by cascade impactor from later Loy Yang runs were analyzed in such a way as to try to separate those Na species which are chemically bound to the

aluminosilicates from those which are simply surface-condensed on these particles. This was accomplished by dissolving a portion of the impactor sample in DI water (to get the surface-condensed sodium, presumably water soluble) and a portion in the standard acid reagant (to get all Na-containing species). There is some evidence that the reaction product of sodium with kaolinite (Punjak et al, 1989) is nephelite ($Na_2O{\cdot}Al_2O_3{\cdot}2SiO_2$). Nephelite is insoluble in cold water and decomposes in hot water. Our DI samples were never subjected to temperatures above 40 °C. Albite and jadite ($Na_2O{\cdot}Al_2O_3{\cdot}6SiO_2$ and $Na_2O{\cdot}Al_2O_3{\cdot}4SiO_2$) were also reported as insoluble. One possible product of reaction between sodium and quartz was $Na_2Si_2O_5$ as evidenced by equilibrium calculations. While this species is soluble, the amount of quartz in the Loy Yang was low overall.

The result of this analysis showed that while a large fraction of the Na captured was indeed water soluble (almost exclusively so in the smaller sizes), there was a substantial fraction of Na in the larger sizes (as high as 50% in some cases) which was water-insoluble. This certainly suggests that chemical reactions to form Na-aluminosilicates plays some role in the fate of Na during coal combustion.

Model Development

In order to mechanistically explain the varied experimental observations reported above, a model was developed to follow the release and capture of sodium species by Al and Si-bearing minerals. The model developed describes the release of sodium from a burning char particle, accounting for char particle shrinkage and sodium capture by silicate minerals, both within and outside the char particle. The assumed chemical reaction between sodium and alumino-silicates is based on work done by Punjak et. al (1989) and Uberoi et. al (1990). Additionally, chemical equilibrium calculations suggested the appropriate reaction to consider between sodium and quartz, the other form of Si considered.

Inside the char particle, species balances on the bound sodium, the "mobile" sodium and the included Si-containing species with which Na can react yield:

$$\frac{\partial C_a'}{\partial t} = D\frac{1}{r^2}\frac{\partial}{\partial r}\left(r^2\frac{\partial C_a'}{\partial r}\right) - C_a'\sum_{i=1}^{n}\frac{\eta_i k_{ai}' S_i k_{mi}' C_i'}{\eta_i k_{ai}' S_i C_i' + k_{mi}'} + k_s' C_s' \qquad 1$$

$$C_a' = 0\ ,\ R = R_0 \quad at\ t = 0 \qquad 2$$

$$\frac{\partial C_a'}{\partial r} = 0 \qquad at\ r = 0 \qquad 3$$

$$-D\frac{\partial C_a'}{\partial r} = k_{mb}'(C_a'-C_b') \quad at\ r = R(t) \tag{4}$$

$$\frac{dC_s'}{dt} = -k_s'C_s' + \frac{C_s'R^{*3}}{(R^3 - R^{*3})}\frac{3}{R}\frac{dR}{dt} \tag{5}$$

$$C_s' = C_{s0}' \quad at\ t = 0 \tag{6}$$

$$\frac{\partial C_i'}{\partial t} = -\frac{\beta_i\eta_i k_{ai}'S_i k_{mi}'C_i'C_a'}{\eta_i k_{ai}'S_i C_i' + k_{mi}'} - \frac{C_i'}{V}\frac{dV}{dt} \tag{7}$$

$$C_i' = f_i C_{i0}' \quad at\ t = 0 \quad for\ i = 1,\ldots,n \tag{8}$$

Once the volatile migrates to the surface of the shrinking spherical char particle it can escape to the bulk flue gas phase. The concentration in the bulk, C_b', can change due to the mobile sodium escaping the char particle, reactions of the volatile species with extraneous silicate species j, particle shrinkage and concentration changes due to temperature effects. The condition given by equation 12 describes a bulk flue gas phase that is initially sodium-free.

$$\frac{dC_b'}{dt} = k_{mb}'a_v(C_a'|_{r=R} - C_b') - C_b'\sum_{j=1}^{n}\frac{\eta_j k_{aj}'S_j k_{mj}'C_j'}{\eta_j k_{aj}'S_j C_j' + k_{mj}'}$$

$$- (C_s' + C_a'|_{r=R})\frac{dR}{dt}a_v - \frac{C_b'}{V_b}\frac{dV_b}{dT}\frac{dT}{dt} \tag{9}$$

$$C_b' = 0 \quad at\ \ t = 0 \tag{10}$$

Finally, a balance on the extraneous silicate species yields

$$\frac{dC_j'}{dt} = -\frac{\beta_j\eta_j k_{aj}'S_j k_{mj}'C_j'C_b'}{\eta_j k_{aj}'S_j C_j' + k_{mj}'} - \frac{C_j'}{V_b}\frac{dV_b}{dT}\frac{dT}{dt} \tag{11}$$

$$C_j' = g_j C_{j0}' \qquad at\ t = 0 \quad for\ j = 1,\ldots,n \tag{12}$$

Parametric description of the reaction kinetics and mass transfer is accomplished with the following models:

$$k_{ai}' = A_i e^{-E_{ai}'/RT} \tag{13}$$

$$k_{mb}' = D_b/R \tag{14}$$

$$k_{mi}' = \frac{D_0 v}{R_i} \frac{4\pi R_i^2}{\frac{4}{3}\pi R_i^3} \frac{f_i C_{i0}'}{\rho_i} = \frac{3vf_i C_{i0}'}{\rho_i} \frac{R_0^2}{R_i^2}\left(\frac{D_0}{R_0^2}\right) \tag{15}$$

$$k_s' = A_s e^{-E_{sa}/RT} \tag{16}$$

$$\eta_{i,j} = 1. \tag{17}$$

$$k_{mb}' a_v = \frac{D_{b0} v}{R}\left(a_{v0}\frac{R^2}{R_0^3 T}\right) = a_{v0}\frac{D_{b0}}{D_0}\frac{vu}{T}\left(\frac{D_0}{R_0^2}\right) \tag{18}$$

$$k_{mj}' = \frac{D_{b0} v}{R_j} \frac{4\pi R_j^2}{\frac{4}{3}\pi R_j^3} \frac{g_j C_{j0}'}{\rho_j} \frac{298}{T} = \frac{D_{b0}}{D_0} \frac{3vg_j C_{j0}'}{\rho_j} \frac{R_0^2}{R_j^2} \frac{298}{T}\left(\frac{D_0}{R_0^2}\right) \tag{19}$$

$$a_v = \frac{(4\pi R^2)(feedcoal)}{(\rho_0 \frac{4}{3}\pi R_0^3)60(feedair)} \frac{298}{T} = a_{v0}\frac{R^2}{R_0^3 T} \tag{20}$$

$$a_{v0} = \frac{(feedcoal)(298)}{\rho_0(20)(feedair)} \tag{21}$$

The temperature was determined by fitting the four parameter model below to the measured temperature profile and residence time calculations.

$$T(t) = a_1(1 - e^{-a_2(t+a_4)})e^{-a_3(t+a_4)} \qquad 22$$

The residence time calculation accounted for geometry and temperature effects.

The char particle radius was determined using a simple char burnout model. According to Smith (1971) the rate of burnout R_{ac} is given by:

$$R_{ac} = Ae^{-E_a/RT_p} \qquad 22$$

Where R_{ac} is in grams of char per second per cm^2 external surface area per atmosphere oxygen. From this equation, the rate of change of particle radius is given by:

$$\frac{dR}{dt} = -\frac{p_{O_2}}{\rho_c}Ae^{-E_a/RT} \qquad 23$$

Where R is the char particle radius, and ρ_c is the char density.

Conclusions

Experiments suggest that the Na could escape the burning char and reach the bulk flue gas phase, as observed by the enrichment of Na in the smallest size classes. For the Loy Yang, the size distribution of the Na was greatly affected by the introduction of the additive, with the fraction of Na found in the smallest sizes being reduced from approximately 75% to 12%. It was clear that, while condensed Na species were dominant in the smaller particle size ranges, Na-containing aluminosilicates were indeed present in the large size particles.

Preliminary modeling results have indicated that (1) the reaction is fast enough for the Na to be captured by the included aluminosilicates during char burnout, and (2) the extent to which this occurs depends strongly on mass transfer of the Na through the char matrix.

REFERENCES

Lindner E.R. and Wall T.F., "An Experimental Study of Sodium-Ash Reaction During combustion of Pulverized Coal", Fourth Engineering Foundation Conference on Mineral Matter and Ash Deposition from Coal, Feb. 21-26, 1988, Santa Barbara, CA.

Punjak, W.A., Uberoi, M., and Shadman, F., "High Temperature Adsorption of Alkali Vapors on Solid Sorbents", AIChE Journal, **35**, 1186 (1989).

Smith, I.W., "Kinetics of Combustion of Size-Graded Pulverized Fuels in the Temperature Range 1200-2270 °K", Combustion and Flame, **17**, 303-314 (1971).

Uberoi, M., Punjak, W.A., and Shadman, F., "The Kinetics and Mechanism of Alkali Removal From Flue Gases by Solid Sorbents", Prog. Energy Combust. Sci. **16**, 205 (1990).

NOMENCLATURE

A_i = frequency factor for reaction of volatile with inherent silicate species i, 1/(cm^2 silicate i per g silicate i)/(g silicate i per cm^3 char)/(s).

A_j = frequency factor for reaction of volatile with extraneous silicate species j, 1/(cm^2 silicate j per g silicate)/(g silicate j per cm^3 flue)/(s).

A_s = frequency factor for release of bound volatile from the char matrix, (1/s).

A_v = char surface area per volume flue, (cm^2 char)/(cm^3 flue).

A_{v0} = reference parameter for A_v, (K).

C_a' = concentration of volatile inside the char particle,(g volatile)/(cm^3 char).

C_b' = concentration of volatile outside the char in the bulk flue gas phase, (g volatile)/(cm^3 char).

C_i' = concentration of inherent silicate species i, (g silicate i) /(cm^3 char).

C_j' = concentration of extraneous silicate species j, (g silicate j) /(cm^3 flue).

C_s' = concentration of volatile bound to the char matrix, (g bound vola- tile)/(cm^3 char).

C_{i0}' = initial concentration of all inherent silicate species,(g silicate)/(cm^3 char).

C_{j0}' = initial concentration of all extraneous silicate species, (g silicate)/(cm^3 flue).

C_{s0}' = initial concentration of volatile bound to the char matrix, (g bound volatile)/(cm^3 char).

D = effective diffusivity of volatile inside the char particle, (cm^2)/(s).

D_{ab} = diffusivity of volatile in a char particle pore, (cm^2)/(s).

D_b = diffusivity of volatile in the bulk flue gas phase, (cm^2)/(s).

D_{b0} = diffusivity of volatile in the bulk flue gas phase at the reference temperature T_0, (cm^2)/(s).

D_0 = effective diffusivity of volatile inside the char particle at the reference temperature T_0, (cm^2)/(s).

E_a = activation energy for char burning, (J/gmole).

E_{ai} = activation energy for reaction of volatile with inherent silicate species i, (J/gmole).

E_{aj} = activation energy for reaction of volatile with extraneous silicate species j, (J/gmole).

E_{as} = activation energy for release of bound volatile from the char matrix, (J/gmole).

f_i = fraction of inherent silicates that is species i.

g_i = fraction of extraneous silicates that is species j.

k_{ai}' = reaction rate coefficient between volatile and inherent silicate species i, 1/(cm^2 silicate i per g silicate i)/(g silicate i per cm^3 char)/(s).

k_{aj}' = reaction rate coefficient between volatile and extraneous silicate species j, 1/(cm^2 silicate j per g silicate j)/(g silicate j per cm^3 flue)/(s).

k_{mb}' = interphase mass transfer coefficient for transport of volatile from the char to the bulk flue gas phase, (cm)/(s).

k_{mi}' = interphase mass transfer coefficient for transport of volatile to inherent silicate species i, 1/(s).

k_{mj}' = interphase mass transfer coefficient for transport of volatile to extraneous silicate species j, 1/(s).

k_s' = reaction rate coefficient for release of volatile from the char matrix, 1/(s).

m = char particle mass, (g).

n = number of silicate species.

p_{O2} = partial pressure of oxygen, (atms).

r = radial position inside the spherical char particle, (cm).

R = char particle radius, (cm).

R_i = inherent silicate particle radius, (cm).

R_j = extraneous silicate particle radius, (cm).

R_0 = initial char particle radius, (cm).

R^* = final char particle radius (burnout complete), (cm).

S_i = specific surface area of inherent silicate species i, (cm^2 silicate i)/(g silicate i).

S_j = specific surface area of extraneous silicate species j, (cm^2 silicate j)/(g silicate j).

t = temporal variable, (s).

T = temperature, (K).

T_0 = reference temperature, (K).

V = char particle volume, (cm^3 char).

V_b = bulk flue gas volume, (cm^3 flue).

$\beta_{i,j}$ = stoicheometric factor, (g silicate i,j)/(g Na).

ϵ = char porosity, (cm^3 void)/(cm^3 char).

η_i = effectiveness factor for inherent silicate species i.

η_j = effectiveness factor for extraneous silicate species j.

ρ_i = inherent silicate density, (g)/(cm^3).

ρ_j = extraneous silicate density, (g)/(cm^3).

ρ_e = initial char particle density, (g)/(cm^3).

feedair = air feed rate into the combustor, (slpm).

feedcoal = coal feed rate into the combustor, (kg/hr).

Table I. Ash analysis for doped and undoped Loy Yang.

Loy Yang	undoped	undoped	doped	doped
oxides	% AR	frac oxide	% AR	frac oxide
Al_2O_3	0.04	0.036	3.36	0.404
SiO_2	0.16	0.132	4.02	0.483
CaO	0.06	0.047	0.05	0.006
Fe_2O_3	0.08	0.066	0.07	0.009
Na_2O	0.60	0.490	0.55	0.066
K_2O	< 0.01	0.004	< 0.01	0.001
MgO	0.28	0.225	0.25	0.030
Total	1.9	1.00	10.21	0.999

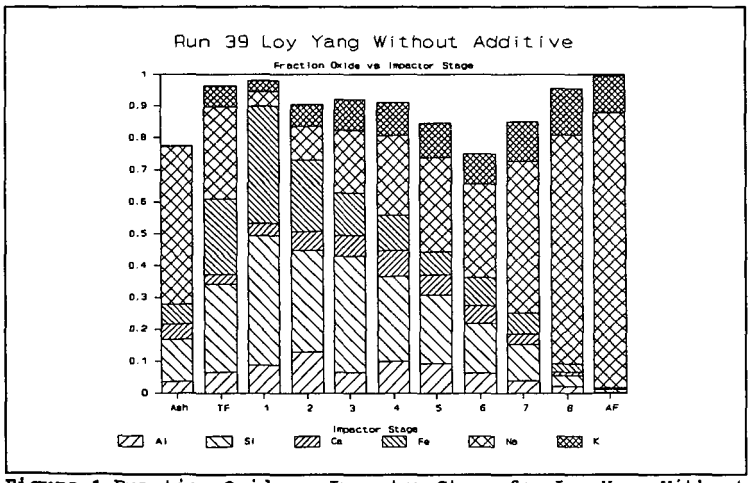

Figure 1 Fraction Oxide vs Impactor Stage for Loy Yang Without Additive

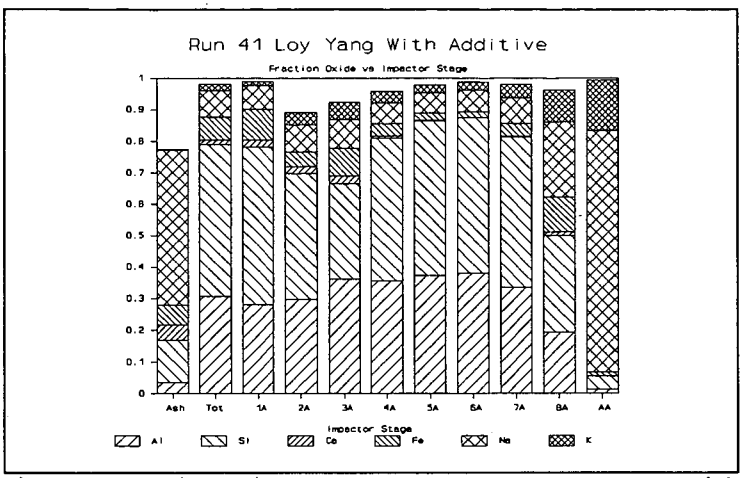

Figure 2 Fraction Oxide vs Impactor Stage for Loy Yang With Additive

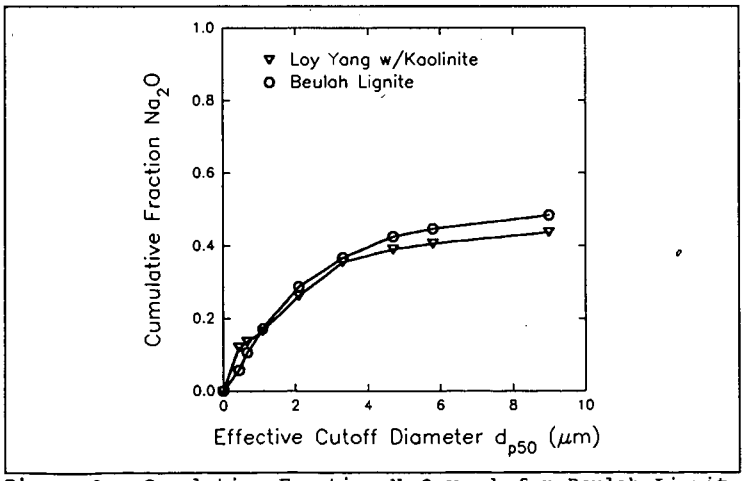

Figure 3. Cumulative Fraction Na_2O vs d_p for Beulah Lignite and Loy Yang doped with Kaolinite

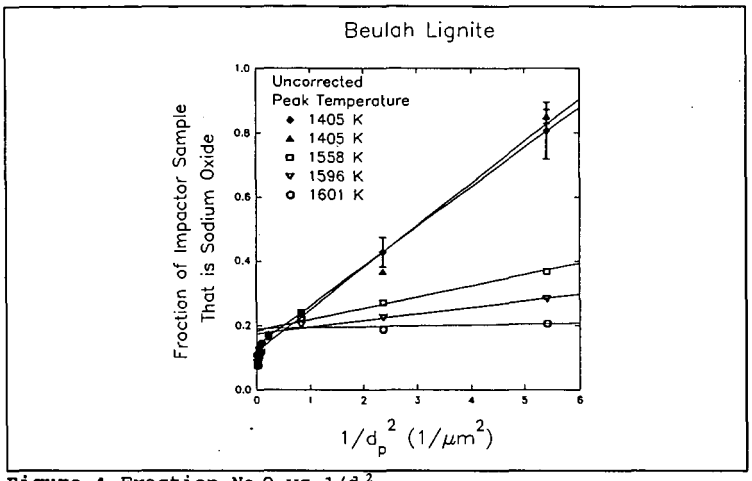

Figure 4 Fraction Na_2O vs $1/d_p^2$.

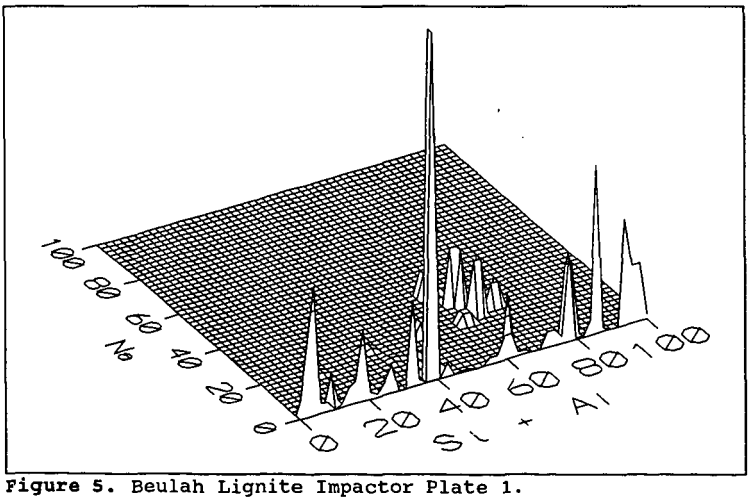

Figure 5. Beulah Lignite Impactor Plate 1.

FRACTAL DIMENSION ANALYSIS OF CHARS PRODUCED FROM SYNTHETIC COAL

Douglas K. Ludlow, Wendy M. Vosen, and Thomas A. Erickson
Department of Chemical Engineering
University of North Dakota
Grand Forks, North Dakota

Keywords: Fractal Dimension, Char, Combustion

ABSTRACT

The fractal dimension, a measure of surface ruggedness, of chars was measured using physisorption techniques. Coals and chars at different stages of combustion were prepared in a laminar flow (drop-tube) furnace. By adjusting the residence time of the coal and char particles in the drop tube, the particles experienced combustion conditions for various lengths of time. The particles were quickly cooled and quenched in an inert atmosphere. The samples were analyzed using a scanning electron microprobe and by using the physisorption of a series of gases. The adsorption data was used to test if the char surface was fractal and to determine the fractal dimension. Changes in the fractal dimension during combustion were quantified. As the char was burned the fractal dimension increased as the carbon matrix burned away leaving mineral moieties. As combustion continued and the carbon burned completely away leaving a mineral fly ash particle the fractal dimension decreased again. Fractal dimension information will be used to model the formation of surface moieties that occur on the char from the inorganic mineral matter dispersed within the coal (Benson *et.al.*, 1988).

BACKGROUND

The morphology and adsorption characteristics of a char surface affect the rate of combustion and the mass transfer processes of the reactants and products involved. A recently developed experimental technique, fractal analysis using physisorption, was used to measure the development of surface morphology during combustion. The conditions at the surface of a burning coal or char particle affect the rate of combustion and the extent of conversion which, in turn, affects the formation of combustion products and unwanted by-products. A laminar flow (drop-tube) furnace was used to produce chars at various stages of combustion for this study.

Background: Physical Adsorption and Surface Area

The adsorption of gases on porous solids is used to measure the surface area of the solid by determining the amount of gas adsorbed as a function of the partial pressure of the adsorbate. Standard surface area determinations are made by adsorbing nitrogen at 77 K and calculating the surface area using the model developed by Brunauer, Emmett and Teller (1938), known as BET (Gregg and Sing, 1982). Other adsorption models can be used. The adsorption model of Dubinin-Polanyi (DP) has been used to determine the surface area of coals and chars(Gregg and Sing, 1982; Marsh and Siemieniewska, 1965). For this research the BET model gave better correlation of the adsorption data (higher correlation coefficients) and was used for all gases. The dynamic flow system was used to determine the gas adsorption isotherms for this research and will be described in the "methods" section.

Background: Fractal Analysis

Adsorption of gases other than nitrogen have been successfully used to measure surface area. Each adsorbing gas has a different molecular size and the surface area covered by an adsorbed molecule of several gases has been determined (Gregg and Sing, 1982, McClellan and Harnsberger, 1967). Mathematical strategies for describing rugged or indeterminate boundaries, known as fractal geometry, developed by Mandelbrot (1977, 1982) have recently been applied to the description of surface structure (Avnir, 1986, 1989; Avnir and Pfeifer, 1983; Avnir *et.al.*, 1983, 1984, 1985; Delfosse *et.al.*, 1988; Fairbridge *et.al.*, 1986; Farin *et.al.*, 1984, 1985a, 1985b; Fripiat *et.al.*, 1986; Jabkhiro and Delfosse, 1988; Ludlow and Moberg, 1990; McEnaney 1988; Moberg, 1990; Ng *et.al.*, 1987; Pfeifer, 1984; Pfeifer and Avnir, 1983; Pfeifer *et.al.*, 1983, 1984; Van Damme and Fripiat, 1985; Van Vliet and Young, 1988; Vosen, 1990; Wilkie, 1990). Theories have been developed to determine a quantity known as the "fractal dimension," which is a measure of the ruggedness of a surface. The value of the fractal dimension varies from the topological dimension of 2 to the euclidean dimension of 3. When a molecule interacts with a surface having a fractal dimension of 2.0 it is essentially encountering a two dimensional plane. When the fractal dimension approaches 3.0, an adsorbing molecule is encountering a three dimensional surface.

Two methods to determine the fractal dimension of solids from adsorption data have been demonstrated. In the first method a single adsorbate is used, and the surface area is measured using different particle sizes of the sample. This technique requires grinding the sample, using a sonic sieve to size the particles into very tight particle ranges, and measuring particle size distribution in each range. This method has been demonstrated (Avnir *et.al.*, 1985; Fairbridge *et.al.*, 1986; Ng *et.al.*, 1987) and has the major advantage that only one adsorbate is required. The disadvantages are the extensive sample preparation required and the possibility that grinding the sample may affect the fractal dimension.

The second method to determine fractal dimension is to adsorb a series of different sized molecules onto a single sample. Because the smaller molecules have access to the "finer" surface structure that the larger molecules do not, a difference in measured surface area is found. Using this difference, a scheme has been developed to determine the fractal dimension. This method has also been demonstrated (Avnir *et.al.*, 1985; Van Damme and Fripiat, 1985). The second method does not explicitly require the sonic sieve, nor the particle size analyzer, but it does require the ability to adsorb different gases onto the sample. Using a mass flow controller and a gas handling manifold, various adsorbate/helium mixtures can be used for surface analysis.

Background: Inorganics in Coal

One objective of this study is to determine the effect that temperature and residence times, found in typical industrial pulverized-coal boilers, have on the formation of char and fly ash morphology. Sodium silicates and sodium sulfates form the major inorganic constituents of coal. These inorganic constituents will affect the surface structure of the chars and fly ash being developed. Western coals contain significant quantities of sodium, sulfur, and silica. The inorganic constituents of coal pass through the combustion zone either as solids, liquids or vapor and ultimately react or condense to form fly ash particles. Some of the fly ash particles are transported to the heat exchange surfaces and form a deposit which will grow with time. As these deposits increase they insulate the heat transfer surface, decreasing the thermal efficiency of the boiler.

Sodium volatilizes upon combustion, becomes dispersed through the gas stream, and later condenses on other ash particles and on the metal surfaces. Wibberly and Wall(1982) proposed that sodium containing materials provide a binding matrix that fuses ash particles together. The mechanism of formation of such a material may be the key to understanding the deposition processes of western coals. Studies by Sondreal(1977) on low rank coals from the western U.S. revealed that the severity of ash fouling deposits correlates not only with sodium concentration but also with total ash content.

One of the major problems in studying the roles of inorganics during coal combustion is the complexity of coal. To alleviate this problem, the interaction of the three inorganic constituents were studied in a model system with use of a synthetic coal (glassy carbon) incorporated with the desired inorganics(Erickson 1988; Erickson 1990).

EXPERIMENTAL METHODS

Synthetic Coal Preparation

The purpose of a synthetic coal is to be able to study the interactions of coal combustion in a system not as complex as actual coal. The synthetic coal must have similar combustion characteristics as well as lending itself to the addition of minerals in a quantitative manner. A furfuryl alcohol polymer has been found to be such a substance(Schmitt 1976; Senior and Flagen 1984; Levendis and Flagen 1987).

The preparation of the synthetic coal was developed by Senior(1984). The technique was slightly modified for this study and is described in detail(Erickson 1990). In brief, the quartz (which had been sized to 5 mm) was added prior to the polymerization so that it would behave as an included mineral. After the polymer was cured, the synthetic coal was ground and sized. Analysis of the sized coal indicated that 0.4 weight percent sulfur was inherent in the synthetic coal polymer due to the p-toluensulfonic acid which is used as a catalyst for the polymerization. Additional sublimed sulfur was added extraneously and mixed with the ground synthetic coal so that the final composition would consist of 1% sulfur. Sodium was added using a solution of sodium benzoate in an ethanol solution. The sodium benzoate/alcohol solution was mixed with the ground coal and the alcohol evaporated. This has been found(Mills 1989) to effectively load the sodium on the coal so that it will easily volatilize.

The chemistry of the polymerization of furfuryl alcohol to form a glassy carbon has been studied extensively(Dunlop and Peters 1953; Riesz and Susman 1960; Conley and Metil 1963; Weswerka et.al 1968; Fitzer et.al 1969). For this study characterization of the synthetic coal included analysis by SEM, CCSEM, TGA, Proximate-Ultimate, Inductively Coupled Plasma (ICP) (with acid digestion and lithium boride extraction), BET surface area from nitrogen adsorption and fractal analysis using gas adsorption. By formulation and analysis the synthetic coal included 10 percent SiO_2 (quartz), 5 percent Na and 1 percent S by weight. The weight loss with respect to temperature from the TGA were in qualitative agreement with TGA results for a low rank coal. The nitrogen BET surface area of the synthetic coal is 50.3 m^2/g.

Laminar Flow Furnace

The prepared samples of synthetic coal were burned in the laminar flow furnace with 20 percent excess air (to ensure complete combustion). The laminar flow furnace is an instrument available through the University of North Dakota, Energy and Environmental Research Center(Zygarlicke *et.al.*, 1989). The pulverized and sized synthetic coal is fed to the laminar flow furnace and burned under preset conditions. The char and fly ash is collected using a water-cooled, nitrogen-quenched probe and collected on filter paper. Six different samples of char and fly ash were prepared using the laminar flow furnace. These six samples along with two samples of synthetic coal were analyzed using the scanning electron microprobe and fractal dimension analysis.

Gas Adsorption

A dynamic flow adsorption instrument is one of the most popular methods to measure gas adsorption. A mixture of adsorbate and helium passes through a thermal conductivity (TC) detector, across the sample, and then through a matched TC detector. The TC detectors are connected in a bridge circuit so that a millivolt signal, which is

proportional to the difference in the concentrations of the adsorbate before and after flowing through the sample, is generated. When flow across the sample is initiated, a signal will be generated from the bridged TC detectors because the concentration of the adsorbate will decrease as it is adsorbed onto the surface. A signal will not be generated by the TC detectors when equilibrium has been achieved. The amount adsorbed is determined from the area under the curve of a plot of the TC signal versus time. To accurately measure the surface area the amount adsorbed should be determined at three to five different adsorbate/helium compositions. However, due to experimental difficulty, some samples were analyzed at only two compositions.

A Micromeritics, Flowsorb 2300 II with a mass flow controller was used to obtain all gas adsorption measurements. The instrument was plumbed so that several different adsorbates (nitrogen, carbon dioxide, ethane, propane and n-butane) can be mixed with helium and used for gas adsorption.

To measure the complete isotherm, each adsorbate was adsorbed at different partial pressures. In order for physical adsorption to occur, the adsorption conditions need to be close to the boiling temperature of the adsorbate. Desorption temperatures are set at any convenient temperature above the adsorption temperature so that desorption will occur.

BET Equation

The BET adsorption model (Brunauer *et.al.*, 1938) is commonly used to determine surface area from physisorption data. The relation:

$$\frac{P}{V(P_o-P)} = \frac{1}{V_m C} + \frac{C-1}{V_m C}\frac{P}{P_o} \qquad (1)$$

is used to determine V_m, the monolayer coverage. In the equation, P is the adsorbate partial pressure (mmHg), P_o is the saturation pressure (mmHg), and V is the volume adsorbed (cm^3 STP/g of sample). The constant C is an experimentally determined constant which is related to the heat of adsorption. The BET equation is considered valid for values of C between 10 and 110. For values of C between 2 and 10 the relationship can be applied but may be within 100% error. For C values greater than 110 the model is expected to be within 20% error. Using Equation 1 the monolayer coverage can be determined from the slope and intercept of a plot of $P/V(P_o-P)$ versus P/P_o.

Fractal Dimension Analysis

The concepts developed by Mandelbrot (1977, 1982) can be applied to the determination of surface ruggedness. Different sized molecules will have different access to surfaces that are rugged or indeterminate. This concept can be visualized in Figure 1. Avnir (1989) developed the relationship:

$$V_m \propto \sigma^{(-D/2)} \qquad (3)$$

where V_m is the monolayer coverage, σ is the cross-sectional area of the adsorbate molecule, and D is the fractal dimension. This equation can be written as:

$$V_m = k\sigma^{(-D/2)} \qquad (4)$$

where k is a prefactor which contains the necessary dimensional conversions. This term is called the lacunarity (Mandelbrot, 1982). The constant k is the monolayer value for unit σ and carries information about the connectivity and porosity of the surface (larger values of k correspond to a greater extent of porosity). The value of D is expected to have a value between 2 and 3.

Equation 4 can be linearized by taking the logarithm of both sides, which results in:

$$\log V_m = \log k - D/2 \log\sigma \qquad (5)$$

Equation 5 is the working relationship, and indicates that a plot of $\log V_m$ versus $\log\sigma$ for various adsorbates on a given adsorbent should be a straight line with slope of -D/2 and intercept of log k.

Experimental Matrix

In order to maintain the experimental integrity of the study and to eliminate any operator bias, the order in which the various adsorptions were performed was randomized. Five sample holders for the gas adsorption unit were available so a suite of five samples were run first followed by a suite of three samples. The order in which the adsorbates were used was randomized, the order in which the various gas compositions were used was randomized, and finally the order in which the samples were analyzed at each composition was randomized. For each adsorbate composition on a given sample, four to six adsorption/desorptions were performed.

RESULTS

The synthetic coal sample was prepared and burned in the laminar flow furnace. The resulting chars and fly ash particles were collected and characterized using the SEM, CCSEM and TGA. The remaining char and fly ash particles were used for the gas adsorption analyses. Figure 2 shows a typical BET plot (nitrogen on sample 3).

Using the gas adsorption data (V_m) and McClellan and Harnsberger's (1967) cross-sectional areas, fractal plots were made for each sample. A sample plot is shown in Figure 3. The fractal dimension determined for each sample is found in Table 1.

DISCUSSION OF RESULTS

As the synthetic coal particles burn the carbon matrix is removed and the remaining mineral constituents form small beads on the char surface. There is evidence of the interaction of the sodium with the silica because the mineral

particles have rounded edges corresponding to a sodium silicate particle. At the operating temperatures, silica is not expected to be molten. However, the heat released during the combustion, may be enough to raise the particle temperature to point above the melting point of silica.

The formation of the sodium silicate moieties on the surface of the char drastically changes the surface morphology of the chars at the different stages of combustion. This was evident in the SEM micrographs. The determination of the fractal dimensions gives a quantitative description of the surface ruggedness. For the synthetic coal particles the surface fractal dimension is initially close to 2. As the particle burns and there is an increase in the ruggedness and the fractal dimension increases. Finally as the carbon matrix completely burns away and the remaining minerals coalesce, the fractal dimension decreases. This is demonstrated in Figure 4 which shows the plot of fractal dimension versus carbon loss. The lacunarity (prefactor) also gives some information about the degree of connectivity and porosity of the surface. The lacunarity also increases in the initial stages of combustion and again decreases as the mineral matter starts to coalesce. This is shown in Figure 5.

Sample Size

The results for some of the samples are less than satisfactory. The primary difficulty with these samples was that there was not enough sample produced in the laminar flow furnace. The Flowsorb II 2300 has resolution down to 0.002 cm^3 STP, however, the accuracy falls off for adsorptions below 0.2 cm^3 STP. Typical procedures for samples with a total volume adsorbed less than 0.2 cm^3 STP is to load the sample cells with more sample. Due to the prohibitive cost of producing more char and fly ash samples, it was decided to attempt the analyses with the existing samples (samples 7 and 8) which were smaller than desired. It was evident from the results that the range of the instrumentation had been exceeded for the smaller sized samples.

Sample Analysis Time

A difficulty that may prevent fractal dimension analysis from becoming a "routine" analysis is the time involved in obtaining the adsorption data. For each sample, five different adsorbates were used, and each adsorbate was adsorbed at three to five different compositions. In addition, at each composition from four to six adsorption/desorption cycles were performed. Each adsorption/desorption cycle requires from one to one and a half hours to complete. Thus the analysis time to determine the fractal dimension of a single sample takes on the order of 100 hours of instrument (operator) time.

However, due to the quantitative nature of the resulting measure of surface ruggedness, the technique still has applications with selected samples of important research applications. There is the possibility that the technique can be further refined to decrease the total analysis time required for each sample.

Cross-sectional areas

An additional difficulty with the analysis is that of determining to correct cross-sectional area of the molecules. This is a notorious problem of surface science (Farin et.al., 1985; Meyer et.al. 1986; McClellan and Harnsberger, 1967) and has yet to receive satisfactory solution. The current state of knowledge is the predictions given by McClellan and Harnsberger (1967). The difficulty with these correlations is that the predictions are based on the idea that different adsorbates should give the same surface area. This can only be true if the adsorbent has a molecularly smooth surface with a fractal dimension of 2. Since McClellan and Harnsberger's work was completed before the concept of fractal surfaces appeared in the literature, these considerations were not taken into account.

CONCLUSIONS

The surface fractal dimension of burning synthetic coal at different stages of combustion have been determined (Vosen, 1990). The experimental technique of using dynamic flow adsorption instrument to determine fractal dimension from gas adsorption data has been demonstrated (Ludlow and Moberg, 1990; Moberg, 1990; Vosen, 1990; Wilkie, 1990). Information (experience) obtained from this study will lead to further improvements of the technique. The fractal dimensions determined, for samples with sufficient sample size, corresponded well with the apparent changes in surface structure at the different stages of combustion.

ACKNOWLEDGEMENTS

The PI would like to acknowledge the assistance of Dr. Steven Benson and Thomas Erickson of the Energy and Environmental Research Center for the preparation of the Synthetic coal and the preparation of the chars in the laminar flow furnace. The PI would also like to acknowledge Wendy Vosen who took on this project as a Senior Honors Thesis and who performed most of the gas adsorptions. Ms. Vosen was assisted in the adsorption studies by Annette Wilkie and Wendy Spenst whose efforts are also acknowledged.

REFERENCES

Avnir, D., "Fractal Aspects of Surface Science - An Interim Report," in *Better Ceramics Through Chemistry II*, Brinker, C. J., Clark, D. E., and Ulrich, D. R. (eds), Materials Research Society, Pittsburgh, PA, 321-329 (1986).

Avnir, D. ed., *The Fractal Approach to Heterogeneous Chemsitry - Surfaces, Colloids, Polymers*, John Wiley & Sons, New York, (1989).

Avnir, D., Farin, D., and Pfeifer, P., "Chemistry in Noninteger Dimensions Between Two and Three. II. Fractal Surfaces of Adsorbents, " *The Journal of Chemical Physics*, **79**(7), 3566-3571 (1983).

Avnir, D., Farin, D., and Pfeifer, P., "Molecular Fractal Surfaces," *Nature*, **308**(5956), 261-263 (1984).

Avnir, D., Farin, D., and Pfeifer, P., "Surface Geometric Irregularity of Particulate Materials: The Fractal Approach," *Journal of Colloid and Interface Science*, **103**(1), 112-123 (1985).

Avnir, D. and Pfeifer, P., "Fractal dimension in chemistry. An intensive characteristic of surface irregularity," *Nouveau Journal De Chimie* **7**(2), 71-72, (1983)

Benson, S. A., Sweeny, P. G., Abrahamson, H. B., Radonovich, L. J., Puffe, W. H., and Zygarlicke, C. J., "Combustion Inorganic Transformations," Ninth Quarterly Technical Progress Report, DOE/DE/FC21-86MC10637, July (1988).

Brunauer, S., Emmett, P. H., and Teller, E., "Adsorption of gases in multimolecular layers, " *Journal of American Chemical Society*, **60**, 309-319 (1938).

Conley, R. T. and Métil, I., "An Investigation of the Structure of Furfuryl Alcohol Polycondensates with Infared Spectroscopy," *Journal of Applied Polymer Science*, **7**, 37-52 (1963).

Delfosse, L., Ponsolle, L. and Jabkhiro, E.H., "The Evolution of Porosity During the Combustion of Char: The fractal Approach and the Statistic Description," In: *Twenty-Second Symposium on Combustion*, The Combustion Institute, , 39-45, (1988)

Dunlop, A. P., and Peters, F. N., *Industrial and Engineering Chemistry*, 34, 814 (1953).

Erickson, T. A. *The Fate of Flame Volatilized Sodium During the Combustion of Pulverized Coal in Reaction with Silica and Sulfur (Studied with the Aid of a Synthetic Coal)*, M.S. Thesis, University of North Dakota (1990).

Erickson, T. A. *The Role of Sodium and Sulfur in High Temperature Reaction with Silica Particles*, Senior Honors Thesis, University of North Dakota (1988).

Fairbridge, C., Ng, S. H., and Palmer, A. D., "Fractal Analysis of Gas Adsorption on Syncrude Coke," *Fuel*, **65**(12), 1759-1762 (1986).

Farin, D., Avnir, D. and Pfeifer, P., "Fractal dimensions of surfaces. The use of adsorption data for the quantitative evaluation of geometric irregularity," *Particulate Science and Technology* **2**, 27-35, (1984)

Farin, D., Peleg, S., Yavin, D. and Avnir, D., "Applications and limitations of boundary-line fractal analysis of irregular surfaces: Proteins, aggregates, and porous materials," *Langmuir* **1**, 399-407, (1985a)

Farin, D., Volpert, A., and Avnir, D., *Journal of the American Chemical Society*, **107**, 3368, 5319 (1985b).

Fitzer, E., Schaefer, W. and Yamada, S., "The Formation of Glasslike Carbon by Pyrolysis of Polyfurfuryl Alcohol and Phenolic Resin," *Carbon*, **7**, 643-648 (1969).

Fripiat, J.J., Gatineau, L. and Van Damme, H., "Multilayer physical adsorption on fractal surfaces," *Langmuir* **2**, 562-567, (1986)

Gregg, S. J., and Sing, K. S. W., *Adsorption, Surface Area and Porosity, 2nd Edition*, Academic Press, New York (1982).

Jabkhiro, E. H., and Delfosse, L., "The Evolution of Porosity During the Combustion of Char, The Fractal Approach and the Statistic Description," 22th International Symposium on Combustion, The Combustion Institute, Pittsburgh, PA (1988).

Levendis, Y. A. and Flagen, R. C., " Combustion of Uniformly Sized Glassy Carbon Particles," *Combustion Science and Technology*, **53**, 117-136 (1987).

Ludlow, D. K. and Moberg, T. P., "Technique for Determination of Surface Fractal Dimension Using a Dynamic Flow Adsorption Instrument," *Analytical Instrumentation*, **19**(2&3), 113 (1990).

Mandelbrot, B. B., *The Fractal Geometry of Nature*, W. H. Freeman & Co, New York (1982)

Mandelbrot, B. B., *Fractals - Form, Chance, and Dimension*, W. H. Freeman & Co, San Francisco (1977)

Marsh, H., and Siemieniewska, T., "The Surface Areas of Coals as Evaluated from the Adsorption Isotherms of Carbon Dioxide using the Dubinin-Polanyi Equation," *Fuel*, **44**(5), 355-367 (1965).

McClellan, A. L. and Harnsberger, H. F., "Cross-sectional Areas of Molecules Adsorbed on Solid Surfaces, " *Journal of Colloid and Interface Science*, **23**, 577-599 (1967).

McEnaney, B., "Adsorption and structure in Microporous carbons," *Carbon* **26**(3), 267-274, (1988)

Meyer, A. Y., Farin, D. and Avnir, D., *Journal of the American Chemical Society*, **108**, 7897 (1986).

Mills, M.E., *Sodium Release from Solids in Flames Studied using Laser Induced Flourescence Spectroscopy*, Ph.D. Thesis, University of North Dakota (1989)

Moberg, T.P., *The Fractal Analysis of Catalytic Glass Fabrics*, M.S. Thesis, University of North Dakota, Grand Forks, ND (1990)

Ng, S. H., Fairbridge, C., Kaye, B. H., "Fractal Description of the Surface Structure of Coke Particles," Langmuir, The ACS Journal of Surface and Colloids, 3(3), 340-345 (1987).

Pfeifer, P., "Fractal dimension as working tool for surface-roughness problems," In: *Applications of Surface Science, Vol. 18*, edited by Park, R.L., North-Holland Physics Publishing, Amsterdam, The Netherlands, 146-164, (1984)

Pfeifer, P., and Avnir, D., "Chemistry in Noninteger Dimensions between Two and Three. I. Fractal Theory of Heterogeneous Surfaces," *The Journal of Chemical Physics*, **79**(7), 3558-3565 (1983).

Pfeifer, P., Avnir, D., and Farin, D., "Ideally Irregular Surfaces, of Dimension Greater Than Two, in Theory and Practice," *Surface Science*, **126**, 569-572 (1983).

Pfeifer, P., Avnir, D., and Farin, D., "Scaling Behavior of Surface Irregularity in the Molecular Domain: From Adsorption Studies to Fractal Catalysts," *Journal of Statistical Physics*, **36(5/6)**, 699-716 (1984).

Riesz, C. H. and Susman, S. *Procedings of the 4th Carbon Conference*, Pergamon Press, Oxford, 621 (1960).

Schmitt, J. L., *Carbon Molecular Sieves as Selective Catalyst Supports*, Ph.D. Thesis, Pennsylvania State University (1976).

Senior, C. L., *Submicron Aerosal Production During Combustion of Pulverized Coal*, Ph.D. Thesis, California Institute of Technology (1984).

Senior, C. L. and Flagan, R. C., "Synthetic Chars for the Study of Ash Vaporization," *Twentieth Symposium (International) on Combustion*, The Combustion Institute, 921-929 (1984).

Sondreal, E. A., Tufte, P. H., and Beckering, W., "Ash Fouling in the Combustion of Low-Rank Western U.S. Coals," *Combustion Science and Technology*, **16**, 95 (1977).

Van Damme, H.; and Fripiat, J. J., "A Fractal Analysis of Adsorption Processes by Pillared Swelling Clays," *The Journal of Chemical Physics*, **82**(6), 2785-2789 (1985).

Van Vliet, B.M. and Young, B.D., "The use of fractal dimension to quantify the effect of surface roughness on film mass transfer enhancement," *Chem. Eng. Comm.* **69**, 81-94, (1988)

Vosen, W. M. *Fractal Dimension Analysis of Fly Ash Development from Char Combustion*, Senior Honor Thesis, University of North Dakota (1990).

Weswerka, E. M., Walters, K. L. and Moore, R. H., "Differential Thermal Analysis of Furfuryl Alcohol Resin Binders," *Carbon*, **7**, 129-141 (1968).

Wibberly, L. J. and Wall, T. F., "Alkali-Ash Reactions and Deposit Formation in Pulverized-Coal-Fired Boilers: The Thermodyamic Aspects Silica, Sodium, Sulfur, and Chlorine," *FUEL*, **61**, 87-92 (1982).

Wilkie, A. M. *Fractal Dimension Analysis of Carbon Fiber Composites*, Senior Honors Thesis, University of North Dakota (1990).

Zygarlicke, C. J.; Benson, S. A.; Abrahamson, H. B.; Mills, M. E., *Departmant of Energy Annual Report*, DOE-DE-FC21-86MC10637 (1989)

TABLE 1
Results

Run	Combustion Temperature (K)	Residence Time (sec)	Sample Size (g)	Mineral[A] Diameter (mm)	Carbon[B] Loss (%)	BET Surface[C] Area (m^2/g)	Fractal Dimension D	Prefactor K ($Å^D$ cm^3 STP)
1	Synthetic Coal	-	0.6319	3.84	0.0	49.0± 1.6	1.89± 0.49	9.35 ± 2.18
2	Synthetic Coal	-	0.6576	3.84	0.0	51.5± 1.4	2.10± 0.28	10.69± 2.10
3	1173	0.1	0.6142	4.04	14.3	55.1± 1.3	2.70± 0.83	16.05± 2.31
4	1173	0.5	0.1568	4.06	66.5	124.7± 3.3	2.85± 0.30	22.67± 2.11
5	1173	1.5	0.1816	27.0[E]	100	121.4± 3.1	2.47± 0.72	16.86± 2.26
6	1773	0.1	0.3089	5.06	48.7	110.4± 3.0	2.81± 0.46	21.79± 2.17
7	1773	0.5	0.0253	4.20	83.5	(5.6± 0.5)[F]	1.98± 1.15	3.26± 2.30
8	1773	1.5	0.3071	8.50[E]	100	(0.8± 0.1)[F]	2.26± 1.84	1.78± 2.48

[A] Determined using CCSEM
[B] Determined using TGA
[C] Nitrogen Adsorption data at 77 K
[E] Average diameter of coalesced fly ash particles
[F] Insufficient sample size to accurately determine surface area

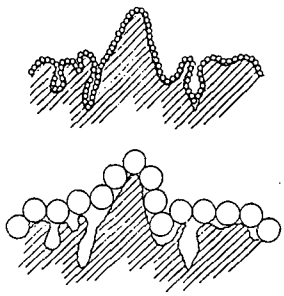

Figure 1. Pictorial representation of fractal dimension analysis.

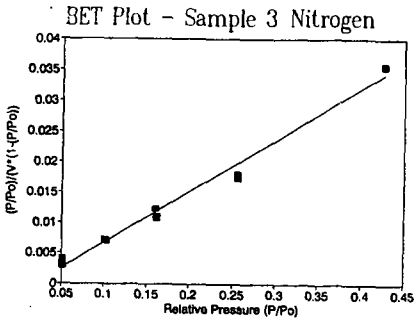

Figure 2. Example of BET plot used to determine monolayer volume adsorbed (V_m).

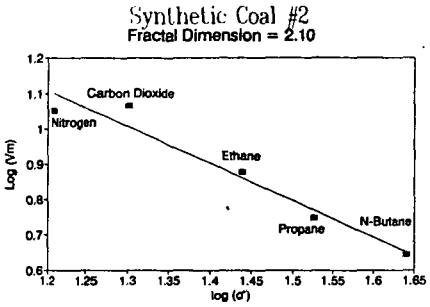

Figure 3. Example of fractal dimension plot used to determine the fractal dimension, D, and the lacunarity.

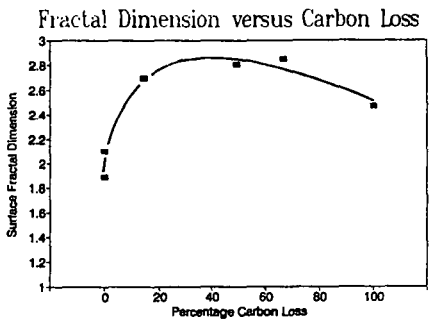

Figure 4. Surface fractal dimension versus carbon loss during char combustion.

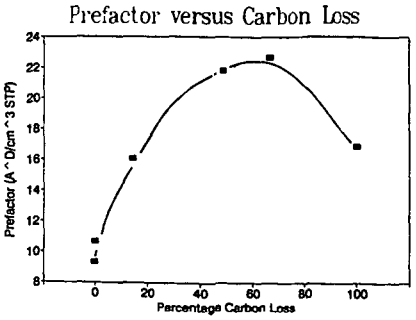

Figure 5. Lacunarity versus carbon loss during char combustion.

PERFORMANCE CHARACTERISTICS OF AN MHD PILOT PLANT ELECTROSTATIC PRECIPITATOR

J. S. Lindner, P. R. Jang, W. P. Okhuysen
Diagnostic Instrumentation and Analysis Laboratory
Mississippi State University
Mississippi State, MS 39762
and
J. K. Holt
Energy Conversion Program
University of Tennessee Space Institute
Tullahoma, TN 37388

Keywords: Magnetohydrodynamics, ESP, Real-time diagnostics

INTRODUCTION

In magnetohydrodynamic (MHD) power generation a seed material, normally K_2CO_3, is added to enhance the conductivity of the coal-fired gas stream. The plasma is passed through a magnetic field and electricity is produced by the Hall effect. Future large scale MHD facilities are expected to be more efficient than conventional coal-fired power plants not only because of the DC electricity produced but also from increased heat recovery owing to the large (3000 K) combustion temperatures employed.

There is, however, a finite cost for the seed material and the resulting K_2SO_4 particles (SO_2 emissions are minimized by combination with seed potassium) must be collected, converted back to K_2CO_3 or KCO_2H, and recycled back to the combustor. Although estimates vary it is well recognized that a large portion ($\geq 95\%$) of the spent seed must be recycled for viable economic operation.[1]

The performance characteristics of the MHD electrostatic precipitator (ESP) are therefore of interest. As an added condition recent experimental and theoretical studies of K_2SO_4 homogeneous nucleation[2] have indicated that these particles grow to Sauter diameters of between 1 and 1.2 μm. These sizes are in a range where ESP performance may be degraded.[3]

In this work, we describe Mie scattering and electric field measurements on an MHD pilot scale ESP located at the Coal Fire Flow Facility (CFFF) at the University of Tennessee Space Institute. Results are reported for the determination of near-real-time collection efficiencies, the variation of the ESP performance with seed percentage, and initial studies on the extent of particle re-entrainment.

EXPERIMENTAL

The theoretical framework for determination of the Sauter mean diameter, D_{32}, using two-color laser transmissometry has been reported previously.[4,5] Briefly, transmissions ($T = I/Io$) measured at two well-separated monochromatic wavelengths (λ_1, λ_2) are related to an extinction efficiency ratio which is proportional to D_{32}

$$\frac{\ln T(\lambda_2)}{\ln T(\lambda_1)} = \frac{\overline{Q}_2}{\overline{Q}_1} \sim D_{32} \qquad (1)$$

Mie theory is used to calculate the variation of $\overline{Q}_2/\overline{Q}_1$ (bars indicate averages over a distribution) on D_{32}. For the case of a polydisperse particle size distribution (PSD) $\overline{Q}$ is expressed in terms of an effective extinction cross section, $\overline{\sigma}_e$ and an assumed distribution

$$\bar{Q} = \int_0^\infty \bar{\sigma}_e f n(r) dr / \pi \int_0^\infty r^2 f n(r) dr \tag{2}$$

where $\bar{\sigma}_e$ is calculated from the theory with knowledge of the complex refractive index, m.

The theoretical response curve used to interpolate D_{32} from the measured transmissions (insert Figure-1) is generated by scaling the assumed PSD. Each distribution corresponds to a unique D_{32} value. The effect of the PSD shape on D_{32} has been determined by sensitivity studies[6] to be within -2% or +9% of the integrated D_{32} value. This result is consistent with the fact that D_{32} is, by definition, a z-average quantity.

Studies have also been carried out on the effect of the complex refractive index on D_{32}[6]. Using the reported values[4] of m for Illinois #6 and Montana Rosebud with and without spent seed (K_2SO_4) and the m value for K_2SO_4 it was determined the D_{32} varies by $\pm 0.1 \mu m$. The above result has some implications on the work reported here as the chemical composition of the particles[7] entering the CFFF ESP are about 85% K_2SO_4 with the remainder flyash. Thus the use of the complex refractive index for K_2SO_4 is not expected to have a significant effect on the Sauter diameters determined.

Although the primary observable in two-color extinction measurements is D_{32} additional information concerning mass and number loading can be obtained. Number densities, C_n values, are available from Beer's law

$$T(\lambda) = \exp(-l \bar{\sigma}_\lambda C_n) \tag{3}$$

where l is the effective optical path length. The mass density C_m is related to C_n through the chemical density, d, of the particles and the volume density, C_v

$$C_m = d C_v = (d 4\pi r_{32}^3 C_n)/3 \tag{4}$$

Electron micrographs of particles collected downstream of the CFFF superheater indicate spherical shape.[7]

The optical configuration of one of the two-color laser transmissometer (TCLT) units is shown in Figure 1. The second optical unit is similar to that shown with the exception that only two lasers, an argon ion ($\lambda = 0.488$ or $0.5145 \mu m$) and a helium-neon ($\lambda = 3.39 \mu m$) are used. For the efficiency measurements both units were interfaced to the microprocessor unit. Because of a small but finite time delay of 100 ms (the processor collects raw intensities from one optical unit followed by the intensities from the second unit) the measurements reported here are classified as nearly simultaneous. For the experiments on rapid temporal response the microprocessor unit was replaced by an IBM PC/AT type microcomputer with an analog to digital board.

Electric field meter (EFM) measurements were performed using a laboratory built unit similar to that reported by Castle et al.[8] The field was sensed by four circular electrodes whose signals were modulated using a 4-hole chopper wheel powered by an air motor. Laboratory experiments indicated that the output of the meter was constant to within ±1 mv over the frequency range from 220 to 270 hr. Initially the meter was calibrated[9] using parallel plates where

$$E = V / D \tag{5}$$

Here E is the electric field, V the applied plate voltage and D the distance between the meter and the charged plate. Knowledge of the duct geometry permits the solution of Poisson's equation for the space charge density, ρ. Expressions for E in terms of ρ for cylindrical[8] and rectangular[10] ducts have been reported. Calculations for the trapezoidal exit duct of the CFFF ESP have not yet been performed; consequently, only raw voltages are reported here. These data are, however, directly related to ρ which is usually expressed in C/m^3 units. Each particle exiting the ESP will carry some charge, q, thus ρ/q yields a measure of number concentration. Results from the EFM are then comparable to the scattering method but also provide the charge density which is an important parameter in models of electrostatic precipitation.[11]

Location of the TCLT units and the EFM with respect to the CFFF ESP is given in Figure - 2. Experiments reported here correspond to facility tests LMF4-N, LMF4-S and LMF4-U. Near-real-time collection efficiencies determined during LMF4-N were calculated from the penetration, P

$$P = \left(\frac{Cn(out)}{fCn(\text{in})}\right)(100) \qquad (6a)$$

$$Efficiency = 100 - P \qquad (6b)$$

in the above equation f is that fraction of the total flow diverted to the ESP. The values of f were taken from the CFFF records where information on the electrical conditions of the ESP, temperatures, vibrator and plate-rapping frequencies and other pertinent conditions are collected.

RESULTS AND DISCUSSION

As stated previously, the behavior of the MHD ESP is critical to the successful economic operation of the facility. The three studies below represent only a fraction of the results collected to date. The data on efficiency and the performance of the ESP as a function of the ratio K_2/S have practical bearing on future commercial scale facilities. The final study concerns our initial efforts to characterize rapid temporal variations of ESP performance and the application of the field meter.

Near - Real - Time Efficiency Measurements - Average Sauter diameters determined upstream of the ESP are collected in Figure - 3. An average of 1.2 μm was calculated. Measurements on May 6 and 7 yielded D_{32} values of 1.18 and 1.25 μm respectively. Average number densities were 5.6, 4.8 and 4.2 x 10^6 cm^{-3}.

Extinction measurements downstream of the ESP permit the application of Eq. 6. Corresponding efficiency values are presented in Figure - 4. To our knowledge this data represents the first reported determination of near - real - time efficiencies for an electrostatic precipitator. In this regard it should be noted that the application of standard sample extraction methods can only provide an estimate of the efficiency since the sampling times before and downstream of the ESP will not be the same. Additionally, any changes in facility operation cannot be quantified rapidly.

Although some scatter is observed in Fig. 4 the majority of efficiencies lie above 90% with many values larger than 95%. The radical decrease in efficiency between 1348 and 1408 hours corresponds to a baghouse cleaning cycle. During this process the flow normally partitioned to the fabric filter device was diverted to the ESP, thereby increasing the flow by approximately 5000 cfm. The decrease in efficiency, albeit of short duration, indicates that the ESP cannot completely

adjust to the additional mass loading. This result is expected based on the flow entering the device, 16,400 cfm compared to the design set point of about 8600 cfm.[12]

Some comments are required concerning the factor f appearing in Eqs. 6. Using C_n values of 2.5 x 10^5 (outlet) and 5.98 x 10^6 cm^{-3} (inlet) it is possible to determine the effect of errors in the mass flow on the efficiency. For the data in Fig. 4 (excluding the cleaning cycle) the flow to the ESP was measured as 11,000 cfm. The flow to the baghouse was 5400 cfm and the calculated efficiency was 94.3%. Assuming flows to the ESP of 9000 and 13,000 cfm yielded efficiencies ranging from 93 - 95.2% or a difference of slightly larger than 2%. So long as the flow rate to the ESP is known to within 20% the calculation of the efficiency is adequate.

Effect of the Ratio K_2/S - Initially feed rates to the MHD combustor were controlled to provide sufficient K atoms for plasma enhancement and the total conversion of SO_2 to K_2SO_4. Recently it has been noted that generator power levels could be increased by overseeding.[13] This practice led to variations in the performance of downstream components as noted by increased bridging in the platen superheater and decreased ESP performance[14] presumably due to K_2CO_3 or other K species.

Measurements of the particle size and loading downstream of the CFFF ESP were conducted at different K_2/S (molar ratio of K in seed to S in coal) ratios during facility test LMF4-S. Figure - 5 illustrates Sauter diameters for time periods corresponding to different K_2/S ratios. Clearly, as the K_2CO_3 percentage decreases the D_{32} values increase.

During these measurements the facility conditions such as gas stream temperatures, soot blowing frequency, total coal flow and combustion stoichiometry, etc. were reasonably constant. The mass flow rates to the ESP were approximately 6000 cfm for the data in panels A and B and 7800 cfm in panel C. The previous efficiency results indicate that as the mass loading is increased (i.e. fabric filter cleaning cycles) the efficiency decreases. This corresponds to an increase in C_N (or a decrease in D_{32}, Eqs. 1 and 3) at the downstream location. The fact that D_{32} is increased at the K_2/S ratio of 1.04 (Fig. 5 panel C) indicates that the excess K_2CO_3 (panels A and B) has a significant effect on ESP performance.

The decreased ESP performance at large K_2/S ratios may indicate that the K_2CO_3 particles are nucleating to smaller particle diameters than K_2SO_4. Changes in particle resistivity do not appear to be responsible for the observed behavior. Further studies are in progress.

Initial Studies of ESP Temporal Performance - The standard means of characterizing ESP operation involves the extraction of sample, preferably isokinetically, from the gas stream. The extraction requires some time and, thus, events occurring over periods of seconds or even minutes cannot be quantified. Such events are thought to be those due to collection plate rapping and the vibration of the wire racks. Experiments were initiated to evaluate the extent of particle re-entrainment from the CFFF ESP.

For these experiments conducted during test LMF4-U the electric field meter (EFM) was installed at the exit duct of the ESP and the TCLT was located slightly downstream. The K_2/S ratio was held constant at 1.0. Figure 6 illustrates the average Sauter diameters (top trace) and the raw EFM signal (lower trace) over a typical collection period. The average particle size is similar to that observed in panel C of Fig. - 5. Of interest in Fig. 6 is the increase in field meter voltage and the decrease in D_{32} observed at approximately 1217. The locations of the peaks are shifted relative to one another owing to the fact that the computer clocks were not synchronized (the residence time between the instrument locations has been calculated at 1 sec.).

Examination of the facility data records led to the assignment of the increase in C_N to the vibration of the field 4 wire rack. Although there could be similar information on the effects of the vibrators for fields 1, 2 and 3 as well as on plate rapping the noise in the data precludes unequivocable assignment. The apparent lack of particle re-entrainment from rapping may arise from the 2 min. frequency for this process. Further studies wherein the frequency of rapping and wire rack vibrating are varied are in progress.

CONCLUSIONS

Our studies of the CFFF pilot plant ESP have yielded some valuable information concerning the performance of the component under different MHD facility operating conditions. To our knowledge, this is the first report of the determination of ESP efficiency in near-real-time. Studies on the ratio K_2/S indicate that ESP performance degrades as the ratio is increased. Work is in progress to further quantify this effect and to establish the conditions for efficient ESP operation at overseeding conditions. Initial temporal studies conducted downstream of the ESP indicate that particle re-entrainment from vibration of the wire racks is more pronounced than increased emission from collection plate rapping.

ACKNOWLEDGEMENTS

We acknowledge support of this work through DOE contract DE-AC01-80ET-15601 to the Diagnostic Instrumentation and Analysis Laboratory at Mississippi State University and DOE contract DE-AC02-79ET-10815 to the Energy Conversion Program at the University of Tennessee Space Institute.

REFERENCES

1. Petrick, M.; et al., in Open Cycle Magnetohydrodynamic Electrical Power Generation, M. Petrick and B. Ya Shumyatsky, eds. Argonne National Laboratory, Argonne, IL (1978).
2. Wang, C. and Lindner, J. S., J. Prop. Pow. 6, 552 (1990).
3. ASHRAE Handbook - Equipment, American Society of Heating, Refrigerating and Air Conditioning Engineers Atlanta, GA (1988).
4. Ariessohn, P. C., HTGL Report No. 119, Stanford University, Stanford CA(1980).
5. Dobbins, R. A. and Jizmagian, G. S., J. Opt. Soc. Am. 56, IO (1966).
6. Lindner, J. S.; et al., Proceedings of the 27th Symposium on the Engineering Aspects of Magnetohydrodynamics p. 8.5.1 Reno NV. (1988)
7. Holt, J. K. et al., Proceedings of the 25th Symposium on the Engineering Aspects of Magnetohydrodynamics p. 8.2.1, Bethesda, MD (1986).
8. Castle, G. S. P.; et al. IEEE Trans. Ind. Appl. 24, 702 (1988).
9. Blitshteyn, M. Eval. Eng. p. 70 Nov. (1984).
10. Carruthers, J. A. and Wigley, K. J., J. Inst. Pet. 48, 180 (1962).
11. Lawless, P. A. and Sparks, L. E., IEEE Trans. Ind. Appl. 24, 922 (1988).
12. Morehead, B. K. and Foote, J. P., Proceedings of the 23rd Symposium on the Engineering Aspects of Magnetohydrodynamics p. 585 Somerset, PA (1984).
13. Stepan, I. E.; et al., Proceedings of the 28th Symposium on the Engineering Aspects of Magnetohydrodynamics p. 1.1-1, Chicago IL (1990).
14. Attig, R. C.; et al., Proceedings of the 27th Symposium on the Engineering Aspects of Magnetohydrodynamics p. 1.2-1 Reno NV (1989).

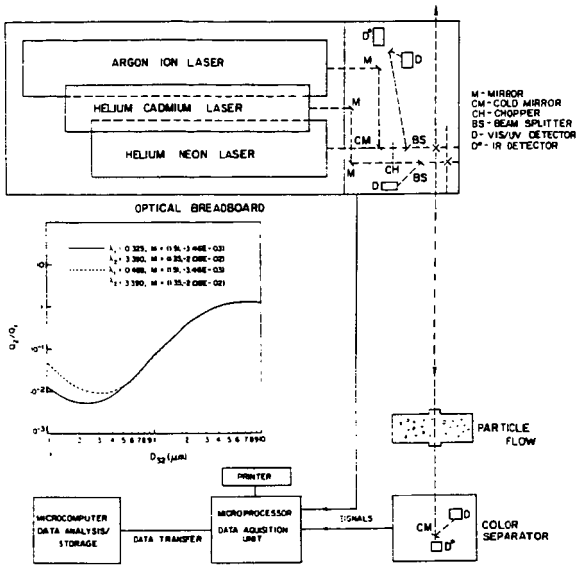

Figure 1. Experimental configuration and theoretical response curve for the Two-Color Laser Transmissometer.

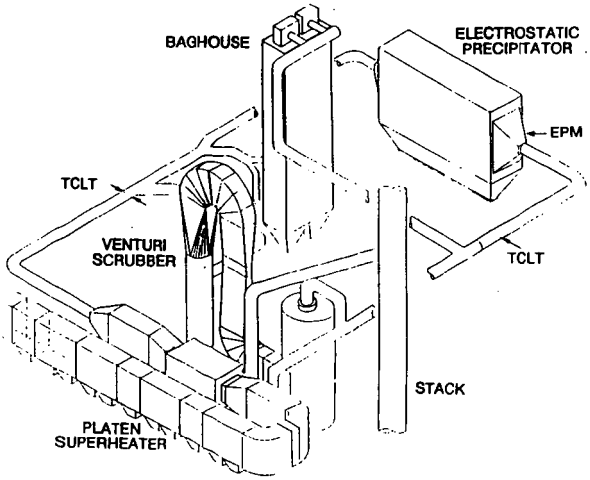

Figure 2. Instrument locations with respect to the downstream facility components of the Coal-Fired Flow Facility.

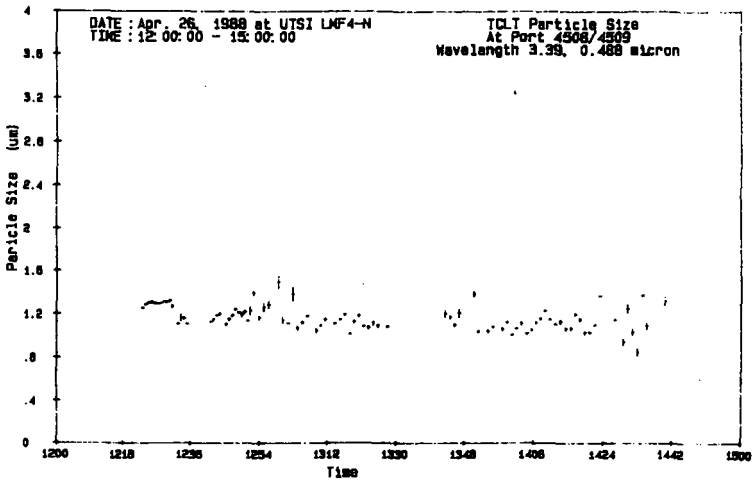

Figure 3. Average particle sizes (D_{32} values) at the baghouse/ESP inlet.

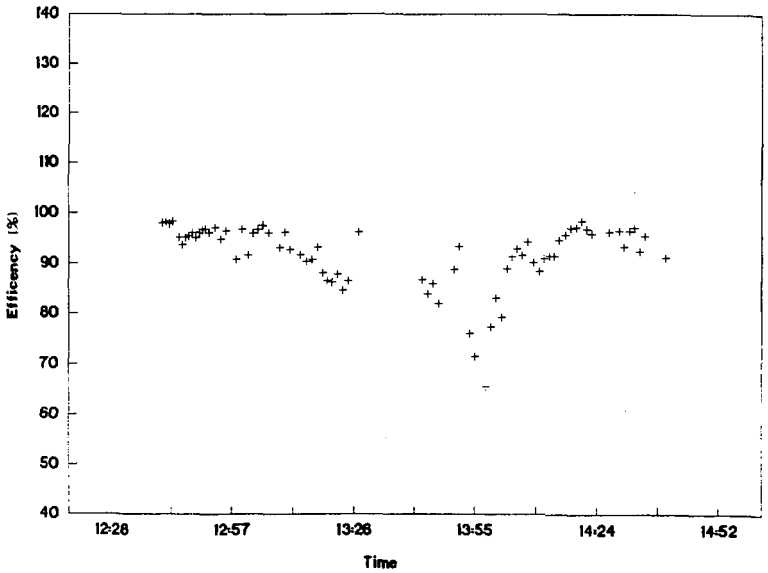

Figure 4. Near-real-time ESP efficiencies measured during LMF4-N. The decrease in efficiency around 1355 corresponds to a baghouse cleaning cycle with all flow diverted to the ESP.

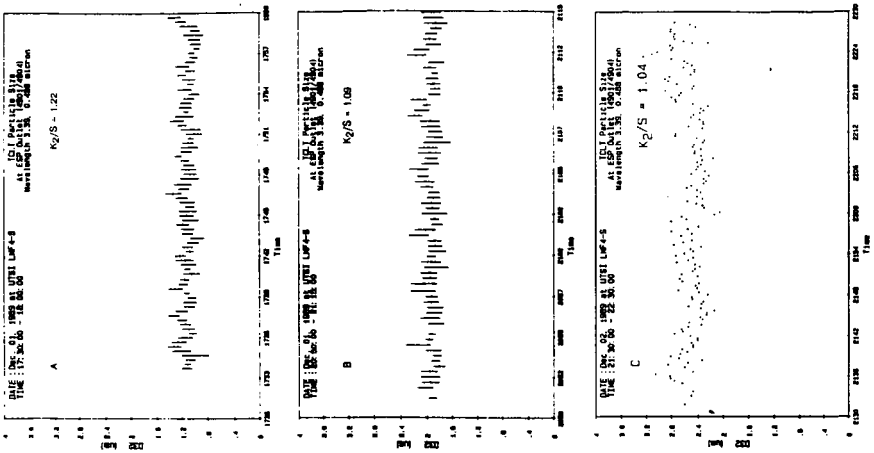

Figure 5. Average Sauter diameters measured at the outlet of the ESP during facility test LMF4-S. Values of the ratio K_2/S decrease in going from panel A to panel C.

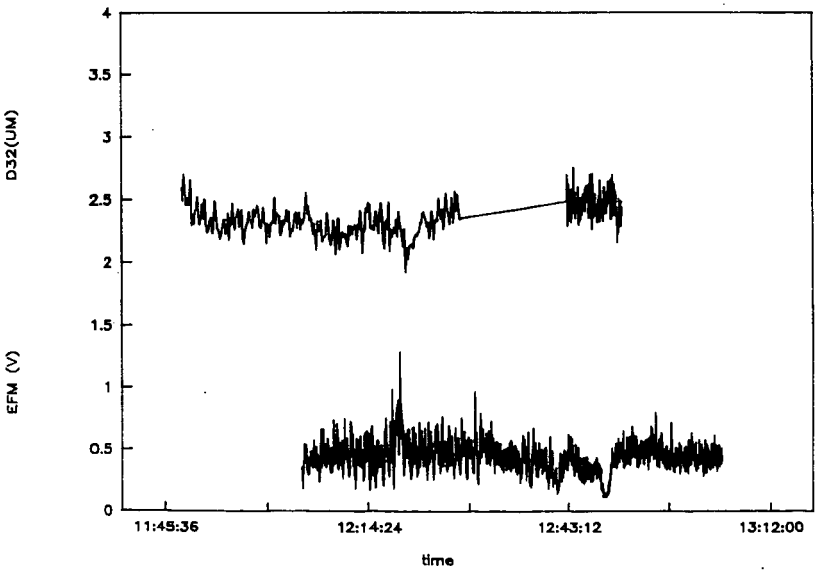

Figure 6. Average Sauter diameter (top trace) and EFM voltage measured during facility test LMF4-U. The decrease in D_{32} and increase in EFM voltage corresponds to particle re-entrainment originating from vibration of the field 4 wire racks.

CHEMICAL PHASES IN PETROLEUM COKE GASIFICATION SLAG

John C. Groen and James R. Craig
Department of Geological Sciences, Virginia Polytechnic Institute & State University,
Blacksburg, VA 24061-0420

Mitri S. Najjar
Texaco Research Center, Box 509, Beacon, NY 12508

Keywords: petroleum coke, slag, gasification

ABSTRACT

The gasification of petroleum coke results in the generation of complex slags. The broad variability in the physical and chemical properties of these slags will be described. The slags were examined primarily by means of reflected light optics using standard polished sections. These sections were also used directly for electron microprobe analysis where quantitative data on elemental distribution and partitioning was gathered and will be presented. Scanning electron microscopy (SEM) techniques were also used to characterize the presence of numerous phases including spinels of variable composition, glass droplets of variable composition, iron sulfide/oxide intergrowths often with tiny Fe-Ni alloy grains, and calcium silicates.

INTRODUCTION

The Texaco partial oxidation gasification process makes use of petroleum coke to produce a synthesis gas for use as a fuel for power generation or process heat, a chemical feedstock, or as a reducing gas. The petroleum coke feedstock is reacted with a controlled, sub-stoichiometric quantity of oxygen in a fuel rich, exothermic reaction. The process is carried out in a pressurized reaction chamber at 2200-2600°F (1200-1450°C), which promotes efficient reaction and facilitates the formation of a partially to wholly molten slag by controlling the feed rates of the reactants. The feeds are introduced together, through the top of the gasifier, and pass through it concurrently with the product gases transporting the solids, making it an entrained flow gasifier. The slags that form in the gasifiers result from the accumulation of residual, noncombustible elements either on the refractory linings of the gasifiers, or as droplets that fall into water quench baths.

The slags produced during the high temperature gasification of petroleum coke can be generally characterized into three principal types: 1.- relatively fluid homogeneous silicate melts that solidify on cooling to brownish-black glass with minor to significant amounts of sulfide droplets, spinel crystals $(Fe,Mg,Ni)^{2+}(Fe,Al,V,Cr)_2{}^{3+}O_4$, plus other minor phases; 2.- sulfide dominant slag of generally troilitic composition (FeS), frequently but not always symplectically intergrown with wüstite (FeO), and usually containing smaller amounts of native Fe-Ni alloy grains, spinels (as above), glass droplets, and other phases; 3.- highly viscous slags comprised of masses of coarse interlocking vanadium-oxide-rich crystals, with major amounts of CaV_2O_6, $(Fe,Ca)VO_4$ or $CaFeV_2O_7$, VO_2, spinels (as above), glass droplets, plus other minor phases. These generalized compositions are shown in Table 1, which also lists in more detail the specific nature of some of the minor phases observed.

CHEMICAL PHASES

Spinels are both the most ubiquitous and the most compositionally variable crystalline phase. Hence it is instructive to consider the potential structural site occupancies and the degree of partitioning that the spinels exhibit with coexisting phases. The most apparent spinel compositional trend, as shown in Figure 1, is that which exists among spinels hosted by Ca-Fe-V oxides. Most of these spinels lie in the Ni to Mg, Al-V-(Fe^{3+}+Cr) prism, and cluster toward the Al-rich corner. These spinels commonly contain more than 20 mol% Ni in the 2+ site, and some contain more than 80%. In contrast, the spinels in sulfide-rich slags tend to be Ni-poor; the Ni in such slags concentrates in the Fe-Ni-S monosulfide solid solution and in the Fe-Ni alloy.

The spinels in FeS-FeO-rich, glassy, and Ca-Fe silicate-rich slags are in general considerably more V-rich (Fig. 2) than are the spinels in Ca-Fe-V oxide-rich slags where the V is more highly partitioned into the host phases. The lower V contents of the spinels in Figure 1 is compensated by increases in the Al and Fe^{3+}+Cr contents. The scarcity of Fe^{2+} in these spinels implies that the oxidation potential at the time of slag generation was high enough to keep most of the iron in the Fe^{3+}

state; this is also supported by the observation that the vanadium in the coexisting Ca-Fe-V oxides is all present as V^{4+} and V^{5+}.

Spinels that occur in the sulfide rich slags (Fig.'s 2a-c) exhibit a fairly tight clustering of compositions that are relatively Fe^{2+} and V-rich and Al-poor. The enrichment of these spinels in Fe^{2+} is obviously due to the abundant available reduced iron in the Fe-S-O melt. Vanadium, as a general rule, partitions out of Fe-S-O melts, however, residual V that is present, clearly prefers filling 3+ sites, and then 2+ sites in spinel to forming V-sulfides. Strong verificaton of this phenomenon comes from the common observation of V-bearing spinels occurring in V-deficient Fe-Ni sulfides. The efficacy of V-partitioning into spinels is so strong, in fact, that even when present as V^{2+}, the V ions still enter spinel structures preferentially to forming sulfides as analyzed in several samples. Furthermore, only one sample of slag was found to contain V-rich sulfides, and in that sample, the euhedral spinels had already been virtually saturated with V, such that their compositions were essentially that of the pure endmember V_3O_4 (unplottable in Figure 2, and unknown as a mineral), leaving no oxygen for the additional V to react with, instead only sulfur. The oxidation state present during the formation of this slag must have been unusually low to facilitate the formation of V-sulfides. The low Al content of many of the spinels in the sulfide-rich slags (Fig. 2b), no doubt results from the virtually complete exclusion of Al from Fe-S-O melts. The relative deficiency of Mg in these spinels (Fig. 2c), can most likely be explained by a similar argument. The sulfide-rich slags also contain an interesting spinel with a rather unique composition approaching that of the mineral coulsonite (FeV_2O_4).

Glass-rich chunks of slag contain variable to large quantities of sulfide droplets, and thus form a continuum of slag types between sulfide-rich and glass-rich. This is probably the main reason that the spinels within glass hosts are compositionally similar to spinels within sulfide hosts. The primary compositional difference between these two groups is the Al-content (Fig. 2b), which is considerably higher in the glass-hosted spinels. Such a variation would be expected, because of the relatively high Al-content of the glasses, where Al substitutes for Si. The analyses of glass-hosted spinels that plot on or near the V - Fe^{3+}+Cr join, are of spinels in sulfide-droplet-rich glassy slags (as described above), suggesting that these spinels experience compositional influences from both sources. The "ideal" glass hosted spinel composition, therefore, appears to be represented by the higher Al-content points shown in Figure 2b. The anomalous, isolated group of V-poor, and Fe^{3+}+Cr-rich spinels in the glass-hosted family are unusually Cr-rich, and are interpreted to result from reaction with the refractory brick in the gasifiers.

Only a few pieces of slag have been found which contain significant quantities of crystalline Ca-Fe silicates; hence any discussion of the composition of their associated spinels is very preliminary. The highly variable V-content of all the spinels (and probably of the slags in general) most likely reflects the variable nature of the source petroleum for the feed cokes. Many crude oils are naturally enriched in V (carried as organic porphyrin complexes), as a result of the type of source materials and source rocks from which the oil was derived. Ni is another common element in petroleum and is also carried in large part as porphyrin complexes; hence its abundance in the slags may also be largely a function of its source crude. The Fe, Al, Si, Mg, Ca, Na, and S found in the slags are derived primarily by residual accumulation of minute entrained mineral particles (such as clays, Fe-oxides, Fe-sulfides, etc.) and hence tend not to vary considerably from slag to slag because of the common, but variable occurrence of these minerals. Chromium contents of petroleum are very low, hence, most of the Cr found in the slags probably originates from reaction of the molten slag with the Cr-rich refractory brick lining the gasifiers. The elemental Cr-content of most of the spinels is generally less than 15 mol%; and as of yet has not been found to show any relationship to host slag type.

The dominant sulfide phase found in the petroleum coke gasification slags is troilite (FeS). This composition may, however, grade from pure FeS to that of hexagonal pyrrhotite ($Fe_{1-x}S$, $0.0<x\leq\sim0.125$) as shown in Figure 3. Distinguishing the compositions of these phases by means of electron microprobe analysis is quite difficult, and is better accomplished (if sufficient quantities exist), by X-ray diffraction, TEM, or other such techniques. The iron-sulfide often occurs as a very fine symplectic intergrowth with iron oxide (presumably wüstite, FeO), that can barely be resolved by optical techniques. These intergrowths appear to be the result of the rapid cooling of an initially homogeneous Fe-S-O melt; such melts cannot be quenched to glasses. Nickel can substitute for iron in pyrrhotite in minor amounts, but may also form a discrete Ni-sulfide phase (Heazlewoodite, Ni_3S_2) and an Fe-Ni-sulfide phase (Pentlandite, $(Fe,Ni)_9S_8$). The crystals/grains of free metal (F.M.) that form in the sulfide matrix generally contain iron plus 10 to 28 atomic percent Ni but have been found to range from pure Fe to more than 70 atomic percent Ni (Fig. 3). In addition to the Fe-monoxide wüstite phase observed in the sulfide bearing slags, NiO (bunsenite) has also been found as well as a few grains of mixed (Fe,Ni)O composition.

Vanadium oxide rich slags have been found to contain at least five distinct V-bearing phases. One

is CaV_2O_6 which is not known as a mineral but has been synthesized in phase equilibria studies. Euhedral Na-V-oxide crystals of apparent stoichiometry equal to NaV_6O_{15} occur with CaV_2O_6 crystals, and correspond well with a ß-solid solution phase along the experimental Na_2O-V_2O_5 join. This experimental ß-solid solution phase has been found to be in equilibrium with CaV_2O_6 at 650°. A third phase, which occurs with the two phases above, has an apparent chemical formula of $NaCaV_8O_{20}$; this phase, however, does not correspond to any phases known from the literature. A fourth V-phase which is quite common, is problematic in that it is most favorably represented as a Ca-bearing variety of the synthetic $FeVO_4$ phase, from charge balance considerations; yet it is conceptually difficult to imagine a Ca ion substituting for Fe^{3+} in the structure. Alternatively, this phase might be a hypothetical $CaFeV_2O_7$ phase extrapolated from such known phases as $Ca_2V_2O_7$ and $Ni_2V_2O_7$; however, $CaFeV_2O_7$ does not charge balance well, and, the coexistence of Fe^{2+} and V^{5+} in the same structure may be unlikely. A fifth and less common V-phase is VO_2. VO_2 is known as the mineral paramontroseite, however, this mineral forms as a metastable, low temperature oxidation product of the mineral montroseite and is a polymorph of synthetic VO_2. The euhedral VO_2 crystals we observe in the slags grew at high temperatures and are therefore most likely not paramontroseite, but instead equivalent to its synthetic, high temperature polymorph. Spinels and variable composition glasses are the other main constituents of this type of slag; many additional minor phases occur in this type of slag as listed in Table 1.

The sulfide-dominant slags occasionally contain pieces of slag which have several different euhedral Ca,Mg,Fe ± Na silicates worth noting. Though still in need of further verification, some of the phases have tentatively been identified as Akermanite ($MgCa_2Si_2O_7$, observed= $(Mg,Fe)Ca_2(Si,Al)_2O_7$), Fayalite (Fe_2SiO_4, observed=$(Fe,Mg,Ca,Na)_2(Si,Al)O_4$), and Pigeonite ($(Mg,Fe,Ca)(Mg,Fe)Si_2O_6$, observed=$(Ca,Fe,Mg,Na)(Mg,Fe)(Si,Al)_2O_6$). These phases are well known in geological realms and should be useful for estimating the conditions under which crystallization occurred.

TABLE 1.

SLAG TYPE	COMMOM PHASES	MINOR PHASES
Glassy	* Glasses of variable composition * Spinels of variable composition (Fig.'s 1&2) * Droplets of Fe sulfide and/or Fe sulfide/oxide intergrowths, often with tiny Fe-Ni alloy grains (Fig. 3)	* Al_2SiO_5: Andalusite or sillimanite, needs crystal structure work * Corundum: Al_2O_3, needles * Eskolaite: Cr_2O_3, exsolution lamellae in Cr-rich spinels * Karelianite: V_2O_3, crust on sulfide bleb * Hematite: Fe_2O_3, irreg. chunk
Sulfide rich ...	* Fe-sulfide: ~FeS, and/or FeS/FeO intergrowths, often with tiny Fe-Ni alloy inclusions (Fig. 3) * Spinels of variable composition (Fig.'s 1&2) * Glass droplets of variable composition * FeO dendritic crystals and blebs	* long acicular sulfide crystals of unknown phase, need crystal structure analysis to identify) * ~1 μm blocky sulfide crystals ? * Pentlandite: $(Fe,Ni)_9S_8$ or monosulfide solid solution (?) * $(Fe,Ni,Cr)VS_2$: not a known mineral * Unknown euhedral CaFeMg-silicate phase * Hercynite: $FeAl_2O_4$, or (?) $FeAlO_3$: (not a known mineral) * V_3O_4: (not a known mineral)
CaFeMg-silicate rich subgroup of sulfide rich slags:	* CaFeMg-rich glasses * Akermanite: $Ca_2MgSi_2O_7$, with Fe and Al partially substituting for Mg * Pigeonite: $(Mg,Fe,Ca)(Mg,Fe)Si_2O_6$, with minor Na substituting for Ca and minor Al substituting for Si * Fayalite: Fe_2SiO_4, with Mg,Ca and Na partially substituting for Fe and minor Al substituting for Si * Unknown euhedral CaFeMg-silicate phase * Spinels of variable composition (Fig.'s 1&2) * Droplets of Fe-sulfide and/or Fe-sulfide/oxide intergrowths, often with tiny Fe-Ni alloy grains (Fig. 3)	
V-oxide rich ...	* CaV_2O_6: not a known mineral * NaV_6O_{15}: not a known mineral * $NaCaV_8O_{20}$: not a known mineral * $FeCaV_2O_7$ or $(Fe,Ca)VO_4$: need crystal structure analysis to determine actual phase * VO_2: Paramontroseite polymorph * Spinels of variable composition (Fig.'s 1&2) * Glass droplets of variable composition	* Hematite: Fe_2O_3, with Al & V partially substituting for Fe * Corundum: Al_2O_3, with an unknown element partially substituting for Al * Sarcolite: $(Ca,Na)_4Al_3(Al,Si)_3Si_3O_{24}$ with Mn(?) partially substituting for Ca * Heazlewoodite: Ni_3S_2 * Bunsenite: NiO * FeV_2O_6: not a known mineral * unidentifiable submicroscopic V-oxide bearing crystals

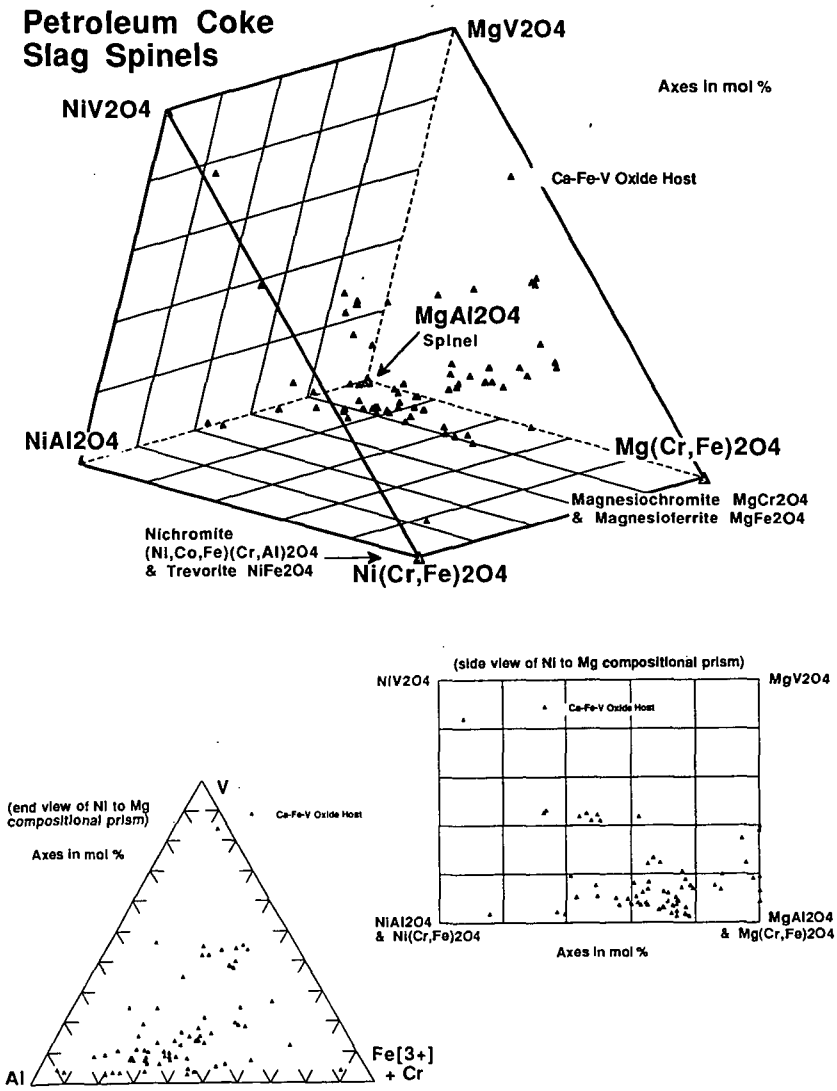
Petroleum Coke
Slag Spinels
MgV2O4
Axes in mol %
NiV2O4
Ca-Fe-V Oxide Host
MgAl2O4
Spinel
NiAl2O4
Mg(Cr,Fe)2O4
Magnesiochromite MgCr2O4
& Magnesioferrite MgFe2O4
Nichromite
(Ni,Co,Fe)(Cr,Al)2O4
& Trevorite NiFe2O4
Ni(Cr,Fe)2O4
(side view of Ni to Mg compositional prism)
NiV2O4
MgV2O4
Ca-Fe-V Oxide Host
NiAl2O4
& Ni(Cr,Fe)2O4
MgAl2O4
& Mg(Cr,Fe)2O4
Axes in mol %
V
(end view of Ni to Mg compositional prism)
Ca-Fe-V Oxide Host
Axes in mol %
Al
Fe[3+]
+ Cr

FIGURE 1.

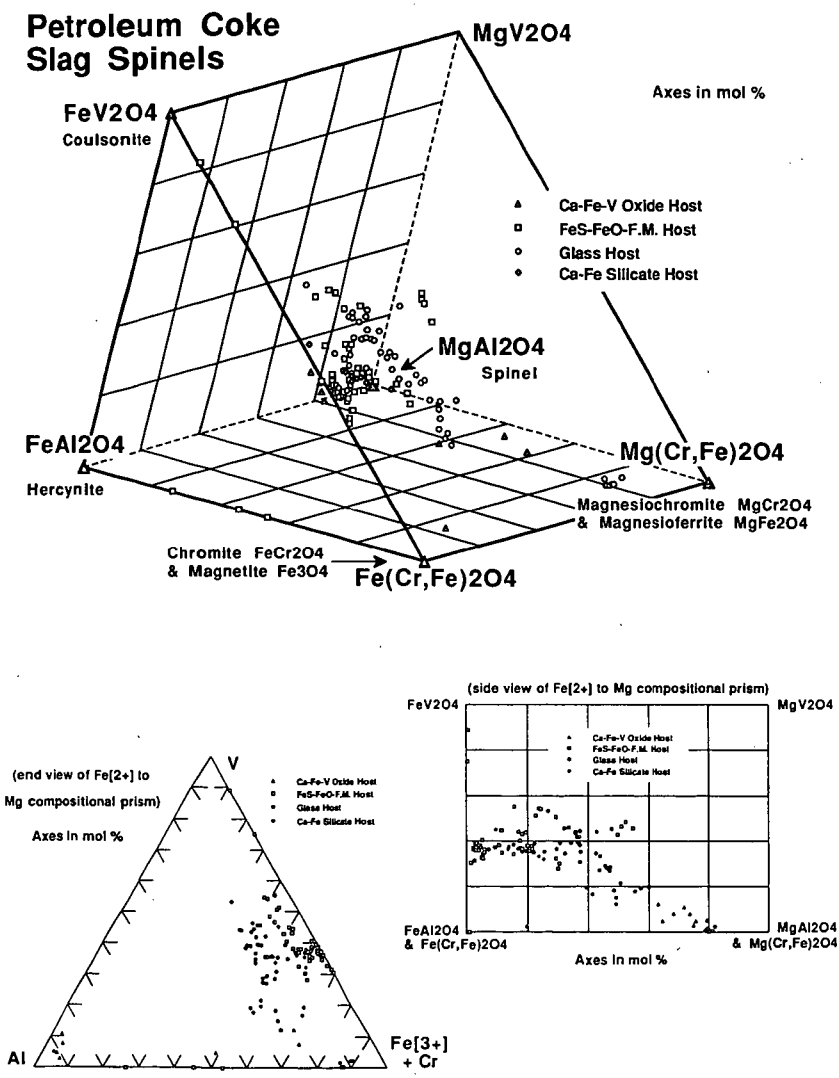
Petroleum Coke
Slag Spinels
MgV2O4
Axes in mol %
FeV2O4
Coulsonite
Ca-Fe-V Oxide Host
FeS-FeO-F.M. Host
Glass Host
Ca-Fe Silicate Host
MgAl2O4
Spinel
FeAl2O4
Hercynite
Mg(Cr,Fe)2O4
Magnesiochromite MgCr2O4
& Magnesioferrite MgFe2O4
Chromite FeCr2O4
& Magnetite Fe3O4
Fe(Cr,Fe)2O4
(end view of Fe[2+] to
Mg compositional prism)
Axes in mol %
V
Al
Fe[3+]
+ Cr
(side view of Fe[2+] to Mg compositional prism)
FeV2O4
MgV2O4
FeAl2O4
& Fe(Cr,Fe)2O4
MgAl2O4
& Mg(Cr,Fe)2O4
Axes in mol %

FIGURE 2a.

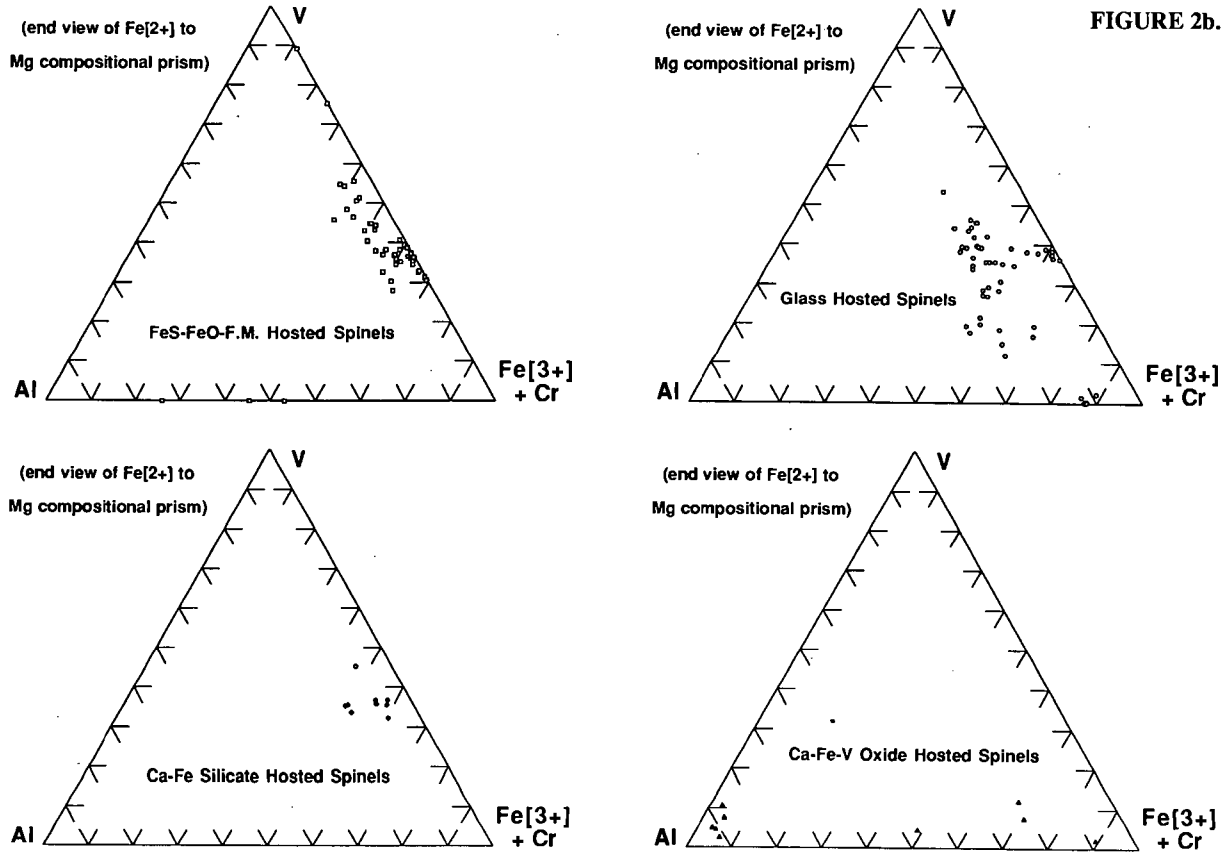
(end view of Fe[2+] to
Mg compositional prism)
V
Al
Fe[3+]
+ Cr
FeS-FeO-F.M. Hosted Spinels
Glass Hosted Spinels
Ca-Fe Silicate Hosted Spinels
Ca-Fe-V Oxide Hosted Spinels

FIGURE 2b.

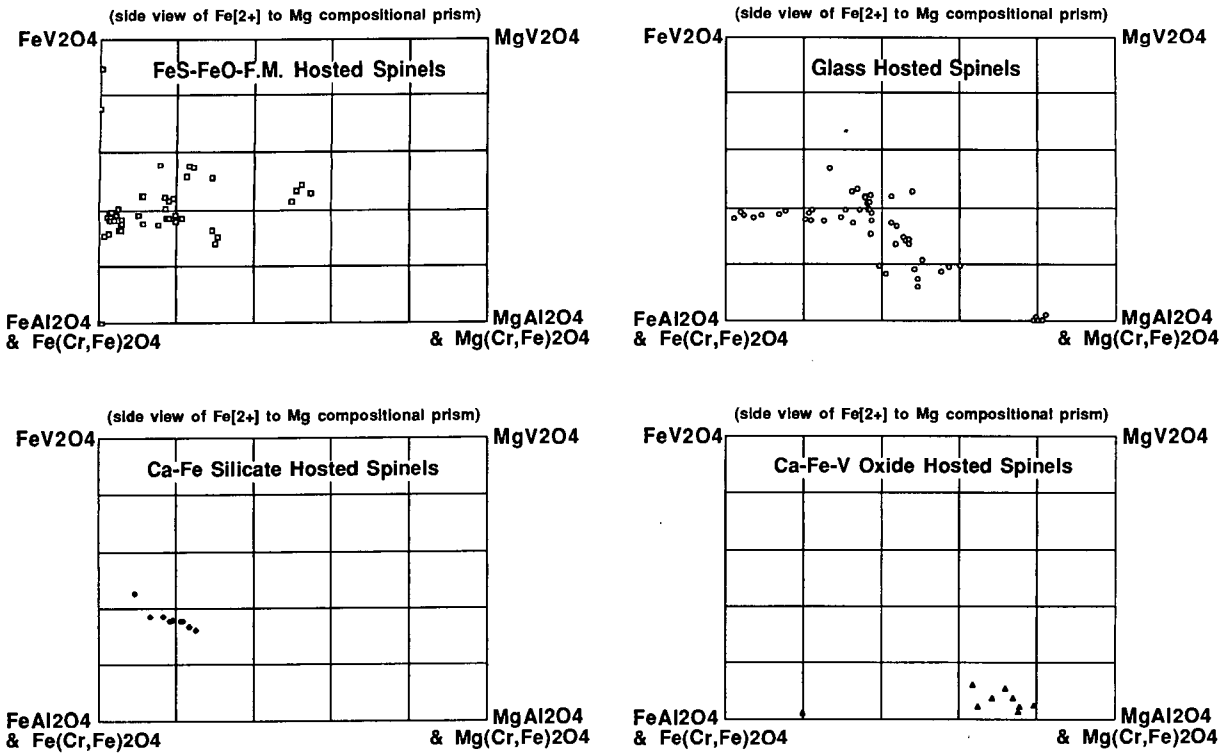
(side view of Fe[2+] to Mg compositional prism)
FeV2O4
MgV2O4
FeS-FeO-F.M. Hosted Spinels
FeAl2O4
& Fe(Cr,Fe)2O4
MgAl2O4
& Mg(Cr,Fe)2O4
(side view of Fe[2+] to Mg compositional prism)
FeV2O4
MgV2O4
Glass Hosted Spinels
FeAl2O4
& Fe(Cr,Fe)2O4
MgAl2O4
& Mg(Cr,Fe)2O4
(side view of Fe[2+] to Mg compositional prism)
FeV2O4
MgV2O4
Ca-Fe Silicate Hosted Spinels
FeAl2O4
& Fe(Cr,Fe)2O4
MgAl2O4
& Mg(Cr,Fe)2O4
(side view of Fe[2+] to Mg compositional prism)
FeV2O4
MgV2O4
Ca-Fe-V Oxide Hosted Spinels
FeAl2O4
& Fe(Cr,Fe)2O4
MgAl2O4
& Mg(Cr,Fe)2O4

FIGURE 2c.

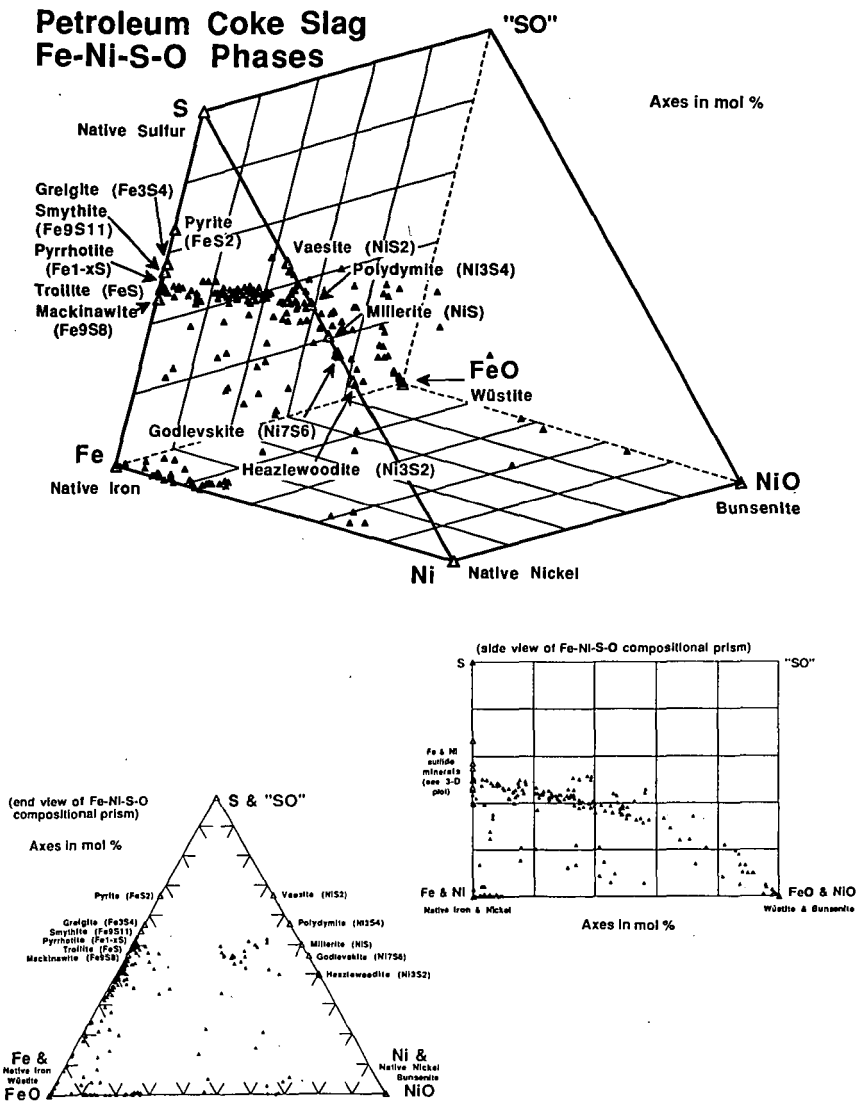
Petroleum Coke Slag
Fe-Ni-S-O Phases
"SO"
Axes in mol %
S
Native Sulfur
Greigite (Fe3S4)
Smythite
(Fe9S11)
Pyrrhotite
(Fe1-xS)
Troilite (FeS)
Mackinawite
(Fe9S8)
Pyrite
(FeS2)
Vaesite (NiS2)
Polydymite (Ni3S4)
Millerite (NiS)
FeO
Wüstite
Godlevskite (Ni7S6)
Heazlewoodite (Ni3S2)
Fe
Native Iron
NiO
Bunsenite
Ni
Native Nickel
(side view of Fe-Ni-S-O compositional prism)
S
"SO"
Fe & Ni
Native Iron & Nickel
FeO & NiO
Wüstite & Bunsenite
Axes in mol %
(end view of Fe-Ni-S-O
compositional prism)
Axes in mol %
S & "SO"
Pyrite (FeS2)
Vaesite (NiS2)
Polydymite (Ni3S4)
Millerite (NiS)
Godlevskite (Ni7S6)
Heazlewoodite (Ni3S2)
Fe &
Native Iron
Wüstite
FeO
Ni &
Native Nickel
Bunsenite
NiO

FIGURE 3.

AUTOMATED IMAGE ANALYSIS OF THE ASSOCIATION OF ASH-FORMING MINERAL MATTER WITH COAL PARTICLES

Warren E. Straszheim and Richard Markuszewski

Fossil Energy Program, Ames Laboratory,
Iowa State University, Ames, IA 50011.

ABSTRACT

Scanning electron microscopy (SEM), energy-dispersive x-ray spectroscopy (EDS) and automated image analysis (AIA) techniques were used for the characterization of the association of ash-forming mineral particles with coal particles. Mineral matter can be found as grains free from the coal matrix or embedded within particles of coal in various proportions and in a range of compositions of the mineral phases. Such mixtures will influence the chemistry of the ash particles generated from the coal, so that the behavior of the ash can be quite different from the behavior predicted by the bulk ash chemistry. SEM-based AIA conducted for several thousand composite coal and mineral particles provides data which can be used to predict the range of ash particles that will be produced from a coal. Results of analyses are reported for a number of bituminous coals.

INTRODUCTION

Over the years, changing practices in coal combustion have led to a need for more detailed characterization of the ash-forming mineral matter in coal. Traditional characterization methods have been performed on bulk samples of ash derived from burning off the coal at relatively large particle sizes (1). That ash is compacted during fusibility tests, so that there is considerable opportunity for interaction of the ash particles and so the ash may be expected to behave in accordance with its average chemistry. Such a test is suited to the ash environment in a stoker-fired boiler where the ash particles do have extensive contact with other ash particles. However, in many modern pulverized coal boilers, ash particles are more likely to result from single particles of coal and remain relatively unaffected by other ash particles. Thus, ash behavior might be expected to be more dependent on the mineral/ash chemistry of individual particles rather than on the bulk ash chemistry. This hypothesis appears to be born out by operating experience where coals of similar bulk ash chemistry can lead to significantly different ash behaviors (2).

Scanning electron microscopy (SEM) along with energy-dispersive x-ray spectroscopy (EDS) offer many insights into coal and mineral particles which should be helpful in predicting ash behavior. These techniques are able to characterize samples for size and elemental composition on a scale appropriate for determining particle ash chemistry. In conjunction with automated image analysis (AIA) techniques, the above analyses can be automated to provide statistical significance in the results.

For the past few years, methodologies have been developed and applied at the Ames Laboratory and elsewhere for the characterization of mineral grains in coal (3,4,5). In much of that work, attention was focused on the fundamentals of measuring particle size and determining a mineral particle's identity from its x-ray spectrum. Less work has been directed toward determining the association of the minerals grains with the coal. Moza et al. (3) reported rather interesting efforts to measure the average elemental content of composite coal and mineral particles. However, there were certain limitations to their approach and the work was not followed up. At the Ames Laboratory, we have continued to develop AIA methodology for the determination of the association of

mineral grains with coal. Work has focused on determining the weight fraction of the mineral and coal phases within the particles. The results have been used primarily in the field of coal preparation to predict the partitioning of phases during physical cleaning (6). However, the data on particle mineral content could just as well be presented in a manner suitable for predicting the nature of the resulting ash particles based on information about their mineral precursors.

METHODOLOGY

Coal samples were prepared for analysis by embedding approximately 2 g of coal in 10 g of carnauba wax according to procedures described elsewhere (7). Samples were embedded at the particle size of interest (i.e., approximately 80% passing 200 mesh for pulverized coal). The ground coal was mixed with molten carnauba wax and the mixture was poured into a cylindrical mold where it was allowed to cool and harden under pressure. The cylindrical pellet was cut vertically along its axis to expose a section through the coal and mineral particles. The exposed section was polished using standard petrographic procedures and then coated with 150 Å of carbon to provide electrical conductivity during SEM examination.

Samples were characterized with an image analysis system consisting of a JEOL JSM-840A electron microscope, a KEVEX model DELTA V energy-dispersive x-ray analyzer, and a LeMont Scientific model DB-10 automated image analyzer. Samples were imaged using the backscattered electron (BSE) signal at magnifications of 100, 200, and 500 times, and with a resolution of 512 pixels (i.e., sampling points) across the field of view. The multiple magnifications were used to provide sufficient resolution across the range of particle sizes present in the sample. Coal and mineral particles were identified, based on the brightness of their BSE signal, and were then characterized for particle area, diameter, perimeter, and other basic parameters. The electron beam was then returned to the center of each mineral particle and the x-ray analyzer was used to collect an x-ray spectrum (2 to 4 seconds acquisition time). The integrated intensities were determined for 20 common mineral-forming elements ranging from oxygen to zinc, and those intensities were compared with up to 20 sets of mineral definitions based on the relative abundance of the elements to identify the mineral phase (4,5). Minerals were identified as the first phase with elemental definitions matching the measured intensities.

The size and elemental data for each coal and mineral phase were recorded on magnetic disk for later data reduction. Significantly, the LeMont Scientific image analysis software recorded the data for associated coal and mineral particles together in such a manner that it was possible to determine the association of particles. For a composite assemblage, the measured areas of each of the phases present were used in conjunction with tables of densities of the phases to calculate the weight fraction of each phase within the particle.

The above measurements were made for thousands of composite coal-mineral particles in order to achieve a measure of statistical reliability. It then remained to tabulate the particle data in a format that was of technological interest.

For this paper, 200-mesh samples of Upper Freeport and Pittsburgh No. 8 coals were used to illustrate the capabilities of the AIA measurements. The general characteristics of these coals are summarized in Table 1. Both coals are bituminous coals with about 15% mineral matter. The amount of pyritic sulfur varied and thus the pyrite fraction of the mineral matter was considerably different between the two coals.

Table 1. General characteristics of the Upper Freeport and Pittsburgh No. 8 coals (results are on a dry basis unless otherwise noted).

	Upper Freeport	Pittsburgh No. 8
Moisture[a]	1.74	3.50
Total S	2.36	4.27
Pyritic S	1.98	3.15
Sulfate S	0.02	0.12
Organic S	0.36	1.00
Ash	12.4	11.4
Mineral Matter[b]	14.9	14.4

[a] As-received basis

[b] From modified Parr formula MM=1.13(Ash)+0.47(Pyr.S) (ref. 8, in which MM = mineral matter)

RESULTS AND DISCUSSION

Typical measurements available using the current technology are shown in Table 2 for some selected coal-mineral particles. The identity of each phase is given along with its area, average diameter, and significant x-ray signals. These results were used to calculate the abundance of phases within the particle as shown in Table 3. The total area of each phase was multiplied by that phase's density to estimate its weight contribution. These tables illustrate that a wide range of particles are encountered in coal, including nearly pure coal particles with very small, isolated mineral particles, coal particles with a large amount of a single mineral phase, and coal particles with a mixture of two and more minerals in a wide range of relative abundances.

The particles can be classified in any number of ways depending on the characteristics of interest. Currently, particles are tabulated according to the weight fraction of the combined minerals within them. This results in distributions as shown in Table 4 and in Figures 1 and 2. Such distributions indicate significant differences between these coals regarding the closeness of association of the mineral phases with coal. Minerals are more closely associated with the coal matrix in the Pittsburgh sample than they are in the Upper Freeport sample. Also, relatively more of the mineral matter in the Pittsburgh coal is pyrite which is somewhat more closely associated with the coal than it is in the Upper Freeport coal. Relatively more of the mineral matter in the Pittsburgh sample consists of quartz, clays, and other silicates.

These formats were developed with utility for density-based coal cleaning in mind. The particle density can readily be calculated, given the mineral composition of each particle. Predictions can then be made about the amount of sample and which phases and particles are likely to report to the clean coal stream.

However, weight fractions calculated from AIA results could also be used to calculate the overall elemental composition for the particles. Such compositions could then be used in conjunction with ash modeling efforts to predict ash particle characteristics.

For the prediction of ash characteristics, the particles may be treated in two ways. One model of ash formation assumes that each mineral grain will

Table 2. Typical SEM-AIA measurements for selected particles of Upper Freeport coal.

Phase	Area (μm^2)	Avg. Diam. (μm)	X-ray elemental intensities (as % of all x-rays)
Coal	561	26.7	none
Coal	1650	45.8	none
Pyrite	89	10.6	S=81, Fe=19
Coal	11	3.8	none
Quartz	30	6.2	O=4, Si=93, K=3
Illite	36	10.5	O=4, Al=33, Si=49, K=14
Coal	17	4.7	none
Coal	362	22	none
Misc.	10	3.7	O=5, Al=95
Quartz	62	8.9	O=3, Si=97
---	---	---	
Total	2267	53.7	
Coal	1320	41.0	none
Kaolinite	20	5.1	O=7, Al=43, Si=50
---	---	---	
Total	1340	41.3	
Coal	181	15.2	none
Iron Sulfate	157	14.2	O=9, Al=7, S=68, Fe=16
Quartz	24	5.6	O=5, Si=95
Coal	347	21.0	none
---	---	---	
Total	709	30.0	
Coal	59	8.7	none
Coal	81	10.2	none
Iron Sulfate	821	32.3	O=12, S=62, Fe=26
---	---	---	
Total	961	35.0	

Table 3. Abundance of coal and mineral phases for the particles shown above in Table 2 (as weight % of particle).

	Identified Phase and its Density (g/cm^3)						
	Coal 1.30	Pyrite 5.00	Fe Sulfate 3.00	Quartz 2.65	Kaolinite 2.65	Illite 2.75	Other 2.50
Particle 1	100.0	---	---	---	---	---	---
Particle 2	78.9	13.2	---	7.2	---	2.9	0.7
Particle 3	97.0	---	---	---	3.0	---	---
Particle 4	56.0	---	38.6	5.4	---	---	---
Particle 5	6.9	---	93.1	---	---	---	---

Table 4. Association of coal and ash-forming minerals in Upper Freeport coal as a function of particle mineral content.

Category	Mineral content % 0	1-20	21-40	41-60	61-80	81-100	Sum
Coal	55.05	22.42	5.42	2.53	1.37	0.33	87.10
Mineral Matter[a]	0.00	1.87	2.23	2.38	3.09	3.33	12.90
Total	55.05	24.29	7.64	4.91	4.46	3.66	100.00
[a] Where "Mineral Matter" includes:							
Pyrite	0.00	0.32	0.66	0.87	0.91	1.96	4.73
Fe-sulfate	0.00	0.04	0.06	0.06	0.04	0.15	0.35
Kaolinite	0.00	0.30	0.28	0.38	0.18	0.11	1.24
Illite	0.00	0.25	0.28	0.40	0.44	0.16	1.53
Quartz	0.00	0.20	0.30	0.13	0.68	0.46	1.77
Silicates	0.00	0.52	0.47	0.46	0.67	0.39	2.51
Other	0.00	0.25	0.17	0.07	0.18	0.10	0.76

produce one mineral particle, while another model assumes that all of the mineral grains in a single coal particle coalesce to form a single ash particle. For either model, AIA results could be used to predict the overall composition and mass/size distributions of the ash particles. The appropriate phase diagrams could then be used to help predict the character of the ash particles. For example, some particles may contain clay particles along with pyrite. The iron could serve as a flux and lead to a low melting point (i.e., sticky) ash particle, whereas clay particles associated with quartz or with no other minerals could lead to more refractory ash particles.

Or again, predictions could be made using both scenarios. First, each mineral particle could be assumed to follow a known transformation during combustion, apart from the influence or contribution of other mineral grains in the same composite. For example, quartz by itself would be relatively unaltered during combustion, while pyrite would lose its sulfur and form a particle of iron oxide, Fe_2O_3. Secondly, for each composite particle, the mineral grains could be assumed to interact. The iron from pyrite might be expected to serve as a flux for clay particles and lead to a low melting point mixture when both are present in the same composite.

However, we are not currently involved in developing models of mineral transformations during combustion. Instead, we are involved in developing the unique capabilities of SEM-based AIA to provide the necessary data for those who are interested in modeling mineral transformations to ash. We leave it to other researchers to determine the relative importance of the various modes of production of ash particles, whether they are produced one per mineral grain, are produced one per composite particle, or are produced as a result of ash particles agglomerating during combustion. We do seek to provide reliable data as input for those models.

CONCLUSIONS

AIA is able to provide detailed characterization of ash-forming mineral particles which can be used as input to models of ash formation and behavior. Significant differences have been observed in the distribution of mineral particles in different coals in the areas of mineral abundance, mineral size distributions, and the extent of association of mineral particles with coal.

Since such differences exist, it is not surprising that coals behave in markedly different ways even though they have the same nominal ash chemistry.

Further development of AIA applications for the prediction of ash behavior is necessary. Particularly, more work needs to be done on preparing the results into formats that are directly applicable to ash modeling efforts. Perhaps elements of the ash models can be incorporated into the AIA programs to directly provide the desired results. Much work also needs to be done to validate results and predictions based on AIA results. There is nearly always concern over how well two-dimensional AIA measurements can represent three-dimensional reality. And the accuracy of the ash models themselves will need to be determined. Nevertheless, the combination of detailed AIA characterization and ash modeling should provide a much improved indicator of ash behavior than older methods of ash characterization which are less than appropriate in view of current combustion technology.

ACKNOWLEDGEMENT

Ames Laboratory is operated for the U.S. Department of Energy by Iowa State University under contract No. W-7405-ENG-82. This work was supported by the Fossil Energy Program of the Ames Laboratory, funded by the Assistant Secretary for Fossil Energy, through the Pittsburgh Energy Technology Center.

REFERENCES

1. "Fusibility of Coal and Coke Ash", Standard D-1857, Annual Book of ASTM Standards, American Society of Testing and Materials, Philadephia, PA, 1989.

2. W.A. Sleiger and J.H. Singletary, "How Reliable are Correlations Between Coal Ash Chemistry and Ash Fusibilities", in Mineral Matter and Ash Deposition from Coal, R.W. Bryers and K.S. Vorres, eds., Engineering Foundation, New York, 1990, pp. 137-146.

3. A.K. Moza and L.G. Austin, "Analysis of Pulverized Coal Particles (10-100 μm) for Fe, S, Ca, Si, and Al on a Particle-by-Particle Basis", Fuel 62 1468-1473, (1983).

4. F.E. Huggins, G.P. Huffman, and R.J. Lee, "Scanning Electron Microscope-based Automated Image Analysis (SEM-AIA) and Mossbauer Spectroscopy", in Coal and Coal Products: Analytical Characterization Techniques, E.L. Fuller, Jr. ed., Am. Chem. Soc., Washington, D.C., 1982, pp. 239-258.

5. W.E. Straszheim, J.G. Yousling, and R. Markuszewski, "Analysis of Ash-Forming Mineral Matter in Raw and Supercleaned Coals by Automated Image Analysis-Scanning Electron Microscopy", in Mineral Matter and Ash in Coal, K.S. Vorres, ed., Am. Chem. Soc., Washington, D.C., 1986, pp. 449-461.

6. W.E. Straszheim and R. Markuszewski, "Evaluation of Physical Coal Beneficiation Using Computerized Microscopy", in Process Mineralogy IX, W. Petruk, D. Hausen, R. Hagni, and S. Pignolet-Brandom (eds.), TMS-AIME, Warrendale, PA, 1990, pp. 155-166.

7. W.E. Straszheim, K.A. Younkin, R.T. Greer, and R. Markuszewski, "Mounting Materials for SEM-based Automated Image Analysis of Coals", Scanning Microscopy, 2(3), 1257-1264, (1988).

8. P.H. Given and R.F. Yarzab, "Analysis of the Organic Substance of Coals: Problems Posed by the Presence of Mineral Matter", In Analytical Methods for Coal and Coal Products, Vol. II, C. Karr, Jr., ed., Academic Press, New York, 1978, pp. 3-41.

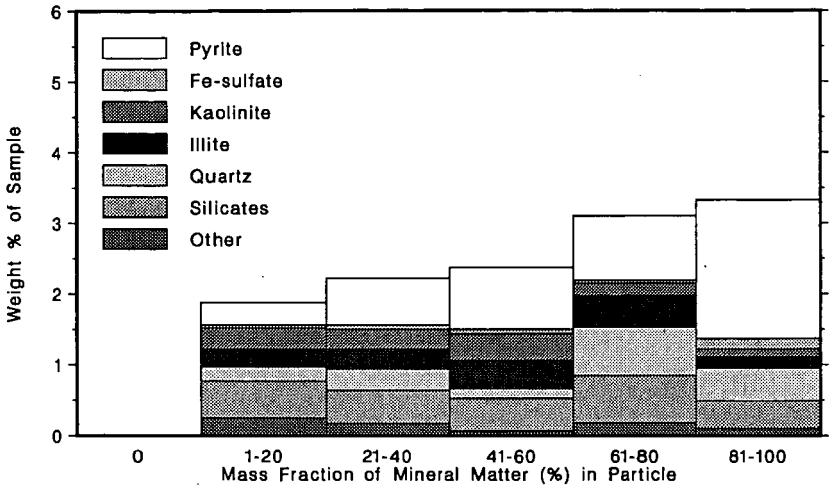

Figure 1. Distribution of ash-forming minerals in Upper Freeport coal as a function of particle mineral content.

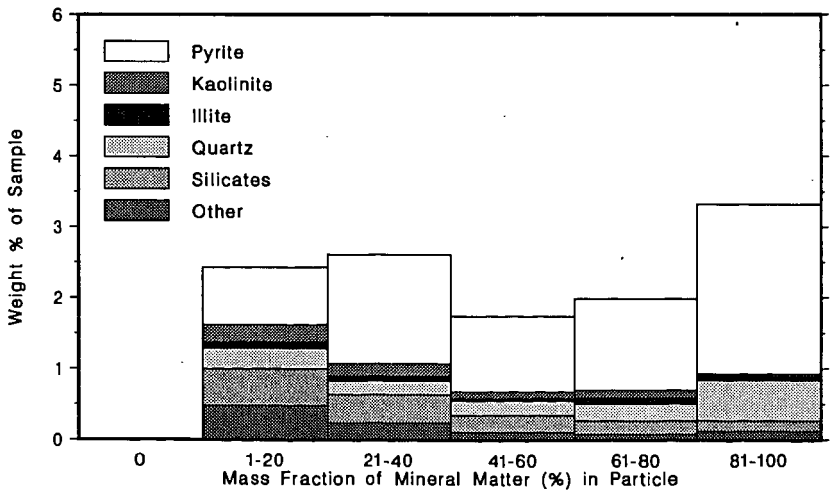

Figure 2. Distribution of ash-forming minerals in Pittsburgh No. 8 coal as a function of particle mineral content.

THERMAL PROPERTIES OF COAL ASHES

RAMONA LEDESMA AND L.L. ISAACS
The City College of CUNY, Dept. of Chemical Engineering, New York, New York 10031

Keywords: Coal ash characterizations, Thermal characterization of ashes, Ash Fusion.

ABSTRACT

The applicability of differential thermal analysis to determine the fusibility behavior of coal ashes was investigated. The technique proved useful to obtain four specific temperature points. These are: the minimum sintering temperature, the softening point, the point of complete fluidity and the reaction temperature which is tentatively identified as a phase boundary crossing or eutectic temperature.

INTRODUCTION

There is an abundance of coal in the United States, much of which is used for power generation. It is envisioned that in the future coal will be converted to "synfuel" as a replacement for crude oil. Coal in itself is a complex mixture of organic and inorganic components, together with large quantities of physically and/or chemically bound water. The inorganic component, which may amount to 15 to 20% by weight of the coal, is a complex mixture of quartz, pyrite, calcite, and silicates. Trace quantities of many metals are present. In the combustion process the coal is converted to ash, steam and other vapors.

Kiss and King [1] consider that the ash forming constituents should be classified into two groups: inorganics and minerals. The inorganic are relatively evenly distributed through the coal, while the minerals occur as discreet particles throughout the coal seam. The minerals are converted to ash via a pathway that includes dehydration, dehydroxylation and gas/solid phase reactions. The inorganics, which are the major ash forming species, are converted to ash via a pathway that includes coal devolatilization, burning of the solid residue (char), reduction of metal oxides, release of fly ash, sulfur, and other species, nucleation and growth of solid particles, gas phase reactions and condensation, and gas/solid phase reactions. Thus the ash material is likely to be a heterogeneous mixture of oxides, phosphates and sulfates.

In an industrial combustion process, a portion of the ash will be carried along with the stack gases. This "fly ash" may differ in composition and/or structure from the remaining "bottom ash". Ash formation is a by-product in reactions such as coal liquification. The inorganic phase itself may

influence the kinetics and the products distribution of various reactions and may have a strong bearing on the service life of the process equipment.

The ash must be removed from the process and disposed of in a safe and economic manner. Intensive research efforts are underway to find uses for ashes of various kind and to overcome the contamination of the environment by leaching from landfills and through the escape of fly ash into the atmosphere.

The efficient design of coal combustors, coal processing reactors, and ash removal systems mandates that the designer has information available on the thermal characteristics of the ash. The data base needed include: Ash fusion characteristics, heat capacities, and thermal conductivities.

The standard test to determine the fusibility behavior of coal ashes is the ASTM D-1857 "Fusibility of Coal and Coke Ash" procedure. It prescribes a preparation and measurement scheme which yields four "call" points which presumably describe the fusing process. The points are empirically defined and bear tenuous relations to actual physical phenomena.

Sintering of a powder leads to the reduction of volume and surface energy. Thus the onset of sintering, i.e. the minimum sintering or agglomeration temperature, can be determined either by dilatometry or by a technique such as differential thermal analysis (DTA).

In dilatometric experiments [2] the powder to be tested is placed into a quartz tube and piston assembly, and the sample is compressed by an adjustable load. The experimental assembly is then heated at some preselected rate and the expansion or contraction of the sample is detected by a linear variable differential transducer and recorded as a function of temperature. In general, the powder dilates on heating due to thermal expansion. Eventually, a temperature is reached where the surface of the particles begin to deform due to viscous flattening and/or sintering at the intergrandular contact points resulting in contraction of the sample. The temperature at which this phenomenon occurs is the minimum sintering temperature, Ts. Ts is a characteristic for each powder and the point where particle agglomeration will first occur.

DTA indicates the onset temperature of change and the direction of change in the internal energy of a material due to heating. Reduction of surface energy is a exothermic event and will show up as such in the DTA signal. Fusion on the other hand is an endothermic event and will manifest itself as such in the DTA signal. Chemical reactions and non-ideal dissolution phenomena will show up as either increases or decreases or as slope changes in the DTA signal. In principle, besides yielding minimum sintering temperatures DTA should provide further fusibility information on ash powders. DTA experiments were performed on a set of coal ashes prepared from coals of the Argonne Premium Coal Bank and are reported here.

EXPERIMENTAL TECHNIQUE

Ashes were prepared from eight coals. These were obtained from the Argonne Premium Coal Sample Bank [3]. In Table I the rank of the original coals and their mineral contents are listed. The ashes were prepared by combustion of 100 mesh size particles at 700°C in a muffle furnace. Part of the ashes were used for DTA measurements and elemental analysis. The rest was heated to 1000°C in a muffle furnace before being used for experiments in the DTA. Elemental analysis was performed using the inductively coupled plasma technique. Results of the elemental analysis are given in Table II. The fusion behavior of the ash powders was investigated with the use of DTA [4]. A DuPont 2100 Thermal Analyzer with a high temperature (1600°C) DTA cell was employed. The samples were heated from 300K to 1900K at the rate of 20°C/min in nitrogen flow. The instrument was calibrated using zinc and gold as standard materials.

RESULTS AND DISCUSSION

The results of the DTA experiments on the ashes derived from the Pittsburgh #8 coal are shown in figure 1. The ordinate of the graph represents the temperature deviation of the ash sample from a baseline which corresponds to the temperature evolution of a sample not undergoing a physical or chemical transformation process.

This set of results is indicative of the results obtained for the other ashes with some variation in details. As was expected, several characteristic temperatures at which significant events occur may be identified. These points of interest, starting with the lowest temperature, are the:

- Onset of particle agglomeration (sintering), Ts.
- Onset of fusion (ash softening), Ti.
- Point of discontinuous change in , Tr.
- Point of complete fluidity, Tf.

In Table III we tabulate these temperature points for all the ashes. One should note that for a given origin ash there is only a relatively small variation in the characteristic temperatures for the ash powders prepared at different temperatures.

The Minimum Sintering Temperature

We previously reported [2] minimum sintering temperatures for a number of coal ashes spanning the same geographic spectrum as those reported here. The method of detection employed in the prior work was dilatometry. In general, the Ts value detected by dilatometry was approximately 100K larger than that detected by DTA. We attribute much of this discrepancy to the way the DTA method was employed in these experiments. However it is important to note that both of these techniques yield a minimum sintering temperature

substantially lower than the initial deformation temperature (IDT) of the ASTM procedure. Rhinehart and Attar [5] have proposed a model for the ash fusion temperatures based on the freezing point depression equation for ideal binary solutions. They used a data base of 263 ashes to perform a seven-parameter correlation analysis. Six of the parameters are statistically determined "pseudo" heats of fusion for the assumed ash components, and the seventh is a fusion temperature for the "average composition" ash. The calculated average ash IDT is 1411K. Experimentally determined IDT's for the Argonne ashes range upwards from 1340K in a reducing atmosphere and upwards from 1445K in an oxidizing atmosphere [3]. It is clear that the IDT temperature is not a measure of the onset of agglomeration.

The Fusion Phenomenon

Melting is a first order phase transition phenomenon accompanied by a discontinuous increase in the enthalpy for pure homogeneous compounds. For dilute solutions the freezing point depression expression may be used to estimate the initial decrease in the freezing point of the solvent due to the addition of the non-volatile solute. Ashes are heterogeneous mixtures and certainly do not act as dilute solutions. The individual compounds which make up the ash mixture each have melting points which are higher than the most of the observed initial softening temperatures, Ti. In the sintering process melting of the powder surface occurs hence several oxides can dissolve in each other. These oxide solutions have substantially lower melting temperatures than the individual oxides. For example the melting point of an iron oxide-silica slag of composition $Fe_2S_iO_4$ has the melting point of 1450K. Thus the initial softening temperature Ti may be considered as the melting point of the lowest melting "component" in the system. The molten component then acts as a solvent and dissolves some of the remaining solid. The dissolution process, unlikely to be ideal (i.e. $H_{sol} = 0$), is accompanied by an enthalpy change. Completion of dissolution is marked by the fluidity temperature Tf. During the dissolution process one reaches eventually a point where the solution composition passes a phase boundary. Such a boundary crossing may be associated with a latent heat or may be athermal. It is our conjecture that the sharp change in at the temperature which we call Tr indicates such an event. It is to be noted that in the vicinity of Tr we have the greatest variability in the nature of the DTA curves.

The Initial Softening temperature

The softening temperature as evaluated by Rhinehart and Attar is 1478K for the average ash. Values for the Argonne ashes, range upwards from 1365K depending on the particular ash and on the furnace atmosphere [3]. For the ash illustrated in Figure 1 we estimate that in an inert atmosphere the initial

deformation temperature, the spherical softening point and the hemispherical softening points are 1520K, 1550K, and 1580K respectively. From the Ti values as defined, we estimate that the initial softening point for a 850°C ash (ashing temperature for the ASTM test) is approximately 1375K.

The Discontinuous Change Temperature

Of the sixteen ashes examined, eight show only a discontinuous endothermic change in , seven show exothermic behavior in prior to the endothermic discontinuity and one ash shows no discontinuity (hence no Tr) of any kind. Tr ranges from 1490K to 1680K. It is likely that Tr is very sensitive to both ash composition and to ashing temperature.

The Fluidity Temperature.

The ASTM test for fusibility defines the fluidity temperature, Tf, as the point where the test sample height has decreased to approximately 10% of its original value. We consider it to be the temperature where there is a final change in indicating the melting (or dissolution) of the last bit of solid ash. The fluidity temperature for the average ash according to the Rhinehart correlation is 1581K (1609 for low Calcium ashes). For the Pittsburgh #8 ash the measured ASTM fluidity point is 1600K in a reducing atmosphere and 1705K in an oxidizing atmosphere. The DTA Tf point is 1720K for this ash.

CONCLUSION

. The DTA technique to determine the fusion behavior of ashes is convenient and yields a set of physically meaningful parameters.
. An accurate model describing the fusion behavior of ashes, based on composition, ashing temperature, and physical structure might be possible once a more extensive experimental data set is collected.

ACKNOWLEDGEMENTS

We wish to acknowledge the support of E.I. Dupont de Nemours and Co., especially the help provided by Peter Compo and J. Creeden to our research efforts. Ramona Ledesma wishes to thank the W.R. Grace Co. for the Graduate Fellowship they provide. This presentation is based on a published article [6].

REFERENCES

1. L.T. Kiss and N.T. King, Fuel 56, 340 (1977)
   Fuel 58, 547 (1979).

2. R. Ledesma, P. Compo and L.L. Isaacs in Fly Ash and Coal Conversion Byproducts: Characterization, Utilization and Disposal III, edited by G.J. McCarty, F.P. Glasser, D.M. Roy and S. Diamond (Mat. Res. Soc. Proc. 86, Pittsburgh, PA 1987) pp.127-136.

3. Users Handbook for the Argonne Premium Coal Sample Program, ANL/PCSP - 89/1. Karl S. Vorres, ed.

4. Thermal Analysis by W.W. Wendland (3rd Ed., J. Wiley and Sons) 1986.

5. R.R. Rhinehart and A.A. Attar, J. of Energy Resources Technology 109, 124 (1987).

6. R. Ledesma and L.L. Isaacs, a Fly Ash and Coal Conversion Byproducts: Characterization, Utilization and Disposal VI, edited by R.L. Day and F.P. Glasser (Mat. Res. Soc. Proc. 178, Pittsburgh, PA 1990) pp. 35-43.

TABLE I - Mineral Composition of the Coals (from [2])

COAL	RANK	MINERAL MATTER Wt % DRY COAL	MINERAL CONTENT (as % of mineral matter) QUARTZ	PYRITE	CALCITE	TOTAL CLAY
UF	HVB	15.53	10	22	7	61
WY	SUBB	8.7	23	1	5	71
ILL	HVB	18.1	19	30	10	41
PITT	HVB	10.9	16	22	5	57
POC	LVB	5.5	5	2	31	62
UT	HVB	5.3	15	9	24	52
WV	HVB	21.6	12	1	1	86
ND	LGN.	8.7	7	3	20	70

TABLE II - Elemental Composition (wt. %) of the Ashes (a)

	UF	WY	ILL	PITT	POC	UT	WV	ND
Ca	1.2	11.3	1.8	1.0	3.1	2.3	0.3	9.4
Mg	0.6	2.4	0.4	0.4	0.8	0.4	0.4	3.2
Na	0.2	1.3	0.6	0.4	1.5	2.9	0.2	5.4
Al	12.3	6.7	7.0	11.4	9.5	6.1	16.1	3.0
Fe	14.7	4.4	17.2	15.2	10.8	6.6	2.1	4.9
Si	21.9	13.9	20.0	24.1	16.7	21.9	28.0	7.9
Ti	0.6	0.7	0.4	0.7	0.8	0.5	1.2	0.2
trace (b)	0.3	1.1	0.4	0.4	0.4	0.2	0.3	1.2
S (c)	1.6	8.8	2.7	0.8	5.0	3.9	0.8	12.0
K (c)	2.2	0.7	2.4	1.7	0.5	1.0	0.8	0.8

(a) Elemental analysis was done using the inductively coupled plasma technique, courtesy of DuPont's Jackson Laboratories.

(b) Trace includes; P, Sr, V, Zn, Ba, Cr, Cu, Mn, Ni and Zr

(c) K and S were calculated from SO_3 and K_2O values reported in the Argonne User's Handbook, sect 3.2, or estimated by interpolation.

TABLE III - Fusion Temperatures (K) for the Ashes

	Onset of Aggl. (Ts)		Onset of Fusion (Ti)		Endotherm. Drop (Tr)		Fluidity (Tf)	
Ashing T	700°C	1000°C	700°C	1000°C	700°C	1000°C	700°C	1000°C
UF	900	1150	1250	1380	1675	1650	1725	1580
WY	950	950	1350	1400	1500	1490	1675	1675
ILL	950	950	1280	1440	1520	1620	1700	1540
PIT	925	950	1130	1450	1680	1660	1700	1740
POC	875	975	1350	1450	1525	1600	1650	1650
UT	975	1000	1400	1380	1620	--	1700	1650
WV	1000	1100	1400	1480	1600	--	1800	1800
ND	950	1150	1325	1375	1590	1625	1650	1640

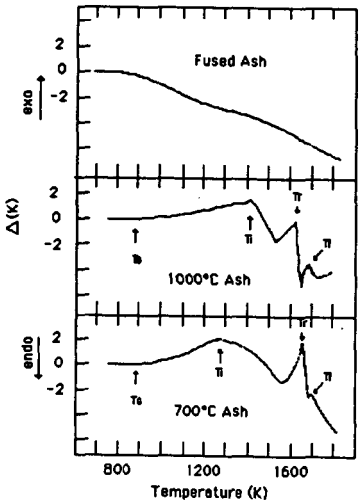

Figure 1 Differential Thermal Analysis of Pittsburgh #8 Ash

THE USE OF AQUEOUS BORON TRIFLOURIDE IN DEASHING ORGANIC RICH ROCKS AND SEDIMENTS.

T. L. Robl and B. H. Davis
Center for Applied Energy Research
University of Kentucky
3572 Iron Works Pike
Lexington, KY 40511.

Introduction.

The study of the organic matter in coal and other organic-rich rocks such as oil shale and petroleum source rocks often requires the isolation of the organic matter. The common approach is to macerate the inorganic fraction of the rock by attack with HF. This unique reagent reacts with the silicates to form SiF_4, a volatile gas, and leaves the organic matter largely unaltered.

Unfortunately HF also reacts with other inorganic components to form fluoride salts, the most pernicious being CaF_2, which is very insoluble. Thus HF is usually used in combination with HCl, which is used first as a pretreatment step to remove calcium carbonates, and then in combination with HF solutions in the final deashing step to prevent additional fluoride formation.

The use of HCl is undesirable, however, as it is a stronger acid than HF and has a stronger affect on the organic matter.[1] (See also Robinson and Saxby for further discussion on the affects of reagents on organic matter).[2,3] Also chlorination reactions are possible and undesirable. The HCl is not needed to dissolve carbonates as the HF is normally used in sufficiently high concentration to dissolve them.

The approach taken in this work is to selectively dissolve neo-formed fluorides in a two step demineralizing process, by reaction with BF_3, which is a highly water soluble gas. The BF_3 is generated by the reaction of H_3BO_3 with HF,

1. $H_3BO_3 + 3HF \rightarrow BF_3 + 3H_2O$

and it then reacts with neo-formed fluoride salts, such as fluorite, to form water soluble fluoroborates.

Methods.

Samples and Sample Preparation. Four oil shales including the Stuart from Australia, the Green River from the U.S. (Rock Springs, Wyoming), the Irati from Brazil (Sao Mateus do Sul) and a sample of the Israeli Rotem (or E'fe) oil shale were used as test materials. The Stuart and Irati are silicates and the Israeli and Green River are carbonate shales. Two coal

samples, obtained from the Argonne National Laboratory (ANL) premium sample bank, were used in the experiments; these are the North Dakota lignite (Beulah-Zap Seam) and the Wyoming subbituminous coal (Wyodak-Anderson Seam).[4]

The oil shale was crushed to approximately -1/4" in a jaw crusher. The -100 mesh material was sieved out and the remainder of the sample passed through a Rieche mill equipped with a 100 mesh screen. The samples were then re-homogenized. The samples of lignite and subbituminous coal from ANL were used as received (-100 mesh).

HF-HCl Demineralization Procedure. For comparison purpose a fraction of the test samples were processed using a typical HCl-HF procedure.[1] Approximately 20 g of sample was stirred for 24 hours at room temperature in a sealed 1 liter heavy duty centrifuge bottle filled with 6 N HCl. The sample was then centrifuged and the residual acid decanted off through 0.45 micron filters. Material trapped on the filters was washed back into the sample containers. The sample was washed by completely resuspending it in distilled-deionized water and centrifuging. Approximately 900 ml of a 1:1 (v/v) solution of 6 N HCL and 48% HF mixture was then added to the sample, which was capped and left at room temperature overnight on a magnetic stirrer. The sample was then centrifuged and washed 5 to 6 times with distilled-deionized water, decanting each time through a 0.45 micron filter and rinsing the filtrate back to the sample. The sample was dried in a vacuum oven at 60°C overnight and disaggregated by crushing with a mortar and pestle.

Boron Trifluoride Procedure. Twenty g of sample was placed in heavy duty 1 liter centrifuge bottles and 800 ml of 1:1 v/v 48% reagent grade HF added. For samples which contained carbonates, the acid was initially added in 10 ml increments to prevent spillage from excessive foaming due to the generation of CO_2. The foaming generally ceased after approximately 40 to 50 ml of HF was added. The sample was sealed, left at room temperature and stirred overnight on magnetic stir plate. The following morning the sample was chilled in an ice bath and 250 g of boric acid was added in two 125 g increments with time left between additions for the sample to recool. The reaction of H_3BO_3 with HF is exothermic and the sample was pre-cooled to 0°C to minimize the loss of BF_3. The sample was again tightly capped and left at room temperature to stir overnight. The following day the sample was centrifuged, the supernate poured through a 0.45 micron filter and washed back to the sample. The sample was each washed 5 to 6 time by completely resuspending it in distilled-deionized water and centrifuging. It was then dried in a vacuum oven at °60 overnight.

Discussion.

The demineralized samples are composed of concentrated organic matter and residual ash which, for the most part, consist of sulfides (pyrite and marcasite). Based upon previous experience rutile and zircon are also expected to be present.[5] The total ash in the test samples varied from ~0.1% in the Wyoming subbituminous and North Dakota lignite samples to ~29% in the Irati oil shale samples. A comparison of the residual ash for sample processed by the two techniques indicate no substantive differences, with the HF-BF_3 technique producing slightly lower ash (Table 1).

Based upon the comparison of FTIR spectra, the organic matter in the samples processed with the HF-BF_3 technique does not appear to be altered more than that processed by the HF-HCl technique. Although additional analysis is needed, the currently level of data suggests that the HF-BF_3 procedure actual results in less organic mater alteration than the

HF-HCL procedure.

The mechanism of the BF_3-fluoride salt reaction is of interest. A search of the literature and consideration of the stoichiometry involve indicated that two reactions are possible,[6,7]

2. $BF_3 + CaF_2 \rightleftharpoons CaF(BF_4)$

or

3. $2BF_3 + CaF_2 \rightleftharpoons Ca(BF_4)_2$

Model compound studies employing optical grade crystalline CaF_2 and $BF_3{\cdot}2H_2O$ were used to explore the possible reactions. The dissolution of CaF_2 was found to depend directly upon the BF_3 concentration (Figure 1) with an equilibrium constant of 0.12. Thus, reaction 2, the formation of calcium fluoride tetraflouroborate, is indicated. During the dissolution experiments, a tan color precipitate was found to begin forming at the point where the calculated concentration of $CaF(BF_4)$ is ~36 g/l, which we believe to be the approximate solubility of this salt.

In summary, the HF-BF_3 technique has certain advantageous over the more traditional approach employing HCl. Because all of the HF is converted to fluoroborates the need to handle large quantities of contaminated HF is eliminated. This approach also results in samples with as low or lower residual ash and does not alter the organic matter any more, and probably less than, more traditional techniques employing HCl.

References.

1. Durand, B. and G. Nicaise, Ch. 2, **In**, *Kerogen, Insoluble Organic Matter from Sedimentary Rocks*, B. Durand (Ed.), Editions Technip, Paris, p. 36, 1980.

2. Robinson, W.E., Ch. 6, **In**, *Organic Geochemistry*, G. Eglington and M.T.J. Murphy (Eds.), Springer Verlag, New York, 1976.

3. Saxby, J.D., **In** *Oil Shale*, Yen, T.F. and G.V. Chilingarian (Eds), Elsevier, p. 104, 1976.

4. Vorres, K.S., 1991, *Energy and Fuels*, **4**, p. 420-426.

5. Robl, T.L., D.N. Taulbee, L.S. Barron and W.C. Jones, 1987, *Energy and Fuels*, **1**, p. 507-513.

6. Paevlenko, S., *Z. anorg. allg. Chemie.*, **301**, p. 337, 1959.

7. Paevlenko, S., *Z. anorg. allg. Chemie*, **315**, p. 136, 1962.

Table 1. Comparison of Residual Ash from Demineralization of Coals and Oil Shales with HF-HCl and HF-BF_3 Procedures.

Demineralizing Procedure	HF-HCL	HF-BF_3
Oil Shales	%Ash	%Ash
Irati Oil Shale-Upper Bench	29.3	26.3
Israeli Oil Shale-E'fe	7.1	6.7
Green River Shale-Tipton Member	9.6	8.8
Stuart-Kerosene Creek Member	9.7	7.2
Coals		
Wyoming Subbituminous-Wyodak	<0.1	<0.1
North Dakota Lignite-Beulah Zap	<0.1	<0.1

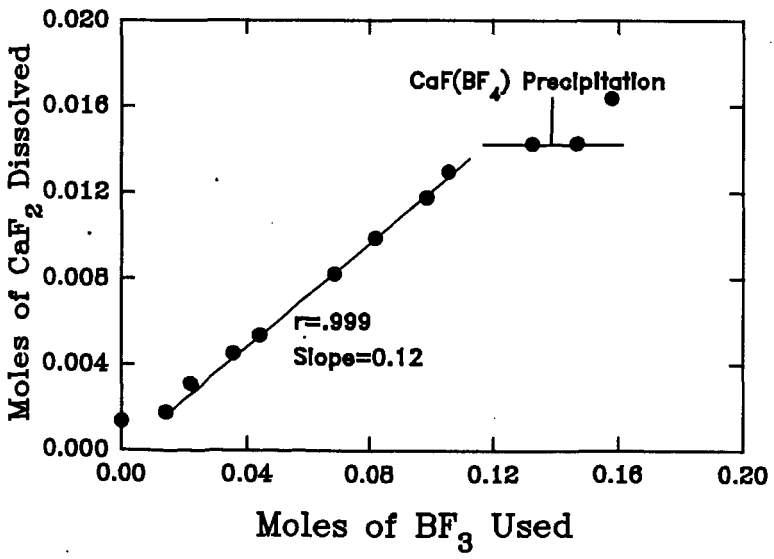

Figure 1. Plot of CaF_2 dissolved versus BF_3 added in modal compound study.

ESTIMATION OF ASH FUSION TEMPERATURES FROM ELEMENTAL COMPOSITION: A STRATEGY FOR REGRESSOR SELECTION

William G. Lloyd, John T. Riley, Mark A. Risen, Scott R. Gilleland, and Rick L. Tibbitts
Department of Chemistry and Center for Coal Science
Western Kentucky University, Bowling Green, KY 42101

INTRODUCTION

Two developments within the past decade have had a major impact upon our ability to infer useful information about ash fusion temperatures from the composition of the ash. The emergence of fast and accurate multielement analyzers means that the chemical composition of an ash can be determined quickly and reliably. At the same time, the proliferation of personal computers, and of statistical software written for them, makes it possible to rapidly estimate an ash fusion temperature, saving the two or three days' time which would be required to determine fusion temperatures in accordance with standard procedures.[1,2]

In order for such an estimate to be useful, a valid and reliable algorithm is needed. Multiple linear regression (MLR) analysis has been used by a number of workers to obtain estimates generally found to be superior to the single-term factors used in the earlier literature.[3-10] The present work re-examines the use of MLR analysis with particular reference to techniques for avoiding the problem of multicollinearity.

EXPERIMENTAL

Seven source coals, of rank from lignite A to medium volatile bituminous, were selected for study. Coal sources, proximate and ultimate analyses, and ash compositions have been reported.[9,10] Table 1 shows the ranges of the analyses. After reduction to -60 mesh (-0.25 mm) three blends were prepared, in the proportions 3:1, 1:1 and 1:3, for each of the 21 binary combinations of source coals. Ash samples from the source coals and the 63 blended coals were then prepared in accordance with ASTM Method D 1857.[2]

Ash samples were fused with lithium tetraborate for elemental analysis by X-ray fluorescence spectrometry, using an ORTEC Model 6141 spectrometer. Calibration and analysis conditions have been reported elsewhere.[9,10] Cross-analyses were made by inductively coupled plasma spectrometry, using a LECO Plasmarray ICP 500 spectrometer. It is necessary to analyze the ashes of each blend, since composition cannot be estimated by interpolation.[10,11]

Ash fusion temperatures (reducing atmosphere) were measured in duplicate or triplicate on ash splits using a LECO Model AF-600 ash fusibility system. Precision for the four ash fusion temperatures is given in Table 2. Except for fluid temperature, the average error estimate is less than 18°F (10 K). Statistical analyses were conducted using the Statistical Analysis System.[12]

RESULTS

Ash properties cannot be adequately described by assuming a mixture of ten discrete oxides. These components obviously interact with one another, in acid-base and in other metathetic reactions. To take account of these, a set of crossterms can be generated, for example, $[Na_2O]*[SO_3]$ from $[Na_2O]$ and $[SO_3]$.[4,5,7-10] For brevity these

oxides and their crossterms will be represented by the parent element symbols, e.g., Na and Na*S.

Limitations Imposed upon Regressor Selection. In developing an algorithm to estimate an ash fusion temperature, the main task is that of selecting regressor terms from among the ten direct analyses and the 45 crossterms. The wealth of candidate regressors requires the use of some selection rules. There are, for example, 29 million six-term combinations of these regressors. We have chosen to focus upon the extent of collinearity among the selected regressors. When a substantial linear dependence exists between two variables, they are said to be collinear.[13] While high collinearity between a predictive variable and the dependent variable indicates a good predictive relationship, high correlations among predictive variables are not desirable. MLR analysis is based upon the assumption of orthogonality: the distribution of values of each predictor is assumed to be independent of the distribution of values of any other predictor. That ideal condition is seldom found in real data, certainly not in coal ash compositional data. Fortunately, multiple regression can tolerate an appreciable amount of collinearity among regressors. Nevertheless, a major hazard in MLR analysis is that in the presence of excessively high collinearities among regressors (multicollinearity) it is easy to get predictive equations which are good-looking in terms of R^2 and root mean square error of estimate (RMSE), but which are in fact useless.

Multicollinearity in a candidate regression analysis is typically detected by instabilities of regression coefficients, such as[14]

(1) large changes in values when a variable is added to or deleted from the model;

(2) large changes in values when datasets are added or dropped from the model;

(3) large standard errors associated with the coefficients of important terms.

All of these regressions are of the form:

$$AFT_{estimated} = b_0 + b_1X_1 + b_2X_2 + b_3X_3 + \ldots \qquad (1)$$

The term common to all regressions on a given AFT is the intercept term b_0. A convenient flag for multicollinearity in any particular candidate regression is the standard error of this intercept term (SEI). Since the RMSE's of the better-looking regressions are found to be about 45°F (25 K), we have adopted as a screening criterion that an acceptable regression must have an SEI value of less than 90°F (50 K).

For the following analysis Pearson's correlation coefficient R is used to express collinearity between pairs of predictor variables, while R^2 when used is the square of the multiple correlation coefficient for a given regression.

If we set the critical value of R (R_c) at 0.99, only 5 of the 55 terms (10 direct analyses and 55 crossterms) are found to have collinearities with other regressor terms for which $R > R_c$. The remaining 50 variables are free of 'significant' correlations [significant in terms of this selected value of R_c] with other predictive variables. At $R_c = 0.99$ the five collinear terms occur in a single cluster [Mg, Mg*Na, Mg*S, Mg*Si, Mg*Ti]. On the other hand, at $R_c = 0.85$, only 7 of the 55 terms are free of significant correlations with others, the other 48 occurring in three correlation clusters.

Our first approach has been to set R_c at each of several values, then for each value of R_c to generate the best available regressions which avoid combinations of regressors for which $R_{x,y} > R_c$.

When R_c is set at 0.99 there are few restrictions on regressors. For ash softening temperature we find a good four-term regression, for which R^2 = .859 and RMSE is an acceptable 58.2°F (32.3 K). When the best (by R^2) five-term regressions were examined, the first three regressions were unacceptable, all having SEI's > 200°F. For the first acceptable five-term regression R^2 = 0.885 and RMSE = 52.9°F (29.4 K). Among the next fifty regressions [the best ten (by R^2) regressions containing 6 to 10 terms] none were acceptable; all were rejected by the SEI criterion.

When R_c is set at 0.85 there are considerably more restrictions on the combinations of regressors which can be used in any particular regression. The best (by R^2) three-, four- and five-term regressions are all acceptable by the SEI criterion, but are not as powerful as those found above. For example, for the best five-term regression R^2 = 0.855 and RMSE = 59.3°F (32.9 K). There is an important difference, however, in this second family of regressions: the SEI's for <u>all</u> regressions are well below 90°F, and it is in fact possible to obtain good regressions with ten or more terms present. Table 3 summarizes the fits of the best regressions for these two values of R_c.

It is evident that there are major changes in the extent and complexity of regressor-regressor correlations in this range of R_c. Figures 1 and 2 illustrate the correlations among 19 regressor terms for two intermediate R_c values, 0.98 and 0.90. (Lines connecting terms indicate $R_{XY} > R_c$.) The clustering of the 55 candidate regressor terms as a function of R_c is shown in Table 4.

<u>A Strategy for Selecting Regressors</u>. Based upon preliminary tests, R_c was set at 0.920, and the 19 terms found to be free of correlations were taken as an initial set.

1. The best regressors were selected, by R^2 ranking, from each of the clusters of terms. The largest of these consists of ten terms (Figure 3). To illustrate this selection process with this cluster, the Ca*Ti term is found to make the greatest incremental contribution to the initial set. When this term is selected, the collinearities shown in Figure 3 require that four other terms (Ca, Ca*Na Ca*Si and K) be excluded. With these exclusions, two other terms in this cluster -- Al*Ca and Ca*S -- are isolated from collinearities and are therefore <u>included</u>. Upon analysis of the three remaining terms, Al*K is found to make the greatest incremental contribution to R^2 and is included; and its inclusion requires the rejection of K*Si and K*Ti. A similar R^2 testing procedure was used to select the most useful terms from each of the other clusters.

2. The best 36 regressions (with four, five and six terms) from this enlarged base were then examined, and several regressors -- which appeared in none of the best regressions -- were dropped. Three of the 36 test regressions exhibited multicollinearity. One term, [Si], appeared in all three multicollinear regressions and in none of the 33 good regressions; this term was also dropped.

3. Starting with 22 terms from the above process, steps 1 and 2 were repeated, to ensure that the most useful terms from each cluster were included. After this second iteration, a group of 23 terms remained.

4. To these final terms were added seven additional terms, selected from the pool of remaining terms on the basis of the greatest incremental improvement in overall R^2. For example, if the 24th term is Na*P, overall R^2 is incremented by 0.0063, more than by any other added term; therefore Na*P is added to the set.

Step 4 clearly introduces collinearities. Na*P, for example, is collinear [$R_{x,y} > R_c$] with P*S. Among other added terms Fe*Ti is collinear with Al*Fe, and Fe and Fe*Si are collinear with both Fe*Ti and Al*Fe. The argument for inclusion of the several terms in step 4 is pragmatic: the regressions with these terms are better estimators than those without these terms, and this step still allows overall collinearity to remain at an acceptable level by the SEI criterion.

Best Predictive Regressions. The best regressions obtained under reducing atmosphere for the set of 70 ashes, following the above strategy, are given in Tables 5-8. Calculations have been carried through ten regressor terms. It is possible to generate predictive equations with even more regressors. However, the incremental improvement falls to small values as the number of terms increases. Furthermore, the probability of significance of each regressor term, which typically is > 99.9% for good regressions with as many as nine terms, falls for at least one regressor below 99% with the inclusion of the tenth term. Thus this appears to be a natural break point for these data.

Figures 4-7 show plots of estimated vs. observed fusion temperatures, using the ten-term equations of Tables 5-8. In the tables the average error is estimated using the approximation of average error for large sets:

$$E(avg) = [RMSE]*[2/pi]^{0.5} \qquad (2)$$

The average observed errors of estimate are given in Figures 4-7. These are similar to but slightly lower than the estimated values.

These calculations use data from all 70 ashes. If the three most remote outliers are dropped from each calculation, the average error is decreased by an average of 3.0°F (1.7 K).

Further Testing for Multicollinearity. The most common indicators of regression fit are R^2 and the standard error of fit (RMSE). Table 9 summarizes key characteristics of four regressions on softening temperature, all with good values of R^2 and rmse. On the basis of these indicators alone, the choice would fall between the 30-term and the 55-term regressions. This choice would be unfortunate.

By the SEI criterion [acceptable regressions must have SEI's below 90°F (50 K)] only the first of these four regressions is acceptable, the other three showing SEI's of 800°F and above, indicating excessively high collinearity.

An additional test for multicollinearity is examination of the precision of the regression coefficients. Virtually all regression programs provide an estimate of the standard error associated with each coefficient. We calculate precision as a relative percentage:

$$P\ (\%) = 100 * [S.E.\ of\ coefficient]/[value\ of\ coefficient] \qquad (3)$$

Coefficients in multiple linear regressions are seldom obtained in high precision, since a moderate displacement in the value of any one coefficient can be balanced by slight shifts in the values of others. For good regressions, precision as defined in Eqn. 3 is typically in the range 5-30%. Table 9 shows the average precision calculated for the ten coefficients of the first regression, and for the first ten coefficients of each of the other regressions. The average error increases tenfold in going to the 20-term regression, and over a hundredfold in going to the 55-term regression.

Another test of the goodness of a regression is made by adding or deleting a dummy variable (a regressor which itself has no predictive power). Instability of a coefficient can then be calculated as:

$$I = [C_{MODIFIED} / C_{ORIGINAL} - 1] * 100\ \% \qquad (4)$$

where $C_{ORIGINAL}$ and $C_{MODIFIED}$ are the regressor coefficients before and after addition/deletion of the dummy variable.

A two-digit random number term was added to each of these regressions, taking the first 70 random numbers listed in a standard statistical reference.[15] For a good regression this dummy variable should have very little effect upon the coefficients of the 'real' regressors. For the 10-term regression in Table 9 the average instability is 0.01%. However, the average instabilities for the first ten terms of the other three regressions are from two to four orders of magnitude larger.

Perhaps the most practical test of the stability of regression coefficients is that of adding or deleting cases from the dataset. If a regression is to have any useful predictive power, it must be reasonably resistant to fluctuation of coefficient values when cases are added or removed. Roughly, variations may be expected to be of the order of magnitude of the precisions of estimate of the coefficients, that is, typically 5-30% for good regressions.

Stability of coefficients to removal of cases was tested by deleting every fifth case in the 70-case dataset, producing a reduced dataset of 56 cases. (This deletion pattern was selected to avoid introduction of systematic bias.) Coefficient instabilities were calculated by Eqn. (4). For the 10-term regression of Table 9 the average instability is 14.1%, consistent with the average coefficient precision of 15.8%. For each of the other regressions in Table 9 the average average instabilities are well over 100%.

These three tests lend support to the use of a critical value of SEI as a convenient indicator of excessive collinearity. The most practical and persuasive showing of the utility of a good regression, however, is to demonstrate its ability to predict from a subset of cases the AFT's of "new" cases. We have taken the coefficients obtained with good ten-term regressions using the reduced set of 56 cases, and have applied them to the 14 excluded cases, treating these as "new" cases. Figure 8 shows the estimated and actual values of softening temperatures for these "new" cases. The average error of estimate is 36.8°F (20.4 K). A similar estimation of hemispherical temperatures yields an average error of estimate of 34.1°F (18.9 K).

DISCUSSION

Gray[7] has recently reviewed various British, American, Australian and international standards for ash fusion temperature determinations. Repeatability (within a laboratory) is 30-40 K for initial deformation temperature, 30 K for hemispherical temperature and 30-50 K for fluid temperature. Tolerated reproducibility (between laboratories) is generally in the range 50-80 K. The repeatability of instrumental ash fusion temperature in this work (Table 2) is considerably tighter than these figures. The average observed error of estimate for the four ash fusion temperatures (Figures 4-7) is 15-18 K. This error includes contributions from coal and ash inhomogeneities, splitting, chemical analysis and AFT determinations, as well as inadequacies of the fitting equations. This approach therefore appears to provide estimates of satisfactory precision.

In the better regressions for estimating softening and hemispherical temperatures certain terms are encountered repeatedly. In softening temperature regressions Al*Ca, Ca*Fe, Na*P and P often occur, always with positive coefficients; Ca*Si, P*S and P*Si also occur frequently, and always with negative coefficients. In hemispherical temperature regressions Al*Ca, Ca*Fe, and Na*P often occur, again always with positive coefficients; Ca*Si, Fe*S and P*S often occur, and always with negative coefficients. Across the ten best ten-term regressions for each AFT the

coefficients in the different regressions are fairly constant, exhibiting standard deviations of 10-20% relative. For example, in ten regressions on hemispherical temperature the coefficients of the common terms and their standard deviations are: Ca*Fe 41,910 +/- 4810, Ca*Si -11,740 +/- 940, Fe*S -47,610 +/- 8300, P*S -411,100 +/- 31,500.

Simple sensitivity analysis calculations have been made to determine, for various regression models, the effect of an analytical error of 1% relative upon the estimated AFT. For the best 10-term regression on softening temperature the average sensitivity for the ten ashes analyzed is 4.0°F per % relative error. The most sensitive analyte is SiO_2, for which a 1% relative analytical error produces an error of estimation of 18°F (10 K). This may be unacceptable for laboratories using atomic absorption analysis, for which repeatability for SiO_2 is 2% absolute or about 5% relative.[16] Using the second best regression (with a loss in RMSE of only 0.1°F) the average sensitivity is 2.9°F per % relative error, and that for SiO_2 is reduced from 18° to 9.8°F. The best ten-term regression on hemispherical temperature shows an average sensitivity of 2.6°F per % relative error, and a sensitivity of 9.2°F per % relative error in SiO_2 determination. The eighth best regression (which gives away 0.4°F in RMSE) shows an average sensitivity of 2.1°F/% and for SiO_2 a sensitivity of 5.2°F/%. As a practical matter it is obviously sensible to determine not only the best valid regression but also a group of regressions, perhaps the ten best valid regressions. The most useful of these can then be selected on the basis of estimated analytical errors and sensitivity analysis for each candidate regression.

ACKNOWLEDGMENT

We gratefully acknowledge financial support of this work through the Robinson Professorship of The Ogden Foundation and a faculty research grant from Western Kentucky University.

REFERENCES

1. Method of Preparing Coal Samples for Analysis, ASTM Method D 2013, Annual Book of ASTM Standards, Vol. 5.05, American Society for Testing and Materials, Philadelphia, PA (published annually).

2. Test Method for Fusibility of Coal and Coke Ash, ASTM Method D 1857 [ISO 540], in reference 1.

3. Rees, O. W., Composition of the Ash of Illinois Coals, Circular 356, Illinois State Geol. Survey, Urbana, IL, 1964.

4. Sondreal, E. A.; Ellman, R. C., Fusibility of Ash from Lignite and its Correlation with Ash Composition, USBM Rept. GFERC/RI-75-1, Pittsburgh, PA, 1975.

5. Winegartner, E. C.; Rhodes, B. T., J. Eng. Power 1975, 97, 395.

6. Vorres, K. W., J. Eng. Power 1979, 101, 497.

7. Gray, V. R., Fuel 1987, 66, 1230.

8. Slegeir, W. A.; Singletary, J. H.; Kohut, J. F., J. Coal Quality 1988, 7, 48.

9. Riley, J. T.; Lloyd, W. G.; Risen, M. A.; Gilleland, S. R.; Tibbitts, R. L., Proc. Intl. Coal Test. Conf. 1989, 7, 58.

10. Lloyd, W. G.; Riley, J. T.; Risen, M. A.; Gilleland, S. R.; Tibbitts, R. L., Energy & Fuels 1990, 4, 360.

11. Riley, J. T.; Gilleland, S. R.; Forsythe, R. F.; Graham, H. D., Jr.; Hayes, F. J., Proc. Intl. Coal Test. Conf. 1989, 7, 32.

12. The Statistical Analysis System, SAS Institute, Inc., Cary, NC 27512.

13. Mason, R. L.; Gunst, R. F.; Hess, J. L., Statistical Design and Analysis of Experiments, Wiley, New York, 1989, p. 490.

14. Chatterjee, S.; Price, B., Regression Analysis by Example, Wiley, New York, 1977, pp 155ff.

15. Arkin, H.; Colton, R. R., Tables for Statisticians, Barnes & Noble, Inc., New York, 2nd ed., 1963, p. 158.

16. Standard Test Method for Major and Minor Elements in Coal and Coke Ash by Atomic Absorption, ASTM Method D 3682, in reference 1.

Table 1

Ranges of Properties of Coals and Ashes[a]

	Low	Mean	High
Coals			
rank	ligA	---	mvb
moisture	1.1%	10.9%	18.4%
% ash[b]	5.8%	11.4%	18.9%
% volatile matter[b]	25.3%	38.2%	44.1%
% carbon[b]	55.3%	67.5%	84.4%
% hydrogen[b]	3.33%	4.19%	5.06%
% nitrogen[b]	0.38%	1.04%	1.57%
% sulfur[b]	0.34%	1.08%	3.78%
Btu/lb[b]	8,770	11,500	14,700
MJ/kg[b]	20.4	26.7	34.1
Hardgrove Index	34	47	90
Free Swelling Index	0	2	9
Ash Composition			
SiO_2	33.1%	40.1%	50.4%
Al_2O_3	14.7%	22.2%	24.7%
CaO	0.55%	10.6%	26.9%
Fe_2O_3	3.49%	8.8%	24.1%
SO_3	0.72%	7.8%	10.5%
MgO	1.06%	2.28%	4.59%
K_2O	0.16%	1.37%	2.63%
P_2O_5	0.01%	0.77%	2.36%
TiO_2	0.82%	1.11%	1.66%
Na_2O	0.51%	0.91%	1.20%

[a] Coal data are from the seven source coals; ash data are from the suite of 70 ashes. [b] Calculated on a dry, ash-included basis.

Table 2

Precision of Ash Fusion Temperature Determinations[a]

Fusion Temperature, °F	DF	Std dev, °F	Avg Error, °F[b]
Initial Deformation	94	20.2	16.1
	(89)	(16.1)	(12.9)
Softening	95	13.4	10.7
	(91)	(11.1)	(8.9)
Hemispherical	94	21.8	17.4
	(89)	(19.1)	(15.3)
Fluid	93	42.0	33.5
	(89)	(35.5)	(28.3)

[a] First figures given are obtained with all 70 ashes. Figures in parentheses are obtained after rejection of three outlier ashes.

[b] Estimated by Eqn. (2).

Table 3

Best Regression Fits at Two Values of R(critical)[a]

	R(critical) = 0.99		R(critical) = 0.85	
terms	R^2	RMSE, °F	R^2	RMSE, °F
3	.825	64.2°	.766	74.2°
4	.859	58.2	.804	68.5
5	.885	52.9[b]	.855	59.3
6	---	[c]	.879	54.5
7	---	[c]	.895	51.2
8	---	[c]	.908	48.5
9	---	[c]	.914	47.2
10	---	[c]	.921	45.5

[a] Regressions meeting the criterion that SEI < 90°F [< 50 K].

[b] Fourth best regression ranked by R^2; SEI's of first three regressions > 200°F.

[c] None of the first ten regressions ranked by R^2 have SEI's below 90°F.

Table 4

Correlation Clusters of Regressors at Various Levels of $R_{critical}$

$R_{critical}$	terms in clusters	total terms in clusters	total free terms
0.99	5	5	50
0.98	6, 4, 3, 2, 2, 2	19	36
0.95	7, 6, 5, 4, 4, 3, 2	31	24
0.92	10, 7, 7, 5, 5	36	19
0.90	19, 8, 7, 5	39	16
0.88	27, 7, 5	41	14
0.85	40, 5, 3	48	7

Table 5

Best Regressions on Initial Deformation Temperature

Intcpt.°F	Terms and Coefficients					SEI.°F	R^2	RMSE.°F	average error.°F
	S*Si	K*P	Ca*Fe	Al*Na					
1,863°F	-8.01E3	1.26E6	1.61E4	1.40E5		36.4	.803	72.1	57.5
	Na*Si	Fe*S	Ca*Ti	Ca*Fe	Al*Na				
1,822	5.60E4	-5.08E4	-3.49E5	7.85E4	1.43E5	34.3	.844	64.8	51.7
	P	S*Si	Ca*Ti	Ca*Fe	Fe*Na				
2,093	1.66E4	-1.82E4	-2.50E5	6.26E4	-3.99E5				
	Al*Na								
	2.96E5					37.1	.877	58.0	46.3
	P	Mg*P	S*Si	Ca*Ti	Ca*Fe				
2,138	1.37E4	1.09E5	-1.94E4	-2.87E5	6.63E4				
	Fe*Na	Al*Na							
	-4.54E5	3.20E5				41.1	.886	56.1	44.8
	P	S*Si	P*Si	P*S	Ca*Ti				
2,080	1.46E5	-1.81E4	-2.49E5	-3.50E5	-3.23E5				
	Ca*Fe	Fe*Na	Al*Na						
	6.28E4	-4.43E5	3.50E5			50.4	.9058	51.5	41.1
	P	P*Si	K*S	P*S	Fe*K				
1,654	1.95E5	-3.08E5	-1.55E5	-6.17E5	1.21E5				
	Ca*Ti	Ca*Fe	Fe*Na	Al*Na					
	-3.90E5	7.68E4	-7.73E5	3.71E5		68.8	.9147	49.5	39.5
	P	P*Si	K*S	P*S	K*Ti				
1,609	1.94E5	-3.21E5	-1.63E5	-5.82E5	7.69E5				
	Fe*K	Ca*Ti	Ca*Fe	Fe*Na	Al*Na				
	9.03E4	-3.54E5	7.40E4	-7.30E5	3.50E5	69.8	.9212	47.9	38.2

Table 6

Best Regressions on Softening Temperature

Intcpt.°F	Terms and Coefficients					SEI.°F	R^2	RMSE.°F	average error.°F
	P*S	K*P	Na*P	Al*Na					
2,004°F	-3.76E5	6.92E5	3.15E6	7.30E4		27.5	.852	59.5	47.5
	Ca*Si	P*S	Al*K	Al*Ca	Na*P				
1,896	-5.34E3	-5.52E5	4.09E4	1.48E4	5.64E6	54.4	.882	53.5	42.7
	Ca*Si	Fe*Si	K*S	K*Na	Ca*Fe				
2,344	-9.04E3	-5.86E3	-5.50E5	7.07E6	5.80E4				
	Fe*Na								
	-3.62E5					55.8	.9047	48.5	38.7
	P	Ca*Si	P*Si	P*S	Al*K				
1,827	1.23E5	-9.31E3	-2.20E5	-8.26E5	5.21E4				
	Al*Ca	Na*P							
	2.23E4	4.64E6				47.9	.9240	43.6	34.8
	Ca*Si	Fe*Si	P*S	Fe*S	K*Na				
2,212	-1.09E4	-2.73E3	-4.27E5	-4.33E4	1.69E6				
	Ca*Fe	Al*Ca	Na*P						
	5.15E4	8.48E3	4.20E6			65.3	.9286	42.7	34.0
	Ti	Fe*Mg	Si*Ti	K*S	P*S				
1,806	1.33E5	-1.75E4	-2.89E5	-3.03E5	-5.48E5				
	K*Na	Fe*K	Al*K	Na*P					
	2.62E6	-7.48E4	1.10E5	4.64E6		53.5	.9356	40.9	32.6
	Fe	Mg*P	Fe*Mg	Al*Fe	S				
2,248	2.97E3	2.29E5	-8.57E4	-2.67E4	1.37E4				
	S*Si	Al*K	Ca*Na	Ca*Fe	Al*Na				
	-5.80E4	7.69E4	-2.28E5	4.65E4	3.28E5	46.8	.9420	39.1	31.2

Table 7

Best Regressions on Hemispherical Temperature

Intcpt.°F	Terms and Coefficients					SEI.°F	R^2	RMSE.°F	average error.°F
	P*S	K*P	Na*P	Al*Na					
2,078	-3.53E5	7.93E5	2.77E6	6.21E4		25.2	.872	54.6	43.6
	Ca*Si	P*S	K*Ti	Al*Ca	Na*P				
1,897	-5.35E3	-4.80E5	1.09E6	1.61E4	4.75E6	69.3	.896	49.7	39.6
	Ca*Si	P*S	Fe*S	K*P	Ca*Fe				
2,070	-4.41E3	-1.09E5	-3.62E4	1.29E6	4.14E4				
	Al*Na								
	1.18E5					25.8	.9127	45.9	36.6
	Ca*Si	K*S	P*S	Fe*S	Ca*Fe				
2,195	-1.18E4	1.34E5	-5.72E5	-4.28E4	4.01E4				
	Al*Ca	Na*P							
	1.46E4	5.60E6				23.1	.9287	41.8	33.4
	P	Ca*Si	P*S	Fe*S	K*Na				
2,066	1.81E4	-1.16E4	-3.61E5	-3.04E4	1.14E6				
	Ca*Fe	Al*Ca	Na*P						
	3.42E4	1.73E4	2.22E6			36.7	.9379	39.3	31.4
	Fe	Ca*Si	Fe*Si	P*S	Fe*S				
2,192	6.54E3	-1.11E4	-1.62E4	-4.65E5	-4.26E4				
	Al*K	Ca*Fe	Al*Ca	Na*P					
	5.33E4	3.34E4	1.43E4	4.55E6		66.2	.9446	37.5	29.9
	P	Fe	Ca*Si	Fe*Si	P*S				
2,256	9.71E5	4.53E3	-1.21E4	-1.16E4	-3.88E5				
	Fe*S	K*Na	Ca*Fe	Al*Ca	Na*P				
	-4.82E4	1.40E6	4.31E4	1.22E4	2.98E6	74.6	.9477	36.7	29.3

Table 8

Best Regressions on Fluid Temperature

Intcpt.°F	Terms and Coefficients					SEI.°F	R^2	RMSE.°F	average error.°F
	S*Si	P*S	K*P	Al*Na					
2,185°F	-8.74E3	-6.09E4	1.00E6	1.73E5		24.9	.892	53.1°F	42.3°F
	Mg*P	S*Si	P*S	K*P	Al*Na				
2,171	9.97E4	-8.52E3	-1.06E5	1.06E6	1.78E5	24.6	.9010	51.2	40.8
	S*Si	K*P	Ca*Ti	Ca*Fe	Fe*Na				
2,319	-1.88E4	6.33E5	-1.11E5	3.30E4	-2.48E5				
	Al*Na								
	2.90E5					34.0	.9172	47.1	37.6
	Mg*P	Fe*Mg	S*Si	P*S	K*P				
2,155	2.19E5	-3.45E4	-1.29E4	-1.39E5	9.50E5				
	Ca*Fe	Al*Na							
	1.27E4	2.40E5				23.2	.9266	44.8	35.7
	Ti	Mg*P	Fe*Mg	S*Si	Si*Ti				
2,203	6.66E4	2.33E5	-3.91E4	-1.45E4	-1.40E5				
	P*S	K*P	Al*Na						
	-2.05E5	1.10E6	2.44E5			55.3	.9313	43.7	34.8
	Ti	Mg*P	Fe*Mg	S*Si	Si*Ti				
2,204	5.02E4	2.35E5	-4.41E4	-1.57E4	-1.10E5				
	P*S	K*P	Ca*Fe	Al*Na					
	-1.89E5	1.11E6	7.83E3	2.57E5		54.1	.9355	42.7	34.0
	Ti	Mg*P	Fe*Mg	S*Si	P*Si				
2,283	6.36E4	2.35E5	-5.13E4	-1.15E4	5.66E4				
	Si*Ti	P*S	K*Na	K*Ti	Al*Na				
	-2.28E5	-2.81E5	-2.01E6	2.21E6	3.14E5	79.9	.9391	41.8	33.3

Table 9

Indicators of Multicollinearity in Softening Temperature Regressions

	10 terms[a]	20 terms[b]	30 terms[b]	55 terms
R^2 (uncorrected)	.942	.9547	.9667	.9770
rmse	39.1°F 21.7 K	37.9°F 21.1 K	36.4°F 20.2 K	50.5°F 28.1 K
SEI	46.8°F 26.0 K	813°F 452 K	>2120°F >1170 K	>21,000°F >11,600 K
Avg precision of first 10 coefficients[c]	15.8 %	159 %	272 %	>2,400 %
Avg instability of first 10 coefficients to a dummy variable[d]	0.01%	4.6 %	32.1%	400 %
Avg instability of first 10 coefficients to removal of 14 cases[e]	14.1 %	111 %	449 %	>1,500 %

[a] Best regression from Table 6.

[b] Selected by forward selection procedure.

[c] [S.E. of coefficient]/[coefficient] * 100%.

[d] Average shift in value of coefficients upon introduction of a random number variable (see text).

[e] Average shift in value of coefficients upon deletion of every fifth case in the dataset.

FIGURE 1

CORRELATIONS AMONG 19 TERMS

R(crit) = 0.98

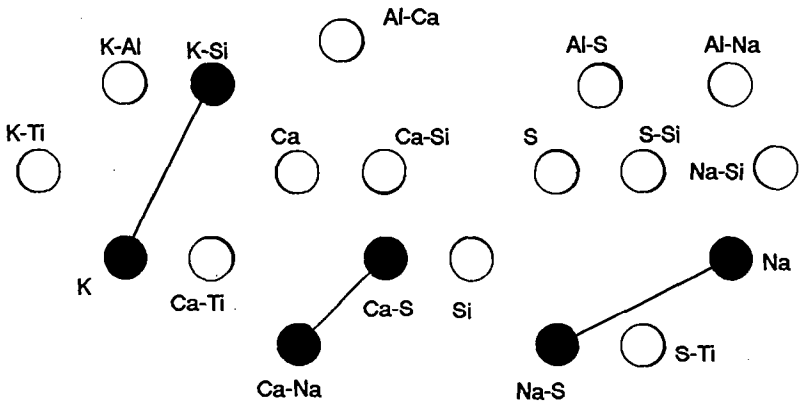

FIGURE 2

CORRELATIONS AMONG 19 TERMS

R(crit) = 0.90

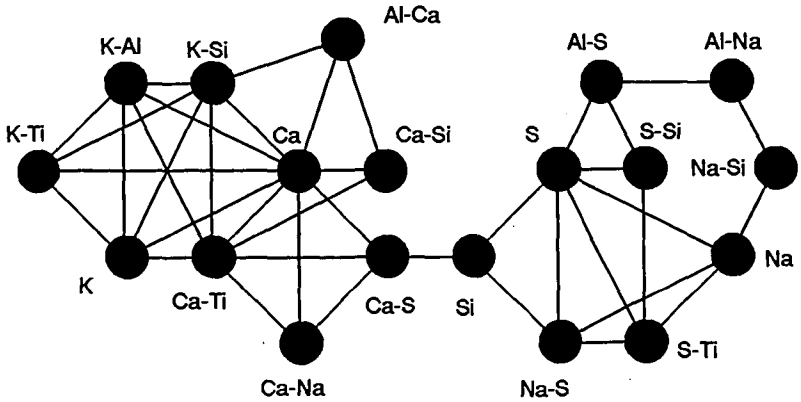

FIGURE 3

SELECTION TO AVOID COLLINEARITIES

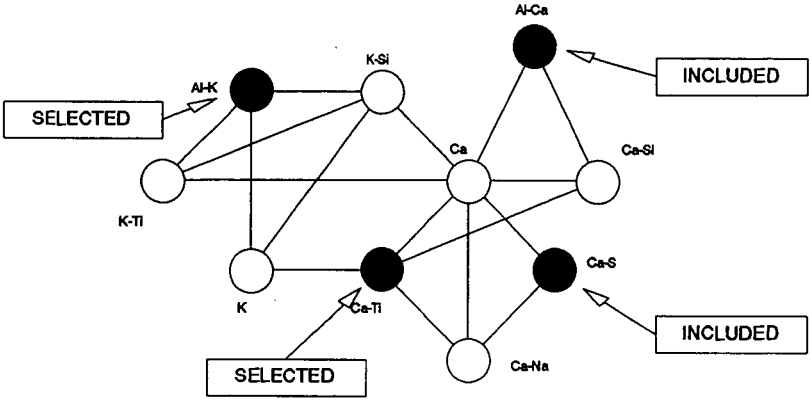

FIGURE 4

ESTIMATE OF INITIAL DEFORMATION TEMP.
70 CASES

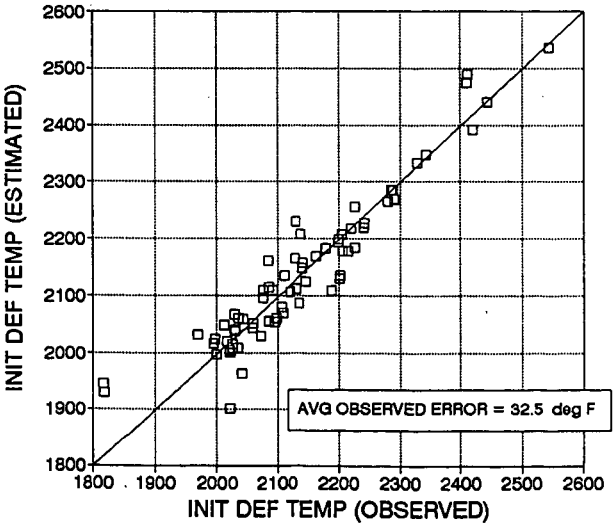

FIGURE 5

ESTIMATE OF SOFTENING TEMPERATURE
70 CASES

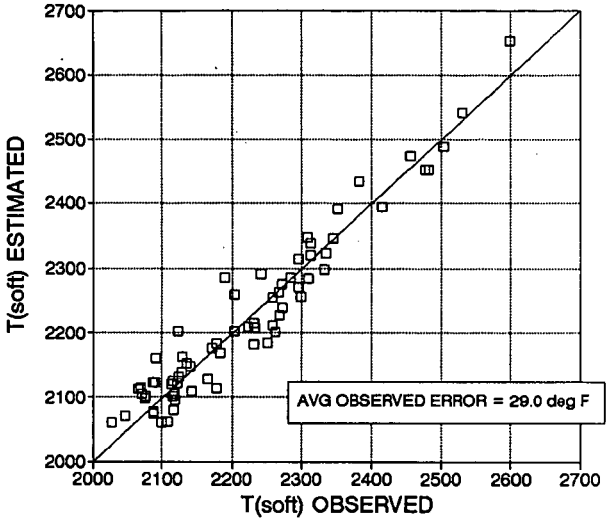

FIGURE 6

ESTIMATE OF HEMISPHERICAL TEMPERATURE
70 CASES

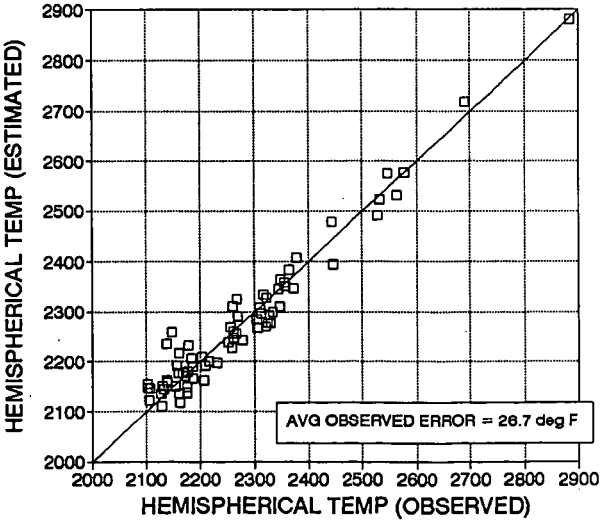

FIGURE 7

ESTIMATE OF FLUID TEMPERATURE
70 CASES

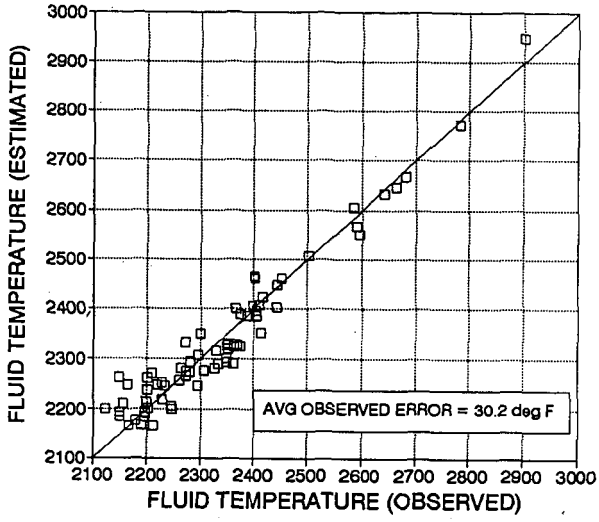

FIGURE 8

SOFTENING TEMPS OF 14 "NEW" ASHES
USING BEST SOFTENING TEMP REGRESSION

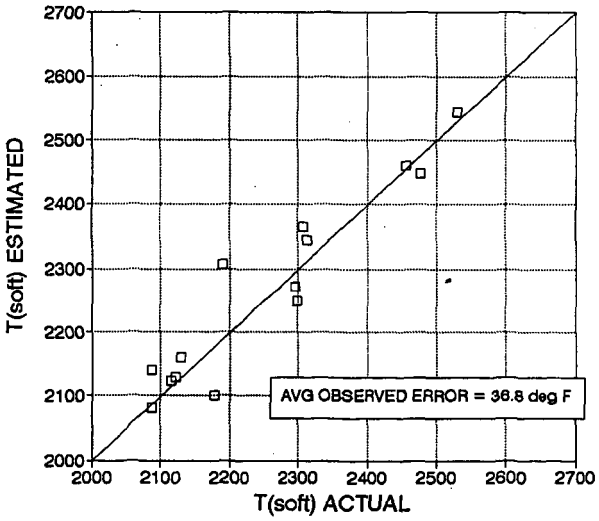

PREDICTING VAPOR PRESSURES OF TAR AND METAPLAST DURING COAL PYROLYSIS*

Thomas H. Fletcher
Combustion Research Facility
Sandia National Laboratories
Livermore, CA 94551-0969

David M. Grant and Ronald J. Pugmire
Department of Chemistry
University of Utah
Salt Lake City, UT 84112

INTRODUCTION

Models of coal pyrolysis have progressed from simple one or two step empirical Arrhenius expressions that correlate total mass release during devolatilization,[1,2] as reviewed by Anthony and Howard,[3] to detailed descriptions of hydrocarbon chemistry and mass transport.[4-8] These models describe the yields and compositions of pyrolysis products from coal under a wide range of heating conditions and ambient pressures. During pyrolysis of softening coals, a liquid phase appears that is referred to as metaplast. Release of pyrolysis gases and tar vapors inside the particle cause bubble formation in the softened coal particle, followed by swelling (increase in the particle diameter) with large internal voids (cenosphere formation). The softened state is followed by crosslinking or repolymerization which solidify the char matrix. As the coal particle is heated to sufficiently high temperatures, the light species in the metaplast are released as hydrocarbon vapors, along with light gases. Coal tar is generally defined to consist of those species which are released from the coal during pyrolysis which condense at room temperature and pressure. Low rank coals and lignites generally give low tar yields, and do not exhibit much softening or swelling behavior; this non-softening behavior may be caused by early crosslinking reactions.[9] High rank coals (i.e., anthracites and low volatile bituminous coals) contain low amounts of volatile matter, and hence coal particles remain relatively intact during pyrolysis unless fragmentation occurs.

Mass transport affects coal pyrolysis in two ways: (1) as the ambient pressure increases, the tar yield decreases, and (2) as particle size increases, the tar yield decreases. However, there seem to be regions where the two mass transport effects are not controlling. For instance, in vacuum, the small pressure generated inside the pyrolyzing coal particle from the release of light gases and tar vapors may control the process. Also, total volatiles yields from a lignite were observed to remain constant with increasing ambient pressure,[10] although this is probably due to the low tar yield of the lignite. Changes in coal pyrolysis yields as a function of particle size for diameters less than 200 μm are small.[11]

* Work supported by the U. S. Department of Energy's Pittsburgh Energy Technology Center's Direct Utilization AR&TD Program and by the Advanced Combustion Engineering Research Center at BYU and the Univ. of Utah, which is supported by the National Science Foundation. Additional support was provided through the Consortium for Fossil Fuel Liquefaction Science by DOE/PETC.

Different theoretical treatments of mass transfer effects on coal tar evolution are reviewed by Suuberg[12]. Bubble transport models have recently been developed to describe intraparticle transport of tar and gases, along with the resultant characteristics of the char particle.[8,13] The radial transport of bubbles from the particle interior to the particle surface is calculated in these models using a momentum equation and an effective diffusivity. Other models[5-7] assume that the particle is small, and do not treat radial transport of material from the interior of the particle. These models are generally applicable for particles less than 200 μm in diameter, where product yields are nearly independent of particle size. In all of these models, however, the effects of pressure are treated assuming some relationship between vapor pressure, molecular weight, and temperature. As the ambient pressure increases, only the species with high vapor pressures (i.e., low molecular weight) are released from the metaplast as tar. In vacuum, even relatively high molecular weight species may have vapor pressures higher than the ambient pressure and are released as tar.

VAPOR PRESSURES OF COAL PYROLYSIS PRODUCTS

Vapor pressure data on coal tar are unavailable, so vapor pressure correlations based on compounds found in coal tar are generally used to develop vapor pressure correlations based on molecular weight. Unger and Suuberg[14] proposed a vapor pressure correlation based on fitting the boiling points of six aromatic hydrocarbons at a total pressure of 6.6×10^{-4} atm (0.5 mm Hg). These compounds were selected because of their high molecular weight (198 to 342) and their lack of heteroatoms. The resulting correlation is:

$$P_i^v = \alpha \, exp\left(\frac{-\beta \, MW_i^{\gamma}}{T}\right) \tag{1}$$

where $\alpha = 5756$, $\beta = 255$, and $\gamma = 0.586$, and units are in atmospheres and Kelvin. The form of Eq. 1 is related to the Clausius-Clapeyron equation, assuming that the heat of vaporization is proportional to molecular weight.

Several investigators have attempted to use the Unger-Suuberg correlation to describe tar release from the metaplast. Many investigators use the form of the Unger-Suuberg correlation, but not the constants proposed by Unger and Suuberg. Solomon and coworkers[5] used the Unger-Suuberg correlation multiplied by an arbitrary factor of 100 in order to fit tar and total coal volatiles yields as a function of pressure. Niksa[6] used a similar form that was easy to integrate analytically, with $\gamma = 1$, and used α and β as adjustable parameters in a comprehensive devolatilization model in order to fit tar molecular weight data from Unger and Suuberg.[15] Oh and coworkers[8] and Hsu[13] found that by using the Unger-Suuberg correlation, good agreement could be achieved with high temperature pyrolysis data ($T > 873$ K) but not with low temperature data ($T < 873$ K). The current work suggests why the Unger-Suuberg correlation does not apply to coal pyrolysis conditions, and suggests an alternate correlation.

The vapor pressure correlation of Unger and Suuberg[14] was based only on low vapor pressures (0.5 mm Hg), and has been extrapolated to much higher pressures and molecular weights in coal devolatilization models. Reid, et al.[16] recommend using the Antoine equation to calculate vapor pressures (if constants are available) when the vapor pressure is in the range 10 to 1500 mm Hg

(.01 to 2 atm). However, Reid and coworkers conclude that no correlation produces good agreement with data for P_i^v < 10 mm Hg (.01 atm). The approach used here is to develop new constants for Eq. 1 based on additional data at both low and high vapor pressures in order to apply to a wide range of coal pyrolysis conditions..

Gray, et al.[17,18] measured vapor pressures as a function of temperature for twelve narrow boiling fractions distilled from coal liquids produced from SRC-II processing of Pittsburgh seam bituminous coal. In their study, temperatures ranged from 267 K to 788 K, and the coal liquids exhibited molecular weights as high as 315 with vapor pressures as high as 35 atm. It is assumed that these are representative of low molecular weight tars released during primary pyrolysis. Gray and coworkers discuss equations of state that fit the vapor pressure data using critical properties of the liquid (i.e., the critical temperature and pressure). However, for the purposes of coal pyrolysis, critical properties are not well known, and simpler correlations are preferable.

The constants derived from a curve fit of the data of Gray, et al.[17,18] using Eq. 1 are shown in Table 1, along with the expressions used by Unger and Suuberg and by Niksa. This correlation, referred to hereafter as the Fletcher-Grant correlation, agrees very well with the measured vapor pressures of the different molecular weight fractions, as shown in Fig. 1. It is interesting that the coefficient on the molecular weight (γ) from the Fletcher-Grant curve fit to the data of Gray and coworkers is 0.590, which is very close to the value of 0.586 found by Unger and Suuberg. The value of β from the Unger-Suuberg correlation is 255, which also compares reasonably well with the value of 299 in the Fletcher-Grant correlation. The major difference between the two correlations is the value for α; the value of α in the Fletcher-Grant correlation is fifteen times greater than in the Unger-Suuberg correlation. This trend is consistent with recent modeling efforts[5], where the vapor pressure from Unger-Suuberg correlation was multiplied by a factor of 100 in order to achieve agreement with a wide range of experimental data.

The Fletcher-Grant vapor pressure correlation presented in Table 1 was compared with boiling point data for 111 compounds at pressures of 5, 60, 760, and 7600 mm Hg (0.0066, 0.079, 1.0, and 10 atm). Boiling point data were obtained from Perry and Chilton;[19] a list of the selected compounds is available.[20] Molecular weights as high as 244 are considered in this set of compounds. Long chain alkanes (hydrogen to carbon ratios greater than 1.5) and heteroatoms with more than two oxygen atoms were not considered in this data set, since they do not occur in coal tars to a significant extent. Boiling point data at 10 atmospheres were only available for five compounds (benzene, phenol, toluene, aniline, and ethylbenzene). The Fletcher-Grant correlation was found to agree surprisingly well with the boiling points of these compounds at all four pressures, as shown in Fig 2a. This is a simplistic vapor pressure expression, and the variations in the chemical structures of the various compounds are not considered. The correlation proposed by Unger and Suuberg[14] agrees with this set of data at the lowest pressure, but predicts higher boiling points than the average of the data at pressures of 1 and 10 atm (see Fig. 2a).

Coal pyrolysis experiments have been conducted at pressures as high as 69 atm,[21] with reported tar molecular weight distributions extending into several thousand amu. Figure 2b shows an extrapolation of three vapor correlations to higher temperatures, pressures, and

molecular weights than shown in the left panel, representing a wide range of pyrolysis conditions. The difference between the Fletcher-Grant correlation and the Unger-Suuberg correlation becomes more pronounced at higher pressures. For example, the predicted boiling point of a species with a molecular weight of 400 amu by the Fletcher-Grant correlation is nearly 500 K lower than that predicted by the Unger-Suuberg correlation. In contrast, the parameters in the vapor pressure correlation used by Niksa[6] were used as fitting parameters to achieve agreement with measured molecular weight distributions. As shown in Fig. 2b, the Niksa correlation gives boiling points that are 800 K lower than predicted by the Fletcher-Grant correlation at atmospheric pressure for a molecular weight of 400 amu. The Fletcher-Grant vapor correlation agrees with measured vapor pressures of coal liquids and boiling points of pure compounds over a wide range of pressures; the constants α, β, and γ used in the correlation are fixed, thereby reducing the umber of unknown parameters in coal pyrolysis models.

APPLICATION TO PRESSURE-DEPENDENT COAL PYROLYSIS CALCULATIONS

The chemical percolation devolatilization (CPD) model was developed by Grant, et al.[7] to describe coal pyrolysis based on the chemical structure of the parent coal. The CPD model treats coal as an array of aromatic clusters, connected by aliphatic labile bridges. As the coal is heated, labile bridge scission creates finite fragments consisting of several aromatic clusters which are no longer attached to the infinitely large coal matrix. Percolation lattice statistics are used to describe the relationship between labile bridge scission and the generation of aromatic clusters of finite size (forming tar and metaplast). This model was extended to treat the effects of heating rate and temperature,[22] and recently extended to treat vapor-liquid equilibrium between tar and metaplast as well as crosslinking of the metaplast.[23] In the CPD model, the assumption is made that all gaseous species (light gases and tar vapors) are convected away from the particle due to the increase in volume between the gas and solid. The convection step is assumed to be instantaneous compared with the chemical reactions of bond scission and char formation. This approach is similar to those of Niksa[6] and Solomon, et al.,[5] who treat the internal mass transfer in an approximate manner, based on the convection of tars by light gases. The low molecular weight clusters are released as tar vapor, while the high molecular weight clusters are not vaporized, and remain in a liquid or solid state within the char matrix as metaplast.

The Fletcher-Grant correlation is combined with Raoult's law and a flash distillation calculation[24] at each time step to determine the partitioning between vapor and liquid for each aromatic cluster size. A detailed description of the equations used is provided by Fletcher and Hardesty.[20,24] The treatments of mass transfer determine where vapor-liquid equilibrium between tar and metaplast may occur. Bubble transport models assume vapor-liquid equilibrium within the small bubbles and at the vapor-liquid interface in the large bubbles. In the CPD model, the tar vapor and light gases leave the vicinity of the particle as they are formed, and only the tar and light gas formed in the last time step are considered to be in vapor-liquid equilibrium with the metaplast. In a different approach used by Solomon, et al.[5] and by Niksa,[6] the tar vapor is convected only by the light gas, and it is assumed that the volume of vaporized tar is insignificant compared to the volume of evolved light gas. If tar vapor is formed, but no light gases are formed at the same time, the tar vapor is trapped within the particle. Other approaches allow for the possibility that some liquid from the metaplast may be entrained in the light gas in an attempt to explain reported molecular weights greater than 1000 amu,[12] where

the molecular weight is too high to allow vaporization. However, there is a large disagreement on the methods for measurement of tar molecular weight distributions, and recent data do not exhibit such large molecular weights.[5,25]

The vapor pressures predicted by the Fletcher-Grant correlation drop steeply with molecular weight, implying that there is little vaporization of high molecular weight compounds. In other words, most of the tar vapor at a given temperature consists of compounds with vapor pressures higher than the ambient pressure. It is assumed that the volume of tar vapor alone is sufficient to cause rapid evolution from the vicinity of the particle, without the necessity of transport by lighter gases. This is consistent with experimental results of Suuberg, et al.[12] which indicate that tar evaporation is more important than transport of liquid tar by light gas.

Comparisons between predictions made with the CPD model and experimental tar and total volatiles yields measured as a function of pressure are presented in Fig. 3. Data for a Pittsburgh #8 bituminous coal are from heated grid experiments by Anthony[10] and by Suuberg and coworkers.[21] Particle heating rates in these experiments were approximately 1000 K/s for the Suuberg data and 700 K/s for the Anthony data, with a final temperature of 1273 K and hold times ranging from 2 to 10 s. Model predictions were made with a heating rate of 1000 K/s and a 5 s hold time at 1273 K using the chemical structure coefficients from Solum, et al.[26] for a Pittsburgh No. 8 coal, with slight adjustments made to two parameters to match the tar and total volatiles yield data at 1 atm.[23]

The dashed line in Fig. 3a represents the predicted yield if there is no pressure drop inside the particle, whereas the solid line represents a minimum internal particle pressure P_{min} of 0.01 atm. A minimum internal particle pressure of 0.2 atm was used by Solomon and coworkers.[5] The pressure buildup inside the particle is due to volume expansion of light gases and tars during coal devolatilization. The predictions made using $P_{min} = 0.01$ agree quite well with the reported total volatiles and tar yields for the bituminous coal.

Model predictions of the pressure-dependent devolatilization behavior of a lignite are shown in Fig. 3b, along with data from Anthony[10] and Suuberg.[27] The tar yield for this lignite is very low, and hence the small effect of pressure on total yield compared to the bituminous coal. Total volatiles yields for the lignite decrease only slightly with increasing pressure in both the experimental data and the model predictions. The predicted tar yield decreases slightly with increasing pressure, but the gas yield increases to compensate, and hence the slight decrease in total volatiles yield with increased pressure.

The lignite contains a large amount of mass in the side chains and bridges; the number of aliphatic carbons per cluster determined by NMR analyses for lignites is twice that determined for bituminous coals.[23,28] At atmospheric pressure, the gas precursors (side chains) attached to the tar are released as tar, and can detach from the tar as light gas if the ambient gas temperature is high enough. In heated grid experiments, the gas is immediately quenched, and the gas precursors remain in the tar. At elevated pressures, more tar remains in the lignite, and the associated side chains are released as light gas. Due to the large mass in the side chains, the increased gas yield largely compensates for the decrease in tar yield, and the total volatiles yields is almost independent of pressure.

REFERENCES

1. Badzioch, S. and P. G. W. Hawksley, *Ind. Eng. Chem. Process Des. Develop.*, **9**, 521 (1970).
2. Kobayashi, H., J. B. Howard, and A. F. Sarofim, *Sixteenth Symp. (Int.) on Comb.*, The Combustion Institute, Pittsburgh, PA, 411 (1976).
3. Anthony, D. B. and J. B. Howard, *AIChE J*, **22**:4, 625 (1976).
4. Gavalas, G. R., *Coal Science and Technology 4: Coal Pyrolysis*, Elsevier, New York, p. 19 (1982).
5. Solomon, P. R., D. G. Hamblen, R. M. Carangelo, M. A. Serio, and G. V. Deshpande, *Energy & Fuels*, **2**, 405 (1988).
6. Niksa, S., *AIChE J*, **34**:5, 790 (1988).
7. Grant, D. M., R. J. Pugmire, T. H. Fletcher, and A. R. Kerstein, *Energy & Fuels*, **3**, 175 (1989).
8. Oh, M. S., W. A. Peters, and J. B. Howard, AIChE J., **35**:5, 775 (1989).
9. Solomon, P. R., M. A. Serio, G. V. Deshpande, and E. Kroo, *Energy & Fuels*, **4**, 42 (1990).
10. Anthony, D. B., "Rapid Devolatilization and Hydrogasification of Pulverized Coal," Sc. D. Thesis, Department of Chemical Engineering, Massachusetts Institute of Technology (1974).
11. Anthony, D. B., J. B. Howard, H. C. Hottel, and H. P. Meissner, *Fifteenth Symp. (Int.) on Comb.*, The Combustion Institute, Pittsburgh, PA, 1303 (1975).
12. Suuberg, E. M., "Mass Transfer Effects in Pyrolysis of Coals: A Review of Experimental Evidence and Models," in Chemistry of Coal Conversion, edited by R. H. Schlosberg, Plenum Press, New York, p. 67 (1985).
13. Hsu, J., "Swelling, Mass Transport, and Chemical Kinetics in Bituminous Coal Pyrolysis," Sc.D. Thesis, Department of Chemical Engineering, Massachusetts Institute of Technology (1989)
14. Unger, P. E. and E. M. Suuberg, *ACS Div. of Fuel Chem.* prepr., **28**:4, 278 (1983).
15. Unger, P. E. and E. M. Suuberg, *Fuel*, **63**, 606 (1984).
16. Reid, R. C., J. M. Prausnitz, and T. K. Sherwood, *Properties of Gases and Liquids*, Third Ed., McGraw-Hill, San Francisco, p. 196 (1977).
17. Gray, J. A., C. J. Brady, J. R. Cunningham, J. R. Freedman, and G. M. Wilson, *Ind. Eng. Chem. Process Des. Dev.*, **22**, 410 (1983).
18. Gray, J. A., G. D. Holder, C. J. Brady, J. R. Cunningham, J. R., Freedman, and G. M. Wilson, *Ind. Eng. Chem. Process Des. Dev.*, **24**, 97 (1985).
19. Perry, R. H. and C. H. Chilton, *Chemical Engineers' Handbook*, Fifth Ed., McGraw-Hill, San Francisco, p. 3-49 (1973).
20. Fletcher, T. H. and D. R. Hardesty, "Coal Combustion Science: Task 1, Coal Devolatilization," DOE/PETC Quarterly Progress Report for January to March, 1990, edited by D. R. Hardesty, Sandia Report No. SAND90-8223, available NTIS (1990a).
21. Suuberg, E. M., W. A. Peters, and J. B. Howard, *Seventeenth Symp. (Int.) on Comb.*, The Combustion Institute, Pittsburgh, PA, 117 (1978).
22. Fletcher, T. H., A. R. Kerstein, R. J. Pugmire, and D. M. Grant, *Energy & Fuels*, **4**, 54 (1990).
23. Fletcher, T. H. and D. R. Hardesty, "Coal Combustion Science: Task 1, Coal Devolatilization," DOE/PETC Quarterly Progress Report for October to December (1990), publication in progress.
24. King, C. J., Separation Processes, McGraw-Hill, San Francisco, pp.70-71,511-512 (1971).

25. Freihaut, J. D., Proscia, W. M., and Seery, D. J., *Energy & Fuels*, **3**, 692 (1989).
26. Solum, M. S., R. J. Pugmire, and D. M. Grant, *Energy & Fuels*, **3**, 187 (1989).
27. Suuberg, E. M., "Rapid Pyrolysis and Hydropyrolysis of Coal," Sc. D. Thesis, Department of Chemical Engineering, Massachusetts Institute of Technology (1977).
28. Pugmire, R. J., M. S. Solum, D. M. Grant, S. Critchfield, and T. H. Fletcher, "Structural Evolution of Matched Tar/Char Pairs in Rapid Pyrolysis Experiments," accepted for publication in *Fuel* (1990).

Table 1
Vapor Pressure Correlations for Coal Pyrolysis Tar and Metaplast

$$P_i^v = \alpha \exp\left(\frac{-\beta\, MW_i^{\gamma}}{T}\right)$$

	α	β	γ
Unger-Suuberg[14]	5756	255	0.586
Niksa[6]	70.3	1.6	1.0
Fletcher-Grant (this work)	87,060	299	0.590

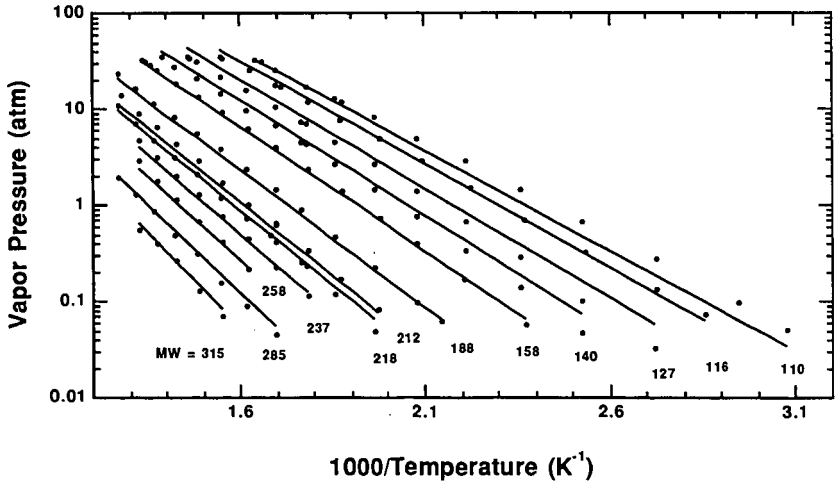

Figure 1. Comparison of the Fletcher-Grant vapor pressure correlation with vapor pressure data from Gray, et al.[17,18] for twelve narrow boiling fractions of coal liquids from a Pittsburgh seam coal.

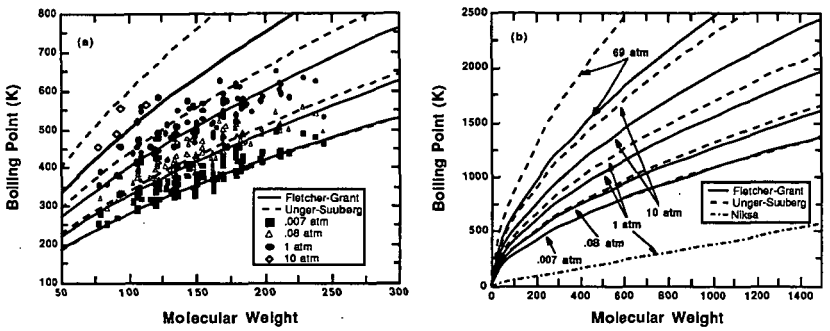

Figure 2. Comparison of the Fletcher-Grant, Unger-Suuberg,[14] and Niksa[6] vapor pressure correlations (a) with boiling point data for 111 organic compounds at pressures of .007, .08, 1, and 10 atm (5, 60, 760, and 7600 mm Hg) and (b) at pyrolysis condictions.

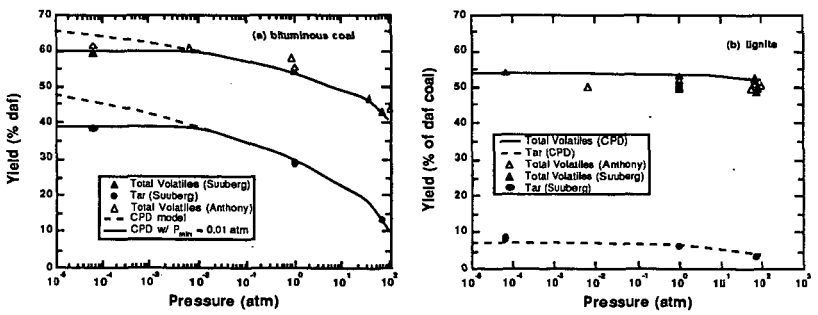

Figure 3. Comparison of CPD model predictions with pressure-dependent tar and total volatiles yield data from Anthony[10] and Suuberg, et al.[21,27] for (a) bituminous coal and (b) lignite. Dashed lines represent predictions with no minimum internal particle pressure; solid lines represent predictions with a minimum internal pressure of 0.01 atm.

SOLVENT SWELLING AS A MEASURE OF THE BREAKDOWN OF THE MACROMOLECULAR STRUCTURE OF COAL

E. M. Suuberg , Y. Otake[1] and S.C Deevi[2]
Division of Engineering
Brown University
Providence, RI 02912

Keywords: Coal Macromolecular Structure, Solvent Swelling, Pyrolysis

Introduction

The characterization of coal's macromolecular structure by the use of solvent swelling techniques has been the subject of renewed interest in recent years (see, for example, a review of the topic[1]). The systematic examination of the swellability of coals in various solvents has its roots in the work of Dryden[2,3], although the first attempts at quantitative analysis of coals macromolecular network structure by this method were made some time later[4]. It is only relatively recently that the technique has begun to find widespread application in the study of processing of coals[5-11].

Generally, solvent swelling is used as an index of the extent of crosslinking of the coal's structure; the more highly crosslinked the structure, the less swellable it is in a good solvent. Solvent swellability of quenched char residues has normally been used to obtain information regarding the conditions that favor so-called "retrograde reactions", which take the thermally degrading coal particle on a path to a char or coke product. This is marked by the loss of swellability in the char (i.e. the retrograde reactions crosslink the structure). The swelling data cannot normally be used to obtain quantitative information concerning the network structure of the chars for the same reason that such information cannot be obtained on coals themselves-- there is a lack of a proven, quantitatively reliable model of coal swelling. This is particularly the case when the swelling data are obtained using strong, specifically interacting solvents (e.g. pyridine). Nevertheless, the change in swellability of the char has been viewed as a valuable qualitative indication of crosslinking.

This presentation explores the application of the solvent swelling technique, using specifically reacting solvents, to the problem of tracking changes in pyrolysis char residues. It does so in the context of a number of new conclusions concerning the nature of the swelling process in specifically interacting solvents. It also explores the use of these techniques in a number of new ways.

---

[1] Present address: Osaka Gas Company, Ltd., Research Center, Osaka, Japan.

[2] Present address: Philip Morris U.S.A. Research Center, Richmond, Va.

Experimental

The general experimental approach involved examining changes in the macromolecular structure of various coals induced by pyrolysis of the coals in an inert gas environment. The effects of different pyrolysis conditions on the macromolecular structure was revealed by solvent swelling of the quenched chars. The pyrolyses were always performed in helium or nitrogen, so as to preclude oxygen contact while the samples were hot. The reactor system has been described in detail elsewhere[5,6]. No attempt was made in this case to prevent oxygen contact with the samples once they were cooled, but the time of exposure of any sample to air, after it was cooled, was generally only as long as necessary for preparation of the sample, as outlined below.

The solvent swelling procedures employed in this study have been described in detail elsewhere[12]. The technique involves a minor adaptation of earlier established methods for studying swelling by immersion in liquid solvents[13,14]. It involves the measurement of the change of height of a column of coal held in a constant diameter glass tube, after addition of liquid solvent to the tube. In our case, the tubes are 3 mm inner diameter and 5 cm in length. The measurements could thus be made on modest amounts of sample (50 to 100 mg). The height of the column of dry coal is determined after centrifugation for 3 min at 7500 rpm in a 30 cm horizontal rotor. Solvent was then added, with vigorous stirring for at least the first one half hour of contact. The height of the column of coal was then remeasured at several times, following centrifugation each time, to establish that equilibrium had been achieved. Normally at room temperature, using good solvents, equilibrium could be achieved within a day or two. The volumetric swelling ratio (Q) is merely the ratio of the height of the swollen column of coal to the height of the dry column of coal. Again, it is generally true that all else being equal, the more highly crosslinked a sample, the lower value of Q it would give.

The elemental analyses of the coals studied in this work are provided in Table 1. Since the method of preparation of samples (particularly how they are dried) has a significant effect on the subsequent swelling behavior of the samples, preparation procedures will be discussed below, together with results. Generally, the coals were sieved prior to use. For most pyrolysis experiments, particles in the size range from 45-100 μm were utilized.

Results and Discussion

Effect of Drying Conditions on Swelling Behavior

It is often difficult to compare solvent swelling values obtained under nominally identical conditions in two different laboratories. This is a consequence of the very significant effect that drying conditions may have upon the swelling behavior. As is well known, coal has a colloidal gel structure that collapses upon removal of moisture. The collapse is significant in the case of lignites and brown coals[15,16], but is quite easily discernible in coals up to high volatile bituminous in rank[17]. The collapse is greater with increasing severity of drying conditions, and is in part irreversible even if drying is carried out at room temperature[16].

An illustration of the problem that this might cause in terms of comparison of

solvent swelling results between laboratories is given in Table 2. The results are all for North Dakota lignites. If coals are dried under such mild conditions that they retain significant moisture, they will give low values of the swelling ratio in a good solvent (e.g. pyridine) because their structure is initially somewhat swollen by water. It can be seen from the first three rows of Table 2 that increasing the time of drying at 298K increases the swelling ratio in pyridine. This probably does not reflect any decrease in crosslink density, but merely the difference in the base value against which swollen coal volume is compared. Drying an initially wet sample at 373 K results in a higher swelling ratio in all but one case (results given in the fourth row). The weight loss in the 373K drying process (carried out in inert gas) is generally only 1 to 2% greater than that obtained by drying at room temperature at zero relative humidity for 30 days. Thus we do not believe that the generally significant differences in swelling ratios reflected between the third and fourth rows reflects the effect of merely removing this small additional volume of moisture (if this were all that happened, the coal would shrink by only 1 to 2% in "dry" volume, and the swelling ratios would not be significantly affected). We believe that drying at elevated temperatures in addition allows some reorganization of the dried coal structure into a more compact form, which then can exhibit an even larger extent of swelling upon exposure to solvent. This is not, however, the only effect that elevated temperature drying may have.

The significant effect that the drying history may have on swelling behavior is seen in comparing the fourth and fifth rows of Table 2. Predrying the samples at room temperature before 373K heating, reduces swellability relative to preparation either by extended room, temperature drying, or direct heating to 373K, in all cases. The last three rows of the table illustrate the continuation of the trend towards lower swellability as the severity of drying conditions is increased by raising temperature. This trend likely illustrates the increase in crosslinking as the temperature of drying is increased. This will be further discussed below.

These observations show the difficulty that will be inherent in any attempts at quantitatively applying the solvent swelling method in an effort to determine the macromolecular structure of "raw" coals. Great thought will have to be given to the preparation of samples, particularly in the case of low rank coals.

The Effect of Pyrolysis Conditions on Solvent Swelling

It has been earlier firmly established that the decrease in swellability of low rank coals during the early stages of pyrolysis correlates well with the evolution of CO_2 as a product of pyrolysis[5,8,10,11], though preliminary results from this laboratory cast doubt upon the conclusion that the correlation between decrease in swellability and carboxyl group loss is linear. This loss of swellability has been interpreted as indicating an increase in crosslinking in the structure of the coal, and this in turn is thought to explain the inability of lower rank coals (lignites and subbituminous coals) to soften during pyrolysis under "ordinary" low and moderate heating rate conditions. Recently, it has been suggested that the process of crosslinking (swellability loss) also correlates with evolution of the water product of pyrolysis[18], in support of an earlier similar conclusion[8].

The general pyrolysis behaviors of low rank coals and high rank coals are illustrated in Fig. 1. The figure illustrates how the observable weight loss correlates with changes in the swellability of the char residue. The heating rate for pyrolysis was about 8 K/min, and the

samples were allowed to cool immediately upon reaching the indicated maximum temperature. Solvent swelling measurements were performed only on cooled chars. The coals were not completely dried prior to pyrolysis, so the weight losses at low temperatures may be viewed as indicative of the moisture content of the samples at the beginning of pyrolysis (some drying, during sieving, occurred in both the low rank coals). These data are in qualitative agreement with results from Solomon et al.[9]. What is important to note from this figure is that periods of apparently rapid crosslinking do not necessarily coincide with periods of rapid mass loss. Crosslinking apparently occurs quite readily at temperatures as low as 423K (150°C).

These data support the conclusion of the previous section, that swellability is lost even at temperatures normally regarded as only causing drying. We have observed by direct measurements changes in the carboxyl group contents of the four lignites shown in Table 2 (using barium cation exchange[19]). The loss of carboxyl content between 373K and 473K is between 5 and 15% of the total. The implication of these results is that if lignites are to be processed to give high yields of low molecular weight products, even very mild preheating might be detrimental.

In contrast to the behavior of the low rank coals, the macromolecular structure of the high volatile bituminous coal apparently changes very little until temperatures in excess of 700K are achieved. This is, however, not entirely accurate. The choice of pyridine as solvent means that most of the internal hydrogen bonding or ordinary acid-base interactions in the coal should be disrupted and that these should not act as virtual crosslinks. The extent to which pyridine is effective at disrupting other non-covalent crosslinks (due to aromatic-aromatic interactions of as yet unknown nature) remains somewhat unclear. Use of a less effective electron donor solvent, such as tetrahydrofuran (THF), would be expected to induce less swelling, because it will not be able to disrupt even the well known donor-acceptor interactions[20,21]. The data of Fig. 2 show that the use of the weaker solvent is quite revealing, in this case.

Whereas in higher rank bituminous coals the swelling of the chars in THF follow the trends shown by swelling measurements in pyridine, in the Pittsburgh No. 8 sample a distinctly different event is revealed by THF than is observable in pyridine. In the neighborhood of 550K, the THF swellability increases abruptly, while the pyridine swellability is constant. Bearing in mind that the measurements are performed on quenched chars, the change revealed by the THF must be an irreversible change in structure, which does not coincide with any particular weight loss events, and to which the pyridine is insensitive. Presumably the event is not observable in pyridine because the swelling in pyridine itself induces the change. This conclusion is supported by the observations by Cody et al.[22] that suggest that pyridine causes irreversible changes in the structure of the Pittsburgh No.8 sample, during the first cycle of swelling. It is also consistent with the observation of Hsieh and Duda[23] that weak solvents may swell coal structure without fully relaxing it.

In the present case, the abrupt change in THF swellability at 550K must reflect an irreversible thermal relaxation of the coal's structure, possibly associated with a phase transition of some kind. The most likely possibility appears to be a glass transition. Lucht et al.[24] have studied glass transitions in coals of similar rank and determined that the it occurs at roughly 600K, at a very similar heating rate of 10K/min., in the absence of solvents. In a rubbery state above the glass transition temperature, the structure of the coal can elastically deform in response to any residual stresses remaining as a result of coalification under geological pressure. Brenner has suggested that the glass transition temperature of pyridine swollen coals is most likely below room temperature[25], and therefore rubbery behavior and full

relaxation of the structure can be expected even at room temperature.

It is noteworthy that the Upper Freeport coal shows an increase in swellability in both pyridine and THF at around the same temperature range of 550 - 600K (see Fig. 2). This coal shows high fluidity and softening in a comparable range of temperatures as the Pittsburgh No. 8 coal[26]. It appears that the softening of both the coals (reported to occur at around 640K, for a heating rate of 3K/min) cannot be governed by whatever processes are initially responsible for the increased swellability. (If the softening phenomenon were governed by an activated process, then increasing the heating rate to a comparable 8K/min would induce fluidity at an even higher temperature). The mass loss from the Upper Freeport coal at 600K, under these heating conditions, is 1%, showing that only moisture loss has occurred, when the large increase in swellability occurs. Thus the conclusion is that as in the case of the Pittsburgh No. 8 coal, the increase in swellability in the Upper Freeport coal probably reflects a glass transition, that allows the structure to relax. Pyridine is not as good a solvent for the Upper Freeport coal as it is for the Pittsburgh No. 8 coal, and is unable to penetrate the structure without thermal relaxation of that structure.

The similarity of the softening temperatures of the Pittsburgh No. 8 and Upper Freeport coals, and the absence of any accompanying decrease in crosslinking in the relevant temperature range lends strong support to the view that the initial softening event, in these coals, is mainly a physical phenomenon[27,28]. This is not thought to be true in the case of the highest rank coal of Fig. 2, the Pocahontas low volatile bituminous.

Figure 3 shows the weight loss and swelling behavior of the Pocahontas coal at two different heating rates, 8K/min and 1800K/min. All phenomena are offset by a bit more than 200K, from the low to the high heating rate case. There is a unique relationship between swelling and mass loss, irrespective of heating rate, as noted in Fig. 4. This coal also softens at a considerably higher temperature (about 730K[26]) than the lower rank bituminous coals of Fig.2. All indications are that in this case, the change in swellability with temperature is an activated process, that depends upon actual pyrolytic bond breakage processes. The higher softening temperature for this coal is expected to be a consequence of the need to initiate true bond breakage as a prerequisite to softening. Fig. 5 shows the relationship between the swelling ratio in pyridine and the temperature range of fluidity in this coal.

Summary

The implications of the above results are that several quite different processes can be responsible for major changes in the nature of the macromolecular structure of coal during pyrolysis. In low rank coals, the process of crosslinking begins almost immediately with the drying of the coal. The changes are very significant, even if they involve very small amounts of pyrolytic mass loss. In higher rank (bituminous) coals, the drying process is not thought to be significant (unless it involves oxidation[9]). There may be a thermally induced glass transition phenomenon (at around 600K) before true softening occurs. This may not be accompanied by significant mass loss, but might be of great importance in terms of increased penetrability of the coal structure. Diffusion phenomena are generally faster in coals that have been partially relaxed by a good solvent, e.g. water[17], and the same would be expected to hold for thermal relaxation.

Initial softening during pyrolysis in most high and medium volatile bituminous coals appears, from other studies, to be a mainly physical phenomenon, and this seems to be

supported by the observations made here. Softening does not appear to coincide with any particular crosslink breakage events. In a low volatile bituminous coal, however, there is evidence that the softening process is indeed tied to bond breakage. This could help to explain why rank appears to play some role in the modeling of pyrolysis phenomena[26].

Acknowledgment

We gratefully acknowledge the financial support of this work by the U.S. Department of Energy, through grant DE-FG22-85PC80527 and contract DE-AC22-91PC91027, and by a grant from the Exxon Education Foundation. We are also grateful to Dr. Karl Vorres for assistance concerning the work with the Argonne Premium Coal Samples.

References

1. Green, T.K. ; Kovac, J.W.; Brenner, D.; Larsen, J. W. *Coal Structure*, R. Meyers, Ed., Academic Press, 1982, Chap. 6.
2. Dryden, I.G.C. *Fuel* **1951**, *30*, 145.
3. Dryden, I.G.C. *Chem. and Ind.* June 7, **1952**, 502.
4. Sanada, Y.; Honda, H. *Fuel* **1966**, *45*, 295 and 451.
5. Suuberg, E.M.; Lee, D.; Larsen, J.W. *Fuel* **1985**, *64*, 1668.
6. Suuberg, E.M.; Unger, P.E.; Larsen, J.W. *Energy and Fuels* **1987**, *1*, 305.
7. Bockrath, B.C.; Illig, E.G. ; Wassell-Bridger, W.D. *Energy and Fuels* **1987**, *1*,227.
8. Solomon, P.R.; Hamblen, D.G.; Carangelo, R.M.; Serio, M.A.; Deshpande, G.V. *Energy and Fuels*, **1988**, *2*, 405.
9. Solomon, P.R.; Serio, M.A.; Deshpande, G.V.; Kroo, E. *Energy and Fuels* **1990**, *4*, 42.
10. Solomon, P.R.; Hamblen, D.G.; Carangelo, R.M.; Serio, M.A.; Deshpande, G.V. *Combustion and Flame*, **1988**, *71*, 137.
11. Ibarra, J.V.; Cervero, I.; Garcia, M.; Moliner, R. *Fuel Proc. Tech.* **1990**, *24*, 19.
12. Otake, Y.; Suuberg, E.M. *Fuel* **1989**, *68*,1609.
13. Liotta, R.; Brons, G.; Isaacs, J. *Fuel*, **1983**, *62*, 781.
14. Green, T.K.; Kovac, J.W.; Larsen, J.W. *Fuel* **1984**, *63*, 935.
15. Evans, D.G. *Fuel* **1973**, *52*, 186.
16. Deevi, S.C.; Suuberg, E.M. *Fuel*, **1987**, *66*, 454.
17. Otake, Y.; Suuberg, E.M. *Prepr. Pap.-ACS Div. Fuel Chem. Prepr.* **1988**,*34(4)*, 898.
18. Ibarra, J.V.; Moliner, R.; Gavilan, M.P., paper presented at the Conference on Coal Structure and Reactivity, Cambridge, U.K., September, 1990.
19. Schafer, H.N.S. *Fuel*, **1984**, *63*, 723.
20. Szeliga, J.; Marzec, A. *Fuel* **1983**, *62* 1229.
21. Suuberg, E.M.; Otake, Y. paper presented at the Conference on Coal Structure and Reactivity, Cambridge, U.K., September, 1990, manuscript submitted for review.
22. Cody, G.D.; Larsen, J.W.; Siskin, M. *Energy and Fuels* **1988**, *2*, 340.
23. Hsieh, S.T.; Duda, J.L. *Fuel*, **1987**, *66*, 170.
24. Lucht, L.M.; Larson, J.M.; Peppas, N.A. *Energy and Fuels* **1987**, *1*, 56.
25. Brenner, D. *Fuel* **1984**, *63*, 1324.
26. Solomon, P.R.; Serio, M.A.; Hamblen, D.G.; Yu, Z.Z.; Charpenay, S. *Prepr. Pap.-ACS*

Div. Fuel Chem. Prepr. **1990**, *35(3)*, 479.
27. Fong, W.S.; Khalil, Y.F.; Peters, W.A.; Howard, J.B. *Fuel* **1986**, *65*, 195.
28. Lynch, L.J.; Webster, D.S.; Sakurovs, R.; Barton, W.A.; Maher, T.P. *Fuel* **1988**, *67*, 579.

Table 1-Coals Studied

SAMPLE	C	H	N	S	ASH	O	Moisture
Beulah lignite[a]	65.6	3.6	1.1	0.8	11.0	17.9	26.0
Freedom lignite[a]	63.5	3.8	0.9	1.4	6.1	24.3	27.9
Glenn Harold lignite[a]	61.1	4.4	0.8	0.4	7.4	25.9	28.9
Gascoyne lignite[a]	60.9	4.2	0.6	1.4	8.2	24.7	30.7
Beulah lignite[b]	65.9	4.4	1.0	0.8	9.7	18.2	32.2
Pittsburgh No.8 (HVBit.)[b]	75.5	4.8	1.5	2.2	9.3	6.7	1.7
Upper Freeport (MVBit.)[b]	74.2	4.1	1.4	2.3	13.2	4.8	1.1
Pocahontas (LVBit.)b	86.7	4.2.	1.3	0.7	4.8	2.3	0.7

•All results on a dry weight percent basis, except moisture which is ASTM value on an as-received, bed moist basis.

•Oxygen by difference.

a- Grand Forks Energy Research Center lignite sample bank.

b- Argonne National Laboratory Premium Coal Samples.

Table 2- Effect of Drying and Thermal Treatments on Solvent Swelling of Lignites in Pyridine

Condition	Beulah	Freedom	Gascoyne	Glenn Harold
Wet	1.48	1.62	1.33	1.60
0% R.H.,298K,24hrs	2.20	2.01	1.90	2.10
0%R.H.,298K, 30days	2.22	2.06	2.10	2.14
Wet, dried at 373K,1hr	2.34	2.50	2.05	2.47
Dry,then 373K,1hr	2.00	1.70	1.68	1.81
", then 473K, 1hr	1.43	1.66	1.54	1.75
", then 573K, 1 hr	1.22	1.45	1.50	1.50
", then 573K, 2 hr	1.14	1.30	1.42	1.45

•"Dry" refers to samples stored at 0% relative humidity for 30 days , before heating.

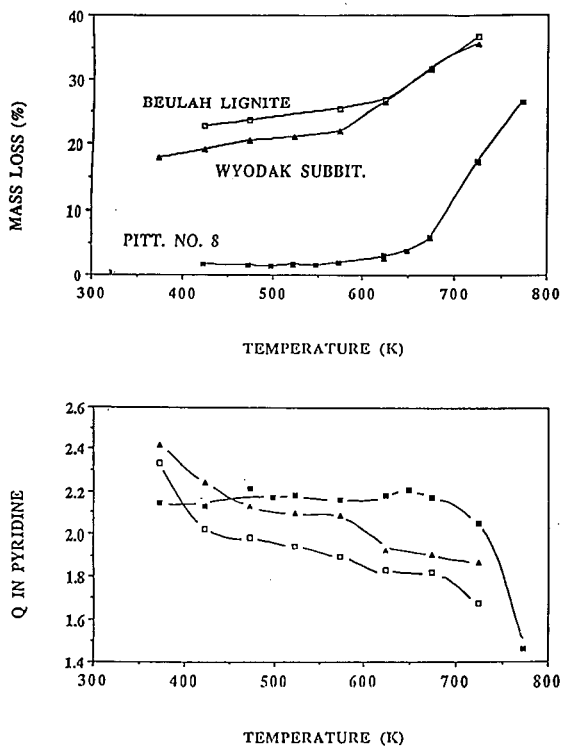

Figure 1. Mass loss and changes in pyridine swelling ratio upon pyrolysis at 8K/min.

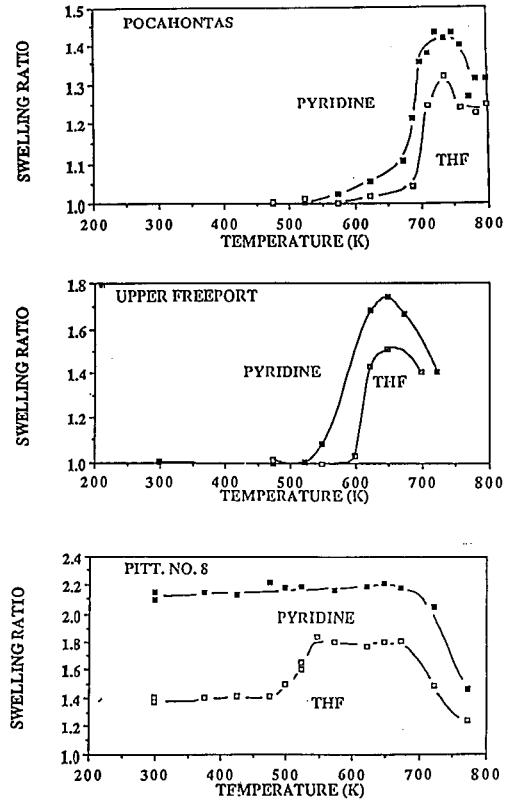

Figure 2. Swelling ratio changes with pyrolysis temperature for pyridine and tetrahydrofuran.

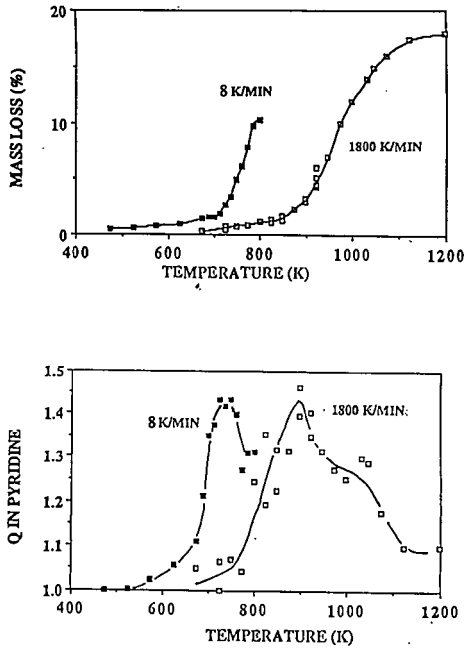

Figure 3. Mass loss and changes in pyridine swelling ratio of Pocahontas coal at two heating rates.

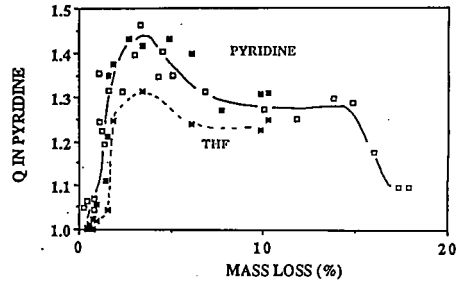

Figure 4. Variation of pyridine swelling ratio with mass loss for Pocahontas coal. Solid points-8K/min, open points 1800K/min. THF swelling ratio for 8K/min only.

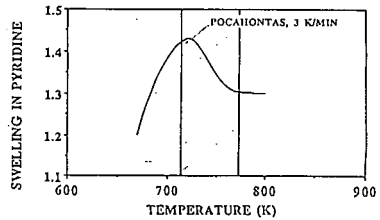

Figure 5. Calculated variation in swelling ratio at 3K/min, and the limits of temperature over which the coal is in a softened state (shaded area).

CAN COAL SCIENCE BE PREDICTIVE

Peter R. Solomon, David G. Hamblen, Michael A. Serio, Zhen-Zhong Yu, and Sylvie Charpenay
Advanced Fuel Research Inc., 87 Church Street, East Hartford, CT 06108

KEY WORDS: Coal, Pyrolysis, Network

ABSTRACT

This paper considers the development of a predictive macromolecular network decomposition model for coal conversion which is based on experimental results from a variety of modern analytical techniques. Six concepts which are the foundation of the Functional Group, Depolymerization, Vaporization, Crosslinking (FG-DVC) model are considered: 1) The decomposition of functional group sources in the coal yield the light gas species in thermal decomposition. The amount and evolution kinetics can be measured by TG-FTIR, the functional group changes by FT-IR and NMR. 2) The decomposition of a macromolecular network yields tar and metaplast. The amount and kinetics of the tar evolution can be measured by TG-FTIR and the molecular weight by FIMS. The kinetics of metaplast formation and destruction can be measured by solvent extraction, by Geissler plastometer and by proton magnetic resonance thermal analysis (PMRTA). 3) The molecular weight distribution of the metaplast depends on the network coordination number (average number of attachments on aromatic ring clusters). The coordination number can be determined by solvent swelling and NMR. 4) The network decomposition is controlled by bridge breaking. The number of bridges broken is limited by the available donatable hydrogen. 5) The network solidification is controlled by crosslinking. The changing crosslink density can be measured by solvent swelling and NMR. Crosslinking appears to occur with evolution of both CO_2 (prior to bridge breaking) and CH_4 after bridge breaking. Thus, low rank coals (which form a lot of CO_2) crosslink prior to bridge breaking and are thus thermosetting. High volatile bituminous coals (which form little CO_2) undergo significant bridge breaking prior to crosslinking and become highly fluid. Weathering, which increases the CO_2 yield, causes increased crosslinking and lowers fluidity. 6) The evolution of tar is controlled by mass transport in which the tar molecules evaporate into the light gas species and are carried out of the coal at rates proportion to their vapor pressure and the volume of light gases. High pressures reduce the volume of light gases and hence reduces the yield of heavy molecules with low vapor pressures. These changes can be studied with FIMS.

The paper describes how the coal kinetic and composition parameters are obtained by TG-FTIR, solvent swelling, solvent extraction, and Geissler plastometer data. The model is compared to a variety of experimental data in which heating rate, temperature, and pressure are all varied. There is good agreement with theory for most of the data available from our laboratory and in the literature.

INTRODUCTION

The question addressed by this paper is, can coal science be predictive? More specifically, is it possible, to accurately predict the way a coal behaves in a coal conversion process, given coal characteristics which can be measured in the laboratory. For example, Fig. 1 illustrates the behavior of coal in combustion. The left hand side of the figure shows a picture of a coal burning in a reactor where the coal is injected into the center of a hot air stream. The processes that occur are illustrated on the right hand side. Starting from the bottom, the figure represents the heating of the coal, coal softening, devolatilization, swelling, the ignition of the volatiles, the formation of soot, the burning of the volatiles, the ignition of the char, the combustion of the char, and finally the fragmentation of the char which determine the ultimate distribution of the ash particles. Can one qualitatively predict pyrolysis yields, swelling, soot formation, char reactivity, etc.?

As a second example, consider coal in a liquefaction process. The important step is the fragmentation of the coal macromolecule into small pieces. As shown in Fig. 2, that fragmentation takes place very quickly for a bituminous coal. The coal dissolves into the solvent, and the subsequent reactions between the solvent and the coal are all liquid-liquid phase interactions, which can occur very rapidly. In a lignite, this fragmentation process is prevented by low temperature crosslinking. The result is that

CAN COAL SCIENCE BE PREDICTIVE

Peter R. Solomon, David G. Hamblen, Michael A. Serio, Zhen-Zhong Yu, and Sylvie Charpenay
Advanced Fuel Research Inc., 87 Church Street, East Hartford, CT 06108

KEY WORDS: Coal, Pyrolysis, Network

ABSTRACT

This paper considers the development of a predictive macromolecular network decomposition model for coal conversion which is based on experimental results from a variety of modern analytical techniques. Six concepts which are the foundation of the Functional Group, Depolymerization, Vaporization, Crosslinking (FG-DVC) model are considered: 1) The decomposition of functional group sources in the coal yield the light gas species in thermal decomposition. The amount and evolution kinetics can be measured by TG-FTIR, the functional group changes by FT-IR and NMR. 2) The decomposition of a macromolecular network yields tar and metaplast. The amount and kinetics of the tar evolution can be measured by TG-FTIR and the molecular weight by FIMS. The kinetics of metaplast formation and destruction can be measured by solvent extraction, by Geissler plastometer and by proton magnetic resonance thermal analysis (PMRTA). 3) The molecular weight distribution of the metaplast depends on the network coordination number (average number of attachments on aromatic ring clusters). The coordination number can be determined by solvent swelling and NMR. 4) The network decomposition is controlled by bridge breaking. The number of bridges broken is limited by the available donatable hydrogen. 5) The network solidification is controlled by crosslinking. The changing crosslink density can be measured by solvent swelling and NMR. Crosslinking appears to occur with evolution of both CO_2 (prior to bridge breaking) and CH_4 after bridge breaking. Thus, low rank coals (which form a lot of CO_2) crosslink prior to bridge breaking and are thus thermosetting. High volatile bituminous coals (which form little CO_2) undergo significant bridge breaking prior to crosslinking and become highly fluid. Weathering, which increases the CO_2 yield, causes increased crosslinking and lowers fluidity. 6) The evolution of tar is controlled by mass transport in which the tar molecules evaporate into the light gas species and are carried out of the coal at rates proportion to their vapor pressure and the volume of light gases. High pressures reduce the volume of light gases and hence reduces the yield of heavy molecules with low vapor pressures. These changes can be studied with FIMS.

The paper describes how the coal kinetic and composition parameters are obtained by TG-FTIR, solvent swelling, solvent extraction, and Geissler plastometer data. The model is compared to a variety of experimental data in which heating rate, temperature, and pressure are all varied. There is good agreement with theory for most of the data available from our laboratory and in the literature.

INTRODUCTION

The question addressed by this paper is, can coal science be predictive? More specifically, is it possible, to accurately predict the way a coal behaves in a coal conversion process, given coal characteristics which can be measured in the laboratory. For example, Fig. 1 illustrates the behavior of coal in combustion. The left hand side of the figure shows a picture of a coal burning in a reactor where the coal is injected into the center of a hot air stream. The processes that occur are illustrated on the right hand side. Starting from the bottom, the figure represents the heating of the coal, coal softening, devolatilization, swelling, the ignition of the volatiles, the formation of soot, the burning of the volatiles, the ignition of the char, the combustion of the char, and finally the fragmentation of the char which determine the ultimate distribution of the ash particles. Can one qualitatively predict pyrolysis yields, swelling, soot formation, char reactivity, etc.?

As a second example, consider coal in a liquefaction process. The important step is the fragmentation of the coal macromolecule into small pieces. As shown in Fig. 2, that fragmentation takes place very quickly for a bituminous coal. The coal dissolves into the solvent, and the subsequent reactions between the solvent and the coal are all liquid-liquid phase interactions, which can occur very rapidly. In a lignite, this fragmentation process is prevented by low temperature crosslinking. The result is that

there is no quick solubilization of the coal, and most of the reaction takes place between the solvent and a solid crosslinked residue. Can one predict macromolecular fragmentation and crosslinking?

The research conducted during the last ten years suggests that many of the steps discussed above can be accurately predicted. Figure 3 shows the concept employed in our laboratory for developing predictive capabilities. We start with a set of laboratory characterization procedures that allow the appropriate kinetic and composition parameters for coal to be determined. Five kinds of experiments allow us to define the parameters for our model. The most important is the TG-FTIR, a thermogravimetric (TG) analyzer with the analysis of the evolved product by Fourier Transform Infrared (FT-IR) spectroscopy (1). This instrument allows us to determine the amount of the volatiles, their composition, the kinetics for their evolution, the reactivity of the char, and also the moisture and ash content of the coal. We also measure the solvent swelling ratio (2,3), the extract yield, and the fluidity in a Geissler plastometer (4), and employ nuclear magnetic resonance (NMR) (5), and Field Ionization Mass spectrometry (FIMS) data (6). These experiments determine the macromolecular network parameters for the model.

The model is the FG-DVC model (7,8). The letters FG stand for Functional Group, and DVC for Depolymerization, Vaporization and Crosslinking. The FG model considers certain functional groups in the coal which decompose to form the light gas species (9-12). At the same time, the DVC model describes the overall depolymerization of the macromolecular network which combines bridge breaking and crosslinking to produce fragments of the coal macromolecular (13-15). These fragments are then subjected to transport behavior, specifically the vaporization of the lightest fragments to form tar. The fragmentation process provides a second mechanism for the removal of functional groups from the coal. The model, whose parameters are determined in the laboratory at moderate temperatures and one atmosphere, can then be used to extrapolate away from the laboratory conditions to predict pyrolysis and combustion in high temperature reactions, or liquefaction at high pressure. Recently, we have explored extrapolation of the kinetics and reactions to low temperature geological transformations in coal beds (16).

The model for coal thermal decomposition has six basic concepts:

- Functional Groups (decompose to produce light gases)
- Macromolecular Network (decomposes to produce tar and metaplast)
- Network Coordination Number (determines fragment molecular weights)
- Bridge Breaking (limited by hydrogen availability)
- Crosslinking (related to gas evolution)
- Mass Transport of Tar (evaporation of light network fragments into light gases)

The first concept is that light gases are formed by the decomposition of certain functional groups in the coal. For example, methyl groups can decompose to form methane, carboxyl groups can decompose to form CO_2, etc. (9-12, 17-20). The second concept is that coal consists of a macromolecular network (2,3,7,13-15,21-36). This network is made up of fused aromatic ring clusters (which are described by their molecular weight) linked by bridges, some of which are relatively weak. There are some unattached parts of the network which can be extracted. Sometimes, there is also a second polymethylene component (37-41). When heated, this network decomposes to produce smaller fragments. The lightest of the fragments evaporate to produce tar (7,42), and the heavier fragments form the metaplast. These heavier molecules are the primary liquid fragments in liquefaction or the fragments that make coal fluid (8,43).

The third concept is that one of the most important properties of the network is its coordination number. The coordination number describes the geometry of the network by specifying how many possible attachments there are per aromatic ring cluster (node) (31-36). For example, a linear polymer chain has a coordination number of 2, because each fused aromatic ring has two possible attachments to link it in the chain. On the other hand, a "fish net" has a coordination number of 4, because there are four possible attachments at each node. The coordination number controls the molecular weight distribution of the network fragments at a given extent of decomposition. The extent of decomposition is specified by the probability that the possible attachments are made. For example, for 20% of broken

bridges, a linear chain is totally fragmented, while a "fish net" will have some holes but is almost totally connected. In describing the network, a crosslink is defined to occur at a node where there are more than two attachments. The coordination number is thus, related to the crosslink density. With no possible crosslinks, the coordination number is two. With increasing crosslink density the coordination number increases.

The second important property of the network is the fraction of possible attachments which are actually made. During thermal decomposition, this fraction is determined by the rates of bond breaking and crosslinking (7,15,44-47). The factors which control how many of the weak links can break are the rate constant and the amount of hydrogen that can be donated from the coal to stabilize the free radicals which form when the links break (10).

A competitive process with the bond breaking is the retrogressive process of crosslinking. Crosslinking reactions appear to be related to the evolution of certain gases (7,15,44,47). Specifically, for low rank coals, crosslinking at low temperature (prior to bridge breaking) seems to be related to the evolution of carbon dioxide (or possibly water). For coals of all rank, a higher temperature crosslinking event (following bridge breaking) seems to be related to the evolution of methane. At high temperatures, the evolution of hydrogen is also related to crosslinking.

The final concept is that the tar evolution is controlled by mass transport. Bridge breaking and crosslinking produce fragments with a molecular weight distribution. The lightest fragments can leave the coal melt by evaporation into the light gas species (7,42). The heavier fragments remain, forming the metaplast which controls the coal's fluidity.

The remainder of the paper describes how these concepts are incorporated into a practical predictive model. Section II considers the FG-DVC model in detail. It discusses each of the six concepts and the evidence for each assumption. Section III considers the experiments employed to obtain the model parameters, and Section IV compares predictions of the model with a variety of experimental data. Section V is the summary.

COAL PYROLYSIS MODEL

Functional Group Decomposition Model

Figure 4 illustrates the phenomena in coal thermal decomposition considered in the functional group model. The figure is not meant to describe the exact structure of coal or the exact chemistry which occurs in pyrolysis. It is meant to illustrate the kinds of structures that are being considered and the classes of phenomena that can occur. The important processes are the decomposition of the individual functional group to form the light gases and the competitive decomposition of the macromolecular network to form fragments, the lightest of which can evaporate as tar.

Figure 4a shows a representative piece of a Pittsburgh Seam coal macromolecule. The structure is based on measurements of the aromatic ring cluster size, the functional group composition and the elemental composition (48). The molecule consists of several fused aromatic ring clusters linked by labile bridges. The ring clusters have various functional groups attached to them. When the coal is heated, two things happen to the functional groups. The first is that certain functional groups can decompose to form light gases. The second is that fragmentation of the network, and removal of light fragments as tar, can cause the same type of functional group to be removed as part of the tar. So, there are two parallel processes for the volatilization of the functional groups.

The way the coal behaves during pyrolysis is illustrated in Fig. 4b. The carbon-carbon aliphatic bridge in the upper left hand corner of the molecule (labeled 2) broke and picked up hydrogen to form two methyl groups. This process creates a fragment which is light enough to evolve as tar. There is also independent decomposition of functional groups to form light gases. The carboxyl group that was shown in the middle of Fig. 4a is shown as a carbon dioxide evolving in Fig. 4b. Methyl groups have decomposed to form methane, there has been a condensation of hydroxyl groups to form water and an ether link (labeled 3), mercaptans decompose to form H_2S, etc.

The evidence for this description is as follows: 1) for bituminous coals and low rank coals heated rapidly, the tar is strikingly similar in elemental and functional group composition to the parent coal (9,10,48-50). The tar appears to consist of representative fragments of the parent coal macromolecule; 2) there is a correlation between the decrease in the functional group sources in the char and the evolution of specific gases (9-12); 3) there is a systematic variation in functional group composition with rank, and this variation is correlated with the evolved gas composition.

While there is good evidence for the above description, the details of the chemistry are not yet well understood. Also, tar produced from low rank coals at low heating rates appears to be significantly different in composition from the coal (51) and is probably dominated by polymethylenes.

Macromolecular Network Decomposition Model

The concept of a macromolecular network decomposition model, is illustrated in Fig. 5, which recently appeared in a paper by Grant and coworkers (36). The figure represents aromatic ring clusters with four possible attachments to their neighbors, arranged in a "fish net" type network, (a network with a coordination number of 4). Figure 5a illustrates what happens when 20% of the possible attachments are broken. As can be seen, there are only three fragments which are created, shown by the clusters with boxes around them. The breaking of 20% of the bridges produces very little fragmentation of the network. On the other hand, consider in Fig. 5b what happens when 45% of the bridges are broken. Now, there is a much higher concentration of fragments and the fragments have a molecular weight distribution from monomers up to 7-mers (consisting of 7 fused ring clusters linked together). The lightest of these fragments, monomers, dimers, and trimers can evaporate into the light gas species and are removed from the coal particles as tar. The heavier fragments make up the metaplast. The lightest of these can be extracted using solvent, while others are too heavy to be extracted. The presence of a sufficiently large fraction of these fragments are what makes these materials fluid.

Network Coordination Number

The importance of the network coordination number is illustrated in Figs. 5 and 6. In Fig. 5a with 20% of the bridges broken in a "fish net", only a small number of fragments are produced, and they are all monomers. On the other hand, if 20% of the bridges in the linear chain are broken, 100% of the material becomes fragments and there will be many dimers, trimers, etc. Thus, the molecular weight distribution of the fragments depends very strongly on the coordination number.

In Fig. 5, the molecular distribution was computed using Monte Carlo calculations in which a representative network is set up in computer memory and the fragment molecular weight distribution is calculated after the broken bridges are randomly distributed. Alternatively, a technique called percolation theory allows a closed form analytical solution of the molecular weight distribution as a function of the number of actual attachments per ring cluster.

Figure 6 shows percolation theory calculations for networks with two different coordination numbers: Fig. 6a is for a coordination number of 2.2 and Fig. 6b is for 4.6. The variable σ is one less than the coordination number. The figure shows the calculated distributions of: i) monomers, ii) up to trimers (i.e., monomer, dimer, trimer) representative of what might be evolved as tar for a ring cluster size of 300 Daltons, iii) the yields of all n-mer up to ten representative of extractable material, and 4) the yield of all n-mers. These are plotted as a function of α, which is the average number of bridges per fused aromatic rings. This term α is equal to the probability, p, that a bridge is occupied times the coordination number of the network divided by two, $\alpha = p(\sigma + 1)/2$. As can be seen, there is a very different distribution of fragments depending on the coordination number. For example, at a value of $\alpha = 0.9$, the network with coordination number 4.6 has most of the fragments in the tar, with only a small number of n-mers between 3 and 10 and almost no n-mers above 10. On the other hand, for a network with a coordination number of 2.2 at $\alpha = 0.9$, there is a smaller number of monomers, a somewhat smaller concentration of tar, but a much higher concentration of n-mers up to 10 and a 100% yield of all n-mers. In other words, for 0.9 bridges per cluster, most of the molecules had decomposed to produce fragments of one size or another.

The DVC model was originally implemented using a Monte Carlo solution method, which allows an arbitrary network geometry. Percolation theory, however, offers significant benefits in computational speed and reproducibility, at the cost of restricting the network geometries.

As we shall see below, in the Monte Carlo version of the model, the starting network is represented by linear chains of monomers (6-12 aromatic clusters) with some amount of crosslinking which tie the chains together. Thus the starting network has a coordination number between 2 (straight chains) and three or more (fully cross linked). As pyrolysis proceeds, the linear chain bonds (bridges) are broken, and crosslinks (the side bonds) are formed. Thus, the coordination number, or degree of branching, increases with extent of pyrolysis. The conventional percolation theory models of coal decomposition do not model this feature. With conventional percolation theory, one can make any identification of the various chemical bonds with the percolation lattice bonds, so that the probability of a bond being occupied tracks the chemistry; but the occupied bonds must be randomly distributed within the lattice. The structure cannot be converted from "chain-like" to "fishnet-like".

The DVC model predicts, and experiments confirm, that there are more than one kind of bond (bridges and crosslinks) which have different coordination numbers, and independent probabilities of being broken. To take advantage of the benefits of percolation theory, we have extended percolation theory on a Bethe lattice (one with no loops) to use two independent sub-networks, as illustrated in Figure 7 (32). In the Figure, double lines represent one of the bond types, while single lines represent the other. As can be seen by comparing Fig 7a and 7b, this lattice has the desired feature of modeling a transition from chain-like structures (a) to fishnet structures (b). The mathematics of this 2-bond percolation theory follows closely that of the standard theory (32). A comparison of the results obtained from the 2-bond percolation theory agree well with those obtained from the original Monte Carlo calculations, as will be discussed in the Results Section.

Bridge Breaking and Hydrogen Utilization

There are two questions with respect to bridge breaking: what is the bridge breaking rate and how many bridges break. Pyrolysis rates have been reviewed by a number of authors (10,52-54). One of the problems in pyrolysis over the last two decades is a very wide variation in the reported rates for either weight loss or tar evolution in pyrolysis.

Figure 8a presents several of the extremes in rates reported prior to 1985 for high heating rate experiments (10,55-58). At 800°C there is almost a four order of magnitude variation in the rate constant which has been reported. An analysis of the data shows that one can not ascribe this sort of variation in kinetics to variations in the coal type, because investigators who measured more than one coal type found that the variations in kinetics rates among coals are typically within a factor of 10. So there has to be another explanation for why there is such a wide variety of reported rates. The answer appears to be the knowledge of the coal particle temperatures (53,54,59-62). Almost none of the experiments are done with direct measurements of the coal particle temperature. For entrained flow reactor experiments, the temperature is usually calculated and the calculations depend critically on the rate of mixing of the preheated gases with the coal stream. A factor of two error in the heating rate can lead to errors of hundreds of degrees celsius in the particle temperature during pyrolysis. For heated grid experiments, temperature measurements are made with a thermocouple and the inference is made that the thermocouple temperature is the same as the coal particle temperature. Recent reviews of experiments for Pittsburgh Seam coal heated at 1000°C/sec show a wide variation in pyrolysis temperatures, suggesting that this is just not a good assumption (60,63).

Since 1985, several experiments have been performed in which coal particle temperatures were measured during pyrolysis (12,53,61,62,64). Careful experiments have also been performed at several low heating rates where the thermocouple temperature is a good measure of the coal particle temperature (65,66). As can be seen from Fig. 8b, the data are much more tightly grouped. There is a systematic variation with the rank of the coal and the kinetic rate constants appear to have an activation energy between 45 and 55 Kcal. This is the magnitude one would expect for the kind of labile bridges depicted in Fig. 4 (14,67).

Besides the kinetic rate for bridge breaking, one needs to know the number of bridges that can be broken. The number depends upon the amount of hydrogen that is available to stabilize the free radicals formed when bridges break. How the hydrogen utilization controls the amount of tar and its hydrogen concentration is illustrated in Fig. 9. The figure is based on the following consideration: every time a bridge is broken, the available hydrogen is used to stabilize the free radicals. Two radicals are assumed to be stabilized per tar molecule. If the tar is made up of large fragments, the utilization of hydrogen per unit weight of tar is very efficient. On the other hand, if the tar consists of small molecules, the utilization of hydrogen is much less efficient. The figure shows the results for 0.3% hydrogen in the coal available for donation to the tar. The figure presents the yield of tar and the percent of additional hydrogen in the tar as a function of the average molecular weight in the tar. For an average molecular weight of 100 Daltons, 15% tar is produced. The amount of additional hydrogen in the tar is 2%. On the other hand, at an average molecular weight of 300 Daltons the yield is up to 45%, while the weight percent of additional hydrogen per unit mass is only 0.7%. The average molecular weight of the tar is affected by crosslinking, pressure, heating rate, and bed geometry.

Crosslinking

During pyrolysis, another important process occurs besides bridge breaking. It is the process of crosslinking, where new bonds are formed between the fused aromatic ring clusters. One of the ways of measuring the crosslink density is through solvent swelling (2,3), in which a solvent (e.g., pyridine) is used to swell the char or coal (7,15,44-47). To understand how solvent swelling indicates the crosslink density, consider the analogy of an air mattress. An air mattress is stitched in long rows along the length of the mattress. When the mattress is inflated there are several connected small tubes, instead of one big round tube. The small tubes have a smaller volume than one large tube and the volume can be used to infer the limiting circumference of the tubes. In a similar manner, the addition of the solvent to a coal indicates the circumference of linked molecules that make a loop to limit the swelling. Since it is crosslinks (more than two attachments per cluster) that allow loops to be formed, the amount of swelling indicates the average molecular weight between crosslinks.

Figure 10 shows the behavior of the solvent swelling ratio as a function of the char temperature for coals of several ranks. Chars are produced by heating up to the indicated temperatures at 30°C/min in an inert atmosphere and then cooling. These chars are subjected to solvent swelling experiments which determines the volume of swollen coal divided by the unswollen volume. Coals have solvent swelling ratios as high as 2.7. As char is formed, new crosslinks reduce the swelling ratio to unity. The solvent swelling ratio in Fig. 10 is normalized. The parameter x is the difference in solvent swelling ratio between the coal and the char divided by the maximum differences that can be achieved. This normalization allows us to compare different coals with different starting solvent swelling ratios in a convenient manner. Figure 10 presents $1 - x$ as a function of the char temperature. If $x = 0$, we have a material that swells the same as coal and if $x = 1$ we have a fully crosslinked char.

There is a wide variation in behavior depending upon rank. This rank dependence of the crosslinking behavior was first noted by Suuberg and coworkers (44) who measured a lignite and a bituminous coal and found the same sort of difference that has been exhibited here. The lowest rank coal, Zap lignite, is shown by the open squares. At temperatures as low as 200°C, the char starts to undergo crosslinking, loosing most of its solvent swelling properties by a temperature of 400°C. It is between 400 and 500°C that most of the pyrolysis weight loss is occurring for this material. Thus, for a low rank coal, the crosslinking occurs well in advance of the bridge breaking.

For higher rank coals, the crosslinking event is delayed relative to bridge breaking. For a highly softening bituminous coal like Pittsburgh Seam coal, or Kentucky No. 9, we find the material swells even more as it is heated into the region of pyrolysis, and only looses its solvent swelling properties after most of the weight loss has occurred in pyrolysis. There is, thus, a very strong rank dependence of the crosslinking behavior. Low rank coals crosslink early, prior to bridge breaking, while high rank coals undergo crosslinking after most of the bridge breaking has taken place.

The results of solvent swelling experiments are not unambiguous because the solvent swelling ratio depends on two things: 1) the crosslink density and 2) the solvent interaction parameter. This

parameter can change with the functional group composition of the coal. Since the functional group composition will change as the coal pyrolyzes, the change in solvent swelling ratio could be due to the change in the functional group composition, not crosslinking. However, an analysis of how much the solvent swelling ratio may change with the functional group composition indicates that the kind of drastic change from a solvent swelling ratio of 2.7, typical for coal, down to 1 for char is not likely to occur for the small changes in the functional group composition with low temperature pyrolysis (47).

Another way of investigating the crosslink density is by experiments done using nuclear magnetic resonance (NMR). The work was performed at the University of Utah in collaboration with Solum and coworkers (68). Results of the NMR experiments are shown in Fig. 11. The NMR experiments employ cross polarization with magic angle spinning and dipolar dephasing (5). Dipolar dephasing allows the determination of the functional group form of the carbons that are being studied. When all the different kinds of bonds are considered, it is possible to determine an average molecular weight for the ring clusters and also the average number of attachments per ring cluster. In Fig. 11, the average number of attachments are compared to the solvent swelling data for Pittsburgh Seam bituminous coal and a North Dakota lignite. The average number of attachments determined by the NMR are also normalized to determine an NMR index which can be compared to 1 - x. Figure 11a compares the results for the lignite. The change in crosslink density determined by NMR is in reasonable agreement with that determined by the solvent swelling ratio. As can be seen, the material starts to crosslink at a reasonably low temperature and is almost completely crosslinked by a temperature of about 700 K (427°C), prior to significant bond breaking. For the Pittsburgh Seam coal shown in Fig. 11b the NMR index is in reasonable agreement with the solvent swelling ratio, and in this case both indices show that the char has not undergone appreciable crosslinking by a temperature of 700.

To develop an understanding of the chemistry of crosslinking, we attempted to determine whether the addition of crosslinks could be correlated with any other observation, specifically, the evolution of gases. In the initial work of Suuberg and coworkers (44), they noted that the one gas species which correlated with the early creation of crosslinking in the lignite was carbon dioxide.

Figure 12 shows the results obtained in our laboratory. Figure 12a presents the parameter x as a function of the carbon dioxide yield divided by 44 so that it is on a molecular basis. In Fig. 12 we have plotted x rather than 1 - x which was plotted in Figs. 10 and 11. For a wide variety of experiments (some at high heating rates and some at low heating rates) there is an very reasonable correlation between the loss of swelling and the appearance of carbon dioxide in pyrolysis. For all the low rank coals studied, there appears to be a good correlation between the appearance of crosslinks and the appearance of carbon dioxide. The line shown in Fig. 12a is from our FG-DVC model, where one crosslink is assumed for each carbon dioxide evolved.

For a higher rank coal, which does not produce significant yields of CO_2, a different correlation is observed. Figure 12b compares the normalized solvent swelling ratio for a Pittsburgh Seam coal with the evolution of methane divided by 16. There is a good correlation between these two parameters for chars created at a number of different temperatures at high heating rates. The line in Fig. 12b is from the FG-DVC model, where it is assumed that one crosslink is formed for each methane evolved.

We examined the correlation of the loss of swelling with other parameters and found the correlation between carbon dioxide and methane to be the best. There is a correlation for low rank coals between the formation of crosslinks and the water evolution, but not quite as good as for CO_2. There was no good correlation for high rank coals between crosslinking and tar evolution.

Three experiments which exhibit the phenomena of bridge breaking and crosslinking are presented in Fig. 13. Figure 13a presents the proton magnetic resonance thermal analysis (PMRTA) experiment done at CSIRO by Lynch, Sakurovs and coworkers (69-71). This experiment, which measures the relaxation time for protons, can distinguish between protons attached to mobile molecules (which are free to rotate) and those attached to a ridged lattice. The higher the concentration of mobile protons, the lower the values of the parameter M_{2T}. The data taken at 4°C/sec was provided by Dr. Sakurovs (72). The decrease in M_{2T} at low temperatures appears to be associated with melting, the sharp drop

in M_{2T} above 400°C is due to bridge breaking and the sharp increase of M_{2T} above 440°C is due to the crosslinking.

Figure 13b shows fluidity data measured with a Geissler plastometer for the same coal at a similar heating rate (3°C/sec) (4). While the fluidity below 400°C is probably due to melting, above 400°C bond breaking becomes important, while above 440°C crosslinking resolidifies the network.

Figure 13c presents data of Fong (73) on the extract yield in chars produced at a high heating rate of 640°C/sec. The maximum extract yield occurs at a much higher temperature than for the other two experiments due to the high heating rate. The increase in extract yield is due to bridge breaking and the decrease to crosslinking.

Transport

The above discussion shows how bridge breaking and crosslinking, can fragment the macromolecular network and allow small pieces to be formed. The evolution of tar is controlled by the formation of these small fragments and their transport out of the metaplast. In our FG-DVC model, we've assumed a very simple transport process. The assumption is that the fragments reach their equilibrium vapor pressure in the light gas species and are removed from the metaplast by convective transport in the light gas species (7). In a highly fluid coal, the expulsion of the light gases occurs by bubble transport. In a low rank thermosetting coal the transport of the light gas species is through the pores. In either case, the degree to which the tar molecules are transported depends upon the volume of light species that evolve and the vapor pressure of the molecule. The low macromolecular weight species that have high vapor pressure are therefore easily transported while heavy molecular weight species are not. The result is that the tar for a bituminous coal pyrolyzed at 1 atmosphere or below consists of molecules up to about 800 Daltons. As the pressure is increased the volume of the light gases is reduced and those marginal heavy products, which were previously transported at one atmosphere, can no longer be transported. Thus, as pressure is increased, the average molecular weight of the tar is reduced. The amount of tar is also reduced because of the reduced efficiency of hydrogen utilization.

For low rank coals, low temperature crosslinking increases the effective coordination number of the network and only small molecules are produced. The yields are low and pressure has little influence on the yield or molecular weight distribution.

Summary of FG-DVC Model

Figure 14 summarizes the FG-DVC model. In Fig. 14a we start with an assumed macromolecular network. In the Monte Carlo version of the model, each piece of this network is actually described in the computer memory. The description of the network contains the molecular weight of the aromatic ring clusters (shown as the number in the circles), and the crosslinking density (shown by the vertical double line). The potential number of labile bridges (related to the donatable hydrogen) are indicated by the single horizontal lines. The starting molecule is constructed from linear chains of a certain length (typically between 6 and 12 aromatic ring clusters) connected by the appropriate number of crosslinks. When this is done a certain number of the chains may be unattached to the rest of the macromolecular network. These are the guest molecules whose molecular weight is less than 3000 Daltons and would be pyridine soluble. The length of the chains is adjusted to obtain the proper pyridine solubles. The number of crosslinks is picked to get a coordination number which yields the right ratio of tar to heavier fragments (e.g., extracts) in the metaplast. The number of labile bridges (amount of donatable hydrogen) is picked to get the proper tar yield in the TG-FTIR experiments.

Figure 14b considers what happens during pyrolysis. As the temperature increases, some of the weak bridges (which are the single horizontal lines), can break according to the bridge breaking rate. The hydrogen limitation is accomplished by requiring that for each bridge that is broken, another one of the labile bridges becomes an unbreakable bridge as its hydrogen is used to stabilize the free radicals caused by the broken bridges. Thus, for each broken bridge, two of the labile bridges are consumed. The broken bridges and new unbreakable bridges are distributed randomly.

In the model, the crosslinking is assumed to correlate with the CO_2 and methane evolution. The evolution of these species is determined from the functional group part of the model and one crosslink is inserted randomly for each carbon dioxide and each methane group which is evolved. If bridge breaking dominates over crosslinking, the macromolecular network is broken up into smaller fragments. On the right hand side of the figure, the molecular weight distribution which results from the bridge breaking and crosslinking events is shown. Molecules below 3000 Daltons are increased, the lightest molecules escape as tar, and the rest of the network is described as pyridine insoluble.

Figure 14c shows the network at the conclusion of the pyrolysis process. When all the labile bridges are consumed, the decomposition of the network is complete. All of the network is completely connected by unbreakable bridges, and is highly crosslinking. All the previously loose fragments have been incorporated into the network by crosslinking or have escaped as tar.

ANALYSIS OF COMPOSITION AND KINETIC PARAMETERS

In this section, the laboratory characterization to determine the model parameters is considered. An analysis by TG-FTIR is employed to determine kinetic rates and functional group compositions. Solvent swelling, solvent extraction, and fluidity measurements in a Geissler plastometer are employed to obtain information on the molecular weight distribution of the metaplast and hence determine the network parameters. NMR and FIMS are used to determine the molecular weight of the ring clusters. These measurements are considered below.

TG-FTIR

Apparatus - As indicated in Fig. 3, TG-FTIR analysis of coal is employed to obtain the composition and kinetic parameter for the model. A schematic of the instrument is presented in Fig. 15. Its components are as follows: a DuPont™ 951 TGA; a hardware interface (including a furnace power supply); an Infrared Analysis 16 pass gas cell with transfer optics; a MICHELSON MB Series FT-IR; (Resolution: 4 cm^{-1}, Detector: MCT); and a PC-AT compatible computer. The cell is connected without restrictions to the sample area and a helium sweep gas is employed to bring evolved products from the TGA directly into the gas cell. This instrument is now available as the TG/plus from Bomem, Inc.

The most difficult volatiles to analyze are the tars which condense at room temperature. In the TG/plus, the rapid cooling from the high thermal conductivity helium sweep gas causes these products to form an aerosol which is fine enough to follow the gas through the analysis cell. The aerosol is also fine enough that there is little scattering of the infrared beam and it thus appears as though the tar was in the gas phase.

As an example of the analysis procedure, the pyrolysis and oxidation of a bituminous coal is described. More detail can be found in Ref. 1. Figure 16a illustrates the weight loss from this sample and the temperature history. A 25 mg sample of Pittsburgh Seam coal, loaded in the sample basket of the DuPont™ 951, is taken on a 30°C/min temperature excursion in the helium sweep gas, first to 150°C to dry, then to 900°C for pyrolysis. After cooling, a small flow of O_2 is added to the furnace at the 57 minute mark and the temperature is ramped to 900°C for oxidation.

During this excursion, infrared spectra are obtained once every forty seconds. As discussed previously (1) the spectra show absorption bands for CO, CO_2, CH_4, H_2O, SO_2, COS, C_2H_4, HCl, and NH_3. The spectra above 400°C also show aliphatic, aromatic, hydroxyl, carbonyl and ether bands from tar. The evolution of gases derived from the IR absorbance spectra are obtained by a quantitative analysis program which employs a database of calibration spectra for different compounds. The routine decides which regions of each calibration spectrum to use for best quantitation with the least interferences. A correlation between the sample spectrum and the reference spectrum is performed to determine gas amounts. A database of integration windows is also available for tracking functional groups absorptions. Tar quantitation is discussed in Ref. 1. The routine is fast enough so that the product analysis can be performed and displayed every 40 seconds during the actual experiment.

Figure 16b illustrates the integral of the evolution curves to obtain cumulative evolved product amounts. Because the data are quantitative, the sum of these curves match the weight loss as determined by the TGA balance. Discrepancies occur because of components such as H_2 which cannot be seen by IR. When O_2 is introduced, the balance shows a net gain in weight due to O_2 chemisorption.

<u>Determination of FG-DVC Model Parameters</u> - The kinetic and composition parameters for the FG-DVC model are obtained from the TG/plus pyrolysis cycle. The pyrolysis cycle for Illinois No. 6 coal (Argonne premium sample) is presented in Fig. 17. Figure 17a presents the weight loss and temperature profile. Also presented (dashed line) is the sum of species (tar, CH_4, H_2O, CO_2, CO, SO_2 NH_3, C_2H_4, and COS). The sum of species is within a few percent of the weight loss.

The water evolution (Fig. 17b) consists of a low temperature moisture peak followed by a pyrolysis peak. To fit the wide pyrolysis peak by the FG submodel, three sources are used for H_2O. Each source evolves according to

$$dW_i/dt = k_i W_i(\text{char}) \tag{1}$$

were W_i is the gas species and W_i(char) is the amount of the functional group source remaining in the char. The rate constant, k_i is given by an Arrhenius expression of the form

$$k_i = A_i \exp((-E_i \pm \sigma_i)/RT) \tag{2}$$

where A_i is the frequency factor, E_i the activation energy and σ_i the distribution in activation energies. Two sources are employed for CH_4, and three sources for CO and CO_2. Note the elimination of the calcite CO_2 evolution peak (Fig. 17d) and the increase in tar (Fig. 17c) for the demineralized coal.

To obtain the model parameters, the model is fit to the TG/plus data at three heating rates (3, 30, and 100°C/min). When there are multiple sources for a given species and the sources have overlapping peaks, the determination of parameters is not unique and some rules must be assumed. Based on chemical arguments, A is restricted between 10^{12} and 10^{15} sec^{-1}. Also, the preexponential for a given species pool is assumed rank invariant based on the observed rank variation of the evolution curves. As the coal is increased in rank, the leading edges and the early peaks (Extra Loose or Loose pools) shift to higher temperatures while the trailing edge (Tight or Extra Tight pools) remain at the same temperature. An example of this is shown for water for five coals in Fig. 18a (16). From this figure it appears that the shift in the evolution curve with rank can be explained by the geological aging process. With increasing aging temperature and time, the maturation process gradually evolve the loosely bounded functional groups and leaves the tightly bounded groups intact.

The shift can be simulated by pyrolyzing a species described by a distribution of activation energies (Eq. 2) up to different bed temperatures. An example is shown in Fig. 18b. Starting with the evolution profile for Zap lignite, the coal is assumed to pyrolyze at 10°C/million years up to temperatures of (60, 120, 150, and 180°C). The resulting geologically aged samples is simulated using the TG/plus temperature profile and the predicted results are plotted. The curves for geological aging at 120, 150, and 180°C are similar to the actual TG/plus evolution curves shown in Fig. 18a for Illinois No. 6, Pittsburgh, No. 8, and Upper Freeport, respectively. Thus, the frequency factor is assumed to be constant as the rank increases, and the activation energy of the pool increased with increasing coal rank to fit the data. We find that the activation energy of tight pools generally change with rank much less than do the loose pools.

A typical comparison of theory and TG-FTIR experiments is shown in Fig. 19 for the Pittsburgh Seam coal for one heating rate. The amounts of the functional group pools are obtained from this procedure. The resolution of the hydrocarbon evolution into paraffins, olefins, ethane, ethylene, propane, and propylene is done in other experiments if required. Figure 20 compares the theory and experiment for three heating rates for weight loss, tar evolution, and methane evolution. The kinetic parameters are derived from these experiments. The agreement between the theory and experiment is quite good.

We have applied these curve fitting procedures for the eight Argonne coals according to the rules cited above (i.e., frequency factor between 10^{12} and 10^{15}/sec and constant for a given gas species pool independent of coal rank). Results for the rates for bond breaking, the evolution of methane (two pools), CO (three pools), CO_2 (three pools) and H_2O (three pools) are presented as a function of the coal's oxygen concentration in Fig. 21. As can be seen, there is a systematic increase in activation energy with increasing rank. The variation in activation energy is maximum for the loose pool and reduces as the activation energy increases. The amounts for these pools are presented in Fig. 22. There is a systematic variation in the amounts with rank.

Solvent Swelling, Extraction and NMR

Solvent swelling and extraction data for the Argonne coals are presented in Table 1. As discussed above, the extract yield is employed to determine the length of the chains (Monte Carlo) or the starting bond probabilities (percolation) used in the model. There appears to be some problem in employing this approach for the highest rank coals (Pocahontas and Upper Freeport). The swelling and extract yields for these coals in pyridine appears to be limited by weak crosslinking (other than hydrogen bonding) forces which are not eliminated by pyridine.

The solvent swelling ratio has been employed to determine the crosslink density (2,3,24-29). The various theories and values for the solvent interaction parameter (24-29) suggest that there are between 4 and 8 ring clusters between crosslinks, indicating a value of $\sigma + 1$ between 2.13 and 2.25 (32). NMR results of Solum et al. (5) for the number of bridges and loops suggest a value of $\sigma + 1$ of between 2 and 3, so a value in the neighborhood of 2.5 seems reasonable. However, the uncertainty of these determinations is too large to employ them in the model. The crosslink density is instead considered an adjustable parameter employed to fit the fluidity data.

Geissler Fluidity

As discussed above, the crosslink density controls the effective coordination number of the network, and hence the molecular weight distribution and amount of the fragments. For bituminous coals, it is the initial crosslink density which is important, since few new crosslinks are formed prior to pyrolysis. A recent theory for fluidity was developed based on the liquid fraction in the coal computed by the FG-DVC model (8,43). Measurements of the tar and the fluidity thus provide a constraint on the molecular distribution of the fragments and hence on the crosslink density.

Figure 23 presents a comparison of theory and experiment for four of the Argonne coals with the kinetic parameters fit from TG-FTIR data. The fitting procedure for fluidity and tar determines a unique combination of the crosslink density and donatable hydrogen.

Monomer Molecular Weight Distribution

The molecular weight distribution of the monomers is chosen based on the ring cluster size determined by NMR (5) and the results of the model checked with FIMS data (6).

RESULTS

Volatiles Evolution

A good test of the validity of using the TG-FTIR method over a range of low heating rates to obtain kinetic parameters is the ability to use the kinetic parameters to extrapolate to high heating rate conditions. Figure 24 presents results for Illinois No. 6 coal (obtained from Combustion Engineering) using the complete FG-DVC model and the most recent kinetic and composition parameters derived from the TG/plus (65). The predicted rates of evolution for each species are in good agreement with the observed rates except for water where moisture sometimes creates measurement errors. The data were obtained in the heated tube reactor where FT-IR emission and transmission measurements of coal particle temperatures determined the heating rate to be over 20,000 K/sec.

Char

A number of char characteristics can be measured and compared with the model. These include fluidity (already discussed in Section III), functional group composition, crosslink density, PMRTA, and extract yield. These are discussed below.

Functional Group Composition - The functional group composition can be determined by FT-IR (74-77) or NMR CP-MS with dipolar dephasing (5). A set of chars was prepared by heating Pittsburgh Seam coal up to temperatures of 200, 300, 400, 500, and 600°C at 30°C/sec and the chars were characterized (68). Figure 25 compares the theory with NMR and FT-IR measurements. The fractions of aliphatic and aromatic carbons are compared in Fig. 25a, and aliphatic, aromatic, methyl, and hydroxyl hydrogens in Fig. 25b. Figures 25c and 25d compare the theory and FT-IR measurements for the same quantities (except methyl and aliphatic hydrogen are lumped together). The tar yield (Fig. 26a), and methane yield (Fig. 26b) are presented for comparison. The model predictions are in excellent agreement with the data.

Crosslink Density - The application of the volumetric swelling ratio to obtain the changing crosslink density in the char was discussed in Section II. Comparison with theory was discussed in Ref. 7. Figure 26c compares the theory and experiment for the set of chars in Figs. 25 and 26. The agreement is good. Figure 27 compares the theory and experiment for two coals (Zap lignite and Pittsburgh Seam). The theory predicts the early crosslinking in Zap lignite (related to CO_2 evolution) not seen for the bituminous coal. The agreement between theory and experiment is good except that the increase in 1 - x for the Pittsburgh Seam coal in Fig. 27 is not predicted.

The NMR data also provide a direct measurement of the number of attachments per cluster (5). Figure 28 presents data (68) for total number of attachments (which includes peripheral groups, bridges, and loops), and just bridges and loops (B & L) as a function of final temperature for Pittsburgh Seam coal heated at 30°C/min to the indicated temperature. The FG-DVC model predicts the number of B & L. This quantity (near 2 for coal) is the coordination number, suggesting that coal is quite chain-like. There is little change in B & L up to 400°C. B&L increased at 500°C and above where crosslinking related to methane evolution is believed to occur.

Notice that the total number of attachments changes very little. This would be reasonable if the methane peripheral groups were replaced by bridges in substitution reactions. This is believed to be the reason for the correlation between methane evolution and crosslinking.

PMRTA - Proton magnetic resonance thermal analysis (PMRTA) is employed at CSIRO as an alternative to fluidity measurements. The measurement of proton mobility can distinguish protons on molecules free to rotate from protons on a rigid lattice. The molecules ability to rotate depends on its freedom from the network (i.e., it must be unattached or attached at only one place) and on the mobility of free molecules to rotate (which depends on the temperature). From the measured M_{2T} values, a "mobile" liquid fraction can be defined by the expression (72)

$$\text{Liquid Fraction} = \frac{M_{2T}\,(\text{room temperature}) - M_{2T}(T)}{M_{2T}\,(\text{room temperature})}$$

At sufficiently high temperature, when the free molecules have sufficient energy to rotate, this quantity should be equal to the FG-DVC liquid fraction. Figures 29a and 29d, compare the measured and predicted liquid fraction using both the Monte Carlo and percolation models. As expected, the theory and experiment do not agree at low temperature, but there is good agreement on the softening temperature, peak fluidity temperature, and solidification temperature. The liquid amounts in the two theories are defined differently and so the absolute amounts do not agree. Also shown for comparison are the fluidity and tar evolution curves for the same coal at a similar heating rate. The agreement between the data and both theories is good.

Extract Yields - Figure 30 compares the FG-DVC predictions to the data of Fong et al. (73) on total volatile yield and extract yield as a function of temperature in pyrolysis at 0.85 atm. The experiment was performed in a heated grid apparatus at heating rates of 640°C to 1018 K, with variable holding times and rapid cooldown. The predictions in Fig. 30 are in reasonable agreement with the data. The predicted extract yields are not as high as the measured yields. However, such high yields of extracts have not been duplicated by others, and there is some possibility that the extracted fraction also contains some colloidal material.

Weathering - Oxidation of a Pittsburgh Seam coal in our laboratory was performed at 80°C for 10, 20, and 62 days. In our model, the loss of fluidity with increasing oxygen concentration is related to the increase in CO_2 evolution and hence increases in low temperature crosslinking. To determine the CO_2 evolution, measurements were made in the TG-FTIR (78). The data in Fig. 31a shows that the low temperature CO_2 evolution was significantly increased after 10 days of oxidation, becoming comparable to that for Illinois No. 6. After 20 days, the early CO_2 evolution was larger than that for the Utah bituminous coal. After three months at 110°C the CO_2 evolution was comparable to that of a lignite. When these increased CO_2 yields were incorporated in the simulation for the oxidized Pittsburgh Seam coal's fluidity, the maximum fluidity was reduced. We compare our predicted maximum fluidity with the measurement of Wu et al. (79) for comparable coal and oxidation treatment in Fig. 31b. The agreement is quite reasonable.

Predicted Molecular Weight Distribution in Char - The dominant event in determining the char's properties is the starting and low temperature crosslinking behavior. Figures 32a and 32b compare the predicted molecular weight distributions in the char for Zap lignite and a Pittsburgh Seam bituminous coal. The bituminous coal (Fig. 32a) exhibits substantial fragmentation of tar precursors (n-mers 1-3), extracts (n-mers 4-10), and liquids (n-mers 11-100). On the other hand, the initial crosslink density in the lignite, and the subsequent increase due to CO_2 related crosslinking, allows almost no n-mers except monomers, dimers, and trimers to be formed (Fig. 32b). These predictions of the model are related to the extract yields, PMRTA analysis fluidity, and tar yields.

Tar

Molecular Weight Distribution - The tar is evolved from the lightest fractions of the metaplast and depends on the metaplast distribution and the transport. This is illustrated in Fig. 32c and 32d, which are the predicted tar distribution for a bituminous coal and a lignite (two cases discussed above). For the bituminous coal, the upper molecular weight is limited only by the vapor pressure for the large molecules. For the lignite, the metaplast distribution limits the amount and molecular weight distribution.

Figures 33c, and 33d show measurements for the Pittsburgh Seam bituminous coal and the Beulah, Zap lignite pyrolyzed in the FIMS apparatus. The data have been summed over 50 amu intervals. While the Pittsburgh bituminous coal shows a peak intensity at about 400 Daltons, the lignite peak is at 100 Daltons. The predicted average tar molecular weight distributions are in good agreement with FIMS data as shown in Figs. 33a and 33b. Since both tar distributions are from the same monomer distribution, the enhanced drop off in amplitude with increased molecular weight for the lignite compared to the bituminous coal must be due to early crosslinking and transport effects in the lignite.

Pressure Effects - The prediction effect of pressure on the tar molecular weight distribution is illustrated in Figs. 34a and 34b. Pressure enters the model through the transport assumption. The internal transport rate is inversely proportional to the ambient pressure. The reduced transport rate reduces the evolution rate of the heavier molecules. Therefore, the average molecular weight and vaporization "cutoff" decrease with increasing pressure. The trends are in agreement with observed tar molecular weight distributions shown in Figs. 34c and 34d. The spectra are for previously formed tars that have been collected and analyzed in a FIMS apparatus (6). The low values of intensity between 100 and 200 Daltons are believed to be due to loss of these components due to their higher volatility.

Yield - The tar yields are measured in the TG-FTIR. Figure 35 compares the measured and predicted yield as a function of temperature. The agreement is good except for the low temperature evolution

of guest molecules, which is not well predicted in the standard model. Improvements to predict this early peak have been made (8).

Network Parameters

Figure 36 presents the adjustable network parameters which have been chosen to fit the tar evolution and fluidity data as functions of the oxygen concentration. The oligomer length and the molecular weight between crosslinks increase smoothly with rank. The concentration of available hydrogen for ring stabilization has a maximum for the high volatile bituminous coals.

In Fig. 37, we compare the predicted and measured extract yield and the predicted and estimated molecular weight between crosslinks. The crosslink density for the bituminous coals is within the range of measured values. The model, however, requires a high molecular weight between crosslinks, M_c, for Pocahontas and Upper Freeport, while the solvent swelling ratios would indicate a low M_c value. The model also requires a high extract yield for Upper Freeport while the measured yields are low. There may be an additional kind of weak crosslink for high rank coals, possibly associated with the aromatic-aromatic interactions suggested by Larsen (80). When the Upper Freeport coal is heated to 300°C and then cooled the solvent swelling ratio increases from 1.32 to 2.13 and the extract yield from 10.4 to 21%, suggesting that this treatment may loosen some of these weak bonds non-reversibly.

SUMMARY AND CONCLUSIONS

The paper poses the question, can coal science be predictive? The answer is yes for coal thermal decomposition in particles small enough to be isothermal. It is possible to construct a model based on reasonable assumptions to predict almost all of the observed behavior. The model has only one parameter which is adjusted for the process conditions. This is the internal pressure in the transport submodel. All other model parameters of the coal are fixed for each coal. The model has composition and kinetic parameters to describe the evolution of each individual gas species. These can be determined in TG-FTIR experiments and exhibit a systematic variation with rank. There are three network parameters in the Monte Carlo version of the model, the chain length, the crosslink density, and the available donatable hydrogen. A similar set of network parameters is used in the percolation theory. These are adjusted to fit the TG-FTIR, tar yields, extract yields, and fluidity. These also exhibit a systematic variation with rank.

The paper explores the six concepts which are the foundation of the FG-DVC model:

1) **The decomposition of functional group sources in the coal yield the light gas species in thermal decomposition.** The amount and evolution kinetics can be measured by TG-FTIR, the functional group changes by FT-IR and NMR. There is good agreement between the model and NMR, FT-IR, and TG-FTIR measurements on a Pittsburgh Seam coal heated at 30°C/min and for gas evolution for a lignite and an Illinois No. 6 bituminous coal at 30°C/min and 20,000°C/sec.

2) **The decomposition of a macromolecular network yields tar and metaplast.** The amount and kinetics of the tar evolution can be measured by TG-FTIR and the molecular weight by FIMS. The kinetics of metaplast formation and destruction can be measured by solvent extraction, by Geissler plastometer and proton magnetic resonance thermal analysis (PMRTA). Reasonable agreement has been demonstrated for solvent extract of a Pittsburgh Seam coal pyrolyzed at 30°C/min and 640°C/sec. Good agreement was shown for four of the Argonne coal samples for fluidity by Geissler plastometer, and for one coal by PMTRA.

3) **The molecular weight distribution of the metaplast depend on the network coordination number.** The coordination number can be determined by solvent swelling and NMR.

4) **The network decomposition is controlled by bridge breaking and the amount of bridge breaking is limited by the available donatable hydrogen.**

5) **The network solidification is controlled by crosslinking.** The changing crosslink density can be measured by solvent swelling and NMR. Crosslinking appears to occur with evolution of both CO_2 (prior to bridge breaking) and CH_4 after bridge breaking. Thus, low rank coals (which form a lot of CO_2) crosslink prior to bridge breaking and are thus thermosetting. High volatile bituminous coals (which form little CO_2) undergo significant bridge breaking prior to crosslinking and become highly fluid. Weathering, which increases the CO_2 yield, causes increased crosslinking and lowers fluidity. There is good agreement between the predicted and measured crosslink densities and fluidities in the FG-DVC model in which crosslinks are correlated with CO_2 and CH_4 gas evolution.

6) **The evolution of tar is controlled by mass transport in which the tar molecules evaporate into the light gas species and are carried out of the coal at rates proportion to their vapor pressure and the volume of light gases.** High pressures reduces the volume of light gases and hence reduces the yield of heavy molecules with low vapor pressure. These changes can be studied with FIMS. The changes in tar yield and molecular weight distribution with pressure have been accurately predicted using the vapor pressure law, of Suuberg and coworkers.

The paper describes how the coal kinetics and composition parameters are obtained by TG-FTIR, solvent swelling, solvent extraction, Geissler plastometer data, NMR data and FIMS data. The model is compared to a variety of experimental data in which heating rate (0.05 to 20,000°C/sec), temperature (100 to 1600°C), and pressure (vacuum to 100 atm) are all varied. There is good agreement with theory (both Monte Carlo and percolation) and most of the data available from our laboratory and in the literature.

The network parameters employed in the model have been presented. The results suggest that there is some form of weak crosslinks for Pocahontas and Upper Freeport coal.

While the experimental results and the model are consistent with the suggested processes, the chemical reactions for bridge breaking, crosslinking, and functional group decomposition are not defined in detail. Also, there is only sparse data to validate the transport assumption and the internal pressure in the particle is an adjustable parameter of the model.

ACKNOWLEDGEMENTS

The authors wish to acknowledge the following organizations for their support over the last ten years: U.S. Department of Energy, Morgantown Energy Technology Center, U.S. Department of Energy, Pittsburgh Energy Technology Center, National Science Foundation, and Gas Research Institute. The authors also wish to acknowledge the extensive contribution from many coauthors who have collaborated on the various aspects of this work: Robert Carangelo, James Markham, Philip Best, Erik Kroo, Yan Ping Zhang, Rosemary Bassilakis, Marie DiTaranto, Girish Deshpande, Po-Liang Chien, H.H. King, Tom Squires, and Kevin Squire who worked at Advanced Fuel Research, Inc., Meredith Colket from United Technologies Research Center, Douglas Smoot and Scott Brewster from Brigham Young University, Eric Suuberg from Brown University, Ronald Pugmire, David Grant, and Mark Solum from the University of Utah, Donald McMillen and Ripudaman Malhotra from SRI International, Rashid Khan from Texaco, Tom Fletcher from Sandia National Laboratory, Leo Lynch and Richard Sakurovs from CSIRO, Bernie Gerstein from Iowa State University, Jean Whelan from Woods Hole Oceanographic Institute, Harold Schobert and Caroline Burgess at Penn State University, Garry Vail, Fred Baudais, Michel Baillargeon, Daniel Gravel from Bomem, Inc. and Dennis Gerson from IBM Instruments.

REFERENCES

1. Solomon, P.R., Serio, M.A., Carangelo, R.M., Bassilakis, R., Gravel, D., Baillargeon, M., Baudais, F., and Vail, G., *Energy and Fuels*, 1990, *4*(3), 319.
2. Green, T.K., Kovac, J., and Larsen, J.W., *Fuel*, 1984, *63*, 935.
3. Green, T.K., Kovac, J., and Larsen, J.W., Coal Structure, R.A. Meyers, Ed., Academic, NY, 1982, p. 199.
4. The Geissler Plastometer data was supplied by Mr. George Engelke from Commercial Testing

and Engineering Company.
5. Solum, M.A., Pugmire, R.J., and Grant, D.M., *Energy & Fuels*, 1989, *3*, 187.
6. St. John, G.A., Butrill, S.E., Jr., and Anbar, M., ACS Symposium Series 71, American Chemical Society, Washington, DC, 1978, p. 223.
7. Solomon, P.R., Hamblen, D.G., Carangelo, R.M., Serio, M.A., and Deshpande, G.V., *Energy and Fuel*, 1988, *2*, 405.
8. Solomon, P.R., Serio, M.A., Hamblen, D.G., Yu, Z.Z., and Charpenay, S., *ACS Div. of Fuel Chem. Preprints*, 1990, *35*(2), 479.
9. Solomon, P.R., in Coal Structure, Advances in Chemistry Series, 1981, *192*, 95.
10. Solomon, P.R. and Hamblen, D.G., "Pyrolysis", in Chemistry of Coal Conversion, (R.H. Schlosberg, Editor), Plenum, New York, NY, 1985, pg. 121-251.
11. Solomon, P.R., Hamblen, D.G., Carangelo, R.M., and Krause, J.L., *Nineteenth Symposium (Int) on Combustion*, 1139, The Combustion Institute, Pittsburgh, PA, 1982, 1139.
12. Serio, M.A., Hamblen, D.G., Markham, J.R., Solomon, P.R., *Energy and Fuel*, 1987, *1*, 138.
13. Solomon, P.R. and King, H.H., *Fuel*, 1984, *63*, 1302.
14. Squire, K.R., Carangelo, R.M., DiTaranto, M.B., and Solomon, P.R., *Fuel*, 1986, *65*, 833.
15. Solomon, P.R., Hamblen, D.G., Carangelo, R.M., Serio, M.A. and Deshpande, G.V., *Combustion and Flame*, 1988, *71*, 137.
16. Solomon, P.R., Serio, M.A., Carangelo, R.M., Bassilakis, R., Yu, Z.Z., Charpenay, S., and Whelan, J., "Analysis of Coal by TG-FTIR and Pyrolysis Modeling", presented at the Pyrolysis '90 Meeting in Holland, June 1990, to be published in Journal of Analytical and Applied Pyrolysis.
17. Suuberg, E.M., Peters, W.A., and Howard, J.B., *Seventeenth Symposium (Int) on Combustion*, The Combustion Institute, Pittsburgh, PA 1979, 117.
18. Gavalas, G.R., Cheong, P.H., and Jain, R., *Ind. Eng. Chem. Fundam.*, 1981, *20*, 113.
19. Gavalas, G.R., Cheong, P.H., and Jain, R., *Ind. Eng. Chem. Fundam.*, 1981, *20*, 122.
20. Xu, W.C. and Tomita, A., *Fuel*, 1987, 66, 627.
21. van Krevelen, D.W., Coal, Elsevier, Amsterdam, 1961.
22. Solomon, P.R., Squire, K.R., and Carangelo, R.M., Int. Conf. on Coal Science, Pergamon, Sydney, Australia, 1985, p. 945.
23. Brenner, D., *Fuel*, 1985, *64*, 167.
24. Lucht, L.M. and Peppas, N.A., *Fuel*, 1987, *66*, 803.
25. Lucht, L.M., Larsen, J.M., and Peppas, N.A., *Energy & Fuels*, 1987, *1*, 56.
26. Larsen, J.W., *ACS Fuel Chem. Div. Preprints*, 1985, *30*(4), 444.
27. Green, T., Kovac, J., Brenner, D., and Larsen, J., Coal Structure, (R.A. Meyers, Ed.), Academic, NY, 1982, p 199.
28. Hall, P.J., Marsh, H., and Thomas, K.M., *Fuel*, 1988, *67*, 863.
29. Sanada, Y. and Honda, H., *Fuel*, 1966, *45*, 295.
30. Suuberg, E.M., Yoshi, O., and Deevo. S., *ACS Div. Fuel Chem. Prepr.*, 1988, *33*(1), 387.
31. Gavalas, G.R., Coal Pyrolysis, Elsevier, NY, 1982 p. 51
32. Solomon, P.R., Hamblen, D.G., Yu, Z.Z., and Serio, M.A., *Fuel*, 1990, *69*, 754.
33. Niksa, S., and Kerstein, A.R., *Combustion and Flame*, 1986, *66*, 95.
34. Niksa, S., *Combustion and Flame*, 1986, *66* 111.
35. Niksa, S. and Kerstein, A.R., *Fuel*, 1987, *66*, 1389.
36. Grant, D.M., Pugmire, R.J., Fletcher, T.H., and Kerstein, A.R., *Energy & Fuels*, 1989, *3*, 175.
37. Nelson, P.F., *Fuel*, 1987, *66*, 1264.
38. Calkins, W.H., Hagaman, E., and Zeldes, H., *Fuel*, 1984, 63, 1113.
39. Calkins, W.H., and Tyler, R.J., *Fuel*, 1984, *63*, 1119.
40. Calkins, W.H., *Fuel*, 1985, *64*, 1125.
41. Calkins, W.H., Hovsepian, B.K., Drykacz, G.R., Bloomquist, C.A.A., and Ruscic, L., *Fuel*, 1984, *63*, 1226.
42. Niksa, S., *AIChE J.*, 1988, *34*, 790.
43. Solomon, P.R., Best, P.E., Yu, Z.Z., and Deshpande, G.V., *ACS Div. of Fuel Chem. Preprints*, 1989, *34*(3), 895.
44. Suuberg, E.M., Lee, D., and Larsen, J.W., *Fuel*, 1985, *64*, 1668.
45. Suuberg, E.M., Unger, P.E., and Larsen, J.W., *Energy and Fuels*, 1987, *1*, 305.
46. Bockrath, B.C., Illig, E.G., and Eassell-Bridger, W.D., *Energy & Fuels*, 1987, *1*, 227.
47. Solomon, P.R., Serio, M.A., Deshpande, G.V., and Kroo, E., *Energy & Fuels*, 1990, *4*(1), 42.

48. Solomon, P.R., "Coal Structure and Thermal Decomposition", in New Approaches in Coal Chemistry, ACS Symposium Series 169, 1981, 61.
49. Brown, J.K., Dryden, I.G.C., Dunevein, D.H., Joy, W.K., and Pankhurst, K.S., *Inst. Fuel*, 1958, *31*, 259.
50. Orning, A.A. and Greifer, B., *Fuel*, 1956, *35*, 318.
51. Freihaut, J.D., Proscia, W.M., and Seery, D.J., *Energy & Fuels*, 1989, *3*, 692.
52. Anthony, D.B. and Howard, J.B., *AIChE J.*, 1976, *22*, 625.
53. Solomon, P.R., Serio, M.A., Carangelo, R.M., and Markham, J.R., *Fuel*, 1986, *65*, 182.
54. Solomon, P.R. and Serio, M.A., "Evaluation of Coal Pyrolysis Kinetics", in Fundamentals of the Physical-Chemistry of Pulverized Coal Combustion, J. Lahaye and G. Prado, Eds.), Martinus Nijhoff, 1987, 126.
55. Kobayashi, H., Howard, J.B., and Sarofim, A.F., *Sixteenth Symposium (Int) on Combustion,* The Combustion Institute, Pittsburgh, PA, 1977, 411.
56. Solomon, P.R., and Colket, M.B., *Seventeenth Symposium (Int) on Combustion*, The Combustion Institute, Pittsburgh, PA, 1979, 131.
57. Anthony, D.B., Howard, J.B., Hottel, H.C., and Meissner, H.P., *Fifteenth Symposium (Int) on Combustion,* The Combustion Institute, Pittsburgh, PA, 1974, 1303.
58. Badzioch, S., and Hawksley, P.G., *Ind. Eng. Chem. Proc. Des., Dev.*, 1970, 9, 521.
59. Solomon, P.R., Fletcher, T.H., and Pugmire, R.J., Progress in Coal Pyrolysis, Pittsburgh Coal Conference, (Sept. 10-14, 1990).
60. Solomon, P.R., Serio, M.A., and Suuberg, E.M., Review of Coal Pyrolysis: Experiments, Kinetic Rates, and Mechanisms, Progress in Energy and Combustion Science, submitted (1990).
61. Fletcher, T.H., *Combustion and Flame,* 1989, *78*, 223.
62. Fletcher, T.H., *Combust. Sci. and Tech.*, 1989, *63*, 89.
63. Freihaut, J.D. and Proscia, W.M., *Energy & Fuels*, 1989, *3*(5), 625.
64. Solomon, P.R., Serio, M.A., and Markham, J.R., Kinetics of Coal Pyrolysis, Int. Conference on Coal Science Proceedings, IEA, Tokyo, Japan, p. 575, (October 23-27, 1989).
65. Serio, M.A., Solomon, P.R., Charpenay, S., Yu, Z.Z., and Bassilakis, R., *ACS Div of Fuel Chem. Preprints,* 1990, *35*(3), 808.
66. Burnham, A.K., Oh, M.S., Crawford, R.W., and Samoun, A.M., *Energy & Fuel*, 1989, *3*, 42.
67. Stein, S.E., Robauch, D.A., Alfieri, A.D., and Miller, R.E., *J. Am. Chem. Soc.*, 1982, *104*, 6567.
68. Solum, M.S., Pugmire, R.J., Grant, D.M., Fletcher, T.H. and Solomon, P.R., Studies of Coal Char Structure Evolution: 1. Solid State ^{13}C NMR, to be submitted, (1989).
69. Lynch, L.J., Sakurovs, R., Webster, D.S., and Redlich, P.J., *Fuel*, 1988, *67*, 1036.
70. Lynch, L.J., Webster, D.S., Sakurovs, R., Barton, W.A., and Maher, T.P., *Fuel*, 1988, *67*, 579.
71. Barton, W.A. and Lynch, L.J., *Energy & Fuels*, 1989, *3*, 402.
72. Dr. Richard Sakurovs, personal communications.
73. Fong, W.S., Peters, W.A., and Howard, J.B., *Fuel*, 1986, *65*, 251.
74. Sobkowwiak, M., Riesser, B., Given, R., and Painter, P., *Fuel*, 1984, *63*, 1245.
75. Riesser, B., Starsinic, M., Squires, E., Davis, A., and Painter, P., *Fuel*, 1984, *63*, 1253.
76. Solomon, P.R. and Carangelo, R.M., *Fuel*, 1988, *67*, 949.
77. Solomon, P.R., and Carangelo, R.M., *Fuel*, 1982, *61*, 663.
78. Solomon, P.R., Best, P.E., Yu, Z.Z., and Charpenay, S., "A Macromolecular Network Model for Coal Fluidity", to be submitted to Fuel, (1990).
79. Wu, M.M., Robbins, G.A., Winschel, R.A., and Burke, F.P., *Energy & Fuels*, 1988, 2, 150.
80. Larsen, J.W., *ACS Div. of Fuel Chem. Preprints*, 1988, *33*(1), 400.

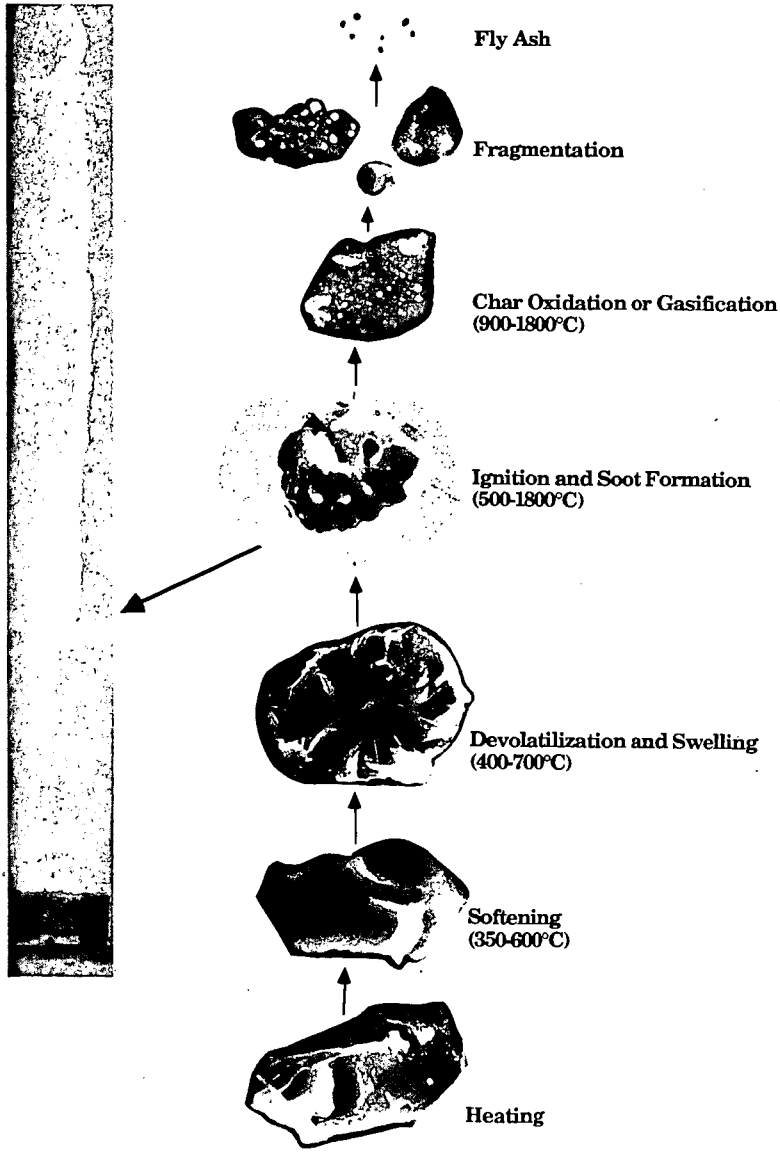

Figure 1. Processes in Coal Conversion.

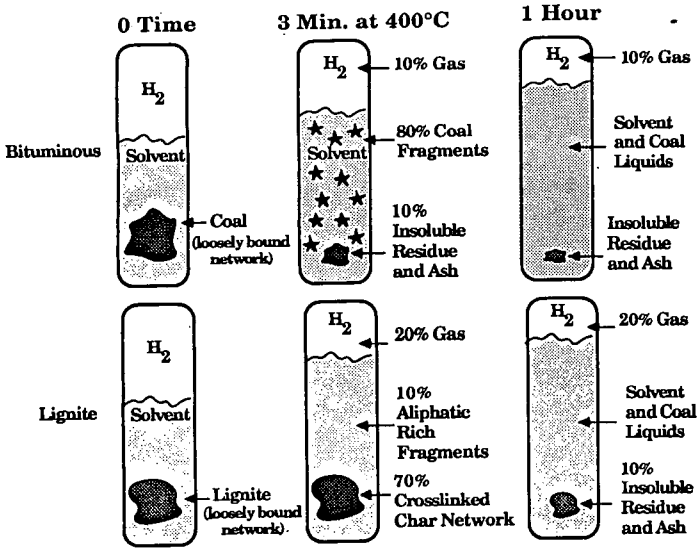

Figure 2. Process in Liquefaction.

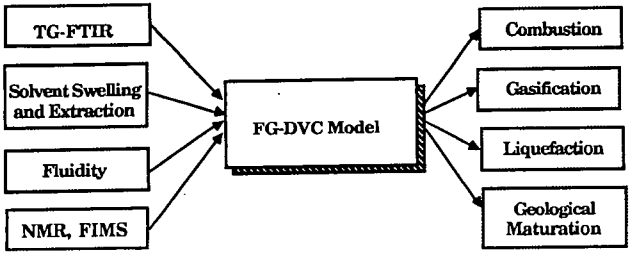

Figure 3. Coal Thermal Decomposition Model.

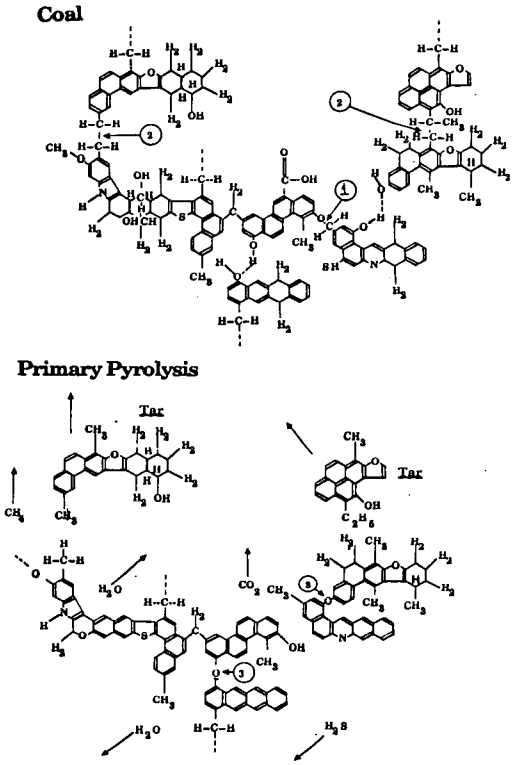

Figure 4. Hypothetical Model for Pittsburgh Seam Coal. a) Starting Coal, and b) During Pyrolysis.

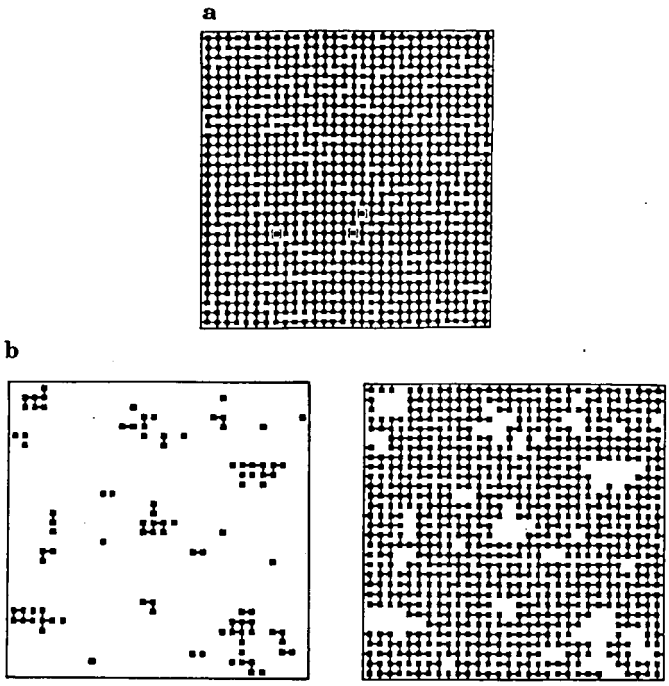

Figure 5. Monte Carlo Calculations for Coordination Number 4. a) 20% Broken Bridges, and b) 45% Broken Bridges (From Ref. 36).

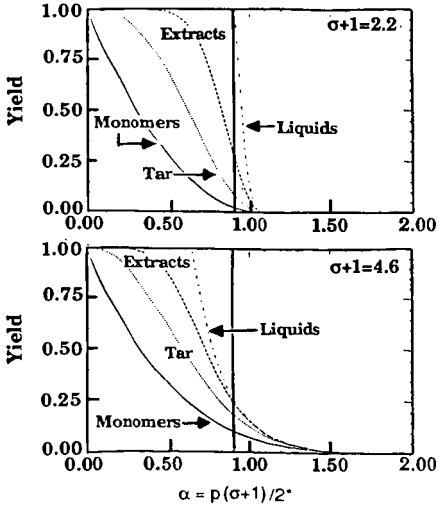

Figure 6. Percolation Theory Predictions for Pyrolysis Products for Two Coordination Numbers.

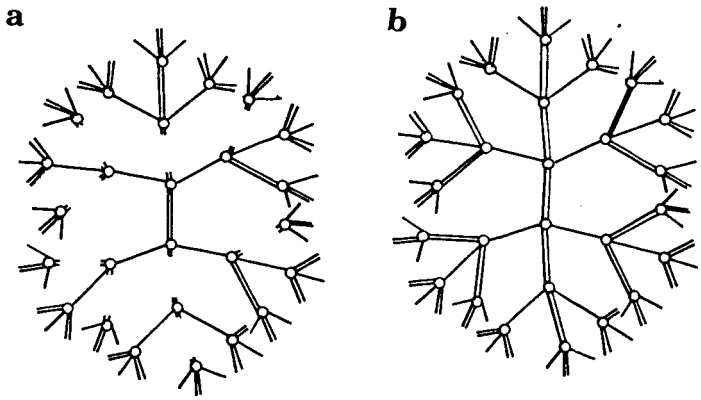

Figure 7. Bethe Lattice for Two-σ Model with σ_1=1 (shown as single bonds). a) Fully Linked Case (p=q=1) is like One-σ Model with σ=3. With Most Double Bands Representing the Crosslinks not yet Formed to Represent the Starting Coal. The Lattice is Like One-σ Model with σ=1, Linear Chains.

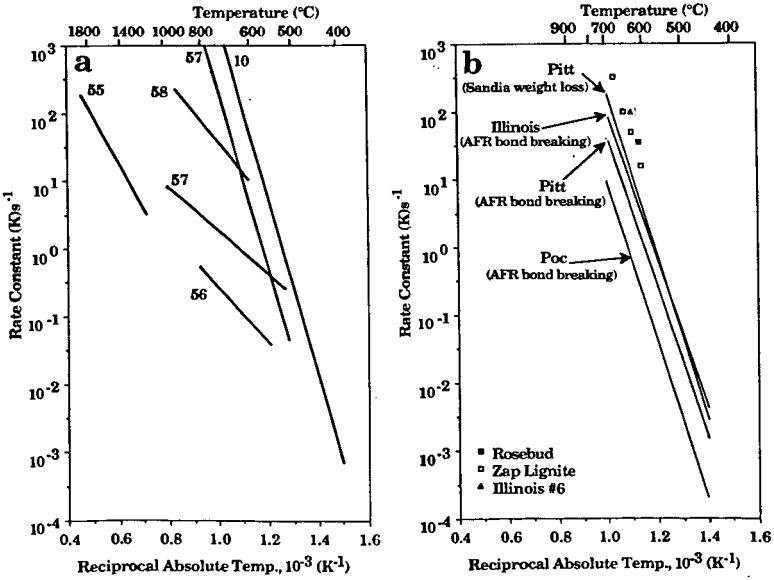

Figure 8. Kinetic Rate Constants for Weight Loss or Bridge Breaking. a) Extremes of Literature Rates from Experiments in which Particle Temperatures were not Directly Measured. b) More Recent Rates from Experiments in which Particle Temperatures were Measured.

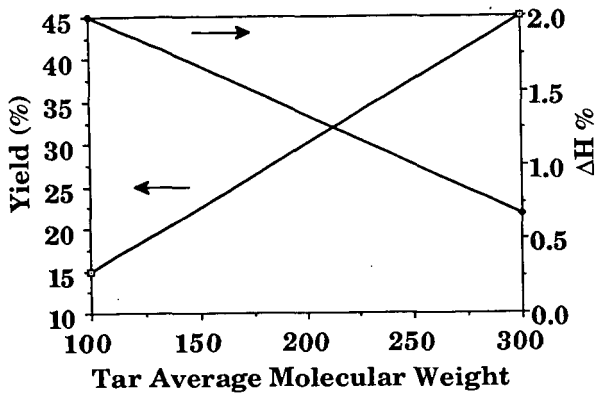

Figure 9. Yield and Hydrogen Concentration of Tar (.3% H available).

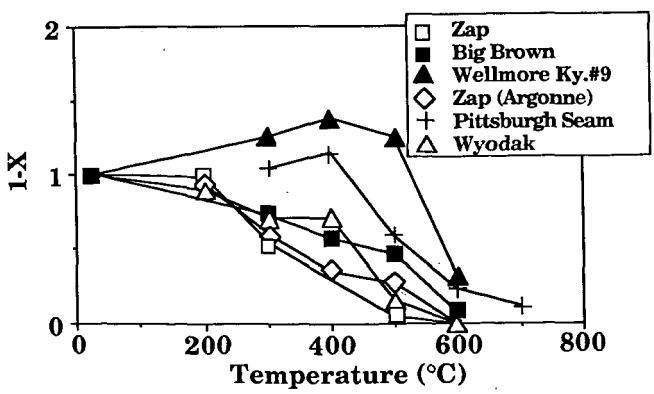

Figure 10. Comparison of Solvent Swelling Ratios for Coals of Various Ranks at a Series of Final Pyrolysis Temperatures at a Heating Rate of 30°C/min to Final Temperature.

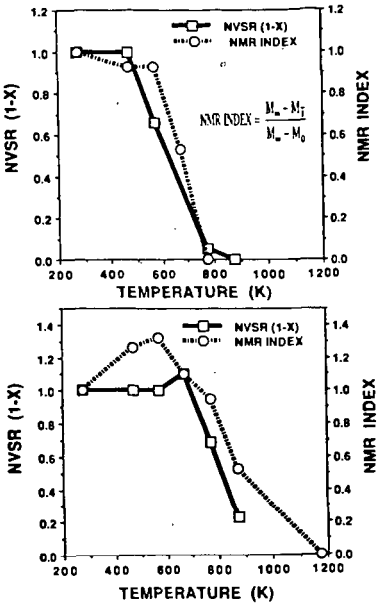

Figure 11. Comparison of NMR and Swelling Data for: a) Zap Lignite and b) Pittsburgh No. 8.

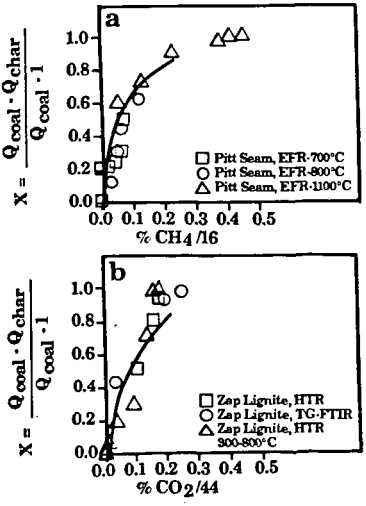

Figure 12. Measured and Calculated Normalized Volumetric Swelling Ratio (VSR) for Coal and Chars: a) Pittsburgh Seam Bituminous Coal Plotted Against the Methane Yield; b) Zap North Dakota Lignite Plotted Against the CO_2 Yield. VSR_{min} is the Value Achieved when Crosslinking is Complete. The Chars were Prepared in an Entrained Flow Reactor (EFR), a Heated Tube Reactor (HTR), and a Thermogravimetric Analyzer with Evolved Product Analysis by FT-IR (TG-FTIR) as Described in Ref.58.

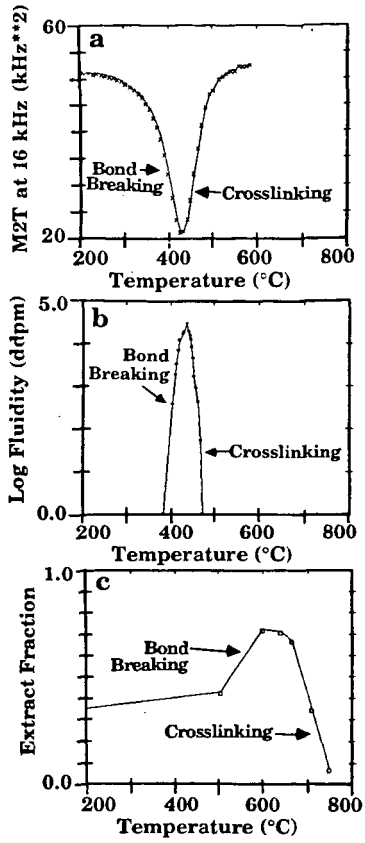

Figure 13. Experiments that Exhibit Bond Breaking and Crosslinking for Pittsburgh Seam Coal. a) PMRTA at 4°C/sec (data of Sakurovs and Lynch (72), b) Fluidity by Geissler at 3°C/sec (data of Commercial Testing and Engineering (4) and c) Extract Yield at 640°C/sec (data of Fong et al. (73).

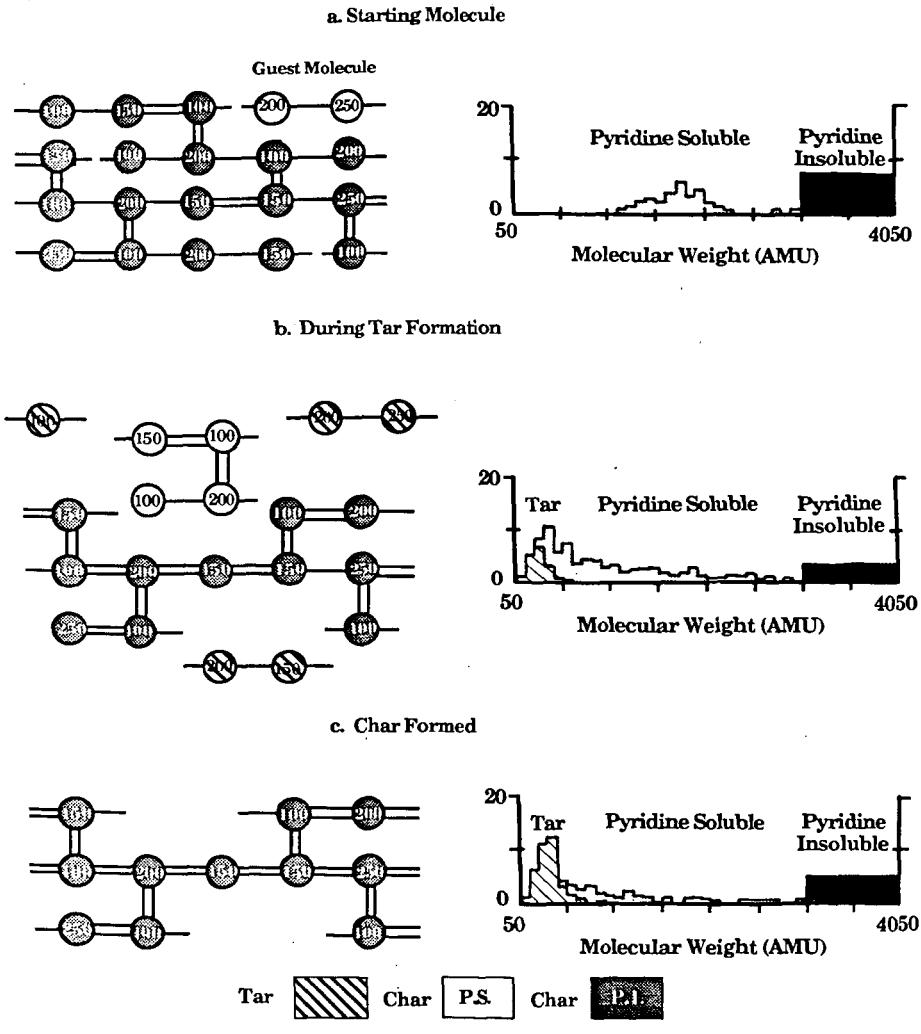

Figure 14. Representation of Coal Molecule in the DVC Simulation and Corresponding Molecular Weight Distribution. In the Molecule, the Circles Represent Monomers (ring clusters and peripheral groups). The Molecular Weight Shown by the Numbers is the Molecular Weight of the Monomer Including the Attached Bridges. The Single-Line Bridges are Breakable and can Donate Hydrogen. The Double-line Bridges are Unbreakable and do not Donate Hydrogen. The Molecular Weight Distribution of the Coal, Tar, and Chars are Shown as a Histogram at the Right. The Histogram is Divided into Tar and Char with Pyridine-soluble and Pyridine-insoluble Fractions. The Area Under the Histogram Corresponds to the Weight Percent of the Oligomers. (From Ref. 58).

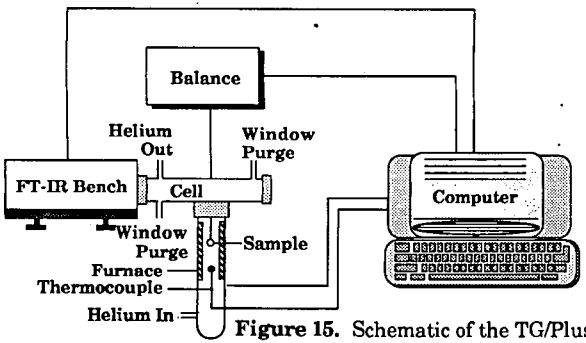

Figure 15. Schematic of the TG/Plus.

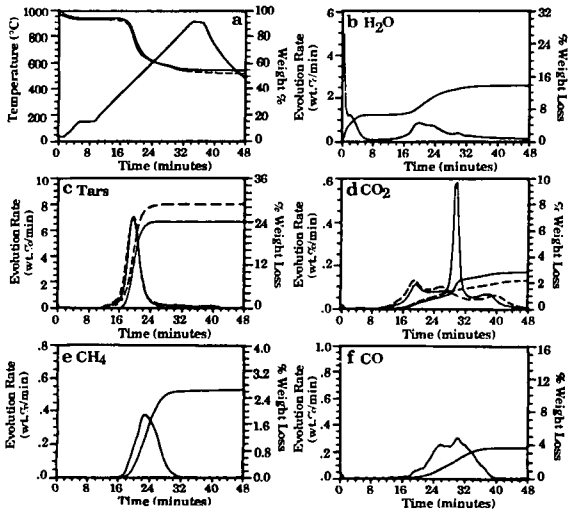

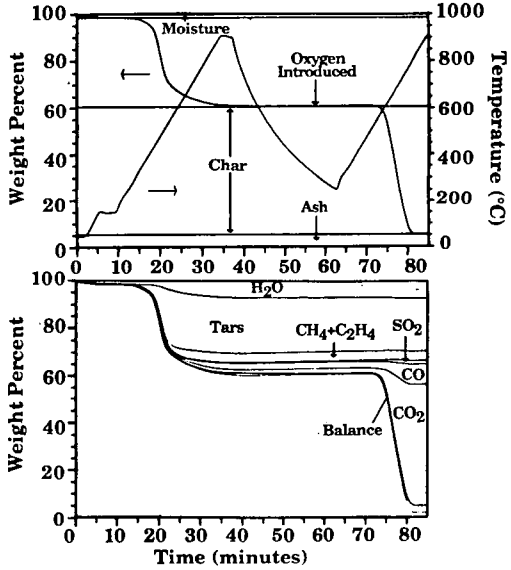

Figure 16. Thermogram and Quantitative Breakdown of Evolved Gases for Pittsburgh Seam Coal.

Figure 17. TG-FTIR Analysis of Raw and Demineralized Illinois No. 6 Coal During the Pyrolysis Cycle. a) Weight Loss (solid), Sum of Evolved Products (dashed), and Temperature Profile; b) H_2O Evolution Rate and Integrated Amount Evolved; c) Tar Evolution Rate and Integrated Amount Evolved (raw coal (solid line); demineralized coal (dashed line)); d) CO_2 Evolution Rate and Integrated Amount Evolved (raw coal (solid line); demineralized coal (dashed line)); e) CH_4 Evolution Rate and Integrated Amount Evolved; f) CO Evolution Rate and Integrated Amount Evolved. All Weight Losses are on an as Received Basis.

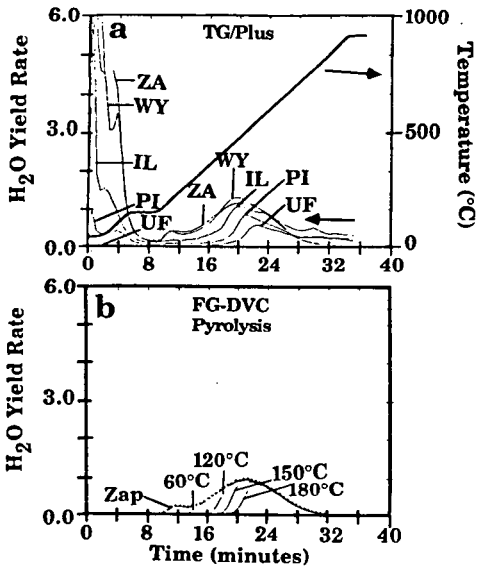

Figure 18. Evolution Curves for H_2O Measured in a a) TG/Plus and b) FG-DVC Predictions for Five Coals fromthe Argonne Premium Sample Collected at 30°C/min. (UF-Upper Freeport, PI-Pittsburgh, IL-Illinois, WY-Wyodak, ZA-Zap Lignite).

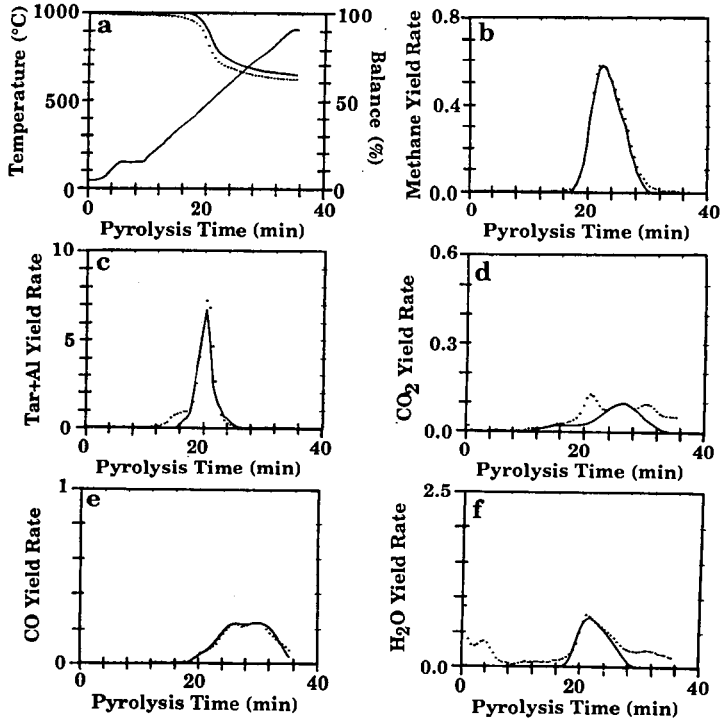

Figure 19. Data from TG-FTIR Heating Rates (···) and Predictions of FG-DVC Model for Pittsburgh No. 8 Bituminous Coal at 30°C/min. a) Weight Loss and Temperature; b) Methane; c) Tar + Aliphatic Gases; d) CO_2; e) CO; f) H_2O.

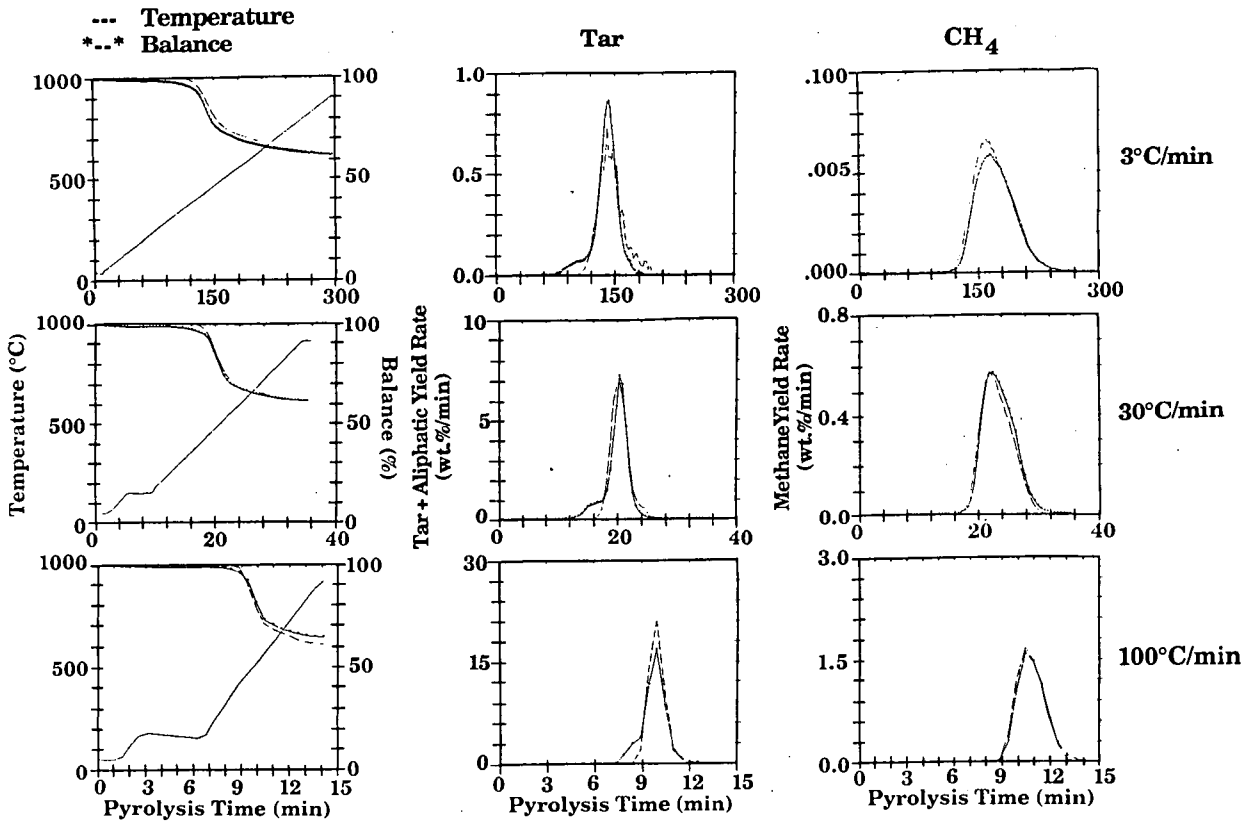

Figure 20. Kinetic Analysis at Three Heating Rates for Pittsburgh Seam Coal. Comparison of Theory (---) and Data (*-*).

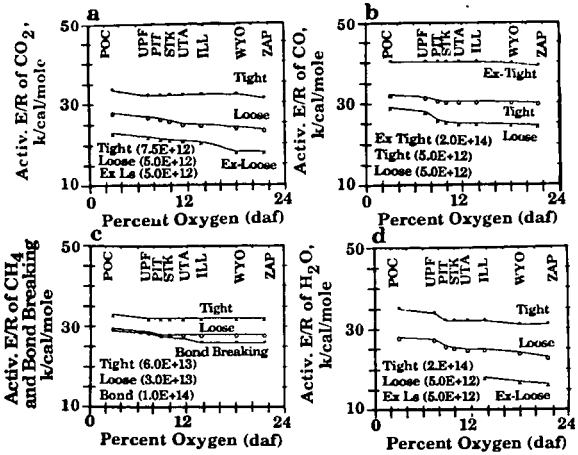

Figure 21. Activation Energies for Functional Group Pools as a Function of the Coal's Oxygen Concentration. The Frequency Factors are Shown in Parenthesis. a) CO_2 Tight, CO_2 Loose and CO_2 Ex-Loose, b) CO Ex-Tight, CO Tight and CO Loose, c) CH_4 Loose, CH_4 Tight and Bond Breaking, and d) H_2O Tight, H_2O Loose and H_2O Ex-Loose.

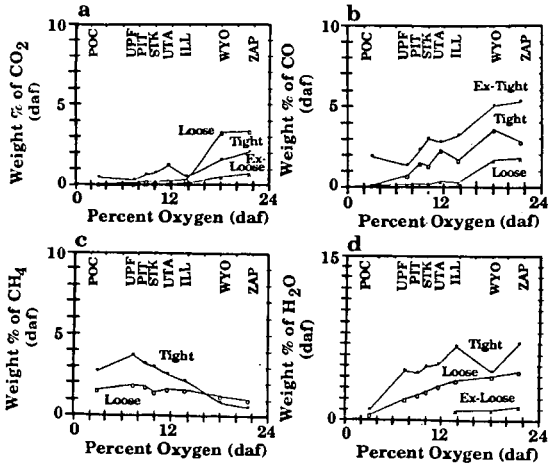

Figure 22. Amounts for Functional Group Pools as a Function of the Coal's Oxygen Concentration. a) CO_2 Tight, CO_2 Loose and CO_2 Ex-Loose, b) CO Ex-Tight, CO Tight and CO Loose, c) CH_4 Loose, CH_4 Tight and CH_4, and d) H_2O Tight, H_2O Loose and H_2O Ex-Loose.

Table 1 - Extract Yields and Volumetric Swelling Ratio (VSR) for Argonne Coals

Coal	Pyridine Extract DAF %	VSR Vacuum Dried
North Dakota	5.4	2.7
WY	10.7	2.7
WV	18.3	2.3
UT	22.5	2.7
Pitt	27.7	2.3
Ill No. 6	35.7	2.5
Poc	1.0	1.1
UF	10.4	1.3

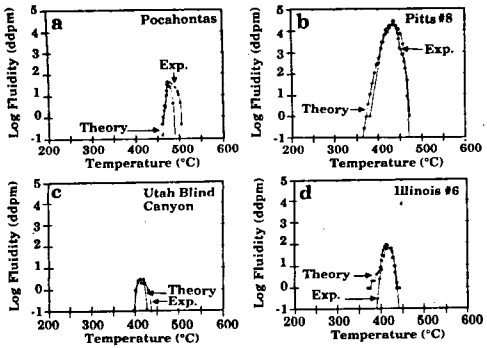

Figure 23. Measured and Predicted Fluidity for Four Argonne Coals.

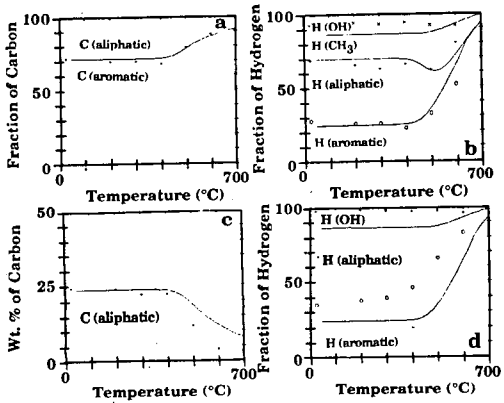

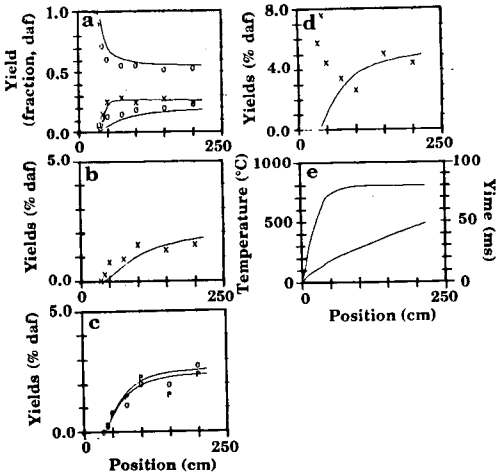

Figure 24. Predictions of FG-DVC Model for Illinois No. 6 Coal Pyrolyzed in the Heated Tube Reactor. a) Char, Tar and Gas, b) Methane, c) Olefins and Paraffins, d) Water and e) Time and Temperature. Data of Solomon et al. (53).

Figure 25. Comparison of Measured and Predicted Functional Group Composition of Pittsburgh Seam Char Heated at 30°C/min to the Indicated Temperature. a) Carbon Distribution by NMR, b) Hydrogen Distribution by NMR, c) Weight Percent Aliphatic Carbon by FT-IR, and d) Hydrogen Distribution by FT-IR. Data from Solum et al. (68).

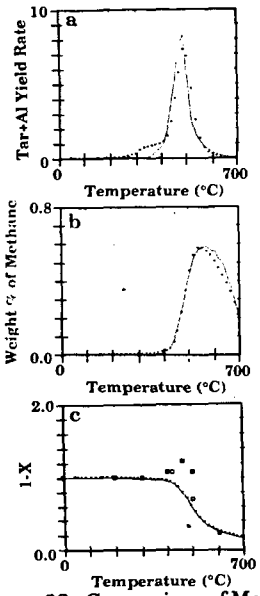

Figure 26. Comparison of Measured and Predicted Pyrolysis Behavior of Pittsburgh Seam Char Heated at 30°C/min to the Indicated Temperature. a) Tar Yield, b) Methane Yield, and c) Solvent Swelling Ratio.

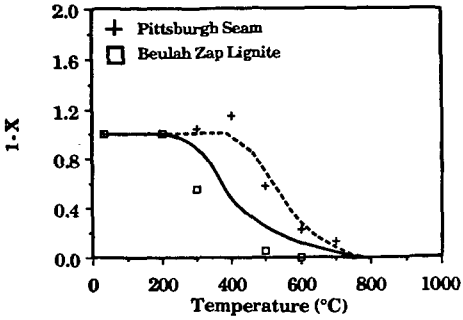

Figure 27. Comparison of Measured and Predicted Normalized Volumetric Swelling Ratio as a Function of Temperature for a Lignite and a Bituminous Coal.

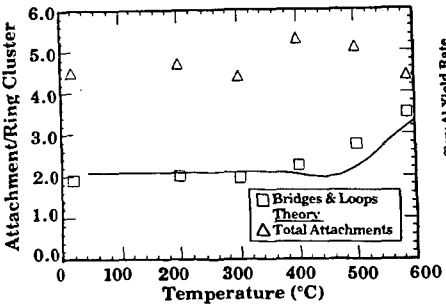

Figure 28. Comparison of Theory with NMR Data for Attachments to Ring Clusters (data from University of Utah).

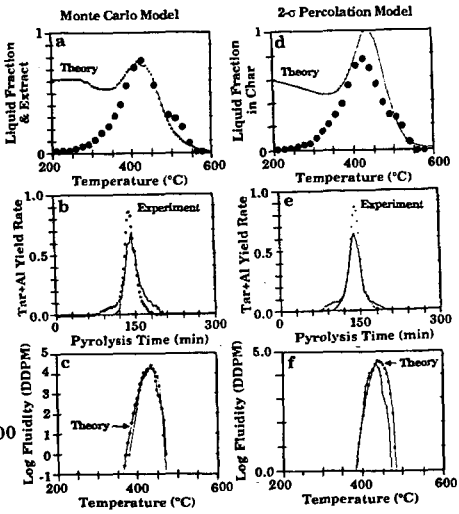

Figure 29. Comparison of Monte Carlo and 2-σ Percolation Theory for Liquid Fraction, Tar Yield and Fluidity for Pittsburgh No. 8 Bituminous Coal at 3°C/min.

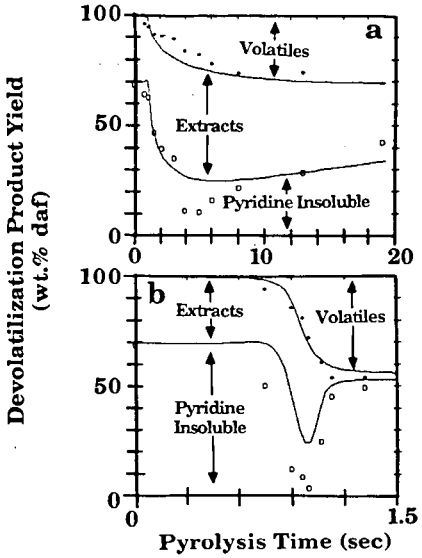

Figure 30. Comparison of FG-DVC Model Predictions with the Data of Fong et al. (73) (symbols) for Pittsburgh Seam Coal. a) 813K @ 470K/s and b) 1018K @ 640K/s. P=0.85 atm. The Solid Lines Assumes Transport by Eq. 4 (ΔP=0 atm) and No External Transport.

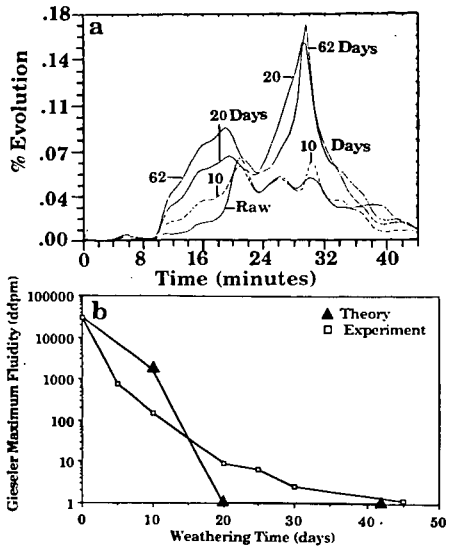

Figure 31. Reduction in Fluidity with Weathering: a) CO_2 Evolutio of Raw and Weathered Coal, and b) Predicted and Measured Fluidity (Measurements of Wu et al. Ref. 79). Weathered Coal was Kept at 80°C for the Indicated Number of Days.

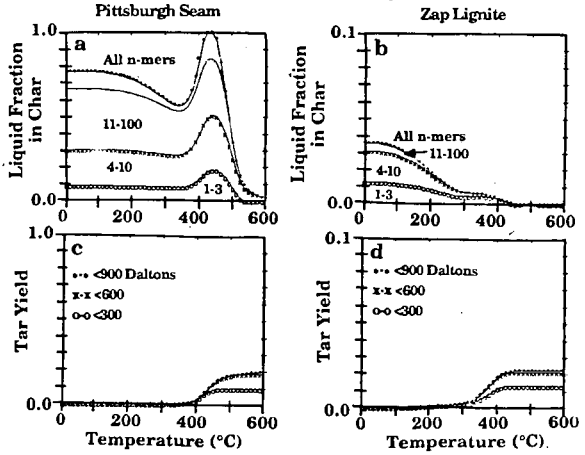

Figure 32. Predicted Molecular Weight Distribution in Char and Tar for a Bituminous Coal and a Lignite. a) and b) Molecular Weight Distribution for Char. and c) and d) Molecular Weight Distribution for Tar.

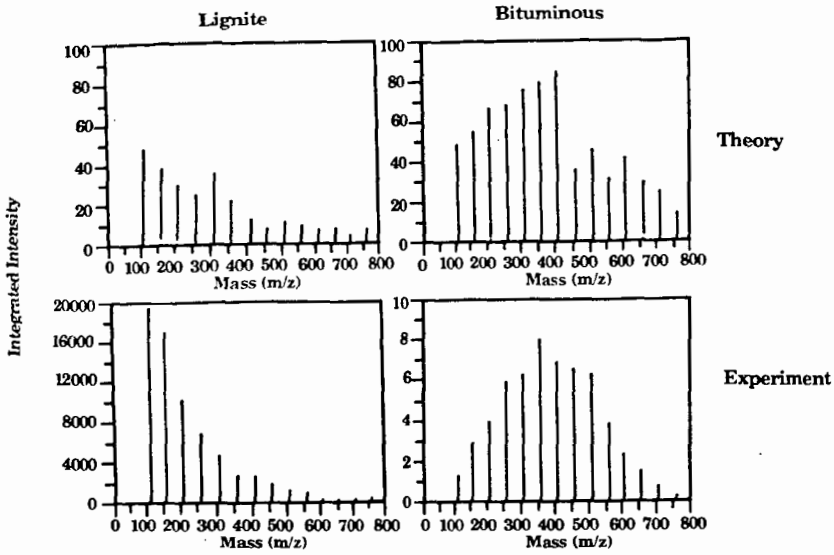

Figure 33. Comparison of Measured and Predicted Tar Molecular Weight Distributions for Lignite and Bituminous Coals. The Experiments are Performed by Pyrolysis of Coal Samples in a FIMS Apparatus. Intensities have been Summed over 50 AMU Intervals.

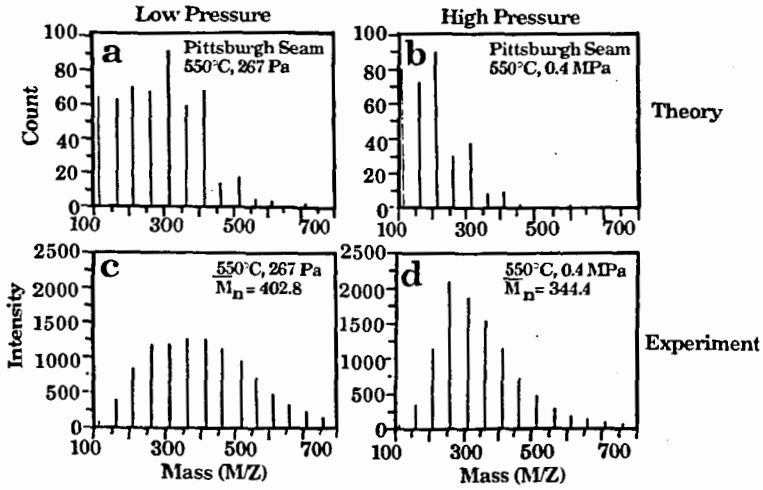

Figure 34. Comparison of Predicted (a and b) and Measured (c and d) Tar Molecular Weight Distribution for Pyrolysis of a Pittsburgh Seam Coal in a Heated-Grid Apparatus at a Heating Rate of 500°C/s to 550°C. Parts a and c Compare the Prediction and the Measurement at 0.00267 atm. Parts b and d Compare the Prediction and Measurement at 4.0 atm. P = 0.2 atm.

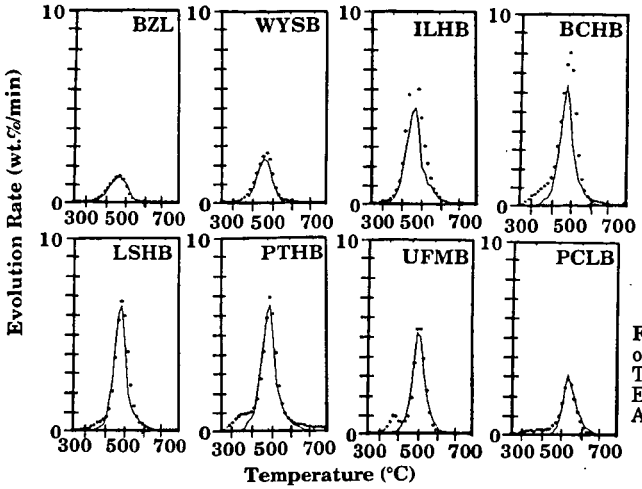

Figure 35. Comparison of Measured and Predicted TG-FTIR Analysis of Tar Evolution for the Eight Argonne Coals.

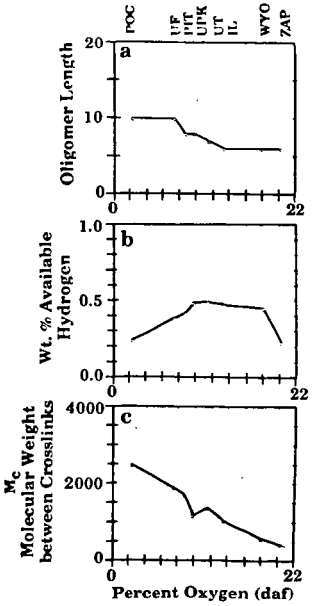

Figure 36. Network Parameters for Monte Carlo Version of FG-DVC Model for Eight Argonne Coals. a) Oligomer Length, b) Weight Percent of Available Hydrogen and c) Molecular Weight Between Crosslinks, M_c.

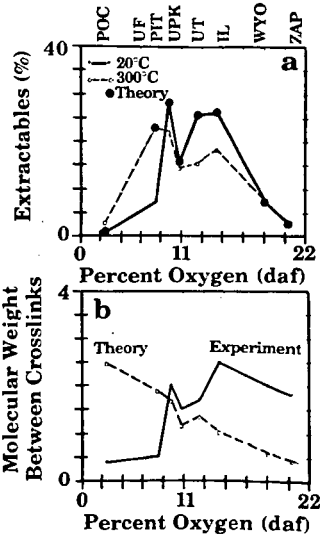

Figure 37. Comparison of Experimental and Theoretical Parameters for a) Extractables and b) Molecular Weight Between Crosslinks.

COMPARATIVE ANALYSIS OF THE ENVIRONMENTAL IMPACT OF ALTERNATIVE TRANSPORTATION FUELS

Robert F. Klausmeier
Radian Corporation
P.O. Box 201088
Austin, TX 78720-1088

INTRODUCTION

Emissions from motor vehicles contribute significantly to air pollution problems. Despite new emission standards and advances in motor vehicle emission control technology, many areas in the country are still projected to have air pollution problems in the year 2000 and beyond. It appears unlikely that there will continue to be significant declines in emissions from gasoline and diesel-powered vehicles. This situation has spurred interest in alternative fuels for transportation.

Substituting alternative transportation fuels for gasoline and diesel fuel may improve air quality in the United States. The goal of this paper is to analyze the impact of alternative transportation fuels on attainment of The National Ambient Air Quality Standards for ozone and carbon monoxide (CO). Although cost and other consumer acceptance factors are not analyzed, all the alternative fuels studied are considered feasible for use by the general public. The term "alternative fuel" is used throughout this report to mean any non-gasoline or diesel fuel, including gasoline mixtures.

This report concentrates on light duty applications of alternative fuels, because light-duty vehicles play a much greater role in ozone and CO non-attainment than heavy-duty vehicles. The emphasis in this report is on how methanol, compressed natural gas (CNG), and liquified petroleum gas (LPG) compare with gasoline.

IMPACT OF ALTERNATIVE FUELS ON ATTAINMENT OF THE NAAQS FOR OZONE

One of the most persistent air quality problems in the U.S. has been the attainment of the NAAQS for ozone. Currently, approximately 90 million people live in areas that have one or more violations of the ambient ozone standard, and a downward trend in ozone levels is not evident. In 1988 there were more ozone violations than in many of the previous years.

Ozone is caused by atmospheric photochemical reactions involving volatile organic compounds (VOCs) and oxides of nitrogen (NO_x). Mobile sources account for about half of these emissions. The ozone formation rate is greater at higher ambient temperatures.

VOCs are emitted from mobile sources as either tailpipe or evaporative emissions. Tailpipe emissions occur as a result of incomplete combustion and/or chemical reactions during combustion. NO_x is largely produced by reactions between nitrogen and oxygen at high temperatures.

EPA policy emphasizes that states should control ozone by reducing VOCs rather than NO_x emissions. However, in areas dominated by VOC emissions (i.e., they have a high HC to NO_x ratio in the ambient air) there is some evidence that reducing NO_x emissions, as well as VOCs, helps reduce ozone.

Impact of Alternative Fuels on Reactive VOC Emissions

VOCs emitted from mobile sources typically are termed hydrocarbons (HCs). In 1988 most (92 percent) of the HC emissions from mobile sources were from light-duty gasoline-powered vehicles (1). Therefore, these vehicles are the target for additional HC controls.

An analysis of VOC emissions impacts must consider both exhaust and evaporative emissions. Furthermore, the photochemical reactivity of these emissions must be considered.

The State of California recently quantified the composite reactivity of emissions from vehicles powered by different fuels. In their study, they speciated emissions for different fuels and calculated the mass-weighted reactivity of the total vehicle emissions. The results of their study are summarized on Table 1 (1). Non-methane VOC emissions from natural gas-powered vehicles are less reactive than those from vehicles powered by other alternative fuels; they are less than half as reactive as non-methane hydrocarbons (NMHC) from gasoline-powered vehicles. Methane emissions were excluded because they have neglible reactivity. VOC emissions from methanol-fueled vehicles include methanol and are estimated to be between 50 and 56 percent as reactive as those from gasoline-powered vehicles. The lower percentage assumes low formaldehyde emission rates (15 mg/mile).

The following discussion compares non-methane VOC emission rates for vehicles powered by different fuels. Exhaust and evaporative emissions rates that are reported in publicly available sources are analyzed.

Reactive VOC Exhaust Emissions for Different Fuels - Reactive VOC emissions from alternative fueled vehicles include non-methane hydrocarbons (NMHCs), methanol, and formaldehyde. Figure 1 summarizes information on NMHC and formaldehyde exhaust emissions from light-duty vehicles burning different fuels. Although a range of values is shown on Figure 1, almost all the emission tests were performed on low-mileage vehicles, so the range may still underestimate in-use emissions. The M100 (100% methanol) numbers are for advanced, dedicated prototypes, while the CNG and LPG numbers are more representative of production dual-fuel vehicles.

For reference purposes, two estimates are presented for VOC exhaust emissions from gasoline-powered vehicles. The high estimate was generated by MOBILE4 (EPA's mobile source emission factor model) for a fleet composed almost entirely of 1981 and newer automobiles. The low estimate for gasoline-powered vehicles equals the exhaust emission standard for 1981 and newer vehicles.

Table 2 summarizes the range of methanol exhaust emissions in grams per mile that were found in the database for M85- and M100-fueled vehicles. Note that the high number (1.6 g/mi) for M85 (85% methanol, 15% gasoline) was a 50,000 mile projection made by EPA (2), so it most likely represents the in-use emission factor in grams per mile. The high value for M100 (1.7 g/mi) is the average of emission test results on vehicles operated on greater than 90 percent methanol (3). If in-use vehicles emit methanol at rates close to the high range shown on Table 2, some ozone impacts, in addition to those from NMHC and formaldehyde emissions, are likely from methanol-fueled vehicles.

Evaporative Emissions for Different Fuels - Evaporative emissions are composed of stationary evaporative losses (hotsoak and diurnal losses), running evaporative losses, and refueling losses. VOC emissions due to fuel evaporation will vary greatly for the different alternative fuels.

Figure 2 shows a comparison of stationary NMHC evaporative losses for different fuels. The database contains information on stationary evaporative losses for vehicles fueled with M85; MOBILE4 was used to estimate evaporative losses from gasoline-powered vehicles. The high value (0.14 g/mi) for M85 shown on Figure 2 is a 50,000 mile in-use projection made by EPA (4). The low value for M85 is based upon test results for two advanced prototype vehicles (5).

Few data are available on the amount of VOC's that is emitted due to running losses or refueling losses for the different alternative fuels. Table 3 shows estimated running and refueling NMHC losses based upon engineering judgment.

Table 4 summarizes the reported range of methanol evaporative emissions while the vehicle is stationary (hot soak and diurnal losses). The high value for M85 (0.37 g/mi) is the 50,000 in-use estimate by EPA (2). The low value (0.02 g/mi) is based on two advanced prototypes tested by the California Air Resource Board (4). Only one test result was available on advanced M100 vehicles (equivalent to 0.12 g/mi) (4).

Total Reactive VOC Emissions from Light-duty Vehicles for Different Fuels - Figure 3 shows estimates of the total exhaust and evaporative reactive VOC emissions from light-duty vehicles during periods when the ambient temperature ranges between 60° and 84°F. Methanol emissions are indicated by the shaded area. Because they have low NMHC emissions in the exhaust and negligible evaporative emission losses, dedicated CNG vehicles are estimated to emit the smallest amount of reactive VOC emissions.

The total emission values for M85 and M100 vehicles include methanol. The totals for M85 are similar to the MOBILE4 estimate for gasoline-powered vehicles, but as discussed earlier M85 vehicle emissions are less reactive than gasoline-powered vehicle emissions. Thus, there may be some ozone benefits for M85, but a clear benefit is not evident. M100-powered vehicles are estimated to have greater ozone benefits than M85 because they appear to emit much less NMHC. Dedicated LPG vehicles may have similar benefits to M100 vehicles; LPG may result in greater NMHC emissions than M100 but M100 will result in substantial methanol emissions.

Dual-fuel LPG and CNG vehicles will emit much greater amounts of VOCs than dedicated LPG and CNG vehicles because of evaporative NMHC losses.

NO_x Emissions for Different Alternative Fuels

The other precursor component in the atmospheric formation of ozone is oxides of nitrogen (NO_x). In 1988 about two-thirds of the mobile source NO_x emissions came from light-duty gasoline-powered vehicles.

Figure 4 compares estimated emissions from light-duty vehicles burning different alternative fuels with emissions from light-duty gasoline-powered vehicles. Unlike the case with NMHC emissions, MOBILE4 estimates of NO_x emissions from 1981 and newer light-duty vehicles are identical to the NO_x standard.

Considering that gasoline-powered vehicles can meet much more stringent emission levels than the Federal NO_x standard, none of the alternative fuels appears to offer clear advantages in reducing NO_x emissions from light-duty vehicles. Emission rates lower than the MOBILE4 estimates were observed for all the fuels; however, emission rates equal to or higher than the MOBILE4 estimates also were observed for most of the fuels. One can conclude that light-duty vehicles can be designed to burn alternative fuels such as CNG, LPG, or methanol and meet emission levels achievable by gasoline-powered vehicles; but it appears unlikely that large reductions are possible. Dual-fuel CNG vehicles are expected to emit about the same amount of NO_x as dedicated CNG vehicles with similar NO_x emission controls.

IMPACT OF ALTERNATIVE FUELS ON ATTAINMENT OF THE NAAQS FOR CARBON MONOXIDE

Exceedances of the NAAQS for carbon monoxide (CO) are less widespread than exceedances of the ozone standard. There has been a significant downward trend in ambient CO concentrations, but several tough CO attainment problems remain. Areas with extreme ambient conditions, such as Alaska and Colorado, are not projected to attain the CO standard without additional controls.

About 80 percent of the nationwide CO inventory is from mobile sources. And most (91 percent) of the mobile source CO emissions are from light-duty gasoline-powered vehicles (1).

Figure 5 shows the range of CO emissions that were observed for light-duty vehicles powered by different fuels. Two estimates of gasoline-powered CO emissions are provided as a reference. One is the MOBILE4 estimate for 1981 and newer vehicles, the other is the CO emission standard for 1981 and newer vehicles.

CNG-powered light-duty vehicles appear to have lower CO emissions than vehicles powered by other fuels. These levels were achieved by vehicles with both advanced emission controls and with no emission controls. These data indicate that CO emissions from CNG-powered vehicles are likely to be very low in actual use, because CO emission levels are less sensitive to vehicle technology or tampering. It is possible to run a CNG engine rich (too much fuel) which greatly increases CO emissions, but these cases should be identified in most inspection/maintenance programs or preventive maintenance checks.

LPG vehicle emissions are higher than CNG vehicle emissions, but are lower than the CO standard for 1981 and newer light-duty vehicles. When M85 and M100 vehicle emissions are compared with the CO emission standard, there appears to be no clear advantage for those fuels. The data are not adequate to project a CO emission value comparable to the MOBILE4 estimate for M85- and M100-powered vehicles. Because most of the emission tests were performed on low-mileage, well-maintained vehicles, it is likely that actual in-use emissions for those fuels would be much higher.

CONCLUSIONS

Impact of Alternative Fuels on Attainment of the NAAQS for Ozone - Efforts to attain the NAAQS for ozone would be enhanced if vehicle fleets in non-attainment areas consumed certain alternative fuels instead of gasoline. Dedicated CNG vehicles appear to have the greatest ozone benefits. LPG and M100 vehicles also offer significant ozone benefits. However, dual-fuel CNG or LPG vehicles and M85 vehicles (vehicles designed to burn mixtures of 85 percent methanol and 15 percent gasoline) may not be much better than gasoline vehicles. The primary reason for this is that evaporative volatile organic compounds (VOCs) emissions from storage of gasoline in the vehicle greatly increase their overall contribution to ozone formation.

This conclusion assumes that each fuel will displace a similar amount of gasoline. It does not consider consumer acceptance or infra-structure issues that will impact the market penetration of an alternative fuel.

Impact of Alternative Fuels on Attainment of the NAAQS for Carbon Monoxide (CO) - Both dedicated and dual-fuel CNG vehicles emit much less CO than gasoline-powered vehicles, so their use will help an area attain the CO NAAQS. LPG vehicles also appear to produce lower amount of CO than gasoline-powered vehicles, but they emit greater amounts than CNG-powered vehicles. Available data are not adequate to project the impact of methanol-fueled vehicles on CO. Preliminary data show that methanol-powered vehicles (both M85 and M100) will emit much more CO than CNG-powered vehicles.

REFERENCES

1. Klausmeier, Rob. Assessment of Environmental, Safety and Health Issues Related to The Use of Alternative Transportation Fuels. Radian Corp., October, 1989.

2. Alson, J. A., M. M. Adler, and T. M. Baines. Motor Vehicle Emission Characteristics and Air Quality Impacts of Methanol and Compressed Natural Gas. U.S. Environmental Protection Agency, Office of Mobile Sources, 1989.

3. Data Base on Emissions from Methanol Fueled Vehicles. U. S. Environmental Protection Agency, Ann Arbor, MI, 1989.

4. Gold, M. D. and C. E. Moulis. Emission Factor Data Base for Prototype Light-Duty Methanol Vehicles. In: Methanol -- Promise and Problems. International Fuels and Lubricants Meeting and Exposition, Toronto, Ontario, 1987.

5. California Air Resources Board. Methanol Fueled Fleet Test Program. Emission Data. CRC Methanol Workshop. March, 1988.

TABLE 1. COMPARISON OF EXHAUST[a] REACTIVITY FOR DIFFERENT FUELS

Fuel Type	Reactivity Factor[b]
Gasoline	1
M85	.56
M85-Low HCHO	.5
LPG (Dual-Fueled)	.85
LPG (Dedicated)	.67
CNG (Dual-Fueled)	.45
CNG (Dedicated)	.36

[a]Emissions include NMHC, formaldehyde, and methanol, but exclude methane.

[b]Relative to gasoline.

Source: Reference 40.

TABLE 2. METHANOL EXHAUST EMISSIONS FROM 1981 AND NEWER AUTOMOBILES BURNING METHANOL

Fuel	Methanol (g/mi) (Range in database)
M85	0.14[a] - 1.6[b]
M100	0.33[c] - 1.7[d]

[a]Average of 3 lean-burn vehicles (42-CARB 88).

[b]50,000 mile projection (2-EPA 87).

[c]One advanced prototype vehicle (1-EPA 89).

[d]Average of emission test results on vehicles fueled with greater than 90 percent methanol (5-EPA 89).

TABLE 3. ESTIMATED NMHC RUNNING LOSS AND REFUELING EMISSIONS 1981+ LIGHT-DUTY VEHICLES - SUMMER

	Running Loss (g/mi) 60 - 84°F	Running Loss (g/mi) 80 - 95°F	Refueling Loss (g/mi)
FLEET LDGV (MOBILE4)	0.28	0.59	0.25
M85	0.13[a]	0.38[a]	0.17
M100	0	0	0
CNG - DUAL FUEL 0.14/0.17	0.23[b]	0.41[b]	0.35[c]
CNG - DEDICATED	0	0	0
LPG - DEDICATED[f]	0[d]	0[d]	.[e]

[a]Determined by multiplying MOBILE4 gasoline projection by ratio of projected M85 evap/MOBILE4 evap

[b]Assumed to be equal to MOBILE4 emissions with RVP = 8.0 psi

[c]Assumes 80% natural gas, 20% gasoline operation.

[d]Assumes no fugitive emissions.

[e]Small amount of refueling losses. Data not available.

[f]LPG - Dual-fuel will be similar to CNG dual-fuel.

LDGV - Light duty gasoline vehicles

NOTE No emission standard has been established for running losses, originally assumed to be zero

TABLE 4. EVAPORATIVE METHANOL EMISSIONS FROM 1981 AND NEWER METHANOL-FUELED VEHICLES

Fuel	Methanol (g/mi)
M85	0.02[a]-0.37[b]
M100	0.12[c]

[a]Two advanced prototypes (42-CARB 88).

[b]50,000 mile in-use projection (2-EPA 87).

[c]One test (2-EPA 87).

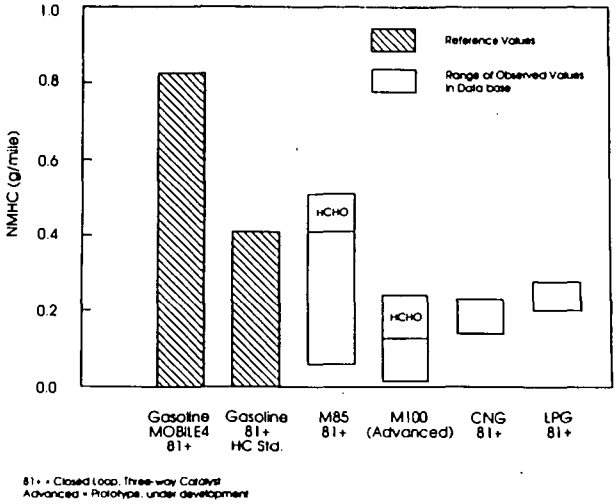

Figure 1. NMHC Exhaust Emissions from Light-duty Vehicles

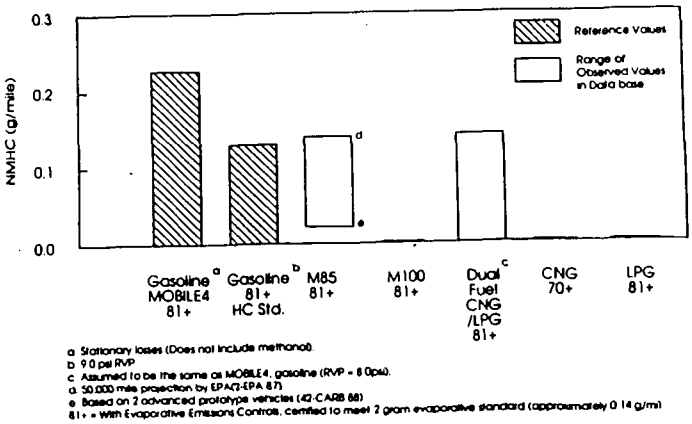

Figure 2. NMHC Evaporative Emissions[a] from Light-duty Vehicles

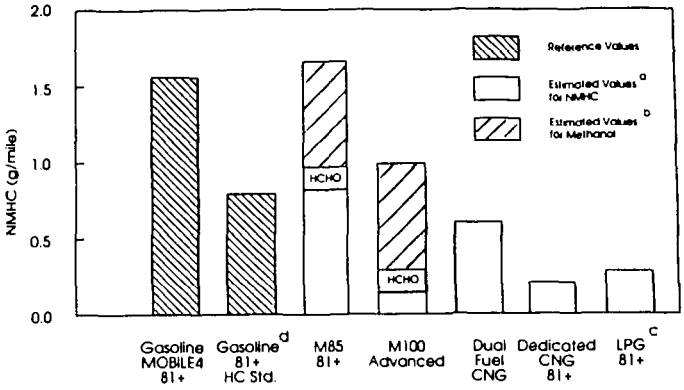

a Values are based on high observed emission levels in data base.
b HC Equivalent
c Assumes no fugitive emissions and dedicated application. Dual fuel LPG will be like dual-fuel CNG
d Assumes no running losses
HCHO Formaldehyde

Figure 3. Estimated Total VOC from Light-duty Vehicles (Exhaust plus Evaporative Losses) during Average Summer Weather (60°-84°F)

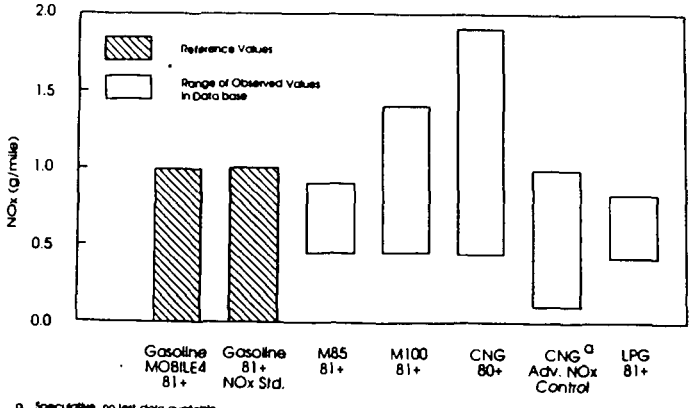

a. Speculative, no test data available
81+ = Closed Loop, Three-way Catalyst
80+ = Oxygen Catalyst, or Three-way Catalyst
Adv. NOx Control = Fast burn, Stoichometric or Lean burn

Figure 4. Estimated NO_x Emissions from Light-duty Vehicles

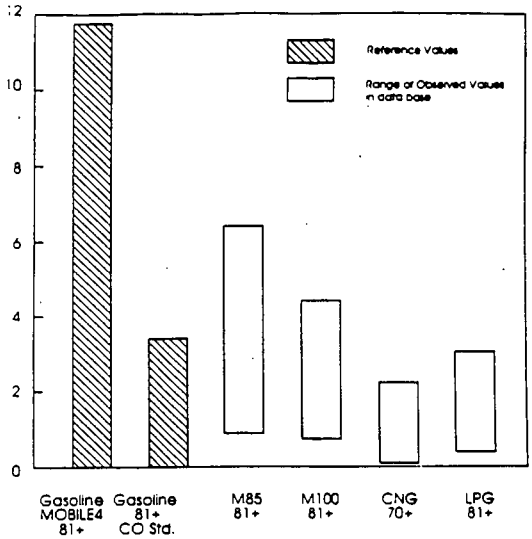

Figure 5. CO Emissions from Light-duty Vehicles

PAH, NITRO-PAH, AND MUTAGENICITY ASSOCIATED WITH DIESEL EMISSIONS MODIFIED BY USE OF A CERAMIC PARTICLE TRAP.

Susan T. Bagley, Linda D. Gratz, David G. Leddy, and John H. Johnson
Michigan Technological University
Houghton, MI 49931

KEY PHRASES: Heavy-duty Diesel Emissions; Polynuclear Aromatic Hydrocarbon Concentrations; and Mutagenicity Characterization.

INTRODUCTION

Whole diesel exhaust has recently been classified as a probable human carcinogen by the International Agency for Research on Cancer (1) and a potential occupational carcinogen by the National Institute for Occupational Safety and Health (2). Much of the research on the possible health effects of diesel emissions has focused on the particle phase and associated organics, which include many polynuclear aromatic hydrocarbons (PAH) with known biological activity (1,3). The particle-free vapor phase exhaust component has been less extensively studied, with mixed results as to its potential health effects (1). However, this phase has also been shown to contain many of the same types of PAH as found with the particles (1,4,5), some of which could adsorb onto atmospheric particles after leaving the diesel engine.

Various federal regulations have been established concerning allowable levels of oxides of nitrogen (NO_x), hydrocarbons (HC), and particles or total particulate matter (TPM) for on-road heavy-duty diesel emissions for 1991 and 1994 (6). Engine manufacturers have generally been able to meet all of the 1991 standards and the 1994 NO_x and HC standards by making engine modifications. However, it is likely that some type of exhaust aftertreatment device will be required on some engines to meet the 1994 TPM standards, even with the use of low sulfur fuels. One type of device that would likely be used with some types of engines is the uncatalyzed ceramic particle trap. Traps will also be used on buses and on underground mine vehicles. The exhaust must pass through the walls of the trap, which typically results in $\geq$ 90% removal of particles depending on the type of engine and how it is operated. However, studies with a 1979 heavy-duty diesel engine indicate that HC and vapor phase organics, including PAH, may be only minimally affected by trap usage (4).

This study was designed to assess the effects of an uncatalyzed ceramic particle trap on the regulated and unregulated emisisons such as PAH from a late-model, heavy-duty diesel engine. In addition to monitoring effects on NO_x, HC, and TPM, detailed analyses were made of organic material from both the particle and vapor phases for levels of selected biologically active PAH and nitro-PAH as well as mutagenicity. These data were obtained as part of a larger study funded by the Health Effects Institute concerned with obtaining some of the quantitative data necessary for the evaluation of the toxicological impact of employing particle trap technology with modern heavy-duty diesel engines.

EXPERIMENTAL

Engine Operation and Emissions Measurements - A 1988 Cummins Engine Co. LTA10-300 heavy-duty diesel engine was used throughout this study. This turbocharged and aftercooled, direct injection engine met the 1988 federal and California Air Resources Board emissions standards (6) without any exhaust aftertreatment and was considered to be representative of engines on the road in the 1990's. The uncatalyzed ceramic particle trap was a Corning type EX-54 four-piece "quad" (0.305 m long and 0.289 m diameter) with a cell density of 15.5 cells/cm^2, a wall thickness of 0.43 mm, and a mean pore size of 26 μm. One batch of AMOCO Premier No. 2 diesel fuel was used, having a cetane index of 48.6, sulfur content of 0.316 wt %, and aromatics content of 22.0 vol %. The engine oil used was Cummins Premium Blue (SAE 15W-40).

Emissions with and without the trap were collected with the engine operating at two rated speed (1900 rpm) modes of the EPA 13-mode steady-state cycle, i.e., modes 9 (75% load)

and 11 (25% load). These modes were selected as being representative of on-highway operation, having similar emission characteristics to data for transient operation of this engine, and having exhaust temperatures below those at which trap self-regeneration should occur. (However, later testing indicated that some trap self-regeneration was occurring at mode 9 due to higher trap temperatures.)

Levels of HC, NO_x, and nitric oxide (NO) were determined in the raw exhaust using a Beckman flame ionization detector HC analyzer and a chemiluminescence NO/NO_x analyzer, respectively. A portion of the raw exhaust with or without (baseline) trap usage was split-off and injected into a dilution tunnel. The volume dilution ratio was calculated by the ratio of measured raw NO_x to measured dilute NO_x.

Portions of the dilution tunnel flow were diverted simultaneously into one of two sampling systems, i.e., a 47-mm filter system used for determination of TPM and component levels [soluble organic fraction (SOF), sulfate, and solids (SOL)] and a 508 x 508-mm filter system used for collection of particle and vapor phase materials for chemical and biological characterization. Both systems contained the same type of Teflon-coated woven glass fiber filters (Pallflex TX40H120-WW). A container with 40 g XAD-2 resin was located immediately behind the 508 x 508-mm filter to collect semi-volatile organics (XOC).

In order to minimize dilution tunnel sampling variablity (7), the filter face temperature under all engine operating conditions was maintained at 45 ± 2°C by allowing the dilution ratio to vary as ambient temperatures (tunnel inlet temperatures) varied for different runs. In order to also minimize the potential for artifact formation, sampling times were held at ≤60 minutes and filter face nitrogen dioxide levels at <5 ppm.

Levels of TPM on the 47-mm filters were determined gravimetrically. Soluble organic fraction levels were determined gravimetrically after filter extraction for four hours with dichloromethane in a Soxhlet apparatus. Sulfate levels were then determined using ion chromatography. Any remaining mass on the filters was considered to be the SOL component. Levels of SOF and XOC associated with the 508 x 508-mm filters and XAD-2 resin, respectively, were determined after Soxhlet extraction for 24 hours with dichloromethane. The mass of each extract was determined gravimetrically by allowing the SOF or XOC to dry on a known mass of Florisil.

Compound Quantitation - The PAH and nitro-PAH selected for quantitation by high performance liquid chromatography (HPLC) were: benz[a]anthracene; benzo[b]fluoranthene; benzo[k]fluoranthene; benzo[a]pyrene; chrysene; fluoranthene; 7-nitrobenz[a]anthracene; 6-nitrochrysene; 3-nitrofluoranthene; 2-nitrofluorene; 1-nitropyrene; and pyrene. These compounds were selected for quantitation due to their known or suspected health effects (1,3), their known occurrence in diesel exhaust (1,3-5,7), the availability of suitable reference materials, and the ability to resolve them from apparent interferences in our quantitation procedure (7).

Separation of the SOF or XOC samples and compound quantitations were conducted using the scheme presented in Figure 1. Quantitation was accomplished by using internal standard method calculations using 2-chloroanthracene and comparison to the National Institute for Standards and Technology standard reference material 1647a as the reference (calibration) standard for PAH and standard reference material 1597 for the nitro-PAH calibration standard. Minimum detection levels (MDL) were determined using dilutions of the calibration standards, with MDL considered to be those quantities injected on the HPLC having a minimum of three times the background noise and areas which could be reproducibly measured. As 1-nitropyrene and 1,3-dinitropyrene coeluted by the method noted for nitro-PAH quantitation, the results are presented as "1-nitropyrene + 1,3-dinitropyrene" levels.

Mutagenicity Analyses - Mutagenicity associated with the SOF and XOC samples was determined using a small dish modification of the microsuspension version of the *Salmonella typhimurium*/microsome mutagenicity bioassay (8-10). Samples for the mutagenicity bioassays were prepared by dissolving a known mass of SOF or XOC in a known volume of dimethylsulfoxide. All samples were tested with tester strain TA98 ± S9 metabolic activation and retested with the nitroreductase-deficient tester strains TA98NR and TA98-1,8-DNP_6 if

responses were detected with TA98-S9. The appropriate solvent, positive control, genotype, sterility, and viability controls were conducted with each test (8).

Data Analysis - As data from two to six test dates per mode and condition were available for analysis, this study was considered to have an unbalanced design with test dates as replicates (11). There was an unequal number of samples per replicate date for each mode and condition; therefore, a mean of means was calculated for most emission parameters, except as noted below. A two-way analysis of variance (ANOVA) was used to compare mode (9 and 11) versus condition (baseline and trap) means at a significance level of 0.05. Where a significant interaction term occurred, a one-way ANOVA was used.

Exceptions had to be made to the statistical analysis procedures (as described above) for many of the PAH and nitro-PAH measurements and the mutagenic activity data. The latter could not be analyzed statistically because the revertants/μg value was calculated using a power function model that was dependent upon the interaction of both the slope and the y-intercept (12). The frequent occurrence of "less than MDL" values in the compound quantitation data sets meant that mean daily values typically could not be calculated. Therefore, mean of median values were determined for each mode/condition for use in the ANOVA. If the majority of values for any test date was above the MDL, then that median value was used for that test date. If 50% or less of the values for each test date were above the MDL, then a value was assigned to each "less than MDL" value for median determinations using several different techniques. The technique that appeared to have the least scattering of residuals was the replacement of the "less than MDL" value with "MDL/2". All ANOVA results reported in this paper involving mean of median analyses were conducted using this technique.

RESULTS AND DISCUSSION

This paper summarizes the results of one of the few large heavy-duty diesel emission sample sets comprising multiple test dates and engine operating modes and conditions. It also represents the first detailed quantitative study specifically of biologically active PAH and nitro-PAH compounds associated with both the particle and vapor phase exhaust from a late-model diesel engine.

Gaseous and Particle-Associated Emissions - Baseline emissions from this 1988 Cummins heavy-duty diesel engine were notably different from older engines tested at Michigan Technological University (MTU) (4, 7, 12). Not only were TPM levels much lower with the 1988 engine, but the proportion of the HC recovered on XAD-2 resin (as XOC) compared to the filters (SOF) was greatly increased.

As indicated in Table 1, use of the trap with the Cummins engine had no significant effects on NO_x (or NO) concentrations at either mode but exerted its effects on the HC (and XOC), TPM, and TPM-associated exhaust components. The greatest effects were found with reductions in SOL concentrations of up to 95%, as this type of control device acts primarily to physically remove this material via engine mode-independent mechanisms. These results are in agreement with previous studies with other types of diesel engines (4, 12-14). The reductions in SOF can be related both to some significant effects on HC levels (at mode 9) and to the decrease in SOL surface sites for adsorption of organic material found at both modes. Sulfates were also decreased with trap use, although a significant change was found only at mode 9. These combined reductions resulted in 92% and 80% TPM-removal efficiencies at modes 9 and 11, respectively. There were consistent mode-dependent differences in trap effects on HC and XOC concentrations, with the latter representing a portion of the vapor phase HC. The significant changes in HC and XOC concentrations (reductions of 43 and 67%, respectively) at mode 9 but virtually no change at mode 11 were most likely related to differences in exhaust temperature between the two modes. The higher trap temperature at mode 9 (450°C) versus mode 11 (325°C) probably resulted in greater oxidation of HC within the trap and, thus, lower HC and XOC levels after the trap. A high proportion of the recoverable HC were still vapor-phase associated (as XOC) even with trap use at mode 9.

Mutagenicity Effects - A summary of the trap and mode effects on TPM and XOC-associated mutagenic activities is presented in Table 2. All detected mutagenicity was direct-acting in nature, regardless of mode, trap usage or particle or vapor phase association, as has

typically been found for diesel exhaust-associated organics. However, in contrast to previous studies with older model engines at MTU (4,12) and elsewhere (13,14) with this same type of control device, trap use with this 1988 engine did not produce increases in TPM-associated mutagenic activities (revertants/μg). The 93% and 86% decreases in exhaust mutagenic concentrations (revertants/m^3) at modes 9 and 11, respectively, were similar to the reductions found in TPM and SOF concentrations (Table 1). Similar to our earlier study with a 1979-model heavy-duty diesel engine (4), about 50% of the recovered mutagenicity (TPM plus XOC) was associated with the XOC. Unlike the earlier study, no mutagenicity was detected at either mode with trap usage with this 1988 engine. Differences in engine configurations and operation, emissions levels (such as for NO_x and NO), and sampling procedures may account for these differences in trends between the present and previous studies.

The responses of the two nitroreductase-deficient tester strains (Table 2) indicated more of the observed TPM-associated activity was due to nitro-substituted compounds under baseline than under trap conditions. The same general relationship was found between baseline TPM and XOC-associated mutagenicity, with the exception of the TA98-1,8-DNP_6 responses at mode 11. This likely indicates differences in the proportion of nitro-substituted compounds in the particle versus vapor phases under baseline conditions and, perhaps, lower levels of these mutagenic compounds with the trap.

PAH and Nitro-PAH Constituents - The ranges of PAH and nitro-PAH concentrations found for each operating condition with and without the trap are presented in Table 3. The baseline particle-associated concentrations for many of these compounds are lower than those in our earlier study with an older engine using similar quantitation techniques (7), in part due to the lower TPM levels with the 1988 engine. However, comparisons to literature values for other studies are difficult due to differences in engines, operating and sampling conditions, and analytical procedures. As noted in the "Experimental - Data Analysis" section, presentation and analysis of most of these data sets were complicated by the presence of "less than MDL" values. With the exception of the fluoranthene TPM and XOC, pyrene TPM and XOC, and chrysene TPM data sets, all of the PAH and nitro-PAH data were analyzed using procedures to estimate medians. Even so, several of these ANOVA comparisons did result in significant differences between either trap use or mode.

Trap usage had significant effects on fluoranthene, benzo[b]fluoranthene, and 7-nitrobenz[a]anthracene TPM-associated concentrations at mode 9 and pyrene and 7-nitrobenz[a]anthracene at mode 11. With the exception of pyrene, the concentrations of these compounds decreased with trap use. The general trend, which was more pronounced at mode 9 than 11, was for decreases in concentrations with use of the trap. Pyrene was the only compound with significant differences in concentrations between modes, although the general trend was for higher concentrations at mode 11 than at mode 9. This trend is in agreement with the higher exhaust temperatures and greater reductions in HC and SOF found at mode 9.

In contrast, the trap was found to have no signficant effects on vapor phase compound concentrations. There were significant differences in fluoranthene, 6-nitrochrysene, and 1-nitropyrene + 1,3-dinitropyrene concentrations between modes, with the lower concentrations again found at mode 9.

Several PAH, such as the benzofluoranthenes and benzo[a]pyrene, were found almost exclusively with particles and some such as fluoranthene and pyrene were proportionally much higher in the vapor phase; these associations were generally in accordance with the known vapor pressures for these compounds (5,15). However, all of the other PAH and nitro-PAH were detected in the vapor phase emissions of this engine with or without the particle trap; a general trend was for an increase in the vapor phase concentration of many of these compounds with trap usage.

CONCLUSIONS

This uncatalyzed ceramic particle trap had consistently significant effects (up to 95% reductions) on TPM and component concentrations regardless of engine operating condition. The PAH and nitro-PAH particle-associated concentrations generally were reduced with trap use, but this was not necessarily true with the vapor phase-associated concentrations. Some

compounds appeared to shift from the particle to vapor phase with the trap. Mutagenicity associated with the particles was generally unaffected with the traps, but mutagenic concentrations decreased due to decreases in particle concentrations. All detectable vapor phase mutagenicity was eliminated with trap use. Therefore, this type of emissions control device appeared to reduce particle concentrations from this late-model heavy-duty diesel engine without increasing particle-associated levels of biologically active PAH or nitro-PAH or mutagenicity. However, the impact of increases in certain types of compounds in the vapor phase should be investigated further.

ACKNOWLEDGEMENTS

Funding for this study was provided by the Health Effects Institute (Agreement No. 87-6). The following MTU graduate students provided invaluable assistance: Cheryl Bohstedt (Biological Sciences) and Kirby Baumgard, Troy Kantola, Kevin King, and Tom Laymac (Mechanical Engineering). Barbara Heard assisted with the chemical analyses. The assistance of Dr. Thomas D. Drummer, Department of Mathematical Sciences, MTU, with the statistical analyses is greatly appreciated. Tester strain TA98 was provided by B. Ames, University of California, Berkeley, and tester strains TA98NR and TA98-1,8-DNP_6 were provided by H. Rosenkranz, University of Pittsburgh.

"Research described in this article was conducted under contract to the Health Effects Institute (HEI), an organization jointly funded by the United States Environmental Protection Agency (EPA) (Assistance Agreement X-812059) and automotive manufacturers. The contents of this article do not necessarily reflect the views of the HEI, nor do they necessarily reflect the policies of the EPA, or automotive manufacturers."

REFERENCES

(1) International Agency for Research on Cancer. *Evaluations of Carcinogenic Risk to Humans. Diesel and Gasoline Exhaust*; IARC: Lyon, France, 1989; Vol. 46.
(2) National Institute for Occupational Safety and Health. *Carcinogenic Effects of Exposure to Diesel Exhaust*. Current Intelligence Bulletin No. 50. DHHS (NIOSH) Publications No. 88-116, 1988.
(3) Hecht, S. S. *Air Pollution, the Automobile, and Public Health*; Watson, A. Y., Bates, R. R., Kennedy, D., Eds.; National Academy Press: Washington, D.C., 1988; pp 555-578.
(4) Dorie, L. D.; Bagley, S. T.; Leddy, D. G.; Johnson, J. H. *Environ. Sci. Technol.* 1987, *21*, 757-765.
(5) Schuetzle, D. EHP, *Environ. Health Perspect.* 1983, *47*, 65-80.
(6) Johnson, J. H. *Air Pollution, the Automobile, and Public Health*; Watson, A. Y., Bates, R. R., Kennedy, D., Eds.; National Academy Press: Washington, D.C., 1988; pp 39-75.
(7) Waldenmaier, D. A.; Gratz, L. D.; Bagley, S. T.; Johnson, J. H.; Leddy, D. G. Society of Automotive Engineers, 1990, Paper No. 900642.
(8) Kado, N. Y.; Langley, D.; Eisenstadt, E. *Mutat. Res.* 1983, *121*, 125-132.
(9) Maron, D. M.; Ames, B. N. *Mutat. Res.* 1983, *113*, 173-215.
(10) Stoltz, S. L.; Bagley, S. T. *Environ. Molec. Mutagen.* 1989, *14* (Suppl. 15), 15.
(11) Zar, J. H. *Biostatistical Analysis, 2nd. Ed.* Prentice-Hall, Inc: Englewood Cliffs, N.J., 1984.
(12) Miller P. R.; Scholl, J.; Bagley, S.; Leddy, D.; Johnson, J. H. *Society of Automotive Engineers Transactions* 1983, *92*, 287-315.
(13) Draper, W. M.; Hartman, H.; Kittleson, D. B.; Watts, W. F.; Baumgard, K. J. Society of Automotive Engineers, 1987, Paper No. 871621.
(14) Mogan, J. P.; Horton, A. J.; Vergeer, H. C.; Westaway K. C. *Heavy-duty Diesel Emissions Control: A Review of Technology*; Mitchell, E. W., Ed; The Canadian Institute of Mining and Metallurgy: Quebec, Canada, 1986; pp 188-197.
(15) Schuetzle, D.; Frazier, J. A. *Carcinogenic and Mutagenic Effects of Diesel Engine Exhaust*; Ishinishi, N., Koizumi, A., McClellen, R. O., Stober, W., Eds.; Elsevier Science Publishing, Inc: Amsterdam, 1986; pp 41-63.

Table 1. *Effect of a Ceramic Particle Trap on Emissions.*

Parameter[a]	Mode 9		Mode 11	
	Baseline (mg/m^3)	Trap Effect (% change)	Baseline (mg/m^3)	Trap Effect (% change)
NO_x	1,390	+1.4	430	+8.8
HC	41.8	-43*	87.2	-6.0
TPM	27.5	-92*	34.0	-80*
SOF	4.40	-89*	7.95	-75*
SOL	17.8	-95*	23.3	-86*
SO_4	5.08	-80*	2.77	-40
XOC	28.0	-67*	42.8	-4.0

[a]NO_x = oxides of nitrogen; HC = hydrocarbons; TPM = total particulate matter; TPM components - SOF = soluble organic fraction, SOL - solids, and SO_4 = sulfates; and XOC = XAD-2 resin organic component.
*Mean significantly different from comparable baseline mean ($p \geq 0.05$).

Table 2. Effect of a Ceramic Particle Trap on Mutagenic Activity.

Mode/ Condition	Component[a]	Mutagenic Activity, TA98-S9[b]		% of TA98-S9 Response		
		Revertants/μg	kRevertants/m^3	TA98+S9	TA98NR-S9	TA98DNP-S9[c]
9 Baseline	TPM	0.60	20.6	55	15	15
	XOC	0.67	18.6	105	55	64
9 Trap	TPM	0.42	1.39	92	60	46
	XOC	NR[d]	NR	NR	NT	NT
11 Baseline	TPM	0.68	27.3	72	24	24
	XOC	0.56	24.7	75	40	13
11 Trap	TPM	0.39	3.96	78	60	61
	XOC	NR	NR	NR	NT	NT

[a]TPM = total particulate matter; XOC - XAD-2 resin organic component.
[b]Revertants/μg based on power function model analysis of dose-response data.
[c]TA98DNP = TA98-1,8-DNP_6.
[d]NR = no response above spontaneous revertant levels; NT = not tested as no activity with TA98-S9.

Table 3. **Range of PAH and Nitro-PAH Concentrations.**

Compound	Concentration Range (ng/m³)[a]							
	9 Baseline		9 Trap		11 Baseline		11 Trap	
	TPM	XOC	TPM	XOC	TPM	XOC	TPM	XOC
Benz[a]anthracene	24-310	82-190	<1.1-76	<0.37-48	120-310	160-280	88-220	8.1-400
Benzo[b]fluoranthene	6.1-190	≤85[e]	<0.97-52*	<0.15-11	15-68	<4.0[d]	<1.2-95	<0.96-180
Benzo[k]fluoranthene	<1.7-24	<2.8[d]	<2.4[d]	<3.0[d]	<1.9-6.7	<4.6[d]	<1.9[d]	≤34[e]
Benzo[a]pyrene	<1.4-22	<2.9[d]	<0.14-1.3	<3.1[d]	<1.3-5.2	<4.8[d]	<1.4-13	<2.9[d]
Chrysene[b]	24-340	1.4-49	4.6-110	<0.35-45	23-360	<0.31-40	12-230	<8.7-450
Fluoranthene[c]	520-23,000	1,300-2,200	57-2,100*	88-3,000	410-780	2,100-3,500	190-2,900	730-6,500
Pyrene[c]	8.1-84	120-590	13-380	99-580	69-130	390-650	260-790*	690-1,600
7-Nitrobenz[a]-anthracene	0.60-3.9	2.5-9.5	0.14-2.1*	≤0.34-60	<4.0-7.2	14-63	≤1.3-18*	<1.1-14
6-Nitrochyrsene	2.1-13	1.7-2.5	<0.88-4.3[e]	0.69-8.0	≤0.27-0.76	≤0.65-12	1.6-11	<0.95-7.9
3-Nitrofluoanthene	≤1.4[e]	<2.8[d]	<2.1[d]	0.015-13	0.17-2.0	3.4-12	≤0.56-4.2	<1.1-7.5
2-Nitrofluorene	5.3-23	2.1-9.9	<2.0-21	<0.12-69	5.2-5.6	1.8-28	7.4-18	≤2.1-26
1-Nitropyrene + 1,3-Dinitropyrene	<2.1-21	<2.7[d]	0.86-25	0.13-45	<3.8-38	12-190	<3.8-47	<1.1-65

[a]TPM = total particulate matter; XOC - XAD-2 resin organic component.
[b]Values above minimum detection limits (MDL) for TPM samples.
[c]Values above MDL for all TPM and XOC samples.
[d]No values > MDL.
[e]Above MDL value for one sample only.
*Mean significantly different from comparable baseline mean ($p = 0.05$).

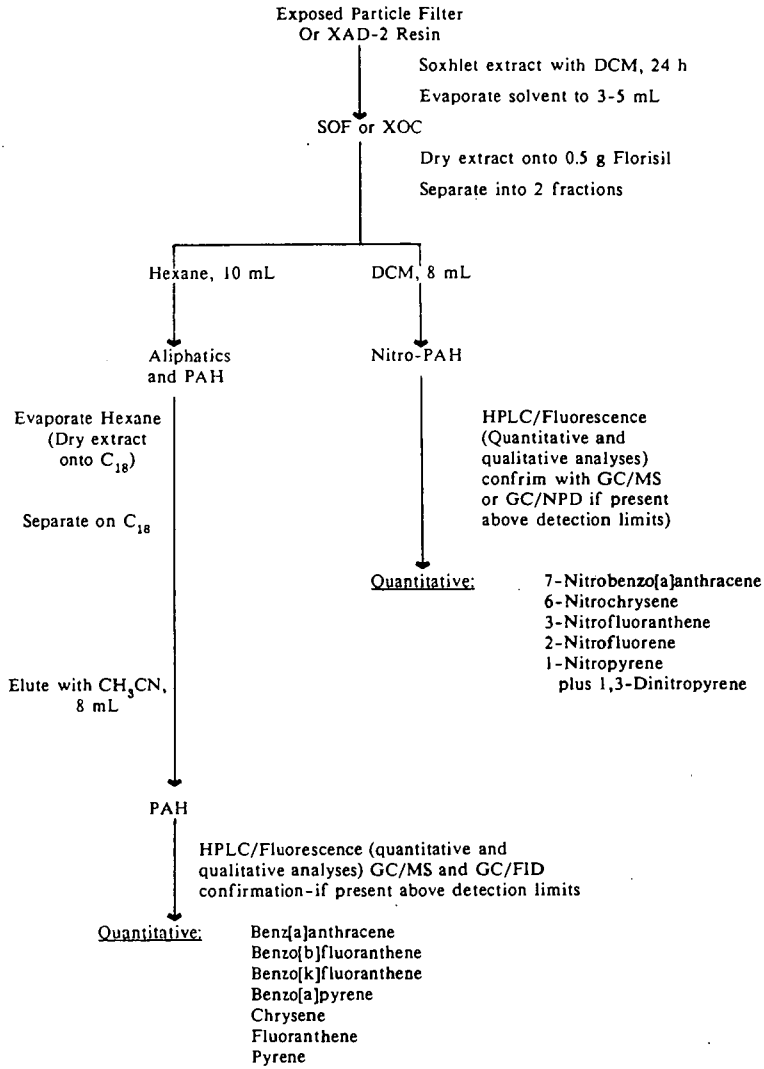

Figure 1. Flow chart for the extraction of SOF and XOC and compound quantitation. DCM = dichloromethane; SOF = soluble organic fraction; XOC = XAD-2 resin organic component; PAH = polynuclear aromatic hydrocarbons; CH_3CN = acetonitrile.

IMPACT OF FUEL CHOICE ON COMPARATIVE CANCER RISK OF EMISSIONS

Joellen Lewtas
Health Effects Research Laboratory
US Environmental Protection Agency
Research Triangle Park, NC 27711

Keywords: cancer risk, combustion emissions, alternative fuels

ABSTRACT

Incomplete combustion of fuels as an energy source results in the emission of products which are mutagenic in short-term genetic bioassays and carcinogenic in animals. Humans occupationally exposed to the incomplete combustion products from certain fuels have an elevated relative risk of cancer. Until recently, it has not been possible to compare the relative cancer risk of emissions from the combustion of various fuels. The combustion emissions from a wide variety of fossil fuels, synthetic fuels, vegetative fuels, synthetic chemicals, and mixed wastes have been characterized for with respect to their comparative genotoxic and tumor initiating activity. This paper evaluates the comparative cancer risk of various fuels in our current data base and identifies critical data gaps in our understanding of the comparative cancer risks from using alternative fuels.

INTRODUCTION

Fossil fuel related mixtures were the first chemicals recognized as human and then animal carcinogens (1). Coal combustion products, chimney soots, and coal tars were the first fossil fuel derived chemical carcinogens studied. Evaluation of the weight of evidence for the carcinogenic risk to humans of many fuel related mixtures has been conducted by the International Agency for Research on Cancer (IARC)(2). Based on these evaluations soots, coal-tars, and shale oils are classified as carcinogenic to humans (Group 1). Carcinogenicity in animals, with limited evidence in humans, has led to diesel engine exhaust and occupational exposures in petroleum refining to be classified as probably carcinogenic to humans (Group 2A). For several other petroleum based fuels (e.g., unleaded gasoline, marine diesel fuel, and residual fuel oils) and their combustion products (e.g., gasoline engine exhaust) the IARC has classified these mixtures as possibly carcinogenic to humans (Group 2B) based principally on the evidence for carcinogenicity in animal studies. Clearly, human exposure to a number of fossil fuel products, especially the combustion products, presents a potential cancer risk.

Vegetative carbon, from non-fossilized plants, was probably the first carbon source used as a fuel. Unfortunately, with the exception of tobacco combustion products, few studies have been conducted to evaluate the human cancer risk from vegetative carbon sources. A lung cancer mortality study in China in a non-smoking female population exposed to high concentrations of indoor burning of either "smoky" coal, "smokeless coal" or wood show that the lung

cancer mortality rates are highest in the populations using the smoky coal (3).

Alternative coal and shale derived fuels and products associated with technologies such as coal liquefaction were evaluated for genotoxicity, carcinogenicity, and other toxicological effects by industry and the U.S. Dept. of Energy (4). In many cases these alternative "synfuels" were compared to conventional petroleum-based fuels. No studies have been conducted on the cancer risk from alternative fuels such as synthetic chemical fuels, oxygenated petroleum fuels and alcohol based fuels.

HUMAN EXPOSURE

The most significant human exposures from fuel use are the air pollution exposures resulting from fuel related combustion emissions from transportation, heating and other area sources (5). Combustion emissions are a complex mixture of gases, condensable organics, and particles. The particles vary from classical submicron carbonaceous soot particles with condensed organics, and inorganic particulate matter to a mixture of condensable organic matter with almost no carbonaceous soot. The condensed or adsorbed organic, often referred to as "tar" in the earlier literature contains the polycyclic organic matter (POM) which induces tumors in animals, mutations in cells, and has been clearly implicated in epidemiological studies as a human carcinogen (5,6).

Polycyclic organic matter (POM) is a general term referring to a complex organic mixture of polycyclic aromatic compounds including many diverse classes of hydrocarbons (e.g. polycyclic aromatic hydrocarbons, PAH), substituted aromatic hydrocarbons (e.g., nitrated-PAH), heterocyclic aromatic compounds (e.g., aza-arenes). Incomplete combustion products, however, also contain gaseous chemicals which are carcinogenic such as benzene, aldehydes, and alkenes (e.g., 1,3-butadiene) and semi-volatile organic compounds which have not been well characterized either chemically or toxicologically (6).

The complexity of the POM emissions, estimated to contain thousands of chemicals, has precluded the quantitative cancer risk assessment of these emissions based on analysis of the components. Since human exposure to these POM emissions occurs as the whole complex mixture, both qualitative, weight of evidence, assessments (2) and quantitative assessments (7) of the human cancer risks have been based on either the whole emissions or the POM component.

CANCER POTENCY AND RISK

Three different approaches have been taken to the quantitative assessment of human cancer risk from fuel related mixtures: 1.Low dose extrapolation of human cancer risks at relatively higher occupational exposures (8), 2.Extrapolation of chronic animal cancer studies to human risk using cross species extrapolation methods (7) and 3.Extrapolation from relative tumor potency data in animals to relative cancer risk in humans based on the comparative

potency method. The first method, relying only on human data, has been the most extensively used for fuel related mixtures (e.g., coke oven emissions (8)), however there is not adequate human data to assess the potential cancer impact of either the currently used conventional fuels (e.g., petroleum derived) or the possible alternative fuels that may be used in the future. The second method, relying on chronic animal cancer data, is also severely limited by the available chronic animal data. The third method, relies on a comparative potency data base for a series of combustion related POM mixtures which have been compared in animal tumor assays and short-term bioassays to the relative human lung cancer risk in a series of related POM mixtures.

The comparative potency method for cancer risk assessment of these complex POM emissions is based on the constant relative potency hypothesis. This method was developed and tested using human lung cancer unit risk estimates, animal tumorigenicity data, and short-term mutagenesis bioassay data (9,10) These mixtures included the extractable organic emissions from coke ovens, roofing coal tar pots, cigarette smoke and automotive emissions. The comparative potency method is based on the hypothesis that there is a constant relative potency between two different carcinogens across human and bioassay data. The mathematical expression for the constant relative potency model is the following:

$$\frac{\textit{bioassay potency of } \dfrac{carcinogen_{\alpha}}{carcinogen_{\beta}}}{\textit{human cancer potency of } \dfrac{carcinogen_{\alpha}}{carcinogen_{\beta}}} = (k)\ constant$$

The constant relative potency assumption is implicit in any comparison which utilizes the relative toxicity of two substances in animals to estimate their relative toxicity in humans. This constant relative potency assumption is an experimentally testable hypothesis, if the relative potency of two mixtures or components in one bioassay (e.g., humans) can be determined and compared to the relative potency in a second bioassay. The test of this hypothesis is whether there is a constant relationship (k) between the relative potencies in the two bioassay being compared.
This hypothesis was tested for three complex organic emissions from a coke oven, roofing coal tar pot and cigarettes by using the human lung cancer data from epidemiological studies of humans exposed to these emissions and comparing the lung cancer unit risk to the potency of these emission sources in a series of bioassays (7,8).

The first application of this method to estimation of the human lung cancer unit risk was for the POM associated with diesel particle emissions (9). In this study, the comparative human data used was for POM from coke ovens, roofing coal tar emissions and cigarette smoke. Evaluation of a battery of bioassay demonstrated that across these three human carcinogens, the constant relative

potency hypothesis could be validated for the mouse skin tumor initiation potency. This is shown in Table 1 by the correlation between the human lung cancer unit risk and the tumor initiation potency for the three human carcinogens.

Table 1.
CANCER UNIT RISK ESTIMATES FOR THE HUMAN COMPARATIVE EMISSIONS

EMISSION SOURCE	HUMAN CANCER POTENCY[a] lifetime risk/ug EOM/m3	TUMOR POTENCY[b] pap/mouse/mg EOM
Coke Oven	9.3 x 10-4 (1.0)[c]	2.1 (1.0)
Roofing Tar (Coal)	3.6 x 10-4 (0.39)	0.41 (0.2)
Cigarette Smoke	2.2 x 10-6 (0.0024)	0.0024(0.0011)

[a]Lifetime cancer unit risk per microgram extractable organic matter (EOM) per cubic meter determined from human epidemiological data(9)
[b]Papillomas per mouse per mg of EOM [c]Relative potency shown in ().

Using this methodology the lung cancer unit risk has been estimated for the following POM emission sources as shown below:

Table 2:
CANCER UNIT RISK ESTIMATES DETERMINED BY THE COMPARATIVE POTENCY METHOD[a]

EMISSION SOURCE	POM UNIT RISK (lifetime risk/ug organic matter/m3)	PARTICLE UNIT RISK (lifetime risk/ug particulate matter/m3)
Automobile-Gasoline Catalyst Non-catalyst	12.0 x 10^{-5}	5.1 x 10^{-5} 1.6 x 10^{-5}
Automobile-Diesel[b]	23.0 x 10^{-5}	2.6 x 10^{-5}
Trucks-Diesel	0.7 x 10^{-5}	0.2 x 10^{-5}
Woodstoves	2.9 x 10^{-5}	1.0 x 10^{-5}
Heating Fuel Oil		0.9 x 10^{-5}

[a]Mouse skin tumor initiation bioassay potency was used as the comparative bioassay.
[b]Average of the unit risk estimate for three light-duty diesel vehicles(9).

The validity of this constant relative potency hypothesis may

depend on the chemical nature of the mixtures being compared as well as the similarity of those mixtures. Comparison of the mutagenic potency of a series of POM from diesel and gasoline vehicle emissions in Salmonella typhimurium with the tumorigenic potency showed high correlations both between the two bioassay and with the concentration of nitrated PAH and PAH in the POM mixture (11).

IMPACT ANALYSIS OF CANCER RISK

Human cancer risk from exposure to a fuel or it's combustion products is dependent on the extent of exposure (e.g., dose or exposure concentration x time of exposure) and the potency of the carcinogen (e.g., cancer risk/unit dose) among other factors (e.g., individual susceptibility). It is important to develop tools to predict the potential impact of cancer risk in the absence of human exposure assessment data so that such assessments can be conducted prior to the widespread introduction of new fuels or technologies into commerce. By combining source emission studies with mutagenicity and tumorigenicity bioassay studies of the combustion source emissions, we are able to estimate the relative impact of various alternative fuels as shown in Table 3.

Table 3.
COMPARATIVE MUTAGENIC AND TUMORIGENIC EMISSION FACTORS

SOURCE	MUTAGENIC EMISSION FACTOR (rev/kg fuel x 10^5)[a]	TUMORIGENIC EMISSION FACTOR (pap/mouse/kg fuel)[b]
RESIDENTIAL HEATING		
wood	50	83
oil	1	3
AUTOMOTIVE SOURCES		
diesel vehicles	40	240
gasoline non-catalyst	10	20
gasoline catalyst	1	2

[a]Revertants (rev) measured using the Salmonella typhimurium mutagenicity bioassay
[b]Papillomas (pap) measured using the mouse skin tumor bioassay

This analysis of the potential impact of sources based on the relative bioassay potency expressed per kg fuel consumption shows even more clearly the comparative differences between these fuels and sources. In this analysis the potential human exposure is assumed to be directly related to the emission rate. Although wood combustion emissions are less potent as carcinogens than many of fossil fuel combustion emissions, the high organic emission rate of woodstoves results in a significant impact when both potential exposure and potency are combined.

To examine the impact of fuel within one combustion source, we have conducted fuels comparison studies by operating motor vehicles, with different qualities and sources of diesel fuels. In several independent studies of diesel fuels we consistently found that alterations in the combustion source (engine type or operating conditions) resulted in greater differences in the mutagenic emission rates that differences in fuel quality or source (e.g. shale derived vs petroleum) (12).

Unfortunately few such fuel comparison studies have been conducted with gasoline vehicles, residential heating sources, waste burning and other significant fuel combustion sources. New oxygenated fuels being widely introduced into vehicle fleets across urban areas are expected to result in reduced POM emissions and reduced risk. However, no studies of the potential genotoxicity or tumorigenicity of these emissions have be conducted. The combustion of synthetic chemicals such as plastics mixed in municipal and hospital wastes and hazardous waste is the least well characterized with respect to the biological activity or potential cancer impact of the complex mixtures emitted from these sources.

DISCLAIMER

The research described in this paper has been reviewed by the US EPA and approved for scientific publication. The contents do not necessarily reflect the views and policies of the Agency.

REFERENCES

(1) Searle, C.E., Ed. Chemical Carcinogens, ACS Monograph 173; American Chemical Society: Washington D.C., **1976**; pp 788.

(2) IARC, IARC Monographs on the Evaluation of Carcinogenic Risks to Humans Vol. 32-46; International Agency for Research on Cancer: Lyon, **1983-1989**.

(3) Mumford, J.L.; He, X.Z.; Chapman, S.; Cao, S.R.; Harris, D.B.; Li, X.M.; Xian, Y.L.; Jiang, W.Z.; Xu, C.W., Chuang, J.C.; Wilson, W.E.; Cook, M. Science, **1987**, 235,217-235.

(4) Biles, R.W.; McKee, R.H.In Developments in the Science and Practice of Toxicology;Hayes,A.W.;Schnell,R.C.;Miya,T.S.,Eds; Developments in Toxicology and Environmental Science, V.11;Elsevier Science,New York, **1983**;pp 13-21.

(5) Lewtas, J. In Air Pollution and Human Cancer; Tomatis, L., Ed.; Springer-Verlag: Berlin, **1990**; pp 49-61.

(6) Lewtas, J. In: Carcinogens and Mutagens in the Environment, Vol. V, H. Stich, Ed., CRC Press, Boca Raton,**1985** pp. 59-74.

(7) Anderson, E.L Risk Analysis **1983**, 3, 277-295.

(8) U.S. EPA. 1984. Carcinogenic assessment of coke oven emissions. Office of Health and Environmental Assessment, Washington, DC. EPA-600-6-828033F. February, **1984**.

(9) Albert, R., J. Lewtas, S. Nesnow, T. Thorslund and E. Anderson Risk Analysis **1983**, 3, 101-117.

(10) Lewtas, J. Tox. and Industrial Health **1985**,4,193-203.

(11) Lewtas, J. Fund. Applied Tox. **1988**, 10, 571-589.

(12) Lewtas, J. In Developments in the Science and Practice of Toxicology;Hayes,A.W.;Schnell,R.C.;Miya,T.S.,Eds; Developments in Toxicology and Environmental Science, V.11;Elsevier Science,New York, **1983**;pp 23-34.

THE CLEAN COAL INITIATIVE: AN APPROPRIATE RESPONSE TO COMPLEX ENVIRONMENTAL ISSUES

C. LOWELL MILLER, PH.D.
ASSOCIATE DEPUTY ASSISTANT SECRETARY
OFFICE OF CLEAN COAL TECHNOLOGY

OFFICE OF FOSSIL ENERGY

U.S. DEPARTMENT OF ENERGY

INTRODUCTION

Little effort is required to confirm the importance of coal as a fuel source for meeting the increasing demands for energy both in the U.S. and internationally. Performing such an exercise would establish that the U.S. should be preparing to use twice as much coal representing an increase in its share of total U.S. energy consumption from today's 34 percent to about 40 percent over the period between now and the middle of the next century.

The challenge is not whether coal will be used, but to assure its use is accomplished in the most efficient way and with the least impact on the environment. Environmental requirements have joined cost reduction as the primary driving forces pushing coal technology development in new directions. A responsive and successful technology development program is essential to realizing sustainable economic and environmental development of our coal reserves on a domestic as well as on a global basis.

TECHNOLOGY DEVELOPMENT

It is an inconvertible fact that the uncontrolled burning of coal will release into the environment carbon dioxide (CO_2), sulfur dioxide (SO_2), oxides of nitrogen (NO_x), particulate matter, and ash. The relative amounts of these emissions will be determined by the amount of coal burned and the effectiveness as well as the degree to which some type of controls are used. The CCTs create the capability to utilize coal as an energy resource with attendant minimal emissions of these pollutants.

Suitably developed CCTs thus provide a unique opportunity to concurrently satisfy two national goals. These are to:

(a) Continue the substantial progress made in emission reductions by resolving the conflicts between coal use and environmental protection.
(b) Meet the rapidly approaching electricity capacity challenge with reduced cost and increased productivity.

Recognizing that in the U.S. 85 percent of all coal produced provides about 60 percent of the Nation's electricity, development of CCT is pursuing two primary objectives. These objectives are to:

(a) Provide an array of retrofittable emission control options which satisfy, at reduced cost the void between present physical coal cleaning capabilities and flue gas scrubbing for existing powerplants.
(b) Provide improved coal utilization alternatives for both repowering and new plant application. Of particular significance are fluidized-bed combustion and coal gasification/combined cycles which combine high levels of emission and effluent control with reduced cost and improved efficiency.

On a global basis, the importance of this linkage between technology development, electricity, coal utilization, and the environment was underscored by the Conservation Commission of the World Energy Conference which stated that:

(a) Future global economic growth particularly in the developing regions will be associated with very large increases in electricity growth.
(b) Coal which provides over 80 percent of the world's nonrenewable energy resource will become increasingly prominent in the coming decades. Worldwide coal usage is expected to exceed the use of petroleum during the first decade of the next century and to continue its preeminence during at least the following 50 years.
(c) Technological innovation to support this expansion in coal use will be essential for the world's economy and its environment.*
(d) The geopolitical importance of coal and the technology for its use are also likely to increase substantially since the bulk of the world's coal resources is controlled by the U.S., U.S.S.R., and China.

*Underlining emphasis added.

These assessments reflect the unique opportunity that low cost, widely distributed coal has to become the source of a versatile, highly available energy form--electricity. Electrification has become a global economic imperative. Growth in electric power production is a major consideration in global energy and environmental projections.

While in the past, the pace of the required advancements in coal utilization technology has proceeded at a acceptable rate, new constraints including escalating capital costs, declining construction productivity, new licensing requirements and growing environmental concerns has shown that a fundamental change in the development of coal-fired technology is required. A principle now being used to guide CCT development is that sustained environmental improvement can only be realized when both emission and cost reduction are achieved concurrently, not pitted against each other.

CLEAN COAL TECHNOLOGY DEVELOPMENT

The importance of these factors in developing an appropriate strategy for the use of the immense coal reserves of the U.S. has been recognized. Positive steps have been taken to ensure that new concepts for the utilization of coal are available to respond to future needs.

The Clean Coal Initiative is one of the largest technology development efforts now underway in the Department of Energy (DOE) . The level of funding responds directly to the strategic importance of coal in the U.S. economy and

the international marketplace and recognizes the need to develop solutions for the problems (economic and environmental) associated with meeting increased demand for this source of energy.

It is an accepted fact that the present and near term future of coal as an energy source depends upon continued advances in coal utilization technology.

The CCT Demonstration Program itself is a technology development effort jointly funded by the Government and industry. In this program, the most promising of the advanced coal based utilization technologies are being moved into the marketplace through demonstration. The demonstration effort is at a scale large enough to generate all data needed by the public sector to judge the commercial potential of the processes being developed. As a goal, the program will make available to the U.S. energy marketplace a number of advanced, more efficient, and environmentally responsive coal utilization technologies. These technologies will reduce or eliminate the economic and environmental impediments that limit the full use of coal.

The program as planned, currently consists of five phases (rounds). It is entering the fourth of the five planned phases. The first three phases were competitive solicitations in which 35 projects with an estimated total cost of $3.7 billion were selected. Of these projects, 29 have been started under the terms of cooperative agreements between the participants and the Government and negotiations are in progress on the remaining six. Of particular importance to DOE in these projects is the level of financial participation of the private sector. Although the U.S. Congress, in its guidance to the program, requires that such participation be a minimum of 50 percent, the participants are providing 63 percent of the funds for the projects in the cooperative agreements signed to date.

The fourth phase of the program has been initiated. The fourth competitive solicitation was released on January 17, 1991, with additional projects to be selected in 1991. Funding in the amount of $600 million each for phases IV and V have been appropriated. When the five phases of the program are completed, two major objectives will have been accomplished:

1. A wide range of more efficient, environmentally responsive coal utilization processes will be available for use that will accommodate almost every combination of specific site requirements.

2. Acid rain precursor emissions will be significantly reduced and significant reductions will have been made in the amounts of CO_2 generated as a result of using coal as an energy source.

WHAT ARE CLEAN COAL TECHNOLOGIES?

This description of something called the CCT Program has little meaning in the absence of some idea about what CCTs are and what type of benefits can be achieved through their use.

The term "clean coal" in itself is to some a conflict in terms. The image of coal certainly is not consistent with "clean." When CCTs are discussed, these

discussions are about advanced coal based utilization systems that offer significant benefits when used for power generation, pollution control, or the conversion of coal into other alternate energy products.

First in the area of power generation, the characteristics of these technologies such as improved thermal efficiencies, modular construction, improved environmental performance, fuel flexibility, repowering capability, etc., will help the power industry accommodate a time of significant change caused by such factors as regulatory reform, uncertain growth in power demand, environmental pressures, and now competition from Independent Power Producers and Cogenerators.

Second, the name clean coal emphasizes its role in pollution control. In this case, most generally through a retrofit application, the technologies can directly remove SO_2 and NO_2 acid rain precursors and substantially reduce the amount of CO_2 generated when combusting coal. The specific type and amounts of pollutants removed will be a characteristic of the individual process. It should be noted also, however, that some CCTs (e.g., Pressurized Fluidized-Bed Combustion (PFBC), Integrated Gasification Combined Cycle (IGCC) have the ability to remove these pollutants while at the same time increasing the power output of the facility itself from 50-150 percent.

In the third case, CCTs can create the opportunity to produce coal derived liquid fuels to replace oil and gas in some applications. This capability will permit coal to have a greater role in providing energy to the industrial, commercial, and transportation sectors.

IMPACT OF THE PROGRAM

With the CCT Demonstration Program implemented to only 60 percent of its proposed full potential, it is premature to evaluate the degree to which it will achieve its objective of making available the technology that will permit the increased use of coal in an environmentally acceptable manner. However, it is not premature to examine the program's accomplishments to date to see how well it is progressing toward that objective.

Thirty-five projects representing ten major categories of technology are in various stages of design, construction, and operation. These projects represent a cost shared effort of private industry and government to achieve mutual objectives. The interest of the private sector in the potential benefits of the program is reflected in a level of cost sharing significantly higher than the required 50 percent (i.e., 63 percent). The technologies being developed are capable of being responsive to the demands of the utility sector for retrofit as well as repowering solutions and key components of industry have used the opportunity to address major pollution issues that threaten their continued existence from an economic and environmental point of view.

The retrofit technologies in the program include six innovative processes for the reduction of sulfur dioxide, six processes for the control of nitrous oxides and six new concepts for their simultaneous removal. These processes introduce combustion modification techniques, new as well as state-of-the-art absorbents employed in new applications and the development and use of new generations of catalysts.

The potential for increased power output is combined with emissions control in the suite of seven repowering technologies being developed. Such promising concepts as pressurized fluidized-bed combustion, coal gasification, circulating fluidized-bed combustion, both atmospheric and pressurized, will be operated as part of a number of innovative integrated power generation systems. These systems offer the potential of increasing the power output of a facility from 50-150 percent, while achieving significant reduction in SO_2 and NO_x emissions.

The three advanced combustor projects are generating new economic systems for coal utilization in both the utility and industrial sectors and the advanced pollution control processes being developed for the steel and the cement industry offer significant and perhaps essential economic solutions to major environmental obstacles.

Finally, a number of projects are introducing the possibility of fuel flexibility through the conversion of coal. While the conversion of coal into other fuel forms is not a new concept, the introduction of environmental issues in conjunction with economic considerations creates a challenge that is being addressed by three of the projects in the Clean Coal Program.

These projects represent options to the utility and industrial user that can accommodate a wide range of site specific requirements to become the solution to emissions control and power production problems.

The role that the technologies play in the reduction and control of acid rain precursor emissions is clearly evident. However, the significant role that some of the technologies can play in resolving some of the complex issues of global warming is not so evident.

Global warming is a critical environmental issue gaining international attention. It focuses on the possibility of significant changes in global climate as a consequence of changes in atmospheric concentrations of "greenhouse" gases--most notably carbon dioxide (CO_2), methane (CH_4), nitrous oxide (N_2O), and chlorofluorocarbons (CFCs).

The question of whether the earth is really warming because of the generation of these greenhouse gases is still a matter of considerable debate and scientific analyses. Moreover, there are significant questions about the relative contributions of various human activities. Nevertheless, if scientific evidence ultimately shows that remedial actions are necessary to mitigate climate change, technology innovation and development is an alternative strategy to regulatory constraints.

Some of the projects now in the CCT Program are developing technologies that can cut the emission of "greenhouse" gases in two fundamental ways. First, many of the CCTs improve the efficiency of the conversion of coal to useful energy. Technologies such as pressurized fluidized-bed combustors, integrated gasification combined-cycle systems, and fuel cells will consume less coal per unit of useful energy produced and thus reduce CO_2 emissions. Second, low-NO_x burners, selective catalytic reduction, and other technologies will reduce NO_x emissions, which should reduce N_2O formation.

As global warming becomes an increasingly important issue, the reduction of emission of greenhouse gases will increase in priority, and the worldwide commercial deployment of CCTs will take on even greater significance.

AN APPROPRIATE RESPONSE

The success achieved thus far in the CCT Program as represented by the number of projects, the degree of industrial participation, and range of technologies included, certainly argues well for the potential of the technology development effort and the possibility of it achieving all of its technical objectives.

The 35 projects that are now underway are equally as significant for the promise they offer in generating solutions to a number of the complex interrelated issues of energy, economics, and the environment. These projects and others to follow permit the continued use of coal as an energy source while:

- Being responsive to the requirements of the Clean Air Act Amendments.
- Reducing the amount of acid rain precursors generated during combustion.
- Improving the ability of the utility industry to meet increased demands for power in a cost effective manner.
- Contributing significantly to improved control over carbon dioxide emissions and thus addressing the issue of global warming.
- Providing environmental control options to accommodate a wide range of specific site requirements.

These capabilities certainly indicate that the CCT Demonstration Program can provide appropriate responses to a wide range of complex environmental issues.

THE DILEMMA OF FOSSIL FUEL USE AND GLOBAL CLIMATE CHANGE

Roddie R. Judkins, William Fulkerson, and Manoj K. Sanghvi*
Oak Ridge National Laboratory
Oak Ridge, TN 37831-6084

*Amoco Corporation
Chicago, IL 60680-0703

Keywords: Global Climate Change; Greenhouse Effect; Fossil Fuels

THE DILEMMA

The energy systems of society are both parts of the means to achieve sustainability and the potential causes of instability. Fossil fuels (petroleum, natural gas, coal, oil shale, etc.) epitomize this dilemma. These are our principal energy sources, yet they are depletable on a time scale that is relevant to human history (~200—1000 years), and although their use may be changing the environment of the planet locally, regionally, and even globally (e.g., changing the greenhouse effect), we live in a developing society that demands more energy for more people. The challenge is to avoid the dilemma by technology and policy intervention so that fossil fuels are used to the net benefit of society and its environment.

Of course, concern about the changing greenhouse effect may ultimately limit the use of fossil fuels, and the issue is fiercely debated (Abelson 1990) because uncertainties permeate the entire matter. Although the increase in the concentrations of greenhouse gases in the atmosphere is indisputable, the evidence of consequential temperature or other climate change is not. Still, we tend to agree with T. A. Sancton (1989) that "it is far too risky to do nothing while awaiting absolute proof of the disaster" and with Senator Albert Gore of Tennessee (1989) that uncertainties about the greenhouse effect and the dire nature of the ecological crisis we face should not be used as excuses for inaction.

We should take those low-cost measures that slow greenhouse gas emissions, and we should be prepared technologically to accomplish much larger reductions if necessary. At present, our technological insurance is not in place, but the opportunities for improvement are great, even for fossil fuels.

WHY ARE FOSSIL FUELS SO POPULAR?

Presently, fossil fuels account for about 88% of the commercial energy sources used (not counting energy supplied directly by the sun and traditional biomass sources not traded in commerce). This situation hasn't changed much over the last 50 years (Table 1) and could persist for 50 more. Considering the environmental problems associated with the increasing use of fossil fuels, why are they so popular?

Fossil fuels are relatively marvelous energy sources. The variety of fossil fuels plus the technology mankind has developed to produce and convert them to useful purposes is a marvelous combination.

Furthermore, as a consequence of biomass production during past geologic epochs, when the planet was apparently much warmer, the reservoirs of fossil fuels were built rather ubiquitously. As a result, fossil fuels are available everywhere, and some (e.g., petroleum) are readily transportable. Technical advances have led not only to discoveries and production from the most inhospitable places but also to more complete resource recovery.

Although fossil fuels are depletable, the estimated resources are still very large (Fig. 1). In this figure, reserves are the discovered quantities in known reservoirs and locations that are technically and economically recoverable using current extraction technology. The undiscovered resources of oil and gas are judgmental estimates of those resources thought to be geologically possible and technically recoverable within a reasonable price range. For coal, ultimately recoverable geological resources is an estimate based on the assumption that 50% of the total coal resources-in-place can be recovered using current mining techniques as well as advanced techniques yet to be developed.

Coal, the most abundant fossil fuel, is located predominantly in the U.S.S.R, the United States, and China. Total world resources of coal are estimated to be over 10,000 Gt, and ultimately recoverable resources are estimated to be about 5,500 Gt, or about 150,000 quads (quadrillion Btu). At present use rates, these resources would last 1,500 years.

Oil resources are much less abundant. At historical recovery rates of about 34%, the remaining recoverable resources of conventional oil are estimated to be about 7,000 quads (Masters 1987); which would last only about 60 years at present use rates. But with enhanced oil recovery and the use of unconventional oils, the recoverable oil resources might be doubled.

The remaining recoverable resources of natural gas are distributed rather ubiquitously, but the U.S.S.R. has more than any other region (Dreyfus 1989). Estimates are similar to those of petroleum (about 8,000

quads), which is approximately 120 years supply at current use rates. The ultimate supply might be double that if unconventional sources such as Devonian shales; tight, deep formations; and coal seam gas are considered.

This resource situation would be much more limiting if it were not for the fact that one form of fossil fuel can be chemically transformed into another; for example, coal can be converted to gaseous or liquid fuels. Also, natural gas can be catalytically reformed to produce liquids for transportation albeit at some cost and thermodynamic penalty. The continuing challenge is to develop efficient and economic processes for performing these chemical conversions. Of course, fossil fuels, particularly petroleum and natural gas, are excellent feedstocks for making useful chemicals and plastics.

Fossil fuels are attractive not only because they are available and relatively inexpensive but also because we have learned to use them so effectively. The relatively simple technology of controlled combustion provides energy for both small- and large-scale applications. Almost exclusively, liquids refined from petroleum power the world's transportation systems (greater than 97% in the United States) because these fuels have such a high energy density, because they are so portable, and because of the development of the internal combustion engine and the modern jet engine.

Although many nonfossil energy sources exist, none, either separately or collectively, are ready to substitute for fossil fuels worldwide at the necessary large scale and with the performance, cost, and social acceptance required to be competitive. Nuclear power is perhaps the nearest to being ready, but a significantly expanded deployment is constrained by concerns over reactor safety, accidental reactor damage, and diversion of nuclear fuel to weapons; by problems with managing waste; and by escalating capital and operating costs. Even France, which produces 70% of its electricity by nuclear power, still uses fossil fuels to provide most of its energy (65%). Biomass and hydropower are resource-limited in many countries. Solar thermal electric, photovoltaics, and wind are still expensive, and the power they provide is intermittent. Geothermal sources are geographically constrained and often expensive to develop, as are ocean thermal, wave, and tidal power. Fusion is considered decades away from practical demonstration.

The environmental problems with fossil fuels that command most of our attention today include acid deposition, urban air pollution, and climate change (global warming or the changing greenhouse effect). The acid deposition problem can be solved over time at reasonable costs. In the United States, all urban air quality probably cannot be brought into compliance with all present standards at reasonable cost, but the problem can be kept within acceptable limits (Russell 1988). However, climate change is a different type of problem for which no technological fix yet exists, and the global consequences could be very serious, if not disastrous.

CONTROLLING CO_2 EMISSIONS

Global warming may occur as a result of the release of the so-called greenhouse gases, notably carbon dioxide (CO_2), methane (CH_4), chlorofluorocarbons (CFCs) (e.g., refrigerant gases such as the Freons), nitrous oxide (N_2O), and O_3 (Smith 1988). Because they are relatively long-lived in the atmosphere, dispersion of these gases is much broader than the acid gases, and, because of this wider dispersion, the concern is truly global as opposed to regional. These gases absorb heat energy (infrared radiation) that would otherwise be radiated from the earth to space, resulting in a warming of the troposphere (lower atmosphere). Of these anthropogenic gases, CO_2 is the major one, presently accounting for about one-half of the changing greenhouse phenomenon, and the burning of fossil fuels is estimated to contribute more than 75% of the increasing CO_2 concentration in the atmosphere. The other major source of CO_2 is from deforestation by slash and burn techniques. The consequences of global warming are poorly understood and are not yet predictable in detail, but they could include a 1.5 to 4°C increase in global annual mean-surface temperature for each doubling of CO_2 concentration; marked changes in the amount and distribution of precipitation; large seasonal changes in mean soil moisture; and reduction of some of the world's great ice masses and thermal expansion of the oceans, which would raise sea levels and flood coastal areas.

Our principal concern is how to control greenhouse gas emissions, particularly CO_2. Depending on the fraction of CO_2 retained in the atmosphere, burning all fossil fuel resources could quadruple the CO_2 concentrations in the atmosphere from the present value of about 350 to 1500 ppmv (parts per million by volume) (Table 2). If current models of warming are correct, such an increase in CO_2 concentration would lead to a global average temperature rise in the range of 3 to 8°C with even higher values at the higher northern latitudes.

If such an increase were to occur over a period of two centuries or so, it would likely be both too much and too fast (in the range of 0.15 to 0.4°C per decade). There exists, however, a CO_2 emission rate at which the atmospheric concentration does not increase, or at least it increases very slowly. A carbon cycle model has been used (Emanuel 1990) to examine several scenarios in which the emission rate is suddenly and dramatically reduced from what it is today and then maintained constant at that reduced rate (Fig. 2). The results indicate that CO_2 emission rates must be very low to prevent any increase in CO_2 concentration (of the order of 1 Gt(C)/year); however, rates of 2 to 3 Gt(C)/year lead to only moderate increases over the next 100 years.

Some have argued that the problem is not warming per se but rather the rate of change. A rate of change <0.1°C per decade has been suggested to be slow enough to be manageable. If we assume that half the increase is due to other greenhouse gases, this rate of change translates into an allowable CO_2 emission rate from fossil fuels of 1.6 to 3.5 Gt(C)/year where the range depends on the value of temperature change assumed for CO_2 doubling. This emission rate range may be extended upward if emissions of other greenhouse gases are also controlled.

The technological and social management challenge is to get maximum energy services from fossil fuels, hold the emission rate as low as practical, and control the rate within an acceptable range. The challenge is definitely formidable if not impossible. If it becomes necessary to reduce CO_2 emissions to a level much less than the present one, it will take decades to accomplish, and the rate will undoubtedly increase significantly before any reduction can be managed.

Also, the idea that there is some CO_2 emission ration raises allocation issues. Who gets to use what? Does the ration go to countries that have below average fossil fuel consumption? Do industrialized nations reduce their use rates so that the developing nations could use more fossil fuels to spur their economic growth? Most of the greenhouse gases are being generated in the developed world that comprises only a fraction of the world population. Of the two most prominent greenhouse gases, only 25% of CO_2 emissions and <10% percent of CFC emissions come from the developing world. On a per capita basis, the developing countries have extremely low absolute levels of energy usage and CO_2 emissions (See Figs. 3 & 4).

Indeed, the emission rates of CO_2 have moderated over the past decade and a half as a result of the Arab oil embargo and subsequent oil price shocks. Controlling emissions of CO_2 may be very expensive. A recent calculation (Manne and Richels 1990) indicates that with current technologies and with a ban on nuclear expansion the tax on a ton of carbon emissions would need to go as high as $600 to force United States emissions to be reduced to 80% of the current emissions of 1.4 Gt(C)/year, and the cost to the United States economy might be 5% of the Gross National Product. With advanced technologies, this cost might be reduced substantially, perhaps by a factor of 5 or more (Williams 1990).

More Efficient Use of Fossil Fuels. Because nonfossil energy sources are currently poor competitors, it has been argued that improving the efficiency of fossil fuel use is the least expensive path to reducing CO_2 emissions (Keepin and Katz 1988). Indeed, the technological opportunities are very large for all segments of the economy. The major attractiveness of this option is that not only do technologies exist, but their increased applications are often economical even at current fuel prices. In addition, the potential seems to be large for developing nations as well as industrialized nations. This conclusion is brilliantly argued by Goldemberg et al. (1988). These authors conclude that the developing nations can achieve a level of affluence equivalent to that of Western Europe in the mid-1970s by a rate of energy use of only about 1.3 kW/person. This compares to the current level actually used by Western Europe, which is about 4.1 kW/person. In other words, it may be possible for developing nations to grow economically along a much more efficient path than those followed by industrialized nations. Despite the attractiveness of such a high efficiency path, it may prove difficult to achieve the degree that is economically justified without significant activity by governments to encourage it. Many barriers must be overcome, not the least of which are the tendency to make investments based on least first costs rather than least life-cycle costs or the tendency for governments to subsidize energy prices.

As more efficient and economical technologies for fossil fuel use are developed and adopted, however, the more difficult it will be for nonfossil sources of energy to compete. The higher efficiency will mean less CO_2 emissions per unit of energy service, but the reduction will be much less than could be achieved if nonfossil sources were substituted. As always, fossil fuel technology gets better and better, and it is a moving target for its competitors. Greater emphasis must be placed on research and development to improve the nonfossil sources.

Substituting Natural Gas for Coal. The second option for reducing CO_2 emissions from fossil fuels is to substitute natural gas for coal (see Figs. 5 & 6). The heat of combustion per molecule of CO_2 produced is 70% greater than for coal, and natural gas can generally be used more efficiently to produce the same energy services. One reason for higher efficiencies using natural gas is that it does not have the sulfur and nitrogen fuel-bound contaminants and ash content that plague coal and result in acid gas and particulate emissions that must be controlled.

Some of the same repowering technologies that are promising for reducing acid gas emissions from coal-fired electricity generation are also important in reducing CO_2 emissions by substituting natural gas for coal. These include advanced gas turbines and fuel cells; the former is much more advanced than the latter, and further improvements in gas turbine technologies are likely, particularly improvements in materials that will permit higher combustion temperatures and pressures. Additionally, Williams (1989) has proposed catalytic chemical reforming of natural gas with steam to produce hydrogen and carbon monoxide which are then burned in an intercooled steam-injected gas turbine (ISTIG). This chemically recuperated ISTIG may further increase power output, and efficiency may be as high as 52.5%.

Although much less developed than gas turbines, fuel cells offer promise for increasing the efficiency of electricity generation from fossil fuels. Fuel cells are devices (like batteries) that convert chemical energy

into electrical energy. The fuel is oxidized at the anode to provide electrons that flow in the external power circuit to the cathode where oxygen is reduced. The anode and cathode are separated by an electrolyte that provides a transport mechanism for ions but not for electrons.

There are two limitations with this natural gas substitution strategy. First, the resources of natural gas are much smaller than those of coal (Fig. 1). However, substitution of natural gas for coal can be an important interim strategy to moderate CO_2 emissions while better nonfossil sources are developed and deployed. Second, leakage of natural gas from production and transport systems may partially offset the advantage of its use. Methane, the principal constituent of natural gas, is a much more effective greenhouse gas than CO_2. The infrared absorption of a methane molecule is almost 30 times that of a CO_2 molecule. However, the effective lifetime of methane in the atmosphere is much shorter. This problem requires much more investigation because the sources and sinks of methane are not well understood, but it should be possible to reduce leakages from the natural gas system to a negligible value.

The slow pace of growth in natural gas use in the developing world has been largely due to the relatively high cost of transporting the gas from the point of production to the point of use in the era of low oil prices. Indeed, historically, there has been little systematic exploration for gas in these regions, and most of the gas reserves were discovered while looking for oil. However, with the generally higher oil prices prevailing since the 1970s, natural gas use has become economic even in markets far from reserves. As a result, natural gas consumption has been rising, especially outside the United States.

Most gas is still consumed in the country where it is produced, but world trade in natural gas has been rising since the early 1970s. Currently, world trade via pipeline accounts for about 11% of total use and liquefied natural gas (LNG) trade accounts for about 3%. The distribution network in the United States is the most extensive in the world, and it is already linked to supplies from Canada by pipeline and from North Africa by LNG. A potentially useful pipeline link to Mexico also exists and projects are being considered to bring additional LNG from Trinidad, Venezuela, and Nigeria to the United States.

The gas distribution network in Western and Eastern Europe is also well developed and is linked by pipeline to large producing fields in The Netherlands, Norway, the U.S.S.R., and North Africa. Countries that are not already linked to the grid (Greece, Portugal, Turkey, etc.) are making plans to join soon. Recently, Iran has reactivated its earlier plan to supply Western and Eastern European countries by pipeline through the Soviet Union. Some LNG is coming into Western Europe from Algeria and Libya currently, and plans are being made to bring LNG from Nigeria.

While the major Eastern European countries have already integrated some natural gas from the Soviet Union into their energy mix, they still face immense environmental problems because of their heavy reliance on coal. These countries offer a very good opportunity for replacing coal with Soviet and Middle Eastern natural gas.

Japan has made considerable progress in natural gas usage with LNG imported from Indonesia, Malaysia, Australia, Alaska, and the Middle East, but consumption elsewhere in Asia is relatively modest, based mostly on available indigenous resources. However, the picture is changing. Korea has recently started LNG imports, and Taiwan will soon begin. A proposal for an Asian grid linking the producing fields in Indonesia, Malaysia, and Thailand with other Pacific Rim countries is also being pursued, and may be implemented during the 1990s (Cedigaz News Report 1990). India is exploring possibilities of importing LNG from the Middle East to supplement its own rising production. Iran is promoting a $12-billion project to bring its prolific natural gas resources to India and Pakistan by a 2000-mile pipeline from Bandar Abbas to Calcutta (Petroleum Economist 1990). The Soviet Union has recently initiated discussions with Japan to build a 3,100-mile pipeline, partly undersea between Siberia and Japan via South and North Korea (Wall Street Journal 1990).

International trade within South America is still limited, but recent bilateral agreements between Argentina, Bolivia, and Brazil portend expansion.

Helping the Soviet Union with advanced gas production, transmission, and utilization technologies would seem to be a stabilizing policy for the OECD countries to adopt in this day of "perestroika." Expanding the use of Middle East gas could make an important contribution, not only to Europe but also, perhaps, to Pakistan and India as well. Resources of Indonesia and Malaysia will likely underpin the growth of natural gas consumption in the Pacific Rim nations. Helping these countries use gas resources is environmentally sound as an interim strategy, and also economically desirable as a developmental strategy. These steps could have a very positive impact on the economics of the Soviet Union, the developing regions of the world, and on urban and regional ambient air environmental quality.

Recovering and Sequestering CO_2. The third strategy for reducing CO_2 emissions from fossil fuel is to capture the emissions and sequester them or find nondispersive uses for the recovered CO_2. This is an expensive proposition, at least for the techniques suggested so far. The difficulty of the problem is evident by the simple realization that 1 ton of carbon in fossil fuel produces almost 4 tons of CO_2.

One technique, of course, is to grow forests and recycle the carbon back into the biomass reservoir. Recently, Advanced Energy Services agreed to fund planting trees in Guatemala sufficient to offset the CO_2 put into the atmosphere during the lifetime of a proposed new coal-fired plant in Connecticut (Pearce 1988).

Although this is an interesting and perhaps important approach to afforestation, it probably cannot be practiced at the scale that would be required to make a significant offset to CO_2 released worldwide from fossil fuel use. For example, offsetting the emissions of a 500 MWe coal fired power plant operating at about 34% efficiency would require about 500 square miles of forest to be grown assuming the forest fixes 2 tons of carbon per acre per year over the lifetime of the coal plant. To sequester the total carbon emissions of the United States would require growing about one million square miles of forests at this productivity and using about 25% of the land area of the United States. Growing trees could, however, do much to offset the deforestation trend.

It should be acknowledged that the role of biomass in the global carbon cycle is still largely unknown. For example, Tans, Fung, and Takahashi (1990) recently analyzed the northern-hemisphere—southern-hemisphere CO_2 gradients and concluded that there must be a large northern hemisphere sink, presumably of terrestrial origin. If the analysis is correct, the effect could be due to CO_2 fertilization causing plants to grow more rapidly or to afforestation in the northern hemisphere. Much more needs to be learned about the natural carbon cycle.

Other strategies have been proposed for recovering CO_2 from the emissions of large fossil fuel facilities such as power plants. These involve recovering CO_2 exhaust gases and permanently sequestering the CO_2 either in the deep oceans or in depleted natural gas reservoirs or other geologic formations such as the hollowed-out salt domes used in the United States for storing strategic petroleum reserves. Steinberg (1985; Horn and Steinberg 1982) was one of the first to look at these possibilities carefully. He estimated that the added cost of recovering and sequestering CO_2 emissions would increase the cost of electricity generation by as much as a factor of 1.8 to 5. However, a recent calculation revises this range substantially downward (Table 3).

In summary, we suspect that CO_2 sequestering schemes (except perhaps for reforestation which, as noted, has its own limitations) will always prove to be more expensive than substituting nonfossil sources, but the calculations of Hendriks, Blok and Turkenburg (1990) clearly narrow the gap and point to needed research.

Hydrogen From Fossil Fuels. Fossil fuels can also be used as a source of hydrogen, an alternative to hydrocarbons as a fuel material. Carbon, hydrocarbons, and carbon monoxide are splendid reducing agents for producing hydrogen from water. Of course, a product of the reduction of water by carbonaceous materials is still CO_2, which must be recovered and sequestered. Nevertheless, we could imagine the use of hydrogen derived from fossil fuels as a clean source of energy for Los Angeles. In fact, it is not inconceivable that it could be an interim step to a situation 50-100 years hence when the principal energy carriers used by society are electricity, hydrogen and biomass-derived liquids for transportation.

To this end, Williams (1990) has used the calculations of Hendriks, Blok and Turkenburg (1990) to estimate the cost of producing hydrogen from coal using the Shell oxygen blown gasifier and sequestering the CO_2 in depleted gas or oil reservoirs. The estimates range from \$4.50 to \$5.74/million Btu on the basis of higher heating value. The lower cost assumes a 6% discount rate whereas the higher cost assumes a 12% discount rate. This is an extremely interesting range of costs given the potential importance of hydrogen as a clean fuel.

By adding heat from nonfossil sources such as from a high-temperature gas-cooled nuclear reactor or perhaps a solar furnace, the yield of hydrogen per unit of CO_2 produced can be increased. For reforming of methane, hydrogen production can be increased by 1/3 and by 70% from coal. Whether such heat sources to boost hydrogen production from fossil fuels will be practical depends on the cost of competing sources of hydrogen such as direct electrolysis of water using nuclear, solar, or wind electricity.

Hydrogen could be produced near coal fields, the CO_2 pumped to sequestering sites, and the hydrogen piped to centers of fuel use. However, hydrogen is not very portable. Gaseous hydrogen at 2400 psi has a volume about 18 times the volume of an equivalent amount of energy stored as gasoline and weighs three times as much if the weight of the storage vessel is included. Hydrogen can be stored as metal hydrides and released by heating. Hydrides weigh about as much as high-pressure gas cylinders but occupy only about 25% more space than a gasoline tank containing the same energy value (Amann 1990). By increasing the efficiency of conversion dramatically, these storage limits may one day be acceptable even for automotive transportation systems. As we have mentioned, hydrogen can be used very efficiently; for example, by fuel cells where conversion of chemical energy to electricity may be accomplished at 60% efficiency, indicating the possibility of a practical hydrogen fuel cell electric vehicle.

From this discussion it is clear that the near-term moderation of the emissions of CO_2 from fossil fuel use depends on two strategies. The first is to use fossil fuels more efficiently across the board from conversion to end uses. This applies both to the conversion to electricity and the efficient use of electricity. Of course, the development and adoption of much more efficient technologies for using petroleum products particularly for transportation is an essential ingredient. The second, related to the first, is to substitute high efficiency gas technologies for coal wherever practical. Stimulation of the use of natural gas at the expense of coal will, of course, increase natural gas prices and hasten depletion of resources. But it can also buy time to develop better nonfossil sources and improve air quality at the same time. Sequestering of CO_2 emissions from the exhausts of fossil fuel combustion or conversion seems presently expensive and impractical except, of course, as it is accomplished by afforestation. Nevertheless, the possibilities including that of hydrogen production should be intensively researched.

CONCLUSIONS – MANAGING FOSSIL FUELS

Fossil fuels can only make a transient contribution to the energy supply for a sustainable planet because they are finite and depletable resources. Nevertheless, that transient contribution is most significant because fossil fuels are mankind's primary commercial energy source, and their use worldwide is growing, especially by the developing nations. Fossil fuels are so important because they are still relatively abundant, cheap, ubiquitous, and some forms (notably petroleum) are readily transportable. Hydrocarbon liquids with high energy density are portable and make superb fuels for powering transportation systems, and one form of fossil fuel can often be readily converted to another (e.g., gases and solids to liquids and solids to gases). Furthermore, they can be used at almost any scale employing simple or complex technology, and they are the source of an enormous variety of chemicals and plastics.

Nevertheless, as the use of fossil fuels has grown, the problems of protecting the environment and human health and safety have also grown, providing a continuing challenge to technological and managerial innovation. Today that challenge is to control atmospheric emissions from combustion, particularly those emissions that cause acidic deposition, urban pollution, and increasing concentrations of greenhouse gases. Technology for reducing acidic deposition is available and needs only to be adopted, and the remedies for urban pollution are being developed and tested. How effective or expensive these will be remains to be determined. The control of emissions of the greenhouse gas, CO_2, seems possible only by reducing the total amounts of fossil fuels used worldwide, and by substituting efficient natural gas technologies for coal. Long before physical depletion forces the transition away from fossil fuels, it is at least plausible and even likely that the greenhouse effect will impose a show-stopping constraint. If such a transition were soon to be necessary, the costs would be very high because substitute energy sources are either limited or expensive or undesirable for other reasons. Furthermore, the costs would be unevenly felt and would be more oppressive for developing nations because they would be least able to pay and, on average, their use rates of fossil fuels are growing much faster than those of many industrialized countries.

It is prudent, therefore, to try to manage the use of fossil fuels as if a greenhouse constraint is an important possibility. This suggests taking several low-cost actions in the near-term such as:

- policies including R&D that encourage the development of more efficient and economical end-use and conversion technologies (e.g., more efficient gas turbines, fuel cells, oxygen-blown gasifiers, and processes for producing hydrogen from fossil sources);

- more intensive R&D to accelerate the development of better nonfossil sources including direct solar, biomass and other renewables, fission, and fusion;

- policies that encourage the substitution of hydrogen-rich for hydrogen-lean fuels and expansion of the natural gas system, particularly in developing nations;

- cooperation by western industrialized countries in providing technical assistance to developing and Eastern Bloc countries for producing energy technologies that are both economically and environmentally more attractive, including expanding the development and use of the natural gas resources of the Soviet Union;

- R&D to increase our understanding of the global cycle of CO_2 releases to the atmosphere and its removal by the oceans and by terrestrial ecosystems so that climate stabilization targets and policies can be better established; and

- experiments with CO_2 recovery and sequestration techniques so that the economic and environmental impacts are better understood.

SOURCES OF INFORMATION

1. Abelson, P. H., "Uncertainties About Global Warming," *Science* 247(4950), p. 1529.

2. Amann, C. A., "Technical Options for Energy Conservation and Controlling Environmental Impact in Highway Vehicles," pp A-41-A-60 in *Energy and the Environment in the 21st Century*, Massachusetts Institute of Technology, March 26-28, 1990.

3. British Petroleum, *BP Statistical Review of World Energy*, July 1989.

4. *Cedigaz News Report*, "Asia," Volume 29, No. 12, pp. 14-15, April 24, 1990.

5. Blok, K., C. A. Hendriks, and W. C. Turkenburg, "The Role of Carbon Dioxide Removal in the Reduction of the Greenhouse Effect," pp. 135-155 in *Energy Technologies for Reducing Emissions of Greenhouse Gases, Proceedings of an Experts' Seminar*, Paris, April 12-14, 1989, Volume 2, International Energy Agency.

6. Blomen, L. J. M. J., "Fuel Cells," in *Electricity Efficient End-Use and New Generation Technologies, and Their Planning Implications*, Lund University Press, pp. 627-64, Lund, Sweden 1989.

7. *Clean Coal Technology, The New Coal Era*, DOE/FE-0149, U.S. Department of Energy, Washington, D. C., November 1989.

8. Dreyfus, D. A., and A. B. Ashby, "Global Natural Gas Resources," pp. 773-784 in *Energy* 14(12), 1989.

9. Emanuel, W. R., "Atmospheric CO_2 Response to Reduced Fossil Fuel Emissions," Oak Ridge National Laboratory, Oak Ridge, TN, personal communication, March 28, 1990.

10. Fulkerson, W. et al., *Energy Technology R&D: What Could Make a Difference*, ORNL-6541/V1&V2, May 1989.

11. Goldemberg, J., T. B. Johansson, A. K. N. Reddy, and R. H. Williams, *Energy for a Sustainable World*, Wiley Eastern, Ltd., New Delhi, 1988.

12. Golomb, D., M. Herzog, J. Tester, D. White, and S. Zemba, "Feasibility, Modeling and Economics of Sequestering Power Plant CO_2 Emissions in the Deep Ocean," Draft Report, MIT Energy Laboratory, December 1989.

13. Gore, A., "What is Wrong With Us," *Time Magazine*, p. 66, January 2, 1989.

14. Hendriks, C. A., K. Blok and W. C. turkenburg, "Technology and Cost of Recovering and Storing Carbon Dioxide from an Integrated Gasifier Combined Cycle," Department of Science, Technology and Society, University of Utrecht, The Netherlands, September 1990, accepted for publication in *Energy—The International Journal*.

15. Horn, F. L. and M. Steinberg, *Possible Storage Sites for Disposal and Environmental Control of Atmospheric Carbon Dioxide*, BNL 51597, September 1982.

16. Keepin, B. and G. Katz, "Greenhouse Warming: Comparative Analysis of Nuclear and Efficiency Abatement Strategies," pp. 538-61 in *Energy Policy*, December 1988.

17. Manne, A. S., and R. Richels, "Global CO_2 Emission Reductions – the Impacts of Rising Energy Costs," pp. E-64-E-99 in *Energy and the Environment in the 21st Century*, Massachusetts Institute of Technology, March 26-28, 1990.

18. Masters, C. D., E. D. Attanasi, W. D. Dietzman, R. F. Meyer, R. W. Mitchell, and D. H. Root, "World Resources of Crude Oil, Natural Gas, Natural Bitumen, and Shale Oil," Twelfth World Petroleum Congress, Houston, April 26-May 1, 1987.

19. Pearce, Fred, "Planting Trees for a Cooler World," *New Scientist*, October 15, 1988.

20. *Petroleum Economist*, "Middle East-A New Role in Gas Exports," Vol. 57, No. 5, pp. 150-151, May 1990.

21. Russell, M., "Ozone Pollution: The Hard Choices," *Science*, **241**, 1275, September 9, 1988.

22. Sancton, T. A., "What on Earth are We Doing," *Time Magazine*, pp. 24-30, January 2, 1989.

23. Schora, F. C., and E. H. Camara, "Fuel Cells, Power for the Future," pp. F-40-F-59 in *Energy and the Environment in the 21st Century*, Massachusetts Institute of Technology, March 26-28, 1990.

24. Smith, I. M., *CO_2 and climatic change*, IEACR/07, IEA Coal Research, London, May 1988.

25. Steinberg, M., "Recovery, Disposal, and Reuse of CO_2 for Atmospheric Control," pp. 69-77, *Environmental Progress* 4(2), May 1985.

26. Steinberg, M., *Production of a Clean Carbon Fuel Derived From Coal For Use In Stationary and Mobile Heat Engines*, BNL--38086 (DE86 011203), April 1986.

27. Steinberg, M., *Clean Carbon and Hydrogen Fuels From Coal and Other Carbonaceous Raw Materials*, BNL--39630 (DE87 009145), April 1987.

28. Tans, P. P., I. Y. Fung, and T. Takahashi, "Observational Constraints on the Global Atmospheric CO_2 Budget," pp. 1431-1438 in *Science*, 247(4949), March 23, 1990.

29. Williams, R. H. and E. D. Larson, "Expanding Roles for Gas Turbines in Power Generation," in *Electricity Efficient End-Use and New Generation Technologies*, and Their Planning Implications, Lund University Press, pp. 503-53, Lund, Sweden 1989.

30. Williams, R. H., "Will Containing Fossil Fuel Carbon Dioxide Emissions Really Cost So Much?", private communication to W. Fulkerson, April 1990.

31. Wilson, C. A., *Coal — Bridge to the Future*, pp. 157-168, Ballinger Publishing Company, Cambridge, Massachusetts, 1980.

32. *Wall Street Journal*, "World Wire-Japan-Siberia Pipeline," p. A8, June 4, 1990.

Table 1. World primary energy use and associated CO_2 emissions by year for the past 50 years

	Oil		Gas		Coal		Fossil		Hydroelectric		Nuclear		Total	CO_2	E/P
	q	%	q	%	q	%	q	%	q	%	q	%	q	Gt(C)/y	MMBtu
1937															
US	7	33	2	11	12	55	21	99	0	1			21	0.4	161
World	12	20	3	5	45	75	60	99	0	1			60	1.2	29
1947															
US	12	36	4	13	16	50	32	99	0	1			32	0.7	221
World	18	24	6	9	48	66	72	99	0	1			72	1.4	32
1957															
US	18	44	10	25	11	27	39	96	2	4			40	0.8	236
World	35	33	12	11	53	50	100	94	6	6			106	2.2	37
1967															
US	25	44	18	31	12	21	55	96	2	4			58	1.0	290
World	70	40	30	17	65	37	165	94	11	6			176	3.3	51
1973															
US	35	47	23	30	13	17	70	95	3	4	1	1	74	1.3	351
World	111	47	42	18	66	28	220	94	13	6	2	1	235	4.5	60
1977															
US	37	49	20	26	14	18	71	93	3	3	3	4	76	1.3	346
World	118	46	46	18	73	28	237	92	15	6	5	2	258	4.8	61
1985															
US	31	42	18	24	17	24	66	90	3	5	4	6	74	1.3	309
World	112	38	59	20	90	31	260	88	20	7	14	5	295	5.3	61
1986															
US	32	43	17	23	17	23	66	89	3	5	4	6	74	1.3	308
World	115	38	59	20	92	31	266	88	21	7	15	5	302	5.4	61
1987															
US	33	43	17	23	18	24	68	89	3	4	5	6	76	1.3	312
World	117	38	62	20	95	31	273	88	21	7	16	5	310	5.5	62
1988															
US	34	43	18	23	19	24	71	89	3	4	6	7	80	1.4	
World	121	38	65	20	96	30	282	88	22	7	17	5	320	5.5	

q - quads (quadrillion Btu); Gt(C) - gigaton (billion metric tons) carbon as CO_2; y - year; E/P - Energy per capita (person); MMBtu - million Btu

Although alternative energy sources, most notably nuclear and hydropower, have become available during the last fifty years, total energy production from fossil energy sources has grown dramatically. Percentagewise, fossil fuels will probably continue to shoulder much of the energy burden for many years to come because alternative energy sources are either not economically competitive or cannot be implemented on a large scale.

[Source: Fulkerson, 1989]

Table 2. If all recoverable resources of fossil fuels were burned, significant increases in atmospheric CO_2 would result, with the absolute magnitude of the increases being dependent on the fraction of CO_2 released that is retained in the atmosphere. Of the fossil fuels, only coal is sufficiently abundant to increase atmospheric CO_2 by more than a factor of two.

Fuel	Recoverable Quantity	Energy Value (1000s of Quads)	Carbon[a] Content 10^{15} g	CO_2 Concentration Increase (ppm)[b] Fraction Retained in Atmosphere 0.4	0.55	0.7
Oil	1255 x 10^9 bbl	7	130	24	34	43
Gas	8200 tcf	8	120	23	31	39
Coal	5500 x 10^{15} g	153	3850	723	994	1265
Totals	(Rounded off)	168	4100	770	1060	1350

Source [Fulkerson, et al., 1989]

[a]In addition to these amounts of carbon, comparable or larger amounts may be available in other fossil resources such as heavy oils, oil shales, tar sands, lower grades of coal, etc. Thus, the quantity of carbon ultimately released to the atmosphere as CO_2 could conceivably be half again as much, or twice as much, as the total shown in the table.

[b]These hypothetical *increases* may be compared with the preindustrial CO_2 concentration (about 270 ppmv), the present concentration (350 ppmv), or the current annual increase (about 1.5 ppmv/year). In the atmosphere, 1 ppm of CO_2 by volume, uniformly distributed, equals about 2.13 Gt of carbon, or 7.81 Gt of CO_2. Thus, 350 ppmv CO_2 corresponds to 745 Gt C. (1 Gt = 10^9 metric tons = 10^{15} g)

Table 3. The estimated costs of CO_2 recovery and sequestration from central power plants are large , but may not be prohibitive. The economically viable method at present appears to be afforestation, but it is severely limited.

Removal Process	Relative Increase In Electricity Cost	Reduction in Efficiency for CO_2 removal	% CO_2 removed
Lime adsorption	2.4[a]	59	90
MonoethanolamineScrubbing	2.3[a]	57	90
O_2 Combustion	1.8[a]	30	100
IGCC/Selexol (Oxygen blown gasifier plus air combustor)	1.3[b]	13	88
Afforestation	1.1	0	100

a--Includes deep ocean disposal
b--Includes disposal in depleted natural gas wells

Sources: Steinberg, 1985, 1986, 1987; Blok, Hendrix, and Turkenburg 1989; Hendrix, Blok and Turkenburg, 1990; Golomb et al. 1989.

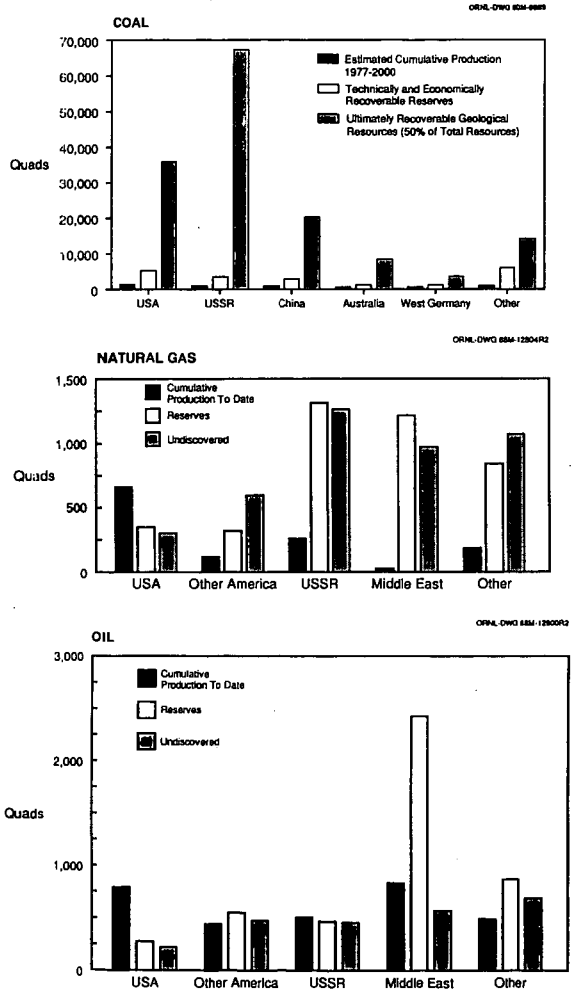

Figure 1. Fossil fuels are presently our most used and obtainable energy resources. They are dispersed throughout the world, and coal is by far the most abundant of the fossil fuels. Although coal is depletable, it would last about 1500 years at present use rates; oil, 60 years; and gas, 120 years.

Sources: Masters, et al., 1987; Wilson, 1980.

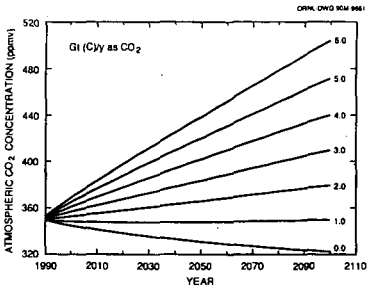

Figure 2. Atmospheric concentrations of CO_2 calculated by assuming that the current rate of emissions is suddenly changed to the values indicated and maintained constant thereafter.

Source: Emanuel 1990.

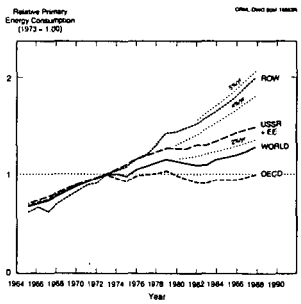

Figure 3. Relative world consumption of fossil energy 1965-1988, by regions.

Source: BP 1989.

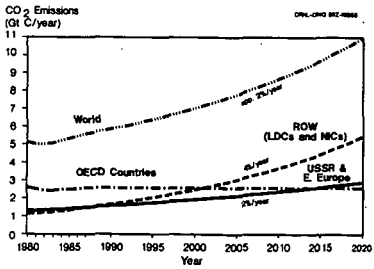

Figure 4. Extrapolation of CO_2 emission growth rates for the decade 1977 to 1987.

Source: Fulkerson 1989.

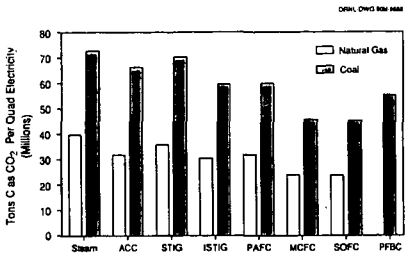

Figure 5. Carbon emissions from electricity generation using fossil fuels depend in large measure on the fuels used and the efficiencies of the generation techniques used. This figure compares emissions of carbon, expressed in terms of millions of tons of carbon as CO_2 per quad of electricity produced, for several electricity generating options using natural gas and coal as fuels. The options include conventional steam-electric plants (Steam), advanced combined cycle (ACC), steam-injected gas turbines (STIG), intercooled steam-injected gas turbines (ISTIG), phosphoric acid fuel cells (PAFC); molten carbonate fuel cells (MCFC), solid oxide fuel cells (SOFC), and pressurized fluidized-bed combustors (PFBC).

[Millions of metric tons C as CO_2 emitted per quad of electricity = 52.5 (natural gas) or 92.0 (coal) x (12/44)/efficiency; for example, for a steam plant fired with an efficiency of 34.6%, the amount of carbon dioxide that is released per quad is 92 x 0.2727/0.346 = 72.5 million tons]

Sources: *Clean Coal Technology*, 1989; Pillai, 1989; Schora and Camara, 1990; Williams and Larson, 1989; Blomen, 1989.

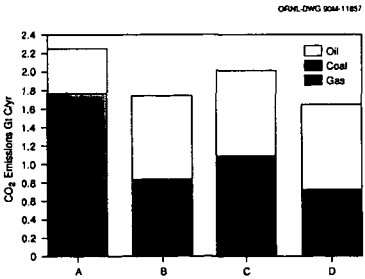

Figure 6. Four scenarios for CO2 emissions from the use of fossil fuel by the USSR, other Eastern European countries, and Western European countries. Scenario A assumes future emissions are the same as for 1988. Scenario B assumes all coal use in Scenario A is replaced by natural gas but with efficiencies 20% greater than coal. Scenario C is the same as Scenario B except that all oil use is replaced by methanol made from natural gas at a conversion efficiency of 60%. Scenario D is the same as Scenario C except that nuclear or solar heat improves the efficiency of conversion to 90% and the CO2 emissions are reduced accordingly. In Scenario A, 34 quads of natural gas are used per year; in Scenario B, 645 quads; in Scenario C, 141 quads; and in Scenario D, 115 quads. The estimated recoverable gas resources and reserves for Europe would last about 90 years for Scenario A, but only 45 years for Scenario B and 21 and 26 years for Scenarios C and D, respectively.

Diversification of Raw Materials for Domestically Produced Transportation Fuels

J. P. Longwell

Department of Chemical Engineering
Massachusetts Institute of Technology
Cambridge, Massachusetts

Keywords: Transportation Fuels, Synthetic Fuels, Alternative Fuels

In the past the transportation fuels, gasoline, jet and diesel fuel, and residual fuels have been almost entirely manuactured from petroleum and natural gas liquids, with growing dependence on foreign sources--currently about 50%.

More recently increasing amounts of oxygenated fuels are blended into gasoline. This change is largely driven by environmental and health concerns. An example is the phasing out of tetraethyl lead which has made limited use of high octane number oxygenated additives cost effective. Urban environmental concerns have resulted in legislation requiring increased gasoline oxygen content. The 1990 clean air act revision requires, for example, 2.7% oxygen content in gasoline by 1992 in some cities during the part of the year when they are prone to high CO levels. At present, oxygenated compounds are based on alcohols from agricultural sources or from natural gas thus providing some resource diversification without major automobile modification. Use of compressed natural gas and methanol fuel, which require vehicle modification, is being introduced for fleet use, largely in urban areas. It is expected that diversification of gasoline composition will continue. Jet fuel and diesel fuel, however, are not expected to undergo major changes.

This paper focuses on the future supply of domestically produced transportation fuels, their cost and the consequent timing for development of fuels from domestic resources. It makes extensive use of information acquired for the National Research Council study "Production Technologies for Liquid Transportation Fuels". [1]
In order to focus the discussion, it is assumed that consumption of transportation fuels will remain constant and that we will work toward the goal of maintaining domestic production at 50% of the total.

In the United States, liquid fuel use is dominated by the transportation sector.I is expected that the transportation sector's share of liquid fuels use will grow as petroleum cost increases and supplies diminish since the other sectors can switch relatively easily to natural gas, solid fuels or electricity.

Within the transportation sector the major fuel is motor gasoline. It is not expected that the distribution will change drastically for the next few decades although jet fuel may well continue to grow in importance.

Table 3 presents estimates of remaining economically producible US. crude oil resources as a function of cost and level of technology used. These estimates were prepared for the National Research Council by ICF Industries and take into account the recent increases in resource estimates based on advances in identification of isolated pockets of oil which had previously been overlooked. Tar (> 10^4 centipoises) is included in these estimates. "Moderate Cost" is taken as 25 $/bbl and "High Cost" 40 $/bbl.

For current practice, which includes secondary recovery, and a cost of $25/bbl, 75 billion bbl can be recovered. The ratio of this resource to the 1989 production of 3 billion bbl of oil/year provides a time scale for this resource. It is, however, not a prediction of suddenly running out of oil in 25 years. It is expected that, in the near term, production will continue to decrease, but that a vigorous drilling and development program can bring production back to the present rate. In time, production for a given price will decrease as the lower cost resources are consumed. This ratio is, however, useful for planning purposes.

Increasing oil price to $40/bbl with no change in technology is estimated to increase the economically producible resource to 95 billion bbl (26%). At this price, however, extended oil recovery techniques become economically feasible and 140 billion bbl can be economically produced with a resource to current annual production ratio of 47. These times are the same general magnitude of the time required to build up an industry and facilities for major production of liquid fuel manufactured from alternative resources such as biomass, coal, and oil shale.

In Table 4 estimates for production of domestic natural gas are presented. The wellhead gas price of 3$/MCF corresponds to an oil price of about 24 $/bbl. Domestic gas production, on a heating value basis, is currently approximately the same as oil production and the base case resource base/current production ratio is 33 years--32% higher than shown in Table 3 for the petroleum base case. It is expected,, however, the use of natural gas for heating and power generation will grow relative to petroleum (2) so the time scales, may not be greatly different from petroleum. While natural gas can be converted to, or used for, transportation fuel, the domestic resource cannot be expected to substitute for petroleum in transportation fuels to a major extent.

Increasing use of solid fuel resources for manufacture of transportation fuel is indicated by the above considerations. Estimates of the magnitude of these resources are presented in Table 5.

Coal and Western oil shale represent resources large enough to replace domestic petroleum for many years. Estimates of the potential for environmentally and economically acceptable biomass production vary widely (about a factor of on either side) of the estimate shown here. This potential can be compared to the 2.4 billion bbl/yr gasoline shown in Table 2. On this basis, the biomass resource is large enough to be an important source of domestic transportation fuel.

The estimated cost of producing transportation fuels from non-petroleum resources has been estimated using a common basis for process and raw material costs. These estimates are based on a study prepared for the National Research Council by SFA Pacific Inc. [4]. These costs are expressed as the crude oil cost that would make a spark ignition vehicle fuel from the alternative resource just as expensive to the end user as gaasoline from crude oil. The cost estimates are for 1988 dollars with 10% DCF return. Capital costs include vehicle modifications for alternative fuels as well as the investment in manufacturing and distribution facilities.

Natural gas costs, for hydrogen and synthesis gas production, increase with increasing crude oil cost according to the formula

$$\$/MCF = 3.91 + .05857\ (P_{oil}-28)$$

P_{oil} is the price of crude oil in $/bbl.

Heavy oil and tar sands, which were counted as petroleum in Table 3, can be converted to transportation fuels by hydroprocessing, using natural gas as a source of hydrogen, at 25 and 28 $/bbl equivalent crude cost. Here, as with natural gas, large foreign resources will probably be available at a lower cost for many years.

The use of compressed natural gas for automative fuel, which includes distribution and vehicle modification costs, was estimated to be 34$/bbl equivalent crude cost. Equivalent crude costs for coal liquefaction and Western Shale oil were estimated to be 38 and 43 $/bbl respectively. Over the last decade significant progress has been made in coal liquefaction; however, the shale oil process has suffered from lack of published activity. Leads for further cost reduction, in both processes, offer the potential of achieving, with continued R&D, a cost of 30 $/bbl for both processes within the next decade.

Methanol by coal gasification is 35-40 $/bbl. In this case the price of domestic gas makes coal gasification the most economic route. Estimated costs for methanol from overseas natural gas are also shown for U.S. investment costs. but with the cost of transportation to the U.S. added. A 15% energy efficiency advantage and a $100 automobile cost differential for methanol was also assumed. On this basis, imported methanol based on low cost gas can be lower cost than domestic production from solid fuel resources.

The use of wood for methanol production is one of the more attractive methods for using biomass. In this study wood and coal feed costs were approximately the same and, for the same size of plant, gasification and process costs would be about the same. The costs shown for coal to methanol, hoever, are based on a large plant (oil equivalent 50,000 bbl/day-oil). Biomass based operations on a smaller scale would have increased costs.

From the above studies it appears that in the 30-40 $/bbl range of equivalent crude cost, use of all the solid resources becomes of economic interest with heavy oil processing becoming economic at 25 $/bbl. The time at which prices in this range will become sufficiently stable to attract unsubsidized private capital is unpredictable. If a decision is made to maintain domestic production at a stable level(say 50%of the total), construction of and operation of facilities before the time of stable international oil prices in the 30-40 $/bbl range will be necessary. Facilities for hydroprocessing of heavy oil and tar are expected to be the first step followed by introduction of use of solid resources. It has been shown that heavy oil hydroprocessing operates successfully with a mixture of coal and oil and that hydrogen, which is used in large quantities can be manufactured from a wide variety of feeds. The possibility exists, therefore, of substantial flexibility in the type of feed used in a given plant with the potential for changing the mix as economic and supply change with time.

These process possibilities are illustrated in Fig. 1. Gasification by partial oxidation is capable of converting any carbonaceous feed to a gaseous mixture from which the hydrogen and CO can be separated. From this hydrogen/carbon monoxide mixture, hydrogen for direct liquefaction can be produced. Methanol or paraffinic liquid fuels, both excellent transportation fuels, can also be manufactured from the hydrogen-carbon monoxide mixture by catalytic conversion.

In direct, or liquefaction, hydrocarbon fuels are produced by reaction of tars or solid fuels with hydrogen produced by gasification.

The production of the greenhouse gas, CO_2, could well have a major effect on the choice of raw materials for transportation fuel. Table 7 presents information on the formation of greenhouse gases, relative to petroleum based gasoline, by production and use of automotive fuels from several starting materials.

Biomass based fuels are considered to be greenhouse gas neutral. This assumes no consumption of fossil fuels in the complete fuel cycle. Methanol from coal, however, produces approximately twice the CO_2 compared to petroleum.

Oil shale is intermediate with the amount of CO_2 produced depending on the degree of carbonate decomposition during the retorting process. Natural gas based fuels are somewhat better than petroleum.

If process heat and hydrogen from non-fossil resources (Biomass, solar, nuclear) becomes available, the greenhouse gas production from gasoline or methanol for all sources is comparable to or better than gasoline from petroleum. Development of non-fossil heat and hydrogen could, therefore, be an important factor in use of our fossil fuel resources.

Conclusions

1. If production of transportation fuels from domestic resources is to be maintained at approximately the current level, it is time to begin the transition from petroleum to alternative raw materials.

2. The 1988 equivalent crude cost, starting with solid resources, is in the 30-40 $/bbl range.

3. Both supply and environmental considerations lead to a diverse set of raw materials.

4. Co-processing of raw materials offers an opportunity for optimizing the transition to use of solid resources.

5. The production of CO_2 from fossil resources can be substantially reduced by developing non-fossil fuel based sources of heat and hydrogen.

References

(1) "Fuels to Drive Our Future", National Academy of Science Press, 1990.

(2) Energy Information Administration - Annual Energy Outlook (1989).

(3) Kuuskra et al. "U.S. Petroleum and Natural Gas Resources, Reserves and Exraction Costs", ICF Industries Inc., Fairfax, Va. 1990.

(4) Shulman, B.L. and Biasca, F.E., "Liquid Transportation Fuels from Natural Gas, Heavy Oil, Coal, Oil Shale and Tar Sands: Economics and Technology" SFA Pacific Inc., Mountain View, CA (1989).

(5) Sperling, D. "New Transportation Fuels - A Strategic Approach to Technological Change": University of California Press-Berkeley, CA 1988.

Table 1

Yearly U.S. Liquid Fuel Use by Sector
(1988)[2]

Sector	Quads (10^{15}BTU)	% of Total
Transportation	21.0	72
Residential	1.2	4
Commercial	1.0	3
Industrial	4.8	16
Electric Utilities	1.3	5
	29.3	100

Table 2

Yearly Transportation Fuel Use
(1988)[2]

Fuel Type	Quads(billion bbl/yr)	% of Total
Motor Gasoline	13.8(2.4)	66
Diesel Fuel	3.5(0.6)	17
Jet Fuel	3.0(0.5)	14
Residual Fuel	0.7(0.1)	3
Total	21.0(3.6)	100

Table 3

Estimated Remaining Economically
Producible US. Crude Oil Resources - 1989[3]

	Current Practice		Advanced Technology	
	Mod. Cost	High Cost	Mod. Cost	High Cost
Billion bbl oil	75	95	115	140
(QUADS)	(435)	(551)	(667)	(810)
Resource base to current annual production ratio	25	32	35	47

Table 4

Estimated Remaining Economically
Producible Natural Gas Resources (3)

	Current Technology		Advanced Technology	
Wellhead Gas Price Dollars/Mcf	3	5	3	5
Tcf Gas (Bbl oil equivalent)	595(107)	770(140)	880(160)	1420(256)
Ratio of Resource Base to Current Production	33	43	50	80

Table 5

Alternative US. Resources (1)

Resource	Recoverable Amount - Quads
Coal	6,000 - 11,000
Western Shale	3,000 - 4,000
Eastern Shale	400
Tar Sands	400
Biomass - Methanol	(~1 billion bbl/yr of oil equivalent)

Table 6

Equivalent Crude Cost of Alternative Fuels
(in 1988 dollars/bbl, at 10% discounted cash flow) (1)

Process	Cost Estimates for Current Published Technology	Cost Targets for Improved Technology
Heavy Oil Conversion	25	-
Tar Sands Extraction	28	-
Coal Liquefaction	38	30
Western Shale Oil	43	30
Compressed Natural Gas	34	-
Methanol via		
Coal Gasification	35-40	-
Natural gas at		
$4.89/Mcf	45	-
$3.00/Mcf	37	-
$1.00/Mcf	24	-

Table 7

Approximate Greenhouse Gas Emission per Mile
Relative to Petroleum-Powered Internal Combustion Engines[5]

Fuel and Feedstock	Percent Change
Current Technology	
Gasoline and diesel from crude oil	0
CNG, gasoline, diesel, or methanol from biomass	-100
Methanol from coal	+ 98
Gasoline from oil shale	+ 27 to + 80
CNG from natural gas	- 19
Methanol from natural gas	- 3
Potential Advanced Technology	
Gasoline from coal or shale using nonfossil sources for process heat and hydrogen	0

Fig. 1

Feeds for Direct and Indirect Solid to Liquid Fuels Conversion

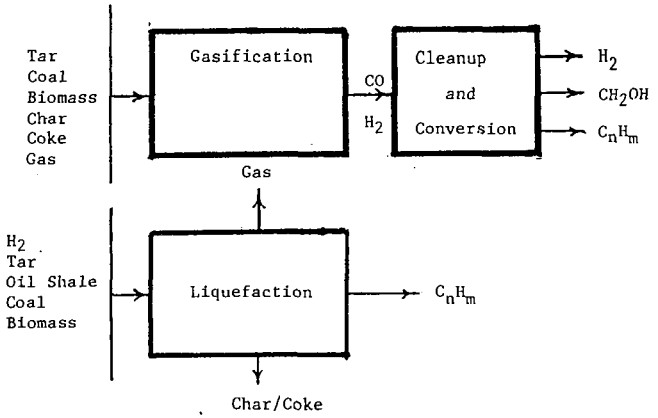

GREENHOUSE GAS EMISSIONS, ABATEMENT AND CONTROL: THE ROLE OF COAL

I.M. Smith, K.V. Thambimuthu, IEA Coal Research, London, UK

Keywords: greenhouse gas, efficiency improvements, CO_2 control technology

ABSTRACT

The basis for quantifying the relative effect of greenhouse gas emissions from coal utilisation is discussed. Emission factors (gC/MJ) need to include greenhouse gas emissions and energy losses throughout the fuel cycle in order to compare the fuels. Nevertheless CO_2 is the most important greenhouse gas from coal. Emission factors have decreased due to improved efficiency of coal use. The scope for further improvements in efficiency of conventional and advanced power generation is assessed. Control of CO_2 emissions is viewed as a less promising option owing to the high cost and energy penalty of most methods.

It is concluded that there is no firm basis for evaluating the effect of reducing emissions on their global warming potential. However it is desirable that available technologies be implemented to reduce emissions by improved efficiency.

INTRODUCTION

Greenhouse gases from coal include methane (CH_4), released during hard coal production, and most important, carbon dioxide (CO_2) as well as nitrous oxide (N_2O) which are emitted when coal is used. Ozone (O_3) is another greenhouse gas formed indirectly from complex reactions with other pollutants in the atmosphere. Here other oxides of nitrogen, nitric oxide and nitrogen dioxide (jointly referred to as NO_x), play a role and are emitted from coal use. The topic of nitrogen oxide emissions from coal combustion was reviewed recently at IEA Coal Research by Sloss (1991). Chlorofluorocarbons (CFC) are important greenhouse gases which are produced in the industrial sector where coal is not involved.

Policy choices over the next few years to reduce greenhouse gas emissions are likely to have a profound effect on the use of coal in many countries. It is therefore essential to examine and monitor the scientific and technical basis for reducing emissions of greenhouse gases from coal use. A major scientific assessment of the greenhouse gas issue is provided by the recent report (Houghton and others, 1990) of Working Group I of the Intergovernmental Panel on Climate Change (IPCC), set up in 1988 by the World Meteorological Organization and the United Nations Environment Programme. The IPCC considered that a reduction in CO_2 emissions >60% would be required to stabilise CO_2 concentrations in the atmosphere. IEA Coal Research has been keeping a watching brief on this issue since 1977 (Smith, 1978, 1982, 1988; Vernon, 1990). This paper examines the basis of the quantitative evaluations which are being commissioned by policy makers in attempting to deal with the greenhouse gas issue and assesses the state-of-the art of abatement and control technologies as they relate to coal use. Information is drawn from a new draft report on this topic (Smith and others, 1991).

GREENHOUSE GAS EMISSIONS

The contributions (%) of trace gases to the greenhouse effect are estimated for the IPCC by Shine and others (1990) over the past decade (based on increased concentrations in the atmosphere) and integrated over the next 100 y (in terms of emissions from human activities in 1990) as follows:

	1980-90	100 y
CO_2	56	61
CH_4	15	15
N_2O	6	4
CFC	24	12
others	-	8
	101	100

The indirect effects of CH_4 oxidation (the production of CO_2, stratospheric water vapour and

tropospheric O_3) are potentially significant but difficult to quantify. This applies also to the indirect effects from other trace gases: CO (1%), NO_x (6%) and non-methane hydrocarbons (0.5%). Shine and others emphasise that the quantification of these indirect effects needs further revision and evaluation and does not include some important chemical reactions. Victor (1990) points out that the indirect effects vary spatially as well as with time.

Further uncertainties arise from different ways of estimating the effective residence time for CO_2 in the atmosphere. The uptake of CO_2 into the various storage sinks of the global carbon cycle can take a short time, for example into non-woody vegetation or a much longer time into the deep ocean. The IPCC adopted a range of 50-200 y for the effective residence time of CO_2 in the atmosphere (Watson and others, 1990). There are uncertainties in accounting for all the CO_2 emissions which do not remain in the atmosphere. Other potential long term carbon sinks (Tans and others, 1990) have not been quantified but would shorten the effective residence time for CO_2.

The contribution to the greenhouse effect of CH_4 relative to CO_2 is important when considering the merits of fuel substitution from coal to natural gas or a carbon tax. The global warming potential of one mole of CH_4 relative to that of CO_2 ranges from 20-35 or more depending on the assumptions of different authors (Selzer, 1989: Zittel and Selzer, 1990). This uncertainty is compounded by differing values for the effective residence time of CO_2, resulting in a wide variety of numbers for the relative global warming potential of CH_4 : CO_2 (see Table 1). The estimates in Table 1 are ranked from the simplest (no consideration of the differences in residence times for CO_2 and CH_4 and a molar global warming potential of 27) to the most sophisticated by Lashof and Ahuja (1990) and Shine and others (1990). The latter use oceanic models for estimating the residence time of CO_2, more complex chemistry for the indirect effects and include the concept of integrating over the short or long term. In the long term, CO_2 assumes greater importance relative to CH_4 than in the short term. Despite current limitations, the concept of applying global warming potentials over different time horizons is the best available means of evaluating emission abatement scenarios but requires further validation.

The contribution of global coal use to the enhanced greenhouse effect is evaluated from CO_2 emissions in 1988 for the low and high estimates of the contribution from deforestation and land use adopted by the IPCC (see Table 2). Shine and others (1990) assume 7.1 GtC/y for the total CO_2 emissions from human activities in 1990. This lies within the range for total CO_2 shown in Table 2 but implies a low value for deforestation and land use if the 1988 CO_2 emissions of 5.7 GtC/y for fossil fuel are extrapolated to 1990. There is little difference between the contributions for one year or over 100 y. Coal, oil and gas would contribute about 20%, 20% and 8% respectively. There would be an additional 1% and 3% for CH_4 from hard coal mining and gas pipeline leakage respectively, assuming these sources contributed 6.3% and 20.8% of CH_4 emissions from human activities (World Resources Institute, 1990). There would also be small contributions from N_2O and NO_x emissions but these have not been quantified reliably.

Average CO_2 emission factors for bituminous coal, crude oil and natural gas, based on the higher heating value (HHV), are 24.1, 19.9 and 13.8 gC/MJ (Marland, 1983; Marland and Rotty, 1984). Those for the brown coals assessed by Couch (1988) averaged 25.2 gC/MJ. Anthracites have CO_2 emission factors of about 26 gC/MJ. When allowance is made for the effect of CH_4, in terms of its CO_2 equivalent, the emission factor for natural gas increases relative to that of coal and oil due to CH_4 leakage from natural gas distribution systems. Mitchell and Sweet (1990) applied the concept of global warming potentials and estimated that coal and natural gas would have the same emission factors at a CH_4 leakage rate of 11.5% over a 100 y time horizon. Over 20 y, the breakeven point would occur at a CH_4 leakage rate of about 5%. Such CH_4 leakage rates are not uncommon in some systems. However, it is unlikely that leakage from new gas supplies for large scale use would exceed 1% (James, 1990).

Similar evaluations including hard and brown coals in the FRG (Zittel and Selzer, 1990) conclude that, over short time horizons, brown coal has a lower effective CO_2 emission factor than hard coal if most of the CH_4 from hard coal mining is vented to the atmosphere. The two fuels would be equal over the 100 y time horizon.

Energy consumption or emission penalties are incurred when coal is upgraded. For example, a coke from a bituminous coal with a CO_2 emission factor of 24.1 gC/MJ (HHV) had an effective emission factor of 31.8 gC/MJ when coal production overheads were included (Thurlow, 1990). Synthetic fuels

from coal generally have much higher CO_2 emission factors than the original coal - even where gasoline is produced at a high thermal efficiency of 65% or more, the CO_2 emission factor is 38 gC/MJ. However this penalty will be offset by the lower CO_2 emission factor and improved combustion efficiency of the resulting synthetic fuels.

ABATEMENT

The proportion of coal used in power generation is about 73% in OECD countries (IEA, 1990) but worldwide it is probably around 50% (Matthews and Gregory, 1989). This section will therefore concentrate on technologies which decrease CO_2 emissions per unit of useful energy in the large scale use of coal for power generation.

The efficiency of coal use in steam power plants has already improved greatly this century. For example, in the FRG increasing operating pressures and temperatures and the use of steam reheat in conventional power plants have resulted in a reduction in the heat rate from 35 MJ/kWhe in the early 1900s to about 9 MJ/kWhe in the 1980s (Schilling, 1990). Emissions and waste heat losses are now only about 25% of what they were in the early steam based power plants.

Current trends show that further improvements are achievable, both on conventional plants and using more advanced technologies (see Table 3). Hence the use of supercritical steam conditions (Riedle and others, 1990) should reduce CO_2 emissions by 20% compared to a conventional 500 MWe pulverised coal (PC) plant with wet limestone flue gas desulphurisation (FGD) and sub-critical steam conditions (US DOE, 1990). Co-firing with natural gas or oil also results in reductions in CO_2 emissions due to a lower emission factor of the blending fuels. The use of flue gas recycling (Wolsky and Brooks, 1989) or selective H_2 combustion (Steinberg and Grohse, 1990) appears to offer 100% reductions of CO_2 emissions but at considerable energy costs for the separation and disposal of CO2 or carbon.

The use of combined cycles with gasification, pressurised pulverised coal or fluidised bed combustion (PFBC) should achieve CO_2 reductions of 13-26%. At the upper end of this range are the hybrid PFBC gasification topping cycle developed by British Coal (Dawes and others, 1990) and a new scheme for pressurised pulverised coal combustion (Weinzierl, 1990). In the latter, pulverised coal is burnt under pressure in an ash slagging combustor with gas expansion through a gas turbine. Pulverised coal-natural gas combined cycles with supercritical steam conditions are expected to achieve a reduction in CO_2 emissions of about 37% (Hebel and Kotschenreuther, 1990).

Commercial MHD generators could reduce CO_2 emissions by up to 27% in the near term and even more in future with a greater efficiency of heat recovery (Morrison, 1988). The development of molten carbonate and solid oxide fuel cell technology is currently in its infancy but is potentially capable of reducing CO_2 emissions by up to 44% when used with gas/steam turbine combined cycles (Kinoshita and others, 1988).

Finally, where waste heat can be used in cogeneration or combined heat and power such as in Denmark (Mortensen, 1989), CO_2 reductions approaching 60% are achievable even with conventional coal combustion technologies.

CONTROL TECHNOLOGIES

In contrast to abatement measures, the control of CO_2 emissions by recovery and disposal is generally regarded as a last resort owing to the high energy costs involved. A recent study by the US Electric Power Research Institute (Smelser and Booras, 1990) concluded that 90% CO_2 recovery by MEA scrubbing, solvent regeneration, compression and removal for disposal in the ocean at a depth of 457 m would incur an energy penalty of 370-374 kWhe/t CO_2. The busbar cost of electricity would increase by 159-178% relative to a coal-fired power plant without CO_2 control. These results lie within a range of 222-988 kWhe/t CO_2 for the energy penalty estimated by several authors for control technologies using absorption or cryogenic separation at 90% CO_2 removal or membrane separation at 80% removal. The estimates of energy use are in the range of 21-95% of the energy released from coal combustion (Smith and others, 1991).

Disposal options include the oceans or sites on land such as salt domes and depleted natural gas or oil

fields. For disposal in the oceans, the transfer of CO_2 as solid blocks of dry ice or hydrate was found to be less practical and more costly than gas or liquid injection owing to the tonnage involved. It is desirable to inject the CO_2 into the ocean at depths >1,000 m and preferably at 3-4,000 m in order to minimise the transfer of CO_2 from the ocean to the atmosphere (Hoffert and others, 1979). More research is required on the long term effects of macromixing in the oceans on CO_2 retention in the deep ocean. On land there is potential for storage of liquid CO_2 in salt domes. For example in the USA, the existing storage capacity of strategic crude oil reserves could accomodate about 15 GtC of CO_2 emissions. Global 1980 natural gas production values suggested that the storage capacity of depleted gas reservoirs could increase at about 0.7 GtC/y with an overall capacity as large as that of past and present reserves of natural gas (Baes and others, 1980). Storage of CO_2 in depleted oil fields can be combined with its use as a solvent for enhanced oil recovery by miscible flooding. In the USA it is estimated that this use could only take up 7.7 MtC/y of CO_2 (Abel and others, 1989). However, there would be a substantial release or recycling of injected gas at active production wells.

Alternative means of controlling CO_2 emissions include its use or recycle by natural or industrial processes. A recent study by Martin and others (1990) of essential growth nutrients in the Antarctic ocean shows that the correction of an iron deficiency could promote a thirty fold increase in phytoplankton growth in the outer continental sea. Estimates indicate that increased growth by iron seeding could sequester up to 1.6 Gt C/y of CO2 over a 50 y period but such an action is undesirable because of unknown ecological effects (Baum, 1990). On land, commercially managed forests in temperate ecosystems could sequester 2.9-5.4 Gt C/y but securing the necessary land areas of 465-733 Mha (Marland, 1989; Sedjo and Solomon, 1989) would pose problems. Unused land in tropical ecosystems (865 Mha) that previously supported forests might however be used to accumulate up to 1.5 Gt C/y over a 100 y period (Houghton, 1990). Two tropical reafforestation projects by US and Dutch utilities are to offset the CO_2 emissions from a new 180 MWe coal-fired power plant in the USA and two 600 MWe coal-fired power plants in the Netherlands (Flavin, 1989; EER, 1990). The reuse of CO_2 in fuel or chemical synthesis is economically viable only if the total energy used can be produced at a lower cost than the fuel or chemical value of the product. Here, biofuels, relying on solar radiation as a 'free' energy source for direct removal of CO_2 from the atmosphere, offer a means to slow the growth of fossil fuel use whilst simultaneously reducing the net accumulation of CO_2 in the atmosphere. The present consumption of CO_2 for process use and the synthesis of industrial chemicals suggests that this sector is unlikely to make a significant contribution to reducing the overall global emissions of CO_2.

CONCLUSIONS

The contributions of the greenhouse gas emissions to the enhanced greenhouse effect are expressed in terms of the equivalent global warming potential of CO_2 when policies to reduce emissions are evaluated. This exercise is however complicated by indirect effects from some, as yet, unquantifiable chemical reactions and by uncertainties regarding the effective residence time of CO_2 in the atmosphere. Thus the concept of applying global warming potentials of greenhouse gases over different time horizons is the best available means but requires further revision and evaluation. It is clear that CO_2 is the most important greenhouse gas from coal. However, consideration of CH_4 affects the relative ranking of different fossil fuels as greenhouse gas emitters. Hence high CH_4 leakage rates of 5-10%, such as occur in some natural gas distribution systems, would virtually offset the advantage of the lower CO_2 emission factor for natural gas over coal; although the leakage rates of <1% claimed for new gas distribution systems would make little difference. Coal use worldwide is responsible for about 20% of the enhanced greenhouse effect, half of which is attributable to coal-fired power generation.

There are many options for the abatement of emissions from coal use in power generation. Apart from reducing the overall demand for energy by conservation, there are technologies which will reduce emissions from an improved efficiency of coal use. Existing technologies based on supercritical steam cycles can achieve CO_2 emission reductions of up to 20%. Over the next decade, technologies such as PFBC and gasification combined cycle offer improvements up to 25% or 37% with the use of pulverised coal-natural gas combined cycles. For the future, MHD and fuel cells should reduce CO_2 emissions by 17-44%. All of these technologies could be improved further with co-generation for CO_2 emission reductions approaching 60% - close to that required to stabilise concentrations of CO_2 in the atmosphere.

The control of CO_2 emissions by recovery and disposal appears to incur too high an energy penalty with uncertain environmental consequences for a practical solution. However systems which offer the possibility of the combined removal of CO_2, SO_x and NO_x might have some role in future in conjunction with energy savings. Reafforestation and recycling of CO_2 in fuels potentially have more scope for reducing the concentration of CO_2 in the atmosphere but probably not on the scale required to stabilise it.

Considerable progress has been made to improve efficiency for economic reasons in the past. Now there is an added impetus to achieve more for both economic and environmental benefits. There is scope for reducing emissions from coal use by both abatement and control measures but their success depends on how quickly they can be implemented.

REFERENCES

Abel A, Holt M E, Parker L B (1989) Controlling carbon dioxide emissions: CRS report for Congress. CRS-89-157-ENR, Washington, DC, USA, Congressional Research Service, Library of Congress, 34 pp (9 Mar 1989).

Baes C F, Beall S E, Lee D W (1980) The collection, disposal, and storage of carbon dioxide. In: Proceedings of the international conference: Interactions of energy and climate, Münster, FRG, 3-6 Mar 1980, W Bach, J Pankrath, J Williams (eds.). Dordrecht, Netherlands, D Reidel, pp 495-519 (1980).

Baum R (1990) Adding iron to ocean makes waves as way to cut greenhouse CO_2. Chemical and Engineering News; 68 (27); 21-23 (2 Jul 1990).

Boden T A, Kanciruk P, Farrell M P (1990) Trends '90: A compendium of data on global change. ORNL/CDIAC-36, Oak Ridge, TN, USA, Carbon Dioxide Information Analysis Center, 278 pp (Aug 1990).

Couch G (1988) Lignite resources and characteristics. IEACR/13, IEA Coal Research, London, UK, 102 pp (Dec 1988).

Dawes S G, Arnold M StJ, Cross P J I, Holmes J (1990) British Coal development of advanced power generation technologies. Paper presented at the Institution of Mechanical Engineers conference on steam plant for the 1990s, London, UK, 4-6 Apr 1990, 9 pp (1990).

European Energy Report (1990) Dutch consider rain forest planting to offer power station emissions. European Energy Report; (312); 4-5 (20 Apr 1990).

Flavin C (1989) Slowing global warming: a worldwide strategy. Washington, DC, USA, Worldwatch Institute, pp 94 (1989).

Hebel G, Kotschenreuther H (1990) Wirkungsgradverbessernde Massnahmen an bestehenden Kraftwerken (Measures to improve the efficiency of existing power plants). In: VGB-Konferenz Kraftwerkstechnik 2000 - Ressourcenschonung und CO_2-Minderung (VGB conference power plant engineering 2000 - Conservation of resources and CO_2 control), Essen, FRG, 21-22 Feb 1990. Essen, FRG, VGB-Kraftwerkstechnik GmbH, pp 200-204 (1990).

Hoffert M I, Wey Y C, Callegari A J, Broecker W S (1979) Atmospheric response to deep-sea injections of fossil-fuel carbon dioxide. Climatic Change; 2 (1); 53-68 (1979).

Houghton J T, Jenkins G J, Ephraums J J (1990) Climate change: the IPCC scientific assessment, Cambridge, UK, Cambridge University Press, 414 pp (1990).

International Energy Agency (1990) Coal information 1990. Paris, France, OECD/IEA, 538 pp (1990).

James C G (1990) Natural gas and the greenhouse. Nature; 347 (6295); 720 (25 Oct 1990).

Kinoshita K, McLarnon F R, Cairns E (1988) Fuel cells: a handbook. DOE/METC-88/6096, Morgantown, WV, USA, United States Department of Energy, Morgantown Energy Technology Center, 156 pp (May 1988).

Lashof D A, Ahuja D R (1990) Relative contributions of greenhouse gas emissions to global warming. Nature; 344 (6266); 529-531 (5 Apr 1990).

Marland G (1983) Carbon dioxide emission rates for conventional and synthetic fuels. Energy; 8 (12); 981-992 (1983).

Marland G (1989) The role of forests in addressing the CO_2 greenhouse. In: Proceedings of the conference on global climate change linkages. J C White, W Wagner, C N Beale (eds.), Washington, DC, USA, 15-16 Nov 1988. New York, NY, USA, Elsevier Science Publishing, pp 199-212 (1989).

Marland G, Rotty R M (1984) Carbon dioxide emissions from fossil fuels: a procedure for estimation and results for 1950-1982. Tellus; (36B); 232-261 (1984).

Martin J H, Gordon R M, Fitzwater S E (1990) Iron in Antarctic waters. Nature; 345 (6271); 156-158 (10 May 1990).
Matthews A K, Gregory K (1989) A global estimate of the proportion of coal used in the production of electricity. Draft report OR/951/20/1, Harrow, UK, British Coal, Operational Research Executive, 4 pp (Feb 1989).
Mitchell C, Sweet J (1990) A study of leakage from the UK natural gas supply system with reference to global warming. London, UK, Greenpeace UK, 112 pp (Aug 1990).
Mortensen H C (1989) Role of CHP in energy conservation and emissions reduction. In: IEA/OECD experts' seminar on energy technologies for reducing emissions of greenhouse gases, Paris, France, 12-14 Apr 1989. Paris, France, OECD\IEA, Vol. 2, pp 173-178 (1989).
Pearman G I (1989) Prediction of climatic change from best scientific models. Paper presented to the first meeting of the Prime Minister's Science Council. Canberra, NSW, Australia, 6 Oct 1989, pp 28 (Oct 1989).
Riedle K, Rukes B, Wittchow E (1990) Die Erhöhung des Kraftwerkswirkungsgrades in Vergangenheit und Zukunft (Improvement of power plant efficiency in the past and in the future). In: VGB-Konferenz Kraftwerkstechnik 2000 - ressourcenschonung und CO_2-Minderung (VGB conference power plant engineering 2000 - conservation of resources and CO_2 control, Essen, FRG, 21-22 Feb 1990. Essen, FRG, VGB-Kraftwerkstechnik GmbH, pp 189-199 (1990).
Rodhe H (1990) A comparison of the contribution of various gases to the greenhouse effect. Science; 248 (4960); 1217-1219 (8 Jun 1990).
Schilling H D (1990) Technology trends in large power plants. Modern Power Systems Supplement; 21-26 (Sept 1990).
Sedjo R A, Solomon A M (1989) Climate and forests. In: Greenhouse warming: abatement and adaptation workshop, Washington, DC, USA, 14-15 Jun 1988. Washington, DC, USA, Resources for the Future, pp 105-119 (1989).
Selzer H (1989) Energiebedingte Methanemissionen (Methane emissions from energy sources). Study A.3.3., Ottobrunn, FRG, Ludwig-Bolkow-Systemtechnik GmbH, 80 pp (Oct 1989).
Shine K P, Derwent R G, Wuebbles D J, Morcrette J J (1990) Radiative forcing of climate. In: Climate change: the IPCC scientific assessment. J T Houghton G J Jenkins J J Ephraums (eds.). Cambridge, UK, Cambridge University Press, pp 41-68 (1990).
Sloss L (1991) Nitrogen oxides from coal combustion. London, UK, IEA Coal Research, 107 pp (In press).
Smelser S C, Booras G S (1990) An engineering and economic evaluation of CO_2 removal from fossil fuel-fired power plants. In: Proceedings of the EPRI 9th annual conference on gasification power plants, Palo Alto, CA, USA, 17-19 Oct 1990. Washington, DC, USA, Electric Power Research Institute, pp 855-2471 (Oct 1990).
Smith I M (1978) Carbon dioxide and the 'greenhouse' effect - an unresolved problem. ICTIS/ER 01, London, UK, IEA Coal Research, 40 pp (Apr 1978).
Smith I M (1982) Carbon dioxide - emissions and effects. ICTIS/TR 18, London, UK, IEA Coal Research, 132 pp (Jun 1982).
Smith I M (1988) CO_2 and climate change. IEACR/07, London, UK, IEA Coal Research, 52 pp (May 1988).
Smith I M, Thambimuthu K V, Clarke L B (1991) Greenhouse gases, abatement and control: the role of coal. Draft Report, London, UK, IEA Coal Research, 88 pp (Jan 1991).
Steinberg M, Grohse E (1990) Economical clean coal carbon fuel co-product gaseous and liquid fuel from coal. In: Processing and utilization of high-sulphur coals III. R Markuszewski, T D Wheelock (eds.). Amsterdam, The Netherlands, Elsevier Science Publishers B.V., pp 709-724 (1990).
Tans P P, Fung I Y, Takahashi T (1990) Observational constraints on the global atmospheric CO_2 budget. Science; 247 (4949); 1431-1438 (23 Mar 1990).
The Changing Atmosphere: Conference Statement Committee (1988) The changing atmosphere: implications for global security. In: The changing atmosphere conference. Toronto, Ontario, Canada, 27-30 Jun 1988, Downsview, Ontario, Canada, Environment Canada, pp 12 (1988).
Thurlow G (1990) Emissions of greenhouse gases. In: Proceedings of the conference on technological responses to the greenhouse effect. G Thurlow (ed.). London, UK, 24-25 Apr 1990, London, UK, Rooster Books, pp 16-24 (1990).
US Department of Energy (1990) A Fossil energy perspective on global climate change. DOE/FE-0164, Washington, DC, USA, US Department of Energy, 99 pp (Jan 1990).
Vernon J L (1990) Market mechanisms for pollution control: impacts on the coal industry. IEACR/27, London, UK, IEA Coal Research, 38 pp (Aug 1990).

Victor D G (1990) Calculating greenhouse budgets. Nature; 347 (6292); 410,431 (4 Oct 1990).
Watson R T, Rodhe H, Oeschger H, Siegenthaler U (1990) Greenhouse gases and aerosols. In: Climate change: the IPCC scientific assessment. J T Houghton G J Jenkins J J Ephraums (eds.). Cambridge, UK, Cambridge University Press, pp 1-40 (1990).
Weinzierl K (1990) New concepts for coal-fired power stations. VGB Kraftwerkstechnik; 70 (5); 333-339 (1990).
Wolsky A M, Brooks C (1989) Recovering CO_2 from large stationary combustors. In: IEA/OECD experts' seminar on energy technologies for reducing emissions of greenhouse gases. Paris, France, 12-14 Apr 1989, Paris, France, OECD\IEA, pp 179-185 (1989).
World Resources Institute (1990) World resources 1990-1991. New York, NY, USA, Oxford University Press, 383 pp (1990).
Zittel W, Selzer H (1990) Die Klimawirksamkeit von Methan (Impact of methane on climate). Erdöl Erdgas Kohle; 106 (9); 364-367 (Sep 1990).

Table 1 **Summary of estimates of CH_4 : CO_2 global warming potential**

Global warming potential CH_4 : CO_2 (molar)	Effective residence time, y		Allowing for indirect effects	Reference
	CO_2	CH_4		
27	(10)	10		
3.5	100	10	CO_2	(Selzer, 1989)
6	60	10	yes	(Pearman, 1989)
10	120	10	O_3, CO_2	(Rohde, 1990)
3.7	230	14.4	O_3, H_2O,	(Lashof and
12 (1% discount of future)	45		CO ≡ CO_2	Ahuja, 1990)
17 (20 y)*			O_3, H_2O,	(Shine and
5.7 (100 y)*	120	10	CO, NO_x,	others, 1990)
2.5 (500 y)*			NMHC	

* integration time horizons NMHC = non-methane hydrocarbons

Table 2 **Contributions to the greenhouse effect** (Boden and others, 1990; Shine and others, 1990; Watson and others, 1990)

	CO_2 emissions, 1988		Greenhouse effect, %	
	Gt C/y	%	over 1 y	over 100 y
Coal	2.4	37-28	21-16	23-17
Oil	2.4	37-28	21-16	23-17
Gas	0.9	14-11	8-6	9-7
Fossil fuel	5.7	88-68	50-38	54-41
Cement manufacture	0.2	2.3-1.8	1.3-1.0	1.4-1.1
Deforestation and land use	0.6-2.6	9-31	5-17	6-19
Total CO_2	6.5-8.5	100	56	61

Table 3 Summary of CO_2 abatement measures for power generation (Smith and others, 1991)

Technology	Steam conditions	Net power plant efficiency (LHV), %	CO_2 emissions, gC/kWhe	CO_2 reduction, %	Comments
Conventional					
PC + FGD	sub-critical	35	262.1	0	reference plant for CO_2 emissions
AFBC	sub-critical	37	257	1.95	in-bed desulphurisation, $deNO_x$
PC + FGD, $deNO_x$	supercritical (250 bar)	41.2	228.1	13	540-560°C, 0.065 bar condenser
PC + FGD, $deNO_x$	supercritical (300 bar)	45	209.4	20	600°C, 0.03 bar condenser
PC-natural gas cofiring	sub-critical	36-37.5	233.3-242.1	7.4-11	15% natural gas input
PC design - coal oil mixture	sub-critical	35	251.2	4.2	40% fuel oil input
PC-CO_2 flue recycle	sub-critical	27.6-28.6	325.9-337.5	(100)	energy use for air separation 187-220 kWhe/t CO_2, additional energy use for CO_2 gas disposal
PC design, H_2 combustion	sub-critical	8.4	-	(100)	energy use for H_2 separation 76% of coal heating value, additional energy use for carbon disposal
Combined cycles					
IGCC	sub-critical	43	212.7	18.9	low temperature gas cleaning
PFBC	sub-critical	42	226.7	13.5	high temperature gas cleaning
PFBC-gasification cycle	supercritical (250 bar)	48-49	195.6-199.5	23.9-25.4	high temperature gas cleaning
Pressurised pulverised coal	sub-critical	48	194.2	26	additional energy used for gas cleaning, CO_2 emissions from desulphurisation
PC-natural gas + FGD, $deNO_x$	sub-critical	40	202.1	22.1	33% natural gas input
PC-natural gas + FGD, $deNO_x$	supercritical (300 bar)	49	166.1	36.6	33% natural gas input
MHD	sub-critical	40-45*	192.5-216.5	17-27	additional CO_2 emissions from desulphurisation
Fuel cells	sub-critical	45-58*	147.1-192.5	26-44	additional CO_2 emissions from desulphurisation
Cogeneration					
Combined heat and power (CHP)	sub-critical	77-84	108.9-118.5	54-59	range for PC + FGD, PFBC, and PFBC-gasification cycle

* HHV

DEMONSTRATION PLANTS: ARE THEY NEEDED?

S. B. Alpert
PESC Division, Building 1
Electric Power Research Institute
Palo Alto, California 94303

Keywords: Demonstration of technology; Coal conversion systems for environmental control

INTRODUCTION

In the evolution of new technologies that demonstrate and challenge existing practice, the concept of a demonstration plant is used to bring the process of research, development and demonstration to conclusion. The incorporation of a demonstration plant in the strategy of realizing commercial application of a new technology was a new step introduced by the availability of support from federal agencies that provided the necessary funds required for large plant scale-up and sustained operation.

A. Commercial Plant Following Bench Scale or Pilot Plant Tests

In the chemical industry commercial plants are often constructed based on small scale (less than 1 ton/day) continuous pilot plant trials where there is a large incentive to realize commercial production of a product that is produced at lower cost or that has improved quality over competing routes. Often the commercial plant is built based on kinetic and yield information from limited pilot plant data (10-50 lbs/day).

In these instances homogeneous phase systems are scaled up to commercial sized plants. Engineering usually does not represent a significant change from existing practice that is in existence. Examples of new technology usually include improvements in reactor design (contacting) and/or in catalyst formulation, representing the primary new steps being proven or modified. Adjustments and plant modifications are made at the time of commercial plant "breakin" and startup. An extra allowance is provided for the "first of a kind" commercial plant which usually is 5-25% of the capital cost of the plant. The advantage of this approach is rapid commercial application that takes advantage of an economic incentive that is significantly large.

B. Modification of An Existing Commercial Plant

In some cases an existing commercial plant can be modified to incorporate new features of a technology. For example, an improved high capacity gasifier may easily be incorporated into an existing coal gasification

commercial plant. This strategy is often used to avoid the cost of installing the raw materials receiving, feed preparation, and product recovery steps which may be relatively unchanged and that may need no modification. Thus, a new technology such as a high capacity reactor can be demonstrated at relatively modest cost at an existing commercial plant. The new gasifier may represent 10-15% of the total capital requirements.

Projects that are demonstrating sorbent absorption of sulfur dioxide in the hot gas path of an existing power plant are examples of this approach. In the petroleum industry new more selective or aging resistant catalysts are incorporated into an existing plant. This approach is usually a low cost approach to bring a new technological advance to commercial realization.

C. Utilization of Large Pilot Plant

For the situation where there is a change in phase a step wise series of continuous bench scale and pilot plants are used to:

(1) provide scientific information on kinetics, selectivity, product characteristics, yields, etc. Often this information is emperical. The chemistry and mechanisms are not very well understood.

(2) provide engineering data on equipment size requirements, maintenance, materials information, engineering design and safety data, and design of special equipment and subsystems. Catalyst life data are defined based on sustained "steady state" operations performed.

On the basis of the continuous pilot plant trials at increased capacity scale up uncertainties are also defined. In the largest pilot plants operated the smallest commercial size equipment from vendors are used to minimize risk of equipment scale up at a pioneer commercial plant. Table 1 shows the features of a pioneer commercial plant. It should be noted that an integrated program requires various size pilot plants to be operated simultaneously. Thus, the program often requires small and large pilot plants to be operated on feed materials used in a commercial plant. The objective of the integrated program is to obtain the engineering equipment design data and yield and product quality information that permits the pioneer plant to be constructed with ordinary financial risk. Trained operations personnel from the large pilot plant serve as a cadre of experience specialists for the pioneer plant.

D. Demonstration Plant

In the development of new technology in which solid feeds (coal or shale) are converted the concept of a Demonstration Plant has been introduced. It usually represents a single full scale train (1000-5000 Tons/day) of a

TABLE 1.
Pioneer Plant Objectives

- Commercial pretested equipment used to prove the technology in full scale module.
- Establish firm basis for investment, operating procedures, costs of commercial plants.
- Establish permitting procedure for plant, transportation of product, utilization by customers
- Complete testing, and handling procedures and health effects in markets
- Ability to expand pioneer plant to full sized commercial plant.

commercial plant that represents an engineering proof of the information from large pilot plants (100-500 tons/day). An important aspect of such plants is the culmination as a technical spectacular.

Such spectaculars, which challenge existing practice, represent step outs that are important "first of a kind" culminations concluding research that may have taken 10 years or more to accomplish. Being first is always an exciting challenge for scientists and engineers.

A demonstration plant has many purposes and objectives including the challenge of using expert knowledge and organizing and managing the skills necessary to achieve technical innovations. Recent demonstration plant experience that featured solid feeds to (coal and shale) indicates that a minimum of 3 years and more appropriately 5 years or more of operations are required to obtain robust information on maintainability and reliability from a utility industry perspective.

Table 2 shows the features of a demonstration plant and its objectives. For a conservative industry like the electric power industry, that must be prudent and is not used to accepting significant financial risk, the added comfort of robust cost, design, reliability and maintenance practice information is an important aspect favoring demonstration plants that represent technological innovations for generating electricity.

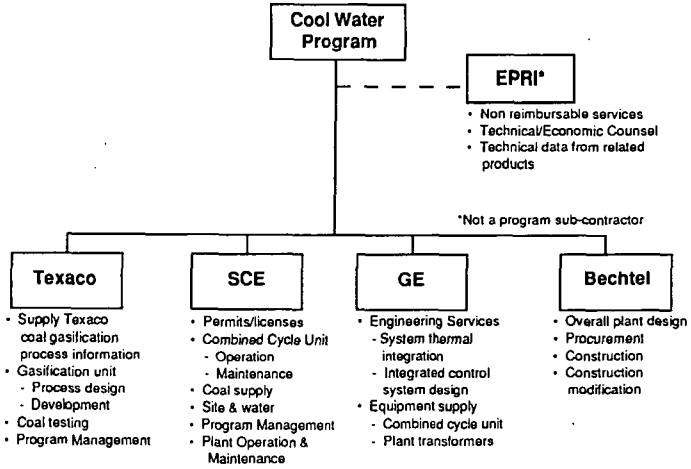

FIGURE 1. Responsibilities of Program Participants

TABLE 2.

Objectives of Demonstration Plant

- Save time to commercial production of products, introduction of new technology
- Complete engineering development from small equipment
- Confirm scaleup parameters, establish sources of commercial equipment
- Operate integrated flow sheet, obtain operating experience, confirm design
- Confirm economics of commercial plant and expand demonstration plant if warranted
- Produce large samples of products for test by customers

While the cost for a demonstration plant is high, new technology acceptance will depend on their outcome. The learnings from demonstration plants guarantee efficient smooth start up and operation of subsequent commercial plants that can reliably proceed with low financial risk.

While there are many advantages for a demonstration plant a major shortcoming is its cost. In the case of the Cool Water program about $300 million was required to build and achieve reliable operations over the course of the 5 year operating program.

Figure 1 shows the responsibilities that were defined for each of the major participants that supplied funds for the Cool Water Program. At the conclusion of the program the demonstration plant was shut down. It is imperative to carefully define the scope of each organizations responsibility at the programs inception.

E. The Cool Water Program

Figure 2 shows a block diagram of the Cool Water plant.

Cool Water is a nominal 120-MW IGCC power plant that uses the Texaco Coal Gasification Process to produce a medium-Btu fuel gas. The gas is combusted in the combined cycle portion of the plant to produce electricity. The plant is designed to process up to 1000 tons of coal per day mixed with water, however, rates as high as 1200 tons per day were achieved. The coal-water slurry is gasified with oxygen at a pressure of approximately 600 psig and a temperature of between 2100 °F and 2500 °F. The raw syngas from the gasifier is first cooled in radiant and convective coolers that generates steam for use in

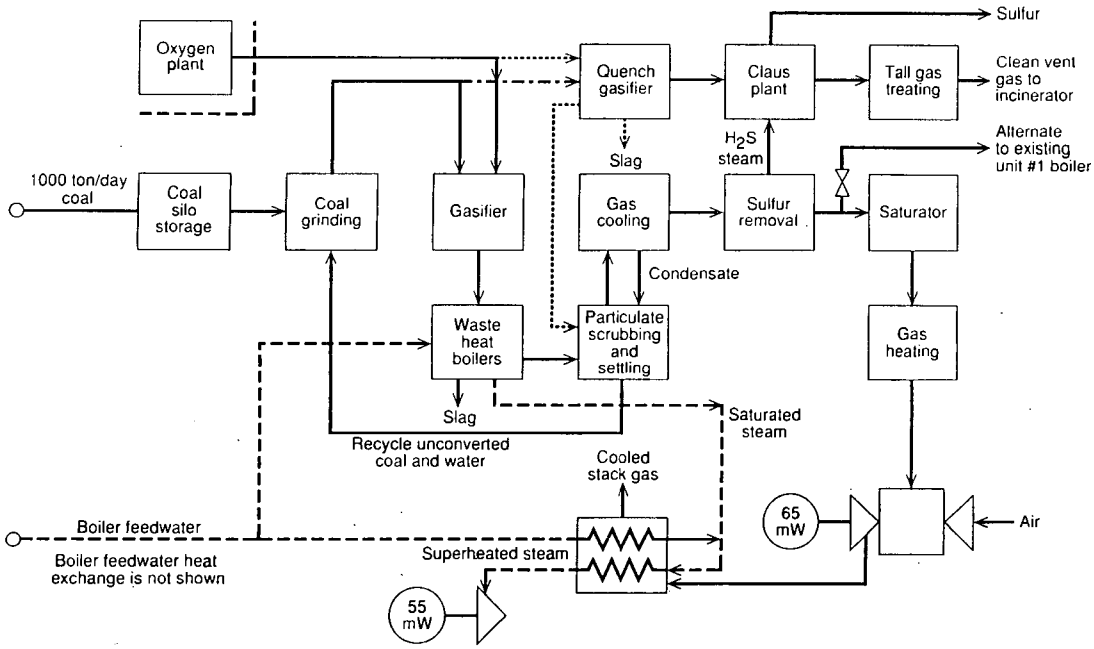

FIGURE 2. Block Flow Diagram of the Cool Water Coal Gasification Plant

power production. The slag solidifies during its fall through the radiant cooler and collects in a water sump at the bottom of the cooler, where it is removed periodically using a lockhopper system.

After leaving the radiant and convective syngas exchangers, the cooled synthesis gas enters a water scrubber where any entrained particulate is removed. After the scrubber, low level heat is recovered from the gas in a series of exchangers, and then air and cooling water trim coolers reduce the gas temperature to appoximately 100 °F. Next, sulfur is removed, primarily in the form of hydrogen sulfide, in a Selexol absorber. A sulfur-rich acid gas is stripped from the Selexol solution and routed through a SCOT/Claus sulfur recovery unit to produce an elemental sulfur product. Following sulfur removal, water is added to the desulfurized gas in a syngas saturator to suppress NO_x formation during combustion.

Subsequently the synthesis gas is fired in a GE MS7001E gas turbine to produce electricity. The exhaust gas from the combustion turbine passes through a Heat Recovery Steam Generator (HRSG) where saturated steam formed in the syngas coolers, and in the middle section of the HRSG, is superheated. After superheating, the steam is utilized in a steam turbine for additional electricity production.

F. Definition of Incentives

The Coolwater Program was started in the late 1970's. A major incentive was the control of emissions of an IGCC plant compared to a pulverized coal plant as shown in figure 3. Demonstration of these environmental features was considered an important incentive for the project.

In addition economic analyses showed that electricity from IGCC plants would be cost competitive with conventional coal plants and offer higher efficiency routes to electric power.

At the time of the start of the program oil an gas prices were expected to escalate in real terms. By the last year of the operating period economic dispatch of the facility on the Southern California Edison Co. system was projected. Projections of oil prices of $40 a barrel or higher were expected.

At the conclusion of the program the plant was not competitive with low cost natural gas in conventional generation plants that produce electric power at a cost of about 3-4¢/Kw-hr, or about 50% of the cost of electricity from the Cool Water plant.

Environmental Trade-offs for Coal-Based Technologies

Flue gas desulfurization (FGD) units and fluidized-bed combustion—both atmospheric (AFBC) and pressurized (PFBC)—have been effective in reducing emissions of SO_2 and NO_x from coal-fired plants, but at the cost of producing substantial volumes of solid waste. Gasification-based generation options (IGCC, IGHAT, and IGMCFC) have the potential to cut those airborne emissions further and minimize solid waste without imposing an efficiency penalty on the overall system.

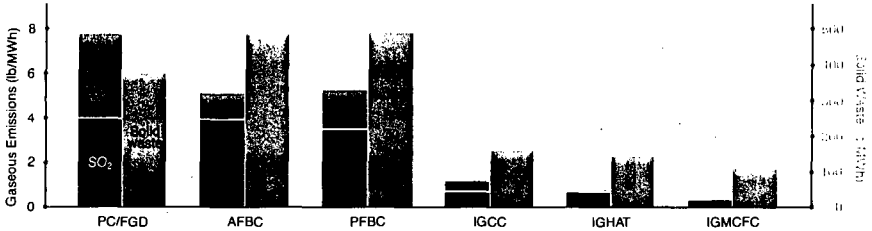

FIGURE 3. Environmental Trade-offs for Coal-Based Technologies

Table 3 shows a summary of the results from the Cool Water program which represented the "know how" produced

TABLE 3.
Major Information From
Demonstration Plants

Management

- Firm basis for capital and operating costs
- Firm basis for plant performance as base load or load following
- Definition of management structure
- Plant reliability as a variable for design
- System integration and performance
- Environmental data for commercial plant licensing

Technical

- Design and equipment requirements
- Performance of equipment from sustained operations on a variety of coals
- Comprehensive information on materials of construction, components, subsystems
- Comprehensive details on environmental impacts and equipment alternatives
- Health and safety information
- Staffing requirements
- Training of future users of the technology, simulator

CONCLUSIONS

Currently a large number of demonstration projects are being performed in the U.S. with funding from federal and private sponsors. The Cool Water Program was a technical success in that all of its objectives were met or exceeded during the 5 year operating period. It's major achievement was to launch a new technological option for the world wide electricity industry--the IGCC plant- which is a clean use of coal.

Of prime importance is agreement by the sponsors on its, objectives and participation by organizations who take the information forward to commercial projects that follow.

MODELING OF CATALYTIC COUPLING OF METHANE

Lucy M. Hair, William J. Pitz, Michael W. Droege and Charles K. Westbrook
Lawrence Livermore National Laboratory
P.O. Box 808 Livermore, CA 94551

Keywords: oxidative coupling of methane, chemical kinetic model, catalysis modeling

Catalytic oxidative coupling to ethane or ethylene is an appealing, direct route to utilization of otherwise low value natural gas located in remote sites. Researchers have focused on oxidative coupling of methane for about 15 years, using metal oxide catalysts to facilitate the reaction (*1-6*). Despite intensive efforts, the best yields to C2 hydrocarbons have been in the 20 to 30 % range, generally accomplished with catalysts which include an alkali metal on an alkali earth oxide, e.g., Li/MgO (*6b*).

In an attempt to understand and overcome the source of this limitation, more fundamental catalyst studies and modeling have been undertaken. Labinger and Ott (*7*) measured kinetic rate constants and modeled the catalytic process for ARCO's oxidative coupling catalyst, achieving good agreement with reactor data. Labinger in a further analysis (*8*) based on their model found that the C2 yield is limited to 30% by sequential oxidation of ethylene as methane conversion increases. Kimble and Kolts were also able to model the catalytic-homogeneous process for their system (*9*).

The importance of the thermally-induced, homogeneous, gas-phase reactions cannot be neglected in any such model. Much of the recent work in oxidative coupling has explicitly recognized the fact that under most conditions, thermally-induced reactions account for a large fraction of products (*10-14*). In previous work (*15-16*), we employed a chemical kinetic model (HCT), developed at this Laboratory, to describe the overall homogeneous gas phase reactions of methane and oxygen. The HCT model can be used to describe reaction pathways and determine products for a wide variety of reactor types and conditions. Its application successfully predicted methane conversions and product distributions found experimentally for a reactor containing no catalyst. In this work, we expand the HCT model to include proposed catalytic reaction schemes. Our purpose is to predict limits in C2 yield, describe product trends as a function of generalized catalyst behavior and use these results as a guide to catalyst design.

Gas-Phase Model

The gas-phase chemical kinetic model used in the present study is the HCT (Hydrodynamics, Chemical kinetics and Transport) model (*17*). This model solves the coupled equations of conservation of mass, momentum and energy in finite difference form, and determines each chemical species concentration. For this study, the reactor is assumed to be essentially a plug flow system where spatial variations in velocity, temperature and species concentrations in the radial direction and diffusion of energy and species in the axial direction are assumed to be negligible. Spatial changes in species concentration and temperature can therefore be replaced by time variations. Thus only the energy equation and the species conservation equations must be solved. Surface reactions at the reactor wall were not considered. In the numerical model, coupling between the different chemical species takes place through the chemical kinetic terms, and these terms are introduced into the model through a detailed reaction mechanism.

The chemical reaction mechanism used here has developed from a number of studies of methane

and natural gas combustion. This mechanism has been extensively validated in a series of studies where numerical results were compared to experimental results from static reactors, stirred reactors, shock tubes, flames and flow reactors (*18-22*).

Inclusion of Catalytic Methane Activation

A schematic of the mechanistic pathways leading to the gas-phase oxidation of methane by oxygen is shown in Fig. 1. We have added reactions to the chemical kinetic mechanism to treat the effect of introducing a catalyst. It is generally assumed that the effectiveness of oxidative coupling catalysts stems from their ability to activate methane. Thus, the first step was to determine the effect of methane activation alone. Considerable experimental evidence suggests that the catalyst activates methane by abstracting a hydrogen (*2,4,6a,i,7,9,11,23,24*). We have modeled this process as the global step,

$$CH_4 + 1/4\ O_2 \rightarrow CH_3 + 1/2\ H_2O \qquad (1).$$

We assumed the reaction rate is given by the expression,

$$R_1 = k_1\ [CH_4][O_2]^a \qquad (2).$$

The dependence of the rate on $[O_2]^a$ serves to turn off the catalytic reaction when the gas phase oxygen is depleted. An exponent "a" of 1.0 serves this purpose satisfactorily, since we do not know the series of elementary reactions. Computationally, it appears that the overall reaction is not critically dependent on the value of the "a" exponent.

. A series of calculations were performed with the above "catalytic" reaction added to the gas-phase chemical kinetic mechanism in order to explore the effect of catalyst activity (k_1) on predicted C_2 yield. The conditions considered were a 2:1 molar ratio of CH_4:O_2 in a 75% Ar mixture. The reactor temperature and pressure were maintained at a constant 750 C and 1 atm, resp. The curve in Fig. 2 shows the results of these calculations, where the residence time for the upper curve was optimized for maximum yield and the residence time for the lower curve was 10 s. The methane conversion and product distributions are shown in Table 1. It is predicted that for k_1 equal to $10^7\ M^{-1}s^{-1}$, the maximum C_2 yield is 84%. When no catalyst is present, the gas-phase reactions result in a C_2 yield of about 0.4% under these conditions of high dilution. The calculations indicate that the catalyst does not substantially affect the yield until the catalytic methane activation rate constant reaches about 10^1. The C_2 yield reaches about 70% for a methane activation rate constant of 10^7. This yield would certainly be adequate to justify production; obviously, either catalysts do not achieve such a high rate constant or they perform another function, such as oxidation.

Although the gas-phase reactions in the absence of catalyst yield only 0.4% C_2's, once the catalyst has generated the methyl radical, it is available for any further reactions. At a sufficiently high level of catalyst activity, the high concentration of methyl radicals will drive the coupling reaction in preference to oxidation steps. Then at short residence times, the catalytic methane activation and gas-phase coupling steps will be sufficient to predict products. Thus it is of interest to know the relative contribution of gas-phase vs catalytic reactions to the overall conversion of methane. To determine these relative contributions, we integrated over time the rates of methane conversion due to the catalyst and to gas-phase reactions for values of k_1 of 10^3, 10^4 and 10^5. These results are shown in Fig. 3. As expected, the catalyst contributes virtually all of the methane conversion at early times until a sufficient radical pool is established for gas-phase reactions. A steady state conversion is reached by about 7 s, 0.3 s and 0.06 s for k_1 of 10^3, 10^4 and 10^5, resp. At steady state, 20%, 50% and 70% of the methane is converted due to catalytic action for values of k_1 equal to 10^3, 10^4 and 10^5, resp. The

catalyst dominates methane conversion for values of the methane activation rate constant greater than 10^4.

Now we investigate the effect of moving away from our optimized residence time. The methane conversion and product distributions corresponding to the predicted maximum C_2 yields for values of k_1 of 10^2 to 10^5 are shown in Table 1. The methane conversion increases from 23.3 to 53.7%, while the selectivity to C_2's increases from 44.5 to 67.1%. The major increase in C_2's is due to an increase in ethane from 18.7 to 41.6%. The residence times which result in maximum C_2 yields decrease from 3.4 to 0.03 s as k_1 increases from 10^2 to 10^5. Since the gas-phase coupling reaction to form ethane is rapid relative to dehydrogenation to ethylene, at shorter residence times, one would expect a higher ethane/ethylene split. The calculated methane conversion and product distributions at 10s residence time, displayed in Table 2, show that this is indeed true. At longer residence times, the C_2 yield decreases slowly, the methane conversion increases, and the C_2 selectivity decreases along with selectivity to ethane. Regardless of residence time, carbon monoxide accounts for the majority of COX products.

Comparison of Model Predictions with Experimental Data

Values of k_1 and the corresponding C_2 yield for catalysts known to be effective in oxidative coupling of methane (*6b-h*) and run under similar conditions to those run for the model are also shown in Fig. 2. In calculating k_1 from literature data, it was assumed that the rate of methyl radical production was equal to the rate of methane conversion and was, therefore, determined from the experimental methane feed rate and the final methane conversion. The rate constant k_1 was then found by dividing that rate by the methane and oxygen concentrations in the feed at reaction temperature. As shown in Fig. 2, the fit of model predictions to rate constants calculated from experimental results is quite good. The values of k_1 that we determined range from 10^2 to 10^5, corresponding to measured C_2 yields of 3-20%, while the model predicts C_2 yields increasing from 8-35%. The methane activation rate constants for these coupling catalysts are too low to achieve the high C2 yields possible from our model calculations. Even the more active catalysts do not give C2 yields of 35%, as the model predicts. In fact, for methane activation rate constants of 10^3 and greater, the experimental C2 yield is fairly flat as a function of catalyst activity. Table 3 shows a selection of data for coupling catalysts (*6b-d*). The fit of the model to C_2 yield, methane conversion and selectivity to C_2's is quite reasonable, matching best at model residence times slightly greater than those optimized for C_2 yield. In a few cases, the predicted ethane/ethylene split is very close to literature values, and fairly good for the others.

The model does not predict carbon dioxide as the only oxidation product, as is seen in the data. It seems likely that the carbon dioxide is produced directly by a catalytic route, bypassing the gas-phase reactions that would lead from ethylene to carbon monoxide. Such a catalytic process could also explain the cap on C_2 yield observed for the coupling catalysts.

Summary

Overall, this simple modification of the gas-phase kinetic model to include a global catalytic step that only produces methyl radicals agrees reasonably well with experimental data. The model predicts that a methane activation catalyst with a sufficiently high rate constant, which performed no other function, could result in a C_2 yield of at least 70%. The high methane activation rate constant is needed

to overcome gas-phase oxidation reactions. The highest methane activation rate constant determined from experimental data was on the order of 10^5 $M^{-1}s^{-1}$, corresponding to a predicted C_2 yield of 35%, but actually yielding only about 20%. A catalytic reaction leading from ethylene to carbon dioxide could account both for the lowered yield and for the absence of carbon monoxide in experimental work.

References

1. Pitchai, R.; Klier, K. **Catal.Rev.Sci.Eng. 1986**, 28, 13.
2. Lee, J.S.; Oyama, S.T. **Catal.Rev.Sci.Eng. 1988**, 30, 249.
3. Hutchings, G.J.; Scurrell, M.S.; Woodhouse, J.R. **Chem.Soc.Rev. 1989**, 18, 251.
4. Lunsford, J.H. **Catal.Today 1990**, 6(3), 235.
5. Garibyan, T.A.; Margolis, L.Y. **Catal.Rev.Sci.Eng. 1989-1990**, 31, 355.
6. a). Keller, G.E.; Bhasin, M.M. **J.Catal. 1982**, 73, 9.
   b). Ito, T.; Lunsford, J.H. **Nature 1985**, 314, 721.
   c). Otsuka, K.; Liu, Q.; Morikawa, A., **Inorg.Chim.Acta 1986**, 118, L23.
   d). Machida, K.I.; Enyo, M. **J.Chem.Soc., Chem.Commun. 1987**, 1639.
   e). France, J.E.; Shamsi, A.; Ahsan, M.Q. **Energy & Fuels 1988**, 2, 235.
   f). Matsuura, I.; Utsumi, Y.; Nakai, M. Doi, T. **Chem.Lett. 1986**, 1981.
   g). Otsuka, K.; Komatsu, T. **J.Chem.Soc.,Chem.Commun. 1987**, 388..
   h). Aika, K.; Moriyama, T.; Takasaki, N. Iwamatsu, E. **J.Chem.Soc., Chem.Commun. 1986**, 1210.
   i). Sofranko, J.A.; Leonard, J.J.; Jones, C.A. **J.Catal. 1987**, 103, 302.
   j). Thomas, J.M.; Kuan, X.; Stachurski, J. **J.Chem.Soc., Chem.Commun. 1988**, 162.
   k). Korf, S.J.; Roos, J.A.; Derksen, J.W.H.C.; Vreeman, J.A.; Van Ommen, J.G.; Ross, J.R.H. **Appl.Catal. 1990**, 59, 291.
   l). Ahmed, S.; Moffat, J.B. **J.Catal. 1990**, 125, 54.
   m). Agarwal, S.K.; Migone, R.A.; Marcelin, G. **J.Catal. 1990**, 121, 110.
   n). Choudhary, V.R.; Chaudhari, S.T.; Rajput, A.M.; Rane, V.H. **J.Chem.Soc.,Chem.Commun. 1989**, 1526.
7. Labinger, J.A.; Ott, K.C. **J.Phys.Chem. 1987**, 91, 2682.
8. Labinger, J.A., **Cat.Lett. 1988** 1, 371.
9. Kimble, J.B.; Kolts, J.H. **Energy Prog. 1986**, 6 (4), 226.
10. Lane, G.S.; Wolf, E.E. **J.Catal. 1988**, 113, 144.
11. Zanthoff,H.; Baerns, M. **Ind.Eng.Chem.Res. 1990**, 29, 2.
12. Yates, D.J.C.; Zlotin, N.E. **J.Catal. 1988**, 111, 317.
13. Nelson, P.F.; Cant, N.W. **J.Phys.Chem. 1990**, 94, 3756.
14. Ekstrom, A.; Lapszewicz, J.A.; Campbell, I. **Appl.Catal. 1989**, 56, L29.
15. Droege, M.W.; Hair, L.M.; Pitz, W.J.; Westbrook, C.K. Lawrence LIvermore National Laboratory Report **UCRL-100568 1989.**
16. Droege, M.W.; Hair, L.M.; Pitz, W.J.; Westbrook, C.K. in **Proc. 1989 SPE Gas Tech. Symp. 1989**, Dallas, TX., p. 247.
17. Lund, C.M. University of California Lawrence Livermore National Laboratory Report **UCRL-52504. 1978** Revised by Lila Chase, 1989.

18. Westbrook, C.K.; Pitz, W.J. **Combust.Sci.Technol. 1984**, 37, 117.
19. Westbrook, C.K.; Creighton, J.; Lund, C.; Dryer, F. **J.Phys.Chem. 1977**, 81, 2542.
20. Westbrook, C.K. **Combust.Sci.Technol. 1979**, 20, 5.
21. Wilk, R.D.; Cernansky, N.P.; Pitz, W.J.; Westbrook, C.K. **Combustion Flame 1989**, 77, 145
22. Pitz, W.J.; Westbrook, C.K.; Proscia, W.M.; Dryer, F.L. **Twentieth Symposium (International) on Combustion**, The Combustion Institute: Pittsburgh, 1985, p.831.
23. Driscoll, D.J.; Martin, W.; Wang, J.-X.; Lunsford, J.H. **J.Am.Chem.Soc. 1985**, 107, 58.
24. Mims, C.A.; Hall, R.B.; Rose, K.D.; Myers, G.R. **Catal.Lett. 1989**, 2, 361.

Table 1
Predictions of Model at Maximum C2 Yield

k1 ($M^{-1}s^{-1}$)	Max %C2 Yld	%CH4 Conv	%C2	%C2H4	%C2H6	%CO	%CO2
10^2	10.4	23.3	44.5	25.8	18.7	51.5	3.1
10^3	15.8	25.0	63.2	32.2	31.0	34.8	0.9
10^4	24.7	35.1	70.2	33.4	36.8	28.2	0.5
10^5	35.1	52.3	67.1	25.5	41.6	14.6	0.1

Table 2
Predictions of Model at 10s Residence Time

k1 ($M^{-1}s^{-1}$)	%C2 Yld	%CH4 Conv	%C2	%C2H4	%C2H6	%CO	%CO2
10^2	7.5	46.4	16.1	13.2	2.9	71.9	11.6
10^3	11.0	51.3	21.5	19.0	2.5	71.0	6.9
10^4	17.9	57.3	31.3	27.5	3.8	64.6	3.1
10^5	30.6	67.5	45.5	39.4	6.1	52.1	1.1

Table 3
Experimental Results from Literature

Ref	%C2 Yield	%CH4 Conv	%C2	%C2H4	%C2H6	%CO	%CO2
6b	19.0	37.8	50.5	31.0	19.5	0.0	49.6
	19.4	42.8	45.5	29.0	16.5	0.8	53.7
6c[i]	18.6	25.9	71.8	56.2	15.6	-.-	-.-
6c[ii]	13.2	25.8	51.3	23.4	27.9	-.-	-.-
6d	31.8	45.1	60.1	36.1	24.0	0.0	39.9

6b. 7%Li/MgO, 4g: 720 C, 2:1 CH_4:O_2, 89% He Diln.
6c. (i) 20 mol% LiCl/NiO (ii) 20 mol%LiOH/NiO: 750 C, CH_4:O_2 2:1, 94% He diln., 1 g cat.
6d. SrCeYbO, 0.6 g: 750 C, CH_4:O_2 2:1, 80% diln with He.

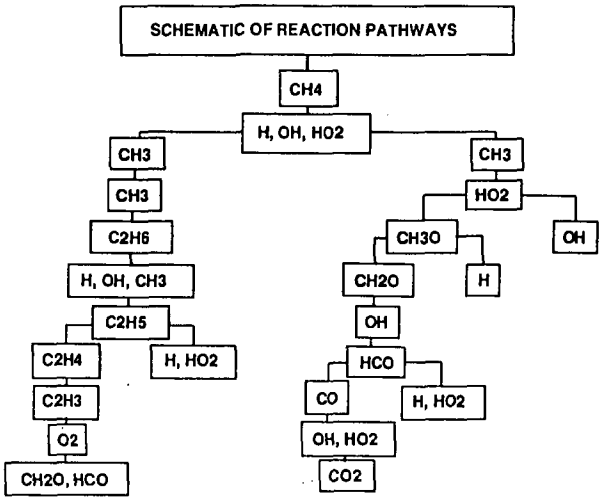

Figure 1. Schematic of gas-phase mechanism for methane oxidation.

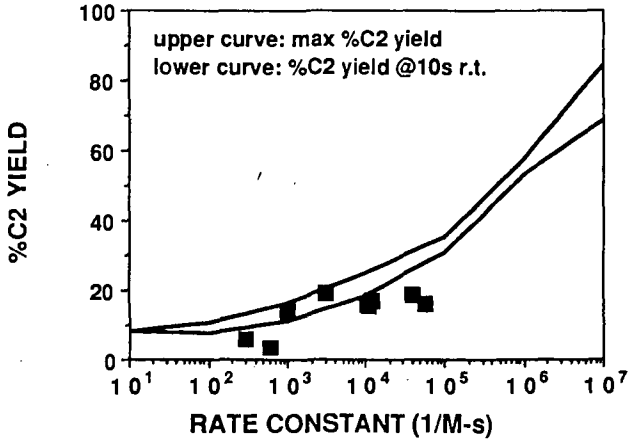

Figure 2. Predicted and experimental C_2 yields as a function of catalytic methane activation rate constant, k_1. Conditions: 750 C, 2:1 CH_4:O_2, 75% Ar dilution.

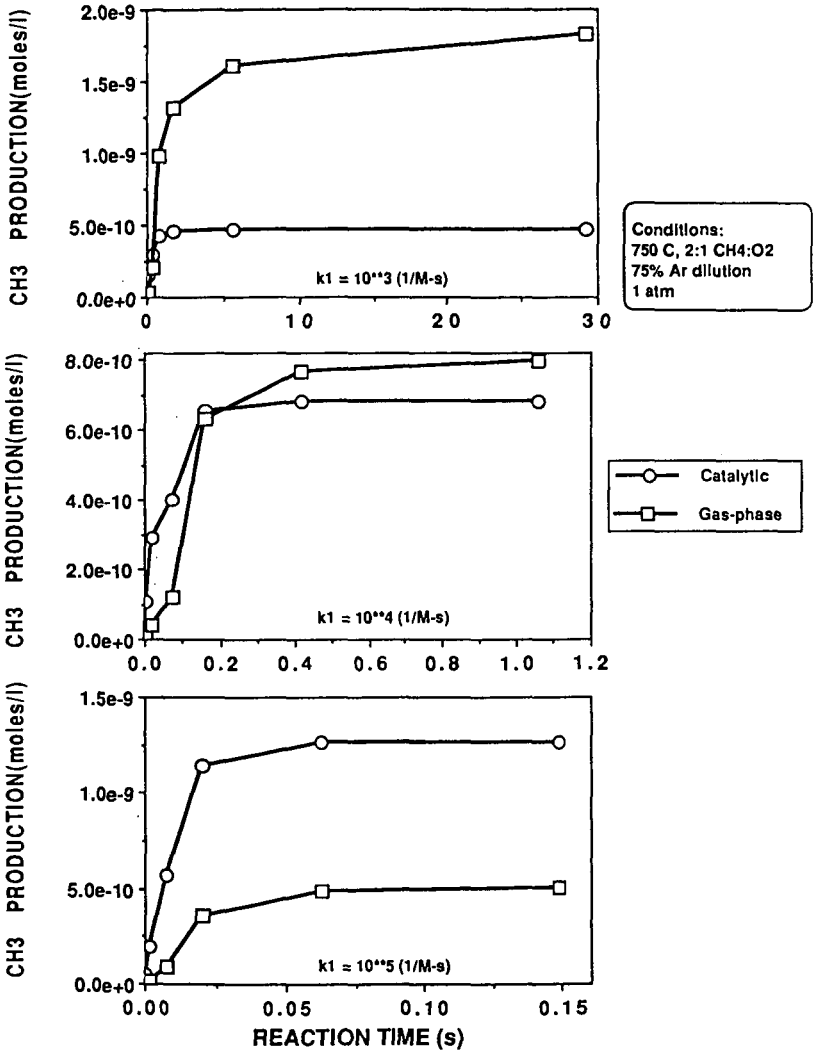

Figure 3. Comparison of methyl production due to catalytic and gas-phase reactions. a) $k_1=10^3$. b) $k_1=10^4$. c) $k_1=10^5$. Units=$M^{-1}s^{-1}$.

SYMPOSIUM ON COMPUTER APPLICATIONS IN FUEL CHEMISTRY
PRESENTED BEFORE THE DIVISION OF FUEL CHEMISTRY
AMERICAN CHEMICAL SOCIETY
ACS INTERNATIONAL MEETING, ATLANTA, GA
APRIL 14-19, 1991

AN ASSESSMENT OF THE PREDICTIVE CAPABILITIES OF A COMPUTATIONAL MODEL FOR FUEL THERMAL STABILITY

Jeffrey A. Pearce, K. V. Reddy, and W. M. Roquemore
Aero Propulsion and Power Directorate
Wright Laboratory
Wright-Patterson AFB, OH 45433

Keywords: Fuel Thermal Stability, Modeling, Computational Fluid Dynamics

INTRODUCTION

The thermal stability of jet fuels is one of the major impediments facing the aerospace community in attempting to increase aircraft performance. Fuel is widely used as a coolant for critical on-board systems, and the thermal loads on the fuel resulting from this practice are steadily increasing. If this trend continues, the thermal stability limit of the fuel will soon be reached and the cooling capacity of current fuels would be exhausted. Restrictions on design parameters, particularly the maximum allowable fuel temperature, will soon be a key limiting factor in attempts to improve overall performance. Ideally, one desires a fuel which remains stable at extreme temperatures (> 1000° F), but realistically any tangible improvement in fuel stability would be welcomed. However, after decades of study, little is known of the fundamental processes leading to the deposition of solid materials on fuel system components largely due to the complexity of the processes involved, which include fuel degradation chemistry, heat transfer, and fluid mechanics.

Recent research has focused on the possibility of modeling fuel thermal stability using Computational Fluid Dynamics (CFD) with a global chemistry model. This approach allows one to examine different hypotheses about deposition mechanisms with relative speed and great flexibility. An essential element in the development of these models regards the formulation of the degradation chemistry. Typical fuels are extremely complex mixtures of hydrocarbons; therefore, attempting to model the specific reactions which contribute to deposition would be a nearly impossible chore. However, global representations of the degradation chemistry are a simple and often effective alternative to applying the full detailed chemistry.

To date, modeling efforts have focused on simulating heated tube experiments using simple, global autooxidation chemistry models[1,2]. These models have performed adequately in predicting the results of other heated tube experiments; however, their ability to predict the results of experiments with significantly different boundary conditions is questionable. Such an experiment has recently been performed at Purdue University[3] in an effort to examine the relative effects of wall and bulk fuel temperature on the deposition process. This experiment features conditions which vary greatly from those encountered in typical heated tube experiments; consequently, this experiment offers a unique vehicle with which to test and improve the current formulation of the models.

The purpose of this paper is to examine the predictive capabilities of a particular thermal stability model. This examination includes addressing the model's ability to predict the results of two basic classes of experiments: (1) constant heat flux heated tube experiments, similar to the experiments from which the model was devised and (2) constant wall temperature experiments. The results of these predictions yield valuable insights into the model's capabilities and indicate areas for possible improvement.

THERMAL STABILITY MODEL

Argonne National Laboratory/Air Force (ANL/AF) Model

The particular model applied in this study was developed by the Argonne National Laboratory in conjunction with the Air Force[1,2]. The intent of this model is to provide the capability to predict

deposition within a given fuel system component. Ultimately, related models will be employed to minimize the ill effects of fuel degradation on various fuel system components. However, it is important to note that the model is in a developmental stage and is not yet suitable for general, widespread use as a design tool.

The approach to predicting deposition with the model is based on a two-dimensional computational fluid dynamics (CFD) code. This approach offers great generality in that given the wall condition (temperature/heat flux), tube geometry, and inlet conditions (velocity and temperature) the code can predict the overall solution of the flow field including the wall and bulk fuel temperatures, pressure, radial and axial velocity components, and constituent concentrations (O_2, precursor, deposit) throughout the domain. By applying the CFD approach, the inherent coupling which exists between the chemistry, heat transfer, and fluid mechanics is preserved.

The essence of modeling fuel thermal stability lies in the degradation chemistry, which for this model is subdivided into two portions: (1) reactions occurring in the bulk fuel and (2) reactions occurring at the wall. In the bulk fuel, the following reactions apply:

$$\text{fuel} + O_2 \xrightarrow{k_1} \text{precursor} \tag{1}$$

$$\text{fuel} + \text{precursor} \xrightarrow{k_2} \text{fuel} + \text{soluble product} \tag{2}$$

where Equation 1 represents the formation of deposit precursors in the bulk fuel and Equation 2 represents the destruction of precursors at high temperatures. It is assumed that any precursor reaching the solid surface by means of diffusive and convective transport immediately forms a solid deposit on the wall. The remainder of the chemistry is a reaction at the wall whereby deposits are formed directly in the following manner:

$$\text{fuel} + O_2 \xrightarrow{k_3} \text{deposit} \tag{3}$$

The specific reaction rates for Equations 1-3 are based on Arrhenius expressions such as Equation 4 below:

$$k_n = A_n \exp(-E_n/RT) \tag{4}$$

Note that Equations 1 and 2 are based on the local *fuel* temperature while Equation 3 is based on the *wall* temperature.

After exercising the code, it becomes apparent that the deposition from the wall autooxidation reaction, represented by Equation 3, is only a small fraction of the overall deposition predicted with this model for cases where the temperature exceeds 475 K. Nonetheless, the low activation energy used for the wall autooxidation reaction (E_3 = 8 kcal/mole) provides a small amount of deposit on the tube walls when the wall temperature is close to room temperature. Since the bulk reactions tend to dominate the deposition process at higher temperatures, it is the bulk fuel temperature along with the dissolved oxygen concentration that are the primary drivers of fuel degradation in this code. Regarding the formation of deposits on the solid wall, which is the eventual product of the calculation, there are two mechanisms by which this occurs : (1) precursors formed in the bulk fuel (Equation 1) can reach the wall by diffusive and convective transport to form deposits and (2) deposits can be formed directly on the wall by Equation 3.

The values of the constants for the activation energies (E_n) and pre-exponential factors (A_n) were determined from experimental data[4,5,6]. These experiments, described below, consisted of flowing JP-5 over an electrically heated tube (constant heat flux) and measuring the deposition accumulated on the tube surface. The oxygen concentration at the tube inlet was taken to be the saturation value of approximately 55 ppm by weight. Values for A_n and E_n can be found in Table 1.

EXPERIMENTS MODELED

Three different experimental test cases were examined using the model described above. Two of these experiments are constant heat flux heated tube experiments which have obvious similarities. The third experiment, however, offers a challenge to the model in that the boundary conditions are quite

different than the heated tube experiments used to calibrate the model. This third experiment is a device developed at Purdue University[3] to examine the relative effects of wall and bulk fuel temperature on the observed deposition.

Heated Tube Experiments

The heated tube experiment is a widely used tool in the study of fuel thermal stability. In these experiments, fuel (initially at ambient temperature) is passed through a cylindrical metal tube which is heated by electrical resistance to thermally stress the fuel. Deposits accumulate on the tube as a result of the thermal stressing, and the deposit mass is measured to determine the degree of degradation. Some characteristics of this test are that a constant heat flux is applied to the fuel as a result of the electrical resistance heating method, and both the bulk fuel and wall temperatures increase at a roughly linear rate over the length of the tube. Data from two sets of heated tube experiments were used for model evaluations in this effort: (1) data from Marteney and Spadaccini[4,5,6] which was used to calibrate the chemical constants in the ANL/AF model, and (2) data from Giovanetti and Szetela[7,8] from similar heated tube experiments using Jet-A fuel. For both data sets the fuel was air sparged and no fuel was recirculated.

Purdue Copper Block Test

Juxtaposed against the heated tube experiments which are typical in thermal stability research, the Copper Block Test developed at Purdue[3] is markedly different. Many differences between this experiment and the heated tube experiments are clearly apparent. Chief among these differences is the manner in which the two experiments endeavor to stress the fuel. In the heated tube experiments, a constant heat flux is applied to the fuel which results in linearly increasing profiles of fuel and wall temperature along the length of the tube. The Purdue test features JP-8 flowing through a cylindrical metal tube which is embedded between two heated copper blocks. The high thermal conductivity of the copper results in a nearly constant tube wall temperature which implies a decreasing heat flux with length as bulk temperature increases. Additional features of the experiment include preheating of the fuel to temperatures (> 500 K) which are in the regime of significant fuel degradation. However, there are other subtle differences that can have a profound effect on the experimental results.

The Purdue test lacks much of the oxygen available in the heated tube experiments as the fuel is recirculated (approximately 4-5 passes through the tube in a 6 hour test) and is not air/oxygen sparged. In fact, further reduction in the fuel's oxygen content results from the practice of maintaining a N_2 overpressure on the fuel in the accumulator. Nonetheless, perhaps the most significant difference between the two experiments is the magnitude of the temperatures in the experiments. In general, the maximum temperature in the heated tube experiments is in the vicinity of 650 K, where the Purdue test reaches temperatures of 750 K. This difference in the maximum temperature could possibly account for a change in the deposition mechanism from oxidative to pyrolytic. In all, it would appear that this test bears little resemblance to the test employed to calibrate the model.

This claim is substantiated by the findings of the researchers at Purdue. In examining deposition data from their experiment against the data of Tevelde and Glickstein[9] (from another constant heat flux heated tube experiment) they found that there was a large discrepancy between the results. Figure 1 shows this discrepancy where the Purdue data appear to show the deposition rate increasing steadily with wall temperature while the Tevelde and Glickstein data clearly show the deposition rate peaking at ~ 650 K and decreasing at higher temperatures. It is our belief that a properly devised model should be able to predict both data sets accurately, and that the differences observed are merely due to the differences in the experimental methodology. Fortunately, these observed differences offer the opportunity to examine some capabilities and shortcomings of the current model formulation.

RESULTS

Predictions of Heated Tube Data

The initial task in terms of exercising the model was to calibrate the chemical constants (A_n and E_n). This was done by modeling the heated tube experiments of Marteney and Spadaccini[4,5,6] carefully tuning the chemical reaction constants (Table 1). In the calibration experiments, JP-5 fuel is driven through a long, thin long metal tube (0.237 cm ID × 2.4 m length) at a velocity of 2.1 m/s while the tube is being heated with a constant electrical power source. The high inlet fuel velocity makes the entire

flow in the tube turbulent; therefore, turbulent flow simulations have been used to predict the deposition rates under these flow conditions. Figure 2 demonstrates that the calibrated ANL/AF model does an extremely good job of representing the experimental data. In particular, the agreement between the model and the data are extremely good in the region between 500-600 K. Note the change in the slope of the curve at ~ 500 K representing the point at which the reaction in the bulk fuel begins to dominate the wall reaction. As a whole, the model is quite capable of accurately representing the data from which it was calibrated.

Figure 3 shows the model's prediction of the experiments of Giovanetti and Szetela[7,8]. One can clearly see that the model predicts the experimental data with reasonable accuracy. There is a wide scatter in the data (greater than an order of magnitude) in the region below 500 K, so it is difficult to say whether the model is representative of the data in this temperature range. However, in the region between 500-560 K, the model yields very good results and follows the sharp rise in the deposition rate. Other key features of the deposition curve are also accurately predicted; in particular, the value of the maximum deposition rate and the temperature at which it occurs are both well represented. Furthermore, the sharp decrease in the deposition rate following the peak value is also well represented by the model. The general accuracy of the model in predicting these data is encouraging, since these are not the experiments used to calibrate the model. Nonetheless, one must consider the basic similarities between the experiments modeled in Figure 3 and the experiments used to calibrate the model. All are constant heat flux heated tube experiments utilizing similar fuels (JP-5 and Jet-A) in nearly identical geometries. Quantities such as the heat flux and the mass flow rate do differ, but the experiments are exceedingly similar. Consequently, the high quality of the model predictions for these cases does not guarantee the model's predictive capabilities.

Predictions of Purdue Data

The initial calculations performed to model the Purdue experiment were done with the model in its calibrated form, and the results are provided in Figure 4. For reference, these calculations were carried out for an inlet fuel temperature of 523 K with the constant wall temperature varied between calculations. One can immediately see that the ANL/AF model fails to represent the experimental data accurately, for it overpredicts the deposition rate at low temperatures while underpredicting the deposition rate at higher temperatures. Annoyingly, the predicted deposition rate starts falling at a wall temperature of ~ 625 K whereas the experimental data indicate a monotonically increasing deposition rate with temperature. These inaccuracies in the prediction can be justified when examining some particulars of the model.

Recall that one of the differences between the calibration experiments and the Purdue experiment dealt with air sparging. While the calibration experiments were constantly supplied with fresh fuel that had been air sparged, the Purdue experiment had no mechanism to saturate the fuel with oxygen. In fact, the Purdue test configuration tends to remove oxygen from the fuel due to the N_2 overpressure on the fuel. Furthermore, since the fuel was recirculated in the Purdue test, the oxygen content in the fuel would decrease steadily with time. Therefore, one can assume that by using the saturation value of oxygen in the model that the model predictions would overemphasize the oxidative deposition in the region below 600 K. This point is clearly demonstrated in Figure 4 where the model overpredicts the deposition rate for temperatures below 600 K.

The drop in the deposition rate at higher temperatures arises from a very different aspect of the model. Recall that two reactions occur in the bulk fuel; one to form precursors in the oxidative regime and one to eliminate precursors at high temperatures. When the temperature is sufficiently high (> 650 K), the precursor destruction reaction (Equation 2) begins to dominate the precursor formation reaction. The result of this is a steadily decreasing contribution to the wall deposition rate from the reactions in the bulk fuel. Eventually, only the wall reaction contributes to the deposition, and as the oxygen is depleted this reaction will also fail to produce appreciable deposits. Therefore, the model in its calibrated form will predict little deposition at high temperatures and no deposition at very high temperatures.

These two shortcomings of the model give rise to a new approach to simulating the Purdue data. The first step being to decrease the oxygen concentration input to the model to match the low temperature deposition data, since in this region the deposition is primarily oxidative. This change is substantiated by the difference in oxygenation of the fuel between the heated tube experiments and the Purdue Copper Block Test. The second step was to derive an additional chemistry expression to simulate a non-oxidative deposition mode that functions primarily at high temperatures. Substantiation for this change arises from a belief that the deposition mechanism changes from autooxidation to pyrolysis at ~ 700 K. This reaction provides a mechanism for deposit formation when the oxidative processes are exhausted.

The results of reducing the inlet oxygen content are given in Figure 4. It was found that an inlet oxygen concentration of 10 ppm by weight (20% of the saturation value) was required to match the low temperature (~ 570 K) deposition data. The final step in the modification of the model was to devise an additional chemistry expression to simulate deposition at high temperatures. The chosen mechanism took the following form:

$$\text{fuel} \xrightarrow{k_4} \text{deposit particle} \tag{5}$$

This reaction represents the formation of deposit particles in the bulk fuel which contribute to the wall deposition only if diffusive and convective transport carry the particles to the wall. This reaction augments the chemistry found in Equations 1-3.

Figure 5 shows the results obtained using the modified model which is a clear improvement over its unmodified counterpart shown in Figure 4. Though the results from the modified ANL/AF model are not exceptionally good, the prediction does manage to capture the essential character of the data which indicate an increasing deposition rate with increasing wall temperature. The magnitude of the deposition rate is also reasonably accurate over a large portion of the temperature range. However, one notes that the data appears to turn downward slightly at higher temperatures while the prediction clearly turns upward. This may well indicate some error in the formulation of the chemistry which is quite likely due to the extremely simple, global nature of the chemistry model.

CONCLUSIONS

The results presented here have focused on attempts to apply a computational model for thermal stability to conditions beyond those for which it was calibrated. Attempts to model experiments which were similar to the model's calibration experiment were very successful; however, deviation from the heated tube experiments to other conditions were not met with immediate success. To reasonably predict the results of the Purdue experiment, modifications to the model input and the model itself had to be made. Clearly this indicates that errors existed in the formulation of the degradation chemistry prior to its modification. Furthermore, even after modifications were made to the model with the specific purpose of better predicting the Purdue experiment, flaws were evident in the prediction.

Unfortunately, the complexity of fuel composition precludes the modeling of the individual chemical reactions leading to degradation. This point is moot, however, since these reactions are not known. The representation of the global degradation chemistry employed by the model is both extremely simple and likely in error. Experimentation is the key to making improvements to such models by pursuing a process of continually evaluating and improving the model. Ultimate success in this endeavor will lead to models which can aid in the future design of fuel system components with minimal deleterious effects from deposition.

NOMENCLATURE

A_n	pre-exponential constant	t	time
E_n	activation energy	T	temperature
k_n	rate constant	[ ]	denotes concentration
R	universal gas constant		

REFERENCES

1. Krazinski, J. L. and Vanka, S. P. (1989), "Development of a Mathematical Model for the Thermal Decomposition of Aviation Fuels," Argonne National Laboratory, WRDC-TR-89-2138.
2. Krazinski, J. L., Vanka, S. P., Pearce, J. A., and Roquemore, W. M. (1990), "A Computational Fluid Dynamics and Chemistry Model for Jet Fuel Thermal Stability," ASME Paper 90-GT-33.
3. Chin, J. S. and Lefebvre, A. H. (1990), "Temperature Effects on Fuel Thermal Stability," Draft copy, to be presented at the 36th ASME International Gas Turbine Conference, June 3-6, 1991.
4. Marteney, P. J. and Spadaccini, L. J. (1984), "Thermal Decomposition of Aircraft Fuel," United Technologies Research Center, NAPC-PE-143C.
5. Marteney, P. J. and Spadaccini, L. J. (1986), "Thermal Decomposition of Aircraft Fuel," *Journal of Engineering for Gas Turbines and Power 108*, pp. 648-653.

6. Marteney, P. J. (1989), "Thermal Decomposition of JP-5 During Long Duration Tests," United Technologies Research Center, NAPC-PE-201C.
7. Giovanetti, A. J. and Szetela, E. J. (1985), "Long Term Deposit Formation in Aviation Turbine Fuel at Elevated Temperature," United Technologies Research Center, NASA CR-179579.
8. Giovanetti, A. J. and Szetela, E. J. (1986), "Long Term Deposit Formation in Aviation Turbine Fuel at Elevated Temperature," AIAA-86-0525.
9. Tevelde, J. A. and Glickstein, M. R. (1983), "Heat Transfer and Thermal Stability of Alternative Aircraft Fuels," United Technologies Research Center, NAPC-PE-87C, Vols. I and II.

TABLE 1: Constants in the Thermal Stability Model

Index, n	Activation Energy, E_n (kcal/mole)	Pre-exponential Constant, A_n
1	30	1.0×10^{14} cm^3/mole$\cdot$ s
2	35	3.0×10^{15} s^{-1}
3	8	4.0×10^{1} cm^4/mole$\cdot$ s
4	40	1.0×10^{10} s^{-1}

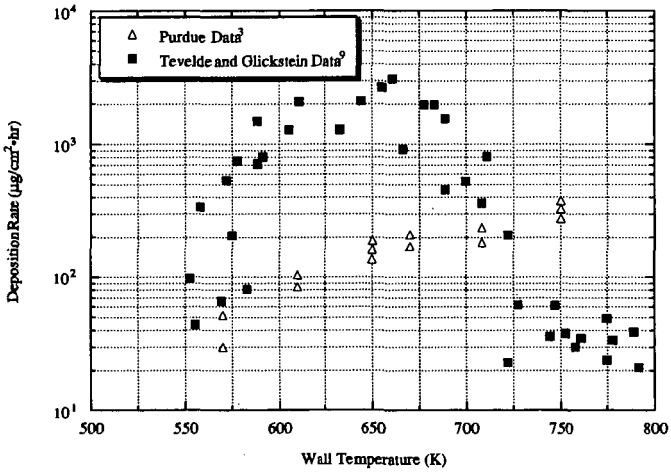

FIGURE 1: Discrepancy in the Results of Purdue and Tevelde and Glickstein

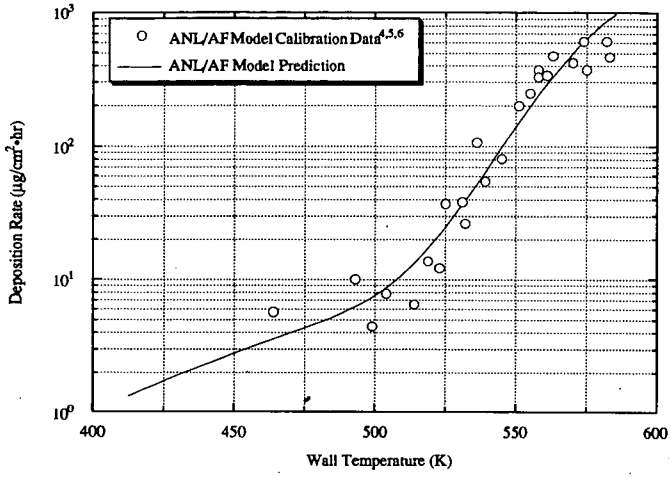

FIGURE 2: Calibration of the ANL/AF Model

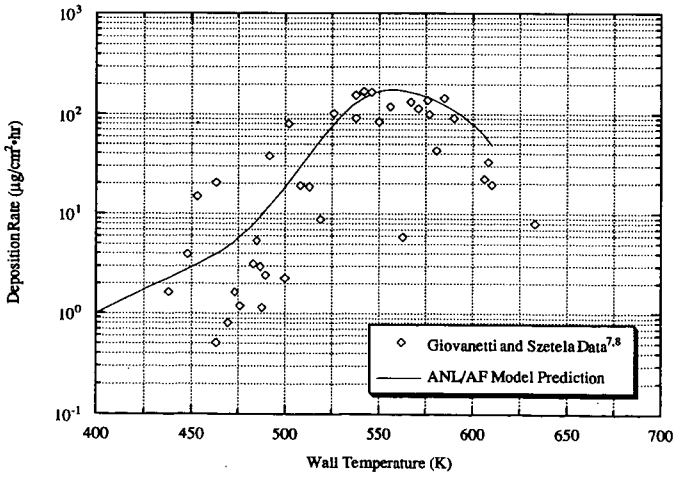

FIGURE 3: Model Calculations of Heated Tube Data

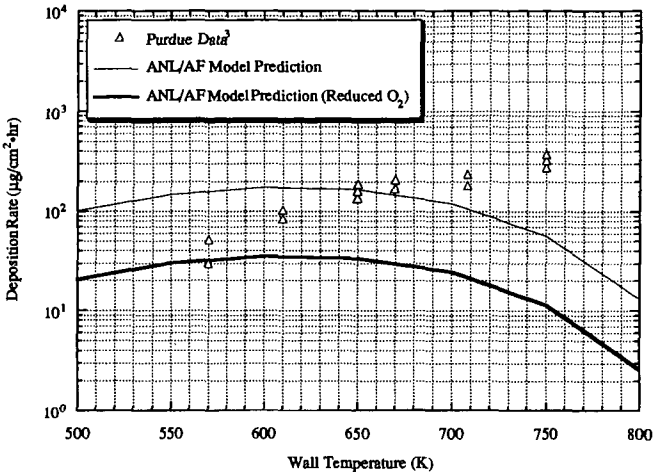

FIGURE 4: Initial Attempts to Model Purdue Copper Block Test

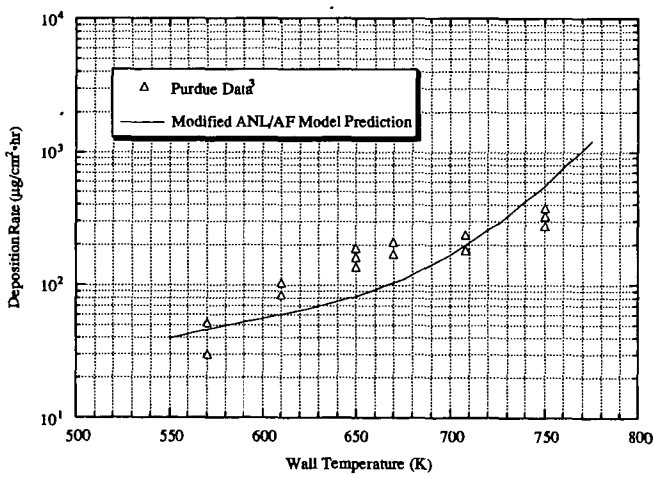

FIGURE 5: Attempts to Predict Purdue Test with Modified Degradation Chemistry

FRACTAL ANALYSIS OF FUEL MOLECULES IN THE BULK LIQUID PHASE

Dennis H. Rouvray
Department of Chemistry
University of Georgia
Athens, Georgia 30602

ABSTRACT

The topological structure and boiling point of individual fuel molecules provide sufficient information for determination of their respective fractal dimensionalities in the bulk liquid phase. Molecules considered need to be members of well-defined series such as homologous series. Our fractal analysis yields a time-averaged molecular conformation for each species. The results are used to estimate the flexibility of each species in the bulk liquid phase. The presence of heteroatoms or multiple bonds in the species can produce marked effects which are alluded to in our conclusion. The present analysis elucidates the behavior of molecules in the liquid phase and sheds useful light on the physicochemical properties of many different types of fuel molecules.

Keywords: Fuel Molecules, Fractal Analysis, Molecular Behavior of Hydrocarbons

INTRODUCTION

Dwindling crude oil supplies and the many uncertainties in world oil markets render it imperative to conserve our oil resources and to utilize them as efficiently as possible. With this in mind, the method introduced here is intended to contribute to the optimal use of fuel molecules. This goal can be accomplished only after the behavior of fuel molecules at the molecular level has been thoroughly elucidated. We show here how it is possible to gain valuable insights into the average conformation of fuel molecules and analyze the factors determining these conformations. In addition, we estimate the flexibility of individual molecules in the bulk liquid phase. All this is achieved by making use of no more than the topological structures of the species under study and their experimentally measured boiling points. Although we focus here on straight-chain hydrocarbon molecules, our methodology can be readily extended to more complex species.

Our approach, originally introduced in 1986 by Rouvray and Pandey [1,2] has recently been employed in the study of species containing heteroatoms [3]. Key to the approach is the description of hydrocarbon and other chains as fractal objects; for a discussion of such objects and appropriate terminology, readers should consult standard texts [4,5]. The fractal dimensionality of each molecular chain can be related to its time-averaged comformation in the bulk liquid phase and then used to estimate the molecular flexibility. A brief mathematical exposition of the salient features of our approach now follows.

MATHEMATICAL FORMALISM

We adopt as a convenient measure for the shape of molecular chains the mean-squared end-to-end length of the species. A molecule M will satisfy a proportionality of the general type:

$$r \propto n^q, \tag{1}$$

where n is the number of atoms in the backbone of the chain, and q is typically some fractional number. An equivalent formulation in terms of the fractal dimensionality of M can also be given thus:

$$r \propto m^{1/d_f}, \tag{2}$$

Because the physicochemical properties of molecules are known [6] to depend on their time-averaged conformation in the bulk phase, we may write for some property P_i of the molecule M_i the following relationships:

$$P_i \propto r_i \propto m_i^{1/d_{f_i}}. \tag{3}$$

Now, if P_i is plotted against n, or some other scalar numerical description such as a topological index [6,7], the plot can be characterized by the proportionality:

$$P_i \propto T_i^{b_i}, \tag{4}$$

where T_i is the descriptor for M_i and b_i is a constant determined from the slope of the curve at T_i. From relations (3) and (4) we can conclude that:

$$m_i^{1/d_{f_i}} \propto T_i^{b_i} \tag{5}$$

The use of scaling arguments at this point, similar to those adopted by de Gennes [8], yields the final result:

$$\frac{b_1}{b_2} = \frac{d_{f_2}}{d_{f_1}} \tag{6}$$

for two molecules M_1 and M_2 in a given series.

RESULTS AND DISCUSSION

For simplicity, we choose for the P_i the boiling points of members of normal alkane species and for T_i the carbon number in the chain. Relevant plots on linear and logarithmic scales are shown in Figures 1 and 2 respectively. The fractal dimensionalities are obtained from the b_1/b_2 ratios by making use of the logarithmic plot; the actual values can be read off from the plot in Figure 3. Because the fractal dimensionalities provide a measure of the distribution of mass with distance [4,5], they can be used as measures of the time-averaged conformation of the species they characterize. Fractal dimensionalities for chain-like molecules all lie within the range $1 \leq d_f \leq 2$, with unity corresponding to a totally rigid chain. As values of d_f become progressively greater than unity they reflect the extent of folding up of the chain. Thus, for the C_1, C_{10}, C_{20}, and C_{30} chains, the respective d_f values are 1.00, 1.18, 1.43 and 1.69.

The d_f values determined from our analysis can be employed to yield an estimate of the flexibility of each of the species in the bulk liquid phase. Our estimate is given as the product of the number of bonds in the chain, n_i-1, and the reciprocal of the mean-squared end-to-end length of the chain, i.e.

$$F_i = (n_1-1)/r_i. \qquad (7)$$

Values for F_i can be determined for any chain containing n_i atoms from our relation (3) above as follows:

$$r_i \propto m_i^{1/d_{f_i}} \propto (n_i m_C)^{1/d_{f_i}} \qquad (8)$$

where m_C is the mass of the carbon atom (C=12). Substitution of appropriate values for the C_2, C_{10}, C_{20}, and C_{30} chains leads to flexibility values of 0.042, 0.156, 0.412 and 0.900 respectively. On this measure of flexibility therefore, the C_{30} chain is roughly 21.5 times more flexible than the C_2 chain.

Our results are in accord with calculations on long alkane and other chains. Flory and Yoon [9] showed that the average shape of polyethylene chains containing 10 or more bonds may be visualized as ellipsoids. Very recent work by Erman et al. [10] has confirmed this picture and presented estimates of chain stiffness that are in broad agreement with the results presented here. Moreover, the effects of heteroatoms in the chain have been studied by us [3] as have the consequences of introducing multiple bonds into the chain. It is known that both the substitution of atoms heavier than carbon and the introduction of multiple bonds into the chain will result in a loss of flexibility or a stiffening of the chain in general [3]. This is only to be expected from the form of the expression we have used, namely relationship (7), for the computation of the chain flexibilities. Clearly, our analysis sheds much useful light on the interactions occurring at the molecular level in the bulk liquid phase. It is hoped that similar analyses in the future can be adapted for the design and optimization of fuel molecules.

REFERENCES

[1]. D. H. Rouvray and R. B. Pandey, J. Chem. Phys. 85, 2286 (1986).
[2]. D. H. Rouvray, in Graph Theory and Topology in Chemistry, ed. R. B. King and D. H. Rouvray (Elsevier, Amsterdam, 1987), p. 17.
[3]. D. H. Rouvray and H. Kumazaki, J. Math. Chem. in press.
[4]. B. B. Mandelbrot, The Fractal Geometry of Nature (Freeman, San Francisco, 1982).
[5]. P. Pietronero and E. Tossati, eds, Fractals in Physics (North Holland, Amsterdam, 1986).
[6]. J. K. Labanowski, I. Motoc and R. A. Dammkoehler, Computers Chem. 15, 47 (1991).
[7]. D. H. Rouvray, Scientific Am. 255, 40 (1986).
[8]. P.-G. de Gennes, Scaling Concepts in Polymer Physics (Cornell University, Ithaca, New York, 1979).
[9]. D. Y. Yoon and P. J. Flory, J. Chem. Phys. 61, 5366 (1974).
[10]. B. Erman, I. Bahar, A. Kloczkowski and J. E. Mark, Macromolecules 23, 5335 (1990).

FIGURES

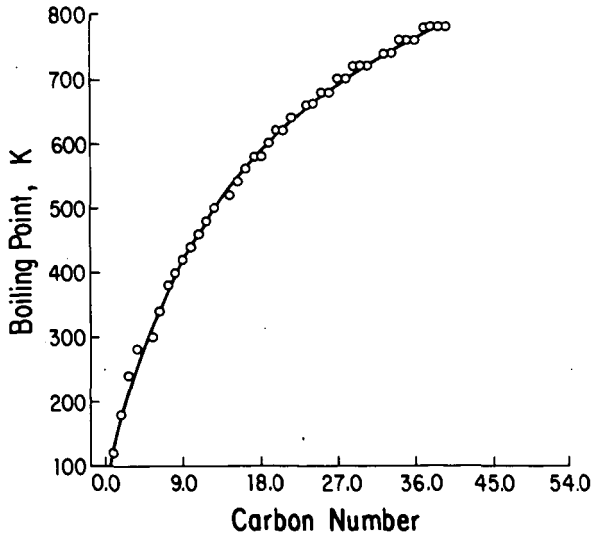

Figure 1. Plot of boiling point against carbon number on linear scales for the first forty normal alkanes.

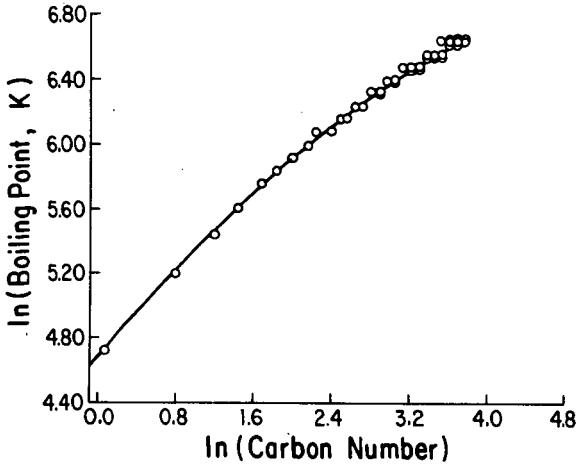

Figure 2. Plot of boiling point against carbon number on logarithmic scales for the first forty normal alkanes.

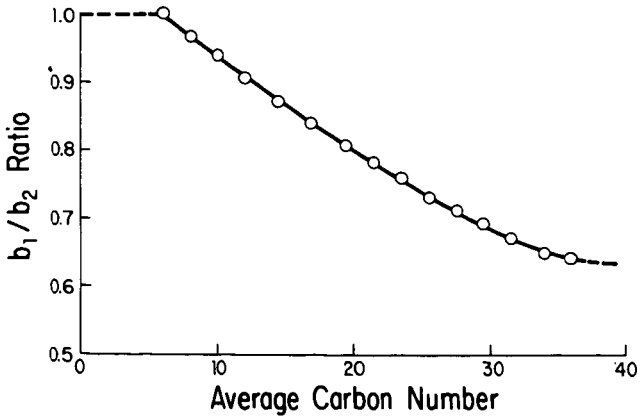

Figure 3. Plot of the b_1/b_2 ratio against carbon number on linear scales for the first forty normal alkanes.

DEVELOPMENT OF A MOLECULAR MECHANICS FORCE FIELD FOR CLAYS
I. STRUCTURE AND IR SPECTRUM OF KAOLINITE

Alan G. Stellpflug, John B. Nicholas, Kathleen A. Carrado,
Glenn L. Keldsen, and Randall E. Winans
Chemistry Division, Building 200
Argonne National Laboratory
Argonne, IL 60439

Keywords: Molecular Mechanics, Force Field, Clays, Kaolinite

INTRODUCTION

The use of layered inorganic silicate clays as catalysts remains technologically vital to industry[1]. It is therefore important to understand the chemistry involved with these compounds. Comprehension of the structure and dynamics of the material, how other ions and molecules interact with the clay, and the reaction mechanisms involved in the catalysis process are all critical issues. Molecular modeling techniques, encompassing energy minimization or molecular mechanics[2], normal mode analysis, molecular dynamics, and computer graphics, is a valuable tool for examination of these properties.

The purpose of this work was to apply molecular modeling techniques to the study of silicate clays to determine their structure and dynamics. Previous studies of related materials[3,4,5] suggested that the results obtained would be of sufficient accuracy to compare to experiment. In addition, more accurate, *ab initio* calculations on such large molecules are nearly impossible at the present time, even on large supercomputers.

THEORETICAL METHODS

Atomic Coordinates

Our modeling efforts begin with kaolinite, an important and common clay mineral from the Kaolin or Kandite group[6]. This class of minerals is made up of a single Si(Al, Fe)-O tetrahedral sheet linked to a single Al(Mg, Fe)-OH octahedral sheet in regular succession, as displayed in Figure 1. As such, these clays are also called 1:1 minerals.

Atomic coordinates were taken from Young and Hewat's Rietvield refinement[7] of both X-ray and neutron powder diffraction data. This refinement was chosen because Young and Hewat measured the most crystalline material available and gave definitive positions for the inner-hydroxyl hydrogen atoms. A space group of P1 was used for this refinement and the resulting cell parameters appear in Table I. The reported values, which were used for this model, must however be viewed with some caution, since aspects[7,8,9] about the actual space group and cell parameters are still being questioned, sixty years after the idealized structure was proposed by Pauling[10]. The major argument about the structure seems to be whether or not the hydrogen atom positions of the inner-hydroxyls are c-face centered. The reason for many of these disputes is that available crystals of kaolinite have not been sufficiently large or coherent enough to allow good single crystal analysis[11].

Peak assignments for comparison to the theoretical infrared (IR) spectrum of kaolinite were taken from a compendium of data on layered materials[12]. Several infrared spectra for kaolinite from different parts of the world and of different purities are contained in this source. To remain consistent with Young and Hewat[7], who used kaolinite from Keokuk, Iowa, the IR spectrum of the Keokuk kaolinite was used.

Simulation

The simulation system was formed by several replications of the unit cell. A 4x2x3 arrangement giving a cell containing 816 atoms and having the dimensions 19.89Å x 17.86Å x 22.16Å was used for the molecular dynamics calculations. Periodic boundary conditions were used to simulate the effects of an infinite lattice framework. The non-bonded interatomic interactions were evaluated for all atoms within a cut-off radius of 8.93Å.

Non-bonded Lennard-Jones and electrostatic interactions were not calculated for atoms that were bonded (1-2 interactions) or for atoms that were involved in a bond angle (1-3 interactions), because these are accounted

for by the bond stretch and bond angle bend potentials. The method of conjugate gradients[13] was used for the energy minimization routines. The molecular dynamics calculations were done using the "leap-frog" algorithm[14] to integrate the equations of motion.

Force Field

Molecular modeling techniques that are based on classical mechanics require a force field to describe inter- and intra-molecular interactions. The force field used in this work is represented by the sum of potential energy terms:

$$V = V_s + V_\Theta + V_{nb}$$

where V_s is the potential caused by bonds stretching from their equilibrium positions, V_Θ is the potential related to the bending of bond angles from their equilibrium positions, and V_{nd} is the potential associated with non-bonding interactions.

Force parameters used in the potential energy terms can be calculated several ways. Quantum mechanical calculations on small molecules that mimic the clay structure can be used to determine force constants, equilibrium geometries, and charge densities. Fitting the force parameters to existing experimental data, such as IR frequencies and crystal structures, is possible and was used to help define some of the force field parameters in this work. The equilibrium values can also be varied over a small range and plotted versus the difference in potential energies of the original structure and its minimized counter-part. This method was also used for some of the force parameters in this work.

The bond stretch potentials in the force field were based on a simple harmonic potential:

$$V(r) = (K_r/2)(r-r_{eq})^2$$

where r is the interatomic distance between atoms, r_{eq} is the equilibrium bond length and K_r is the bond stretching force parameter.

Bond angle bends were also modeled after a simple harmonic potential:

$$V(\Theta) = (K_\Theta/2)(\Theta-\Theta_{eq})^2$$

where Θ is the bond angle bend, Θ_{eq} is the equilibrium bond angle and K_Θ is the bond angle bend force constant.

The non-bonded interactions considered were of two types. The first was the Lennard-Jones 6-12 potential

$$V(r) = B/r^{12} - A/r^6$$

where A and B are Lennard-Jones parameters taken from the MM2[15] force field. The second non-bonded interaction accounted for was that of electrostatic interactions. These were modeled by a Coulomb potential:

$$V(r) = q_i q_r/\epsilon r$$

where q_i and q_j represent the charges of the atoms and ϵ is the dielectric constant. The electrostatic forces are of longer range and can be more important than the Lennard-Jones terms.

RESULTS AND DISCUSSION

An important test for the accuracy of any force field is its ability to reproduce the experimental crystal structure. Energy minimizations were performed starting with the reported crystal structure of kaolinite. The final structure after minimization was then compared to the original structure using both computer graphics and root mean square (RMS) differences (Table II) for each atomic coordinate. In Figure 2 it can be seen that the minimized geometries are very close to that of the original structure, especially for the heavier silicon and aluminum atoms. The oxygen and hydrogen atoms, which are expected to have greater freedom of movement in the actual compound, account for the major differences between the theoretical and actual crystal coordinates. It is interesting to note that the inner-hydroxyl hydrogens in the minimized structure have assumed a c-centered positioning (pointing in the same direction), which deviate from the original coordinates where they point towards

different layers in the clay. However, this may be caused by the absence of a hydrogen bonding potential in the force field. If this potential is added it may cause the hydroxyl hydrogens to point towards the tetrahedral silicon layer.

Another check for the accuracy of the model force field is the force field's ability to predict the infrared spectrum. This can be done in two ways. Normal mode analysis can be used to determine the frequencies of the vibrations of the molecule. A theoretical infrared spectrum can also be calculated from molecular dynamics. This is done by taking the Fourier transform of the total dipole correlation function[16] calculated from the molecular dynamics trajectory. The intensities obtained by either method are, however, strictly qualitative because the quantum corrections needed to give accurate intensities are impractical for such a large system. The force parameters and equilibrium values used in the theoretical force field are summarized in Table III.

The theoretical and experimental[12] infrared spectra for kaolinite are compared in Figure 3. Very good correlation is found in the 14 to 24 micron region of the spectrum. According to both the literature[17] and to the normal mode calculations carried out on the model structure, the peaks at 19 and 21.5 microns are due to the Si-O bond stretch. The fact that the experimental and theoretical peaks match well indicate that the Si-O parameters are correct. The experimental peak at 14.5 microns is due to the Si-O-Al bond angle bend[17], however, the theoretical peak is at a slightly lower energy value (16 microns). The 8 to 13 micron range of the theoretical spectrum does not clearly exhibit all the major peaks in the experimental IR spectrum, but tentative assignments can be made. The Si-O bond stretch at 9.0 microns is calculated to occur at 8.5 microns and the theoretical peak at 10.2 microns is believed to correspond to the experimental peak at 9.9 microns. This peak, along with the band at 14.5 microns, may be due to the Si-O-Al bond angle vibration. Additional molecular dynamics calculations are being performed to adjust the force constants to acheive agreement with experiment in the 8 to 10 micron region.

CONCLUSION

A force field for the clay kaolinite has been developed that gives good results both for reproducing the experimental crystal lattice structure and the infrared spectrum. A final test for this force field will be its ability to be transferred to other 1:1 layered minerals that contain aluminum, silicon, and oxygen.

ACKNOWLEDGMENTS

The Division of Educational Programs at Argonne National Laboratory is acknowledged for providing full support for AGS. This work was performed under the auspices of the Office of Basic Energy Sciences, Division of Chemical Sciences, U.S. Department of Energy, under contract number W-31-109-ENG-38.

REFERENCES

1. Pinnavaia, T.J.; *Science* **1983**, *220*, 365.

2. Boyed, D.B.; Lipkowitz, K.B. *J. Chem. Ed.* **1982**, *59*, 269-274.

3. van Beest, B.W.H.; Kramer, G.J.; van Santen, R.A. *Phys. Rev. Lett.* **1990**, *64*, 1955-1958.

4. Mabilia, M; Pearlstein, R.A.; Hopfinger, A.J. *J. Am. Chem. Soc.* **1987**, *109*, 7960-7968.

5. Sander, M.J.; Leslie, M.; Catlow, C.R.A. *J. Chem. Soc. Chem. Comm.* **1984**, 1271.

6. Grim, R.E. *Clay Mineralogy*; McGraw-Hill: New York, **1968**, pp. 35-38.

7. Young, R.A.; Hewat, A.W.; *Clays Clay Miner.* **1988**, *36*, 225-232.

8. Adams, J.M. *Clays Clay Miner.* **1983**, *31*, 352-356.

9. Thompson, J.G.; Withers, R.L. *Clays Clay Miner.* **1987**, *35*, 237-239.

10. Pauling, L. *Proc. Nat. Acad. Sci.* **1930**, *16*, 123-129.

11. Giese, R.F. *Reviews in Mineralogy*, Vol. 19, S.W. Bailey, Ed., **1988**, pp 30-35.

12. van der Marel, H.W.; Beutelspacher, H. *Atlas of Infrared Spectroscopy of Clay Minerals and their Admixtures*; Elsevier Scientific: New York, **1976**, pp 65.

13. Gunsteren, W.F.V.; Karplus, M.J. *J. Comp. Chem.* **1980**, *11*, 266-274.

14. Hockney, R.W. *Methods Comput. Phys.* **1970**, *9*, 136-211.

15. Allinger, N.L.; Yuh, Y.H.; Lii, J.H. *J. Am. Chem. Soc.* **1989**, *111*, 8551-8566.

16. Berens, P.H.; Wilson, K.R. *J. Chem. Phys.* **1981**, *74*, 4872-4882.

17. van der Marel, H.W.; Beutelspacher, H. *Atlas of Infrared Spectroscopy of Clay Minerals and their Admixtures*; Elsevier Scientific: New York, **1976**, pp 57.

Table I. Lattice parameters of kaolinite from Young and Hewat[7].

a = 5.1497 Å	b = 8.9351 Å	c = 7.3855 Å
α = 91.93°	β = 105.04°	γ = 89.79°

Table II. Room mean square (RMS) differences between X-ray crystal data and minimized structure of kaolinite.

RMS(x): 0.024	RMS(y): 0.016	RMS(z): 0.018

Table III. Force parameters and equilibrium values used in the calculated force field of kaolinite.

O(1): oxygen in silicon-oxygen rings
O(2): oxygen between silicon and aluminum layers
O(3): oxygen in bridging hydroxyls
O(4): oxygen in terminal hydroxyls

BOND TYPE	FORCE PARAMETER (mdyne/Å)	r_{eq} (Å)
Al-O(2)	2.60	1.93
Al-O(3,4)	2.80	1.77
Si-O(1)	4.15	1.65
Si-O(2)	4.15	1.63

BOND TYPE	FORCE PARAMETER (mdyne/deg)	Θ_{eq} (°)
O(1)-Si-O(1)	0.96	106.5
O(1)-Si-O(2)	0.96	106.5
O(2)-Al-O(2)	0.90	90.0
O(2)-Al-O(3)	0.90	90.0
O(3)-Al-O(3)	0.90	90.0
Si-O(1)-Si	0.40	146.5
Al-O(2)-Al	0.10	138.0
Al-O(2)-Si	0.40	135.0
Al-O(3)-Al	0.40	138.0
Al-O(4)-H	0.15	120.0

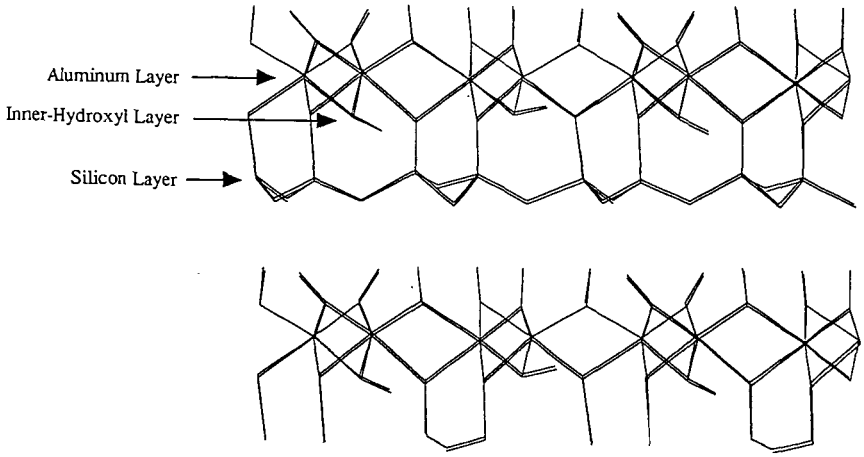

Figure 1. X-ray crystal structure of a 2x2x2 lattice of kaolinite

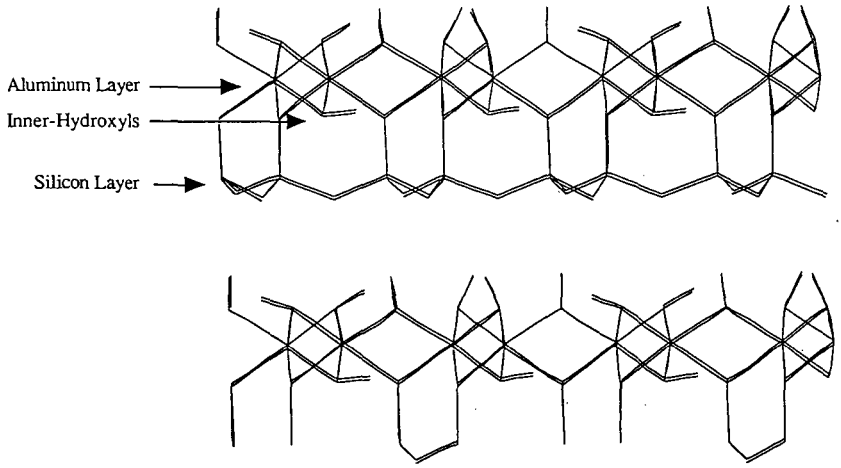

Figure 2. Minimized structure of kaolinite

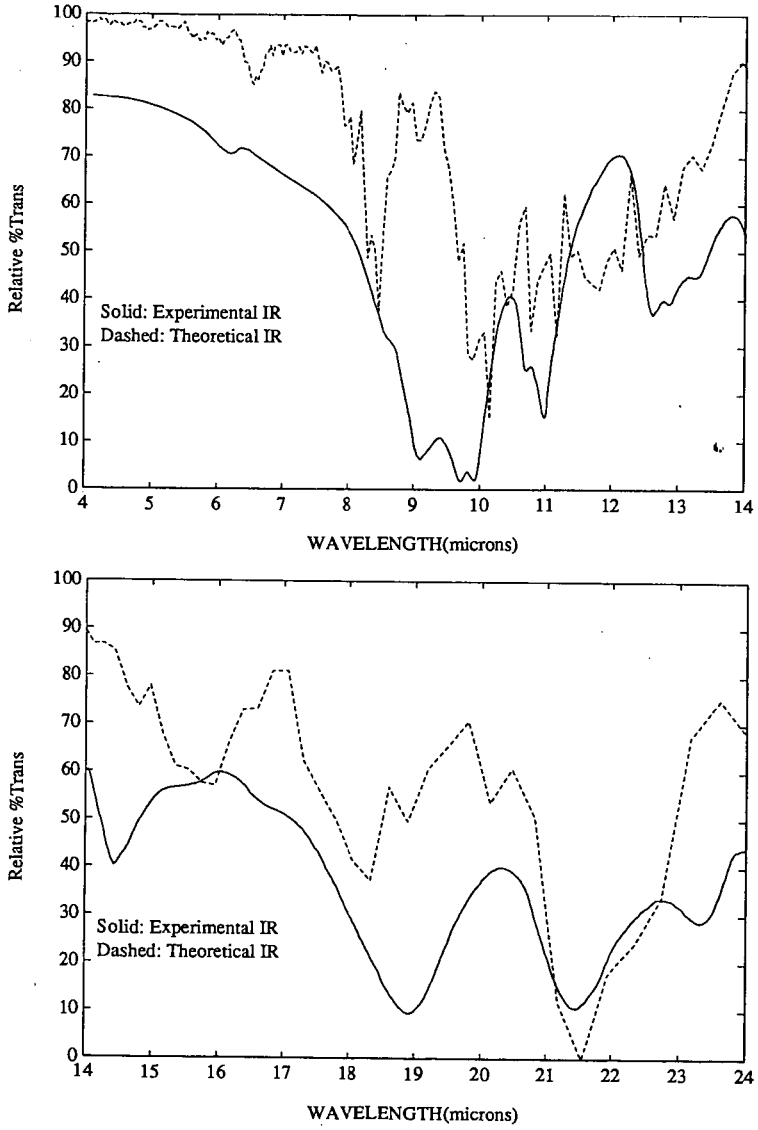

Figure 3. Comparison of theoretical and experimental infrared spectra of kaolinite

MOLECULAR MODELING STUDIES OF BITUMINOUS COAL STRUCTURE*

G. A. Carlson
Division 6211
Sandia National Laboratories
Albuquerque, N. M. 87185

Keywords: molecular modeling; computer-aided molecular design; coal structure

Abstract

Computer-aided molecular design (CAMD) has been used to define the structural conformations and intramolecular interactions of bituminous coal models. Molecular dynamics studies have produced representative minimum energy conformations for several published molecular models. These studies show the importance of van der Waals (vdW) and hydrogen-bonding interactions as cohesive forces responsible for the three-dimensional (folded) structures of the coal models. Calculations on pairs of small ring compounds representative of those found in coal clusters demonstrate that aromatics exhibit stronger vdW interactions compared with saturated ring compounds. Correlations of the vdW interactions with boiling points also show differences between aromatics and saturated rings.

Introduction

Details of coal structure and the nature of bonding within the coal structure are key concepts as one attempts to develop an understanding of coal reactivity. Because of the strong connection between structure and reactivity, there have been many studies directed toward a definition of coal structure. One group of studies has been concerned with the molecular structure of coal, as defined by various chemical and physical properties. Examples of molecular models postulated for bituminous coal are given in references 1-4. Because coal is a highly heterogeneous material, these models are only intended to be representative, or average, structures. These structures generally consist of 2-4 ring polyaromatic hydrocarbons (clusters) containing appropriate numbers of heteroatomic constituents. Most of these clusters are connected together by hydroaromatic, etheric or aliphatic linkages; others remain unconnected and relatively mobile.

The second major emphasis of bituminous coal structure studies has been to define coal as a network solid, i.e., as clusters connected together by three-dimensional cross-links (5-10). In these network models, the average size of clusters and the number of clusters between cross-links are relevant factors, while the molecular details of the clusters are relatively unimportant. Studies assuming a cross-linked structure support the concept that hydrogen bonds within the coal structure are largely responsible for defining the secondary structure of bituminous coal (6,7,9,10). The network models also explain qualitatively the observed solvent-swelling behavior of bituminous coal (6). Bituminous coals swell when intramolecular hydrogen (and perhaps other non-covalent) bonds are broken and replaced with coal-solvent hydrogen bonds. The most effective swelling solvents are those that form strong hydrogen bonds, and thus replace most or all of the original intramolecular hydrogen bonds. However, even with strong solvents, the degree of swelling is ultimately limited by the covalent cross-link structure of the coal, which is unaffected by the solvent. Thus, the extent of solvent swelling is related to the covalent cross-link density.

*This work supported by the U. S. Department of Energy and Sandia National Laboratories under Contract DE-AC04-76DP00789.

In this paper, we explore the relative importance of hydrogen bonding and van der Waals (vdW) interactions in energy-minimized coal molecular structures. While hydrogen bonding has been more widely recognized as a major contributor to the stability of middle-rank coals, vdW interactions have also been characterized as important (7,11), especially for higher-rank coals (> 87% C, daf), which contain larger, predominantly aromatic, ring systems (12). Additional support for the importance of vdW interactions in middle-rank coals is found in the work of White (13), who concluded that vdW forces were most likely the dominant intermolecular forces in liquids derived from Illinois No. 6 coal. To the extent that these liquids are similar in structure to the clusters in the coal from which they are derived, vdW interactions would be expected to be of importance for the coal as well. It has generally been found that coal-derived liquids have molecular structures similar to the parent coal (3), providing support for this view.

Method

As previously described (14), the CAMD studies were carried out using a commercial molecular modeling software program (BIOGRAF, BioDesign, Pasadena, CA), operating on a MicroVAX II computer coupled with an Evans and Sutherland PS390 graphics terminal. The CAMD software allows the construction of molecular structures of desired complexity (up to several thousand atoms) and the subsequent manipulation of those structures using molecular dynamics techniques to determine most probable (i.e., minimum-energy) structures.

The molecular dynamics calculations employ a force field model (15) that describes the potential energy of a structure in terms of interactions between covalently-bonded atoms (bond stretches, angle bends, torsions, inversions) and other, generally longer-range, interactions between non-bonded atoms (van der Waals, electrostatic and hydrogen-bond interactions). BIOGRAF uses DREIDING (16), a force field that treats a wide range of atoms and atom types.

In this paper, we focus primarily on the vdW and hydrogen bond interaction energies calculated for structures before and after molecular dynamics (energy minimization) runs. VdW interaction energies (E_{vdW}) are calculated in DREIDING using a Lennard-Jones 12-6 potential, with vdW bond strength (well depth) D_0 and equilibrium bond length R_0 defined separately for each type of atom pair.

$$E_{vdW}(R) = D_0 \cdot \left\{ \left[\frac{R_0}{R}\right]^{12} - 2\left[\frac{R_0}{R}\right]^{6} \right\} \cdot S \qquad 1)$$

A switching function S is employed to gradually "cut off" the vdW calculations for atom pairs more than 8 angstroms apart. Separate calculations showed that using this cutoff affected the calculated vdW energies by 3% or less, while reducing the time required for the calculations by 4-7 times for the structures being studied (for example, for the modified Shinn structure, containing 1040 atoms, over 500,000 vdW interactions must be calculated in the absence of a distance cutoff. With a cutoff between 8 and 9 angstroms, the number of vdW interactions calculated is reduced to ~75,000).

Hydrogen bond interaction energies (E_{hb}) are calculated using a Lennard-Jones 12-10 potential with an additional dependence on the angle between acceptor atom (A), hydrogen atom (H), and donor atom (D).

$$E_{hb}(R) = D_0 \cdot \left\{ 5\left[\frac{R_0}{R}\right]^{12} - 6\left[\frac{R_0}{R}\right]^{10} \right\} \cdot \cos^2(\theta_{AHD}) \cdot S \qquad 2)$$

All oxygen, nitrogen and sulfur atoms are considered to be potential hydrogen bond acceptors and donors. For all atom types, the equilibrium distance R_0 between donor and acceptor is defined to be 2.75 angstroms, and the equilibrium hydrogen bond strength D_0 is fixed at 9.50 kcal/mol. Since DREIDING uses the same force constants for all hydrogen bonds independent of atom types, energy calculations can be compared for one structure relative to another (providing the relative numbers of heteroatoms are similar, as in the present case), but are not accurate in absolute terms.

Calculations of hydrogen bonding and vdW interaction energies were carried out for three molecular models of bituminous coal, those of Wiser (2), Solomon (3), and Shinn (4), modified as previously described (17). Stabilization energies were determined as the differences in vdW and hydrogen bonding energies for the energy-minimized structures (after molecular dynamics calculations) relative to the initial structures. VdW interactions were also calculated for pairs of simple ring compounds ranging in size from C_6 (benzene and cyclohexane) to C_{24} (coronene and perhydrocoronene). The range of sizes and the extremes of fully-aromatic to fully-hydrogenated molecules were intended to cover the range of molecular cluster sizes and compositions believed to be present in bituminous coal. In each case, two molecules (e.g., two benzenes) were first separated by a sufficient distance to eliminate any intermolecular vdW interactions (~20 angstroms), and the total (intramolecular) vdW energy of the two molecules calculated. The molecules were then allowed to attain a minimum-energy configuration and the vdW energy again calculated. The difference in the two energies was taken to represent the vdW stabilization energy per molecular pair.

Results

Table I shows data related to hydrogen bond formation for each of the models studied. The total number of potential hydrogen bond donors and acceptors for each structure is given, as well as the actual number of intercluster hydrogen bonds formed in the energy-minimized molecular structures. Some additional intracluster hydrogen bonds were observed (i.e., hydrogen bonds between acceptors and donors present on the same cluster, on either the same or adjacent rings), but these do not contribute stability to the folded structure. Interestingly, although the Wiser model had the highest number of donors and acceptors relative to the total number of atoms, it exhibited the least intercluster hydrogen bonding. This was apparently because the donors and acceptors in the Wiser model are most often in close proximity, and preferentially form intracluster hydrogen bonds. The observation may also be partly due to the generally higher degree of cross-linking between clusters observed for the Wiser structure. This strong cross-linking appears to have limited the freedom of the clusters to move relative to one another, and thus may have restricted the access of intercluster donors and acceptors to each other. The average energy calculated for the intercluster hydrogen bonds for all models ranged from 4.5 to 7.9 kcal/mol, in good agreement with Larsen's data based on solvent swelling interactions (5-8.5 kcal/mol, ref. 6). The calculated values are somewhat lower than the maximum calculated bond strength (9.5 kcal/mol, Eq. 2), reflecting less than optimal hydrogen bond angles and bond lengths.

The number of vdW interactions in the energy-minimized structures and the vdW stabilization energies are also given for each model. The stabilization energy was calculated as the difference between the vdW energy of the initial structure and of the energy-minimized structure. As shown, although the number of vdW interactions for each structure is quite large (even with the assumed vdW cutoff distance), the energy per interaction is very small (~0.005 kcal).

Finally, the differences between the vdW and hydrogen bond energies for each model before and after energy minimization were compared, to evaluate their relative contributions to stabilization of the secondary structure. As Table I shows, the vdW stabilization energy was in every case greater than that due to hydrogen bond formation by roughly a factor of 2-3. It is not obvious how to compare the relative importance of vdW and hydrogen bonding interactions based on these total energy data, which sum up tens of thousands of vdW

interactions but only tens of hydrogen bonding interactions. However, it does seem clear from these data that vdW interactions are significant contributors to bituminous coal structural stability.

To further evaluate the significance of vdW interactions in coal, vdW interactions were calculated for pairs of simple aromatic and saturated-ring ring compounds ranging in size from C_6 (benzene and cyclohexane) to C_{24} (coronene and perhydrocoronene). Figure 1 shows the vdW stabilization energies for each molecular pair, normalized to the number of carbon atoms in each molecule and plotted against the molecular weight of the molecule. For the aromatic molecules, there is a well-defined progression toward greater stabilization energy (per carbon atom) with ring size. This is to be expected, since there are more vdW interactions possible for larger molecules. By contrast, for the fully-saturated rings, the vdW stabilization per carbon tends to be smaller than for the aromatics and is relatively unchanged with ring size. Apparently the steric overlap of the non-planar hydrogens in the saturated ring compounds prevents the molecular pairs from approaching to optimal distances for C-C vdW interactions (the C-C distance for equivalent carbons in the aromatic ring pairs is ~ 3.5-3.7 angstroms, relatively near to the equilibrium vdW C-C distance of 3.9 Angstroms; for the saturated ring pairs, the C-C distance ranges from 4.7-5.1 angstroms).

These calculations may overestimate somewhat the vdW interactions for the aromatic ring compounds. The calculated minimum-energy conformations for all the molecular pairs are with rings in a face-to-face parallel configuration. However, Larsen has reported that quadrupole interactions for aromatic ring compounds (which are not calculated in most force field approximations) are repulsive for a parallel ring configuration, and tend to to force rings to orient in a perpendicular (T-shaped) fashion (18). The tendency to form non-planar pairs is strongest for small rings (e.g., benzene), and weakest for large rings. If quadrupole effects were included, vdW interactions for benzene might be reduced by roughly 50%, but for coronene by less than 20% (19). Thus, the actual progression of vdW stabilization energy with size for aromatic ring compounds would likely be even more pronounced than Fig. 1 indicates. The effects of quadrupole interactions on the orientation of saturated ring pairs are not known.

Figure 1 also shows the vdW stabilization energies for the three coal structures previously discussed, expressed in terms of the average molecular cluster size. The average molecular cluster size for each structure was obtained after dividing the structure into "clusters" at apparent linkage sites (aliphatic, etheric bridges, etc.). These coal structure stabilization energies represent all the interactions of the molecular clusters, not just those of pairwise clusters. The tendency of the coal structure stabilization energies to be somewhat lower than the pairwise molecular interaction energies is believed to reflect the constraints of the covalent bonds between coal clusters, which tend to prevent fully-optimal ring overlap.

In earlier studies of hydrocarbon liquids, White found an excellent correlation between boiling point data and gas-chromatographic retention indices for 48 polyaromatic hydrocarbons (20). Such correlations are of value when evaluating the boiling fractions derived from coal liquefaction products. In this work, White did not consider partially- or fully-saturated ring compounds, which also would be important constituents in liquids from coal. Boiling points reflect generally the intermolecular forces, including vdW interactions, between molecules. In Fig. 2, the boiling points for the molecules represented in Fig. 1 (excluding perhydrocoronene, for which data were not found) are plotted against the vdW stabilization energies. The data separate into two quite distinct, relatively linear sets, one for aromatic and one for saturated ring compounds. Additional data would be necessary to determine whether such correlations are sufficiently accurate to provide predictive value for other ring compounds.

Discussion

Calculations of bituminous coal structures using CAMD techniques have demonstrated that intercluster vdW and hydrogen-bond interactions provide significant energy stabilization, with

vdW interactions apparently providing a larger total contribution to stabilization. The importance of vdW interactions for middle-rank coals has been pointed out previously (7,11), but not the possibility that vdW interactions actually may contribute more to energy stabilization than hydrogen bonds. The present calculations based on pairs of ring compounds show the relative effects of ring size and of ring saturation on vdW stabilization energy. These data support the increased strength of vdW interactions reported for higher-rank coals (11,12), for which the average ring size and the degree of aromaticity both increase. The ring pair data also have been shown to correlate reasonably well with boiling point data for a limited range of molecules, with aromatic ring compounds showing a distinctly different relationship than saturated ring compounds. It would be interesting to study partially-saturated rings and heteroatom-containing ring compounds as well, to provide additional data for comparison with coals and coal products.

The present studies were based on molecular models of coal, which do not incorporate the three-dimensional cross-linking that is believed to occur in actual coal structures. To address this issue, CAMD studies of coal as a network structure are planned. In these studies, representative molecular clusters (modified relative to the molecular structures considered in this work, to account for more recent chemical and structural data, refs. 21-23) will be linked together with intermittent cross-links, forming a three-dimensional structure. The structures will be energy minimized, and vdW and hydrogen bond interactions evaluated. Also, the physical density represented by the structures will be calculated, and the presence of void volume (microporosity) determined. Results will be correlated with various experimental data and with theoretical network models for coal.

Acknowledgements

Helpful suggestions and discussions of the van der Waals studies by Malvina Farcasiu and Curtis White, Pittsburgh Energy Technology Center, are gratefully acknowledged.

References

1. Given, P. H., Fuel 1960, 39, 147.
2. Wiser, W. H., Proc. of the Electric Power Research Institute Conf. on Coal Catalysis, 1973.
3. Solomon, P. R., in New Approaches in Coal Chemistry, Am. Chem. Soc. Symp. Series No. 169, 1981; p. 61.
4. Shinn, J. H., Fuel 1984, 63, 1187.
5. Larsen, J. W., Am. Chem. Soc. Div. Fuel Chem. Preprints 1985, 30(4), 444.
6. Larsen, J. W., Green, T. K., and Kovac, J., J. Org. Chem. 1985, 50, 4729.
7. Brenner, D., Fuel 1985, 64, 167.
8. Solomon, P. R., Best, P. E., Yu, Z. Z., and Deshpande, G. V., Am. Chem. Soc. Div. Fuel Chem. Preprints 1989, 34(3), 895.
9. Hall, P. J., Marsh, H. and Thomas, K. M., Fuel 1988, 67, 863.
10. Lucht, L. M., and Peppas, N. A., Fuel 1987, 66, 803.
12. Mallya, N. and Stock, L. M., Fuel 1986, 65, 736.
13. White, C. M., and Schmidt, C. E., Fuel 1987, 66, 1030.
14. Carlson, G. A., Am. Chem. Soc. Div. Fuel Chem. Preprints 1989, 34(3), 780.
15. Fruhbeis, H., Klein, R., and Wallmeir, H., Angew. Chem. Int. Ed. Engl. 1987, 26, 403.
16. BioDesign, Pasadena, CA, unpublished data.
17. Carlson, G. A., "Modeling of Coal Structure Using Computer-Aided Molecular Design", to be published in the Given Symposium Advances in Coal Science series (1991).
18. Larsen, J. W., Am. Chem. Soc. Div. Fuel Chem. Preprints 1988, 33(1), 400.
19. Miller, J. H., Mallard, W. G., and Smyth, K. C., J. Phys. Chem. 1984, 88, 4963.
20. White, C. M., J. Chem. Eng. Data 1986, 31, 198.
21. Solum, M. S., Pugmire, R. J., and Grant, D. M., Energy & Fuels 1989, 3, 187.
22. Carlson, R. E., Brigham Young University, unpublished data.
23. Winans, R. E., Argonne National Laboratory, unpublished data.

Table I

HYDROGEN BONDS AND VAN DER WAALS INTERACTIONS IN COAL STRUCTURES

Parameter	Wiser	Solomon	Shinn
Total # Atoms	394	396	1040
Hydrogen Bonds			
# H-Bond Acceptors	26	20	68
# H-Bond Donors	16	12	30
# Intercluster H-Bonds Formed	5	9	29
Δ H-Bond Energy	-25	-71	-130
Energy/Intercluster H-Bond	-5.0	-7.9	-4.5
Van der Waals Interactions			
Total # vdW Interactions	20451	21706	74882
Δ vdW Energy	-84	-119	-341
Energy/vdW Interaction	-.004	-.005	-.005
Energy Comparison			
Ratio $\frac{\Delta \text{ H-Bond Energy}}{\Delta \text{ vdW Energy}}$	.30	.60	.38

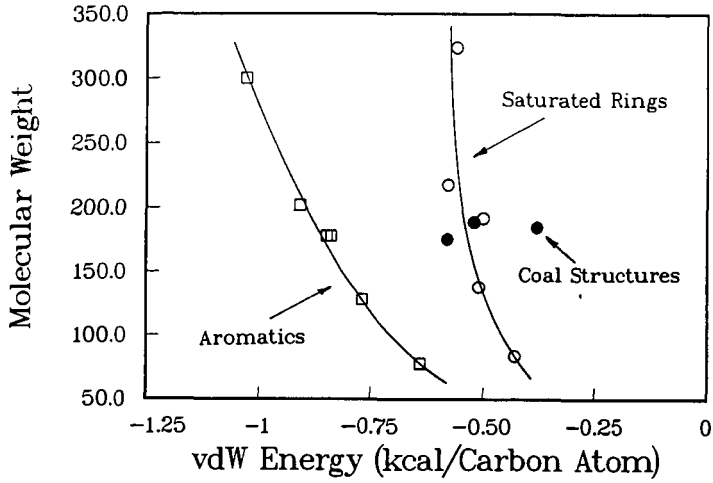

Fig. 1. Van der Waals stabilization energies for pairs of aromatics and saturated ring compounds as a function of molecular weight, and for bituminous coal structures as a function of cluster size. Lines are hand fits to data, drawn to aid the eye.

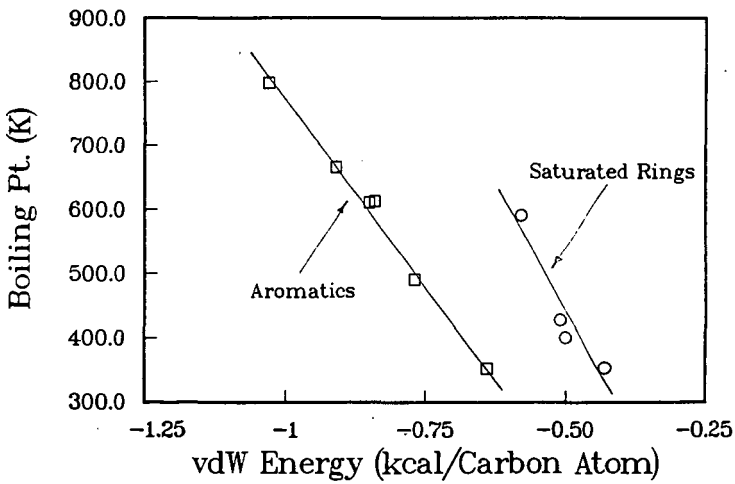

Fig. 2. Van der Waals stabilization energies for pairs of aromatics and saturated ring compounds, plotted as a function of boiling points. Straight lines are hand fits to data, drawn to aid the eye.

AN ALTERNATIVE TO "STERIC C-H COMPRESSION" AS THE SOURCE OF UPFIELD CARBON-13 NMR SHIFTS IN POLYMETHYLARENES.

Brian M. Lynch
Department of Chemistry, St. Francis Xavier University
Antigonish, Nova Scotia B2G 1C0, Canada

KEYWORDS: Carbon-13 nmr, steric extension, C-C bond lengths, MM2 calculations

INTRODUCTION

Vicinal alkyl groups attached to benzenoid rings or cycloalkane moieties in a tetralin-like configuration are commonly postulated features in structural models of bituminous coals [for examples, see [1]]. Formation of cyclic carboxylic acid anhydrides (analogous to phthalic anhydride) from mild oxidations of such coals [2] is one item of evidence in support of this postulate, and it would be expected that features from vicinal alkyl species should be readily identifiable if highly resolved carbon-13 nmr spectra of coals were to be obtained. This expectation should be readily testable since in polymethylarenes, methyl carbon-13 nmr shift patterns are observed in which ortho-related methyl carbon signals are significantly upfield (up to 7 ppm) from those of isolated methyl groups. These patterns are usually interpreted by suggesting that non-bonded repulsion between alkyl hydrogen atoms [3-5] leads to **steric compression** of C-H bonds. Many other carbon-13 "steric shifts" are rationalized similarly, with electron migration postulated in the sense δ^+ H-C δ^- [6,7]. However, bond length and angle distortions occur more readily for C-C bonds than for C-H bonds (compare ν CH, ~ 3000 cm^{-1}; ν CC, ~ 1000 cm^{-1}, and δ CH ~ 1450 cm^{-1}; δ CC ~ 700 cm^{-1}), so hydrogen-hydrogen repulsions are not likely to be the only significant steric factors. Further, the methyl proton shifts in ortho-xylene are also upfield from those in the meta and para isomers [8].

PROCEDURES AND DISCUSSION

I have tested the validity of the **steric compression** postulate, using Allinger's MM2 force field approach [9] with the commercial application Chem3D Plus™ [10] on a Macintosh II microcomputer. I calculated equilibrium geometries of various methylarenes (benzenes, naphthalenes, anthracenes). The steric interactions were minimized iteratively, considering contributions from compression-stretching, bending, stretch-bend, van der Waals, dipole-dipole, and torsional forces. Ten to one hundred iterations are sufficient to reach self-consistent minima. Calculations for ten distinct environments for methyl groups suggest (see Table 1) that the major variations in geometry minimizing non-bonded repulsions are bond extensions of the aryl C - alkyl C bonds, and appropriate angular changes.

Bond length and angle distortions occur more readily for C-C bonds than for C-H bonds, consistent with the appropriate force constants.

The methyl carbon-13 shifts are linearly correlated with aryl C - alkyl C bond lengths: shift increases as bond length decreases (Figure 1). The hybridization of the alkyl carbons is unchanged; one-bond carbon-13 - proton coupling constants are within 0.5 Hz of 125 Hz.

I interpret these results as decreased hyperconjugative interactions between the methyl groups and the attached aromatic species with increasing aryl C - alkyl C bond length, and as a direct consequence, decreased C-methyl carbon-13 shifts. In this series of compounds, there is **steric extension** of carbon-carbon bond lengths to avoid the hydrogen-hydrogen repulsions in the steric compression model proposed by Grant and coworkers.

This is not to discount the possible significance of non-bonded hydrogen-hydrogen repulsion effects under appropriate circumstances. In the polycyclic aromatic phenanthrene a similar MM2 treatment may be applied to deduce the preferred geometry. In this species, the two hydrogens of the C-H bonds in a bay environment are shortened significantly, but the major predicted changes are systematic deformations of the entire ring geometry and bending of the bay C-H bonds with increased angles. The predicted C-C bond lengths in the phenanthrene skeleton show excellent correlations with those observed from neutron diffraction measurements (see Figure 2).

ACKNOWLEDGEMENTS

This work was catalysed by an opportunity provided by a Project SERAPHIM Fellowship held in summer 1988 at the Department of Chemistry of Eastern Michigan University, Ypsilanti, Michigan. Thanks are accorded for this award.

REFERENCES

1. Davidson, R. M. in Gorbaty, M. L.; Larsen, J. W.; Wender, I., Editors. Coal Science. Volume 1. Molecular Structure of Coal. Academic Press, 1982.
2. Lynch, B. M. and MacPhee, J. A. in Nelson, C. R., Editor. Chemistry of Coal Weathering(Coal Science and Technology 14). Elsevier, Amsterdam, 1989, p. 93.
3. Woolfenden, W. R.; Grant, D. M. J. Am. Chem. Soc. 1966, 88, 1496.
4. Grant, D. M.; Cheney, V. B. J. Am. Chem. Soc. 1967, 89, 5315.
5. Dalling, D. K.; Grant, D. M. J. Am. Chem. Soc. 1967, 89, 6612.
6. Perlin, A. S.; Casu, B.; Koch, H. J. Can. J. Chem. 1970, 48, 2599.
7. Dorman, D. E.; Roberts, J. D. J. Am. Chem. Soc. 1970, 92, 1355.
8. Bhacca, N.S.; Johnson, L. F.; Shoolery, J. N. NMR Spectra Catalog. Varian Associates, Palo Alto, California, 1962. Spectra 201-203.
9. Berkert, U.; Allinger, N. L. Molecular Mechanics. American Chemical Society: Washington, D. C., 1982.
10. Cambridge Scientific Computing, Inc., Cambridge, Mass. 02139.

Table 1

Carbon-13 shifts for methyl groups in methylarenes

Compound	Shift, ppm	MM2 bond length, nm
Toluene	21.3	0.1509
o-Xylene	19.6	0.1511
9-Methylanthracene	13.7	0.1516
9,10-Dimethylanthracene	14.1	0.1517
1,2,3-trimethylbenzene	15.2 (2)	0.1514
1-Methylnaphthalene	19.1	0.1511
1-Methylanthracene	19.7	0.1512
2-Methylnaphthalene	21.4	0.1509
1,2,3,5-tetramethylbenzene	14.6(2)	0.1515
	20.9(5)	0.1508

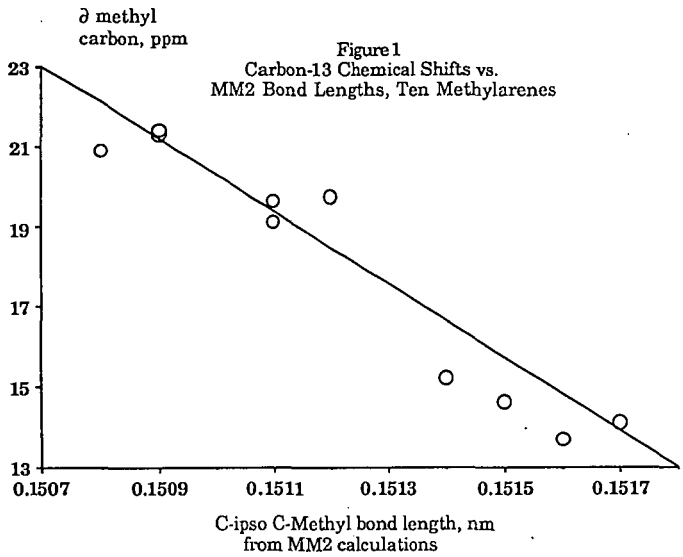

Figure 1
Carbon-13 Chemical Shifts vs.
MM2 Bond Lengths, Ten Methylarenes

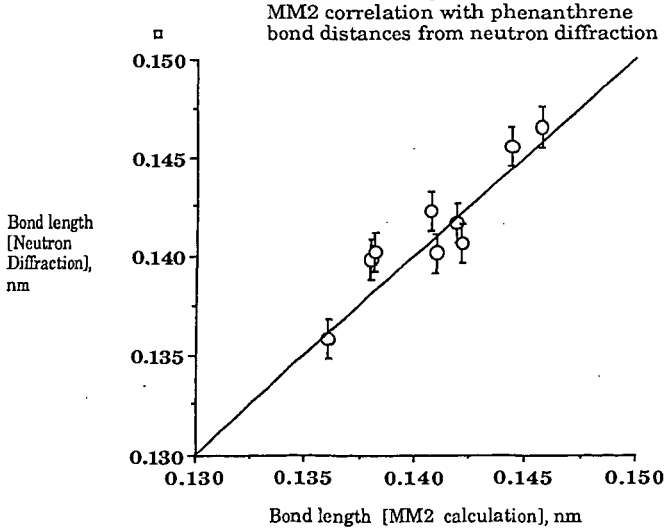

Figure 2
MM2 correlation with phenanthrene
bond distances from neutron diffraction

DEVELOPMENTS IN SIMULATION METHODS FOR SOLID CATALYSTS

C. M. Freeman, A. T. J. Hope, S. M. Levine,
J. M. Newsam, J. Sauer, R. F. Smith and S. Tomlinson

BIOSYM Technologies Inc.
10065A Barnes Canyon Rd., San Diego CA 92121

Keywords: Computer simulation, Catalyst characterization, Catalyst structure

INTRODUCTION

The complexity of most heterogeneous catalyst systems has traditionally hampered the effective application of computer simulation methods. However, increasing sophistication in methodology and application, coupled with the development of tools specifically tailored for solid catalyst systems is now enabling computer modeling to address a number of problems encountered during the development and implementation of a variety of heterogeneous catalysts. We outline here some of our recent progress in this area, and give specific examples taken from (1) the characterization of crystalline catalysts and supports (2), the development and dynamical simulation of metal atoms and clusters on amorphous inorganic matrices (3), the dynamical behavior of hydrocarbons within microporous media and (4) the application of quantum chemical tools to studying local coordination environments and chemistries. In-depth theoretical studies of reaction pathways over real, multicomponent heterogeneous catalysts at process conditions remain a far distant goal, but, as the present examples demonstrate, considerable insight can be gleaned when tailored tools and approaches are applied to appropriately phrased heterogeneous catalyst problems.

CATALYST CHARACTERIZATION

Structural characterization is a key step in the development of a fundamental understanding of catalyst function. Most real heterogeneous catalyst systems are, however, complex and do not lend themselves readily to study by conventional structural characterization tools. Microporous crystals such as zeolites, the basis for current fluid cracking catalysts, and mixed metal oxides of interest in a wide range of oxidation reactions are microcrystalline. Powder X-ray diffraction techniques are therefore a key source of structural data. Powder diffraction data can, using the Rietveld method, be the basis for refinement of an approximate model, but the derivation of the initial model is often difficult. Computer simulations can greatly facilitate the structure solution process, either by direct derivation of an initial model from unit cell and compositional data, combined with established geometrical constraints (1), or by enabling a developing structural model to be manually adjusted while the degree of match between the simulated powder diffraction pattern and that observed is interactively monitored (Figure 1) (2, 3).

AMORPHOUS SUPPORTS

Heterogeneous catalysts are rarely used in a 'neat' form and in many cases the catalyst support or binder can play a significant role in processes. For example, classical reforming catalysts, or a large number of hydrogenation catalysts are comprised of metals dispersed on non-crystalline supports. In such cases a direct determination of structure from scattering data is not possible. Computer simulations can, however, be used effectively to develop models for the surfaces of amorphous

matrices, such as silica (4), and to study the dynamical interactions of metal atoms and clusters with such a support (Figure 2) (5, 6).

HYDROCARBONS WITHIN MICROPOROUS CRYSTALS

The behavior of hydrocarbons within microporous crystals such as zeolites is central to the role of zeolites as catalysts and sorbents. A number of experimental tools can be applied to studying the preferred sites occupied by sorbed hydrocarbons within zeolites, and aspects of the character of the hydrocarbon molecular motion over several time-scales (7). Modeling is already being applied in studies of sorbate location and diffusion (e.g. (2, 8, 9)), and computer simulations will clearly play an increasingly important role as the mechanism by which the experimental insights provided by these various methods can be combined into a self-consistent picture of the zeolite - hydrocarbon interactions. Key areas for development are the potential functions and parameters used in describing the interatomic interactions, and methods for simulating dynamical phenomena that occur on characteristic time scales longer than a few thousand picoseconds for which classical molecular dynamics methods are currently unviable.

APPLICATIONS OF QUANTUM CHEMICAL METHODS

Quantum chemical methods must play a central role in developing an understanding of catalyst reactivity. However, the complexity of real catalysts that hampers the application of structural characterization methods also imposes restrictions on the degree to which quantum chemical methods can be applied to models that approximate actual catalyst centers. Methods are continually being refined and ab initio Hartree-Fock calculations on a complete sodalite cage have recently been described (10). Ab initio methods have also contributed considerably to our understanding of Brønsted acidity in zeolites and to the geometries of such active sites (11, 12). Additionally, ab initio methods provide a powerful means of computing potential energy surfaces and of hence deriving potential energy functions and parameters for both intra- and intermolecular interactions.

ACKNOWLEDGEMENTS

The BIOSYM Catalysis and Sorption project is supported by a consortium of member companies.

LITERATURE CITED

(1) Deem, M. W.; Newsam, J. M. Nature 1989, 342, 260-262.
(2) Freeman, C. M.; Catlow, C. R. A. Chem. Ind. 1990, 3, 796-799.
(3) BIOSYM Technologies Inc, Catalysis and Soprtion Project Software (1991).
(4) Levine, S. M.; Garofalini, S. H. in Surface structure of silica glasses by molecular dynamics simulations; Materials Research Society, Pittsburgh, PA, 1986; pp 29-37.
(5) Levine, S. M.; Garofalini, S. H. Surf. Sci. 1985, 163, 59-66.
(6) Levine, S. M.; Garofalini, S. H. 1990, in preparation.
(7) Newsam, J. M.; Silbernagel, B. G.; Melchior, M. T.; Brun, T. O.; Trouw, F. in Motion of Organic Species Occluded or Sorbed within Zeolites; Atwood, J. L.; Plenum, New York, 1990; pp 325-337.

(8) Newsam, J. M.; Silbernagel, B. G.; Garcia, A. R.; Melchior, M. T.; Fung, S. C. in Structure-Activity Relationships in Hetrogeneous Catalysis (Stud. Surf. Sci. Catal.); Grasselli, R. K. Sleight, A. W.; Elsevier, Amsterdam, 1991, in press.
(9) Schröder, K.; Sauer, J. Chem. Phys. Lett. 1990, 271, 289-296.
(10) Ahlrichs, R.; Bär, M.; Häser, M.; Kölmel, C. M.; Sauer, J. Chem. Phys. Lett. 1989, 164, 199-204.
(11) Sauer, J. Chem. Rev. 1989, 89, 199-255.
(12) Sauer, J.; Kölmel, C. M.; Hill, J. R.; Ahlrichs, R. Chem. Phys. Lett. 1989, 164, 193-198.

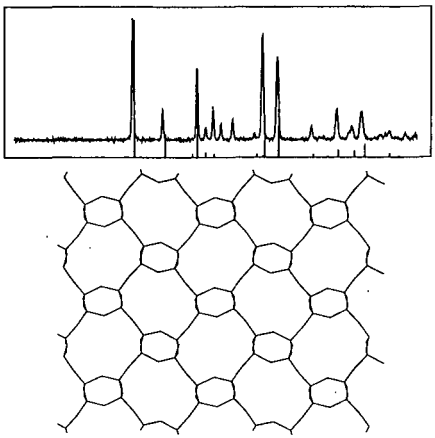

Figure 1: A model of the zeolite ABW-framework drawn as straight lines connecting adjacent Si or Al sites and their coordinating oxygen atoms (lower). The powder X-ray diffraction pattern computed interactively as the structure is edited is shown above as bars, compared with the experimental pattern of an ABW-framework material (continuous line) (3).

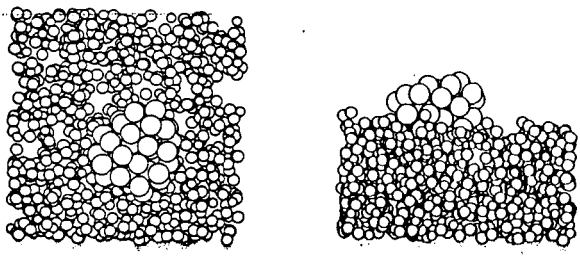

Figure 2: Top (left) and side (right) views of a model Pt cluster on a vitreous silica support generated by a series of molecular dynamics simulations (5, 6).

MOLECULAR MODELLING OF KEROGENS AND RELATED COMPOUNDS AS A TOOL FOR PREDICTION OF FOSSIL FUELS GENESIS

F. BEHAR*, M. VANDENBROUCKE* and J. L. FAULON**
* IFP, 1-4 Avenue Bois Préau, 92506 RUEIL MALMAISON, FRANCE. ** C.A.O. Robotique, Armines, 60 Boulevard St Michel,75272 PARIS Cedex 06, FRANCE

Key-words: molecular modelling of kerogen, thermal cracking, oil, kinetics.

INTRODUCTION

Kerogen is defined as that fraction of sedimentary organic matter which is insoluble in usual organic solvents (1). It is a mixture of macromolecules whose structures evolve under the influence of time and temperature due to increasing sediment burial. Thermal cracking of kerogen (primary cracking) will lead to petroleum generation. Oil is formed first, further thermal degradation of kerogen and oil (secondary cracking) will produce gaseous compounds. Prediction of both quantity and quality of hydrocarbons generated from a given kerogen buried in a given sedimentary basin are of paramount importance as exploration guide. Thus, simulation of thermal degradation of organic matter in laboratory has been performed in order to elaborate kinetic models. These kinetic models can be really predictive only when the three following conditions are fulfilled:

1°) knowledge of chemical structure of reactants,
2°) knowledge of chemical structure of degradation products,
3°) establishment of laws relating chemical structures of reactants and products.

For many years, attention has been focused on characterization of pyrolysis products and establishment of kinetic laws, but a chemical structure was not available when kerogen, coal or heavy ends of petroleum such as resins and asphaltenes were studied. In this paper, we will present the approach we are following for modelling these complex structures and how we can relate kerogen and/or asphaltenes modelling to kinetics.

Many experimental devices have been developed for simulating thermal cracking of kerogen or asphaltenes (2). As these insoluble compounds are generally not vaporisable, experimental simulation of cracking can be done either in open pyrolysis systems swept by an inert carrier gas (3, 4, 5 among others) or in closed pyrolysis systems (6, 7 among others). An open pyrolysis system is very convenient because it allows continuous detection of effluents and programmed temperature increase. Thus, many samples can be studied in a short experimentation time. Nevertheless, transport effects due to the delay between formation and detection of effluents, can both modify kinetic parameters such as the apparent activation energies (8) and underestimate the yield of heavy compounds such as resins and asphaltenes; these latter, if they are only partially swept out of the pyrolysis chamber, can be further cracked together with the residual kerogen. Moreover, secondary cracking reactions cannot be simulated as pyrolysis products are swept away as soon as they are generated. In a closed pyrolysis system, primary cracking can be observed for low conversion yields, whereas secondary cracking will occur for higher severity, but care must be taken regarding both wall effects (9) and overlap of primary and secondary reactions. There are currently not enough available data for doing a real comparison between

open and closed systems. As the aim of our work is to elaborate a complete kinetic scheme including both primary and secondary cracking, we have chosen to perform the experimental work in a closed system.

Compounds involved in thermal cracking reactions can be identified unambiguously when present either as gaseous or liquid products. Therefore, they can be classified according to their chemical structure and carbon number, and their relative thermal stabilities can be compared.
When kerogen and heavy ends of petroleum are pyrolysed, characterization of these latter in terms of chemical bonds distribution and molecular moieties is not available. As a consequence, establishment of a predictive kinetic scheme based on chemical structure for these complex macromolecules, is not yet possible. To overcome this difficulty, we propose to use the molecular modelling software Xmol (10) which, through a combination of atomic and molecular analyses of an unknown insoluble sedimentary organic matter, builds up a self consistent 3D chemical structure. Although the 3D structural representation can be disputed, and is maybe unrealistic, it allows a correct statistical balance of all kinds of bonds present in the macromolecule. Thus, the amount and the distribution of these chemical bonds can be listed and can be related to the distribution of stoichiometric coefficients of the kinetic scheme obtained from experimental simulation.
In this paper, preliminary experimental results on kinetics of cracking of oils and kerogens will be presented. We are currently gathering all the data necessary to link kinetic scheme and molecular structure of reference kerogens.

SAMPLES

Four samples were selected: two kerogens (Type II and Type III) and two oils (Boscan and Pematang), the first one being aromatic and the second one paraffinic. As during thermal cracking each oil produces both lighter and heavier molecules than those present in the initial oil, the resulting pyrolysate will be a complex mixture of new compounds plus reactants not yet degraded. In order to discriminate between reactants and products, we have chosen to study each oil after fractionation into two classes: the first one (distillate) comprising light hydrocarbons ranging from C6 to C16, the second one (topped residue) comprising both hydrocarbons (saturates + aromatics) and polar compounds (resins + asphaltenes). Chemical composition and elemental analysis of the initial samples are reported in tables 1 and 2. .

EXPERIMENTAL SIMULATION

The experiments were carried out in sealed gold tubes under pressure; pyrolysis conditions are listed in table 3.
Pyrolysis products were analyzed according to the following procedure (11):

- non hydrocarbon gases:
  * quantification of individual species such as H20, CO2 and H2S,
  * atomic balance for carbon, hydrogen, oxygen and sulfur.
- C1-C5 fraction:
  * identification and quantification of all hydrocarbons,
  * carbon and hydrogen balances.
- C6-C13 fraction:

* separation of saturates plus unsaturates and aromatics,
* quantification of all saturates,
* quantification and identification of nearly all aromatics,
* carbon and hydrogen balances.

- C14+ extract:
  * separation into saturates, aromatics and NSO compounds and quantification,
  * elemental analysis of total C14+ fraction
- insoluble residue:
  * quantification and elemental analysis.

Consequently, atomic balances are done on the total pyrolysis products recovered in each experiment in order to be compared to the elemental analysis of the initial sample. This allows a check of the experimental data independent of the mass balance. Table 4 presents an example of a set of experimental data obtained at 300[C for the Type II kerogen.

Kinetic model for kerogen and oil cracking

Cracking reactions can be described by a set of first order reactions involving the transformation of the initial reactant into new compounds or new chemical classes of compounds, some of them being stable and others unstable in the limits of the experimental domain considered.
A first order reaction obeys the Arrhenius law: $dx/dt = - kx$ where x is the reactant concentration and k, the first order rate constant, is equal to $Ae^{-E/RT}$. The preexponential factor A and the activation energy E are the parameters to be determined by experimental simulation and they are characteristic of each cracking reaction. From our 245 experiments, a general kinetic scheme can be elaborated. It comprises six stable classes, H20, C02, H2S, C1, ARO.S (C6-C13 stable aromatics such as benzene, toluene, xylenes and naphthalene) and coke and 7 unstable classes, C2, C3-C5, C6-C13 SAT., C8-C13 ARO., C14+ SAT., ARO.U (unstable C14+ aromatics such as alkyl and/or naphtheno aromatics, resins and asphaltenes), condensed C14+ aromatics (ARO.C) and residual kerogen (RK). In this scheme, 9 cracking reactions are involved: .

1. Kerogen ---> H2O + CO2 + H2S + C14+SAT + ARO.U + RK
2. ARO.U ---> H2O + CO2 + H2S + C14+SAT + C6-C13 SAT + ARO.C + coke
3. ARO.C ---> C1 + C3-C5 + coke
4. C14+SAT ---> C3-C5 + C6-C13 SAT + C8-C13 ARO
5. C6-C13 SAT ---> C1 + C2 + C3-C5 + C8-C13 ARO + ARO.C
6. C8-C13 ARO ---> C1 + ARO.S + ARO.C
7. C3-C5 ---> C1 + C2 + C6-C13 SAT + C8-C13 ARO
8. C2 ---> C1 + C3-C5 + C6-C13 SAT
9. RK ---> C1 + coke

In each reaction, stoichiometric coefficients multiply each compound or class of compounds formed. In order to reduce the number of free parameters to be experimentally determined, the preexponential factor A is assumed to be the same for all cracking reactions. Then, from these experiments, kinetic parameters such as activation energies and stoichiometric coefficients were calculated, through

optimization successively on each kerogen, each topped oil and each distillate, then on each total oil and finally on the two total oils. Consequently, we have a unified kinetic model for oil cracking (reactions 2 to 8), provided the proportions of chemical classes as defined above are known in the initial oil. For kerogen cracking (reactions 1 and 9), due to the complexity of the initial chemical composition of kerogen, a specific kinetic model is currently proposed for each sample.

CHEMICAL MODELLING

Various quantitative analytical techniques allow us to define a macromolecular structure of kerogen or asphaltenes more or less precisely. These techniques can be divided into 2 classes (Table 5). One includes atomic analyses such as elemental analysis, spectroscopic techniques and the quantitative determination of some functional groups. The other involves quantitative analysis of molecular moieties obtained by degradation reactions such as pyrolysis (12, 13, 14), chemical attack (15, 16) or natural thermal cracking during burial of sediments (17). After fractionation, these molecular moieties can be identified and quantified by chromatography or mass spectrometry. Results provide molecular level information because the inference is that the small molecules are component fragments of the larger macromolecule. As these analytical data are not sufficient to allow a detailed representation of a macromolecular structure, some assumptions, have to be made (Table 6). In order to combine all these informations and to elaborate a chemical model, a new chemical representation of molecules labelled "molecular signature" is proposed: each molecule is defined by a series of 21 coordinate numbers which characterize the geometric configuration of atoms. It can be applied either to molecular moieties or to the macromolecule. Moreover, it allows to calculate parameters not available by analytical techniques. Then a structure is built from the analyses and assumptions defined above, using the software Xmol™ (10). A first step is to construct in a 3D space the molecular moieties, including biomarkers, analyzed as described above: this is done by an editor of molecules which stores these data into a library. Then, starting from the set of equations describing the analytical results and the assumptions, a prediction program selects quantitatively the required cyclic or aliphatic groups from the library and calculates a list of intergroup bonds. Finally, a third program constructs in a 3D space one macromolecule isomer calculated by the prediction program. Although each run of the third program will give one different 3D isomer of the macromolecule, the prediction program has an unique solution for one set of analytical data plus assumptions. It thus allows to characterize the macromolecule by the list of its molecular groups or chemical bonds, whatever the arrangement of molecular groups is.

Among the advantages of this software it allows:

- to list all parameters to be known in order to describe the chemical structure of a given macromolecule,
- to compare the number of assumptions versus analytical data, thus testing the accuracy of the chemical structure,
- to stress some discrepancies among the set of analytical data,
- to take into account, at any time new analytical data which may eliminate assumptions,

- to build self consistent chemical structures which fit all analytical data and to calculate easily the number of each atom or bond.

DISCUSSION

When both kinetic scheme of kerogen cracking and corresponding chemical modelling are achieved, the last problem is to link the two fields of research. The aims of this remaining work are to check, for reference samples, the validity of the kinetic scheme by chemical constraints and then to help to predict thermal cracking of an unknown sample according to its chemical structure, without starting again a complete experimental study. Xmol allows us to describe kerogen or related compounds as a set of chemical bonds or molecular groups, for instance:

a - number of methyl groups,
b - number of ethyl groups,
c - number of aliphatic chains from C3 to C5,
d - number of aliphatic chains from C6 to C13,
e - number of aliphatic chains C14+,
f - number of functional groups such as carbonyl, carboxyl, phenols, alcohols methoxy groups and other ethers,
g - distribution and amount of naphthenic rings,
h - distribution and amount of naphthenoaromatic rings,
i - distribution and amount of aromatic rings.

Each of these molecular groups can be considered as individual and independent reactant during kerogen cracking. Thus, when a given molecular group is considered in the general kinetic scheme described above, knowing its initial proportion in the kerogen structure is enough to predict either its contribution among pyrolysis products derived from kerogen cracking or the proportion of pyrolysis products when it is degraded. Moreover, as the main difference between kerogen types relies on their relative amounts of the same molecular groups, an unified kinetic model for cracking of kerogen could be established. It means that Xmol allows first to choose chemical classes to be taken into account in the kinetic scheme, secondly to know the chemical composition of the C14+ fraction defined in reaction 1 and finally to constrain stoichiometric coefficients of reactions from 1 to 9. For instance:

- total aliphatic carbon content included in methane, ethane, C3-C5 compounds, C6-C13 saturates and C14+ saturates must not exceed the aliphatic carbon content of the initial sample,
- oxygen content included in CO_2, H_2O and coke must not exceed the oxygen content in the initial sample,
- oxygen content included in CO_2 must not exceed the oxygen content included in both carbonyl and carboxyl functional groups,

CONCLUSION

We have checked the feasibility of this new approach for relating thermal reactivity and chemical structure of kerogen only from a qualitative point of view. In the future, we have to confirm this feasibility with quantitative data. Moreover, we need to improve our knowledge of the chemical structure of kerogen, especially on the quantitative determination of functional groups, in order to relate a given functional

group to the yield of non hydrocarbon species released during pyrolysis of kerogen (reactions 1 and 2). Finally, specific and more precise additional analyses can be performed on asphaltenes, such as liquid ^{13}C NMR and some chemical degradation techniques, which could better constraint structural parameters and thus kinetic scheme. Nevertheless, use of Xmol must be considered at its current stage of development mainly as an useful guide for writing kinetic equations but not as a predictive tool i.e. as a substitute of experimental work. The very first use of this software is to give a chemical model of an unknown sample which, up to now, has been considered as a "black box". Even if it is only a model which will certainly be modified in the future according to new analytical data, it allows to set up appropriate experimental work for kinetic studies as well for temperature and time conditions as for analytical procedure for identification and quantification of pyrolysis products.
A direct application of that work extended to complex products such as resins or asphaltenes could be in refinery processes, for thermal treatment of heavy ends of petroleum. This work allows also to link two fields of research, structure of kerogens (and related compounds) and kinetics, which are generally studied by separate research teams.

REFERENCES

1. Durand B., Kerogen, Editions Technip, Paris, 1980.
2. Ungerer P., Advances in Organic Geochemistry 1989 (Edited by B. Durand and F. Behar), Org. Geochem., Vol 16, Nos 1-3, pp 1-25, (1990).
3. Tissot B., Pelet R. and Ungerer P., AAPG Bull. 71, 12, 1445-1466, (1987). 4. Espitalié J., Ungerer P., Irwin I. and Marquis F., Org. Geochem., 13, 4-6, 893-900, (1988).
5. Burnham A. K. and Braun R. L., In situ, 9 (1), 1-23, (1985).
6. Lewan M. D., Philosophical Transactions of the Royal Society of London, series A, 315, pp. 123-134, (1985).
7. Behar F., Ungerer P., Kressmann S. and Rudkiewicz J. L., Rev. Inst. Fr. du P{trole, in press, (1991).
8. Burnham A. K. and Braun R. L., Advances in Organic Geochemistry 1989 (Edited by B. Durand and F. Behar), Org. Geochem., Vol 16, Nos 1-3, pp. 27-39, (1990).
9. Kressmann S., unpublished data, (1990).
10. Faulon J. L., Vandenbroucke M., J. M. Drappier, F. Behar and Romero M., Advances in Organic Geochemistry 1989 (Edited by B. Durand and F. Behar), Org. Geochem., Vol 16, Nos 4-6, pp. 981-993, (1990).
11. Behar F., Leblond C. and Saint-Paul C., Rev. Inst. Fr. du Pétrole, Vol 44, 3, 387-411, (1989).
12. Behar F. and Pelet R., J. Anal. Appl. Pyr., 8, 173-187, (1985).
13. Nip M., Tegelaar E. W., de Leeuw J. W. and Schenck P. A., Advances in Organic Geochemistry 1985 (Edited by Leythaeuser D. and Rullkotter J.), Org. Geochem.10, pp. 769-778, (1987).
14. Hatcher P. G., Wilson M. A., Vassallo A. M. and Lerch H. E., Int. J. Coal Geol., 13, 99-126, 1989.
15. Micke B. and Michaelis W., Advances in Organic Geochemistry 1985 (Edited by Leythaeuser D. and Rullkotter J.), Org. Geochem.10, pp. 847-858, (1987).
16. Chappe B., Michaelis W. and Albrecht P., Advances in Organic Geochemistry 1979 (Edited by Douglas A. G. and Maxwell J. R.), Pergamon Press, Oxford, (1980).
17. Tissot B. P. and Welte D. H., Petroleum Formation and Occurrence, Springer, Berlin, (1978).

Table 1: Chemical composition (wt%) of Boscan 300+, Pematang 340+ and corresponding distillates.

Sample	C6-C13 SAT.	C6-C13 ARO.	C14+ SAT.	C14+ ARO.	RES.	ASP.	H	C	Distillate
Boscan 300+	0	0	13	37	33	17	10,1	82,4	
Boscan 300-	44	20	20	17	0	0	12,9	87,1	10
Pematang 340+	0	0	59	17	23	1	1,8	86,7	
Pematang 340-	57	7	30	6	0	0	14,3	85,7	37

Table 2: Elemental analysis of the two reference kerogens (wt%)

Sample	C	H	N	O	S org.	Pyrite
Type II	55,34	5,85	1,77	10,7	3,46	22,9
Type III	72,86	5,27	1,86	15,9	1,06	3,08

Table 3: Pyrolysis conditions for experimental simulation of kerogen and oil cracking

Sample	Temperature (°C)	Time (h)	Number of experiments
Type II kerogen	260-500	0,5-1900	70
Type III kerogen	250-500	0,5-1900	50
2 oils	350-500	0,5-1000	60
2 distillates	380-500	0.5-1000	65

Table 4: Mass balances (wt%) obtained for Type II kerogen at 300°C for various heatin times

Time (h)	CO_2	H_2O	H_2S	C1	C2-C5	C6-C13 SAT.	C6-C13 ARO.	C14+ extract	Residue
1	2,0	1,7	0,4	0,0	0,2	0,1	0,0	8,5	86,9
9	3,4	2,4	0,7	0,4	0,3	0,3	0,1	17,3	75,1
24	4,0	2,8	0,8	0,5	0,4	0,6	0,2	24,2	66,0
240	4,6	4,2	1,9	0,7	3,0	2,7	1,5	31,1	50,0
648	5,1	4,9	2,3	1,2	3,5	3,7	1,6	26,7	51,0
1296	6,0	4,9	2,5	1,5	4,0	3,9	1,7	26,4	49,0

Table 5 : Analytical data needed for kerogen modelling

ANALYTICAL TECHNIQUE	RESULTS
ATOMIC INFORMATION	
Elemental analysis	Number of atoms (C.H.O.N.S.)
I.R. Spectroscopy + ^{13}C NMR	Amount of Csp^2 bonded to : - 3 CARBONS - 2 CARBONS and 1 HYDROGEN - 1 OXYGEN or NITROGEN by a single bond - 1 OXYGEN by a double bond Amount of Csp3 bounded to : - Only CARBON and HYDROGEN - 1 OXYGEN by a single bond - 2 OXYGENS by single bonds
Functional-group analysis	Distribution of functional groups
Pycnometer	Density
MOLECULAR INFORMATION	
Pyrolysis + Gas chromatography + Mass spectrometry	Histogram of CARBON NUMBERS in ALIPHATIC CHAINS Histogram of NUMBER of RINGS in CYCLOALKANES Histogram of NUMBER of RINGS in AROMATICS and NAPHTHENOAROMATICS
Csp^2 is a carbon atom with sp^2 hybridization (i.e. aromatic or double bonded). Csp^3 a carbon atom with sp^3 hybridization (i.e. naphthenic or aliphatic).	

Table 6 : Hypotheses done for kerogen modelling

Only the elements C, H.O. N, S. List of molecular groups included in a library List of possible intergroup bonds (only covalent bonds) List of possible functional groups and heteroatoms Elimination of improbable configurations (i.e. a carbon linked to 3 or 4 oxygens) Number of carbon atoms in the model Assumptions which supplement analyses (i.e. : percentage of ether linked to 2 aromatic carbons or 2 aliphatic carbons or 1 aromatic and 1 aliphatic carbon)

BOND DISSOCIATION ENERGY CALCULATIONS FOR COAL FRAGMENTS AND MODEL COMPOUNDS

Harriet F. Ades, Audrey L. Companion, and K.R. Subbaswamy
Departments of Physics and Chemistry
University of Kentucky
Lexington, KY 40506-0055

Keywords: Coal liquefaction, quantum chemical calculations, catalysis modeling.

Abstract

Anderson's modified version[1] of the extended Hückel molecular orbital method and the MNDO and AM1 methods of Dewar have been used to study bond cleavage in molecular fragments of interest to coal liquefaction. Geometric conformations, molecular orbital coefficients for the HOMO's and LUMO 's, bond dissociation energies, and heats of reaction have been computed and compared for the three methods. Qualitative agreement with experiments for bond cleavage is observed for the three methods for the neutral molecule. However, the modified Hückel method appears to best describe bond cleavage in the presence of an electron-accepting catalyst. Heats of reaction are also calculated for reaction conditions appropriate to the presence of a hydrogen donor.

Introduction

Given the complexity of coal at the molecular level, it is not clear at the outset that useful quantum chemical computations of relevance to coal chemistry can be carried out. However, there are two significant developments that are paving the way for quantum chemical calculations to play a useful role in this field. One is the steady escalation in the power of computers. The other is the synthesis of model compounds that mimic, in a controlled way, aspects of the molecular structure of coal. Careful, quantitative experimental studies on reaction pathways and catalytic action in reactions involving model compounds promise to offer new insights into coal chemistry and the possibility of developing more economical processes for direct liquefaction.

For any modeling of coal to be significant, it must first be shown that the method employed in the study gives meaningful results for model compounds for which experimental results are available. We have begun by performing quantum chemical calculations on 4-(1-naphthylmethyl)bibenzyl (referred to hereafter as Model Compound I), studied recently by Farcasiu and Smith.[2,3] In Figure 1 the skeletal structure of Model Compound I is shown. In their experiments Farcasiu and Smith demonstrated the bond breaking selectivity of a novel catalyst, carbon black (BP 2000), and measured kinetic reaction rates and bond activation energies for cleavage of the methylene and ethylene linkages of the compound. We have recently used[4,5] several semi-empirical quantum chemical methods to calculate bond dissociation energies of model compounds and coal fragments. In this paper we describe some further calculations that are designed to elucidate the bond-selective catalytic action in the hydrogenation reaction of 4-(1-naphthylmethyl)bibenzyl studied by Farcasiu and Smith[2,3]

In the earlier papers[4,5] we used Anderson's modified version of the extended Hückel molecular orbital method[1] and the MNDO and AM1 methods of Dewar, *et al.*[6,7] to study bond cleavage in

neutral and positively charged Model Compound I. The interest in the positively charged radical ion formed from Model Compound I by removal of an electron comes from the suggestion of Farcasiu and Smith[2,3] that the BP 2000 catalyst acts as an electron acceptor and removes an electron from the naphthyl portion of model compound I.

Geometric conformations, molecular orbital coefficients for the HOMO's and LUMO's, and bond dissociation energies were computed and compared for the three methods. Qualitative agreement with experiment for bond cleavage was observed for the three methods for the neutral molecule. Our earlier calculations suggest that the ASED-MO method appears to best describe the bond cleavage in the presence of an electron-accepting catalyst. This can be seen from the results shown in Table 1, where the product distributions with and without the catalyst (i.e., for the neutral molecule and the positive radical ion, respectively) calculated by the ASED-MO method are compared with the thermolysis results. The bond labels referred to in the Table are shown in Figure 1. The theoretical relative product distributions were calculated from the computed bond dissociation energies (shown in columns 2 and 5) using the Boltzmann distribution at the experimental temperature. The qualitative agreement between theory and experiment with regard to the bond-selectivity of the catalytic reaction is evident from the Table.

Calculation of Energies of Reaction

In our earlier papers the reactions in the presence of a hydrogen donor, which are more directly relevant to the study of coal liquefaction, were not studied. In this paper we have calculated the energy differences for the five reactions

$$H_2 + \text{Model Compound I} \rightarrow R_\alpha^{(1)} + R_\alpha^{(2)}, \tag{1}$$

where α = a,b,c,d,e denotes the bond that is cleaved in the reaction (as labeled in Figure 1), and in each instance, $R^{(1)}$ denotes the product molecule containing the naphthyl portion of the starting Model Compound I and $R^{(2)}$ the product molecule containing the remainder of Model Compound I. This is a rather simplistic model of the reaction in the presence of the hydrogen donor; clearly, the energy of reaction for hydrogen extraction from the donor (e.g., 9,10-dihydrophenanthrene) will be involved. However, our interest is in the relative product stabilities for the different bond cleavages, and the hydrogen extraction contribution should be essentially the same in all the cases. We present results for ASED-MO, MNDO, and AM1 methods. It should be noted that only the relative energies of reaction for the five paths indicated above within any given method are significant. The absolute numbers calculated by the different methods depend on the calculated dissociation energy for the hydrogen molecule. For example, the dissociation energy for the hydrogen molecule is overestimated by about 5 eV by the ASED-MO method, and by about 1 eV by the AM1 method.

In Table 2 we show the energies of reaction for the hydrogenation reactions of the neutral and charged Model Compound I calculated by the three methods. As explained above, only the relative magnitudes within each method are meaningful. For reactions involving the positive radical ion, the positive charge is kept with the product species containing the naphthyl fragment; the justification for this has been given in our earlier papers. The main conclusion from Table 2 is that the energies of reaction for the five different paths are similar; the product stabilities relative to the reactants are not greatly different, and further there is no correlation between product stability and the observed product distributions. This is true for reactions involving the neutral molecule as well as the positive radical ion.

Discussion and Conclusions

From these calculations we conclude that the driving force behind the bond-selectivity found in the reaction is not the relative thermodynamic stabilities of the products formed. Other possible factors for the bond selectivity are the differences in the activation energies for the different bond cleavages, and/or the charge distribution in the radicals formed after bond cleavage. We will consider first whether the experimentally found product distribution might be accounted for by the differences in the hydrogen affinity of the radicals formed by the bond cleavage. To test the importance of this factor, we have compared the charge localized on the terminal carbon atoms of the cleaved bond for the neutral and the charged Model Compound I in the different methods. We find no correlation between the charge build-up in the radicals and the observed product distributions.

Since the entropy changes in all the reactions are expected to be small, the bond dissociation energies, which are directly calculated by the theoretical methods, should be an upper bound to the the activation energies and appears to be the most important factor in determining the product distributions. The ASED-MO method predicts the difference between the neutral molecule and the positive radical ion in qualitative agreement with experiment. The fact that this simple method succeeds where the more sophisticated semi-empirical methods fail is surprising. Of course, the MNDO and AM1 methods have not really been parameterized for charged species, and this may be the reason for their apparent failure. We are presently carrying out more calculations both to further elucidate the catalytic action, and to test the methods for other model compounds.

Acknowledgments

This research was supported in part by the USDOE through contract DE-FC22-90PC90029. We are grateful to Dr. Malvina Farcasiu for providing us with the experimental data on Model Compound I prior to publication.

References

1. Anderson, A.B. *J. Chem. Phys.*, **1974**, *60*, 2477.
2. Farcasiu, M.; Smith, C. *Prepr., Div. Fuel Chem., Am. Chem. Soc.* **1990**, *35*, 404.
3. Farcasiu, M.; Smith, C. *Energy Fuels* (in press)
4. Ades, H.F.; Companion, A.L.; Subbaswamy, K.R. *J. Phys. Chem.* (in press).
5. Ades, H.F.; Companion, A.L.; Subbaswamy, K.R. (to be published).
6. Dewar, M.J.S.; Thiel, W. *J. Am. Chem. Soc.* **1977**, *99*, 4899.
7. Dewar, M.J.S.; Zoebisch, E.G.; Healy, E.F.; Stewart, J.J.P. *J. Am. Chem. Soc.*, **1985**, *107*, 3902.

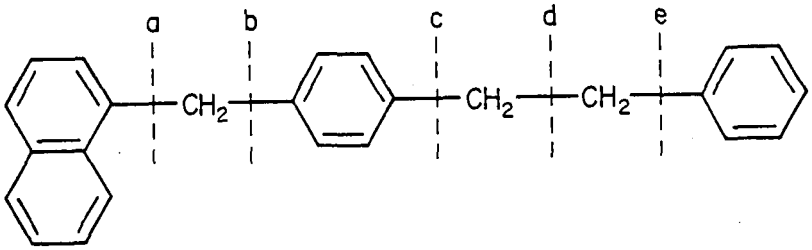

Figure 1: The skeletal structure of 4-(1-naphthylmethyl)bibenzyl. The methylene and ethylene linkages, whose cleavage is of interest here are labeled for use in the text.

Bond	Neutral			Charged (+1)		
	BDE(eV)	Product %		BDE(eV)	Product %	
	ASED	ASED	Expt.[a]	ASED	ASED	Expt.[a]
a	4.09	0.4	17	2.80	94	51
b	3.89	11	3	3.08	0.7	7
c	4.23	0.0	16	3.01	2	8
d	3.77	88	64	3.00	3	34
e	4.18	0.1	-	3.40	0.0	-

[a]From Farcasiu and Smith (Ref. 2)

Table 1: Bond dissociation energies (BDE) and product distributions for the thermolysis of Model Compound I. The results for the positively charged radical ion are appropriate to the presence of BP 2000 catalyst, as described in the text. From Ades, *et al.*, Ref. 5.

Bond	ASED-MO		MNDO		AM1	
	Neutral	Charged	Neutral	Charged	Neutral	Charged
a	0.90	0.96	-0.60	-0.54	-0.12	0.00
b	0.93	0.98	-0.43	-0.44	-0.02	-0.09
c	0.93	0.93	-0.37	-0.43	0.05	-0.02
d	1.07	1.07	-0.50	-0.55	-0.03	-0.10
e	0.93	0.93	-0.37	-0.42	0.05	-0.03

Table 2: The calculated energies of reaction (in eV) for the neutral and charged (+1) Model Compound I using three semi-empirical methods. As explained in the text the numbers are only meaningful for the comparison of the thermodynamic stability of the products relative to the reactants within a particular method.

AN INVESTIGATION INTO THE REACTIVITY OF ISOTETRALIN

M. W. Bedell, C. W. Curtis
Department of Chemical Engineering
Auburn University, Auburn, AL 36849

Keywords: molecular orbital, hydrogen transfer, isotetralin

ABSTRACT

Molecular orbital calculations were used to explore proposed reaction mechanisms of isotetralin (ISO) and tetralin (TET). Heats of formation and electronic data were determined for ground states and intermediate species. Since the reaction mechanisms was not known a priori, calculations were performed for anionic, cation and free radical dehydrogenation mechanisms. The electron density in the frontier molecular orbitals was used to assess the relative reactivity of sites within ground state and radical species. Model reactivity studies examining the thermal and catalytic reactivity of ISO and TET were performed. ISO was much more reactive than its isomeric analogue TET. Possible reaction pathways are proposed based upon the product slate obtained in the model compound reactivity experiments that were performed at 225, 380 and 425°C with ISO, TET, 1,4-dihydronaphthalene and 1,2-dihydronaphthalene. The results from the experimental study were evaluated in light of the results obtained from the molecular orbital calculations.

INTRODUCTION

The cyclic olefin, isotetralin, (1,4,5,8-tetrahydronaphthalene) is a highly effective donor for coal conversion at liquefaction temperatures. In previous experimental work, isotetralin converted more coal to THF solubles under thermal liquefaction conditions in both nitrogen and hydrogen than did tetralin (1,2). The results of experimentally evaluated reactivities and reaction pathways under a variety of conditions have recently been reported by Bedell and Curtis (2). The observed high reactivity and hydrogen donability of isotetralin warrants further investigation to understand its mechanism of hydrogen donation and a subsequent investigation of how that information can be applied to processing.

The focus of this report is to examine the dehydrogenation mechanism of ISO and TET using molecular orbital calculations and to compare the calculated results with those obtained experimentally. To achieve this goal, calculations were performed using a semi-empirical method of modified neglect of diatomic overlap (MNDO), developed by Dewar and Thiel (3). The second part of the investigation determined the most likely site for hydrogen donation from each donor molecule, by using frontier molecular orbital electron densities (4).

EXPERIMENTAL RESULTS

Isotetralin Reactivity. Isotetralin (ISO) showed much greater reactivity than did tetralin when reacted at temperatures of 225 and 380°C under both nitrogen and hydrogen atmospheres in stainless steel tubing bomb reactors at different reaction times. ISO converted rapidly and formed the reaction products of 1,2-dihydronaphthalene (1,2-DHN) 1,4-dihydronaphthalene (1,4-DHN), tetralin (TET) and naphthalene (NAP). The same products were formed regardless of the atmosphere, but different amounts were present as shown in Table 1. After two minutes of reaction at 380° C in either nitrogen on hydrogen, nearly 50% of the ISO converted producing 1,4-DHN as

the primary product. Longer reaction times in either nitrogen or hydrogen resulted in all of the ISO being converted. Conversely, TET showed little reactivity at 380 or 425°C. Even after 30 minutes of reaction in either atmosphere at 380°C, less than 5% conversion of TET was obtained. Reactions of TET for 15 minutes at 425°C resulted in 20% conversion in nitrogen and ~ 12% in hydrogen. The products formed in each case were 1,2-DHN, 1,4-DHN and NAP.

Reaction Pathway for Isotetralin. A proposed thermal dehydrogenation reaction pathway based on the products obtained from reactions performed with ISO at 225 and 380°C in nitrogen and hydrogen atmospheres is presented in Figure 1. In addition, reactions were performed using reaction products from ISO as the reactants to further elucidate the reaction pathway. The product distributions from reactions involving 1,2-DHN and 1,4-DHN are presented in Table 2. Short time (2 minute) reactions of 1,4-DHN in either nitrogen or hydrogen at 225 or 380°C resulted in ~ 25% or less of the 1,4-DHN being converted to the products, NAP and 1,2-DHN. No TET was formed. The reaction products observed from a 30 minute reaction of 1,4-DHN at 380°C were TET, 1,2-DHN, and NAP in hydrogen and NAP and TET in nitrogen; 1,4-DHN readily isomerized to 1,2-DHN. More NAP was produced in nitrogen than in hydrogen and substantially more TET was produced from 1,4-DHN in hydrogen after 30 minutes of reaction than in nitrogen.

The reaction of 1,2-DHN was also examined under a variety of conditions as presented in Table 2. Thermal reactions were performed at 425°C for 15 minutes while catalytic reactions using two different hydrogenation catalysts were performed at 225 and 380°C for short 2-minute reactions. Under catalytic conditions in hydrogen, 1,2-DHN preferentially produced TET as a product while under thermal conditions NAP was the preferred product. Some isomerization of 1,2-DHN to 1,4-DHN did occur indicating that the isomerization pathway to TET may also be available.

The thermal reactions of TET shown in Table 1 are inconclusive of a preferential pathway for TET reaction to 1,2-DHN. This pathway is obscured because of the observed isomerization of 1,2-DHN to 1,4-DHN. However, the reaction of 1,2-DHN particularly under catalytic conditions indicated that TET was the preferred product. On the basis of microscopic reversibility, it would be appropriate to suggest that TET may preferentially form 1,2-DHN in the dehydrogenation reaction.

The thermal dehydrogenation pathway of ISO proposed then is (1) the isomerization of ISO to form TET as indicated by the formation of TET in the 380°C reactions in both nitrogen and hydrogen and in (2) the dehydrogenation of ISO to form 1,2-DHN or 1,4-DHN as indicated by both the short time and longer reaction products in both atmospheres. 1,4-DHN appeared to be the favored product except at 60 minute reaction time in hydrogen. The isomerization step from ISO to TET in the pathway resulted in further dehydrogenation of TET to 1,2-DHN or 1,4-DHN. The DHN's then dehydrogenated to form NAP as indicated by the dehydrogenation of 1,4-DHN to NAP at all reaction conditions.

MOLECULAR ORBITAL CALCULATIONS

It has been reported in the literature on polyaromatic hydrocarbons that the electron density in the frontier molecular orbitals of the carbon or heteroatoms can be used, with some degree of success as an indicator of reactivity (4, 6-8). Sato et al. (6) found good agreement between the experimentally determined reactivity ranking of 1-methylnaphthalene, tetralin, decalin, and 9,10-dihydroanthracene, with that predicted by the electron density in the frontier molecular orbitals. Obara et al. (7) experimentally found that for a series of compounds, the ease of hydrogenation was acenaphthylene > anthracene > phenanthrene, and reported that "this order is in good agreement

with that in the terms of frontier electron density at a given position of the compounds" (7). Sukano et al. (8) found that the conversion of the donor increased with increasing electron density of the carbon and oxygen atoms of the carbonyl groups in the hydrogen acceptors.

Molecular orbital (MO) calculations were performed to elucidate the reasons for the greater reactivity observed for ISO in comparison to TET and to more fully investigate the dehydrogenation pathway proposed from experimental results. These MO calculations were performed using SYBYL (licensed from Tripos Associates, Inc.), which is an integrated molecular modeling package with graphics and interfaces to various computational methods. The desired structures were input using the graphics capabilities of SYBYL, with standard bond lengths and angles. These structures were next optimized using the Tripos 5.2 force-field (5) and conjugate gradient minimization. The resulting optimized structures were used as input to AMPAC (QCPE 506) using the MNDO Hamiltonian, with complete geometry optimization. MO calculations were performed on a VAX 5320 computer, while the force-field calculations were done on a MicroVaxII and Sparcstation 1+ workstation.

Since the actual dehydrogenation mechanism was not known a priori, three separate routes were investigated; they were cationic, anionic, and two proposed free radical pathways. MNDO calculations were performed on the ground state reactants (ISO or TET), the single radical or charged intermediate, the bi-radical or dual charge species, and finally the ground state product. The molecular orbital procedures used are capable of determining energetic, electronic and structural data. For the current investigation, the thermodynamic stability of each step was assessed through heats of formation.

Calculations on the open shell species (free radicals) were performed using the half electron approximation, in which the unpaired electron is represented by two "half electrons" with opposite spin. The repulsive energy introduced by this convention is subtracted from the final energy value. The energies calculated in this way can be directly compared to those for closed shell species.

Frontier orbital density was determined as the electron density in the highest occupied molecular orbital (HOMO) for closed shell species, and the singly occupied molecular orbital (SOMO) for radicals. These values are determined as the sum of squares of the atomic orbital coefficients for a given atom. These values are multiplied by one and two for open and closed shell structures, respectively.

DEHYDROGENATION MECHANISM

Based on the experimental results that have been previously discussed and presented in Figure 1, MNDO calculations were performed for the transitions between reactants and products from ISO to 1,4-DHN and TET to 1,4-DHN, and the other dehydrogenation paths illustrated. Initial work focused on the former pathways, since they appear to be preferred to the 1,2-DHN pathway. As indicated, cationic, anionic, and radical routes were examined. The calculated heats of formation for the proposed compounds in each step are shown in Figures 2 and 3.

Frontier Orbital Electron Density Calculations. Based on these results, the distribution of electron densities was examined for each step in the free radical pathway. As indicated in the cited literature, it has been proposed that the higher the frontier electron density Fr(R), the more reactive the site; i.e., the hydrogen most likely to be removed will have the highest electron density. The results of these frontier orbital electron density calculations for ISO and TET are presented in Figures 4 a-d and 5 a-e, respectively.

Figure 4-a shows the frontier electron density for the donable hydrogen in ground state ISO. As can be seen, the hydrogen on carbons 1,4,5, and 8 are approximately equivalent, and the loss of a hydrogen is not expected to be preferential to any one of the four positions. For illustrative purposes, if the hydrogen is lost from carbon 8, the radical species shown in Figure 4-b will be formed. Evaluating the resulting electron densities, the second hydrogen will be lost from carbon 5, which has the highest electron density. The resulting bi-radical species formed is shown in Figure 4-c. Once this species is formed, the double bond will isomerize to either the 7-8 or 5-6 positions, both of which are equivalent. The new bi-radical species formed is shown in Figure 4-d, and once the radicals are on adjacent carbon centers, a double bond will form to produce 1,4-DHN (Figure 4-e). These frontier molecular orbital electron density calculations predict that ISO will dehydrogenate preferentially to 1,4-DHN which is in good agreement with the experimental results.

Figure 5-a shows Fr(R) for the donable hydrogen in ground state TET. The electron densities for the hydrogen atoms at carbons 1 and 4, using the IUPAC numbering system for naphthalene parent compound are greater than those of the hydrogen atoms on carbons 2 and 3. Assuming that the loss of hydrogen occurs at the position with the highest electron density indicates that dehydrogenation occurs at carbon 4. Removal of the hydrogen at carbon 4 level forms the single radical species shown in Figure 5-b. It is predicted that the second hydrogen will be removed from carbon 3, the position with the highest electron density in the single radical species, to form the bi-radical shown in Figure 5-c. Once the bi-radical species is formed, the free electrons will combine to form a double bond, producing 1,2-DHN (Figure 5-d). The frontier orbital electron density calculations predict that TET will preferentially be dehydrogenated to 1,2-DHN, which appears to be what the experimental results previously described suggest. From the calculations for the frontier orbital electron density of ISO and TET, and the comparison with experimental results, Fr(R) appears to be a useful predictive and explanatory tool in the investigation of the dehydrogenation of cyclic olefins and hydroaromatic compounds.

SUMMARY OF THEORETICAL STUDY

The MNDO calculations, coupled with the frontier molecular orbital electron density calculation, are in good agreement with the experimentally determined results in the following points: 1) ISO is readily converted to 1,4-DHN and TET, and only to a small extent to 1,2-DHN. 2) TET is preferentially converted to 1,2-DHN. 3) ISO is more reactive than TET because of its lower energy barrier for 1,4-DHN formation, more possible reaction pathways, and its larger Fr(R) value on the greater number of donable hydrogen. These results illustrate the potential of molecular orbital calculations to be a useful tool in the understanding of fundamental dehydrogenation chemistry of model hydrogen donor compounds.

1. Curtis, C.W.; Guin, J.; Kwon, K.; "Coal Solvolysis in a Series of Model Compound Systems," Fuel; 63; 1984.
2. Bedell, M.W.; Curtis, C.W.; "The Chemistry and Reactivity of Cyclic Olefins as Donors in Coal Liquefaction," Submitted to Energy and Fuels; 11/90.
3. Dewar, M.; Thiel, W.; Am. Chem. Soc. 1977, 99, 4899.
4. Fukui, K.; Yonezawa, T.; Nagata, C.; Bull. Chem. Soc. Japan, 1954, 27, 423.
5. TRIPOS ASSOCIATES, INC., St. Louis, Missouri, 1989.
6. Sato, Y.; Uemasu, I.; Kushigama, S.; Proceeding 1985 International Conference on Coal Sciences; Sydney, Aust.
7. Obara, T.; Yokono, T.; Sanada, Y.; Fuel, 1983, 62, 813-816.
8. Sukeno, Toshio; Tsutsumi, Kinto; Oyama Kogyo Koto Senmon Gakko Kenky Kiyo, Vol. 14, 94-97, 1982.

Table 1. Reactivity of Isotetralin and Tetralin

Donor	Temperature (°C)	Atmosphere	Time (min)	NAP	1,2-DHN	1,4-DHN	TET	ISO
ISO	225	N_2	2	0.0	0.0	2.8(0.3)	0.0	97.2(0.3)
	380	N_2	2	3.6(0.1)	0.0	48.4(0.3)	1.6(0.1)	46.4(0.3)
	380	N_2	30	55.1(1.5)	4.6(0.5)	36.7(1.0)	3.6(0.4)	0.0
ISO	225	H_2	2	0.0	0.0	1.7(0.3)	0.0	98.3(0.3)
	380	H_2	2	2.2(0.2)	3.1(0.7)	39.1(1.8)	3.3(1.5)	52.3(2.9)
	380	H_2	15	30.5(0.5)	23.8(4.6)	27.9(12.3)	17.8(6.0)	0.0
	380	H_2	30	52.6(2.3)	10.0(2.6)	26.8(3.7)	10.6(1.2)	0.0
	380	H_2	60	61.1(2.1)	11.5(1.7)	1.1(0.3)	26.3(3.5)	0.0
TET	380	N_2	30	0.8(0.2)	0.0	0.0	99.2(3.8)	0.0
	425	N_2	15	1.2(0.02)	12.5(0.6)	6.3(0.6)	80.0(1.2)	0.0
TET	380	H_2	30	0.7(0.1)	1.0(0.1)	2.1(0.3)	96.2(2.3)	0.0
	425	H_2	15	0.0	3.5(0.2)	8.6(0.1)	87.9(0.3)	0.0

Table 2. Reactivity of 1,4-Dihydronaphthalene and 1,2-Dihydronaphthalene

Donor	Temperature (°C)	Atmosphere	Time (min)	Catalyst	NAP	1,2-DHN	1,4-DHN	TET	ISO
1,4-DHN	225	N_2	2	none	10.7(1.7)	10.9(0.3)	78.4(1.5)	0.0	0.0
	380	N_2	2	none	13.3(0.2)	11.3(0.2)	75.4(0.2)	0.0	0.0
	380	N_2	30	none	60.2(1.7)	0.0	28.5(1.6)	11.3(0.8)	0.0
	225	H_2	2	none	9.2(0.3)	11.0(0.2)	79.8(0.3)	0.0	0.0
	380	H_2	2	none	13.0(0.2)	12.8(0.9)	74.2(1.1)	0.0	0.0
	380	H_2	30	none	44.9(0.3)	11.5(0.3)	1.7(0.5)	41.9(0.6)	0.0
1,2-DHN	425	N_2	15	none	43.6(0.04)	42.4(0.3)	9.3(0.3)	4.7(0.1)	0.0
	425	H_2	15	none	40.9(0.6)	46.1(0.8)	8.2(0.3)	4.8(0.1)	0.0
	225	H_2	2	Mo/Al_2O_3	trace	44.7(0.4)	trace	55.3(0.4)	0.0
	225	H_2	2	$NiMo/Al_2O_3$	0.0	17.3(8.5)	3.1(0.5)	79.6(8.0)	0.0
	380	H_2	2	Mo/Al_2O_3	6.8(3.5)	0.0	0.0	93.2(3.5)	0.0
	380	H_2	2	$NiMo/Al_2O_3$	9.1(4.7)	0.0	0.0	90.9(4.7)	0.0

Reaction Conditions: 425 cpm, 1250 psig N_2 or H_2 charge at ambient temperature, 2.0 g charge of 0.5 weight percent donable hydrogen in hexadecane.

Abbreviations: NAP = naphthalene; 1,2-DHN = 1,2-dihydronaphthalene; 1,4-DHN = 1,4-dihydronaphthalene; TET = tetralin; ISO = isotetralin.

Figure 1. REACTION PATHWAY FOR ISOTETRALIN.

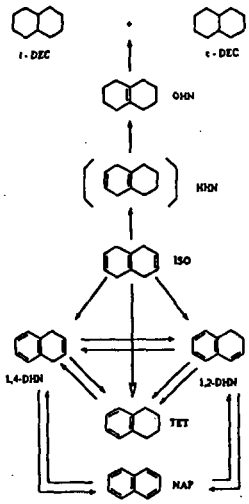

Figure 2. HEAT OF FORMATION DATA FOR THE TRANSITION OF ISO TO 1,4-DHN : THREE MECHANISMS .

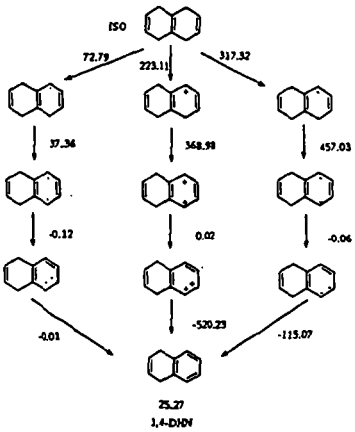

Figure 3. HEAT OF FORMATION DATA FOR THE TRANSITION OF TET TO 1,4-DHN : THREE MECHANISMS.

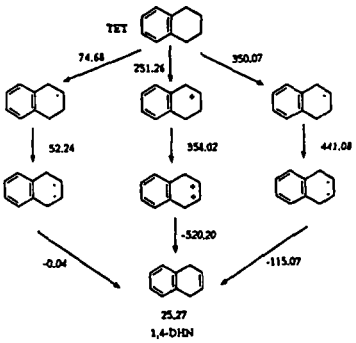

Figure 4. ELECTRON DENSITIES IN THE TRANSITION OF ISO TO 1,4-DHN .

a)

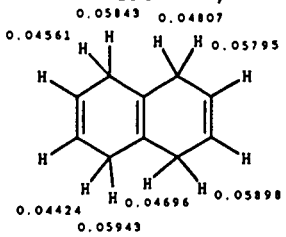

b)

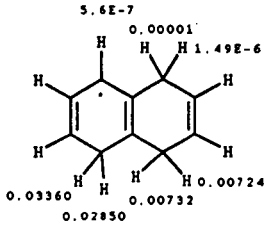

c)

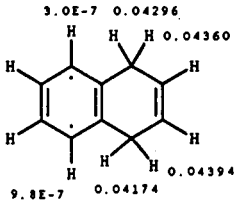

d)

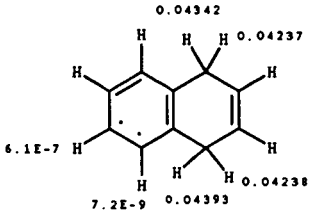

e)

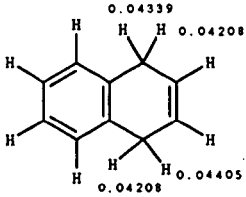

Figure 5. ELECTRON DENSITIES IN THE TRANSITION OF TET TO 1,2-DHN.

a)

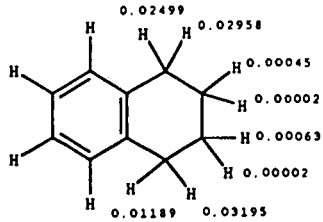

b)

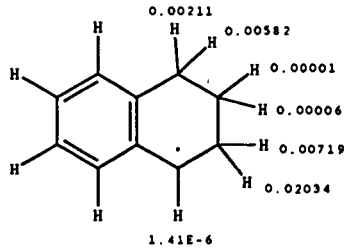

c)

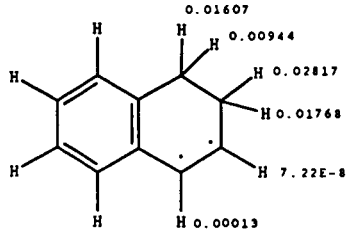
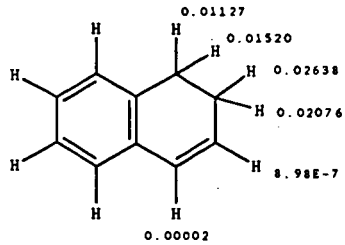
d)